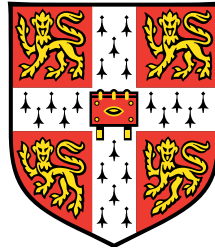


Scattering of Internal Gravity Waves

Abigail Leaman Nye

Selwyn College



A dissertation submitted
to the University of Cambridge
for the degree of Doctor of Philosophy

April 2009

Summary

Internal gravity waves play a fundamental role in the dynamics of stably stratified regions of the atmosphere and ocean. In addition to the radiation of momentum and energy remote from generation sites, internal waves drive vertical transport of heat and mass through the ocean by wave breaking and the mixing subsequently produced. Identifying regions where internal gravity waves contribute to ocean mixing and quantifying this mixing are therefore important for accurate climate and weather predictions. Field studies report significantly enhanced measurements of turbulence near ‘rough’ ocean topography compared with those recorded in the ocean interior or near more gradually varying topography (e.g. Toole *et al.* 1997, *J. Geophys. Res.* 102). Such observations suggest that interaction of waves with rough topography may act to skew wave energy spectra to high wavenumbers and hence promote wave breaking and fluid mixing. This thesis examines the high wavenumber scatter and spatial partitioning of wave energy at ‘rough’ topography containing features that are of similar scales to those characterising incident waves.

The research presented here includes laboratory experiments using synthetic schlieren and PIV to visualise two-dimensional wavefields produced by small amplitude oscillations of cylinders within linear salt-water stratifications. Interactions of wavefields with planar slopes and smoothly varying sinusoidal topography are compared with those with square-wave, sawtooth and pseudo knife-edge profiles, which have discontinuous slopes. Far-field structures of scattered wavefields are compared with linear analytical models.

Scatter to high wavenumbers is found to be controlled predominantly by the relative slopes and characterising length scales of the incident wavefield and topography, as well as the shape and aspect ratio of the topographic profile. Wave energy becomes highly focused and the spectra skewed to higher wavenumbers by ‘critical’ regions, where the topographic slope is comparable with the slope of the incident wave energy vector, and at sharp corners, where topographic slope is not defined. Contrary to linear geometric ray tracing predictions (Longuet-Higgins 1969, *J. Fluid Mech.* 37), a significant back-scattered field can be achieved in near-critical conditions as well as a forward scattered wavefield in supercritical conditions, where the slope of the boundary is steeper than that of the incident wave. Results suggest that interaction with rough benthic topography could efficiently convert wave energy to higher wavenumbers and promote fluid mixing in such ocean regions.

Preface

This dissertation is the result of my own work and includes nothing which is the outcome of work done in collaboration except where specifically indicated in the text.

Acknowledgements

I am extremely grateful for the support and help given to me by so many people during the preparation of this thesis. In particular, I would like to thank Dr Stuart Dalziel for his wisdom, endless enthusiasm and sense of humour (which included him pirouetting like a ballerina during a conference presentation and not being offended when accused of being a crocodile). Many thanks also to Dr Matthew Scase for his advice on aspects of this thesis.

I am also especially grateful for the expertise, hard work and entertainment of the laboratory technicians of the G.K. Batchelor laboratory: David Page-Croft, John Milton, Trevor Parkin and Rob Raincock.

My time at Cambridge has overlapped with that of many others, who have all helped me at some point and in some way. In particular, I would like to thank Martin Seaton, Alison Hart, Michael Patterson, Nastja Bethke, Christian Ihle and Andrew Lawrie for their friendship and assistance. Thank you also to Samantha Carr and Margaret Hay at Selwyn College for organising me!

On a personal level, I have enjoyed immense support and encouragement from my wonderful husband, Mike, my delightful children Isaac and Eleanor, my *amazing* parents, Helen and Terry, and my family and friends. *Thank you all.* And, of course, *thank you God!*

This research was funded by grant NER/S/A/2003/11205 from the Natural Environment Research Council.

Contents

1	Introduction	1
1.1	Overview	1
1.2	Characterisation of stratifications	1
1.2.1	Stratification stability	1
1.2.2	Internal gravity waves within continuous stratifications	3
1.2.3	Instabilities of a stable stratification	4
1.3	Motivations	6
1.3.1	Internal gravity waves in the ocean	6
1.3.2	Ocean circulation and mixing	7
1.4	Research aims and methodology	8
1.4.1	Outline of thesis	9
2	Background	10
2.1	Overview	10
2.2	Wave motion in an unbounded fluid	10
2.2.1	Linearisation and approximations	11
2.2.2	Dispersion relation	13
2.2.3	Characteristic variables	15
2.3	Internal wave generation by an oscillating cylinder	16
2.3.1	Internal Gravity Wave Beams	16
2.3.2	Wave beam structure: wave amplitudes	18
2.3.3	Wave beam structure: beam widths	21
2.4	Wave interaction with boundaries	22
2.4.1	Reflection at a horizontal or vertical boundary: linear inviscid theory	23
2.4.2	Reflection at an inclined boundary: linear inviscid theory	25
2.4.3	Reflection at an inclined boundary: nonlinear and viscous effects	29
2.5	Scatter at rough boundaries	34
2.5.1	Linearised boundary conditions	37
2.5.2	Boundary variations comparable with wave scales: large amplitudes	40
2.5.3	Discontinuous boundaries: sharp corners	42

2.6	Summary	44
3	Experimental Methods	46
3.1	Overview	46
3.2	Stratification	46
3.2.1	Double-bucket method	46
3.2.2	Stratification measurement	47
3.3	Visualisation	52
3.3.1	Visualisation techniques	52
3.3.2	Synthetic schlieren	53
3.3.3	Pattern matching	56
3.4	Image optimisation and accuracy	56
3.4.1	Camera	56
3.4.2	Dot mask	59
3.4.3	Error reduction	62
3.4.4	Reference image and world coordinates	63
3.4.5	Error estimate	64
3.5	Particle Image Velocimetry (PIV)	65
3.5.1	Light sheet	67
3.5.2	Particles	69
3.5.3	Camera	73
3.6	Internal gravity wave generation	73
3.6.1	Wave generation by an oscillating cylinder	75
3.7	Features of the wavefields	78
3.7.1	Removal of unwanted waves	91
3.8	Topography	95
3.8.1	Smooth horizontal boundary	95
3.8.2	Smooth sloping boundaries	96
3.8.3	Rough topographic profiles	97
3.9	Summary	103
4	Smooth topography	104
4.1	Overview	104
4.2	Reflection at a smooth horizontal boundary	104
4.2.1	Qualitative results	104
4.2.2	Quantitative results: amplitudes	107
4.2.3	Scatter to higher harmonics	121
4.3	Reflection at a smooth sloping boundary	124
4.3.1	Qualitative results: subcritical and supercritical	124

4.3.2	Quantitative results: supercritical	126
4.3.3	Qualitative results: near-critical	131
4.4	Reflection at a smooth curved boundary	133
4.5	Reflection at a smoothly varying rough topographic profile	135
4.5.1	Ray tracing analysis	136
4.5.2	Energy density spectra	143
4.6	Summary	155
5	Wave generation by different cylinder shapes	156
5.1	Overview	156
5.2	Wave generation by elliptical cylinders	156
5.2.1	Across-beam amplitudes	158
5.2.2	Across-beam spectra	162
5.2.3	Higher harmonics	167
5.2.4	Influence on background stratification	169
5.3	Wave generation by rectangular cylinders	171
5.3.1	Across-beam amplitudes	172
5.3.2	Across-beam spectra	176
5.3.3	Higher harmonics	178
5.3.4	Influence on background stratification	180
5.4	Summary	183
6	Subcritical rough topography	185
6.1	Overview	185
6.2	Sawtooth topography	186
6.2.1	Subcritical ray tracing	186
6.2.2	Basic sawtooth (T_G)	187
6.2.3	High wavenumber sawtooth (T_H)	199
6.2.4	Varying the slope (T_I)	205
6.3	Topographic shape	210
6.3.1	Scatter from a sinusoid (T_A)	210
6.3.2	Scatter from a square-wave (T_K)	217
6.3.3	Corners, slopes and curves	224
6.4	Scatter to higher harmonics	227
6.5	Summary	229
7	Supercritical rough topography	231
7.1	Overview	231
7.2	Sawtooth topography	231
7.2.1	Basic sawtooth (T_D)	231

7.2.2	High wavenumber sawtooth (T_E)	236
7.3	Topographic shape	243
7.3.1	Scatter from a square-wave (T_J)	243
7.3.2	Scatter at a knife-edge (T_L)	249
7.3.3	Corners, slopes and edges	256
7.4	Scatter to higher harmonics	256
7.5	Summary	260
8	Near-critical rough topography	262
8.1	Overview	262
8.2	Sawtooth topography	262
8.2.1	Varying the wavenumber	262
8.2.2	Varying the slope	265
8.2.3	Varying the aspect ratio	268
8.3	Topographic shape	270
8.3.1	Curves versus corners	270
8.3.2	Corners versus knife-edges	272
8.4	Summary	273
9	Conclusions	274
9.1	Summary of results	274
9.1.1	Wave generation by oscillating cylinders	274
9.1.2	Reflection at horizontal and sloping boundaries	275
9.1.3	Scatter at slowly varying topography	276
9.1.4	Scatter at rough topographic profiles	276
9.2	Future work	278
9.2.1	Extensions of experimental work	279
9.2.2	Extensions of theoretical work	280
9.2.3	Numerical work	280
9.3	Geophysical and environmental implications	283
9.4	Final remarks	286

List of Figures

1.1	Schematic describing forces acting on a displaced fluid parcel within discrete two-layer stratifications. The density of the upper and lower layers are denoted by ρ_1 and ρ_2 respectively. Arrows in (b) and (c) indicate directions of buoyancy force.	2
1.2	Schematic describing the Meridional Overturning Circulation and processes causing density changes of constituent water masses.	7
2.1	Characteristic coordinates for wave energy propagating along lines inclined at angles θ to the vertical.	15
2.2	Schematic of two-dimensional internal gravity wave beams produced by an oscillating cylinder. Phase and group velocity directions are indicated for each beam. Grey shading indicates regions where wave beams overlap. Bounding envelopes of amplitudes of the along-beam fluid motion are sketched on the lower left-hand beam. The sketch depicts the transition from a bimodal form at small along-beam distances to a unimodal structure further from the cylinder as viscosity attenuates the wave energy.	17
2.3	Schematic of wave beams reflecting at (a) a horizontal boundary and (b) a vertical boundary. Red and blue lines denote the lines of constant phase associated with incident and reflected wave beams respectively. Arrows positioned on phase lines indicate the directions of energy propagation.	25
2.4	Schematic of wave beams reflecting at subcritical boundaries of different orientations. Arrows and colouring are defined as in figure 2.3.	27
2.5	Schematic of wave beams reflecting at supercritical boundaries of different orientations. Arrows and colouring are defined as in figure 2.3.	28
2.6	Schematic of wave energy scatter at a sinusoidal boundary with $\hat{A}_T \hat{k}_T \ll 1$	38
3.1	Calibration of conductivity probe for density values.	50
3.2	Vertical density profiles of stratifications measured using a conductivity probe (red and black solid lines). Both stratifications displayed yielded buoyancy frequencies of 1.5 rad s^{-1} . Dashed lines indicate upper and lower vertical limits of linear density profiles.	51
3.3	Synthetic schlieren experiment configuration.	54
3.4	Error dependence on gain. Multiples n of unit gain.	59

3.5	Schematic graphs of image sensor pixel intensities for (a) transparent dots within a black background and (b) black dots against a transparent background. Blue lines show ideal pixel intensities across a dot; red lines are representative of actual dot intensities due to optical blurring and electronic effects; green lines show dot intensities possible after manipulation of output from the image sensor.	60
3.6	Synthetic schlieren dot mask sections measuring 50×50 mm (a) as generated by the PostScript file and (b) as viewed by the camera. Section shown in (b) is taken from an image of a typical field of view with dot diameters 0.53 mm.	62
3.7	Close-up pictures of dot masks with $F_d = 26\%$ and dots having PostScript specified diameters of (a) 0.53 mm, (b) 0.45 mm and (c) 0.35 mm.	63
3.8	Root mean square values of the perturbed buoyancy field for a sequence of images recorded of fluctuations in the laboratory environment in daytime conditions.	65
3.9	PIV experiment setup.	66
3.10	Close-up picture of artificial pearlescence. Particles shown in (b) are enlarged by a factor of 5 from the dashed square in (a).	72
3.11	Image of particle suspension used in PIV as viewed by camera.	73
3.12	Internal gravity wave generation mechanism: the cylinder was oscillated vertically by a cam mechanism remotely controlled to oscillate at specific frequencies.	76
3.13	Vertical displacement of cylinder oscillating with temporal period T about a mean position. The displacement was averaged over nine oscillations, with the standard deviation of the displacement of each individual oscillation from this average lying in the range 0.12 – 0.21 mm. The pixel diameter was approximately 0.27 mm. The maximum displacement amplitude was 2.36 mm.	78
3.14	Sequence of transient start-up wavefield at times $t = 1T, 2T, \dots, 9T$ s. The cylinder oscillation was initiated at $t = 0T$ s with $T = 8.64$ s and $\sigma/N = 0.54$	80
3.15	Sequence of transient start-up wavefield at times $t = 1T, 2T, \dots, 9T$ s. The cylinder oscillation was initiated at $t = 0T$ s with $T = 2.86$ s and $\sigma/N = 1.63$	81
3.16	Development of wavefield after cylinder oscillation initiated at $t = 0$ relative to the wavefield at times $t \in [7T, 8T)$	82
3.17	Graph to compare the forcing frequency with the cosine of the measured angle of internal wave beams.	83
3.18	RMS_T values of $\Delta N^2/N^2$ at σ corresponding to (a) $\theta_1 = 56.8^\circ$, (b) $\theta_1 = 72.8^\circ$ and (c) $\theta_1 = 74.7^\circ$. The beams shown are in positions corresponding with those of the upper and lower right-hand wave beams in figure 3.14.	84
3.19	RMS_T values of $\Delta N^2/N^2$ after harmonic filtering for secondary and tertiary harmonics relating to figure 3.18 (c). Scales for $\Delta N^2/N^2$ are as in figure 3.18 except with colour scale values corresponding to the ranges (a) $[-1.0 \times 10^{-4}, 1.0 \times 10^{-3}]$ and (b) $[3.7 \times 10^{-4}, 1.2 \times 10^{-3}]$ respectively.	85

3.20	RMS _T values of $\Delta N^2/N^2$ for σ/N values (a) 1.45 and (b) 1.63. The vertical line visible above the cylinder is due to the presence of the cylinder rod.	86
3.21	Transient decay of established wave beams after cylinder oscillation halted at $t = -T/4$ s. $T = 8.64$ s.	87
3.22	Schematic of the influence of boundaries on stratifications.	88
3.23	RMS _T images showing development of horizontal intrusions near the cylinder after cylinder oscillation at frequency $\sigma = 0.79$, <i>i.e.</i> $\sigma/N = 0.59$, for durations of (a) $\hat{t} + 0$, (b) $\hat{t} + 40$ and (c) $\hat{t} + 80$ minutes, with $\hat{t} = 4$ minutes.	89
3.24	Zoom of section near cylinder in figure 3.23 (c). Scaling as in figure 3.23.	89
3.25	Zoom of section near cylinder in figure 3.24. Scaling as in figure 3.23.	90
3.26	Wavetrap schematic.	92
3.27	Experiment picture of focusing of wave beams wave trap. Wave trap is highlighted with dashed white line.	92
3.28	Schematic of wave beam reflection and transmission behaviour at layers of sponge. Red lines denote lines of constant phase associated with the incident wave beam. Blue dashed lines denote lines of constant phase associated with partial reflection at the sponge layers. Only primary reflections are shown for each of the layers. Arrows denote the direction of energy propagation. A 20 mm square section of the sponge material is also shown and a typical pore (~ 3 mm) is highlighted in white.	93
3.29	Wave damping by sponge layers (highlighted by white dashed lines).	94
3.30	Amplitude reduction in wave beam reflections from sponges compared with those from a solid horizontal boundary. The curves are magnitudes of the perturbed buoyancy field throughout a period of the motion. Curves represent cross-sections taken from the incident beam (cyan); a beam after reflection from a solid horizontal boundary (dark blue) and a beam after interaction with the sponge formation (red). Amplitudes are normalised by the maximum amplitude of the incident beam.	94
3.31	Topography side profiles and dimensions.	98
3.32	Camera view.	101
3.33	RMS _T images showing development of horizontal intrusions near sawtooth topography after cylinder oscillation at frequency $\sigma = 0.79$, <i>i.e.</i> $\sigma/N = 0.59$, for durations of (a) $\hat{t} + 0$, (b) $\hat{t} + 40$ and (c) $\hat{t} + 80$ minutes, where $\hat{t} = 4$ minutes.	102
4.1	Images of the instantaneous perturbed buoyancy field for reflections at a smooth horizontal boundary with beams angles θ equal to (a) 44.8° and (b) 54.4° respectively, and corresponding RMS _T images shown in (c) and (d).	105
4.2	Coordinate systems used for incident and reflected wave beams.	105
4.3	Time series images for cross-sections of established wave beams at positions (a) $s_I = 7$ and (b) $12R_c$ and (c) $s_R = 7$ and (d) $12R_c$ for $\sigma/N = 0.58$ and $T = 7.4$ s.	108

4.4	Instantaneous across-beam values of the perturbed buoyancy field along cross-sections of (a) incident and (b) reflected beams associated with figure 4.1 (b) and comparisons of the measured cross-sections with linear theory in (c) and (d) respectively.	110
4.5	Across-beam RMS_T amplitudes at different values of s_I and s_R for $\sigma/N = 0.58$. Grey dashed lines indicate locations of tangents to cylinder in along-beam directions. The dashed black line indicates the cross-section measured closest to the horizontal boundary, positioned at $s_I/R_c = 17$	111
4.6	Tests of spectral methods for a specified data set. Here (a) plots a prescribed data set and its individual wavenumber components and (b) plots power spectra calculated with Fourier and maximum entropy methods. \tilde{k} is a nondimensional wavenumber representing the number of waves in an across-beam section of length R_c	114
4.7	Two-dimensional power spectra for the sequence of images associated with the experiment of figure 4.1 (b) and (d). Power, P , is normalised by total power, \hat{P} . \tilde{k}_x and \tilde{k}_z denote nondimensional wavenumbers representing the number of waves in horizontal and vertical sections, respectively, of length R_c . The dashed white line indicates the orientation of the corresponding nondimensional across-beam wavenumber \tilde{k} , <i>i.e.</i> the wavenumber aligned with those directions making an angle $\theta = 54.4^\circ$ with the horizontal. Marks along the dashed line indicate magnitudes in the across-beam direction of $\tilde{k} \in [0, 3]$ incremented by 0.5.	115
4.8	Power spectra of across-beam sections associated with figure 4.5. Power, P , is normalised by total power, \hat{P} , associated with the section at $s_I = 4R_c$. The dashed black line indicates the cross-section in (a) measured closest to the horizontal boundary, positioned at $s_I/R_c = 17$. Predictions of linear theory (dashed lines, HK = Hurley & Keady 1997) are compared in (b) with power spectra calculated from experiment cross-sections (solid lines) located at $s_I/R_c = 7, 11$ and 15	116
4.9	Wavenumber calculations from across-beam sections associated with figure 4.5. Here (a) shows variation of maximum normalised power, P_{max}/\hat{P} , of spectra with s and corresponding exponential fits and (b) shows variation of wavenumbers of spectra peaks with s and corresponding linear fits. Triangular symbols in both panels indicate predictions of linear theory, with colours corresponding to those of predicted spectra plotted in figure 4.8 (b).	117
4.10	Power spectra variation with forcing frequency at along-beam distances s_I/R_c equal to (a) 7, (b) 11 and (c) 15. Corresponding RMS_T amplitudes along these sections are shown in (e), (f) and (g) respectively. Peaks of spectra for black dashed line are located at (a) $\tilde{k} = 0.34, 0.77$; (b) $\tilde{k} = 0.33, 0.74$; and (c) $\tilde{k} = 0.32, 0.72$. Power, P , is normalised by the total power, \hat{P} , in the spectra corresponding to $\sigma/N = 0.58$ at $s_I/R_c = 4$	119

4.11	Power spectra variation with forcing frequency for three frequencies $\sigma/N = 0.71, 0.58$ and 0.33 at along-beam distances s_I/R_c equal to (a) 7, (b) 11 and (c) 15. Solid lines indicate spectra calculated from experiment data (<i>c.f.</i> figure 4.10) whilst dashed lines indicate predictions of linear theory (Hurley & Keady 1997). Corresponding RMS_T amplitudes for both experiment data and theoretical predictions along these sections are shown in (e), (f) and (g) respectively. Power, P , is normalised by the total power, \hat{P} , in the spectra calculated from experiment data corresponding to $\sigma/N = 0.58$ at $s_I/R_c = 4$	120
4.12	Variation of power spectra maxima, P_{max}/\hat{P} , with σ/N for different along-beam distances. Symbols indicate values of P_{max}/\hat{P} predicted by linear theory (Hurley & Keady 1997). Grey dashed vertical lines highlight the frequency values $\sigma/N = 1/2$ and $1/3$, below which the generation of second and third temporal harmonics, respectively, is possible.	121
4.13	Temporal filtering for primary and secondary harmonics of reflection at a horizontal boundary with primary frequency $\sigma/N = 0.46$. Here (a) and (b) show amplitude components for the primary ($i = 1$) and secondary ($i = 2$) harmonics respectively with maxima $M_1 = 5.6 \times 10^{-2}$ and $M_2 = 3.8 \times 10^{-3}$; (c) and (d) show phase components corresponding to (a) and (b) respectively; (e) and (f) are products of the amplitude and phase components for (a) and (b) respectively.	123
4.14	Images of the instantaneous perturbed buoyancy field for sub and supercritical reflections with slope ratios θ/α equal to (a) 0.89 and (b) 2.17 respectively, with corresponding RMS_T images shown in (c) and (d). Regions on right-hand side of slopes are shaded grey.	125
4.15	Coordinate systems used at boundaries inclined at an angle α to the vertical.	125
4.16	(a) Across-beam RMS_T amplitudes for cross-sections positioned at different s_I and s_R along incident and reflected beams in a supercritical configuration; and (b) corresponding energy flux, \mathbf{F} , spectra, normalised by total flux, \hat{F} , in cross-section $s_R/R_c = 6$. Grey dashed lines indicate locations of tangents to cylinder in along-beam directions. The dashed bold red line corresponds to measurements along the section located at $s_I/R_c = 11$. The cyan line in (b) represents predictions of inviscid linear theory for reflected spectra. Green solid and dashed lines indicate viscous adaptations of inviscid linear theory.	127
4.17	Comparison of measured peak wavenumbers with inviscid linear theory for supercritical slopes with $\alpha = 32.4^\circ$ (red symbols), 37.0° (blue symbols) and 37.3° (green symbols). Grey dashed line is a linear fit with gradient $= 4.86 \times 10^{-1}$ and y -intercept $= 3.25 \times 10^{-2}$	130
4.18	RMS_T image of perturbed buoyancy field for near critical reflections with slope ratios θ/α (a) 0.95, (b) 1.02 and (c) 1.08. Here $\alpha = 50.1^\circ$	131

4.19	Contours of instantaneous perturbed buoyancy field for near-critical reflection with $\theta/\alpha = 1.02$. Colour scaled with magnitudes four times that of figure 4.18.	132
4.20	RMS _T images of perturbed buoyancy field for scatter at a curved boundary. The boundary and regions enclosed therein are shaded grey.	134
4.21	Example of positioning of cross-sections taken for incident (B_I, B_I^*) and reflected (B_F, B_F^*) beams at (top of picture) sinusoid, T_A , and (bottom of picture) horizontal boundary, respectively.	136
4.22	Geometrical ray tracing predictions for upper and lower bounds of reflection coefficients in forward and backward propagation directions (Longuet-Higgins 1969).	137
4.23	Comparison of RMS _T beam structures (a) B_I^* and (b) B_I , for topographic profile T_A and $\sigma/N = 0.67, \theta/\alpha_s = 0.95$. Similarly, (c) and (d) compare RMS _T beam structures B_I^* and B_I respectively, for parameter values $\sigma/N = 0.54, \theta/\alpha_s = 1.14$	138
4.24	RMS _T images for topographic profile T_A with (a) $\sigma/N = 0.58, \theta/\alpha_s = 1.08$ and (c) $\sigma/N = 0.33, \theta/\alpha_s = 1.41$. These are compared with linear geometrical ray tracing predictions in (b) and (d) respectively. Blue lines denote wave rays within the incident ray tube; red lines denote forwards reflected rays; and cyan lines denote downwards reflected rays.	140
4.25	Ray tracing predictions for T_A . Here (a) $\sigma/N = 0.58, \theta/\alpha_s = 1.08$ and (b) $\sigma/N = 0.33, \theta/\alpha_s = 1.41$. Blue lines denote incident rays (constituents of B_I); red denote forwards reflected rays from primary reflection ($\in B_F$); green denote forwards reflected rays after multiple reflections ($\in B_F$); magenta denote back-reflected rays after multiple reflections ($\in B_I$). Cyan, dark green, dark red, grey and yellow denote topography-topography reflections.	140
4.26	RMS _T images for topographic profile T_B with (a) $\sigma/N = 0.63, \theta/\alpha_s = 0.98$ and (c) $\sigma/N = 0.41, \theta/\alpha_s = 1.27$. These are compared with linear geometrical ray tracing predictions in (b) and (d) respectively. Line colouring as is figure 4.24.	142
4.27	Ray tracing predictions for T_A . Here (a) $\sigma/N = 0.63, \theta/\alpha_s = 0.98$ and (b) $\sigma/N = 0.41, \theta/\alpha_s = 1.27$. Line colouring as in figure 4.25.	142
4.28	Forward-scattered energy density spectra for T_A are plotted in (a, c, e, g). Corresponding spectral differences are plotted in (b, d, f, h). Frequencies decrease down the page.	145
4.29	Error estimation for energy density spectra. Spectral differences, $ E_\Delta = E_1 - E_2 $, between energy density spectra calculated at different along-beam distances for two simultaneously generated wave beams, B_1 and B_2 respectively, at $\sigma/N = 0.54$, where $ E_\Delta $ is normalised by the total energy, \hat{E} , associated with the closest cross-section to the cylinder.	146
4.30	Back-scattered energy density spectra for T_A are plotted in (a, c, e, g). Corresponding spectral differences are plotted in (b, d, f, h). Frequencies decrease down the page.	150

4.31	Forward-scattered energy density spectra for T_B are plotted in (a, c, e, g). Corresponding spectral differences are plotted in (b, d, f, h). Frequencies decrease down the page.	152
4.32	Back-scattered energy density spectra for T_B are plotted in (a, c, e, g). Corresponding spectral differences are plotted in (b, d, f, h). Frequencies decrease down the page.	154
5.1	Geometrical schematic of an elliptical cylinder and definition of c_e are shown in (a). Variation of c_e with θ for elliptical cylinders, C_i , $i = A - E$, is plotted in (b).	158
5.2	Across-beam RMS_T amplitudes at different values of s for $\sigma/N = 0.36, 0.50, 0.59$ and 0.73 (corresponding to columns from left to right) are plotted for ellipse aspect ratios $0.3, 0.5, 1.0, 2.0$ and 3.0 (corresponding to rows from top to bottom). Perturbed buoyancy values are multiplied by the factor $1/\hat{A}_e = (R_c/c_c)^2$	159
5.3	Across-beam RMS_T amplitudes at different values of s for $\sigma/N = 0.36, 0.59$ and 0.73 (corresponding to columns from left to right) are plotted for ellipse aspect ratios $0.3, 0.5, 1.0, 2.0$ and 3.0 (corresponding to rows from top to bottom). Perturbed buoyancy values are multiplied by the factor $1/\hat{A}_e = (R_c/c_c)^2$	163
5.4	Across-beam power spectra corresponding to figure 5.2. Perturbed buoyancy values are multiplied by the factor $1/\hat{A}_e = (R_c/c_c)^2$. Power is normalised by the total power, \hat{P} , associated with the cross-section for C_C at $s/c_e = 4$ and $\sigma/N = 0.59$. Wavenumbers \tilde{k} represent the number of waves per across-beam section of length c_e	164
5.5	Variation of maximum power, P_{max} , with (a) aspect ratios a_e/b_e of the elliptical cylinders at seven forcing frequencies, σ/N , for cross-sections at along-beam distance $s = 7c_e$ and (b) forcing frequency for each cylinder aspect ratio for $s = 7c_e$	165
5.6	Comparisons of power spectra from experiments and predictions of viscous linear theory corresponding to the amplitude plots of figure 5.3 for the three forcing frequencies (increasing across page) $\sigma/N = 0.36, 0.59$ and 0.73 and five elliptical cylinders $C_A - C_E$ (aspect ratios increase down page). \hat{P} is the total power associated with the cross-section at $s/c_e = 4$ and $\sigma/N = 0.59$ for C_C	166
5.7	Spectra calculated from measurements of undisturbed stratification in circular cylinder case, C_C , relating to figures 5.4 and 5.6.	167
5.8	Amplitude and phase images of temporal harmonics generated by elliptical cylinders at forcing frequency $\sigma/N = 0.32$. RMS_T images of primary, secondary and tertiary harmonics are shown in (a-c) and (g-i) for C_B and C_D respectively. Corresponding phase images are shown in (d-f) and (j-l). Dashed lines are shown at angles $71.6^\circ, 50.9^\circ$ and 18.7° to the vertical, corresponding to predicted values of θ_i for primary ($i = 1$), secondary ($i = 2$) and tertiary ($i = 3$) harmonics respectively. Amplitude maxima M_i have values $7.8 \times 10^{-2}, 7.8 \times 10^{-3}$ and 7.8×10^{-4} for $i = 1, 2$ and 3	168

5.9	RMS _T images of $\Delta N^2/N^2$ fields in regions adjacent to cylinders $C_A - C_E$ (centre-left of field of view) are shown in (a)-(e) respectively. Amplitudes are multiplied by the factor $\hat{A}_e = (R_c/c_c)^2$	170
5.10	Zoom of section near cylinder in figure 5.9 (e). Scaling as in figure 5.9.	171
5.11	Ray geometry for rectangular cylinders.	173
5.12	Across-beam RMS _T amplitudes at different values of s for $\sigma/N = 0.36, 0.50, 0.59$ and 0.73 (corresponding to columns from left to right) are plotted for a circular cylinder (top row) and rectangle aspect ratios $0.65, 1.0$ and 1.53 (corresponding to rows from second from top to bottom). Perturbed buoyancy values are multiplied by the factor $1/\hat{A}_r = (R_c/c_c)^2$. Dashed lines indicate across-beam positions of corners of rectangular cylinders.	174
5.13	Across-beam RMS _T amplitudes at different values of s for $\sigma/N = 0.36, 0.59$ and 0.73 (corresponding to columns from left to right) are plotted for a circular cylinder (top row) and rectangle aspect ratios $0.65, 1.0$ and 1.53 (corresponding to rows from second from top to bottom). Perturbed buoyancy values are multiplied by the factor $1/\hat{A}_r = (R_c/c_c)^2$. Dashed grey vertical lines indicate across-beam positions of corners of rectangular cylinders.	175
5.14	Across-beam power spectra corresponding to figure 5.12. Perturbed buoyancy values are multiplied by the factor $1/\hat{A}_r = (R_c/c_c)^2$. Power is normalised by the total power, \hat{P} , associated with the cross-section for C_C at $s/c_e = 4$ and $\sigma/N = 0.59$. Wavenumbers \tilde{k} represent the number of waves per across-beam section of length c_e and \tilde{c}_e for the circular and rectangular cylinders respectively.	177
5.15	Comparisons of power spectra from experiments with rectangular cylinders $C_F - C_H$ (aspect ratios increase down the page) and predictions of viscous linear theory (Hurley & Keady 1997) for analogous elliptical cylinders corresponding to the amplitude plots of figure 5.13. Forcing frequencies $\sigma/N = 0.36, 0.59$ and 0.73 increase across the page. \hat{P} is the total power associated with the cross-section at $s/c_e = 4$ and $\sigma/N = 0.59$ for C_C	178
5.16	Amplitude and phase images of temporal harmonics generated by circular and square cylinders. RMS _T images of primary, secondary and tertiary harmonics are shown in (a-c) and (g-i) for C_C and C_G respectively. Corresponding phase images are shown in (d-f) and (j-l). Dashed lines are shown at angles $71.6^\circ, 50.9^\circ$ and 18.7° to the vertical, corresponding to predicted values of θ_i for primary ($i = 1$), secondary ($i = 2$) and tertiary ($i = 3$) harmonics respectively. Amplitudes relating to square cylinder are scaled by the factor $1/\hat{A}_r = (R_c/c_c)^2$. Amplitude maxima M_i have values $5.6 \times 10^{-2}, 5.6 \times 10^{-3}$ and 5.6×10^{-4} for $i = 1, 2$ and 3	179

5.17	Amplitude and phase images of temporal harmonics generated by rectangular cylinders. RMS _T images of primary, secondary and tertiary harmonics are shown in (a-c) and (g-i) for C _F and C _H respectively. Corresponding phase images are shown in (d-f) and (j-l). Dashed lines are shown at angles 71.6°, 50.9° and 18.7° to the vertical, corresponding to predicted values of θ _i for primary (i = 1), secondary (i = 2) and tertiary (i = 3) harmonics respectively. Amplitude maxima M _i have values 9.5 × 10 ⁻² , 9.5 × 10 ⁻³ and 9.5 × 10 ⁻⁴ for i = 1, 2 and 3.	181
5.18	RMS _T images of regions adjacent to cylinders (centre-left of field of view) (a) C _C and (b) to (d) C _F to C _H respectively. Amplitudes are multiplied by the factor $\hat{A}_r = (R_c/c_c)^2$	182
5.19	Zoom of section near cylinder in figure 5.18 (e). Scaling as in figure 5.18.	182
6.1	RMS _T image of perturbed buoyancy field for subcritical scatter at sawtooth T _G and θ/α = 0.88 after filtering at the primary frequency, σ.	189
6.2	Two-dimensional wavenumber domain represented as (a) a schematic indicating the orientation of group velocity vectors for fluid motion associated with each quadrant (nomenclature as defined in figure 2.2); magnitudes, M/ĤM, of the two-dimensional FFT of data relating to figure 6.1 (b) before and (c) after filtering for wavenumber components associated with c _{g++} (i.e. forwards scatter), where ĤM denotes the maximum value of the transform in (b).	189
6.3	RMS _T image of perturbed buoyancy field for subcritical scatter at sawtooth T _G and θ/α = 0.88 after filtering at the primary frequency, σ, and for wavenumbers associated with forwards scatter. Scale for ΔN ² /N ² as in figure 6.1.	189
6.4	RMS _T images of perturbed buoyancy fields for subcritical scatter at sawtooth T _G , with α = 63.5°, at forcing frequencies such that θ/α is equal to (a) 0.77, (b) 0.88 and (c) 0.97. Images of corresponding forward and back-scattered wavefields after filtering using the Hilbert transform are shown in (d)-(f) and (g)-(i) respectively, with upper edge of topography highlighted in grey. Fields of view measure 449 × 186 mm.	192
6.5	Ray geometry for subcritical sawtooth.	193
6.6	Variation with θ/α of coefficients for focusing, C _f , and defocusing, C _{df} , of wave energy incident at sawtooth topographies.	193
6.7	Forward-scattered energy density spectra for sawtooth T _G are plotted in (a, c, e). Corresponding spectral differences are plotted in (b, d, f). Frequencies decrease down the page with θ/α equal to (a,b) 0.77, (c,d) 0.88 and (e,f) 0.97.	196
6.8	Back-scattered energy density spectra for sawtooth T _G are plotted in (a, c, e). Corresponding spectral differences are plotted in (b, d, f). Frequencies decrease down the page with θ/α equal to (a,b) 0.77, (c,d) 0.88 and (e,f) 0.97.	198

6.9	Close-up RMS_T images of perturbed buoyancy field near corners of topography for profile T_G with subcritical θ/α equal to (a) 0.76, (b) 0.86 and (c) 0.96, and supercritical θ/α equal to (d) 1.05, (e) 1.09 and (f) 1.13. Fields of view measure 188×59 mm.	200
6.10	Close-up of figure 6.9 (c) for profile T_G and $\theta/\alpha = 0.96$. Colour scale as in figure 6.9 except with maximum value 0.12. Field of view measures 68×29 mm.	201
6.11	RMS_T images of perturbed buoyancy fields for subcritical scatter at sawtooth T_H , with $\alpha = 63.5^\circ$, at forcing frequencies such that θ/α is equal to (a) 0.77, (b) 0.88 and (c) 0.97. Images of corresponding forward and back-scattered wavefields after filtering using the Hilbert transform are shown in (d)-(f) and (g)-(i) respectively, with upper edge of topography highlighted in grey. Fields of view measure 449×193 mm. Colour scale as in figure 6.4.	202
6.12	Forward-scattered energy density spectra for sawtooth T_H are plotted in (a, c, e). Corresponding spectral differences are plotted in (b, d, f). Frequencies decrease down the page with θ/α equal to (a,b) 0.77, (c,d) 0.88 and (e,f) 0.97.	204
6.13	Back-scattered energy density spectra for sawtooth T_H are plotted in (a, c, e). Corresponding spectral differences are plotted in (b, d, f). Frequencies decrease down the page with θ/α equal to (a,b) 0.77, (c,d) 0.88 and (e,f) 0.97.	206
6.14	RMS_T images of $\Delta N^2/N^2$ fields for subcritical scatter at sawtooth T_I , with $\alpha = 69.5^\circ$, at forcing frequencies such that θ/α is equal to (a) 0.80, (b) 0.87 and (c) 0.95. Images of corresponding forward and back-scattered wavefields after filtering using the Hilbert transform are shown in (d)-(f) and (g)-(i) respectively, with upper edge of topography highlighted in grey. Fields of view measure 449×193 mm and 449×148 mm. Colour scale as in figure 6.4.	207
6.15	Forward-scattered energy density spectra for sawtooth T_I are plotted in (a, c, e). Corresponding spectral differences are plotted in (b, d, f). Frequencies decrease down the page with θ/α equal to (a,b) 0.80, (c,d) 0.87 and (e,f) 0.95.	208
6.16	Back-scattered energy density spectra for sawtooth T_I are plotted in (a, c, e). Corresponding spectral differences are plotted in (b, d, f). Frequencies decrease down the page with θ/α equal to (a,b) 0.80, (c,d) 0.87 and (e,f) 0.95.	209
6.17	RMS_T images of perturbed buoyancy fields for subcritical scatter at sinusoid T_A , with $\alpha = 62.0^\circ$, at forcing frequencies such that θ/α is equal to (a) 0.78, (b) 0.88 and (c) 0.97. Images of corresponding forward and back-scattered wavefields after filtering using the Hilbert transform are shown in (d)-(f) and (g)-(i) respectively, with upper edge of topography highlighted in grey. Fields of view measure 449×182 mm. Colour scale as in figure 6.4.	212
6.18	RMS_T velocity images of primary harmonics generated by subcritical scatter at sinusoid T_A with θ/α equal to (a) 0.68, (c) 0.87 and (e) 0.98 with σ/N equal to 0.74, 0.59 and 0.49 respectively (topography shaded in grey). Corresponding phase images are shown in (b), (d) and (f) (topography shaded in black).	213

6.19	Ray tracing predictions for T_A . Here (a) $\sigma/N = 0.66$, $\theta/\alpha = 0.78$, (b) $\sigma/N = 0.58$, $\theta/\alpha = 0.88$ and (c) $\sigma/N = 0.50$, $\theta/\alpha = 0.97$. Blue lines denote incident rays (constituents of B_I); red denote forwards reflected rays from primary reflection ($\in B_F$); green denote forwards reflected rays after multiple reflections ($\in B_F$); magenta denote back-reflected rays after multiple reflections ($\in B_I$). Cyan, dark green, dark red, grey and yellow denote topography-topography reflections.	214
6.20	Forward-scattered energy density spectra for sinusoid T_A are plotted in (a, c, e). Corresponding spectral differences are plotted in (b, d, f). Frequencies decrease down the page with θ/α equal to (a,b) 0.78, (c,d) 0.88 and (e,f) 0.97.	216
6.21	Back-scattered energy density spectra for sinusoid T_A are plotted in (a, c, e). Corresponding spectral differences are plotted in (b, d, f). Frequencies decrease down the page with θ/α equal to (a,b) 0.78, (c,d) 0.88 and (e,f) 0.97.	218
6.22	RMS $_T$ images of perturbed buoyancy fields for subcritical scatter at square-wave T_K , with $\alpha = 61.0^\circ$, at forcing frequencies such that θ/α is equal to (a) 0.79, (b) 0.89 and (c) 0.99. Images of corresponding forward and back-scattered wavefields after filtering using the Hilbert transform are shown in (d)-(f) and (g)-(i) respectively, with upper edge of topography highlighted in grey. Fields of view measure 449×177 mm. Colour scale as in figure 6.4.	220
6.23	RMS $_T$ velocity images of primary harmonics generated by subcritical scatter at square-wave T_K with θ/α equal to (a) 0.63, (c) 0.70, (e) 0.89 and (g) 1.00 with σ/N equal to 0.79, 0.74, 0.59 and 0.49 respectively (topography shaded in grey). Corresponding phase images are shown in (b), (d), (f) and (h) (topography shaded in black).	221
6.24	Ray tracing predictions for T_K . Here (a) $\sigma/N = 0.67$, $\theta/\alpha = 0.79$, (b) $\sigma/N = 0.58$, $\theta/\alpha = 0.89$ and (c) $\sigma/N = 0.49$, $\theta/\alpha = 0.99$. Line colouring as in figure 6.19.	222
6.25	Ray tracing predictions for forward scatter coefficients at square-wave profiles T_J and T_K and pseudo knife-edge T_L , derived from method of Longuet-Higgins (1969). Dashed green line indicates the predicted lower bound for C_F at sinusoid T_A and horizontal dashed grey lines indicate lower bounds for C_F at T_J , T_K and T_L . Vertical dashed grey line indicates critical value for θ/α . Curve for T_J is truncated for clarity. Dashed cyan, red and blue lines are explained in chapter 7.	223
6.26	Forward-scattered energy density spectra for square-wave T_K are plotted in (a, c, e). Corresponding spectral differences are plotted in (b, d, f). Frequencies decrease down the page with θ/α equal to (a,b) 0.79, (c,d) 0.89 and (e,f) 0.99.	225
6.27	Back-scattered energy density spectra for square-wave T_K are plotted in (a, c, e). Corresponding spectral differences are plotted in (b, d, f). Frequencies decrease down the page with θ/α equal to (a,b) 0.79, (c,d) 0.89 and (e,f) 0.99.	226

6.28	Amplitude and phase images of temporal harmonics generated by marginal subcritical scatter at sinusoidal, sawtooth and square-wave profiles T_A , T_G and T_K with $\sigma/N = 0.50, 0.48$ and 0.50 , $\theta/\alpha = 0.97, 0.97$ and 0.99 . RMS $_T$ images of primary and secondary harmonics are shown in (a-b), (e-f) and (i-j) respectively. Corresponding phase images are shown in (c-d), (g-h) and (k-l). Amplitude maxima M_i have values of 5.4×10^{-2} , 5.4×10^{-3} and 5.4×10^{-4} for $i = 1, 2$ and 3	228
7.1	RMS $_T$ images of perturbed buoyancy fields for supercritical scatter at sawtooth T_D , with $\alpha = 45.0^\circ$, at forcing frequencies such that θ/α is equal to (a) 1.23, (b) 1.36 and (c) 1.55. Images of corresponding forward and back-scattered wavefields after filtering using the Hilbert transform are shown in (d)-(f) and (g)-(i) respectively, with upper edge of topography highlighted in grey. Fields of view measure 449×203 mm and 449×133 mm, with unit aspect ratio. Colour scale as in figure 6.4.	233
7.2	Ray schematic of shadow zone for supercritical scatter at sawtooth T_D	234
7.3	Close-up of scatter at profile T_D for $\theta/\alpha = 1.23$. Colour scale as in figure 6.9 except with maximum value 11.72×10^{-2} . Field of view measures 68×29 mm.	235
7.4	RMS $_T$ velocity images of primary harmonics generated by supercritical scatter at sawtooth T_D with θ/α equal to (a) 1.01, (c) 1.08 and (e) 1.49 with σ/N equal to 0.70, 0.66 and 0.39 respectively (topography shaded in grey). Corresponding phase images are shown in (b), (d) and (f) (topography shaded in black).	235
7.5	Forward-scattered energy density spectra for sawtooth T_D are plotted in (a, c, e). Corresponding spectral differences are plotted in (b, d, f). Frequencies decrease down the page with θ/α equal to (a,b) 1.23, (c,d) 1.36 and (e,f) 1.55.	237
7.6	Back-scattered energy density spectra for sawtooth T_D are plotted in (a, c, e). Corresponding spectral differences are plotted in (b, d, f). Frequencies decrease down the page with θ/α equal to (a,b) 1.23, (c,d) 1.36 and (e,f) 1.55.	238
7.7	RMS $_T$ images of perturbed buoyancy fields for supercritical scatter at sawtooth T_E , with $\alpha = 45.0^\circ$, at forcing frequencies such that θ/α is equal to (a) 1.20, (b) 1.38 and (c) 1.56. Images of corresponding forward and back-scattered wavefields after filtering using the Hilbert transform are shown in (d)-(f) and (g)-(i) respectively, with upper edge of topography highlighted in grey. Fields of view measure 449×205 mm and 449×134 mm, with unit aspect ratio. Colour scale as in figure 6.4.	240
7.8	Forward-scattered energy density spectra for sawtooth T_E are plotted in (a, c, e). Corresponding spectral differences are plotted in (b, d, f). Frequencies decrease down the page with θ/α equal to (a,b) 1.20, (c,d) 1.38 and (e,f) 1.56.	241
7.9	Back-scattered energy density spectra for sawtooth T_E are plotted in (a, c, e). Corresponding spectral differences are plotted in (b, d, f). Frequencies decrease down the page with θ/α equal to (a,b) 1.20, (c,d) 1.38 and (e,f) 1.56.	242

7.10	RMS _T images of perturbed buoyancy fields for supercritical scatter at square-wave T_J , with $\alpha = 45.0^\circ$, at forcing frequencies such that θ/α is equal to (a) 1.20, (b) 1.38 and (c) 1.56. Images of corresponding forward and back-scattered wavefields after filtering using the Hilbert transform are shown in (d)-(f) and (g)-(i) respectively, with upper edge of topography highlighted in grey. Fields of view measure 449×190 mm and 449×121 mm, with unit aspect ratio. Colour scale as in figure 6.4.	245
7.11	Ray tracing predictions for T_J . Here (a) $\sigma/N = 0.59$, $\theta/\alpha = 1.20$, (b) $\sigma/N = 0.47$, $\theta/\alpha = 1.38$ and (c) $\sigma/N = 0.34$, $\theta/\alpha = 1.56$. Line colouring as in figure 6.19.	246
7.12	Forward-scattered energy density spectra for square-wave T_J are plotted in (a, c, e). Corresponding spectral differences are plotted in (b, d, f). Frequencies decrease down the page with θ/α equal to (a,b) 1.20, (c,d) 1.38 and (e,f) 1.56.	247
7.13	Back-scattered energy density spectra for square-wave T_J are plotted in (a, c, e). Corresponding spectral differences are plotted in (b, d, f). Frequencies decrease down the page with θ/α equal to (a,b) 1.20, (c,d) 1.38 and (e,f) 1.56.	248
7.14	Ray geometries for critical configurations at knife-edge with critical configurations (a) as defined for analogous sawtooth and (b) where reflection of incident rays is purely supercritical (green lines in the latter indicate region where incident ray reflection is possible).	249
7.15	RMS _T images of perturbed buoyancy fields for supercritical scatter at knife-edge T_L , with $\alpha = 46.6^\circ$, at forcing frequencies such that θ/α is equal to (a) 1.22, (b) 1.40 and (c) 1.56. Images of corresponding forward and back-scattered wavefields after filtering using the Hilbert transform are shown in (d)-(f) and (g)-(i) respectively, with upper edge of topography highlighted in grey. Fields of view measure 449×175 mm and 449×112 mm, with unit aspect ratio. Colour scale as in figure 6.4.	251
7.16	RMS _T velocity images of primary harmonics generated by supercritical scatter at knife-edge T_L with θ/α equal to (a) 1.01, (c) 1.22, (e) 1.36 and (g) 1.54 with σ/N equal to 0.68, 0.54, 0.45 and 0.32 respectively (topography shaded in grey). Corresponding phase images are shown in (b), (d), (f) and (h) (topography shaded in black).	252
7.17	Ray tracing predictions for T_J . Here (a) $\sigma/N = 0.58$, $\theta/\alpha = 1.22$, (b) $\sigma/N = 0.45$, $\theta/\alpha = 1.45$ and (c) $\sigma/N = 0.34$, $\theta/\alpha = 1.56$. Line colouring as in figure 6.19.	253
7.18	Forward-scattered energy density spectra for pseudo knife-edge T_L are plotted in (a, c, e). Corresponding spectral differences are plotted in (b, d, f). Frequencies decrease down the page with θ/α equal to (a,b) 1.22, (c,d) 1.40 and (e,f) 1.56.	254
7.19	Back-scattered energy density spectra for pseudo knife-edge T_L are plotted in (a, c, e). Corresponding spectral differences are plotted in (b, d, f). Frequencies decrease down the page with θ/α equal to (a,b) 1.22, (c,d) 1.40 and (e,f) 1.56.	255

7.20	Amplitude and phase images of temporal harmonics generated by supercritical scatter at sawtooth, square-wave and knife-edge profiles T_E , T_J and T_L with $\sigma/N = 0.38$ and $\theta/\alpha = 1.51$, 1.51 and 1.46 . RMS $_T$ images of primary and secondary harmonics are shown in (a-b), (e-f) and (i-j) respectively. Corresponding phase images are shown in (c-d), (g-h) and (k-l). Amplitude maxima M_i have values of 5.4×10^{-2} , 5.4×10^{-3} and 5.4×10^{-4} for $i = 1, 2$ and 3	258
7.21	Amplitude and phase images of temporal harmonics generated by supercritical scatter at sinusoidal, sawtooth and square-wave profiles T_A , T_G and T_K with $\sigma/N = 0.33$, 0.35 and 0.33 , $\theta/\alpha = 1.14$, 1.10 and 1.16 . RMS $_T$ images of primary and secondary harmonics are shown in (a-b), (e-f) and (i-j) respectively. Corresponding phase images are shown in (c-d), (g-h) and (k-l). Amplitude maxima M_i have values of 5.4×10^{-2} , 5.4×10^{-3} and 5.4×10^{-4} for $i = 1, 2$ and 3	259
8.1	RMS $_T$ images of $\Delta N^2/N^2$ fields for near-critical scatter at sawtooth profiles T_D and T_E with θ/α equal to (a-b) 1.08 and (c-d) 1.05 respectively. Fields of view shown in (a) and (c) measure 449 mm across and have unit aspect ratio. Colours are scaled as in figure 6.4. Corresponding zooms by factor $24/7$ and colours scaled with maxima 10% greater than the larger fields of view are shown in (b) and (d).	264
8.2	RMS $_T$ images of $\Delta N^2/N^2$ fields for near-critical scatter at sawtooth profiles T_G and T_H with θ/α equal to 1.02 in each case. Fields of view shown in (a) and (c) measure 449 mm across and have unit aspect ratio. Colours are scaled as in figure 6.4. Corresponding zooms by factor $24/7$ and colours scaled with maxima 10% greater than the larger fields of view are shown in (b) and (d).	265
8.3	RMS $_T$ images of $\Delta N^2/N^2$ fields for near-critical scatter at sawtooth profiles T_C , T_E and T_G with θ/α equal to (a-b) 1.06 , (c-d) 1.05 and (e-f) 1.02 respectively. Fields of view shown in (a), (c) and (e) measure 449 mm across and have unit aspect ratio. Colours are scaled as in figure 6.4. Corresponding zooms by factor $24/7$ and colours scaled with maxima 10% greater than the larger fields of view are shown in (b), (d) and (f).	266
8.4	RMS $_T$ images of $\Delta N^2/N^2$ fields for near-critical scatter at sawtooth profiles T_H and T_I with θ/α equal to (a-b) 1.02 and (c-d) 0.99 respectively. Fields of view shown in (a) and (c) measure 449 mm across and have unit aspect ratio. Colours are scaled as in figure 6.4. Corresponding zooms by factor $24/7$ and colours scaled with maxima 10% greater than the larger fields of view are shown in (b) and (d).	267
8.5	Schematic of rays (red and blue lines - incident from top left) reflecting specularly at a discontinuity in the background stratification (green dashed line) near a corner of a sawtooth topographic profile.	268

8.6	RMS _T images of $\Delta N^2/N^2$ fields for near-critical scatter at sawtooth profiles T_D and T_G with θ/α equal to (a-b) 1.08 and (c-d) 1.02 respectively. Fields of view shown in (a) and (c) measure 449 mm across and have unit aspect ratio. Colours are scaled as in figure 6.4. Corresponding zooms by factor 24/7 and colours scaled with maxima 10% greater than the larger fields of view are shown in (b) and (d).	269
8.7	RMS _T images of $\Delta N^2/N^2$ fields for near-critical scatter at sawtooth profiles T_E and T_F with θ/α equal to (a-b) 1.05 and (c-d) 1.02 respectively. Fields of view shown in (a) and (c) measure 449 mm across and have unit aspect ratio. Colours are scaled as in figure 6.4. Corresponding zooms by factor 24/7 and colours scaled with maxima 10% greater than the larger fields of view are shown in (b) and (d).	270
8.8	RMS _T images of $\Delta N^2/N^2$ fields for near-critical scatter at sinusoid T_A , sawtooth T_G and square-wave T_K with θ/α equal to (a-b) 1.01, (c-d) 1.02 and (e-f) 0.99 respectively. Fields of view shown in (a), (c), (e) and (g) measure 449 mm across and have unit aspect ratio. Colours are scaled as in figure 6.4. Corresponding zooms by factor 24/7 and colours scaled with maxima 10% greater than the larger fields of view are shown in (b), (d) and (f).	271
8.9	RMS _T images of $\Delta N^2/N^2$ fields for near-critical scatter at sawtooth T_E , square-wave T_J and knife-edge T_L with θ/α equal to (a-b) 1.05, (c-d) 1.05 and (e-f) 1.02 respectively. Fields of view shown in (a), (c), (e) and (g) measure 449 mm across and have unit aspect ratio. Colours are scaled as in figure 6.4. Corresponding zooms by factor 24/7 and colours scaled with maxima 10% greater than the larger fields of view are shown in (b), (d) and (f).	273
9.1	Sequence of transient start-up wavefield at times $t = 1T, 2T, \dots, 9T$ s. The cylinder oscillation was initiated at $t = 0T$ s with $T = 11.64$ s and $\sigma/N = 0.54$. Simulations run at domain resolution of 1024×1024 . Smaller regions with resolutions 915×787 are shown for direct comparison with figure 3.14.	282
9.2	RMS _T images of $\Delta N^2/N^2$ from numerical simulations of scatter with $\sigma/N = 0.54$ at (a) an isolated step and (b) a four step staircase topographic profile. Colour scale as in figure 6.4, with amplitude maxima 2×10^{-2} and topography shaded in black. Simulations run at resolutions of 512×512 , with whole domain shown.	283
9.3	Variation with distance from topography of total wave enstrophy, En_F , measured along cross-sections of subcritical forwards scattered wavefields at sawtooth (T_G), sinusoid (T_A) and square-wave (T_K) profiles. Enstrophy is normalised by the total, $\hat{E}n$, in the cross-section measured closest to the topography in each case. Values of θ/α for configurations with T_G , T_A and T_K are 0.77, 0.78 and 0.79 (dotted lines); 0.88, 0.88 and 0.89 (dashed lines) and 0.97, 0.97 and 0.99 (solid lines) respectively.	286

List of Tables

3.1	Specifications of topographies used in experiments. Lengths are given to an accuracy of ± 0.05 mm.	99
5.1	Specifications of cylinders used in experiments. Length scales a and b denote a_e or a_r and b_e or b_r for elliptical and rectangular cylinders respectively.	157

Chapter 1

Introduction

1.1 Overview

A fluid in which density varies in the direction parallel to gravity is said to be vertically stratified. Density inhomogeneities that promote stratification occur through spatial variations in temperature and composition of a fluid and hence regions of transient or sustained stratification are characteristic of many environmental and industrial flows. In particular, stratifications are sustained throughout constituent layers of both the atmosphere and ocean. Such layers have a fundamental influence on weather systems and climate. It is therefore critical that the features and dynamics of stratifications are understood if the evolution of global conditions on both daily and decadal timescales is to be accurately predicted.

This thesis examines oscillatory disturbances known as internal gravity waves that can propagate through stratified fluids. The study focuses specifically on the interaction of internal gravity waves with topography in order to determine those interactions that promote mixing of a stratified fluid. The characterisation of stratifications and conditions under which internal gravity waves may propagate are described in section 1.2. Motivations for this study are discussed in section 1.3. Overviews of the research methods employed and structure of this thesis are given in section 1.4.

1.2 Characterisation of stratifications

The form of the vertical density profile of a stratification determines the types of fluid motion it supports. A stratification is defined as discrete in regions of a fluid consisting of two or more horizontal layers of finite depth within which the density is homogeneous. Regions in which the vertical density profile varies smoothly are described as having a continuous stratification.

1.2.1 Stratification stability

In the absence of horizontal density gradients, an initially static stratification remains in equilibrium regardless of its discrete or continuous nature. A small perturbation introducing horizontal density

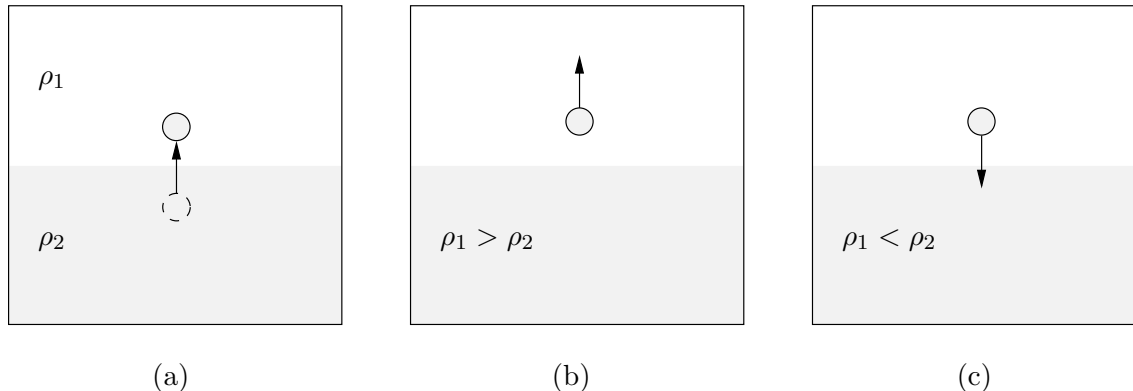


Figure 1.1: Schematic describing forces acting on a displaced fluid parcel within discrete two-layer stratifications. The density of the upper and lower layers are denoted by ρ_1 and ρ_2 respectively. Arrows in (b) and (c) indicate directions of buoyancy force.

gradients induces fluid motion with a character that is controlled by both the vertical density profile of the stratification as well as the nature of the initial perturbation. In particular, the direction of the vertical density gradient has a dominant influence on the dynamic stability of a perturbed stratification. Such stability can be understood in terms of simple physical arguments. In systems where there are spatial variations in density, gravity induces buoyancy forces directing ‘heavy’ fluid downwards and comparatively light fluid upwards. Depending on the gradient of the initial stratification, these buoyancy forces either act to enhance an initially small perturbation or they can act, to some degree, to counteract it. Figure 1.1 (a) depicts a discrete two layer stratification where the fluid densities of the upper and lower layers are denoted ρ_1 and ρ_2 respectively. Fluid motion following vertical displacement of a fluid parcel from the lower layer into the upper layer is qualitatively different for configurations having a positive, $\rho_1 > \rho_2$, or negative, $\rho_1 < \rho_2$, vertical density gradient (see figure 1.1 (b) and (c) respectively).

A fluid parcel moved upward into fluid of greater density experiences a buoyancy force acting in the same direction as the initial displacement (see figure 1.1 (b) where $\rho_1 > \rho_2$). Without a restoring force, the parcel accelerates away from it’s equilibrium level and the perturbation of the stratification is therefore enhanced. More generally, a perturbation of a density configuration having a positive vertical density gradient triggers an instability between the regions of different density. In the absence of a significant mean shear between the two layers, a Rayleigh-Taylor type instability is triggered (see for example Chandrasekhar 1961; Drazin & Reid 2004). Horizontal gradients produced by the perturbation induce baroclinic generation of vorticity. In turn, the torque imposed on the fluid leads to small scale convective overturning with the sinking of heavy fluid in narrow fingers and the reciprocal rise of light fluid in bubble-like structures. These localised overturning events merge and grow into larger scale convective motions that turbulently mix the stratification, eventually resulting in a homogeneous fluid with a lower potential energy. A stratification having a positive vertical density gradient is therefore described as unstable since there are no forces produced in response to perturbations that are capable of restoring the original density profile.

Alternatively, a stratification can have a negative density gradient as depicted for the two-layer discrete system in figure 1.1 (c) where $\rho_1 < \rho_2$. A fluid parcel moved upward from the lower layer into the less dense fluid above experiences a buoyancy force acting in the opposite direction to that of the displacement. As a result, such a fluid parcel is directed back towards the layer in which it is neutrally buoyant. A stratification with a negative density gradient is therefore able to recover from small perturbations through the generation of counteracting buoyancy forces. Hence this density configuration is described as stable. The existence of a restoring force implies the ability of stable stratifications to support oscillations and therefore waves, introducing a mechanism for the transport of information and energy throughout the fluid.

1.2.2 Internal gravity waves within continuous stratifications

The induction of oscillatory motion in a stable stratification may be more clearly illustrated by considering a system with a larger number of fluid layers. In the limit where the discrete layers become infinitesimally thin, the stratification is representative of a continuous density profile. In this generalisation each layer may be identified as a surface of constant density, or isopycnal. A perturbation of the density profile through displacement of fluid parcels therefore corresponds to a deformation of isopycnals. A fluid parcel displaced upward within a continuous stable stratification in a similar manner to that shown in figure 1.1 is returned to the vertical level at which it is neutrally buoyant by buoyancy forces induced by its initial displacement. This coincides with the return of density surfaces to their horizontal form. However, in an inviscid fluid, the potential energy imparted on the parcel by the original displacement is entirely converted to kinetic energy as the parcel reaches its equilibrium level. Hence the parcel's inertia carries it past this level and the parcel overshoots into the heavier fluid below, also deforming the isopycnals in this direction. The downward displacement of the fluid parcel into the denser fluid subsequently induces an upwards directed buoyancy force. In response, the parcel decelerates and at some depth in the stratification below its neutral buoyancy level changes its direction of motion and begins to rise. With no damping force, the competition between inertia and buoyancy continues and the fluid parcel oscillates about the region at which it is neutral buoyant, with the simultaneous oscillation of isopycnals about their horizontal form.

The magnitude of the buoyancy force induced on the fluid parcel as it moves vertically through the stratification is determined by the density difference between the parcel and the surrounding fluid. The vertical distance over which the buoyancy force acts to counteract the kinetic energy of the parcel therefore specifies the depth to which it sinks below or rises above the neutral buoyancy level respectively and hence also the duration of an ensuing oscillation. In this way buoyancy forces suppress vertical motion in a statically stable stratification and the extent to which they do this is controlled by the vertical density gradient. Formulating this mathematically, the buoyancy force per unit volume, \mathbf{F}_B , experienced by a fluid parcel of density $\rho = \hat{\rho}$ that is displaced a small distance

vertically within a linear stable stratification with background density field ρ_0 is

$$\mathbf{F}_B = [\hat{\rho} - \rho_0(\hat{z} + \delta)] \mathbf{g}, \quad (1.1)$$

where $\mathbf{g} = (0, -\hat{g})$ is the gravitational acceleration and $\delta = \delta(t)$ denotes the vertical displacement of the fluid parcel at time t from its vertical equilibrium position located at $z = \hat{z}$. Expanding as a Taylor series and neglecting second and higher order terms in δ , yields the second order differential equation for the vertical displacement

$$\hat{\rho} \frac{\partial^2 \delta}{\partial t^2} = \left(\hat{g} \frac{\partial \rho_0}{\partial z} \right) \delta, \quad (1.2)$$

which has harmonic solutions for $\partial \rho_0 / \partial z < 0$. An otherwise unconstrained frequency of oscillation, the Brunt Väisälä, or buoyancy, frequency N , can therefore be defined for a particular stratification as

$$N = \sqrt{-\frac{\hat{g}}{\hat{\rho}} \frac{\partial \rho_0}{\partial z}}. \quad (1.3)$$

The Brunt Väisälä frequency corresponds to the temporal frequency of oscillation of a fluid parcel, or an isopycnal, trying to recover a position of neutral buoyancy after being disturbed vertically.

Parcels of fluid within a stratification subject to a sustained disturbance with a forcing frequency σ that is only a fraction of N are acted on by only a fraction of the restoring buoyancy force experienced by a fluid parcel displaced vertically by a transient disturbance. The reduction in buoyancy force is achieved by the fluid moving along lines at a specific angle, θ , to the vertical corresponding to directions along which $N \cos \theta$ is equal to the forcing frequency σ . Fluid parcels disturbed in this manner are therefore constrained to oscillate along one of these directions as they endeavour to achieve a level of neutral buoyancy. Within this constraint, the spatial distribution of the fluid motion is further determined by the boundary conditions associated with the forcing disturbance. These oscillations are known as internal gravity waves of frequency σ . Internal gravity wave energy travels away from sites of disturbances and parallel to the fluid particle motion at the angle θ designated by the relationship between σ and N . Physical descriptions of internal wave generation may also be found in Phillips (1966), Roberts (1975), Lighthill (1978), Turner (1979), Pedlosky (2003). This thesis is concerned with internal gravity waves propagating within continuous stable stratifications. A short overview of conditions under which a stable stratification can develop instabilities and support mixing are given below.

1.2.3 Instabilities of a stable stratification

The ability of buoyancy forces to maintain the vertical density profile of a stratification that is subject to perturbations is dependent on the magnitude and character of the imposed disturbance. Although a stratification with a negative vertical density gradient is convectively stable to small perturbations of its equilibrium state and will not develop Rayleigh-Taylor instabilities directly,

conditions exist under which such stratifications can be destabilised, resulting in overturning of isopycnals and mixing within the fluid. Instabilities of stable stratifications arising as a result of shear or wave breaking are introduced briefly here.

Shear instabilities

Instabilities and so turbulence and mixing can arise when stratifications are subject to shear - *i.e.* there is some region in the fluid where the vertical gradient, du/dz , of the horizontal velocity field, u , is nonzero. Such shear instabilities occur if the influence of the shear becomes significantly larger than that of the buoyancy. The Richardson number, Ri , compares the relative influence of these two effects according to

$$Ri = \left(\frac{N}{du/dz} \right)^2. \quad (1.4)$$

The effects of shear are only sufficiently dominant over those of buoyancy to allow the growth of a small perturbation of the stratification into an instability for values of $Ri < 1/4$ (Howard 1961; Miles 1961). The exact nature of the instability generated under these conditions depends on the vertical profiles of both the density and the horizontal velocity fields. For example, if the variations of the velocity and density fields are characterised by similar vertical distances then, for sufficiently small Richardson numbers, shear instabilities are commonly Kelvin-Helmholtz in form (Helmholtz 1868; Kelvin 1871), whilst at larger Richardson numbers Holmboe instabilities may develop (Holmboe 1962; Browand & Wang 1972). See Chandrasekhar (1961) and Drazin & Reid (2004) for more detailed descriptions of these instabilities and the associated mixing.

Wave breaking

Instabilities can also be generated through internal wave processes, with the nature of instabilities depending on the wave properties as well as the background flow and stratification. The vertical amplitude, A_m , of a wave is defined here as the vertical displacement of the associated isopycnals from their vertical equilibrium positions. It is illustrative to define a nondimensional parameter, \tilde{A} , comparing the wave amplitude with horizontal length scales of the wave according to

$$\tilde{A} = kA_m, \quad (1.5)$$

where k is the horizontal wavenumber of the wave. Such a parameter can be used as an indicator of the nonlinear character of the fluid response, e.g. the proportion of wave energy fed into higher frequency harmonics of the primary wave motion.

Internal wave breaking events can occur whenever the waves become steep enough to overturn isopycnals. A second parameter, a measure of the steepness of a wave, is given by

$$S_t = mA_m \quad (1.6)$$

where m is the vertical amplitude of the wave (e.g. Thorpe 1994). In regions where $S_t > 1$, *i.e.* fluid particles are displaced vertically a greater distance than the vertical wavelength so that the vertical density gradient becomes locally positive with heavy fluid forced to overlie light fluid, Rayleigh-Taylor instabilities are induced and the ensuing fluid motion generates mixed fluid. Factors promoting wave steepness are therefore factors promoting wave breaking and so mixing. In particular, breaking events are only associated with those interactions resulting in high wavenumber waves, which correspond to small length scales (Garrett & Gilbert 1988). Detailed reviews of wave instabilities and breaking can be found in Staquet & Sommeria (2002), Miropol'sky (2001) and Fritts & Alexander (2003).

Mixing events can themselves generate internal gravity waves that have spatial and temporal forms determined by the instability. Regions of mixed fluid formed within an otherwise stably stratified fluid are subject to buoyancy forces imposed by the surrounding fluid. Such fluid patches are therefore suppressed vertically and slowly spread horizontally to form thin homogeneous density layers at vertical levels where they are neutrally buoyant within the stratification. The mixing induced by mechanisms such as shear instabilities and wave breaking thereby introduces relatively fine scale structure to stratifications. The sharp gradients in the vertical density profiles caused by intruding layers are smoothed on longer time scales by diffusion mechanisms. Fluid mixing and the subsequent evolution of mixed fluid patches is discussed further in Barenblatt (1996).

1.3 Motivations

The previous section described propagation of internal gravity waves through stable stratifications. Research of internal gravity waves has been largely motivated by their significance in mixing and transport within the mainly stably stratified stratosphere, an atmospheric layer separated from the Earth's surface by the turbulent troposphere, and the ocean thermocline, located between surface and 'deep waters'. The density profile of the stratosphere is predominantly controlled by gradients in temperature that position this layer at altitudes $\sim 10 - 50$ km above sea level. The density profile of the ocean thermocline, however, is specified by a combination of both temperature and salinity gradients and, as a result, the thermocline has a vertical density profile with a depth and form that is subject to considerable regional and seasonal variation. Whilst internal gravity waves greatly influence both atmospheric and ocean dynamics, the emphasis of the present study is towards oceanic applications. Further information on internal gravity waves in the specifically atmospheric context can be found in, for example, Holton (1979), Gill (1982), Andrews *et al.* (1987) and Fritts & Alexander (2003).

1.3.1 Internal gravity waves in the ocean

Oceanic internal gravity waves are principally generated by wind forcing at the ocean surface or tidal forcing along irregular ocean floor. The latter of these contributions is the most significant

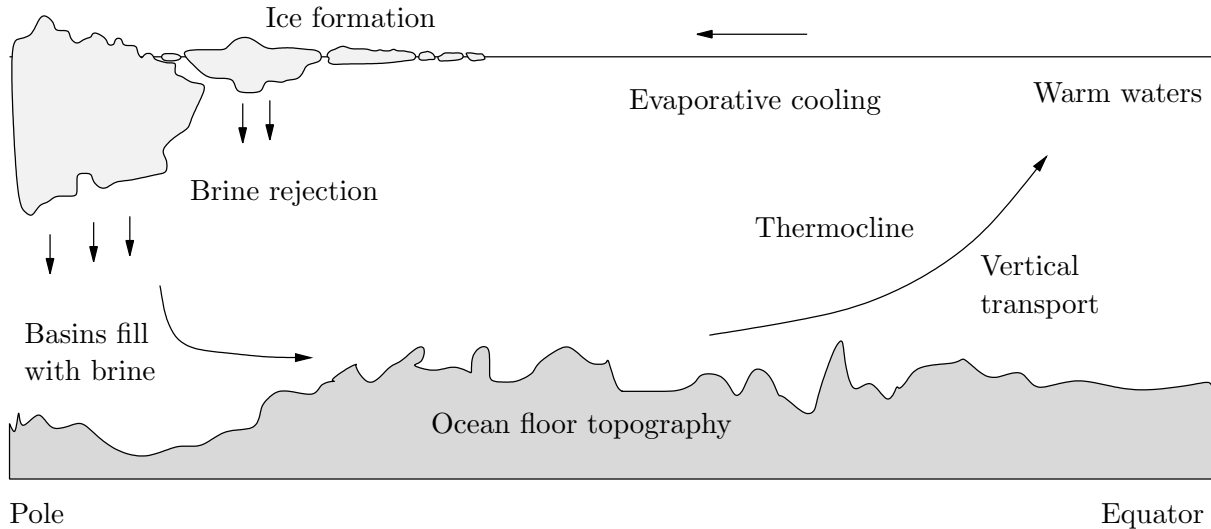


Figure 1.2: Schematic describing the Meridional Overturning Circulation and processes causing density changes of constituent water masses.

and is known as the ‘internal tide’ (Wunsch 1975). The tidal power input in global energy budgets is estimated to be $\sim 3.5 TW$, of which $\sim 1 TW$ has been associated with internal gravity wave generation in the abyssal ocean (Munk & Wunsch 1998; Egbert & Ray 2000). Waves generated through these various mechanisms transport energy from their source towards the ocean interior, where the wavefield is generally modelled by the spectrum calculated by Garrett & Munk (1975). Subsequent interactions of the waves with topography, with other waves, or with variations in the background stratification and flow all act to alter wave properties such as wavenumbers and energy densities, hence causing local skews in the wavenumber spectra. The waves undergo viscous diffusion, resonance and breaking events, which in turn induce turbulence and mixing within the ocean.

1.3.2 Ocean circulation and mixing

Estimates of mixing attributed to internal wave processes have been used to explain deficiencies in energy calculations relating to the meridional overturning circulation or ‘MOC’ (e.g. Sandström 1908; Munk 1966; Baines & Turner 1969; Munk & Wunsch 1998). The MOC is a large scale global system that transports thermal energy as well as salt and other substances between the equator and poles (see schematic in figure 1.2). The cycle may be seen to begin at the equator where warm surface waters are cooled and made more saline as a result of several mechanisms including evaporation, wind cooling experienced by pole-ward surface currents such as the Gulf Stream (North Atlantic Current), radiative cooling (if a water mass is warm, such as the Gulf Stream, radiative cooling may dominate over radiative heating at higher latitudes), and through brine rejection during ice formation. At high latitudes, the dense water formed sinks below polar ice and seas into deep ocean

basins and is channelled by topography as bottom currents travelling away from the poles. Within the ocean interior, the thermocline is dominantly stably stratified. This suggests that instead of the ocean eventually being filled by the fluxes of dense water sinking to the ocean floor at high latitudes, mechanisms of significant vertical transport and therefore mixing (since this is the only mechanism by which there can be a net vertical transport in a stable stratification) must exist between the buoyant surface layer and abyssal waters (e.g. Sandström 1908; Munk 1966; Baines & Turner 1969; Munk & Wunsch 1998). A recent review of these ideas can be found in Wunsch & Ferrari (2004). Accurate climate models therefore depend on detailed understanding and quantification of processes contributing to such diapycnal mixing (*i.e.* exchange between isopycnals) in the deep ocean.

Measurements of turbulence, which convert large to small scales, are indicative of levels of mixing within the ocean. Comparisons of diapycnal mixing rates based on turbulence data collected in field studies above continental slopes or seamounts and ridges imply that mixing levels are elevated in these regions and as much as $O(10^4)$ times greater near ‘rough’ topography than those estimated elsewhere (e.g. Cox & Sandstrom 1962; Munk 1966; Armi 1978; Eriksen 1982; Kunze & Toole 1997; Lueck & Mudge 1997; Polzin *et al.* 1997; Toole *et al.* 1997; Ledwell *et al.* 1998; Egbert & Ray 2000; Ledwell *et al.* 2000; Rudnick *et al.* 2003; Nash *et al.* 2004; Nash *et al.* 2007). Turbulence generated by breaking internal gravity waves near such topography is considered to be the principle cause of mixing there (e.g. Eriksen 1982; Gilbert & Garrett 1989; Müller & Lui 2000; St Laurent & Garrett 2002). It is therefore of interest to identify conditions that act to promote wave breaking and hence the cascade from internal wave energy to turbulent mixing.

1.4 Research aims and methodology

This research focuses on the scattering behaviour of internal gravity waves that interact with ‘rough’ topography, *i.e.* boundary profiles exhibiting features characterised by length scales comparable with incident wavelengths. A number of recent research articles investigate the generation of internal gravity waves by the flow of a stratified fluid over rough topography (e.g. Balmforth *et al.* 2002; Gyüre & János 2003; Legg 2003; St Laurent *et al.* 2003; Aguilar *et al.* 2006; Peacock *et al.* 2008). The present study considers the scattering behaviours of the waves in stratifications where there is no mean background flow. The research aims to determine how incident wave energy is partitioned spatially after interaction with topography (*i.e.* scattered forwards, backwards, to higher harmonics or trapped locally), where the wave energy is dissipated (*i.e.* locally or remotely from the topography) and to what effect (e.g. isolation of topography by local changes in background stratification caused by mixing there). The interactions of an incident wavefield with rough topography are characterised here in terms of those promoting conditions for mixing of the stratified fluid. Whilst the nature of the related instabilities are beyond the scope of this thesis, mixing in the immediate vicinity of the topography, *i.e.* the ‘near-field’, is discussed. Features such as localised changes to the background stratification and regions of large shear are also used to indicate regimes of decreased stability. The structure of the fluid motion in the near-field is used to give an insight into

the physical processes controlling the wave scattering behaviour. This thesis describes the scattered wavefield in regions remote from the topography, *i.e.* the ‘far-field’, in terms of the directions of the scattered wave energy propagation and the relative energy fluxes and energy density spectra of the wavefields in each of these directions. In particular, the present research highlights regimes where the energy density spectra of wavefields interacting with topography are skewed to higher wavenumbers, since these have been identified as conditions promoting mixing (Garrett & Gilbert 1988).

Ocean topography is composed of a broad range of length scales and slopes and exhibits features such as rapid variations in gradient and, in particular, abrupt changes that are described here as ‘sharp corners’. The effects of each of these properties on the scattered wavefields is investigated here using a series of laboratory experiments and the results compared with predictions from linear theories. The study is concerned specifically with two-dimensional wavefields propagating through continuous linear stratifications.

The influence of variations in the relative slope of the boundary and the direction of the incident wave energy flux is studied in chapter 4. Experiment results are presented of the reflection behaviours of waves of a range of frequencies at smooth boundaries inclined at different angles. These are compared with scattering of wavefields at topographies with sinusoidal profile in order to examine the effect of an introduction of a smooth boundary variation on the scattered wavefields. The effect of an increase in wavelength of the topography for a given wavefield is illustrated by the use of two different sinusoidal topographies with different wavelengths.

Chapter 5 investigates the effect of surface curvature and sharp corners on wavefields generated by vertically oscillating cylinders. The wavefields generated by five elliptical and three rectangular cylinders with different aspect ratios are compared.

Near-field and far-field structures of experiment wavefields scattering at topographies with sinusoidal, sawtooth, square-wave and pseudo knife-edge profiles are presented and analysed in chapters 6, 7 and 8 for sub, super and near-critical values of θ/α respectively. The influence of topographic shape and changes in parameters comparing slopes and length scales of the incident waves and topography are investigated.

1.4.1 Outline of thesis

An introduction to the basic properties of internal gravity waves and a synthesis of relevant literature is given in chapter 2. Chapter 3 describes and validates the experimental methods employed in this research. Results from this study are presented and analysed in chapters 4 - 8. The main results from this research together with areas for further research are summarised and discussed in chapter 9.

Chapter 2

Background

2.1 Overview

The previous chapter outlined the motivations, aims and structure of the present study. This chapter provides a context for the research and introduces key concepts and terminology. A synthesis is presented here of the properties and reflection behaviour of internal gravity waves established in other studies. Both kinematic and physical descriptions are given of wave motion remote from boundaries (section 2.2). In particular, the generation of waves by an oscillating cylinder is discussed in section 2.3. Boundary and radiation conditions are detailed in section 2.4 and wave interactions with smooth horizontal, vertical and sloping boundaries (sections 2.4.1 - 2.4.2) and rough topographies (section 2.5) are described. This chapter concludes by clarifying the limits of current understanding of internal gravity wave scatter at topography and the specific role of this study.

2.2 Wave motion in an unbounded fluid

The equations governing propagation of internal gravity waves are derived and discussed here. The present research is predominantly concerned with scattering behaviours of internal gravity waves under conditions applicable to those in the ocean, though most aspects of oceanic internal wave generation, propagation, wave-wave and boundary interactions, breaking and dissipation are directly analogous with those occurring in the atmosphere. It is assumed here that, in general, deep oceanic waters behave incompressibly and rotational effects are also neglected in order to exclude contributions to the dynamics from inertial waves that arise from the Coriolis effect and assess only those due to internal gravity waves. The equations governing the motion of an incompressible, nonrotating fluid are given by the continuity equation

$$\nabla \cdot \mathbf{u} = 0 \tag{2.1}$$

and expressions for conservation of momentum and mass,

$$\rho \frac{D\mathbf{u}}{Dt} = -\nabla P + \rho \mathbf{g} + \mu \nabla^2 \mathbf{u} \quad (2.2)$$

and

$$\frac{D\rho}{Dt} = -\kappa \nabla^2 \rho, \quad (2.3)$$

where \mathbf{u} is the velocity field, ρ the fluid density, P the pressure field, \mathbf{g} is the gravitational acceleration and μ and κ are constants denoting coefficients of dynamic viscous and molecular mass diffusion respectively (e.g. Phillips 1966).

2.2.1 Linearisation and approximations

Several assumptions and approximations may be made in order to reduce these equations to a set which may be solved more readily. The Schmidt number compares the relative magnitudes of viscous and molecular diffusion and is defined as $Sc = \nu/\kappa$, where the kinematic viscosity, ν , is the quantity μ/ρ . In salt-water stratifications the Schmidt number is large ($O(10^3)$) and so the effect of molecular diffusion of mass is generally assumed to be much less significant than diffusive effects on the fluid motion caused by viscosity. This assumption becomes less valid in regions where $\nabla^2 \rho$ is large however.

The fluid motion is assumed to be Boussinesq so that it comprises small perturbations of field variables relative to a base state, which corresponds to that of an undisturbed continuous stable stratification with density profile $\rho_0 = \rho_0(z)$. Within this approximation, perturbations in the density field have a negligible influence on inertia terms and only become significant as factors of buoyancy terms, so that factors of ρ in inertia terms may be replaced by ρ_0 . The pressure and density fields relating to ensuing fluid motion are therefore decomposed as $P = p' + p_0$ and $\rho = \rho' + \rho_0$, where p_0 is the ambient pressure and p' and ρ' are deviations from the base state such that $\nabla p' \ll \nabla p_0$ and $\rho' \ll \rho_0$. Linearising about the base state reduces equations (2.1), (2.2) and (2.3) to the set

$$\nabla \cdot \mathbf{u} = 0, \quad (2.4)$$

$$\hat{\rho} \frac{\partial \mathbf{u}}{\partial t} = -\nabla p' + \rho' \mathbf{g} + \mu \nabla^2 \mathbf{u} \quad (2.5)$$

and

$$\frac{\partial \rho'}{\partial t} + \mathbf{u} \cdot \nabla \rho_0 = 0, \quad (2.6)$$

respectively (e.g. Lamb 1932; Phillips 1966), where $\hat{\rho}$ is a reference density as defined in 1.3. This linear set of equations describes fluid motion arising from disturbances of a Boussinesq stratification that are characterised by vertical scales much smaller than that over which the background stratification varies. Notably, solutions to these equations are invertible in the vertical direction and can be superposed.

An inviscid approximation, neglecting the term $\mu \nabla^2 \mathbf{u}$, is made on the basis that, in general for

the fluid considered, this term makes a negligible contribution relative to the inertial terms, except in small regions near boundaries.

Two-dimensional approximation

Solutions to equations (2.4) - (2.6) are symmetric in the coordinates perpendicular to the gravitational field and so a two-dimensional approximation is also made, restricting consideration to fluid motion in the vertical cartesian plane $\mathbf{x} = (x, z)$.

A slowly varying background density profile, ρ_0 , may be approximated locally, i.e. on the scale of the fluid displacements, as a linear function of height. In an unbounded linear stratification, the vertical gradient, $\partial\rho_0/\partial z$, is constant and the horizontal gradient, $\partial\rho_0/\partial x$, vanishes. Hence the two-dimensional equations governing the evolution of perturbations to the density profile can be expanded into their cartesian components as the set of equations

$$\hat{\rho} \frac{\partial u}{\partial t} = -\frac{\partial p'}{\partial x}, \quad (2.7)$$

$$\hat{\rho} \frac{\partial w}{\partial t} = -\frac{\partial p'}{\partial z} - \rho' \hat{g}, \quad (2.8)$$

$$\frac{\partial \rho'}{\partial t} + w \frac{\partial \rho_0}{\partial z} = 0, \quad (2.9)$$

$$\frac{\partial u}{\partial x} + \frac{\partial w}{\partial z} = 0, \quad (2.10)$$

where $\mathbf{g} = (0, -\hat{g})$ and $\mathbf{u} = (u, w)$ is the horizontal and vertical decomposition of the velocity field. After some manipulation, equations (2.7) - (2.10) are amalgamated into the partial differential equation for the vertical velocity

$$\left(\frac{\partial^2}{\partial t^2} \nabla^2 + N^2 \frac{\partial^2}{\partial x^2} \right) w = 0, \quad (2.11)$$

where $\nabla^2 = \partial^2/\partial x^2 + \partial^2/\partial z^2$ and the Brunt Väisälä frequency (see section 1.2.2)

$$N^2 = -\frac{\hat{g}}{\hat{\rho}} \frac{\partial \rho_0}{\partial z} \quad (2.12)$$

is constant for a linear stratification.

A two-dimensional stream function, $\psi(x, z, t)$, is also defined such that

$$u = -\frac{\partial \psi}{\partial z} \quad \text{and} \quad w = \frac{\partial \psi}{\partial x}. \quad (2.13)$$

2.2.2 Dispersion relation

For monochromatic disturbances of a stratification, *i.e.* those characterised by a single temporal frequency σ , that cause small fluctuations of the density profile relative to the variation of the background density profile, the field variables ρ' , ψ , u , w and p' may all be assumed to evolve according to a plane wave form, within which lines of constant phase are parallel. Internal gravity waves of small amplitude are therefore expected to be described by field variables, denoted generally by ϕ , having the form

$$\phi \sim \Re[\hat{\phi}(x, z)e^{-i\sigma t}]. \quad (2.14)$$

Substituting a plane wave (*i.e.* infinite extent) spatial dependence

$$\hat{\phi}(x, z) \sim e^{i(kx+mz)}, \quad (2.15)$$

where $\mathbf{k} = (k, m)$ is the two-dimensional wavenumber, with horizontal and vertical components k and m , into (2.11) yields the dispersion relation

$$\sigma = \pm N \frac{k}{\sqrt{(k^2 + m^2)}} = \pm N \cos \theta. \quad (2.16)$$

Here θ is the angle of the direction of fluid particle motions relative to the vertical, indicating that the fluid motion is anisotropic. The relationship $\chi = kx + mz - \sigma t$ is the phase of the wave, which is definitively linear in x , z and t for a plane wave.

Phase and group velocities

The phase, \mathbf{c}_p , and group, \mathbf{c}_g , velocities of such fluid motions, describing the propagation of the wave phase and energy respectively, are therefore calculated to be

$$\mathbf{c}_p = \frac{Nk}{(k^2 + m^2)^{\frac{3}{2}}}(k, m) \quad \text{and} \quad \mathbf{c}_g = \frac{Nm}{(k^2 + m^2)^{\frac{3}{2}}}(m, -k). \quad (2.17)$$

Notably

$$\mathbf{c}_p \cdot \mathbf{c}_g = 0, \quad (2.18)$$

indicating that the phase propagates in a direction perpendicular to the energy propagation, and vertical components of the phase and group velocities are related by

$$c_{p_z} = -c_{g_z}. \quad (2.19)$$

Directions of particle motions coincide with that of the group velocity.

A reformulation of the phase and group velocities in terms of coordinates aligned across and

along the wave beam, with unit vectors $\mathbf{e}_{\mathbf{k}}$ and \mathbf{e}_{θ} respectively, as

$$\mathbf{c}_p = \pm \frac{N}{|\mathbf{k}|} \cos \theta \mathbf{e}_{\mathbf{k}} \quad \text{and} \quad \mathbf{c}_g = \mp \frac{N}{|\mathbf{k}|} \sin \theta \mathbf{e}_{\theta}, \quad (2.20)$$

illustrates the dependence of the speed of energy propagation on the frequency and wavenumbers associated with the fluid motion. For a given wavenumber, the group velocity increases with increasing θ , *i.e.* decreasing frequency σ by the dispersion relation; a consequence of the inhibiting effect of the stratification on vertical motions. For a given wave frequency, and therefore for a fixed angle θ , the group velocity is inversely related to the magnitude of the wavenumber so that energy associated with the largest length scales (*i.e.* small $|\mathbf{k}|$) is transferred most rapidly through the fluid. Derivations and discussion of the equations and approximations above can be found in Lighthill (1978) and Turner (1979).

Frequency regimes

Inspection of (2.16) indicates that restrictions apply to internal gravity wave generation, since the nature of the governing equation for field variables, (2.11), depends on the magnitude of the frequency parameter σ/N . In particular, the dispersion relation (2.16) is invalidated by values of the forcing frequency, σ , that exceed N . In this case, with $\sigma/N > 1$, (2.11) is elliptic and the resulting fluid motion is not wave-like in character but instead decays exponentially in space. The governing equation (2.11) becomes hyperbolic for parameter values $0 \leq \sigma/N \leq 1$ and the dispersion relation is valid in this regime. Fluid disturbances of frequency equal to the Brunt Väisälä frequency correspond to fluid particle motion at an angle $\theta = 0^\circ$ and a zero group velocity at first order. The fluid parcels in this configuration therefore undergo simple harmonic oscillations and wave energy is confined to the disturbance region. More generally, a disturbance characterised by frequency σ/N in the hyperbolic range generates wave motion, with energy propagating at the angle θ to the vertical determined from the nontrivial dispersion relation (2.16). Hence the waves generated are both hyperbolic and dispersive in nature (see e.g. Whitham 1974 for typical properties of such classifications of waves). Wave propagation resulting from a monochromatic forcing in two dimensions is therefore only possible along characteristics or rays directed along four directions, and in three dimensions may only occur along the surface of two cones originating at the source.

Wave groups

In general, a disturbance characterised by frequency σ does not generate individual wavenumber components in isolation but rather generates *groups* (also referred to as ‘packets’) of waves that travel along the directions specified by θ . Wave groups consist of a superposition of a range of wavenumbers, where the exact composition and hence form of such a wave group is determined by the nature and spatial structure of the disturbance region. The plane wave representation of each of the wave group components is appropriate only in domains that vary slowly on the scale

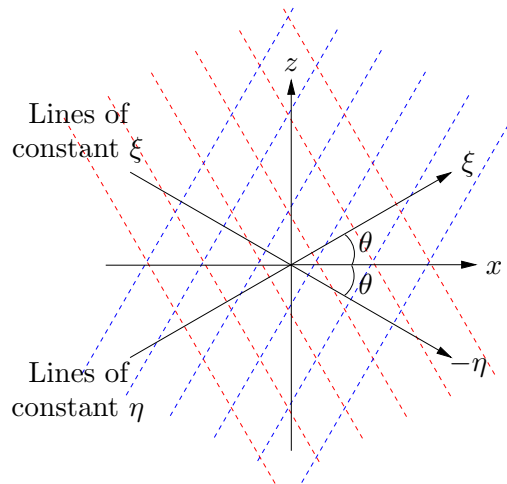


Figure 2.1: Characteristic coordinates for wave energy propagating along lines inclined at angles θ to the vertical.

of the waves. In this case, the components of a wave group have a constant phase relationship. The plane wave model of a wave group becomes inadequate in the vicinity of rapid variation of a domain, which can be caused, for example, by nonlinear variation of the background stratification or the presence of a rough boundary. The wave group can be deformed in such regions and energy transferred between the component wavenumbers. Abrupt changes in the fluid domain, such as discontinuities in the background density profile or at sharp corners of topography, are supported by the hyperbolic nature of the wave solutions of (2.11), with such ‘events’ being propagated as shocks throughout the fluid that also travel along the characteristic ray paths.

2.2.3 Characteristic variables

As a result of the hyperbolic nature of the waves, a convenient analytical description of a monochromatic wavefield can be given by consideration of the characteristic variables

$$\xi = z + cx, \quad \text{and} \quad \eta = z - cx, \quad (2.21)$$

where $c = \cot \theta$ (e.g. Baines 1971a; Mied & Dugan 1976; Liu 1998). These variables are constant on lines corresponding to the directions of wave energy propagation, which are straight lines in a slowly varying domain. Hence a rotation from a cartesian frame of reference to the characteristic coordinates (ξ, η) allows the spatial dependence of field variables, $\hat{\phi}(x, z)$, to be decomposed into a sum of its components that are directed in each of the permitted directions of energy propagation, *i.e.*

$$\hat{\phi}(x, z) \rightarrow \hat{\phi}(\xi, \eta) = f(\xi) + g(\eta). \quad (2.22)$$

A plane wave with $\hat{\phi} = f(\xi) = \exp(ik\xi)$, for example, therefore has a phase propagating along the ξ coordinate and a group velocity directed downwards and aligned parallel to lines of constant ξ (see

the coordinate system shown in figure 2.1). This formulation is revisited in section 2.4.

2.3 Internal wave generation by an oscillating cylinder

The previous section introduced characterising properties, such as the dispersion relation and phase and group velocities predicted by linear theory, of small amplitude two-dimensional internal gravity waves propagating in an inviscid linear Boussinesq stratification. Wave fields in the experimental component of the present study (see chapters 3-8) are generated by the vertical oscillation of cylinders in linear stratifications. This section therefore outlines previous theoretical, experimental and numerical research of internal gravity wave beam generation by oscillating cylinders. Physical descriptions are given of the wave beams such as their inclinations, amplitudes and widths. The limits of linear theory to accurately describe the wave motion and the influence of viscous diffusion and boundary layers on the wavefields are also discussed.

2.3.1 Internal Gravity Wave Beams

The linear inviscid theory of Lamb (1932) (see section 2.2.1) was supported and analysed further in experiments by Görtler (1943) and Mowbray & Rarity (1967). Linear theory predicts that a two-dimensional point or finite circular wave source making small amplitude vertical oscillations at a sustained temporal frequency, σ , within a Boussinesq linear stratification characterised by the Brunt Väisälä frequency N , generates four wave beams. In experimental contexts, the two-dimensional system is approximated by the oscillation of cylinders with circular cross-section such that the axis of symmetry is aligned perpendicular to the wavefields produced. Mowbray & Rarity's experiments confirmed that each beam in the resulting wavefield, often referred to as a 'St Andrew's Cross', is inclined at an angle θ relative to the vertical that is specified by the dispersion relation (2.16). The energy introduced into the system by small amplitude vertical oscillations of the source is equally partitioned between the four beams and propagates along each beam at the group velocity (2.17), where the wavenumber components of a generated wave group are determined by the dimensions of the source. The phase of a wave group propagates in the across-beam direction at the phase velocity (2.17). Figure 2.2 illustrates this configuration for a circular source with diameter D_c and vertical amplitude of forcing oscillation A_c . The coordinates (a, s) denote along-beam and across-beam directions respectively, where the origin is taken as the source center. The suffices $+$ and $-$, respectively, denote positive and negative directions so that in the context of a_{+-} , for example, the suffices indicate that the across-beam coordinate is oriented with a positive horizontal sense and a negative vertical sense.

The effects of viscosity on the wavefield were first modelled by Thomas & Stevenson (1972). Their similarity solution used a boundary layer approximation that is valid in regions where gradients of the wavefield in the along-beam direction are much smaller than those in the direction of phase propagation. This assumption is invalidated in regions close to the oscillating source,

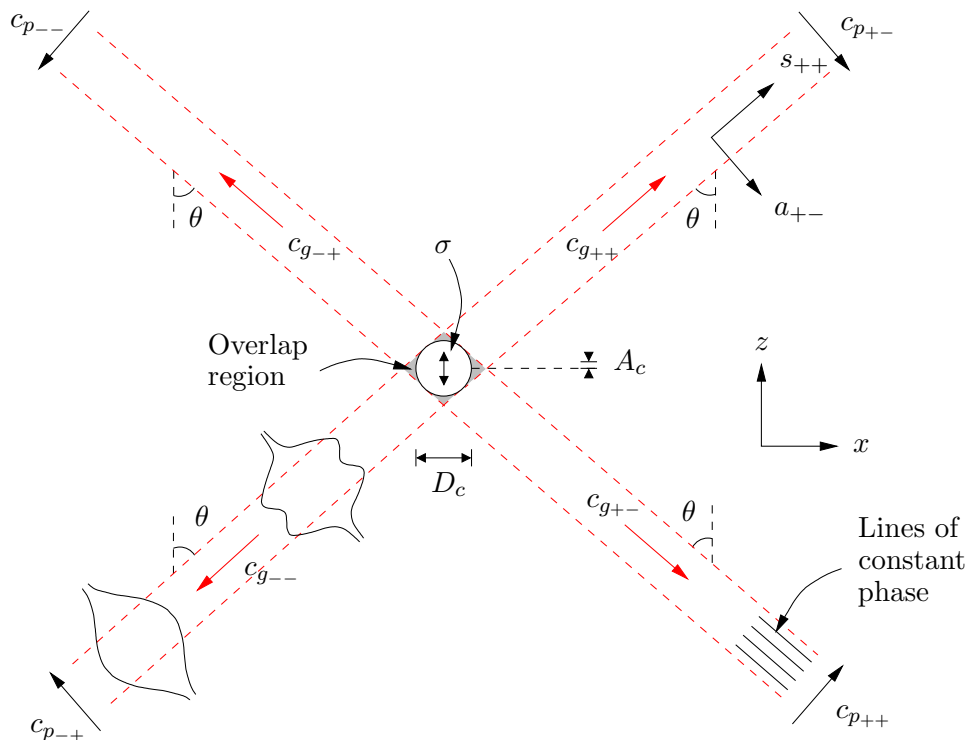


Figure 2.2: Schematic of two-dimensional internal gravity wave beams produced by an oscillating cylinder. Phase and group velocity directions are indicated for each beam. Grey shading indicates regions where wave beams overlap. Bounding envelopes of amplitudes of the along-beam fluid motion are sketched on the lower left-hand beam. The sketch depicts the transition from a bimodal form at small along-beam distances to a unimodal structure further from the cylinder as viscosity attenuates the wave energy.

where gradients in the fluid motion perpendicular to the surface of the source are significantly enhanced as a result of the oscillating boundary layer there. Thomas & Stevenson's solution also assumed linear fluid motion and therefore requires that the forcing amplitude of the system is small, *i.e.* $A_c/D_c \ll 1$. The linear model derived becomes less applicable at forcing frequencies near to zero or to the buoyancy frequency, N (Thomas & Stevenson 1972; Tabaei & Akylas 2003). Makarov *et al.* (1990) also studied the changes caused by viscosity to properties of wave groups as they propagate along beams. Inviscid limits of their solution do not agree with inviscid theory of Hurley (1972) and Hurley (1997) at small along-beam distances, s . Hurley & Keady (1997) developed inviscid solutions to include the influence of viscosity and, although their treatment of the region immediately surrounding the source remained inviscid with no boundary layer accounted for on the basis that the Reynolds number there is large, the resulting theory does compare well with viscous solutions of Makarov *et al.* (1990) and also with that of Thomas & Stevenson (1972) in regions further from the source. More detailed analysis of structures of internal wave beams has resulted from advancements in experimental schlieren techniques (e.g. Peters 1985; Dalziel *et al.* 1998; Sutherland *et al.* 1998; Sutherland *et al.* 1999; Dalziel *et al.* 2000). In general, experiments have both qualitatively and

quantitatively supported theoretical predictions. Quantitative discrepancies are attributed to the neglect in theoretical models both of nonlinear terms and of the boundary layer about the source.

The following sections give descriptions, determined by the studies outlined above, of across-beam structures of generated wave groups and their evolution as they propagate along beams.

2.3.2 Wave beam structure: wave amplitudes

Amplitudes of the wave motion are defined as the distance that fluid parcels are displaced in the along-beam direction away from their positions of neutral buoyancy. A measure of these amplitudes can be given experimentally as the change in the square of the local Brunt Väisälä frequency relative to that of the background stratification, *i.e.* $\sim \Delta N^2/N^2$ (e.g. Sutherland *et al.* 1999). Lines of constant phase are oriented parallel to the direction of the group velocity and propagate across-beams at the phase velocity. Amplitudes of wave groups are bounded by an ‘envelope’ as the phase propagates across the width of a beam. These amplitude envelopes are found in both theoretical and experimental studies to be characterised by either a ‘bimodal’ structure, with two peaks of the amplitude at $a \simeq \pm R_c$, where R_c is the radius of the source, or a ‘unimodal’ structure, with a single peak amplitude value at $a \simeq 0$ (Makarov *et al.* 1990; Hurley 1997; Hurley & Keady 1997; Sutherland & Linden 2002). Linear theory predicts that the amplitude envelope of a wave group generated by an oscillating cylinder in an inviscid fluid will have a bimodal form that is sustained as it propagates away from its source (Hurley 1972; Hurley 1997). The influence of viscosity and the magnitude of the forcing amplitude and frequency on this across-beam structure are discussed here.

Influence of viscosity

In a viscous fluid, the form of the bounding envelope of a propagating wave group depends on the ratio of the viscous length scale,

$$L_\nu = \frac{(\hat{g}\nu)^{\frac{1}{3}}}{N} \quad (2.23)$$

(Makarov *et al.* 1990), to source size, D_c , as well as the distance that the wave group has propagated away from the source. The viscous length scale is derived from scaling analysis using a subset of characterising length scales of the wave motion. These include $\Lambda = \hat{g}/(2\pi N^2)$, a length scale associated with the background stratification, $\lambda = 2\pi U/N$, a wavelength characterising generated internal gravity waves (Lighthill 1978), where U is the velocity of the cylinder, and the depths of the stationary and periodic boundary layers for the velocity field $\delta_u = \nu/U$ and $\delta = (2\nu/\sigma)^{1/2}$ respectively (Batchelor 1970). The viscous length scale (2.23) is therefore formulated by the combination $(\Lambda\lambda\delta_u)^{1/3}$.

In regions near to the source the envelope of a wave group takes a bimodal form provided that $L_\nu/D_c \ll 1$, whilst at larger values of this parameter the envelope degenerates to a unimodal form (Hurley & Keady 1997). Regardless of the initial form of its envelope, viscosity acts to

gradually reduce the amplitudes of the fluid motion associated with a wave group as it propagates away from the source. Wave amplitudes are therefore greatest near to the source and decrease with distance along wave beams. As well as causing this reduction in the energy density of the wave group, viscosity also modifies the *form* of the envelope as the group propagates along the beam (e.g. Sutherland *et al.* 1999). This is a result of the fact that viscous action is enhanced in regions of the fluid where there is greater shear. Shearing motions are generated along lines parallel to the fluid motion, which is aligned along the wave beam. The wave phase dictates the gradients in these fluid motions in the across-beam direction. Shear motions are therefore the most pronounced for high wavenumber components of a propagating wave group since these produce larger gradients in the across-beam direction. Hence the amplitudes of fluid motions associated with these higher wavenumber components are reduced by viscosity faster than those associated with smaller wavenumbers and hence smaller across-beam gradients. The across-beam structure of a wave group propagating in a viscous fluid is therefore controlled at large distances from the source by its smaller wavenumber components, *i.e.* those associated with larger length scales. Where the length scale ratio L_ν/D_c is non negligible, viscosity is thereby able to erode the bimodal envelope of the inviscid limit to a unimodal envelope with a smaller amplitude and a larger width over a finite along-beam distance s_ν (Makarov *et al.* 1990; Hurley & Keady 1997; Sutherland *et al.* 1999). This transition distance is calculated by Makarov *et al.* (1990) to be

$$s_\nu = \frac{NR_c^3}{\nu}. \quad (2.24)$$

However, much smaller values for s_ν are found in experiments by Sutherland *et al.* (1999) - they suggest that (2.24) is not a correct measure of the transition distance. Schematics of the bimodal and unimodal envelope structures are shown in figure 2.2. Viscosity continues to reduce the energy density of unimodal wave groups subsequent to envelope transition as they propagate further along wave beams, with the amplitudes of the fluid displacement caused by propagating wave groups calculated to decrease inversely with radial distance, s , from the source (Thomas & Stevenson 1972; Peters 1985).

Variation with forcing amplitude

Amplitudes of linear internal waves are expected to increase linearly with the source oscillation amplitude A_c , for $\varepsilon \sim A_c/R_c \ll 1$ (Hurley 1997). This is confirmed in experiments with oscillating cylinders by Sutherland *et al.* (1999) and in the three-dimensional case with oscillating spheres for values as large as $A_c/R_c < 0.27$ (Flynn *et al.* 2003).

Nonlinear effects are also expected to become more significant as the ratio of source amplitude to source size, A_c/D_c , is increased. One such effect is the generation of ‘higher harmonics’. In the nonlinear formulation, the dispersion relation permits the generation of additional sets of wave beams with frequencies $n\sigma$, where n is a positive integer, provided that $n\sigma \leq N$. These additional

harmonics are associated with beams inclined at angles relative to the vertical θ_n , which also satisfy the linear dispersion relation according to

$$\theta_n = \cos^{-1} \left(\frac{n\sigma}{N} \right). \quad (2.25)$$

As the ratio A_c/D_c is increased, a greater proportion of the wave energy is distributed to the higher harmonics, and so this reduces the energy associated with the primary harmonic frequency σ . Secondary harmonic beams were first observed in experiments by Mowbray & Rarity (1967) and have been noted in subsequent studies such as Sutherland *et al.* (1999) and Sutherland & Linden (2002). No studies are known that have successfully demonstrated the presence of tertiary harmonic generation by an oscillating cylinder however, presumably as a result of the fact that the amplitudes of these wave beams, $\sim (A_c/D_c)^3$, are relatively weak and their visualisation is therefore inhibited by the error associated with the experimental technique being used. Sutherland & Linden (2002) suggest that the nonlinear generation of these secondary (or more) sets of wave beams develop as a result of the interference between the internal wave beams generated by the source oscillations and standing waves that are generated in the boundary layer along the surface of the source (e.g. Batchelor 1967; Riley 2001). Boundary layers of width δ form about the surface of a source oscillating with small amplitude in homogeneous viscous flow (Batchelor 1967), where

$$\delta \simeq \sqrt{\frac{2\nu}{\sigma}}, \quad (2.26)$$

and with experimental values for the boundary layer thickness typically measuring a few millimetres. The influence of this boundary layer on fluid motion is clearly enhanced for larger values of the ratio of boundary layer thickness to source size, δ/D_c . Sutherland & Linden (2002) argue that the interaction between the wave beams and the fluid motion generated in the boundary layer is the mechanism for the generation of the higher harmonic beams, rather than as a result of nonlinear interactions caused by the overlap of upper and lower beams of the primary harmonic set of beams, since the secondary harmonic set is seen to originate at the boundary layer and is not present in numerical studies in which the source boundary layer is absent. The second set of internal wave beams becomes more pronounced as the aspect ratio of the source is increased (with major axis aligned perpendicular to the direction of oscillation) (Sutherland & Linden 2002). Hence, this also supports the theory that the secondary harmonic wave beams are generated in the boundary layer since the larger curvature of more elliptical cylinders is known to enhance boundary layer effects (Batchelor 1967). The influence of source curvature on generated wavefields is investigated further in chapter 5.

Outside the boundary layer region, linear theory is assumed valid, and hence the generation of higher harmonic beams may generally be considered negligible, provided source amplitudes are small relative to source size, *i.e.* $A_c/D_c \ll 1$. However, even for small values of this parameter, the resulting fluid motion may contain regions where large amplitudes are realised and the linear

assumptions thereby invalidated. For example, regions where two or more wave beams interact can support constructive interference and significantly enhanced amplitudes (Sutherland *et al.* 1999; Sutherland & Linden 2002). This is possible in the immediate vicinity of the source where the fluid motion along wave beams has the largest amplitude and the beams also overlap (see figure 2.2). The area of overlap increases as source frequency approaches zero, implying that the associated nonlinear interactions could be enhanced at smaller source frequency. Such wave beam interactions are believed to be the cause of oscillations of twice the source frequency, 2σ , that were observed to propagate horizontally away from the source in experiments by Sutherland *et al.* (1999). These disturbances oscillated vertically about the mean vertical position of the source and were enhanced at larger source amplitudes, A_c .

Variation with forcing frequency

Amplitudes of the wave motion are also dependent on the forcing frequency. The group velocity decreases, with increasing frequency, σ , so that the rate of energy transport decreases resulting in larger energy densities at each position along the wave beam. Amplitudes are therefore expected to increase as wave frequencies approach the buoyancy frequency. This general trend is confirmed by experiments (Sutherland *et al.* 1999; Sutherland & Linden 2002). Experimental errors at frequencies close to the buoyancy frequency and the increasing influence of nonlinear wave motion as forcing frequencies approach zero lead to quantitative discrepancies between theory and experiments.

2.3.3 Wave beam structure: beam widths

The width of a wave beam at a particular along-beam distance s from the source is defined to be the standard deviation of the bimodal or unimodal amplitude envelope of an internal wave group there (Sutherland & Linden 2002). Linear inviscid theory of Hurley (1997) and Hurley & Keady (1997) suggests that the widths of internal gravity wave beams are equal to the source diameter, D_c , at their generation at $s = 0$. As wave groups propagate along beams away from the source, their bimodal envelope narrows slightly for a brief distance before widening again to the width of the source for the entire length of the beam. However, inspection of the velocity field along the predicted bounding characteristics of the inviscid wave beam, coincident with tangents to the source inclined at the angle θ to the vertical (red dashed lines in figure 2.2), reveals unphysical singularities there (Hurley 1997). Experiments report similar patterns of width behaviour as those deduced using linear theory. The infinite values of the velocity field predicted along the source tangents indicate that, in a real fluid, boundary layers around the source and the action of viscosity are very significant in smoothing the fluid motion in this region. Hence, inclusion of these influences into theoretical models is necessary if accurate quantitative calculations of the beam properties are to be made.

No analytical studies are known that satisfactorily allow for boundary layer formation about the source. Experimentally observed widths of beams in regions close (*i.e.* at distances $s < D_c$)

to the source are poorly modelled by inviscid theory. Viscous theory that neglects boundary layer formation calculates beam widths to be close to that of the source diameter, as in the inviscid limit, but with viscosity gradually widening wave groups as they propagate along wave beams and the wavenumber spectra of the group becomes skewed to lower wavenumbers (Hurley & Keady 1997). Experiments agree qualitatively with these calculations but find beams are wider than expected by the same order of magnitude as the predicted boundary layer depth. This discrepancy is therefore attributed, in part, to boundary layers forming and ‘adding’ to the width of the source (Batchelor 1967; Sutherland *et al.* 1999). Thomas & Stevenson (1972) calculate that viscous action widens unimodal beams according to the cube root of the distance from the source, $s^{1/3}$. Kistovich & Chashechkin (1993, 1995) deduced the same behaviour by modelling the propagation of wave groups with a Green’s function approach. Few experiments have verified this result since internal wave beams are generally viewed over inadequate distances, though those of Peters (1985) were supportive and analytical studies show similar behaviour at large s (Hurley & Keady 1997; Makarov *et al.* 1990).

2.4 Wave interaction with boundaries

The previous section described the wavefields generated in an unbounded domain by an oscillating cylinder. This thesis is concerned with the interaction of wavefields with boundaries. A description of a system within which an incident wavefield, represented by the incident stream function ψ_I , interacts with a boundary, B , is given as the superposition of the streamfunctions

$$\psi = \psi_I + \psi_S, \quad (2.27)$$

where ψ is the stream function describing the complete wavefield and ψ_S is the stream function of the scattered wavefield. The exact partitioning of scattered wave energy associated with ψ_S in physical and wavenumber space is determined by the shape of the boundary and the spatial and temporal form of the incident wave, ψ_I . The various conditions imposed by the presence of a boundary are discussed here.

At an impermeable rigid boundary the velocity field, \mathbf{u} , must satisfy

$$\mathbf{u} \cdot \mathbf{n} = 0, \quad (2.28)$$

where \mathbf{n} is the inward normal at the boundary. The vanishing of normal velocity components at the boundary therefore implies that, at first order, the frequency of scattered waves must be equal to the incident wave frequency. Hence, in the notation of section 2.2.3, a small amplitude monochromatic incident wavefield of the form

$$\psi_I = \hat{\psi}_I \exp(-i\sigma t) \quad (2.29)$$

generates a scattered wavefield with the similar form

$$\psi_S = \hat{\psi}_S \exp(-i\sigma t), \quad (2.30)$$

where $\hat{\psi}_I$ and $\hat{\psi}_S$ are purely spatially varying functions. The complete wavefield is therefore separated into spatial and temporal variations as

$$\psi = (\hat{\psi}_I + \hat{\psi}_S) \exp(-i\sigma t). \quad (2.31)$$

Together with the dispersion relation for small amplitude disturbances of a linear Boussinesq stratification,

$$\sigma = \pm N \cos(\theta) \quad (2.32)$$

(Lord Rayleigh 1883), the boundary condition (2.28) imposes the constraint that wave energy scattered at a boundary must propagate with the same slope as that of the incident energy flux, though not necessarily with the same directional sense. In the characteristic coordinate description, the scattered wavefield can therefore be decomposed into a sum of the contributions propagating in each of the four possible directions. Notably, the angle of propagation of the the scattered wave energy is *independent of the slope of the boundary* with which the incident wave energy interacts and depends solely on the frequency of the incident wave.

Scattered waves are also required to satisfy the ‘radiation condition’, which stipulates that scattered energy must propagate *away* from the boundary (Sommerfeld 1949). More rigorously, this requires that a Fourier decomposition of the scattered wavefield can have no component with group velocity vector directed into the boundary. A wave component with this orientation could only exist if the system included sources of energy other than the incoming energy flux associated with the incident wave. The subtlety of this condition needs to be understood in order to prevent its misapplication. Baines (1971a) demonstrates the misuse of the radiation condition by its application to a wave group instead of its application to each of its individual plane wave Fourier components. Discussions on the enforcement of the radiation condition are also given by e.g. Gilbert & Garrett (1989) and Voisin (1991).

It remains to determine the partitioning of the incident wave energy between the various directions permitted by the conditions outlined above and the spatial form (*i.e.* spectral scatter) of the wavefields in each direction. This is controlled by the exact shape of the boundary. The following sections describe scattering behaviours in terms of parameters comparing the relative slopes and length scales of the incident wavefield and topography, as well as features of the topography such as its aspect ratio and the presence of sharp corners.

2.4.1 Reflection at a horizontal or vertical boundary: linear inviscid theory

The simplest reflection configuration to consider is that of a small amplitude monochromatic wave beam, characterised by a temporal frequency σ and a wavenumber k_I that is aligned with the characteristic coordinate ξ , reflecting inviscidly at an infinite smooth and impermeable horizontal

boundary (Lamb 1932; Phillips 1966). Each wave group propagating along such a beam is a superposition of different wavenumber components and hence such a group's fate after interaction with a boundary may be described, in the linear limit, as a direct aggregate of those of each of its wavenumber components. Conservation of frequency, and hence the angle θ determined by (2.32), together with the radiation condition constrains the reflected energy to propagate away from the boundary in two possible directions, each making an angle θ to the vertical. By continuity, the wavenumber aligned parallel to the boundary, \hat{k}_I , where in this case $\hat{k}_I = k_I \cos \theta$, must also be conserved on reflection so that $\hat{k}_R = \hat{k}_I$, where \hat{k}_R is the component of the reflected wavenumber aligned parallel with the boundary. Hence at a horizontal boundary, the magnitude of the wavenumber of the reflected wave oriented in the direction of phase propagation is $k_R = k_I$. The wavenumber component of the reflected wave directed normal to the boundary is therefore $\hat{m}_R = -\hat{k}_R \sin \theta = -\hat{m}_I$, where \hat{m}_I is the component of the incident wavenumber normal to the boundary. At first order, wave energy incident at a horizontal boundary is therefore predicted to reflect forwards, *i.e.* the reflected wave energy propagates with the same sense parallel to the boundary as does the incident wave energy. The reflected wave has the same frequency and wavenumber as the incident wave except that the reflected energy and wave phase propagate with the opposite sense to that of the incident wave with respect to the direction normal to the boundary. The wave phase of the reflected wave therefore propagates in the direction $-\eta$. Since the group velocity is conserved and the characteristic wavenumber is unchanged on reflection, energy densities are also maintained on reflection. If the incident wave is assumed to have plane wave form with maximum amplitude $\varepsilon \ll 1$ then the spatial variation of the incident and reflected waves are

$$\hat{\psi}_I = \varepsilon \exp(ik_I \xi) \quad \text{and} \quad \hat{\psi}_R = \varepsilon \exp(-ik_I \eta) \quad (2.33)$$

and so the complete wavefield can be written

$$\psi = \varepsilon [\exp(ik_I \xi) + \exp(-ik_I \eta)] \exp(-i\sigma t). \quad (2.34)$$

Similar arguments can be applied to characterise wave reflection at a vertical boundary. Linear inviscid theory predicts that the frequency and wavenumber (aligned with characteristic coordinates) of a wave reflecting at a vertical boundary are preserved except for a change in orientation of the wavenumber of the reflected wave, and hence also those of the phase and group velocities, relative to the direction normal to the boundary. The reflected wave phase therefore propagates along the direction η . The conservation of the properties discussed above is illustrated in figure 2.3 (a) and (b) by ray tube schematics of reflections at horizontal and vertical boundaries, respectively. The schematics use 'ray tracing', which is commonly used in linear geometrical optics to describe the behaviour of wave characteristics in slowly varying domains (e.g. Lighthill 1978). In this configuration, ray tracing correctly preserves both the wavenumber parallel to the boundary, *i.e.* for each characteristic incident (red lines) at the boundary there is exactly one reflected (blue lines)

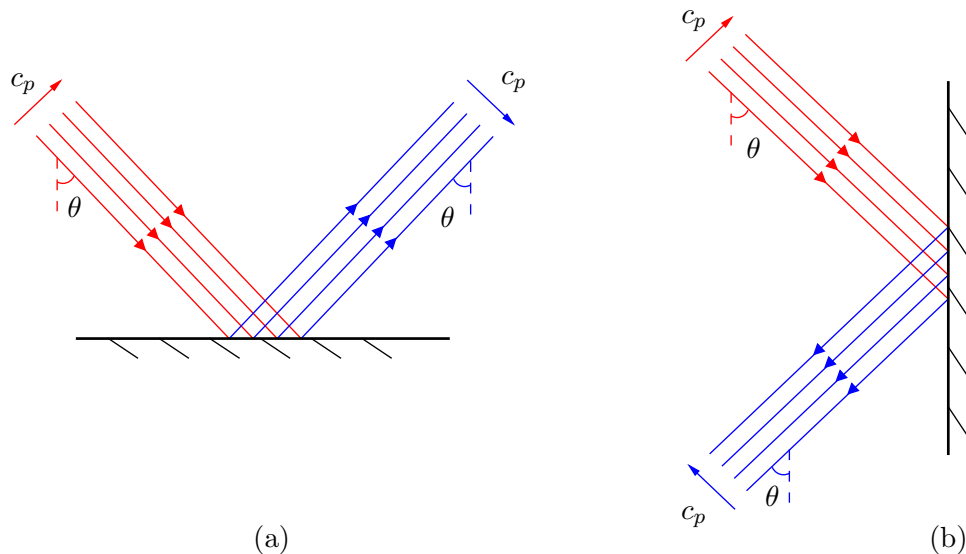


Figure 2.3: Schematic of wave beams reflecting at (a) a horizontal boundary and (b) a vertical boundary. Red and blue lines denote the lines of constant phase associated with incident and reflected wave beams respectively. Arrows positioned on phase lines indicate the directions of energy propagation.

characteristic there, as well as the angle θ that the wave characteristics can make with the vertical.

2.4.2 Reflection at an inclined boundary: linear inviscid theory

The linear inviscid reflection of internal gravity waves at a horizontal boundary was generalised by Phillips (1966) to that at a boundary inclined at an angle α to the vertical, where $\alpha \in [0, 90)^\circ$ (reformulations can be found in e.g. Wunsch 1969, Thorpe 1987 and Tabaei *et al.* 2005). Consideration of wave propagation in such a configuration introduces the parameter θ/α , which compares the relative slopes of the wave energy vector and the boundary. Reflection at an infinitely long smooth sloping boundary is referred to here as subcritical, supercritical and near-critical for the parameter ranges $\theta/\alpha < 1$, $\theta/\alpha > 1$ and $\theta/\alpha \approx 1$ respectively.

The linear inviscid reflection behaviour at a sloping boundary is again prescribed by the radiation condition, the conservation of frequency, and so slope θ of the wave energy vectors, and conservation of the components of the wavenumber in the direction parallel to the sloping boundary. An incident wave with wavenumber k_I aligned with the characteristic coordinate ξ has components aligned parallel and normal to the sloping boundary denoted by \hat{k}_I and \hat{m}_I respectively. Linear inviscid theory predicts that the wave energy reflects in one direction to a wave that is characterised by a single wavenumber, k_R , parallel to the characteristic coordinate η , where both the direction and wavenumber of the reflected wave are determined by the slope ratio θ/α (Phillips 1966). The

complete wavefield can therefore be written

$$\psi = \varepsilon [\exp(ik_I \xi) + \exp(ik_R \eta)] \exp(-i\sigma t). \quad (2.35)$$

The components of the reflected wavenumber aligned parallel and normal to the boundary are denoted by \hat{k}_R and \hat{m}_R respectively. The parallel component of the incident wavenumber is necessarily conserved on reflection so that

$$|\hat{k}_R| = |\hat{k}_I| = |k_I| \sin(\alpha + \theta). \quad (2.36)$$

For incident wave-boundary configurations where both the horizontal or vertical components of the incident group velocity vector are oriented in the opposite sense to those of the outward normal of the boundary, the component of the reflected wavenumber normal to the boundary is

$$\hat{m}_R = -k_I \sin(\alpha + \theta) \cot(\alpha - \theta). \quad (2.37)$$

The reflected wavenumber parallel to the coordinate η is therefore

$$k_R = -k_I \frac{\sin(\alpha + \theta)}{\sin(\alpha - \theta)}. \quad (2.38)$$

Otherwise, if either or both the horizontal or vertical components of the incident group velocity vector are mutually oriented with the outward normal at the boundary then the component of the reflected wave normal to the boundary is given by

$$\hat{m}_R = k_I \sin(\alpha - \theta) \cot(\alpha + \theta) \quad (2.39)$$

and the reflected wavenumber is given as

$$k_R = -k_I \frac{\sin(\alpha - \theta)}{\sin(\alpha + \theta)}. \quad (2.40)$$

Hence, linear theory predicts that each wavenumber component of a wave group reflecting at a smooth sloping boundary undergoes the same simple linear scaling. The wavenumber spectra of the wave group therefore undergoes a scaling in Fourier space. Since the magnitude of the group velocity is dependent on the wavenumber, an increase/ decrease of the wavenumber results in an increase/ decrease, respectively, in the energy density and hence the wave amplitude. This is discussed in more detail in chapter 4. Singularities of k_R exist for (2.38) and (2.40) when $\theta = \alpha$ or $(\theta + \alpha) \rightarrow 180^\circ$ respectively. The components of the reflected wavenumbers perpendicular to the boundaries given by (2.37) and (2.39) are zero for $(\theta + \alpha) \rightarrow 180^\circ$ and $\theta = \alpha$ respectively. These unphysical solutions occur when the incident wave energy approaches either perpendicular or parallel to the slope. The reflection regimes as determined by linear theory for different values of the slope parameter θ/α

and the break down of the linear theory are described here.

Subcritical reflection

Wave reflections occurring at a slope with $\theta/\alpha < 1$ are described here as subcritical. Ray tube schematics of two subcritical reflections are shown in figure 2.4 (a) and (b). The configuration

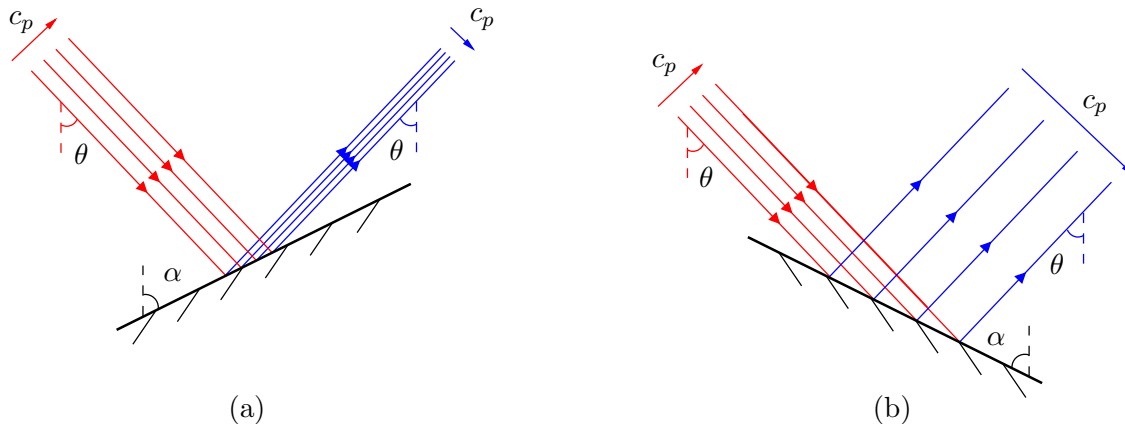


Figure 2.4: Schematic of wave beams reflecting at subcritical boundaries of different orientations. Arrows and colouring are defined as in figure 2.3.

shown in figure 2.4 (a) is of a ray tube incident on a boundary where the horizontal and vertical components of the outward normal at the boundary are oriented with the opposite sense to those of the direction of the incident wave energy propagation. The rays are squeezed, or ‘focused’, together into a narrower ray tube that is reflected forwards. Throughout this thesis, the term ‘focusing’ is defined as a process that collects energy from an incident wave over some length scale and emits it over a smaller length scale. The focusing leads to an increase both in the wavenumber of the reflected ray tube, as predicted by (2.38), and in energy density as a result of the associated decrease in group velocity and the confinement of the energy flux within a narrower tube. Since a propagating wave group is composed of a range of wavenumbers, the narrowing of the ray tubes associated with each Fourier component of the group results in its spatial contraction in the direction of phase propagation and an amplification of the along-beam fluid motion. The reflected wavenumber has the same horizontal orientation but opposite vertical orientation as that of the incident wavenumber.

The configuration shown in figure 2.4 (b) is of a ray tube incident on a boundary where the horizontal and vertical components of the outward normal at the boundary are oriented in the same and opposite senses, respectively, to those of the direction of the incident wave energy propagation. The rays are stretched apart, or ‘defocused’, and so define a broader ray tube that is reflected forwards. The defocusing leads to a decrease both in the wavenumber of the reflected ray tube, as predicted by (2.40), and hence also in energy density. The broadening of the ray tubes associated with each Fourier component of a wave group results in its spatial expansion in the direction of phase propagation and the enervation of the along-beam fluid motion. As in figure 2.4 (a), the

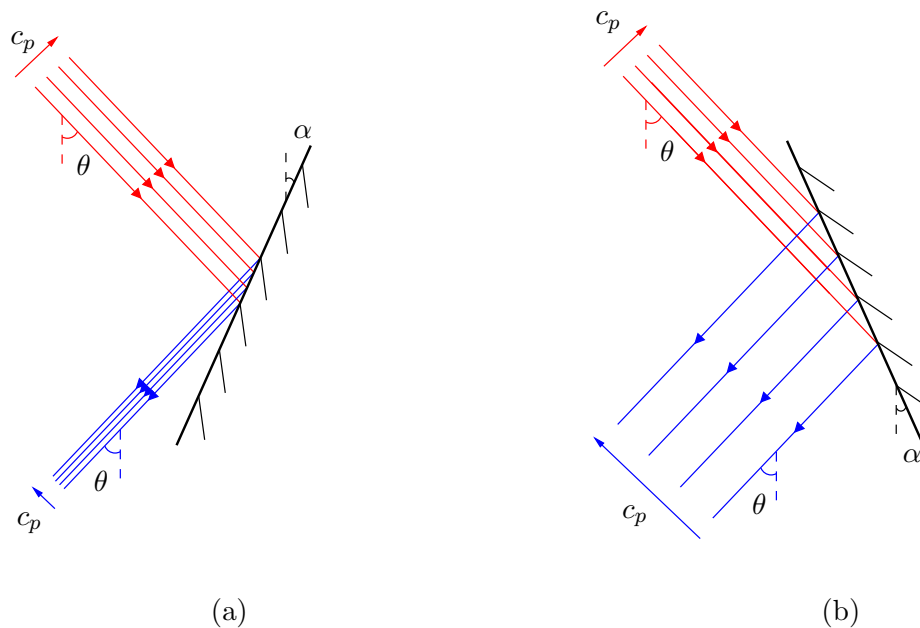


Figure 2.5: Schematic of wave beams reflecting at supercritical boundaries of different orientations. Arrows and colouring are defined as in figure 2.3.

reflected wavenumber in this configuration has the same horizontal orientation and the opposite vertical orientation to that of the incident wavenumber.

Supercritical reflection

Wave reflections occurring at a slope with $\theta/\alpha > 1$ are described as supercritical. Ray tube schematics of two supercritical reflections are shown in figure 2.5 (a) and (b). The configuration shown in figure 2.5 (a) is of a ray tube incident on a boundary where the horizontal and vertical components of the outward normal at the boundary are oriented with the opposite sense to those of the direction of the incident wave energy propagation. As in the reflection behaviour depicted in figure 2.4 (a) for the analogous subcritical configuration, the forwards reflected rays are focused. The wavenumber and energy density associated with the narrower reflected ray tube are therefore increased. Wave groups are compressed and so the amplitudes of the fluid motion are amplified. The reflected wavenumber has the opposite horizontal orientation but the same vertical orientation as that of the incident wavenumber.

The configuration shown in figure 2.5 (b) is that of a ray tube incident on a boundary where the horizontal and vertical components of the outward normal at the boundary are oriented in the opposite and same senses, respectively, to those of the direction of the incident wave energy propagation. The rays are defocused and the wider ray tube reflected forwards. The wavenumber and energy density are reduced and wave groups hence broadened by the reflection. As for the reflection shown in figure 2.5 (a), the reflected wavenumber in this configuration has the opposite

horizontal orientation and the same vertical orientation to that of the incident wavenumber.

Near-critical reflection

Wave reflections occurring in configurations with $\theta/\alpha \approx 1$, so that either of the characteristic coordinates ξ or η become aligned with the boundary, are described as ‘near-critical’. Under critical conditions, inviscid linear theory (Phillips 1966) makes unphysical predictions that the reflected wavenumber and energy density parallel to the boundary are infinitely large as the ray tube is compressed to an infinitesimal width and the reflected group velocity, calculated from (2.17), tends to zero (Wunsch 1969; Eriksen 1985). Observations and attempts made in analytical studies to resolve the fluid motion of the near-critical regime are discussed in more detail in the next section.

2.4.3 Reflection at an inclined boundary: nonlinear and viscous effects

The predictions of linear inviscid theory outlined in sections 2.4.1 and 2.4.2 have been replicated by other theoretical approaches, e.g. using linear geometrical ray tracing (Keller & Mow 1969) or those using Green’s function approaches to model the evolution of wave *groups*, which have finite extent in the direction of phase propagation, instead of tracing the individual plane wave components (Kistovich & Chashechkin 1993). The general trends of sub and supercritical reflection, such as the transfer between wavenumbers at the slope and the relative amplitudes of incident and reflected waves, have been confirmed in laboratory experiments (e.g. Sandstrom 1966; Wunsch 1969; Cacchione & Wunsch 1974; Thorpe & Haines 1987).

As critical conditions are approached, the linear analysis infers that the group velocity of wave energy incident at a sloping boundary tends to zero and the energy therefore becomes confined to the region of incidence. Experimental and numerical studies as well as field observations of these configurations have reported complicated and energetic fluid behaviour close to the boundary (e.g. Cacchione & Wunsch 1974; Eriksen 1982; Eriksen 1985; Thorpe & Haines 1987; Ivey & Nokes 1989; De Silva *et al.* 1997; Slinn & Riley 1998; Ivey *et al.* 2000; McPhee-Shaw & Kunze 2002; Nash *et al.* 2004; Venayagamoorthy & Fringer 2007). In particular, the high energy densities and shear in these regions promote nonlinear effects such as the generation of higher harmonics, which propagate energy away from the boundary, and flow instabilities, which develop into turbulence and cause mixing of fluid along the boundary. The primary reflected wave and higher harmonics are described here as ‘far-field’ fluid responses, whilst fluid structures forming along the boundary and the associated fluid mixing are described as ‘near-field’ responses. The partitioning of the incident wave energy between the far-field and near-field responses is determined by subtleties in the values of θ/α as well as the significance of viscous and buoyancy driven boundary layers.

The breakdown of linear inviscid theory in near-critical conditions together with the wave-field observations have therefore prompted many analytical studies (e.g. Thorpe 1987; Kistovich & Chashechkin 1993; Kistovich & Chashechkin 1995; Dauxois & Young 1999) investigating the influence of nonlinear, time dependent, viscous and nonBoussinesq contributions to the dynamics.

The unphysical singularities are found to prevail under inviscid linear nonBoussinesq (Kistovich & Chashechkin 1993) as well as in inviscid nonlinear (Thorpe 1987; Tabaei *et al.* 2005) treatments of the problem. However, the singularities have been successfully removed in analytical models by the inclusion of viscous diffusion (Kistovich & Chashechkin 1995; Dauxois & Young 1999) and also by consideration of the time dependence of the problem (Dauxois & Young 1999). The inclusion of viscosity introduces a mechanism for significant diffusion of wave energy. Kistovich & Chashechkin (1995) deduced that whilst they propagate within the boundary layer along a slope, wave groups experience exponential decay in amplitude, $\sim \exp(-z_\alpha/\delta_\alpha)$, where z_α is a coordinate oriented perpendicular to the slope and δ_α is the depth of the boundary layer given as

$$\delta_\alpha = \sqrt{\frac{2\nu \cos \theta}{N (\cos^2 \alpha - \cos^2 \theta)}}. \quad (2.41)$$

Elsewhere, the amplitude was found to decay according to $s_R^{-1/3}$, where s_R is the distance of propagation of the reflected wave energy away from the reflection region on the slope. Wave groups propagating in near-critical conditions are therefore subject to strong attenuation, since the wave group necessarily propagates within the boundary layer for a greater time in this geometry due both to the direction and the vanishing magnitude of the group velocity. The nonlinear scatter of incident wave energy amongst wave components of frequencies different to that of the incident wave and to the generation of turbulent motion and mixing in the boundary layer are discussed in the following sections.

Far-field dynamics: energy scatter to higher harmonics

Within the linear description of reflection at a sloping boundary, incident and reflected wavefields simply superpose in regions where they overlap. Under a nonlinear description, however, the wavefields interact at higher orders, with respect to the forcing amplitude ε , and generate additional wavefield components. The second and third order inviscid behaviours of wavefields were derived by Thorpe (1987)¹ from iterations of Phillips' (1966) linear solution. The nonlinear treatment highlighted resonance regimes occurring between the incident and reflected wavefields. In particular, the singularity of the linear solution at the critical value $\theta/\alpha = 1$ is not removed by the inviscid nonlinear analysis. Higher harmonics are generated by interactions between the incident, primary reflected and higher order reflected wavefields. The interaction of wave components defined by the frequencies σ_1 and σ_2 , with $\sigma_1 \geq \sigma_2$, and corresponding wavenumber components parallel to the slope \hat{k}_1 and \hat{k}_2 , for example, can produce higher harmonics with the frequencies $\sigma_1 \pm \sigma_2$ that have the parallel wavenumber components $\hat{k}_1 \pm \hat{k}_2$ respectively. In general, the wavenumber components normal to the boundary are determined in the same manner from sums and differences of those of the interacting waves. The exceptions are those harmonic components that are predicted specifically

¹Note that a variety of definitions of sub and supercritical are used in different studies. Results of these studies are presented here in terms of the definitions used in this thesis.

to ensure that the boundary and radiation conditions are satisfied at each order. In accordance with the dispersion relation, the higher harmonics are nonevanescant waves provided that their frequency is less than N and they propagate at angles $\theta_n = \cos^{-1}(n\sigma/N)$, where $n\sigma$ is the frequency of the harmonic expressed as an integer multiple n of the primary frequency σ . Thorpe's analysis indicates that an along slope Eulerian flow, corresponding to zero frequency, is generated at second order. Resonances are indicated by singularities in the nonlinear solution and occur at second order for reflections at shallow slopes, $\alpha > 81.6^\circ$, provided that the secondary harmonics are nonevanescant, *i.e.* $2\sigma < N$, and also at third order at slopes with $\alpha > 78.2^\circ$. The nonlinear behaviour of the wavefield becomes pronounced in near-critical or near-resonant conditions.

The generation of secondary harmonics were also predicted by Dauxois & Young (1999) and both secondary and tertiary harmonic generation were predicted by the nonlinear inviscid analysis of Tabaei *et al.* (2005). The presence of secondary (Peacock & Tabaei 2005; Gostiaux *et al.* 2006) and tertiary (Gostiaux *et al.* 2006) harmonic components have been confirmed in experimental studies as well as by numerical simulations (Javam *et al.* 1999; Tabaei *et al.* 2005). The energy associated with higher harmonic components of the scattered wavefield is in general a small proportion of the incident wave energy (e.g. Gostiaux *et al.* 2006). In accordance with the predictions of Thorpe (1987), the amplitudes of nonevanescant secondary harmonics were found to be most pronounced in near-critical conditions and to become substantially weaker for supercritical configurations in both numerical (Slinn & Riley 1998; Tabaei *et al.* 2005) and experimental (Peacock & Tabaei 2005; Gostiaux *et al.* 2006) studies. The directions in which energy associated with nonevanescant higher harmonic components propagates are determined by the geometry of the configuration. In particular, numerical simulations (Tabaei *et al.* 2005) and experiments (Peacock & Tabaei 2005; Gostiaux *et al.* 2006) have demonstrated the scatter of higher harmonic energy in the opposite vertical direction to that of the primary reflection for configurations that are supercritical with respect to the primary reflection but subcritical with respect to the secondary harmonic.

The accurate measurement of wavenumbers of reflecting wavefields has been restricted by the resolution of experimental and numerical techniques. However, the recent experimental study of Gostiaux *et al.* (2006) has been successful in analysing the wavenumbers both of the primary reflections as well as secondary and tertiary excited harmonics. The study isolated each harmonic component with application of a temporal filter to results of near-critical and supercritical reflections at a slope with $\alpha = 68^\circ$. Analysis of the results revealed that in the marginally subcritical ($\theta/\alpha = 0.96$) configuration, both secondary and tertiary harmonics were visible and were associated with wavenumbers that were twice and three times that of the primary reflection respectively (see e.g. Thorpe 1987 and Tabaei *et al.* 2005). In the marginally supercritical ($\theta/\alpha = 1.08$) configuration, however, the wave energy was scattered dominantly between the primary reflection and a tertiary harmonic, which was associated with a wavenumber *equal* to that associated with the primary reflection. The wavenumber selection for the tertiary harmonic was attributed to unexplained subtleties of the nonlinear interaction. The study also demonstrated evidence of an evanescent tertiary harmonic confined to a small region near the slope.

Near-field dynamics: Boundary layer structure and fluid mixing

The nature of the fluid motion in regions in close proximity to a boundary is described here. Fluid motion near a boundary is influenced by both buoyancy driven (e.g. Phillips 1970; Wunsch 1970; Woods 1991) and viscous boundary layers (e.g. Batchelor 1967). For the fluids considered here, buoyancy driven boundary layers are typically $\sim O(0.1)$ mm in depth and so, in general, their influence can be neglected. The effects of buoyancy driven layers in the context of undisturbed stratifications, however, are discussed further in section 3.7.

The effects of viscosity have been shown to be significant in near-critical configurations (Kistovich & Chashechkin 1995; Dauxois & Young 1999), where its inclusion surmounts the unphysical singular fluid behaviour predicted by linear inviscid theory. Shear motions and hence the viscous influence are enhanced in these configurations by the large gradients that occur in the direction normal to the boundary, resulting from the singular tendencies of the reflected wavenumber, together with the large energy densities, caused by vanishing group velocities. The degree to which viscosity is able to stabilise the singular critical fluid motion predicted by inviscid linear theory has been parameterised by the Reynolds number defined by

$$Re = \frac{\varepsilon^2 \sigma}{\nu} \quad (2.42)$$

(Ivey & Nokes 1989), where ε is a characteristic amplitude of the incident wave motion, σ is the frequency of the incident wavefield and ν is the kinematic viscosity. At small Reynolds number ($\sim O(1)$), the fluid motion along the boundary layer is stabilised by the viscous dissipation and the fluid responds to the strong shearing motions near critical conditions by the development of regular structures along the boundary, with only local generation of mixed fluid. The development of regular along-slope structures of vortices were reported in experiments with $Re \sim 2$ (Cacchione & Wunsch 1974). The vortex structure was most significant for near-critical and supercritical conditions, having the largest diameters when critical. The presence of vortices was also noted for some subcritical configurations with $\theta \not\approx \alpha$. Though they did not detail parameter values at which the subcritical vortices were observed, it is conjectured here that these occurred near resonance singularities of the nonlinear solution of Thorpe (1987). The second order resonance predicted for $\alpha > 81.2^\circ$ would have coincided with their experiments with slope angle $\alpha = 93^\circ$ for sufficiently low forcing frequencies. The boundary layer vortices observed in the near- and supercritical configurations of Cacchione & Wunsch (1974) were typically characterised by sizes smaller than the incident wavelength, with their size oscillating in phase with the wave propagation. Boundary layer fluid was mixed in the vortex cores through convective instabilities and subsequently propagated horizontally away from the boundary region into the stratification at the level where it was neutrally buoyant. The study also reported ‘fronts’ (characterised by a region of relatively large density gradients) generated by each wave that propagated up shallow slopes, with $\alpha = 75^\circ$, 93° , for near- and supercritical conditions as well as more pronounced upslope fronts exhibiting the generation of a vortex at the leading end of the front in subcritical cases. The collapse of the fronts induced local mixing along the boundary, with the mixed fluid intruding into the stratification

as described above. Mixing associated with breaking waves became more vigorous in subcritical conditions and for steeper slopes ($\alpha = 45^\circ, 60^\circ$).

The fronts observed by Cacchione & Wunsch (1974) are reminiscent of the upslope Eulerian flows predicted in the nonlinear inviscid analysis of Thorpe (1987) and similar structures have been described in other studies as a ‘surge’, a ‘bore’, or an ‘internal bolus’. The generation and evolution of internal boluses are considered in detail in Thorpe (1992) and the set of numerical studies by Venayagamoorthy & Fringer (2005, 2006, 2007). Fronts like those described by Cacchione & Wunsch (1974) were also observed in experiments with $Re \sim 20$ for $\alpha = 70^\circ$, $\theta/\alpha = 0.98$ (Thorpe & Haines 1987); at similar values of the Reynolds number for critical reflection at $\alpha = 60^\circ$ (Ivey & Nokes 1989); and with $23 \leq Re \leq 57$, $\alpha = 55^\circ$ for the marginally subcritical conditions $\theta/\alpha = 0.89$ (Dauxois *et al.* 2004). Dauxois *et al.* (2004) also reported fronts in the supercritical regime, $\theta/\alpha = 1.15$, where the fronts and associated mixing were more pronounced than in the subcritical case, developing convective instabilities at the head of the fronts. This effect was attributed to the geometrical confinement of the propagating energy between the slope and the incident wave. Whilst secondary harmonic generation was not discussed in detail in these studies, for the sake of completeness the possible angles, θ_2 , of propagation of these modes are given here. For the experiments of Thorpe & Haines (1987), Ivey & Nokes (1989) and in the supercritical case of Dauxois *et al.* (2004) values for angles of propagation of secondary harmonics can be calculated as $\theta_2 \approx 44^\circ, 0^\circ$ and 26° respectively. The discussion of the previous section suggests that these were most significant for the experiments with larger Reynolds number (*i.e.* larger forcing amplitude) and in near-critical conditions, so that perhaps the study of Ivey & Nokes (1989) was most influenced by this nonlinear effect. As an additional note, Thorpe (1999) predicts that fronts are also generated in configurations that are near-critical with respect to generated higher harmonic components of the wavefield.

The near-critical instability characterised by the structure of vortices along the boundary was not observed in the higher Reynolds number experiments of Thorpe & Haines (1987), Ivey & Nokes (1989) or Dauxois *et al.* (2004). Ivey & Nokes (1989) studied the transition between laminar and turbulent boundary layer responses for different Reynolds numbers by varying the incident wave amplitudes, and suggested that it occurred at $Re \sim 15 - 20$. In contrast to the structured boundary layer observed by Cacchione & Wunsch (1974), Ivey & Nokes (1989) reported the development of a turbulent boundary layer characterised by an average depth of 5ε in critical experiments with $\alpha = 60^\circ$ and at $Re \sim 170$. Transient events described as “backward-breaking rollers” were also noted, which perhaps suggest the structure of the boundary layer at Reynolds numbers intermediate between those associated with more regular boundary features for $Re < 15$ and the turbulent behaviour at $Re \sim O(100)$. The transition from front formation along a sloping boundary to a more turbulent boundary layer at larger Reynolds numbers was also seen in numerical simulations of critical reflections at slopes with $\alpha > 85^\circ$ by Slinn & Riley (1998). They observed a boundary layer depth of magnitude $\sim \lambda_z/2$, where λ_z is the vertical component of the incident wavelength. In all experimental and numerical studies, features of both laminar and turbulent boundary layers were consistently enhanced during fractions of the wave period that the incident wave phase propagated

up the boundary.

The instabilities and degrees of fluid mixing generated by near-critical reflections have been the subject of much debate. Some authors argue that the initial along-slope instability occurring for a near-critical reflection is shear driven (e.g. Eriksen 1985; Slinn & Riley 1998), whilst others have suggested a convective mechanism (e.g. Cacchione & Wunsch 1974; Thorpe & Haines 1987; Dauxois & Young 1999; Dauxois *et al.* 2004; McPhee-Shaw & Kunze 2002), with vortices along the slope overturning fluid layers (see sections 1.2 and 1.2.3). Dauxois & Young (1999) studied the temporal evolution of the boundary layer structure and deduced that the convective instability is initiated first. Their analysis predicts the initial development along the boundary of a structure of vortices, with alternating sign, that narrow in the direction perpendicular to the boundary inversely with time with the growth of oscillations in this direction. The growth is interrupted by the convective instability. Dauxois & Young (1999) also note, however, that the apparent prevalence of convective over shear mechanisms is subject to the definition of the Richardson number used. Ensuing turbulence generates mixed fluid that can propagate horizontally away from the boundary, forming thin intrusions into the surrounding stratification. Such intrusions have been observed in experiments and numerical simulations (e.g. Cacchione & Wunsch 1974; Slinn & Riley 1999) and are studied in greater detail by McPhee-Shaw & Kunze (2002). McPhee-Shaw & Kunze (2002) found that intrusions are generated by mixing caused by convective overturning within the boundary layer at lower Reynolds numbers and are characterised by vertical scales proportional to $\sim \cos \theta / \cos \alpha$. The regularity of the intrusions is lost as critical conditions are approached and intrusions are not generated at larger Reynolds numbers as the mixing becomes more homogeneous along the boundary.

This section has outlined reflection behaviours of wavefields incident at sloping boundaries inclined at a constant angle α to the vertical as a function of θ/α . The insufficiency of the parameter θ/α in the categorisation of reflection regimes has been demonstrated through the critical breakdown of inviscid linear theory and the reported near-critical enhancement of the nonlinear generation of higher harmonics as well as along boundary features that produce mixed fluid. Experimental studies have concluded that sub and supercritical behaviours are generally accurately predicted by linear theory provided that θ/α is sufficiently less than or greater than unity. The determination of the bounding values of θ/α of the near-critical regime is more complex and has not been analysed rigorously in previous studies. The following section discusses scattering behaviours at rough boundaries, for which θ/α is not a constant.

2.5 Scatter at rough boundaries

The previous sections, 2.4.1-2.4.3, described subcritical, supercritical and near-critical reflection behaviours of waves at sloping boundaries that were inclined at a constant angle α , where the boundaries were long with respect to the length scales associated with the wavefields. In the vernacular of the field of geometrical optics, reflection behaviour in these configurations is often termed

‘specular behaviour’ as a convenience for comparison with wavefields scattered from more complicated boundaries (e.g. Mied & Dugan 1976). This description refers to the directions, wavenumbers and amplitudes of a wavefield reflecting at a smooth slope for a given value of α and will be used throughout this thesis.

The present section considers wave interactions with boundaries that have spatially dependent height, $A_T(x)$, where x is the horizontal coordinate of the two-dimensional Cartesian plane (x, z) , and for which the angle made between the tangent to the boundary at a position x and the vertical, $\alpha = \alpha(x)$, is not constant. Consideration of such boundaries therefore introduces additional length scales as well as nonzero higher order derivatives of the boundary slope and the possibility of discontinuities of the boundary slope at features such as sharp corners. Unless otherwise stated, stream functions of the incident wavefields, ψ_I , referred to in this section, as in section 2.4, are assumed to have the form

$$\psi_I = \hat{\psi}_I \exp(-i\sigma t), \quad (2.43)$$

where the frequency σ is constant, $\hat{\psi}_I = \varepsilon \exp(ik_I \xi)$, and the maximum wave amplitude satisfies $\varepsilon \ll 1$. Wavefields interacting with rough boundaries are subject to the boundary and radiation conditions applied in sections 2.4.1 and 2.4.2 so that on reflection

1. the temporal frequency, σ , is conserved in order to satisfy (2.28), so that scattered wave components therefore evolve in time as $\exp(-i\sigma t)$;
2. the parallel component of the incident wavenumber along the boundary is conserved;
3. the normal components of incident and reflected waves must sum to zero;
4. all components of scattered wave energy must propagate away from the boundary according to the radiation condition.

At first order, scattered wavefields, ψ_S , are therefore represented by

$$\psi_S = \hat{\psi}_S \exp(-i\sigma t). \quad (2.44)$$

Recall that, as a consequence of the dispersion relation, the phase of components of $\hat{\psi}_S$ is hence restricted to propagate in either of the four directions η , $-\eta$, ξ or $-\xi$.

Slowly varying boundaries

A boundary is described as ‘slowly varying’ provided that the radius of curvature of the boundary, $R_T(x)$, is everywhere much greater than the length scales associated with the incident wavefield, where $R_T(x)$ at a point along the boundary is defined as the distance from the centre of curvature of that point. In such cases, plane wave assumptions and linear ray tracing analyses (e.g see sections 2.4.1 and 2.4.2) may be assumed to be appropriate in regions of the boundary where the angle parameter, θ/α , is not critical (e.g. Sandstrom 1966, 1972) since all components of the incident

wave group experience almost identical reflection conditions. Within the ray tracing description, the propagation paths of wave energy are identified with infinitesimally narrow rays that are aligned with the group velocity vector of the incident wave. At first order, the rays are assumed to respond at the boundary according to the specular reflection analogy corresponding to the local value of θ/α at the point of incidence. As a result, scatter at locally critical regions of the boundary, where the inviscid specular solution becomes singular, or at discontinuities, where the local slope is not defined, are not resolved. Wave energy incident on a slowly varying boundary is therefore predicted to be focused or defocused by varying degrees along the boundary (see figures 2.4 (a) and (b)). These effects correspond to regions of high and low wavenumber scatter respectively. Since the rays are assumed to obey specular behaviour, at each point along a slowly varying boundary wave energy is reflected in only one direction parallel to η , where the direction along this coordinate is specified by the relative orientations of the incident group velocity and the normal to the boundary at that particular point.

The efficiency of high wavenumber scatter of wavefields interacting with slowly varying slopes having concave and convex curvatures was studied both analytically, using ray tracing methods, and numerically by Müller & Liu (2000a,b). The studies found that convex boundaries were marginally more efficient at high wavenumber scatter than boundaries with constant slope, whilst the least high wavenumber scatter was observed for concave boundaries. As for boundaries with constant slope (sections 2.4.1-2.4.2), the scattering behaviours of wavefields at slowly varying boundaries in near-critical regions, *i.e.* $\theta/\alpha \approx 1$, of the boundary, the effect of nonlinear interactions between wavefields that overlap near the boundary and the influence of viscosity are not well understood.

Rough boundary categorisation

The main focus of this thesis is to determine the scattering behaviours of waves encountering rough boundaries. A boundary is defined as rough if the length scales of variation of $A_T(x)$ are comparable with the length scales associated with a given incident wavefield. In such cases, characteristics associated with an incident wave group are subject to different reflection conditions across the extent of the wave group. Wave groups can therefore be deformed significantly, rather than just scaled as is the case of reflection at a smooth slope, and the associated wave energy can also be scattered away from the boundary in a number of directions, rather than solely along the direction specified by specular theory. The complexity of scatter at rough boundaries becomes apparent when attempts are made to parameterise the problem. As a result, previous research has been restricted to a few specific idealised, generally linear, inviscid analytic cases with little or no experimental or numerical results to compare to predictions.

In addition to the angle ratio, θ/α , a rough boundary can be characterised by the parameter $\hat{A}_T \hat{k}_T$, where \hat{A}_T is the maximum vertical amplitude of the boundary and $\hat{\lambda}_T = 2\pi/\hat{k}_T$ is a characteristic horizontal lengthscale of the boundary variation. This length scale ratio therefore provides a description of the maximum aspect ratio of the boundary. For convenience, the scattering behaviour

at rough boundaries is divided in this section into three main categories (see Baines 1971a,b for similar categorisations) according to

1. boundaries that have continuous spatial derivatives and for which $\hat{A}_T \hat{k}_T \ll 1$;
2. boundaries that have continuous spatial derivatives and for which $\hat{A}_T \hat{k}_T \sim O(1)$;
3. discontinuous boundaries that contain features such as sharp corners at which the angle α is not defined.

2.5.1 Linearised boundary conditions

Boundaries for which $\hat{A}_T \hat{k}_T \ll 1$ and that have continuous spatial derivatives are described here as ‘linearised’ boundaries. This terminology is similar to that used in e.g. Baines (1971a,b) and is adopted for reasons described later in this section. Wave interactions with linearised, or ‘small aspect ratio’, boundaries are necessarily subcritical everywhere, with reflection behaviour in the limit $\hat{A}_T \hat{k}_T \rightarrow 0$ expected to tend to that occurring at a smooth horizontal boundary. The radiation condition therefore constrains the phases of scattered wave components to propagate along the characteristic directions $-\eta$ or $-\xi$. Linearised boundaries have been studied analytically and numerically by e.g. Longuet-Higgins (1969), Baines (1971a,b), Mied & Dugan (1976), Fels (1977,1978), Baines (1978), Rubenstein (1988) and Thorpe (2001). Although there are a number of experimental studies that research the *generation* of internal gravity wavefields by flow over rough topography, there are no published experimental studies known to the present author that report the scatter of a remotely generated wavefield that interacts with a rough boundary. The predictions for the scatter made in the studies listed above are presented here.

The scattering behaviour of wavefields incident at infinitely long sinusoidal, sawtooth and square-wave boundary roughness profiles, where the boundaries have no mean slope, was studied using inviscid linear ‘geometrical’ ray tracing by Longuet-Higgins (1969). As described above, the ray tracing approach predicts locally specular reflection behaviour of wave energy at each point along the boundary. Of the boundary shapes considered by Longuet-Higgins, only the sinusoidal profile can be described as a ‘linearised’ boundary for sufficiently small values of $\hat{A}_T \hat{k}_T$. Such a boundary is described here by the height function

$$A_T(x) = \hat{A}_T \cos(\hat{k}_T x). \quad (2.45)$$

Longuet-Higgins (1969) applied ray tracing generically, without the formal restriction of the boundary length scales and therefore predicted that, in accordance with specular theory, all wave energy incident at an exclusively subcritical sinusoidal boundary is forwards reflected so that the phase of the scattered wavefield, ψ_S , propagates along the characteristic coordinate direction $-\eta$. Since the angle α varies along the boundary and changes sign at the maximum and minimum elevations, incident wave energy therefore becomes focused along sections of the boundary that have positive

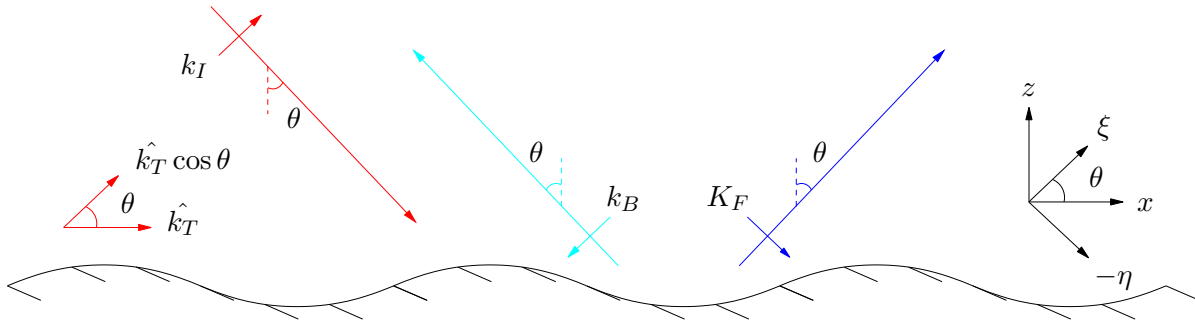


Figure 2.6: Schematic of wave energy scatter at a sinusoidal boundary with $\hat{A}_T \hat{k}_T \ll 1$.

slope and defocused in regions with negative slope (see figures 2.4 (a) and (b)). Hence the periodicity of the focusing and defocusing induced by the regular boundary profile imposes the length scales associated with the boundary variation onto the scattered wavefield.

A general solution for the inviscid scatter of wavefields incident at linearised boundaries was calculated by Baines (1971a). Baines determined an expression for the radiation condition (see section 2.4) within the characteristic coordinate system (ξ, η) associated with the incident wavefield. In particular, Baines solved the radiation condition by expanding to first order in the parameter $\hat{A}_T \hat{k}_T \ll 1$ (hence the description of ‘linearised’ boundaries) for wavefields scattering at sinusoidal topography described as in (2.45), with the additional condition that $k_I \hat{A}_T \ll 1$ and also allowing for nonzero mean slope of the boundary. In contrast to the predictions of ray tracing, this solution indicates that, while most of the incident wave energy flux is forward scattered in the specular direction with phase propagating along $-\eta$, the scattered wavefield can also contain a ‘back-scattered’ flux component that propagates *back along the direction of the incident wave energy flux*, i.e. the phase of the back-scattered component is aligned with the coordinate $-\xi$. The spatial component of the stream function describing the scattered wavefield can therefore be expressed as functions of ξ and η according to

$$\hat{\psi}_S = \hat{\psi}_B(\xi) + \hat{\psi}_F(\eta), \quad (2.46)$$

where $\hat{\psi}_B$ represents the back-scattered component and $\hat{\psi}_F$ represents the forward scattered component. The following discussion is restricted to configurations for which the boundary has zero mean slope, as illustrated in figure 2.6. The propagation directions and wavenumbers of the scattered waves are determined by the parameter $k_I c / \hat{k}_T$, where $c = \cot \theta$ (see also section 2.2.3), which compares the projected wavenumbers of the incident wave (coloured red in figure 2.6) and boundary variation. For simplicity, the projected boundary wavenumber \hat{k}_T / c is denoted k_T and in this notation the parameter $k_I c / \hat{k}_T$ is written k_I / k_T . The forward scattered energy flux predicted by Baines (coloured blue) is characterised by the set of wavenumbers denoted here by K_F , where each wavenumber is aligned with $-\eta$. K_F consists of up to three components. One of these is equal to the incident wavenumber k_I and a second is equal to the sum of the incident wavenumber and a wavenumber associated with the boundary variation $k_I + k_T$ (i.e. high wavenumber scatter). A

third forward scattered component is also possible that has wavenumber equal to the difference $k_I - k_T$ provided that $k_I/k_T > 1$ (*i.e.* low wavenumber scatter). The latter component becomes back-scattered (coloured cyan), however, for values of $k_I/k_T < 1$. There is no back-scattered flux predicted for values $k_I/k_T > 1$. The possible components of $\hat{\psi}_F$ therefore have forms

$$\sim \exp[-i\eta(k_I)], \quad \sim \exp[-i\eta(k_I + k_T)], \quad \sim \exp[-i\eta(k_I - k_T)] \quad (2.47)$$

and the possible back-scattered component, $\hat{\psi}_B$, has form

$$\sim \exp[-i\xi(k_T - k_I)]. \quad (2.48)$$

The energy fluxes associated with the sum components for $k_I/k_T < 1$ and $k_I/k_T > 1$, and difference components for $k_I/k_T > 1$ are $O(k_I^2 \hat{A}_T^2)$. However, Baines (1971a) notes that the back-scattered component could become significant beyond the limits of the linearised boundary condition since the associated energy flux is calculated to be $O(k_I k_T) \hat{A}_T^2$. The discrepancies between the calculations of Longuet-Higgins (1969) and Baines (1971a) result from the failure of ray tracing to satisfy the radiation condition at the boundaries considered.

A numerical study by Mied & Dugan (1976) extended the solution of Baines (1971a), described above, to calculate contributions from scattered components with wavenumbers of the form $k_I \pm nk_T$, where n is a positive integer. The numerical solution is therefore nonlinear in $\hat{A}_T \hat{k}_T$ but was shown to compare well for values of $\hat{A}_T \hat{k}_T < \cot \theta / 6$ with the first order approximation calculated by Baines (1971a) for the linearised limit $\hat{A}_T \hat{k}_T \ll 1$. In general, the numerical solution converged provided $\hat{A}_T \hat{k}_T < \cot \theta / 2$, and hence was restricted to wave-boundary interactions that were everywhere subcritical. In particular, the numerical results show strong agreement with Baines' solution for the back-scattered fluxes with $k_I/k_T < 1$ but also report a back-scattered flux for $k_I/k_T > 1$. Such components were predicted, though not formally calculated, by Baines (1971a) at second order and above, and correspondingly this contribution appears in the numerical flux calculations with values several orders of magnitude smaller than the first order predicted back-scatter.

Properties of the scattered wave components were investigated further with analytical and numerical approaches by Fels (1977) (see also Baines 1978 and Fels 1978). Fels calculates that scatter to nonspecular components is enhanced significantly for incident waves with vertical wavelength of magnitude $\sim \hat{A}_T$. Baines (1978) considers interactions of first order (in the wave amplitude) components of the wavefield at higher orders and predicts the generation at second order of a "steady streaming" that propagates horizontally away from the boundary. Another extension of Baines (1971a) is the work of Thorpe (2001) that expands the two-dimensional linear theory for boundaries of the form given by (2.45) to three dimensions. The study also considered higher order components and the possibilities for resonant interactions, which produce wave components of higher order in the wave frequency. In order for there to be resonant interactions between the different

wave components, the sum of the wavenumbers of the two interacting waves is required to satisfy the dispersion relation for a wave with frequency 2σ , with $2\sigma \leq N$. Conditions for resonance between the incident and specular components are as those described in section 2.4.3 for smooth sloping boundaries. Besides this, no other resonant interactions were identified involving the specular component. Scatter at sinusoidal topography was also considered by Rubenstein (1988), though this study will not be discussed here due to critical errors in calculations within the paper, highlighted by Müller & Xu (1992) and Thorpe (2001), which affect those details most relevant to this study.

2.5.2 Boundary variations comparable with wave scales: large amplitudes

Boundaries with continuous spatial derivatives that contain regions not satisfying the linearised boundary condition $\hat{A}_T \hat{k}_T \ll 1$ are classified here as ‘steep’ boundaries. In addition to the scattering behaviours exhibited by linearised boundaries, steep boundaries can support both critical and supercritical wave-boundary interaction regions. As a consequence, these boundaries can permit downward scattered wave components propagating with phase aligned with the characteristic directions η and ξ . The introduction of supercritical interaction regions can also allow regions of the boundary to be sheltered geometrically from the incident wave energy flux, described here as ‘shadow’ regions (see e.g. Baines 1971b and Sandstrom 1966, 1972).

Calculations from the geometrical ray tracing study of Longuet-Higgins (1969) apply also to scatter at *large amplitude* sinusoidal boundaries. For a given sinusoidal boundary, the angle α_s denotes here the minimum angle made between a tangent to the boundary and the vertical, which corresponds to the point of greatest slope of the boundary. Results of the ray tracing analysis for the case of $\theta/\alpha_s < 1$ were discussed in the previous section. In the case that $\theta/\alpha_s > 1$, then critical and supercritical interaction regions exist along the boundary. For a given incident ray, such interactions, which can produce downward directed fluxes, can result in repeated reflections with the boundary that may thereby produce back-reflected fluxes with phase propagating along $-\xi$. The proportion of the incident flux that is back-reflected, by repeated reflection, or forwards reflected, either at subcritical regions of the boundary or through repeated reflections, is highly dependent on the slope of the incident wave and the aspect ratio of the topography. Longuet-Higgins calculates that for increasing θ/α_s , the forwards transmitted energy coefficient, C_F , oscillates between 1 (*i.e.* the incident wavefield is completely forward scattered) and $\sin^{-1}(\tan \alpha_s / \tan \theta) / 180$ (*i.e.* the incident wavefield is partially back-reflected with coefficient $C_B = 1 - C_F$). However as noted above, though this provides a first geometrical based approximation for the scatter this analysis does not satisfy the radiation condition at the boundary, hence excluding the prediction of back-scatter through mechanisms other than repeated specular reflections, nor does it provide wavenumber analyses of the scattered wavefields or describe behaviour at critical regions of the boundary.

Scatter at a critical point of a convex boundary region

Scattering behaviours of wavefields incident at boundaries featuring a single critical point along a convex region of the boundary were calculated by Baines (1971b), using similar methods to those used in Baines (1971a). This scenario can be divided into two classes of configuration - those for which the incident group velocity vector is directed *parallel* to the tangent to the boundary at the critical point, and those for which the incident group velocity vector is *perpendicular* to the tangent at the critical point. Baines (1971b) refers to these configurations as diffraction and split-reflection respectively. In the case of diffraction, scattered waves are geometrically permitted to propagate with phases aligned with $-\xi$ (*i.e.* back-scattered components), with $-\eta$ (*i.e.* forwards scattered components), and with ξ (*i.e.* downward diffracted components). Since there is just one critical point, the portion of the boundary lying below the critical point is a supercritical interaction region and is shadowed from (*i.e.* not directly exposed to) the incident energy flux. Baines calculates that amplitudes of forwards scattered wave components tend to the form $1/|\xi|$ as the waves propagate away from the critical point. In accordance with specular behaviour, the wavefield becomes singular along the tangent to the critical point, *i.e.* in those scattering directions corresponding to phases aligned with $\pm\xi$. The singularity arises as high wavenumber components of the scattered field, with vanishingly small group velocities, are generated, so that energy remains in this region. The singular velocity fields of the back-scattered and diffracted wave components are found to differ from the incident wave velocity by the factor $(k_I/|\xi|)^{1/2}$. In particular, Baines notes the significance of this result, which indicates that this scattering behaviour is the same regardless of the radius of curvature of the boundary feature. For the specific case of a boundary that has symmetric form about the normal through the critical point, and which asymptotes to planes in the far-field, the diffracted wave is calculated to propagate a distance of about the incident wavelength away from the critical point.

In the case of split-reflection, the scattered wavefield becomes singular along the tangent to the boundary at the critical point, *i.e.* oriented with the directions of energy propagation of the forwards scattered and split-reflected components. In contrast to the diffraction configuration, the singular velocity fields in these directions are found to differ from the incident wave velocity by the factor $(R_T/|\eta|)^{1/2}$, so that the singularity is enhanced at more abruptly varying boundary profiles. Baines finds that for a boundary feature that has a form similar to that for the specific configuration discussed for diffraction, a back-reflected component is not generated.

Scatter at a critical point of a concave boundary region

Scatter in the vicinity of a critical point positioned along a concave boundary region was considered by Baines (1974), with minor amendments in Gilbert & Garrett (1989). In regions near the critical point the geometry only permits scattered components with phases aligned with $-\xi$, $\pm\eta$. Baines found that the critical singularity predicted for the convex boundary scatter was absent in the concave case and Gilbert & Garrett (1989) suggest that this is possible through the cancellation

in the region adjacent to the critical point of the equal and opposite phases of scattered components propagating along $\pm\eta$. However, a fully nonlinear numerical study by Legg & Adcroft (2003) disputed this cancellation mechanism on the physical grounds that, in general, nonlinear components of the wavefields prevent the symmetry required for this to be true. Legg & Adcroft considered the scatter at planar slopes, concave and convex sections of boundaries, where the ratio of the horizontal length scales of the wavefield and those of the topography was 2.5. The study investigates nonlinear features of the scattered wavefields and in particular reports upslope travelling bores for all boundary shapes, though with less prominence in concave configurations. These bores, present in subcritical, supercritical and critical boundary regions, were compared with those reported in studies of larger scale planar slopes, discussed in section 2.4.3. Legg & Adcroft deduce that bore generation occurs for values of the Froude number, Fr , greater than unity and defined by

$$Fr = \frac{\hat{U}_I}{c_p} \left(\frac{\sin(\theta + \hat{\alpha})}{\sin|\theta - \hat{\alpha}|} \right)^2, \quad (2.49)$$

where \hat{U}_I is the amplitude of the velocity field associated with the incident wave and c_p is the phase velocity of the incident wave.

2.5.3 Discontinuous boundaries: sharp corners

A region of a boundary that has a radius of curvature much smaller than the length scales associated with the incident wave is defined here as a sharp corner. Corners pointing outwards (*i.e.* into the fluid) or inwards (*i.e.* recessed into the boundary) are referred to here as convex and concave respectively. The previous section considered diffraction and split-reflection and the associated singularities occurring at critical regions of a steep boundary. In the region of a sharp corner, the slope of a boundary varies rapidly or can even become discontinuous. Hence, wave groups encountering such regions experience discontinuous reflection conditions across their span and this can impose singular behaviour in the scattered wavefield, which is permitted by the hyperbolic nature of the system. Configurations involving convex and concave sharp corners were considered using inviscid linear analyses by Longuet-Higgins (1969), Wunsch (1969), Hurley (1970), Robinson (1970), Hurley (1972), Fels (1977,1978) and Gilbert & Garrett (1989), and the limiting case of an infinitesimally thin ‘knife-edge’ was studied by Sandstrom (1966, 1969), Larsen (1969) and Robinson (1969).

Convex sharp corners

Scatter at a convex corner with finite radius of curvature was calculated by Sandstrom (1972) by application of the radiation condition to the scattered field predicted by specular reflection theory. Sandstrom deduced that specular theory was appropriate except in a region of high boundary curvature where a back-scattered flux, with phase directed along $-\xi$, was generated. Amplitudes associated with this flux were found to be most pronounced as the radius of curvature of the corner

decreased. Configurations where the boundary slope was discontinuous at a point, i.e. the boundary had an infinitesimally small radius of curvature there, were considered by Gilbert & Garrett (1989) using an extension of an earlier analysis by Hurley (1970) that, in particular, identified singular velocities along characteristics passing through a sharp corner. Gilbert & Garrett (1989) calculated the intensity of the back-scattered flux and found it to be a maximum in configurations where characteristics passing through the corner on either side each make the same angle with the boundary on their respective sides of less than 10° , with a gradual decrease in the back-scattered flux for larger values of this angle. However, this maximum only amounts to $\sim 1.5\%$ of the incident wave energy flux when averaged over a period and when the beam width is equal to one wavelength. The study conjectured that the predicted back-scattered flux generated in this sharp corner limit represents an upper bound to that generated at corners that have finite radius of curvature, such as those discussed in Sandstrom (1972). Gilbert & Garrett (1989) also suggest that the back-scatter at continuous sharp corners originates across the whole region of high curvature of the boundary and hence is likely to be less highly focussed than that emanating from a point of discontinuity.

Concave sharp corners

Linear geometrical ray tracing (e.g. Longuet-Higgins 1969) predicts that incident wave energy can undergo multiple, or even infinite repeated reflections within a concave region of a boundary. In configurations allowing the latter case, incident wave energy is reflected repeatedly towards the corner, or ‘trapped’, hence resulting in repeated focusing of the wave energy. The wavenumbers and so energy density therefore increase as the wave propagates towards the corner. In the inviscid limit, the reflection behaviour becomes singular near the corner with wavenumbers and energy density becoming infinitely large (e.g. Hurley 1970). In configurations for which specular theory predicts that wave energy is not trapped within the corner but instead reflects out of the corner after a finite number of reflections, a singularity was shown to exist along the characteristic that passes through the corner point by inviscid linear theory (Wunsch 1969). Wunsch (1969) demonstrates the removal of such singularities in particular configurations. However, this was not possible in configurations where the boundary on either side of the corner had critical slope. A singularity through the corner was also shown to exist in the linear inviscid analysis of Robinson (1970). Robinson (1970) considered nonlinear contributions to the fluid motion and found that their inclusion removed the singular behaviour, whilst specular predictions for the scatter remained valid away from the corner characteristic.

Scatter at a knife-edge

A limiting case of scatter at both a sharp corner and at steep topography is that of the ‘knife-edge’, which constitutes a infinitesimally thin vertical feature of finite height, along an otherwise horizontal boundary. Scatter at knife-edges have been studied by the linear inviscid analyses of Larsen (1969), Robinson (1969) and Sandstrom (1969). A knife-edge configuration, confined within a channel, was

studied in experiments and analytically with characteristic ray tracing by Sandstrom (1966, 1969). In this description, wave energy incident on the exposed side of the knife-edge reflects supercritically, *i.e.* the scattered phase propagates along η . Such downward scattered energy subsequently undergoes repeated reflections with the upper and lower boundaries of the channel. Incident wave energy passing over the tip of the knife-edge also undergoes specular reflections at the horizontal boundaries of the channel. In particular, Sandstrom predicted the formation of ‘shadow’ zones within the channel to the rear of the knife-edge, as a result of the geometrical ‘shading’ caused by the knife-edge from the incident wave energy. However, Larsen (1969) argues that such shadow zones are not possible since they could only occur through the deconstructive interference of two waves, with one of these having a nonzero group velocity component directed into the boundary so that the radiation condition is not satisfied. Larsen’s analysis of scatter at a knife-edge positioned within a channel used a normal mode approach with a correct application of the radiation condition. The analysis mapped particle motions throughout the channel. Particles moved rectilinearly in regions where the wave energy was forward transmitted beyond the knife-edge. The motions became more ellipsoidal in regions where wave characteristics overlapped, such as in reflections regions at the channel boundaries ahead of and beyond the knife-edge, ahead of the knife-edge where the incident and back-reflected wavefields overlapped and also in the region directly above the knife-edge itself. Larsen attributed an inverse square root singularity in the velocity field at the top of the knife-edge to be a result of the infinitesimal width of the knife-edge. The results of Larsen (1969) were supported by numerical simulations by Müller & Liu (2000a). Robinson (1969) also used normal modes to model the knife-edge configuration, representing the knife-edge as an array of vortices within a channel and with an exponential stratification. As in Larsen’s analysis, Robinson (1969) calculated there to be infinite velocities along wave characteristics passing across the top of the knife-edge. In particular, Robinson noted that the gradient of the density perturbation became comparable in magnitude to that of the background density field in the region at the top of the knife-edge and argued that the influence of both nonlinear dynamics and diffusion therefore become important there.

2.6 Summary

This chapter has outlined basic linear theory and properties of internal gravity waves, in particular in the context of their generation by an oscillating cylinder. Previous work on reflections of internal gravity waves at horizontal, vertical and inclined smooth slopes has been reviewed and the classification of reflections into sub, super and near-critical regimes defined. Scatter at small amplitude ‘linearised’ boundaries as well as at rough boundary features such as isolated critical points, sharp corners and knife-edges has also been described. In general, former consideration of scatter at rough boundaries has been restricted to linear inviscid analyses, with predictions remaining largely unverified by experimental or numerical results. However, the insufficiency of linear and inviscid treatments is clearly evident from the unphysical predictions of singular fluid motion that have

been made for configurations containing a near-critical region, or in the vicinity of rapid variations or discontinuities in the slope of the boundary. The role of nonlinear fluid motion and viscous or molecular diffusion in modifying this behaviour is not well understood, due in particular to the complexity in parameterising the stratification, wavefield and boundary.

This thesis aims to determine limits of linear inviscid theory in describing scatter at various boundary profiles with experimental results as well as assessing the significance of nonlinear and diffusive contributions to the scattering problem.

Chapter 3

Experimental Methods

3.1 Overview

This chapter outlines experimental procedures employed in the present research. Internal gravity waves were generated in the laboratory by small amplitude vertical oscillations of a cylinder in stable linear saltwater stratifications. The waves were scattered off topographies with flat, sinusoidal, sawtooth, square-wave and knife-edge profiles. Resulting wavefields and other related flow structures were visualised using synthetic schlieren and PIV (Particle Image Velocimetry) techniques.

Section 3.2 describes methods for making stratifications and measuring the resultant density profiles. Sections 3.3 and 3.4 give details of the synthetic schlieren technique used for visualisation of experiments and procedures followed to optimise image quality and minimise error. A description of the PIV technique used to view near-field structures of the wavefields (discussed in chapters 6 and 7) is given in section 3.5. Internal gravity wave generation is discussed in section 3.6 and the dampening of unwanted wave reflections is described in section 3.7. Experiment data from this study illustrating key features of wavefields is presented in section 3.7. The chapter concludes with a description of topographic profiles that were used in experiments and the parameters these introduce.

3.2 Stratification

3.2.1 Double-bucket method

Stable linear saltwater stratifications were formed in a tank with internal dimensions of length 2350 mm and height 570 mm. The front and rear tank walls were made of transparent acrylic sheets of thickness 10 mm held within an aluminium frame. After filling, the tank interior had an approximately constant width with height of value 150 mm.

Stratifications were created using the ‘double-bucket’ or ‘two-tank’ method (Fortuin 1960; see also Oster 1965 and Hill 2002 for further detail on double-bucket methods). The basic technique uses an apparatus consisting of two large connected compartments: the first containing a volume

of saltwater, and the second containing a volume of fresh water. The saltwater was prepared with a specific concentration of common salt (NaCl). Each of the compartments, or buckets, had a capacity of 0.13m^3 . Saltwater was pumped from the first bucket at a fixed flow rate and was added slowly to the surface of the deepening stratification in a manner such that there was minimal disturbance and mixing of the fluid below. This process was aided by directing the pumped fluid onto a sponge ‘float’ with polystyrene walls that sat on the surface of the stratification as it rose. The sponge diffused the momentum of the the saltwater as it seeped through. This ensured a consistent filling process and caused less mixing so that fewer discrete layers were formed within the stratification. As saltwater was pumped out of one side of the double-bucket, the pressure difference between the two buckets drove water at a nearly constant flow rate across from the fresh water side, hence maintaining hydrostatic equilibrium between them. Fluid in the saltwater bucket was continually mixed by a motorised pump in order to maintain a homogeneous concentration as it was diluted by the flux of fresh water in from the second bucket. Linear stratifications characterised by particular Brunt Väisälä frequencies may thereby be achieved by careful specification of the initial concentrations and volumes contained in both buckets. The solutions required were formed by precise dilution of saltwater (brine) with a typical density of about $1.18 \times 10^3 \text{ kg m}^{-3}$ (at 20.0°C) corresponding to approximately 24 percent by weight salt solution. The saltwater was formed under cooler conditions than those in the laboratory. On standing in the laboratory, the solubility of gases dissolved in the saltwater was reduced by the warmer conditions and the gases therefore came out of solution. There were also dissolved gases present in the tap water used, where the gas concentration had a seasonal variation. To reduce bubble formation within the stratified tank, the double-buckets were therefore left to stand for at least a day before stratifying to allow bubbles to nucleate and rise. In experimental contexts the bubbles formed could distort views as they developed on tank walls, as well as rising under buoyancy causing transient but significant disturbances to the stratification in their wake. Care was taken to submerge the water and brine hose jets whilst filling the buckets so that less air could be entrained into the solutions during this process. The delay period before stratification also allowed the temperature of the bucket solutions to equilibrate to that of the surrounding environment and so avoid double diffusive effects when the tank was filled. Whilst empty, the tank was levelled using spirit levels to ensure the base was horizontal and was cleaned and dried carefully for the next set of experiments. Any moisture left on the interior walls and base was found to significantly increase the rate of bubble nucleation after stratifying. Stratifications generally took between 1.5 – 2 hours to complete.

3.2.2 Stratification measurement

Measurements were made in order to confirm that initial density profiles, $\rho_0 = \rho_0(z)$, were linear with depth and thereby validate the method of stratification. The value of the reference density, $\hat{\rho}$,

was taken as the average of ρ_0 over the total depth, and the Brunt Väisälä frequency N given by

$$N = \sqrt{-\frac{\hat{g}}{\hat{\rho}} \frac{\partial \rho_0}{\partial z}}, \quad (3.1)$$

where $\hat{g} = |\mathbf{g}|$, was determined from the profiles obtained. Profile measurements were repeated at intervals over the course of experiments to determine how density profiles evolved in time.

Several methods were available for such measurements, the most direct being discrete sampling of stratifications. This involved slowly lowering a long narrow needle attached to a syringe into a stratification and taking small samples of the saltwater at different vertical levels. The density at each level could be determined using either a digital handheld refractometer or a density meter. The refractometer available (Atago Palette PR-101) was calibrated with distilled water and was then able to determine densities of just a few drops of each sample placed on a small back-lit prism by relating the sample's refractive properties to its density. Densities were given by the refractometer in the form of Brix percentages ($\pm 5 \times 10^{-2}$ Brix%) and could be converted to densities measured in the units kg m^{-3} by standard conversion tables. Slightly larger samples, greater than 1 ml, were required for measurement by a density meter. An 'Anton-Paar DMA 500' density meter was used which determined densities of samples to an accuracy of $\pm 5 \times 10^{-3} \text{ kg m}^{-3}$. Samples were injected into a small 'U' shaped tube within the density meter and, depending on the initial temperature of the sample, cooled or warmed to a temperature of $20^\circ\text{C} \pm 1 \times 10^{-2} \text{ }^\circ\text{C}$, controlled by a built-in 'Peltier' thermostat. The tube was oscillated and the density of the sample inferred from a relation between its mass and resonant frequency. Between each measurement residual traces of the previous sample were removed by air which was forced through the U-tube by a peristaltic pump.

The discrete nature of the sampling described above prevented fine scale vertical structure of density profiles being captured dependably. However, more continuous measurements of density with depth were possible by traversing a conductivity probe at a constant speed from the free surface of a stratification to the tank base. The probe produced a conductivity profile of the saltwater over the depth of the tank. Electrical conductivity of a saltwater solution is related to the concentration of salt-ions present, since these are the means by which charge is transferred throughout the fluid. After calibration, conductivity data therefore provided a measure of the density of the solution.

Although density meter readings were taken at a temperature of 20°C , a typical temperature of saltwater in the tank was $21^\circ\text{C} \pm 0.25^\circ\text{C}$. A discussion of the relationship between density, conductivity and temperature can be found in Leppinen (1997). For a fixed saltwater concentration, conductivity increases with temperature introducing a small scaling discrepancy between the measured conductivity and the density that it represents at 20°C compared with its density at the temperature of the fluid in the tank. However, for the purposes of this study, the density values were not of direct interest and it was sufficient that the measurements that were made of the vertical density gradients were precise and these inferred accurate values for the Brunt Väisälä frequency, N . Since the choice of a reference density, $\hat{\rho}$, was arbitrary, the scaling discrepancy was inconsequential

with respect to the density gradient and the corresponding value of N .

The conductivity probe was 720 mm long and consisted of an inner (2 mm diameter) and an outer (6.35 mm diameter) stainless steel tube. The tubes were insulated from one another and acted as an anode and cathode when they were included within an electrical circuit and a potential voltage difference setup between them. The circuit was bridged by an alternating current, so that the direction of polarisation changed periodically, to prevent electrolysis of the solution. The end of the probe was fitted with a short tapered tip of height 6 mm made of an insulating material Delrin. A narrow hole of diameter 0.3 mm connected the fluid at the nose of this tip to the interior of the hollow inner steel tube. The capacity of the probe tip was therefore calculated to be 0.4 mm^3 . Fluid could be sucked through the tube from the tip by setting up a pressure difference across the length of the tube, for example by using a large syringe to extract air from the probe. The probe was cleaned before use by syphoning a quantity ($\sim 10^{-3} \text{ m}^{-3}$) of water through the probe to ensure there was no crystallised salt retained within the tube. Water used in this process was first purified by reverse osmosis so that it was more receptive to solutes. The surface of the probe tip absorbed a small amount of fluid during its immersion, causing expansion of the tip material and a reduction in the size of the inner hole. Provided it was kept immersed, however, the tip could be considered nonporous and hence the hole size constant during subsequent traverses.

A linear traverse was fixed to the tank and aligned so that the conductivity probe was moved vertically. The traverse was automated via a computer and set so that the probe made downward transits of the undisturbed stratification at a constant speed. The speed at which the probe was lowered into the stratification was constrained by the residence time of fluid in the tip, t_r . The residence time was calculated as the ratio of fluid volume contained in the probe tip to the rate at which fluid is syphoned through the probe, Q . A volume of 12 mm^3 was syphoned over a time 150 s with the probe positioned at a depth of 250 mm below the surface of a stratification. Hence the average rate at which fluid was passed through the probe during this period was $Q = 80 \text{ mm}^3 \text{ s}^{-1}$ and so the residence time in the probe tip was calculated to be $t_r = 5.2 \text{ ms}$. The probe speed was therefore chosen to be 1 mm s^{-1} , which allowed fluid contained in the probe tip, corresponding to an earlier conductivity reading, to syphon completely through before the conductivity of fluid from a deeper level in the stratification was measured. During each pass, conductivity readings were taken every 1 s, producing several hundred data points over the depth of the tank.

Density profiles of stratifications were determined from conductivity data after careful calibration of the probe. Eight samples were prepared for the calibration over the range of the densities within stratifications. The conductivity probe was used to measure the conductivity of the samples and the conductivity readings were subsequently plotted against the corresponding densities of each sample as measured with the density meter. A constant of proportionality relating conductivity to density was calculated from the line of best fit (found using a least squares linear regression) to the data and used to determine the density profiles required. A typical example of this calibration is shown in figure 3.1. The line of best fit has a gradient of 0.29 and an extrapolated conductivity value of $0.13 C_O$ at the density value of 998 kg m^{-3} corresponding to pure water, where C_O is

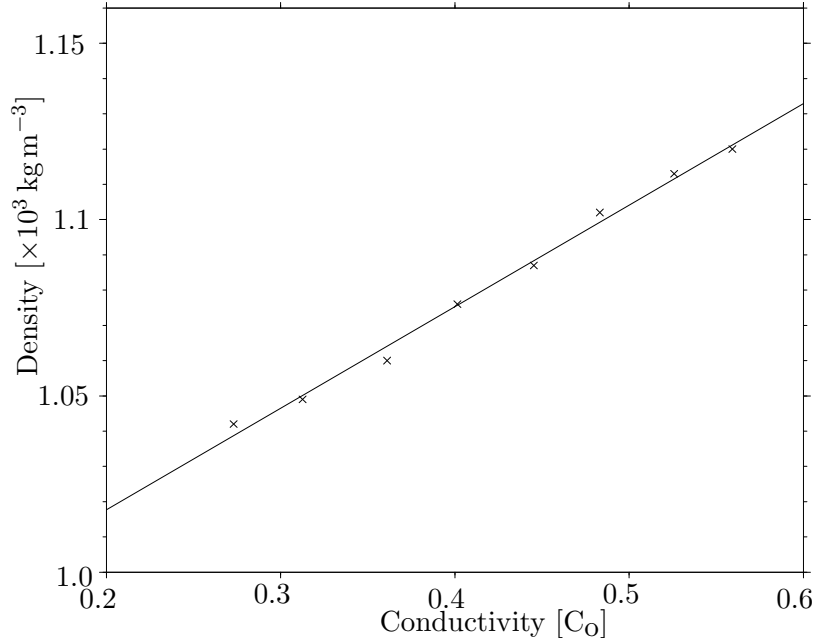


Figure 3.1: Calibration of conductivity probe for density values.

a unit representing conductivity. The prediction of a nonzero conductivity at this density from the linear extrapolation arises due to slight voltages being present across even the open circuit and also as a result of the nonlinear relationship between conductivity and density at densities close to 1000 kg m^{-3} . Figure 3.2 displays measurements of typical density profiles obtained from calibrated conductivity data. The red solid line shows the density variation with height measured one hour after stratification. This particular stratification represents an upper bound for the range of densities contained in stratifications used in this study. The black solid line, taken from a stratification that was a week old, represents a lower bound. The majority of stratifications used in this study had profiles close to this bound. The range of Brunt Väisälä frequencies used in this study were $N \in [0.68, 1.5] \text{ rad s}^{-1}$. At mid depths, the stratifications were characterised by a linear vertical density profile, with minor localised fluctuations. The interior stratifications generally improved with time, becoming closer to linear profiles as the fine scale structure was eroded slowly by molecular diffusion ($\sim 1.5 \times 10^{-3} \text{ mm}^2 \text{ s}^{-1}$) and lateral spreading, and hence vertical narrowing, of any localised mixed patches. A 12 hour period was allowed before experiments so that fine scale structure of the vertical density profile was smoothed by diffusion. A Boussinesq parameter, β_o , could be defined within the interior regions by

$$\beta_o = \frac{H_{\beta_o} N_0^2}{\hat{g}}, \quad (3.2)$$

where $\hat{g} = |\mathbf{g}|$, $H_{\beta_o} \approx 500 \text{ mm}$ was taken to be a typical vertical length scale of a stratification, and N_0 was a reference Brunt Väisälä frequency taken to be 1.5 rad s^{-1} so that $\beta_o \approx 0.11$. For the

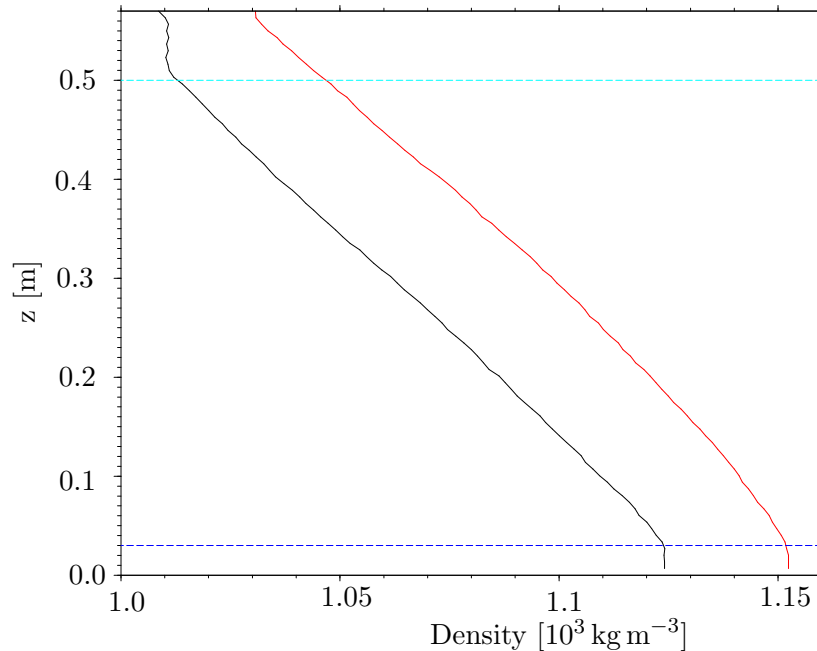


Figure 3.2: Vertical density profiles of stratifications measured using a conductivity probe (red and black solid lines). Both stratifications displayed yielded buoyancy frequencies of 1.5 rad s^{-1} . Dashed lines indicate upper and lower vertical limits of linear density profiles.

purposes of this study the Boussinesq parameter gave an indication of how symmetrical features of the fluid dynamics were in the vertical direction for a particular stratification. Values of $\beta_o \ll 1$ indicate strong symmetry.

The linear profiles did not extend to the base of the tank as a result of mixing that, despite precautions, inevitably occurred in that region during the filling process. With care, the layer could be minimised to an initial depth of $\sim 20 \text{ mm}$. The layer gradually thickened with time due to mixing and diffusion, and thereby narrowed the interior linear region of the stratification. Section 3.8 discusses strategies to cope with the effects of this layer on reflecting wavefields. A layer with lower vertical density gradients also formed at the surface of the stratification due to evaporation and mixing from removal of the sponge float used whilst stratifying or from insertion of the wave generator or topographic profiles (see sections 3.6 and 3.8). This layer was typically initially 10 mm in depth. As for the layer at the tank base, the surface layer extended deeper with time, affecting the choice of position of the wave generator and topographic profiles within the tank (discussed in sections 3.6 and 3.8) since focusing and reflection of waves occurred at changes in the vertical density profile.

3.3 Visualisation

The type and quality of information that may be obtained about the response of a stratified fluid to a disturbance is determined by the methods employed for the data extraction. Ideally, non-intrusive techniques are required that yield detailed qualitative and quantitative data about changes to the initial density profile over the entire spatial field of interest. Flow structures present in a fluid with a spatially varying density profile may be revealed by exploiting the refractive properties of light. A local change in the refractive index of a medium results in a deflection of a propagating light ray away from its original path and towards the induced gradient in the refractive index field. The dependency of the refractive index of light on the density of a transparent medium through which it propagates can therefore give rise to optical distortions of images viewed through the medium. In the terminology used in lens development, the inhomogeneities of the medium that result in such distortions are called schlieren.

3.3.1 Visualisation techniques

The linkage between changes in refractive behaviour of light passing through a fluid and inhomogeneities in the fluid density field has spawned a number of well-established visualisation techniques including shadowgraphy, schlieren, Moiré methods and interferometry. These all feature various schemes to filter light transmitted through a strategically lit experiment and thereby generate images from which the light intensity field can be related to specific flow properties such as the density field and its spatial derivatives. Shadowgraphy (e.g. Dvorak 1880¹) uses an approximately collimated light to produce a shadow image or ‘shadowgraph’ of an experiment that yields information about the second spatial derivatives of the density field. Classical schlieren (e.g. Foucault 1859 and Toepler 1864²) employs parabolic mirrors to collimate, then focus the light with the addition of a carefully positioned knife-edge that acts to filter light rays passing through the experiment. Angles of deflection of light rays by the experiment can be measured from the resulting schlieren images. The Moiré method uses a pair of masks consisting of parallel slits aligned in front of and behind the experiment to form patterns (Moiré fringes) of light. The patterns are indicative of the effective phase changes occurring between the masks due to the fluid motion between them (e.g. Weller & Shepard 1948). Schlieren and Moiré methods thereby yield first spatial derivatives of the density field. Interferometry, however, produces direct measures of the perturbed density field (Mach & von Weltrusbsky 1878). Interferometry uses a semitransparent mirror to split a beam of light between two directions of propagation. One of these beams passes through the experiment whilst the other is directed around it. The two beams are reconciled by a particular four (e.g. Tanner 1956, 1957; Zienkiewicz 1959) or six (e.g. Laws *et al.* 1982) mirror arrangement. Two interference

¹Although shadowgraphs are more commonly associated with Dvorak 1880, the basic principle was first used by German optician Johann Wiesel to assess eye cataracts as early as 1649 and was later implemented in a more recognisable form to visualise convection above candles and lamps (Hooke 1705).

²Optical, or ‘classical’, schlieren methods were first used in observations of candle flames by Hooke (1672), though experiments by Foucault (1859) and Toepler (1864) are more well known.

images are produced that indicate the phase difference between the beams caused by the passage of only one of the beams through the experiment. The visualisation techniques briefly outlined above are described in more detail in Merzkirch (1974), Rienitz (1975, 1997), Patorski (1993) and Settles (2001).

The data supplied by each of these techniques has been useful in various experimental studies of internal gravity waves. Visual demonstrations of internal gravity wave beams were first presented by Görtler (1943) using a shadowgraph and subsequently by the use of classical schlieren in the more well known experiments of Mowbray & Rarity (1967). Schlieren images produced by the latter experiments (and also e.g. Stevenson 1969) gave a qualitative insight into the development of the structure of wave beams with increasing distance from their source. Angles that beams made with the vertical could also be measured from the images and so the dispersion relation (2.16) was confirmed for the known forcing frequencies, σ , of oscillation of the internal gravity wave source. More quantitative results including measurements of beam widths and of amplitudes of the fluid displacement parallel to the wave beams were achieved by interferometry (Laws *et al.* 1982; Peters 1985; Merzkirch & Peters 1992) and the Moiré fringe method (Sakai 1990).

3.3.2 Synthetic schlieren

Although schlieren and Moiré methods are able to produce some useful quantitative data about fluid motion, their experimental arrangement is difficult and restrictive. Synthetic schlieren (e.g. Dalziel *et al.* 1998; Sutherland *et al.* 1999; Dalziel *et al.* 2000) is a digital technique combining elements of both methods to give data at the precision required for this study. The experimental layout is relatively simple compared with those used in the visualisations described above and it allows the user extensive control over the choice of resolution and field of view that is not as easily achieved by the alternative methods. Applications of synthetic schlieren have included the study of internal gravity wave beams generated by cylinders (e.g. Sutherland *et al.* 1999, 2000; Sutherland & Linden 2002; Onu *et al.* 2003) or by stratified flow over topography (e.g. Aguilar & Sutherland 2006; Aguilar *et al.* 2006; Sutherland & Aguilar 2006) as well as for visualising micro-scale fluid phenomena at high resolutions (Yick *et al.* 2007).

A schematic of a typical synthetic schlieren experiment layout used in this study is given in figure 3.3. A random pattern of transparent dots within an otherwise opaque black mask was fixed to a diffuse light source placed behind the stratified tank. The mask spanned the field of view seen by a digital video camera that was situated at a distance L_c in front of the tank. Light rays emitted through the dots and propagating along paths that passed through the tank and camera lens were incident on the image sensor of the camera comprising a rectangular array of ‘pixels’. Light rays incident on a camera pixel generated a charge with magnitude proportional to the light intensity.

It is necessary to formulate the relationship between the light intensity field associated with the images and the fluid properties in order to gain an insight into the fluid motion from images obtained of experiments. Perturbations to the density profile, $\rho'(\mathbf{x})$, of a quiescent stratification,

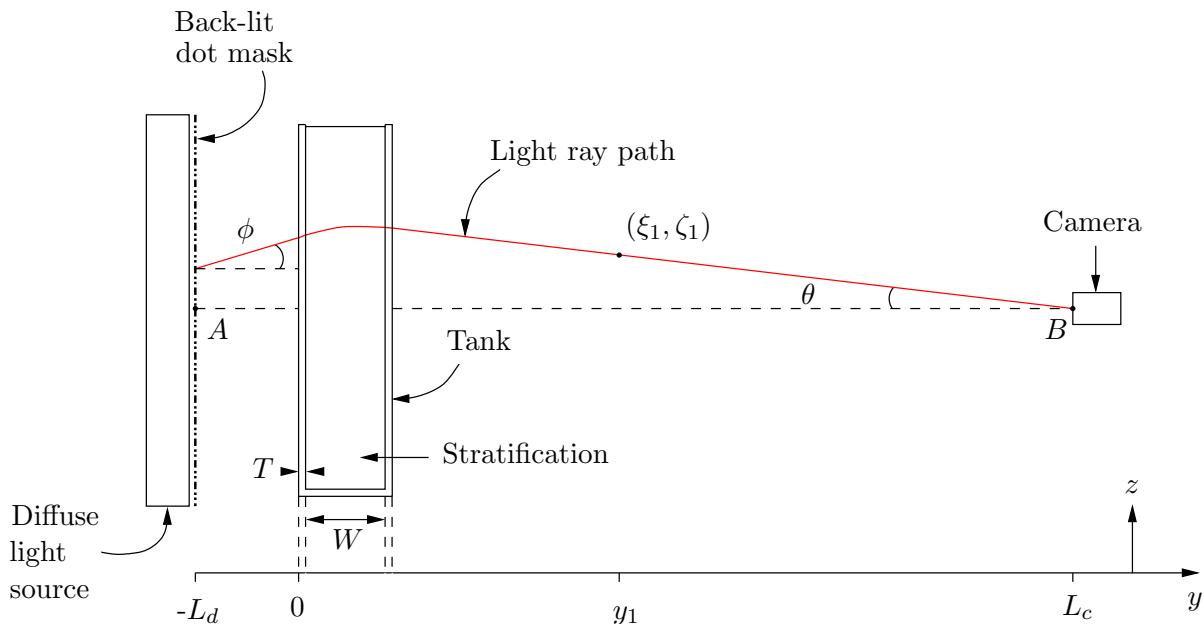


Figure 3.3: Synthetic schlieren experiment configuration.

$\rho_0(z)$, result in changes, $n'(\mathbf{x})$, to the refractive index field associated with the undisturbed or base state, $n_0(z)$. After transformation of the base state by a representative reference refractive index, \hat{n} , the refractive index field relative to the transformed base state, $\hat{n} + n_0(z)$, can be expressed as $n(\mathbf{x}) = \hat{n} + n_0(z) + n'(\mathbf{x})$. The relationship between perturbations of the density and refractive index fields is given by the formulation

$$\nabla n = \frac{dn}{d\rho} \nabla \rho = \beta \frac{\hat{n}}{\hat{\rho}} \nabla \rho, \quad (3.3)$$

where $\hat{\rho}$ is a reference density and the relevant value of β for saltwater is approximately 0.184 (Weast 1981).

Perturbations in the refractive index field resulting from changes in the fluid density profile deflect the path of light rays passing through the experiment and distort the view of the dot pattern compared with that seen by the camera when the stratification is undisturbed. Comparing dot positions before and during a disturbance therefore gives a measure of the deflection of the light rays caused by the disturbance. The deflection field can then be used to calculate perturbations of the refractive index field from which the causal density perturbations are inferred by the linear relationship given in (3.3). It therefore remains to relate a given deflection field to the corresponding perturbed refractive index field.

A light ray must satisfy Fermat's Principle of Least Action (1657), which requires that the path followed by a light ray passing through two points is the path that minimises the transit time rather than the path length. Hence the first variational derivative of the integral of the refractive index

along the light ray vanishes. The path of a light ray originating at the dot mask, $\mathbf{x} = (\xi(y), y, \zeta(y))$, is determined by the partial differential equations (Weyl 1954)

$$\frac{d^2\xi}{dy^2} = \left[1 + \left(\frac{d\xi}{dy} \right)^2 + \left(\frac{d\zeta}{dy} \right)^2 \right] \frac{1}{n} \left(\frac{\partial n}{\partial x} - \frac{d\xi}{dy} \frac{\partial n}{\partial y} \right), \quad (3.4)$$

$$\frac{d^2\zeta}{dy^2} = \left[1 + \left(\frac{d\xi}{dy} \right)^2 + \left(\frac{d\zeta}{dy} \right)^2 \right] \frac{1}{n} \left(\frac{\partial n}{\partial z} - \frac{d\zeta}{dy} \frac{\partial n}{\partial y} \right). \quad (3.5)$$

If the position of the light ray is assumed to have small spatial gradients in the direction perpendicular to the field of view as it progresses through the experiment, so that $d\xi/dy \ll 1$ and $d\zeta/dy \ll 1$, and the disturbance is assumed to be two-dimensional (*i.e.* $\partial n/\partial y = 0$), then (3.4) and (3.5) may be approximated by the uncoupled ordinary differential equations

$$\frac{d^2\xi}{dy^2} = \frac{1}{n} \frac{\partial n}{\partial x}, \quad (3.6)$$

$$\frac{d^2\zeta}{dy^2} = \frac{1}{n} \frac{\partial n}{\partial z}, \quad (3.7)$$

which may be solved to give the components of the ray path

$$\xi(y) = \xi_i + y \tan \phi_\xi + \frac{y^2}{2n} \frac{\partial n}{\partial x}, \quad (3.8)$$

$$\zeta(y) = \zeta_i + y \tan \phi_\zeta + \frac{y^2}{2n} \frac{\partial n}{\partial z}. \quad (3.9)$$

Deflections of light rays from their base state paths are seen by the camera as ‘apparent’ shifts in the positions of dots within the mask behind the experiment. Snell’s law may be applied to account for the deflections of light rays as they enter or leave the solid tank walls (Dalziel *et al.* 2007). The apparent translations, $\Delta\xi_s$ and $\Delta\zeta_s$ in the x and z directions respectively, are therefore related to the causal changes in the refractive index field for the experiment geometry described in figure 3.3 according to

$$\Delta\xi_s = -\frac{W}{2} \left(W + 2\frac{\hat{n}}{\hat{n}_a} L_d + 2\frac{\hat{n}}{\hat{n}_t} T \right) \frac{1}{\hat{n}} \left(\frac{\partial n'}{\partial x} \right) \quad (3.10)$$

and

$$\Delta\zeta_s = -\frac{W}{2} \left(W + 2\frac{\hat{n}}{\hat{n}_a} L_d + 2\frac{\hat{n}}{\hat{n}_t} T \right) \frac{1}{\hat{n}} \left(\frac{\partial n'}{\partial z} \right), \quad (3.11)$$

where \hat{n}_a and \hat{n}_t are the refractive indices of air and the tank walls respectively. Horizontal and vertical gradients in the perturbed density field, $\partial\rho'/\partial x$ and $\partial\rho'/\partial z$, are then given by (3.3) as

$$\frac{\partial\rho'}{\partial x} = -\frac{2}{W} \left[W + 2\frac{\hat{n}}{\hat{n}_a} L_d + 2\frac{\hat{n}}{\hat{n}_t} T \right]^{-1} \frac{\hat{\rho}}{\beta} \Delta\xi_s, \quad (3.12)$$

$$\frac{\partial \rho'}{\partial z} = -\frac{2}{W} \left[W + 2\frac{\hat{n}}{\hat{n}_a} L_d + 2\frac{\hat{n}}{\hat{n}_t} T \right]^{-1} \frac{\hat{\rho}}{\beta} \Delta \zeta_s. \quad (3.13)$$

3.3.3 Pattern matching

The spatial gradients of the perturbed density field were calculated by applying (3.12) and (3.13) to the displacement fields relating to a sequence of digitised images, collected during an experiment, and using the ‘pattern matching’ algorithm of the image processing package DigiFlow (Dalziel 2007). The pattern matching found the displacements of the dot pattern by dividing each image into a grid of ‘tiles’ or ‘interrogation windows’ and performing correlations of the positions of the dots between tiles in consecutive images. Accuracy and resolution of the calculated displacements could be controlled to a degree by the choice of tile sizes. In general, smaller tiles yielded displacement fields of higher resolution but also increased computation times. In all cases, the optimal settings for high accuracy and resolution were used. More detail on the pattern matching algorithm can be found in the DigiFlow user manual (Dalziel 2007).

Regions of an image that contain topography or other solid boundaries were excluded from the pattern matching calculations of the density perturbations by masking. Masks that set image values to zero at pixels representing a solid boundary were applied to each experiment movie prior to pattern matching. The masked points were subsequently ignored during the pattern matching, hence reducing artificially large gradients in these regions.

3.4 Image optimisation and accuracy

It was critical to ensure that data collected from experiments had suitable resolution and extent in space and time as well as having an accuracy that allowed the information retrieved from the data through processing to be reliable. Every effort was made in the present study to enhance the precision of measurements made and also to reduce or, where possible, eliminate possible sources of error. Experiment procedures associated with the visualisation and methods of evaluating and minimising error are discussed here.

3.4.1 Camera

The field of view and the spatial resolution of the camera chosen for a particular experiment depended on the information required from the experiment and also the limitations imposed by the camera, lens and the dot pattern selected. The camera used was a DALSA (Stop Action PT-41-04 M60-02E) camera, with a high resolution of 2352×1728 pixels. The pixelated digital images produced were saved on a computer and processed using DigiFlow (Dalziel 2007). The camera was mounted with a Canon lens having an adjustable zoom of maximum focal length of 210 mm. This focal length allowed the camera to be positioned at a typical distance of $L_c \sim 3$ metres in front of the tank whilst also maintaining a sufficiently large field of view so that the larger scaled spatial

data could be collected. A large value of L_c was preferred as this decreased parallax effects caused by light rays passing into the camera lens at nonzero angles, θ , relative to the optical axis $A - B$ shown in figure 3.3. Ideally, all light rays passing into the lens would satisfy $\theta = 0$, which can only be achieved when the separation distance between the camera and experiment, L_c , is infinite or by using a large parabolic mirror. However, provided θ is small then parallax effects may be ignored. The largest field of view used in this study spanned a region of approximately $681 \text{ mm} \times 500 \text{ mm}$. The corresponding values of θ_ξ in the horizontal and θ_ζ in the vertical directions were therefore calculated as 6.48° and 4.76° respectively. The camera's high pixel resolution allowed fluid features with spatial magnitudes that were a fraction of a millimetre to be captured at the largest field of view. Decreasing this field of view at a fixed value of L_c increased the spatial resolution of the images and decreased the effects of parallax.

A spirit level was used to ensure the camera was upright. A mirror was placed against the side of the tank and the camera positioned such that the image of the camera was in the centre of the view. This ensured that the camera lens, and so therefore the field of view at a given distance from the camera, was aligned parallel to the sides of the tank. After positioning and alignment, the camera was focused on the dot mask attached to the light source behind the tank. The light source contained four pairs of high frequency fluorescent tubes each with power 58 W and luminous flux (*i.e.* the perceived power) 5200 lm. A DigiFlow macro was used to aid focusing of the camera. The macro calculated the quantity

$$H = \overline{(P_{i,j} - P_{i+1,j})^2}^{\frac{1}{2}} \quad (3.14)$$

over all pixels where $P_{i,j}$ is the pixel intensity for the i, j^{th} pixel of the image sensor. Gradients between intensities registered by adjacent pixels were a maximum when the image was in sharp focus.

An image was considered to be good quality if, amongst other attributes but most importantly, the subject was in sharp focus and the image data representative of the light intensity field was spread over a broad range of values that was not clipped abruptly at the minimum or maximum values. A careful balance was required between the different camera settings, such as the aperture size, the gain value and the exposure time, in order to optimise the image quality.

Aperture dilations, controlling the size of the region through which light entered the lens, are measured by the 'f-number' or 'focal ratio'. For an aperture of diameter D_a and focal length of the camera L_f , the focal ratio, N_f , is given by

$$N_f = \frac{L_f}{D_a}. \quad (3.15)$$

A smaller aperture dilation (*i.e.* larger N_f) acted as a filter by reducing the range of possible angles that light rays entering the lens could make with the optical axis $A - B$. This filtering increased the distance over which the camera could remain focused, known as the 'depth of field' of the camera.

Synthetic schlieren visualisation required that the dot pattern and the experiment, separated by a distance L_d , were in focus simultaneously. Hence the aperture was optimally as small as possible, *i.e.* the focal ratio was as large as possible, so that the depth of field was maximised to include focused images of both the dots and the experiment. A smaller depth of field was required for smaller values of L_d . However, a reduction in L_d decreased the distance that light rays could diverge between the dots and the experiment and so made the apparent shifts in the dot pattern less pronounced and harder to detect.

The aperture dilation also determined the total quantity of light that entered the lens at any time. Too much light incident on the image sensor resulted in an overexposed image and hence a loss of resolution. Too little light caused an image to be underexposed and therefore have a smaller signal to noise ratio resulting in noisier processed images. A further constraint on the aperture size was the unavoidable bending of light (diffraction) at the edges of the aperture opening. This could cause slight blurring at the edges of images and became most significant for small aperture dilations. At larger dilations, almost the entire surface area of the lens was utilised and distortions or aberrations of the image could result from any imperfections in the lens itself. The choice of aperture size was therefore nontrivial but provided the image was neither over or underexposed, the sharpest focus combined with the greatest depth of view was achieved by smaller aperture sizes.

For an adequately lit experiment, the exposure of the image was affected by the exposure time and camera gain. Although the camera was capable of 61 frames per second (fps), images were captured at a rate of 25 fps. The exposure time of the image sensor during each frame affected both the sharpness and light intensity of the image produced. A typical time scale for changes to the fluid structure was $O(1)$ s since the upper frequency limit for non-evanescent internal gravity wave generation is the Brunt Väisälä frequency which had maximum values $\sim 1.5 \text{ rad s}^{-1}$ and hence a period of wave motion of 4.2 s. This corresponded to a temporal resolution of 105 frames per period. Images were exposed for the entire frame period of $1/25$ s. This choice of exposure time resulted in sharp images, without blurring due to fluid motion in that period, which had the greatest intensity of light for the given frame rate.

The gain was a factor by which the output from the image sensor was amplified to increase the brightness of images and so the range of intensity values. The increased intensity range improved the contrast between different intensity values. However, such an intensity multiplication also amplified the noise in the image, which was in part an artifact of resistance in the electrical circuitry of the camera and so, at least for this albeit minor contribution, was unavoidable in this study. Hence the gain could be increased to allow the aperture size needed for optimal image exposure to be reduced (and hence maximise the depth of field) provided the additional error introduced by the larger gain value was not significant.

A measure of the error and its dependence on the gain was found by taking a series of movies at different values of the gain with tracing paper covering the camera lens to diffuse the light entering the camera. The aperture was adjusted before recording at each gain setting so that each movie was taken at approximately the same basic light intensity. The root mean square light intensity was

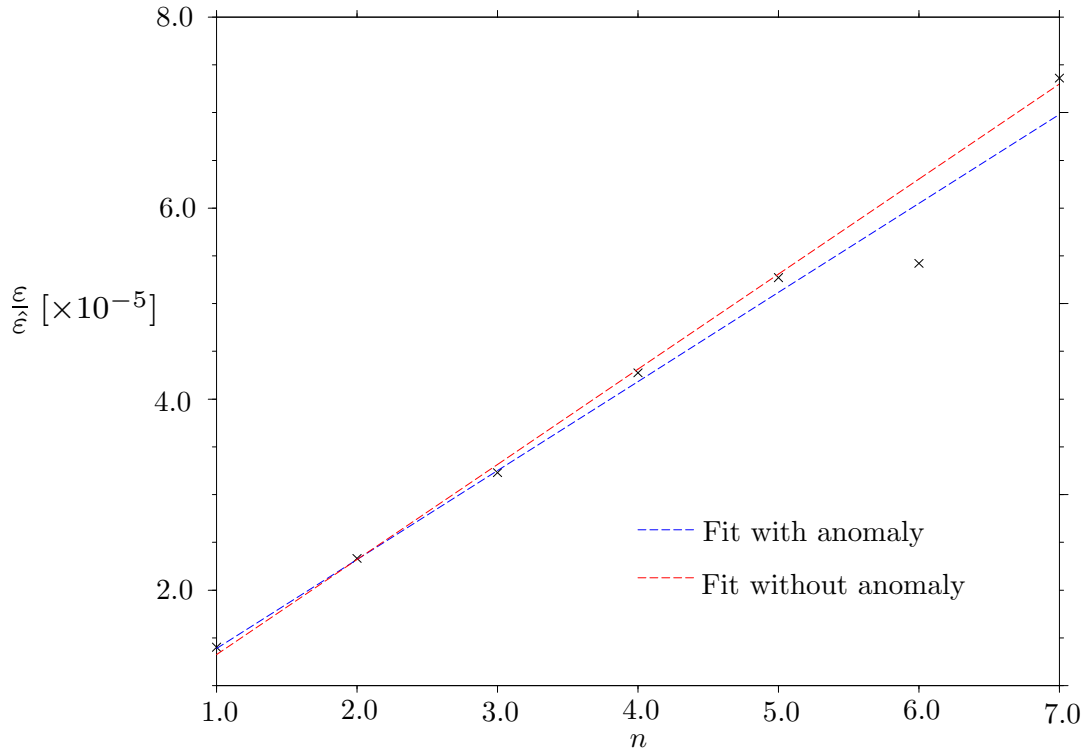


Figure 3.4: Error dependence on gain. Multiples n of unit gain.

calculated for each frame in a sequence of 400 and the standard deviation, ε , and mean, $\hat{\varepsilon}$, of the RMS values determined for each sequence. Figure 3.4 compares $\varepsilon/\hat{\varepsilon}$ at each gain setting. The error increases from the minimum value at 1.40×10^{-5} as the gain value is increased. Least square fits are also displayed for the data set with and without the anomalous point at 6 times the unit gain. This anomalous point is believed to be the result of the light source being inadvertently obscured at the time of experiment. The gradients of these fits are 9.32×10^{-6} and 9.96×10^{-6} respectively. Despite the relatively small increase in error with an increase in the camera gain, unit gain was used in all experiments.

3.4.2 Dot mask

Dot masks required for the pattern matching consisted of transparent circles (dots), of diameter D_d , which were randomly positioned within an opaque black background. Figure 3.5 (a) shows a schematic graph of the spatial distribution of the response of the camera optics and sensor to light passing through a transparent dot within such a mask. The blue line depicts the ideal response of the camera, having a value of 1 (*i.e.* full exposure) across the centreline of the dot and an intensity of 0 (*i.e.* zero exposure) anywhere across the surrounding black background. In reality, optical and electronic effects result in blurring of the dot so that the actual image sensor intensity profile is

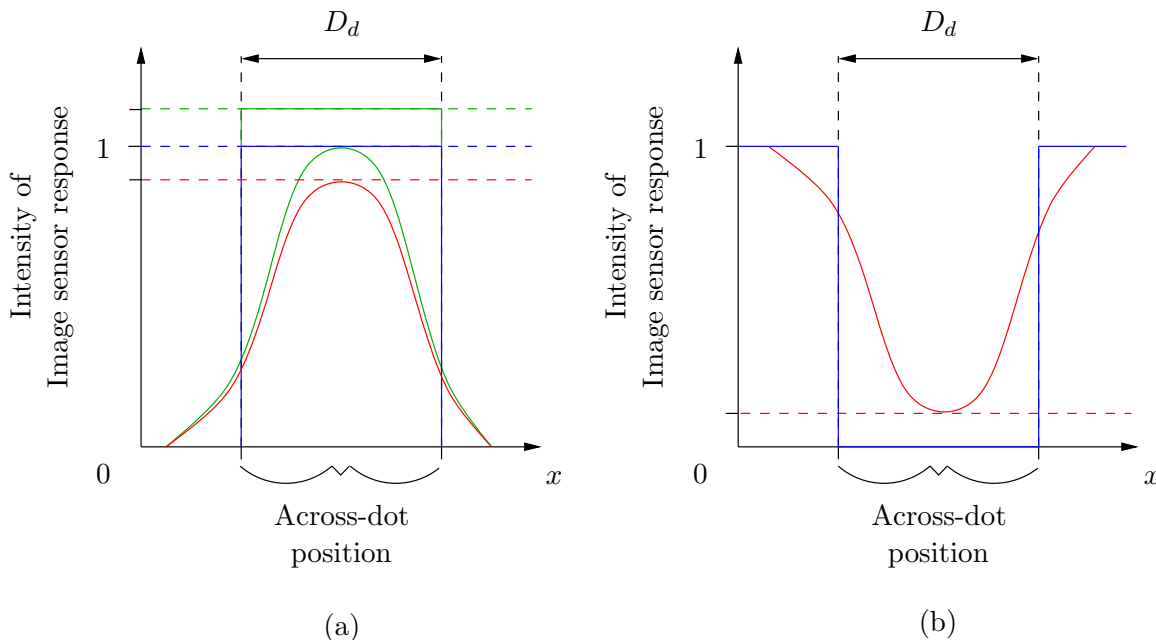


Figure 3.5: Schematic graphs of image sensor pixel intensities for (a) transparent dots within a black background and (b) black dots against a transparent background. Blue lines show ideal pixel intensities across a dot; red lines are representative of actual dot intensities due to optical blurring and electronic effects; green lines show dot intensities possible after manipulation of output from the image sensor.

better described by the red curve. The intensity for this curve does not reach the maximum and there is a nonzero intensity measured beyond the circumference of the dot. However, the camera gain can easily be adjusted to rescale the intensity profile, as depicted by the green lines, and so maximise the contrast between the dot and the black background. Intensities relating to the alternative choice of black dots within an otherwise transparent mask are shown in figure 3.5 (b). Again, the blue line depicts the ideal intensity profile of the response of the image sensor. This has a value of 0 anywhere across the black dot and a value of 1 elsewhere. The actual intensity profile after the influence of optical and electronic effects is described by the red curve, which again fails to reach the maximum contrast between the dot and the background. In this case however, unless the intensity value defined to be black by the camera can be shifted to a higher intensity corresponding to the actual minimum (dashed red line in figure 3.5 (b)) seen by the camera, then there is no way to improve the contrast between the dot and the background. Whilst most cameras cannot compensate for this, the DALSA camera used in this study had this capability and so the choice to use transparent dots within a black background was largely arbitrary. Some benefit was gained by using transparent dots within a black background, however, since the fraction of the light source covered by dots was about a quarter of that covered by the background (discussed below). Hence for this polarisation of the dot mask, less light was available to produce unwanted reflections from the tank walls, etc., within the experiment area and thereby introduce sources of error into

the visualisation.

Dot patterns were generated with PostScript files and printed onto transparencies using a high contrast printer. Transparencies were carefully attached together with clear tape with an overlap of less than 1 mm to create a large enough mask to cover the field of view required for a particular experiment. Dot masks were fixed to a large diffuse light source aligned parallel to the tank and positioned a distance $L_d = 250$ mm behind it. Since the light source was finite in size, the emitted light intensity inevitably decreased towards the edges of the source. The mask being used was therefore mounted at the centre of the light source so that it was back-lit as uniformly as possible.

The resolution of images produced was influenced by both the size of the dots and also the fraction of the total area of the patterned mask that they occupied. Diameters of dots, D_d , were necessarily large enough that sufficient light could be emitted through the mask and also so that the camera could be easily focused on the dots. Smaller dot sizes allow the motion of density surfaces of the viewed stratification to be resolved to smaller scales. However, a reduction in dot size also increased the sensitivity of the visualisation to changes in the environment external to the tank - with even nearby hand-clapping causing intensity ‘pulses’ in the images for dot sizes less than 1 mm. Measures used to minimise external influences on the experiment are discussed in section 3.4.3. A wide range of dot sizes were tested and it was found that optimally each dot occupied one or two pixels when viewed by the camera. The dot diameter used for the minimum field of view was $D_d = 0.45$ mm and that for the maximum field of view was $D_d = 0.53$ mm.

A random pattern of dots was used so that dots could be identified in terms of their position relative to neighbouring dots, making it clearer where each particular dot ‘moved’ as the density field was perturbed. Dot ‘movement’ within a regular pattern was more difficult to track since each dot in the pattern was not easily distinguished from the others. The visualisation technique was therefore more concerned with the apparent movements of *groups* of dots, rather than those of individual dots. The PostScript file used to generate the random dot patterns first produced a regular array of dots and then perturbed the position of each of the individual dots by random amounts in the horizontal and vertical directions, restricting its perturbation to within a radius of 0.6 mm from its position in the regular array.

The dots acted as data points and so the fraction of the random pattern occupied by dots was chosen to be as large as possible provided that the dots could be easily distinguished apart. It was more difficult to track ‘movement’ of the dot patterns at higher dot fractions since the number of data points was effectively decreased by dot clustering. Masks used in this study were specified in PostScript files to have a dot fraction, F_d , of 26 %. Figure 3.6 (a) shows a section of a dot mask as generated by the PostScript file and (b) an equal sized section of a digitised image produced by the camera of a typical dot mask and with typical camera positioning and settings. Despite their equal size, the two regions do not exactly coincide since the dot mask is positioned a distance ~ 350 mm behind the plane at which the camera is primarily focused. As a result, figure 3.6 (b) appears with a higher dot fraction and relatively smaller dots than those shown in (a).

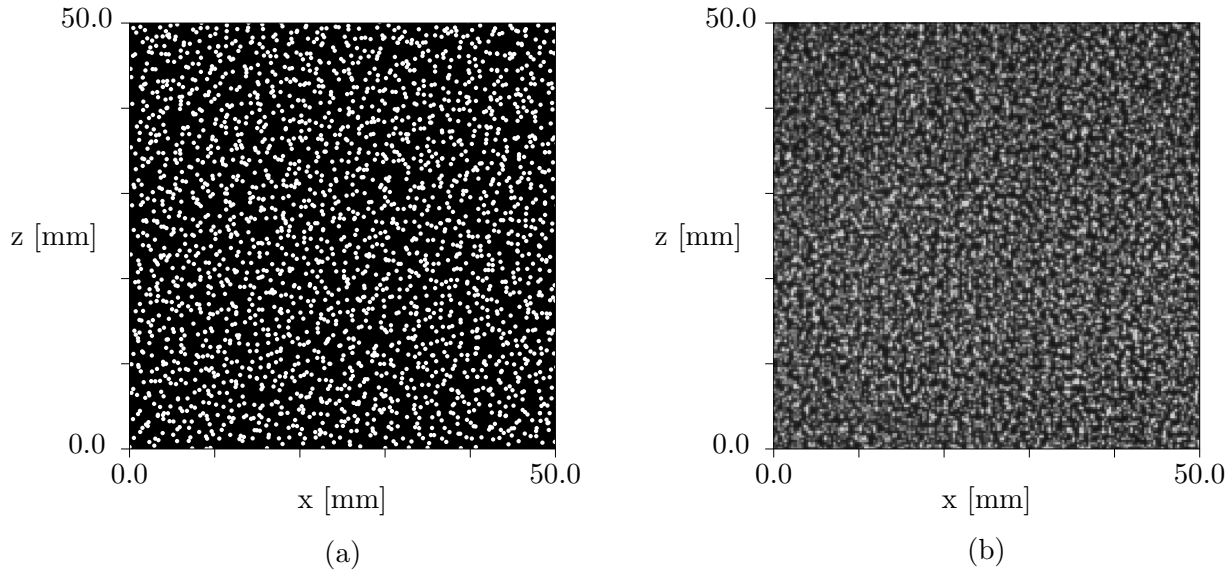


Figure 3.6: Synthetic schlieren dot mask sections measuring 50×50 mm (a) as generated by the PostScript file and (b) as viewed by the camera. Section shown in (b) is taken from an image of a typical field of view with dot diameters 0.53 mm.

Figure 3.7 shows pictures taken with a microscope¹ of dot masks with $F_d = 26\%$ and comprising dots with diameters, as specified in the generating PostScript files, of (a) 0.53 mm, (b) 0.45 mm and (c) 0.35 mm. The printer produced images by superposing many approximately circular dots of toner. The resolution limits of this printing method are clearly evident in the magnified images and the dots were typically printed with irregular perimeters and smaller diameters than specified. However, the dots were still distinct and approximately circular even at diameters below those used in this study (figure 3.7 (c)) and it is expected that the deformities of the dots produced during printing were not significant factors in this study.

3.4.3 Error reduction

Synthetic schlieren is highly sensitive to changes of the density field and so thermal convection within the environment outside the tank introduced a significant source of error to experiments. Several measures were therefore taken to reduce inevitable temperature or pressure fluctuations near to the camera. Heavy black curtains isolated the entire experiment area from computers, people and doorways or windows. Experiments were also automated to run during the nighttime when the surrounding environment was less active and the heating was turned off (starting after several hours of inactivity in the laboratory). As an additional precaution, a tunnel of diameter 635 mm and length 1100 mm was positioned between the experiment and camera with one end sealed off except for a few millimetres around the circumference of the camera lens. This gap isolated the camera from any movement of the tunnel. The tunnel isolated the lens from density changes occurring in the immediate vicinity of the camera, which had the strongest influence on results due to their

¹Microscope photographs were kindly taken by J-W. van de Meent

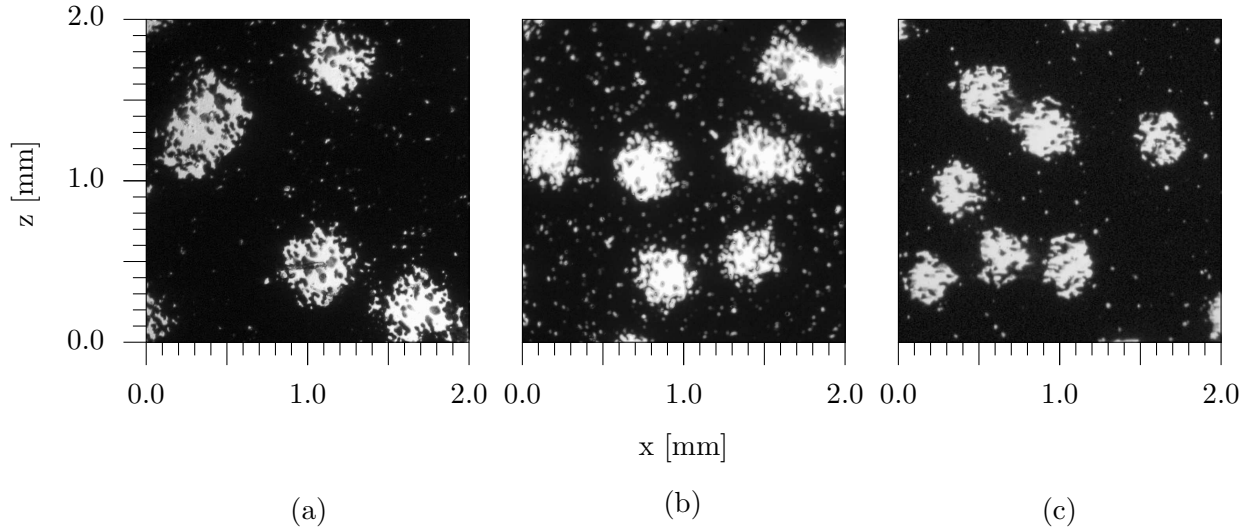


Figure 3.7: Close-up pictures of dot masks with $F_d = 26\%$ and dots having PostScript specified diameters of (a) 0.53 mm, (b) 0.45 mm and (c) 0.35 mm.

proximity. In particular the lens was largely shielded from the body of the camera that acted as a heat source.

Another source of error was that of light rays entering the camera lens that had followed paths reflecting off surfaces within the tank and laboratory. Surfaces capable of producing reflections detectable by the camera were blacked out with curtains or matt black paper, and the interior of the camera isolation tunnel was sprayed black. Other sources of light besides the back-lit mask were also removed where possible. This included switching off overhead lights and blacking out parts of the light source not covered by the dot mask. Heat generated by the light source was also directed away from the experiment by strategically positioned card, even to the extent of constructing chimney like structures at the open ends of the light source. As a result of this care, there was a significant improvement in the general quality of movies recorded from experiments. This was qualitatively observed by the flow features becoming more distinct in images. Also, prior to the adoption of the various practices described above, typically one in every three experiments had to be repeated due to significant inconsistencies in the surrounding environment caused by doors shutting, close proximity of people or air temperature fluctuations caused by open windows and heating. However, following the adoption of these error reducing practices, it was rarely necessary to repeat experiments because of poor or interrupted visualisation.

3.4.4 Reference image and world coordinates

Processing of images of a perturbed stratification using pattern matching (see section 3.3.3) required a reference image of the undisturbed stratification in order to determine the apparent translations of the dots as a result of disturbances of the stratification. Ideally, the translations calculated by

the pattern matching represented changes in the refractive index field caused exclusively by perturbations, ρ' , to the linear stratification, ρ_0 . It was therefore essential that the reference image was recorded when the laboratory conditions, such as the temperature of the surrounding environment, and the unperturbed component, ρ_0 , of the density profile of the stratification were as close to those present during the course of the experiment. Any dynamic fluid structures present whilst reference images were captured became unavoidably included in all subsequent processing. Reference images were therefore taken immediately before experiments. Localised density fluctuations in the laboratory air were inevitable during the recording of reference images and added noise to the gradient fields produced by the pattern matching. Various methods were tested for collecting reference images that had minimal noise. A single recent reference image collected under controlled conditions was preferred for use in the pattern matching over the use of an average of several such images. Processed images tended to be blurred when an average of a set of reference images was used for the pattern matching due to the high frequency nature of the noise present.

DigiFlow permitted the association of a coordinate system with recorded images so that pixel positions of points on an image could be identified in terms of a ‘real world’ location. In order to apply a coordinate system to a particular set of experiments, an additional image was recorded of a grid marked at 10 mm intervals in the horizontal and vertical directions and attached flush to the tank wall closest to the camera in the relevant field of view. The image of the grid was then used to specify the real world position of five or more points on the image, preferably chosen to fix the positions at the extrema of the field of view. A linear transformation was subsequently performed by DigiFlow to infer the coordinate system over the entire image. Such a coordinate system allowed meaningful length and angle measurements to be made from recorded images as well as compensating for any slight inaccuracies in the camera alignment.

3.4.5 Error estimate

A sequence of schlieren images were recorded of the tank filled with water as a means of estimating errors associated with the visualisations caused by fluctuations in daytime laboratory conditions. The movie was taken with typical camera settings and positioning and with most of the error controls detailed above employed. The movie was, however, taken during the daytime in a moderately active laboratory environment. Measurements of root mean square (RMS) values of the perturbed buoyancy field corresponding to changes in the laboratory conditions are presented in figure 3.8. The values calculated are two orders of magnitude smaller than typical measurements obtained of the dominant wavefields in experiments. These error estimates may be considered an upper bound to those associated with actual experimental runs that were performed in more stable nighttime conditions and under more rigorous controls.

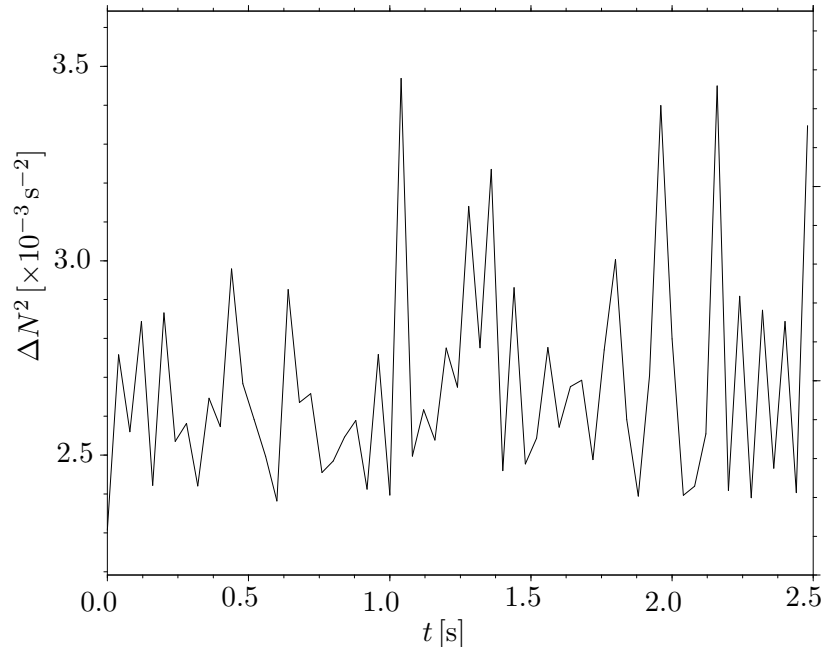


Figure 3.8: Root mean square values of the perturbed buoyancy field for a sequence of images recorded of fluctuations in the laboratory environment in daytime conditions.

3.5 Particle Image Velocimetry (PIV)

As discussed in section 3.3.2, synthetic schlieren allowed direct calculation of gradient fields of density perturbations to the stratification. It was possible to use these fields to calculate the perturbed horizontal and vertical velocity fields according to

$$u' = \frac{1}{N^2} \int (N^2)_t dx, \quad w' = \frac{1}{N^2} \int (N^2)_t dz \quad (3.16)$$

(Sutherland *et al.* 1999). Calculation of the velocity fields using (3.16) was valid provided that the background stratification was both incompressible and linear, and the wave motion controlled by dominantly linear processes (see Wunsch 1985 for related discussions). These conditions were not guaranteed in the vicinity of topography. Wave focusing by topography as well as the interactions between incident and scattered wavefields could enhance energy densities and hence the amplitudes associated with the waves. To a lesser extent, the necessary curvature of isopycnals in narrow layers near boundaries and the development of mixed layers also prevented accurate application of (3.16).

Particle image velocimetry, or PIV, is an alternative technique that yields direct information about the fluid displacement and velocity fields. PIV has been used in other experimental studies of stratified fluids that focused on wave generation by towed or oscillating cylinders (e.g. Merzkirch & Peters 1992; Zhang *et al.* 2007) or by a spatially periodic wave generator (Gostiaux *et al.* 2007). PIV visualisations have also been used to examine the interactions of existing waves with various

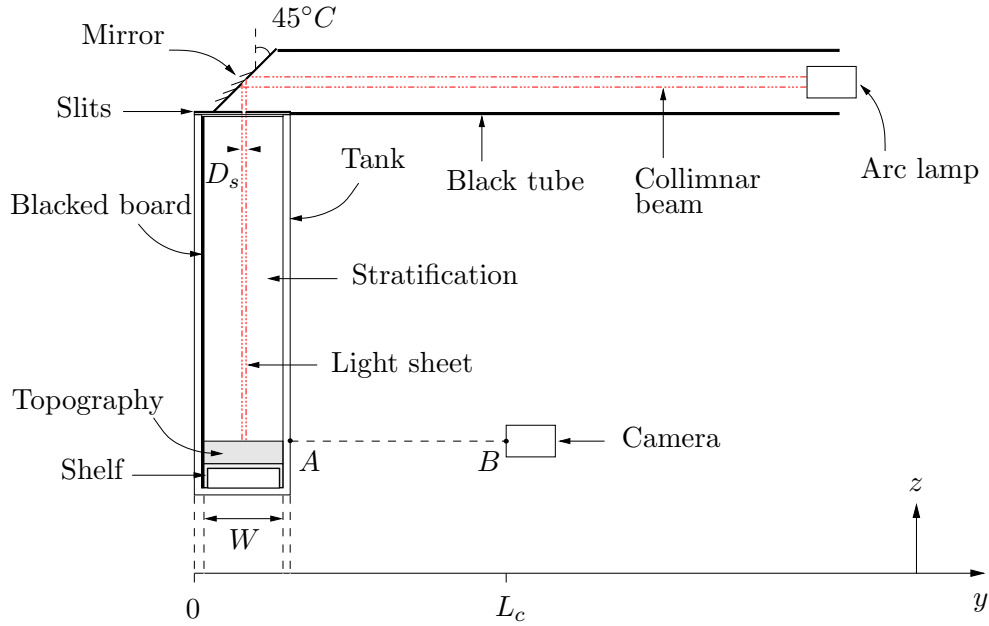


Figure 3.9: PIV experiment setup.

topographies (e.g. Gostiaux & Dauxois 2007). PIV was used in the present research for near-field (i.e. regions close to topography) studies of the scattering behaviour at the topographic profiles *A* (sinusoid), *D* (sawtooth), *K* (square-wave) and *L* (knife-edge) (see section 3.8).

For the most part, the PIV experiment setup was similar to that used for the synthetic schlieren measurements that were described in section 3.3.2. The synthetic schlieren method required a camera to be focused on a patterned mask that was fixed into position behind the tank. During PIV measurements however, the camera was focused on a vertical light sheet aligned with the field of view and positioned approximately midway between the front and back walls of the tank. Small particles suspended within those stratifications studied using the PIV technique acted as passive tracers of the fluid motion. Particles positioned within the region of the light sheet were illuminated so that they appeared bright. This enabled their motion, corresponding to the motion of the stratified fluid, to be recorded and followed so that particle displacements and hence fluid velocities could be determined. These calculations were performed within DigiFlow, which used similar algorithms to those employed in the synthetic schlieren pattern matching described briefly in section 3.3.3. More detail can be found in the DigiFlow manual (Dalziel 2007). A general reference for PIV techniques is Raffel *et al.* (1998). In contrast to the synthetic schlieren experiment arrangement, the topographic profiles in PIV experiments were positioned at the base of the tank prior to stratification (see sections 3.3.2 and 3.8). This permitted the stratification to be more easily lit by a light sheet and seeded with particles for the visualisation. The experiment configuration used for PIV measurements is shown in figure 3.9.

Sveen & Dalziel (2005) proposed a technique that allowed the simultaneous visualisation of fluid motion by synthetic schlieren and PIV. This employed an LCD monitor (in place of a dot

mask attached to a light source as described in section 3.4.2) positioned behind experiments that periodically displayed a random dot pattern or blank screen. The fluid was seeded with particles as in a standard PIV setup, and synthetic schlieren and PIV measurements were synchronised with the alternating monitor display. However, resolutions of the synthetic schlieren images visualised in this manner were constrained by the resolution and brightness of the monitor available. Since the fluid motion in this research was not turbulent and the wave motion repeatable, it was found unnecessary to have simultaneous information about the density and velocity perturbations and so a simpler setup could be used.

3.5.1 Light sheet

Light sheets were formed by directing an initially horizontal collimated beam of light at a mirror that was positioned above the free surface of the tank. The mirror measured 450 mm in the along-tank direction and was inclined at 45° to the vertical so that light from the lamp reflected through 90° and was directed vertically downwards into the stratification. The light source used was a 300 W arc lamp². This produced a beam within which component light rays were approximately, but not exactly, parallel. The initially collimated beam therefore slowly spread out as it travelled away from the lamp. Positioning the lamp ~ 2.8 m from the mirror allowed the beam to diverge sufficiently in the lateral direction so that it spanned the required field of view within the tank.

Light reflecting from the mirror could only enter the tank through a gap separating two 2 mm thick aluminium plates of length 500 mm and width 200 mm. These were attached to the top of the tank such that the 450 mm long slit formed between the plates was aligned in the along-tank direction. The width of the slit, and hence the width of the light sheet, could easily be adjusted by spacing the plates closer together or further apart. Several factors controlled the choice of width of the light sheet. To a good approximation the fluid motion could be assumed to be two-dimensional, except perhaps near the tank walls. It could therefore be expected that velocity data obtained from following particle motion within a light sheet with a finite width was consistent with velocity data for a plane section of the fluid obtained through the use of an infinitesimally thin light sheet - provided that the light sheets were positioned sufficiently far from the tank boundaries. For a given suspension of tracer particles, a wider light sheet increased the spatial resolution of the data since a larger number of tracer particles (data points) were illuminated. However, the contrast in the intensity field of an image obtained using a wider light sheet was reduced. The motion of individual particles became less distinct where the particles were located at different depths within the light sheet but occupied approximately, but not identically, the same position in the field of view. This effect was more significant for wider light sheets where more particles were visible across the thicker region. Also, although the entire width of the light sheet was contained within the focal depth of the camera, there were nevertheless slight variations in the sharpness of the focusing of the camera lens at depths of the light sheet away from the focal plane on which the camera lens was

²300 W Xenon Perkin Elmer Cermax Lamp, type B Parabolic (PE300BF).

primarily focused. Consequently, images of particles suspended within the light sheet but not in the primary focal plane of the camera appeared slightly blurred. This reduced the contrast between a region occupied by a particle and that occupied by fluid surrounding the particle. A narrower light sheet therefore promoted a higher resolution of image intensities. The width of the slit used in experiments was 4 mm. This width was found to produce images with an optimal balance between spatial and intensity resolutions as compared with those produced in trials of experiments using light sheets with widths ranging between 2 mm and 10 mm.

The arc lamp contained a Dichroic reflector that acted to minimise the radiation of Infrared (heat) components of light in the light beam. Despite this, the light source and the beam that it produced inevitably radiated heat to air surrounding the lamp. This heating and the resulting convective motions affected PIV measurements in the same way that motion caused by temperature inhomogeneities in the laboratory air, through various causes, were detected in synthetic schlieren visualisations (see section 3.4.3). In order to shield the surrounding air from the heat produced, a 2.4 m tunnel was constructed between the arc lamp and the mirror above the tank. The tunnel was made from 4 mm thick black corrugated plastic card and had a rectangular interior cross section with width 550 mm and height 200 mm. The tunnel served the additional purpose of preventing light from the lamp straying in directions other than directly towards the mirror and so creating unwanted reflections around the laboratory and tank that would contaminate the visualisations. Also to this end, gaps at the ends of the tunnel shielding the lamp and light beam were covered using black card or cloth.

The positioning of the lamp several metres from the tank resulted in attenuation of the light sheet both through heating of the air in the tunnel and by the divergence of light rays over that distance. The light sheet also transferred a small amount of heat to the saltwater of stratifications and had its greatest heating effect on the saltwater where the sheet was the most intense near the slits at the top of the tank. Density profiles of stratifications had their smallest values in this region. Divergence of the light sheet resulted in further attenuation of the intensity of the sheet as it travelled downwards away from the slit. The heat transferred by the light sheet therefore decreased with depth into stratifications and was minimal in the region near the bottom of the tank. Since the heating gradient acted in the same direction as the vertical density gradient of the stratification, double diffusive effects were insignificant and the density profile and fluid motion were only influenced through a slight local steepening of the density gradient confined near the top of the tank. In order to reduce heating effects further, a 2 mm thick sheet of transparent perspex was placed between the aluminium sheets used to make the slit and the top of the tank so that the saltwater was insulated from heat radiated by the metal. The aluminium plates were kept silver in colour on the side facing the mirror so that light reflecting from the mirror onto the metal was reflected back to the mirror to some degree rather than heating the plates, which in turn would transfer the heat to the stratification. The sides of the aluminium plates facing away from the mirror and the interior 2 mm edges of the slit were sprayed black in order to reduce light reflections and light refracted by the slit edges propagating inside the tank. A further reduction in the heating of

the plates was achieved by blacking out the area of the mirror not reflecting light directly downwards through the slits. This also served to ensure that the light sheet diverged less in the across-tank direction as it travelled deeper into the stratification as well as preventing multiple light sheets being produced by light passing through the slits obliquely from other regions of the mirror.

Light reflections off the interior tank walls were a source of error in the experiment visualisations. Reflections from the rear tank wall were removed by a 4 mm thick PVC board, measuring 1.9 m wide and 0.57 m high and covered in matt black covering film, being placed within the tank prior to stratifying. The blacked board was wedged firmly into position at each end by small blocks of sponge. The board effectively reduced the width of the tank by 4 mm and the length of the cylinder used to generate internal gravity waves was reduced by 4 mm to compensate. Additionally, the measures taken in synthetic schlieren experiments (see section 3.3.2) to remove other sources of superfluous light reflections and the noise introduced by the presence of computers, people or open windows and doors, etc., were repeated here. The majority of PIV experiments were run during the night and the laboratory was unoccupied, except for the necessary reseeding of stratifications with particles between experiments.

3.5.2 Particles

PIV measurements rely on particles moving *passively* with the fluid in which they are suspended. The particles used must therefore be chemically inert in the fluid and preferably have negligible settling velocities. PIV visualisations of stratified fluids require that a range of densities of particles are used. This ensures that an even suspension of particles is achieved over the entire field of view, rather than the particles just being concentrated in a narrow band about a particular vertical level. Stratifications used in this study had vertical profiles with density values in the range $\sim 1.02 - 1.15 \times 10^3 \text{ kg m}^{-3}$. However, small enough particles exhibiting this exact range of densities are not readily available commercially. Particles with densities that were close to those of the fluid could therefore be assumed to act as approximately passive tracers of the fluid motion provided that their sedimentation or rise velocities had sufficiently smaller magnitudes than the velocities characterising the bulk fluid motion. For a given density of particle, an even distribution of particles over the whole field of view could be achieved by ensuring there was a range of particles sizes present, hence ensuring the particles sedimented at different rates and so covered the field of view, or alternatively by reseeding the fluid intermittently with similar sized particles.

Particles played a similar role in PIV to that of the dots in the synthetic schlieren method (see section 3.4.2). Many of the optimisations of the dot masks used in synthetic schlieren experiments, applied in order to achieve high spatial and intensity resolutions in the data recorded, therefore had direct analogies with the optimisations of particle suspensions used in PIV. In particular, the size of particles and the fraction of the field of view occupied by the suspension were important factors in controlling resolutions of the experiment data. Particles ideally measured one or two pixels in diameter on images recorded of the experiments. Like the dots, particles represented data points and

so, for an approximately evenly distributed particle suspension, an increase in the particle fraction increased the number of data points, provided significant visual clustering did not occur. Unlike the dots however, the particles were actually suspended in the fluid and at very high particle fractions *physical* clustering of the particles could occur and result in the suspension having a non-negligible influence of the fluid motion.

In order to achieve high resolutions of the intensity field of images, the particles needed to appear as bright as possible against the surrounding fluid. The contrast could be controlled to some degree by adjusting the intensity and width of the light sheet as discussed above. For a light sheet with a particular intensity field and width, the contrast and so resolution of image intensities could be reduced if the particle fraction became too high causing adjacent particles to become less distinct from one another.

Particle description

The particles used for the PIV were artificial pearlescence³ made of mica coated with a surface of silver-white iron oxide and having a range of particle sizes 10 – 60 μm , though the samples inevitably also contained particles of smaller sizes referred to here as ‘dust’. In contrast, natural pearlescence consists of minute flat ellipsoidal fish scales. The surface of the scales is reflective and so a suspension of pearlescence shimmers when positioned in a light sheet. Pearlescence is ordinarily used in experiments as a fluid tracer since the scales have the useful tendency to align themselves with the shear fields within the fluid (Savaş 1985). The patterns of shear in a fluid may therefore be deduced from the light intensity field of an image taken of a suspension due to the preferential tilt of the scales. Owing to the complex dependencies of the shear fields, the use of pearlescence in this manner does not however allow the more useful quantitative information about fluid properties such as velocity or density gradient fields to be inferred from the illuminated fluid patterns. Pearlescence is rarely used in quantitative studies but has been successfully used to study turbulence, where data is generally only obtained through analysis of the statistical properties of the visualised fluid motion (e.g. Davidson *et al.* 2006; Staplehurst *et al.* 2008).

Artificial pearlescence is largely qualitatively the same as the natural version but may be obtained in a wide variety of colours and scale sizes. This control over the brightness and size of the scales made the artificial pearlescence a good choice for use as passive tracers in the PIV experiments. Natural pearlescence also has the disadvantageous property of degenerating in water after periods of a few hours. Artificial pearlescence is also significantly denser than natural pearlescence.

The fluid motion in experiments was approximately two-dimensional, with the fluid shear directed along wave beams and parallel to the fluid particle displacements. The pearlescence aligning itself with these shear motions therefore tilted so that the flat surface of each scale was perpendicular to the field of view of the camera. It might be expected therefore that the scales were not visible from the perspective of the camera since they could not reflect light perpendicular to the

³Iriodin[®] 103 Rutile silver sterling. Item no. 1.04246, www.Merck.de.

field of view whilst they were orientated in this manner. However, scales tended to intermittently ‘flip’ through 180° . These ‘flipping’ events were witnessed in visualisations as flashes. The scales statistically spent a very small fraction of the time flipping than remaining aligned with the flow. The flipping allowed partial glimpses of the individual scales that were sufficient to indicate their positions due to their highly reflective nature. This property of the pearlescence was also a major disadvantage as compared with the use of the spherical particles ordinarily used for PIV studies. The flipping events of the larger pearlescent scales were a source of error in the intensity fields of images and resulted in significant localised overestimates of the fluid displacements and hence velocities. These larger flashes were therefore ‘masked’ from movies by using a filter on each frame. The filter set intensities to zero in regions that exceeded a specified size where pixel intensities exceeded a specified threshold value. The area and threshold values were determined through a trial and error process from studying the unmasked raw movies. The contribution from the masked points was then ignored in the subsequent PIV processing using DigiFlow.

The small sizes of the artificial pearlescence available allowed the high spatial resolutions required from the data obtained from experiments to be achieved. It was found through test experiments that a subset of the range of particle sizes $10 - 60 \mu\text{m}$ was suitable for the passive particle suspension required. The pearlescence was more dense than the saltwater and so the different component sizes of the particles sedimented at different rates when placed into stratifications. Unfortunately, the composite nature of the artificial pearlescence prevented the assignment of a specific density range for the particles. Consequently, the behaviour of the particles in solution had to be characterised through trial and error. The largest of the range of particles sedimented too rapidly, taking minutes to fall completely through the designated field of view. Sedimented particles collected at the base of the tank and reflected light from the light sheet, creating a glare in that region. The smallest particles, however, remained in suspension for several days. These finer dust-like particles were too small to act as well-defined tracer particles in the visualisations and instead served to reduce the contrast in images between the other larger particles and the surrounding fluid. The dust also ‘clouded’ the light sheet in the region where it was inserted into the stratification and so reduced the light intensity reaching lower regions of the tank. The subrange of particles selected for use in experiments were those that were large enough to be distinct in images viewed through the camera but small enough that their sedimentation velocities permitted them to remain in suspension in stratifications for at least an hour after being introduced near the top of the tank. The method used to separate this optimal subrange of sizes from a mixed sample of the pearlescence and their seeding within stratifications is described below.

Suspension seeding

A concentrated homogeneous solution of pearlescence was made by mixing ~ 6 heaped spatula measures of the pearlescence powder with 1 litre of water in a large beaker. The particles were allowed to settle for approximately 30 minutes before the water and remaining suspension were

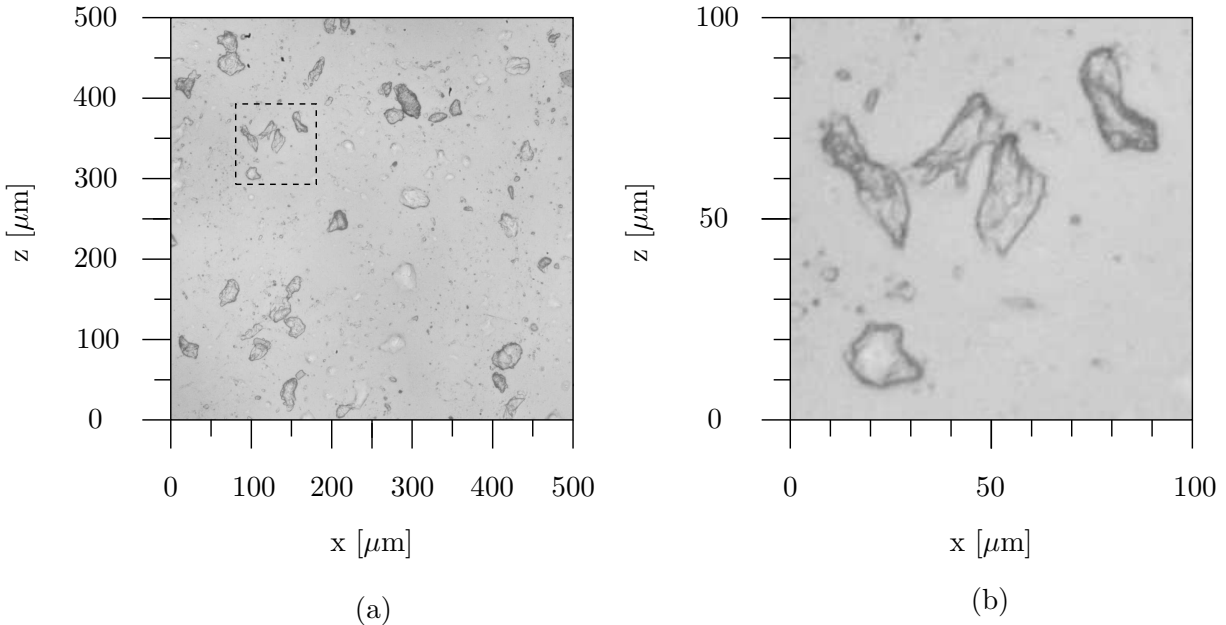


Figure 3.10: Close-up picture of artificial pearlescence. Particles shown in (b) are enlarged by a factor of 5 from the dashed square in (a).

carefully drained away and discarded. This process removed a large proportion of the unwanted finer particles. A homogeneous solution was again made as above from the thick mixture of sedimented particles collected from the base of the beaker and left undisturbed for a further 30 minutes. Those particles still in suspension after this time were slowly poured into a second beaker. The slushy mixture deposited at the base of the beaker contained the larger particles, which had the larger sedimentation velocities, and was discarded. The retained suspension was left to stand undisturbed for a further 15 minutes before the sedimented particles were again removed as above. The final suspension was allowed to stand for several hours before any particles remaining in solution were poured away and the mushy deposit that was retained was used for seeding stratifications. Figure 3.10 shows a photograph taken with a microscope of a sample of the artificial pearlescence that was considered suitable for use⁴. The particles in this sample were typically characterised by lengths $\sim 10 - 30 \mu\text{m}$. A 10 ml syringe was filled with the thick particle mixture and a long needle was used to slowly inject the pearlescence solution into stratifications just below the free surface. Care was taken to inject the particles evenly across the whole field of view and, as much as possible, only into the region of the fluid lit by the light sheet so that the contrast of viewed images was optimised (preventing reflections from particles outside the light sheet).

The particle suspension generally took about 40 minutes to settle into a useful form over the whole area of the field of view. Particles settled at slower rates in a stratified fluid, as compared with settling velocities in a homogeneous fluid, due to the entrainment of lighter fluid in their wake,

⁴Microscope photographs were kindly taken by J-W. van de Meent

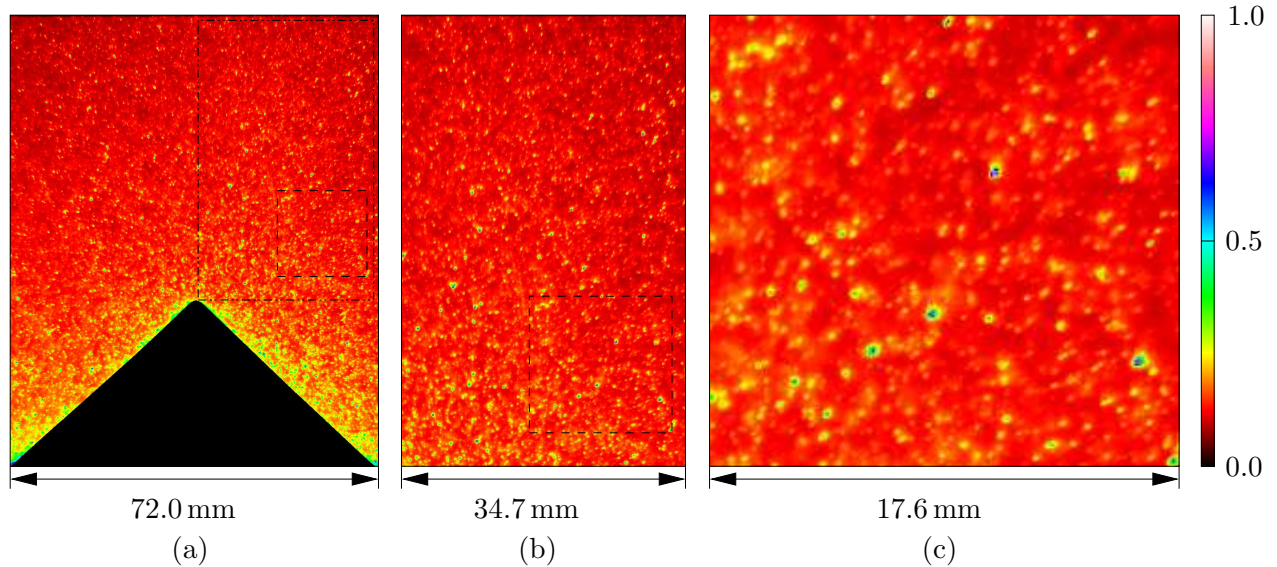


Figure 3.11: Image of particle suspension used in PIV as viewed by camera.

which increased their buoyancy and retarded their motion (see e.g. Srdić-Mitrović *et al.* 1999; Yick *et al.* 2007). The suspension was reseeded and allowed to settle again when required, typically after every 2 – 4 experiments (i.e. $\sim 50 - 150$ minutes). A typical suspension is shown in figure 3.11.

3.5.3 Camera

The same camera was used for the PIV experiments as that used for the synthetic schlieren. A large aperture lens with a short focal length of 50 mm was used however since the PIV was applied to much smaller fields of view with areas typically $\sim 220 \times 220 \text{ mm}^2$. A 5 mm spacer was also fitted between the camera lens and image sensor for even smaller fields of view. The small focal length of the camera lens allowed only the particles in the light sheet to be in focus, whilst the large aperture (with focal ratio $N_f = 0.95$) allowed more light to enter the lens. The camera was positioned at distances $\approx 200 - 300 \text{ mm}$ away from the tank at the level of the topography, with the vertical centre of the field of view aligned at the crests of the topographic profile in use. This minimised parallax (though parallax was not significant for thin light sheets) at these points of particular interest. Results of the PIV study are given in chapters 6 and 7.

3.6 Internal gravity wave generation

The mechanism by which monochromatic internal gravity wave beams were generated determined the spatial and temporal structure of the resulting wave beams. It was desirable to be able to specify the temporal frequency, σ , associated with wave beams (and thereby their angle of propagation, θ) as well as the position within the stratification at which they were generated. The combination of these two details allowed a degree of control over the location of the region where beams interacted with

topography. In order to determine the influence on the wavefield of interactions with topography, wave beams were also required to have a well defined across-beam structure that had small along-beam gradients and that could be sustained over many periods of the phase propagation.

A common approach to the generation of internal gravity waves in experiments has been to make sinusoidal vertical oscillations of cylinders within linear stratifications (originally presented by Görtler 1943 and in the classical experiments by Mowbray & Rarity 1967). Such a method has the advantage of producing beams with structures that have been well documented in experimental studies (e.g. Thomas & Stevenson 1972; Laws *et al.* 1982; Peters 1985; Merzkirch & Peters 1992; Gavrilov & Ermanyuk 1997; Sutherland *et al.* 1999; Dalziel 2000; Dalziel *et al.* 2000; Sutherland & Linden 2002; Zhang *et al.* 2007) and are accurately modelled analytically to first order in both the inviscid approximation (e.g. Lamb 1932; Hurley 1972, 1997) and with consideration of viscous effects (e.g. Thomas & Stevenson 1972; Makarov *et al.* 1990; Hurley & Keady 1997; Hurley & Hood 2001). At first order, four beams are produced by a cylinder oscillating with a small amplitude, A_c , and at a fixed frequency σ , where the energy propagates along the beams directed at an angle θ relative to the vertical. The angle of inclination, θ , is determined by the dispersion relation (Lord Rayleigh 1883)

$$\theta = \cos^{-1} \left(\frac{\sigma}{N} \right). \quad (3.17)$$

As discussed in chapter 2, each of the beams has a width approximately equal to the cylinder diameter, D_c , near to the forcing region and gradually widen with distance due to the influence of viscous diffusion. However their across-beam spatial structure is not characterised by any one dominant wavenumber. At fixed along-beam positions, profiles mapped out by the maxima and minima of the amplitude of the wave phase for each across-beam position over the course of one period of the motion are approximately symmetrical across the beam centreline. Slight symmetry deviations to this phase ‘envelope’ are attributed to viscous and nonlinear interactions in the region where beams overlap near the cylinder. The envelope has a bimodal form close to the cylinder that is gradually eroded to a unimodal form further from the cylinder by viscosity, which has a more rapid influence on the smaller length scaled structure of the motion (see section 2.3). The interpretation of power spectra for spatial properties of beams produced by oscillating cylinders is therefore nontrivial. However, beams generated by an oscillating cylinder may be sustained over long periods of time from a predetermined region in the fluid, in contrast to wave beams created by objects towed through the stratification (e.g. Merzkirch & Peters 1992; Bonneton *et al.* 1993; Dupont & Voisin 1996; Dupont *et al.* 2001; Gyüre & Jánosi 2003; Scase & Dalziel 2006), by flow over stationary objects (e.g. Baines & Hoinka 1985; Sutherland & Linden 1998; Sutherland 2002; Aguilar & Sutherland 2006; Sutherland & Aguilar 2006; Aguilar *et al.* 2006) or by parametric excitation where the stratified tank itself is oscillated in a chosen direction producing wave beams that focus into attractors determined by the geometry of the tank (e.g. Maas & Lam 1995; Maas *et al.* 1997; Benielli & Sommeria 1996, 1998; Maas 2005; Hazewinkel *et al.* 2008; Lam & Maas 2008). Also, for small amplitude oscillations of a cylinder, the wave motion may be assumed to be associated with

dominantly linear processes - a property difficult to achieve with paddle generation mechanisms for example (McEwan 1973; Cacchione & Wunsch 1974; Teoh *et al.* 1997; De Silva *et al.* 1997; Ivey *et al.* 2000; Gostiaux *et al.* 2006).

A camshaft generation mechanism has recently been proposed (Gostiaux *et al.* 2007) that is capable of producing a single broad monochromatic beam of a specified temporal frequency and a spatially periodic across-beam structure with a width of several wavelengths. Such a structure is preferable over those of beams generated by an oscillating cylinder since analysis yields spatial spectra that may be more reliably interpreted as a result of more tangible peaks at the dominant wavenumbers. Notably though, even an across-beam structure which is very strongly spatially periodic near to the generation site will be modified with along-beam distance by viscous action, with the far-field structure resembling that of a beam generated at a point source. However, the across-beam spatial periodicity is likely to be preserved over along-beam distances ~ 10 times the characteristic length scale of the across-beam structure (c.f. transition distance for beams generated by oscillating cylinders, section 2.3). The camshaft mechanism was not implemented since it was designed at a late stage in the present study.

Internal gravity wave beams were generated in the present study by sinusoidal vertical oscillations of a cylinder ('cylinder' and 'source' are henceforth used synonymously). It was also found to be advantageous that, unlike the camshaft mechanism of Gostiaux *et al.* (2006), an oscillating cylinder simultaneously generated more than one beam with similar spatial and temporal structures during each experiment. The scattering behaviour of one of these beams directed at rough topography could therefore be compared directly with the behaviour of a simultaneously generated second beam that did not interact with topography. Descriptions of visualisation and processing methods employed in order to overcome difficulties associated with the beam structure are described in chapters 4-8.

3.6.1 Wave generation by an oscillating cylinder

Unless otherwise stated, internal gravity waves were generated in experiments by a PVC cylinder that measured 148 mm in length and that had a circular cross-section of diameter $D_c = 35.6$ mm (see figure 3.12). The cylinder was attached at the midpoint of its length to a rigid metal rod with a diameter of 6 mm and a length of 40 mm. The rod was connected to a rigid pivoting arm oscillated at the far end by a motor-driven rotating circular disc, with a centre of revolution that could be offset to adjust the amplitude of the motion. The rod passed through a hole of diameter 8 mm within a PVC block of thickness 10 mm that was fixed to the top of the tank and was aligned vertically using a plumb line. The block acted as a guide to keep the rod vertical whilst it was in motion. After stratification, the cylinder was lowered slowly and smoothly into the tank such that the axis of symmetry of the cylinder was aligned across the width of the tank (i.e. perpendicular to the field of view) with the flat cylinder ends parallel to the tank walls. The cylinder was positioned close to half way along the tank so that it was the furthest from both of the end walls of the tank, from

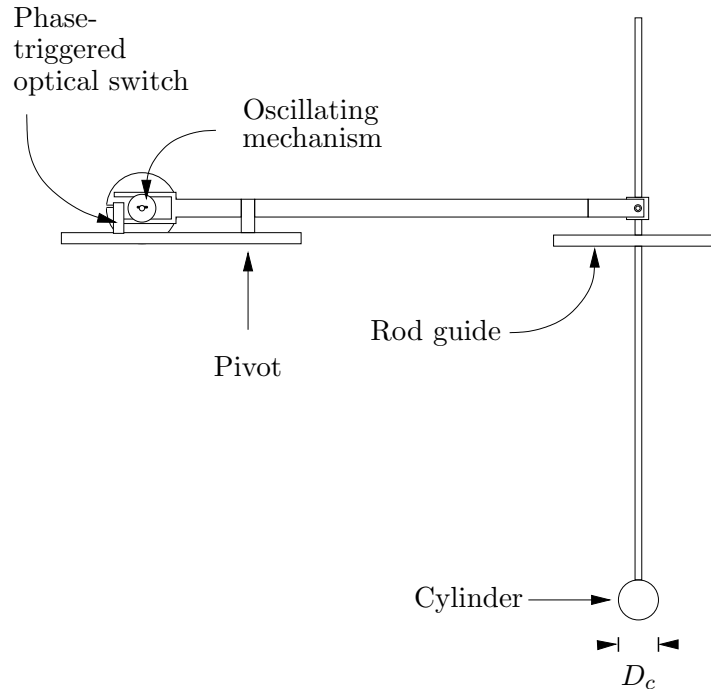


Figure 3.12: Internal gravity wave generation mechanism: the cylinder was oscillated vertically by a cam mechanism remotely controlled to oscillate at specific frequencies.

which reflected waves could propagate back towards the cylinder region and influence wavefields generated by it. The stratification was allowed to settle for several hours before experiments to allow the density profile to recover from the disturbance caused by the cylinder insertion.

Oscillation frequency

During experiments, the cylinder was set to oscillate at a chosen frequency and for a selected duration of time via a computer controlling the motor. An optical switch connected to the oscillating mechanism triggered a red LED at the beginning of each period of oscillation (corresponding physically to the point where the cylinder was at the midpoint of its vertical oscillation). The LED was triggered (without considering electrical response times or the effectively instantaneous warming-up of the LED to full intensity) for a percentage

$$\frac{\sin^{-1}\left(\frac{a}{d}\right)}{\pi} \times 100 \quad (3.18)$$

of the oscillation period, where a was the diameter of the slot in the rotating circle and d was the diameter of the circle mapped out by the sensor position on the rotating circle. For $a = 2$ mm and $d = 55$ mm this had a value of 1.158%. For a maximum wave generating frequency of oscillation bounded by the Brunt Väisälä frequency $N \sim 1.5 \text{ rad s}^{-1}$, the period was a minimum value of $4\pi/3$ s. The LED was triggered for a minimum time in this case of 0.0485 s. More generally the LED trigger

time was given by

$$\frac{2 \sin^{-1} \left(\frac{a}{d} \right)}{\sigma} \text{ s.} \quad (3.19)$$

The LED could be used to indicate the position in the phase at a particular stage in a movie recorded from an experiment and hence allowed ensembles of movies, for example, to be accurately phase-averaged where necessary. However, the accuracy of the use of the LED was bounded by the frame rate of the camera and the frequency of the cylinder oscillation, as well as being affected by the warm-up time taken by the LED and electrical delays.

The period of wave motion could also be determined to resolutions greater than the camera frame rate through processing movies of established wavefields using the ‘Qualitative’ pattern matching algorithm of DigiFlow. By choosing a reference image from a sequence of images of the established wave field, the processed fields could be tracked to identify experiment times when the wavefield became completely in or out of phase with the reference image. The period for a particular experiment was therefore calculated by averaging these times over several complete oscillations of the phase. The forcing frequency was therefore inferred by $\sigma = 2\pi/T \text{ rad s}^{-1}$.

Oscillation amplitude

The oscillation amplitude of the cylinder, A_c , was defined as the maximum vertical distance that the cylinder moved away from the midpoint of its oscillation. This introduced the parameter A_c/D_c relating the amplitude of the cylinder oscillation to the cylinder diameter. The cylinder was required to approximately mimic a point source in order that the generated wavefields correlated well with the predictions of linear theory (e.g. Hurley & Keady 1997). A small amplitude of oscillation, i.e. $A_c/D_c \ll 1$, was therefore chosen so that the cylinder remained at approximately the same position in the stratification. However the amplitude was also required to be sufficiently large that displacements of the density surfaces caused by the generated wavefields could be visualised by the camera distinctly from density fluctuations in the surrounding environment. The amplitude was therefore chosen to be such that $A_c < 0.1 D_c$, with the lower bound determined for a typical experiment layout from a series of tests comparing the quality of the observed wavefields. The amplitude was measured by recording a sequence of images over many oscillations and producing a time series over the course of the sequence of a vertical section passing through the centre of the cylinder and the surrounding region. The vertical position of the cylinder could be determined directly from the time series as the position at each time that the pixel intensity crossed a specified threshold. The cylinder was oscillated sinusoidally with a vertical amplitude of $A_c = 2.36 \text{ mm}$, corresponding to $A_c/D_c = 0.066$, as shown in figure 3.13. The slight irregularity of the curve is believed to be introduced during the interpretation of the time series, since the irregularity remained despite an average over many oscillation periods. The motion of the cylinder was recorded against a dot mask background. At each time step of the oscillation period recorded, the cylinder occupied a different region of the dot mask. Consequently, the viewed contrast between light intensity measurements for pixels located at the cylinder edge relative to those located within the region of

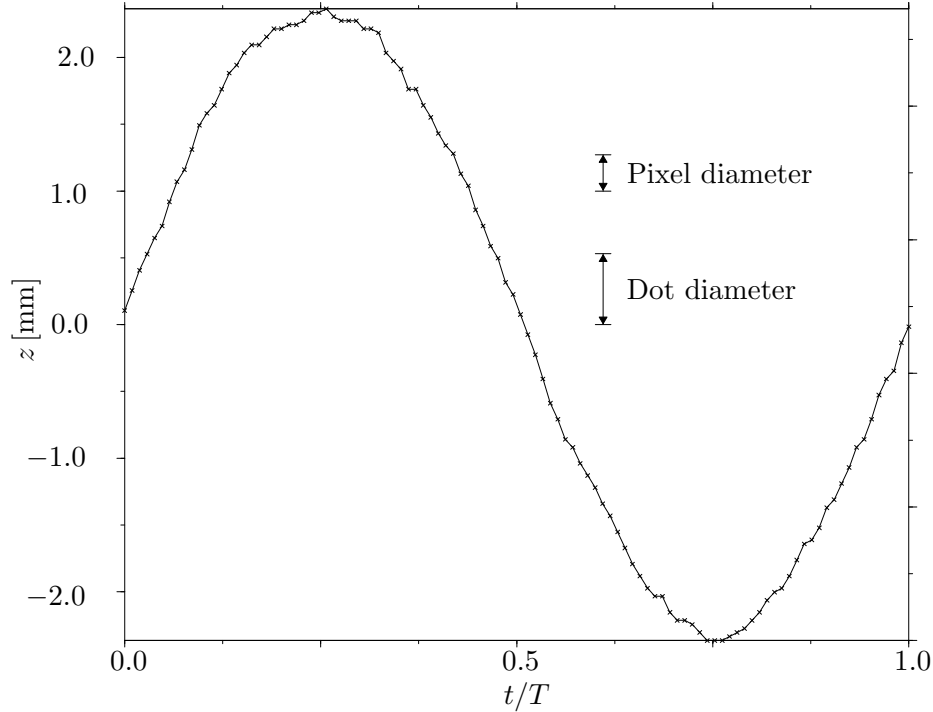


Figure 3.13: Vertical displacement of cylinder oscillating with temporal period T about a mean position. The displacement was averaged over nine oscillations, with the standard deviation of the displacement of each individual oscillation from this average lying in the range 0.12 – 0.21 mm. The pixel diameter was approximately 0.27 mm. The maximum displacement amplitude was 2.36 mm.

the dot mask viewed adjacent to the cylinder also varied during a period. In particular, the location of the vertical position of the cylinder edge became less well defined when the edge was located against a dark region of the dot mask, *i.e.* when the light intensity contrast across the edge was reduced. However, the value of the threshold light intensity used to identify the vertical position of the cylinder edge in the time series recorded was specified to be constant for all time steps.

3.7 Features of the wavefields

The main features of the wavefields generated by an oscillating cylinder in experiments are described qualitatively here, with these preliminary experimental results either presented for the first time here or to a greater resolution and degree of accuracy than in previous studies. Quantitative descriptions are given in chapter 5.

Transient ‘start-up’ motion

A study was made of both the transient ‘start-up’ and the established wavefields generated by an oscillating circular cylinder prior (physically) to the interaction of the wavefields with boundaries.

The established wavefields are compared in chapter 5 with those produced by elliptical and rectangular cylinders in order to determine the influence of aspect ratio and sharp corners of the cylinder cross-sections on the spatial structure of the generated wave beams.

The cylinder was started from rest and set to oscillate vertically at a frequency $\sigma/N = 0.54$ for $\sim 16T$, where the period $T = 2\pi/\sigma$ s. The cylinder initially generated a transient ‘start-up’ wavefield while it accelerated to the specified oscillation frequency. During this adjustment interval, a spectrum of waves was generated with transient frequencies σ_{tr} in the range $0 < \sigma_{tr} \leq N$, both above and below the value of σ . This wavefield was seen as a fan of characteristics around the cylinder along which energy propagated away from the cylinder (see figure 3.14 with $\sigma < N$ and more distinctly in figure 3.15 where $\sigma > N$). The range of values observed was a result of the continuous range of frequencies induced as the cylinder accelerated from rest and the angular dependence of the wave frequency given by the dispersion relation

$$\sigma_{tr} = N \cos \theta_{tr}, \quad (3.20)$$

where θ_{tr} denotes the angle of energy propagation corresponding to σ_{tr} . The initial transients propagated away from the cylinder at the respective group velocity. Recall that the group velocity (2.20) increases with decreasing frequency σ , *i.e.* with increasing values of θ , so that transients inclined closer to horizontal propagated across the field of view most rapidly. As time progresses, the fluid response shown in the sequence in figure 3.15 is seen to become characterised by increasingly smaller length scales. This is a result of the inverse relationship between the group velocity and magnitude of the wavenumber for each wave component generated by the impulsive start-up of the cylinder oscillation. Smaller wavenumber components, *i.e.* those characterised by larger length scales, are seen to propagate rapidly across the field of view within a few periods of the cylinder motion, whilst groups of larger wavenumber components, with smaller length scales, take a time greater than $9T$ to propagate across the field of view. Dark curving fronts can also be seen in figure 3.15 to propagate away from either side of the cylinder with increasing time. Approximating the surface of the cylinder as an array of point sources, the fronts can be understood to be regions of destructive interference between waves generated at each of the point sources.

After $\sim 8T$, the wavefield shown in figure 3.14 narrowed into four wave beams (similar beams are not seen in figure 3.15 since established cylinder oscillation does not generate propagating modes for frequency values $\sigma > N$). These were approximately bounded by the tangents to the cylinder that made angles $\theta = \cos^{-1}(\sigma/N) = 57.4^\circ$ with the vertical. Figure 3.16 shows the evolution of the wavefield during the first eight periods of oscillation after the cylinder was started from rest at $t = 0$ s relative to the evolution of the wave field during the eighth period of oscillation. Values shown represent normalised differences in amplitude between a time $t_i \in [(i-1)T, iT)$ of the i^{th} period of oscillation and a corresponding time $t_8 \in [7T, 8T)$ in the eighth period of motion (*i.e.* $t_i = t_8$ modulo T). The rapid decrease at the start of the eighth (*i.e.* the reference) period indicates that the wavefield for this field of view still contains transient components during the seventh period. An

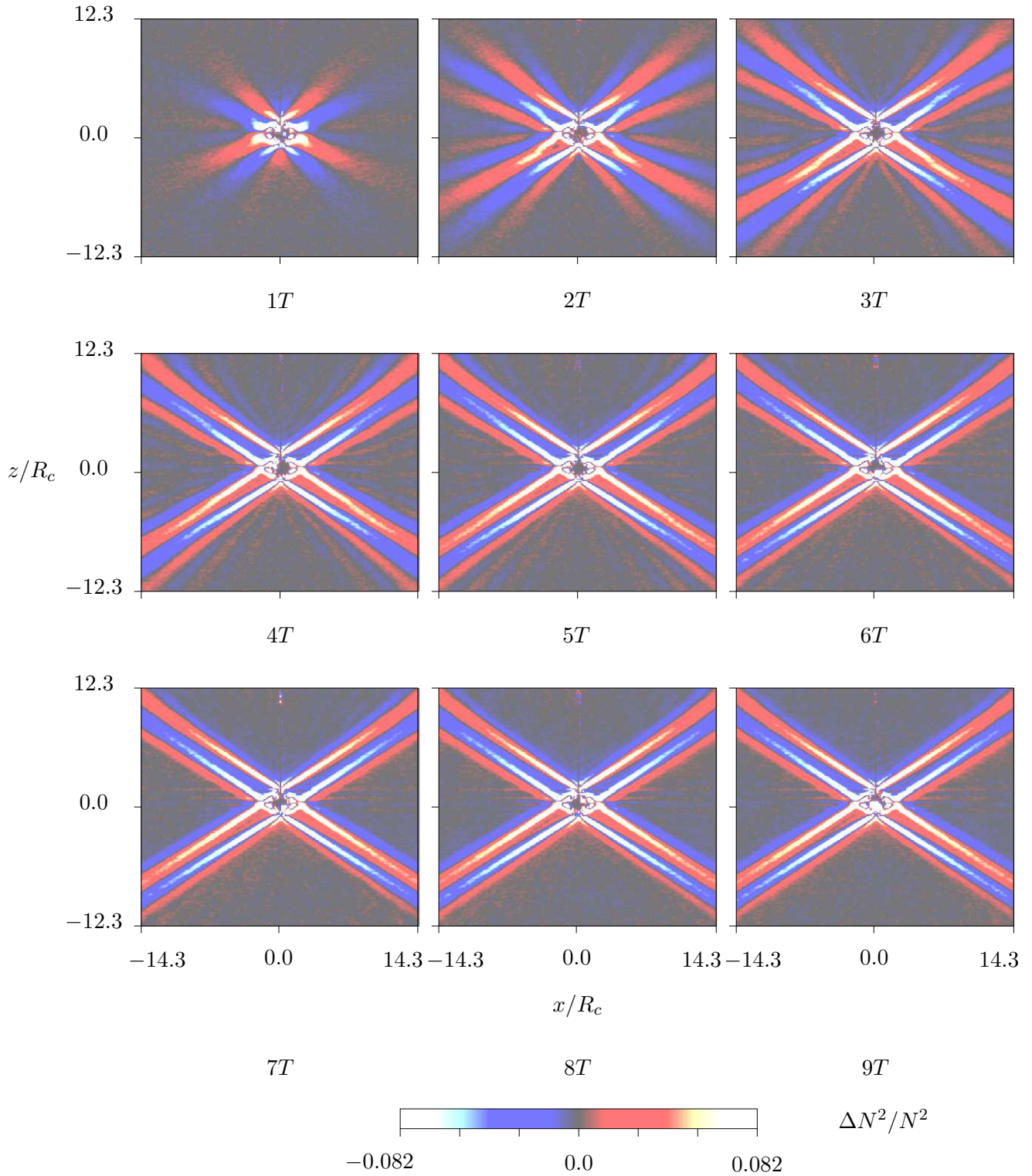


Figure 3.14: Sequence of transient start-up wavefield at times $t = 1T, 2T, \dots, 9T$ s. The cylinder oscillation was initiated at $t = 0T$ s with $T = 8.64$ s and $\sigma/N = 0.54$.

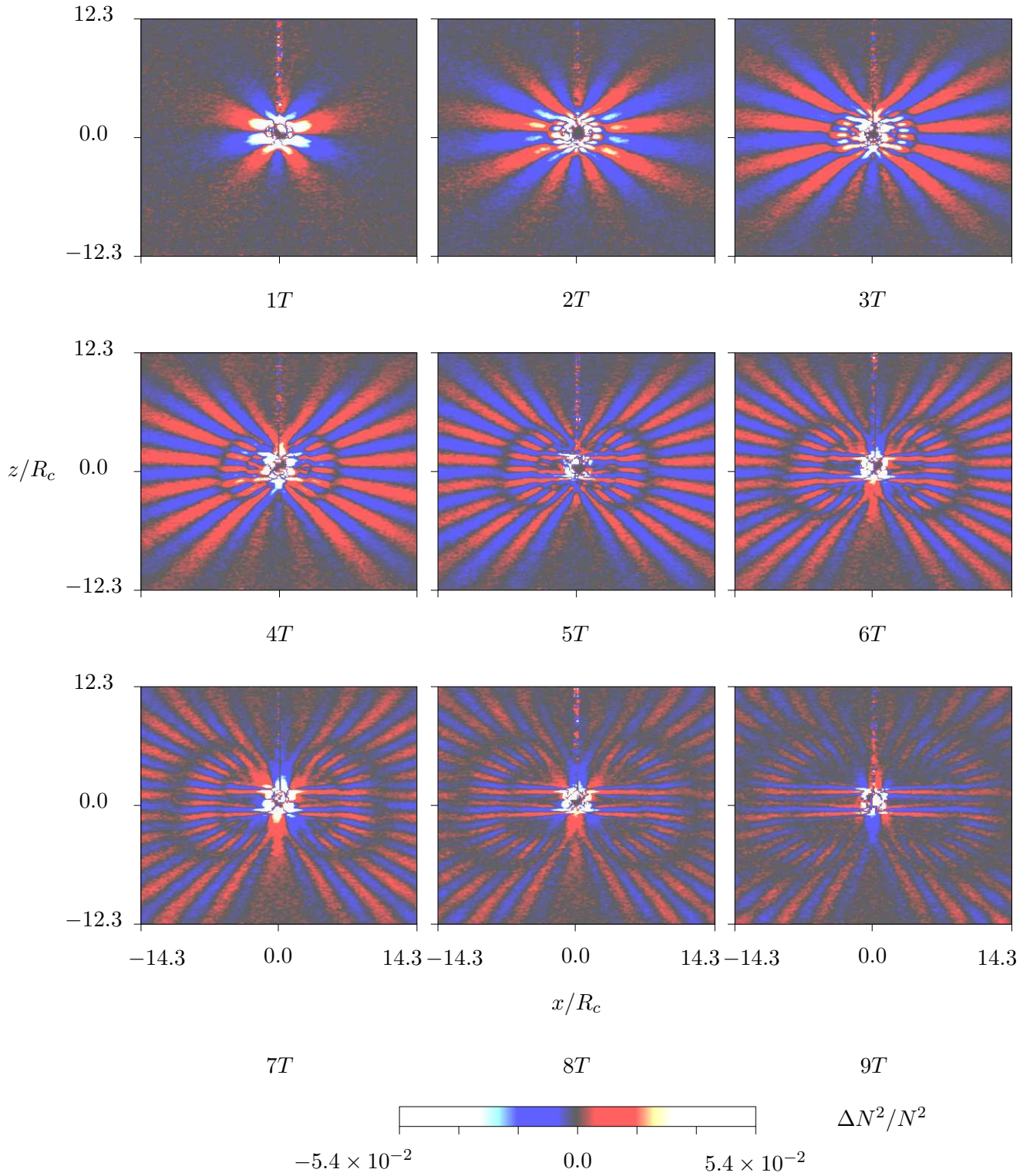


Figure 3.15: Sequence of transient start-up wavefield at times $t = 1T, 2T, \dots, 9T$ s. The cylinder oscillation was initiated at $t = 0T$ s with $T = 2.86$ s and $\sigma/N = 1.63$.

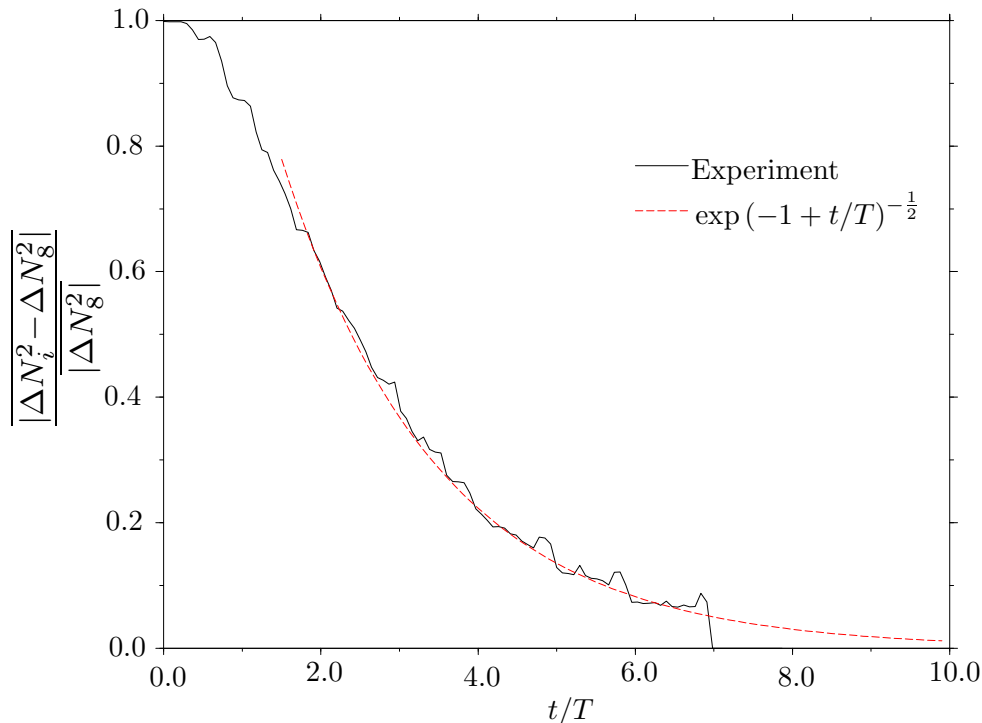


Figure 3.16: Development of wavefield after cylinder oscillation initiated at $t = 0$ relative to the wavefield at times $t \in [7T, 8T)$.

extrapolation of the fit shown to the data suggests that the wavefield converges on an ‘established’ periodic form at $t \sim 10 - 11 T$. Wave beams contained in similar sized fields of view as that shown are therefore referred to here as ‘established’ for times $t \geq 10 T$ after the cylinder oscillation was initiated.

Established motion: $0 \leq \sigma/N \leq 1$

For forcing frequencies in the range $1/2 \leq \sigma/N \leq 1$, the dispersion relation only permitted wave generation at temporal frequencies of σ corresponding to energy propagation at angles $\theta = \cos^{-1}(\sigma/N)$. Secondary harmonics with frequency 2σ could be generated for $0 \leq \sigma/N < 1/2$. More generally, the condition for the n^{th} harmonic, with frequency $\sigma_n = n\sigma$ and angle of energy propagation $\theta_n = \cos^{-1}(\sigma_n/N)$, to exist was that $0 \leq \sigma/N \leq 1/n$ for $n \in \mathbb{Z}_{\geq 0}$. Characterising amplitudes of fluid displacements associated with the n^{th} harmonic, ε_n , are related by $\varepsilon_n \sim O(\varepsilon^n)$, where $\varepsilon \ll 1$ is a characteristic amplitude associated with the primary harmonic.

Angles, θ , of inclination of wave beams were measured along the centrelines of beams from RMS (the average taken over several periods of the cylinder oscillation) images of the perturbed buoyancy fields. Root mean square fields calculated over integer multiples of the period T associated with the forcing frequency are henceforth denoted RMS_T . Measurements of angles were made directly from digital images within DigiFlow using coordinate systems defined as described in section 3.4.4.

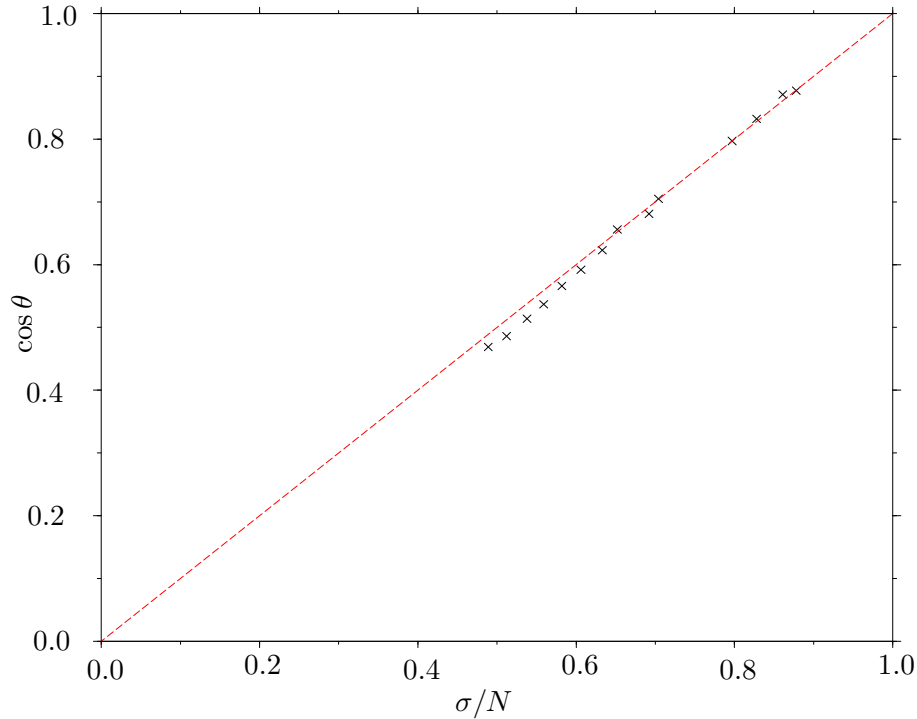


Figure 3.17: Graph to compare the forcing frequency with the cosine of the measured angle of internal wave beams.

(Colour schemes were manipulated for this purpose in order to enhance the visibility of the structure of the wave beams.) The value of θ was taken as the average of at least five measurements. Figure 3.17 compares the cosine of measurements of wave beam angles at 14 different forcing frequencies in the range $\sigma/N \in [0.46, 0.86]$ with the ratio σ/N . The data points closely follow the dispersion relation satisfying $\cos \theta = \sigma/N$ as illustrated by the dashed line. Figure 3.18 shows RMS_T images of wave beams generated at forcing frequencies σ/N equal to (a) 0.54, (b) 0.31 and (c) 0.27. These correspond to primary harmonic beams at angles $\theta = \theta_1$ of (a) 57.4° , (b) 71.8° and (c) 74.4° ; secondary harmonics at angles θ_2 of (b) 51.3° and (c) 57.5° and tertiary harmonics at angles θ_3 of (b) 20.4° and (c) 36.2° . The primary harmonics are clearly visible in all images, with bimodal structures and higher energy densities at small along-beam distances from the cylinder centre gradually transitioning to a unimodal structure associated with lower energy densities at further distances. Beam widths were approximately equal to the cylinder diameter at their origin and broadened with along-beam distance. Energy densities were higher in beams associated with higher frequencies, for which the forcing mechanism put energy into the system at a greater rate. The energy densities were also smaller at these higher frequencies, corresponding with smaller angles, because energy propagation was more efficient in directions closer to horizontal, i.e. when the wave beams were directed along isopycnals rather than across them. Secondary harmonics, associated with significantly lower energy densities than the respective primary harmonics, and their bimodal

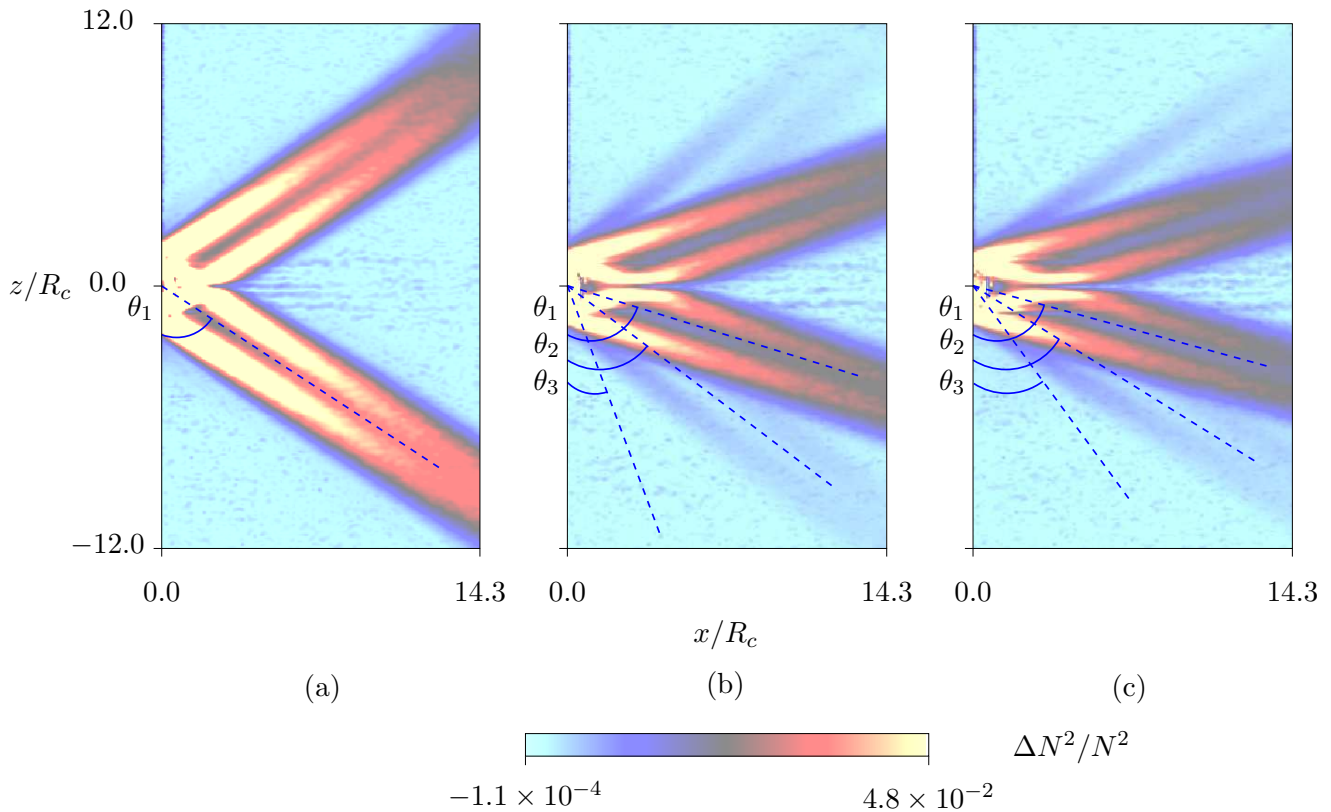


Figure 3.18: RMS_T values of $\Delta N^2/N^2$ at σ corresponding to (a) $\theta_1 = 56.8^\circ$, (b) $\theta_1 = 72.8^\circ$ and (c) $\theta_1 = 74.7^\circ$. The beams shown are in positions corresponding with those of the upper and lower right-hand wave beams in figure 3.14.

structure are also evident in figure 3.18 (b) and (c). The presence of the predicted tertiary harmonics for (b) and (c) is not evident in the RMS_T images, although could be faintly observed in movies of the wavefield corresponding to (c). Figure 3.19 (a) and (b) shows RMS_T images of the second and tertiary harmonics from harmonic filtering of the experiment represented in figure 3.18 (c). The poorer image quality is a consequence of the fact that amplitudes of these higher harmonics approach the order of that of background wavefields and also due to the relatively larger influence of noise. It is believed that these are the first experimental pictures of the tertiary harmonic generated by an oscillating cylinder.

Established motion: $\sigma/N > 1$

The dispersion relation is invalidated at forcing frequencies $\sigma/N > 1$ and the wavefield becomes evanescent so that energy from the disturbance is predicted to decay exponentially with distance from the source region with no propagating modes being produced. Figure 3.20 shows RMS_T images of wavefields generated at forcing frequencies σ/N equal to 1.45 and 1.63 respectively. Only small disturbances were evident and were confined to the regions close to the cylinder. Short beam-like structures inclined at small angles to the vertical and associated with low energy densities became

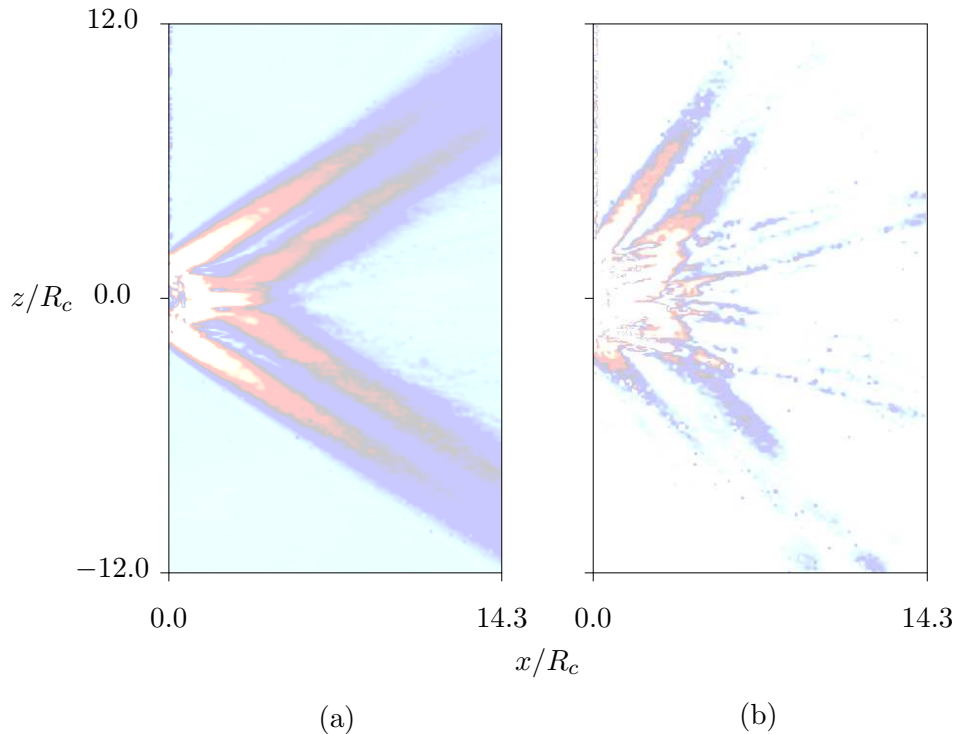


Figure 3.19: RMS_T values of $\Delta N^2/N^2$ after harmonic filtering for secondary and tertiary harmonics relating to figure 3.18 (c). Scales for $\Delta N^2/N^2$ are as in figure 3.18 except with colour scale values corresponding to the ranges (a) $[-1.0 \times 10^{-4}, 1.0 \times 10^{-3}]$ and (b) $[3.7 \times 10^{-4}, 1.2 \times 10^{-3}]$ respectively.

weaker as σ/N was increased from 1.45 to 1.63. Horizontal intrusions of mixed fluid protruding into the stratification after formation at the levels of the upper and lower extrema of the cylinder became more pronounced with the increase in frequency however.

Decay of wavefield

Figure 3.21 shows a sequence of images at intervals of $1T$ of the decay of wave beams and the transient wavefield produced when the cylinder oscillation was abruptly stopped after 16 oscillations at $\sigma/N = 0.54$. As in the transient start-up interval, the deceleration of the cylinder from the oscillation frequency σ to rest generated a spectrum of wave frequencies satisfying the dispersion relation and bounded above by the forcing frequency. This wavefield propagated away from the cylinder, leaving the field of view by $\sim 8T$ after the cylinder oscillation was halted. The persistence of wave modes associated with larger length scales is evident at these later times, since a weak wave beam reflection from the tank bottom and walls and the free surface can be seen crossing the field of view from the bottom left-hand corner (most clear in the images corresponding to $6T$ - $8T$).

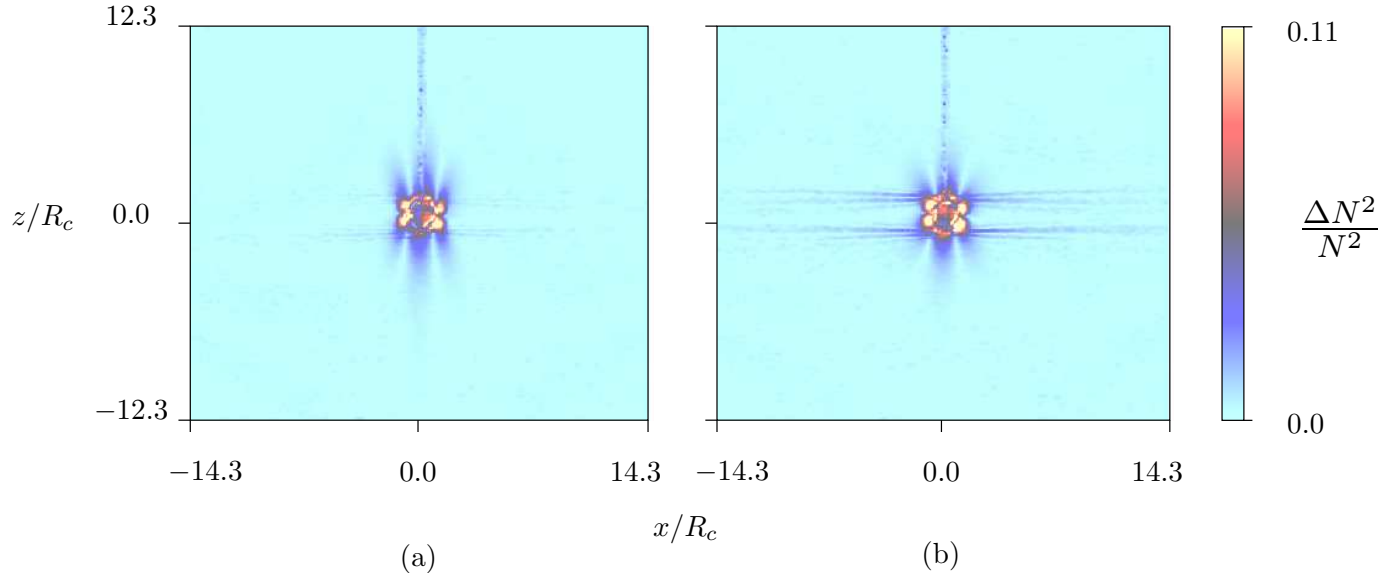


Figure 3.20: RMS_T values of $\Delta N^2/N^2$ for σ/N values (a) 1.45 and (b) 1.63. The vertical line visible above the cylinder is due to the presence of the cylinder rod.

Influence of a stationary cylinder on background stratification

The presence of an obstacle such as a cylinder within a stratification imposes certain boundary conditions on the fluid even when stationary. The boundary condition at an impermeable surface prevents a mass flux directed into it, requiring that the gradient in density of the fluid perpendicular to a boundary has to vanish there. This can only be satisfied when isopycnals contact boundaries at right angles. Hence, at boundaries that are neither horizontal or vertical, the otherwise horizontal isopycnals of an undisturbed stable linear stratification are forced to curve in order to meet this condition. Such curvature creates a horizontal gradient in the density field near the boundary that gives rise to baroclinic generation of vorticity there. Figure 3.22 (a) shows an exaggerated schematic of the curvature of isopycnals meeting a flat sloping boundary and, (b), those around a circular cylinder. At a sloping boundary with negative gradient (i.e. the angle, $0 < \alpha < 90^\circ$, made between the boundary and the vertical is anticlockwise from vertical), as shown in (a), the horizontal density gradient induced is positive so that vorticity is generated there with a positive sign and hence a clockwise rotational sense. This in turn sets up flow near to the boundary that is directed along the boundary with a positive vertical component in a region characterised by the length scale

$$\delta_N = \left(\frac{N^2 \cos^2 \alpha}{4\kappa\nu} \right)^{\frac{1}{4}} \quad (3.21)$$

(Phillips 1970; Wunsch 1970). Similar arguments can be used to deduce the direction of the induced boundary surface flow over the whole surface of a cylinder (e.g. Baydulov & Chashechkin 1996) as shown in figure 3.22 (b), with stagnation points where the slope of the surface is vertical or horizontal. In linear stratifications the horizontal density gradient (and so amount of vorticity

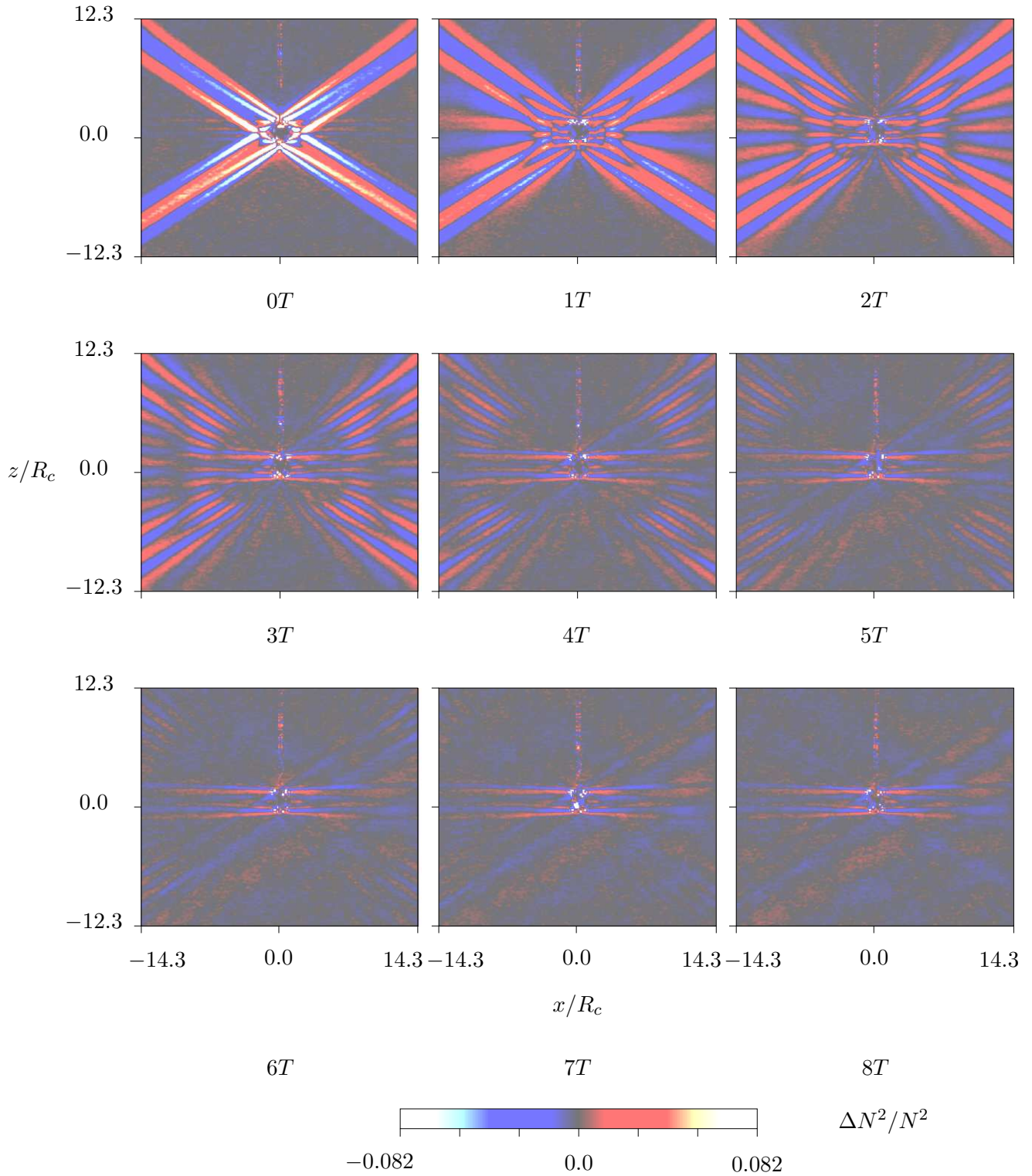


Figure 3.21: Transient decay of established wave beams after cylinder oscillation halted at $t = -T/4$ s. $T = 8.64$ s.

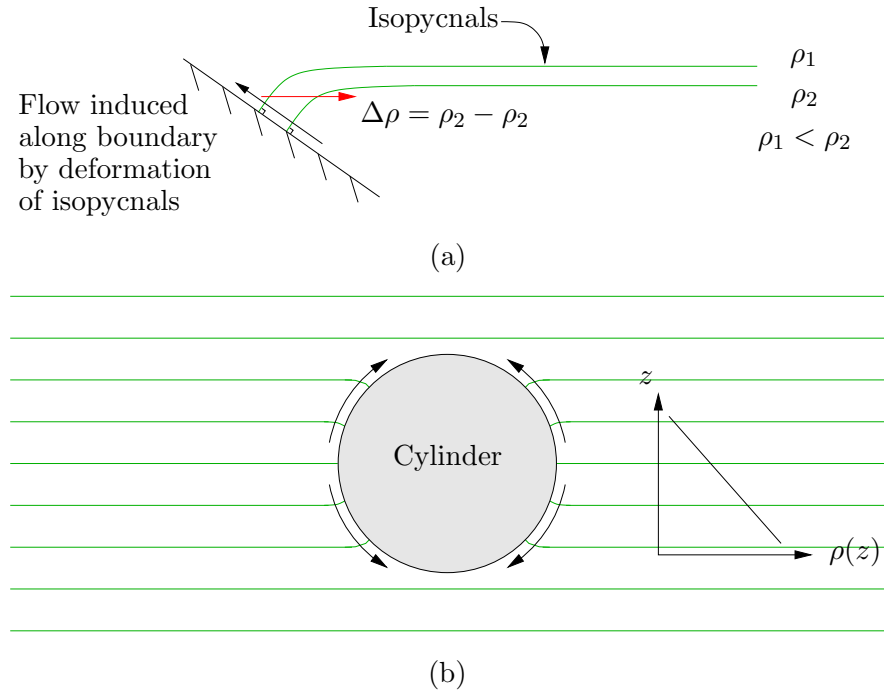


Figure 3.22: Schematic of the influence of boundaries on stratifications.

produced by this mechanism as a result) varies with the slope angle. The Phillips-Wunsch theory predicts an increase in the along-slope velocities for decreasing slope angles in the range $0 < \alpha < 90^\circ$, with the average velocity directed along the boundary in the buoyancy-driven layer given as

$$u = -\frac{\kappa}{\delta_N} \tan \alpha. \quad (3.22)$$

Experimental results comparing diffusion-driven flow along an inclined wall compare well with (3.22) except for small angles of inclination in the approximate range $0 < \alpha < 2.8^\circ$ where the slope velocities decreased rapidly with decreasing slope angles from a maximum value at $\sim 2.8^\circ$ (Peacock 2004).

In this study, whilst the cylinder was stationary, the along surface flows enhanced diffusive mixing in a boundary region adjacent to the cylinder that had a thickness comparable with δ_N . Fluid drained into the stratification from this boundary region at the level where it was neutrally buoyant and spread laterally at that level. The boundary layer associated with this process hence gradually eroded the stratification in the vicinity of the cylinder over time scales comparable with the diffusion time scale.

Influence of an oscillating cylinder on background stratification

The effect on the background density profile induced by the presence of a cylinder in a stratification can be expected to increase significantly when it is forced to oscillate, though the mechanism for changes in the background N should still be controlled by diffusion when $A_c/D_c \ll 1$. Experiments

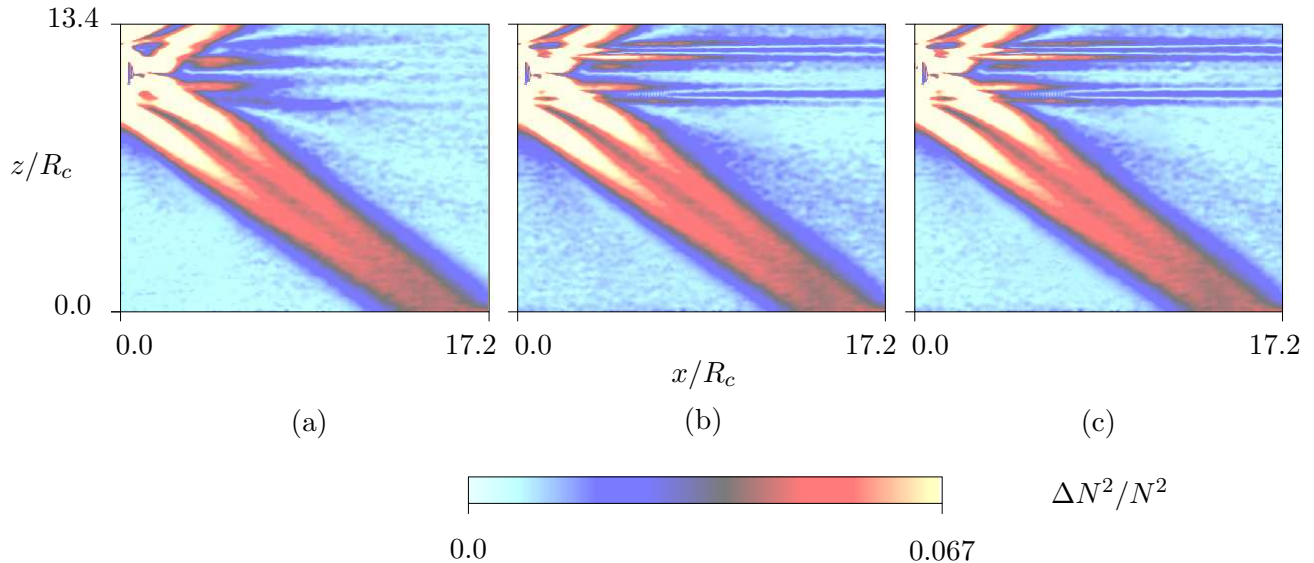


Figure 3.23: RMS_T images showing development of horizontal intrusions near the cylinder after cylinder oscillation at frequency $\sigma = 0.79$, *i.e.* $\sigma/N = 0.59$, for durations of (a) $\hat{t} + 0$, (b) $\hat{t} + 40$ and (c) $\hat{t} + 80$ minutes, with $\hat{t} = 4$ minutes.

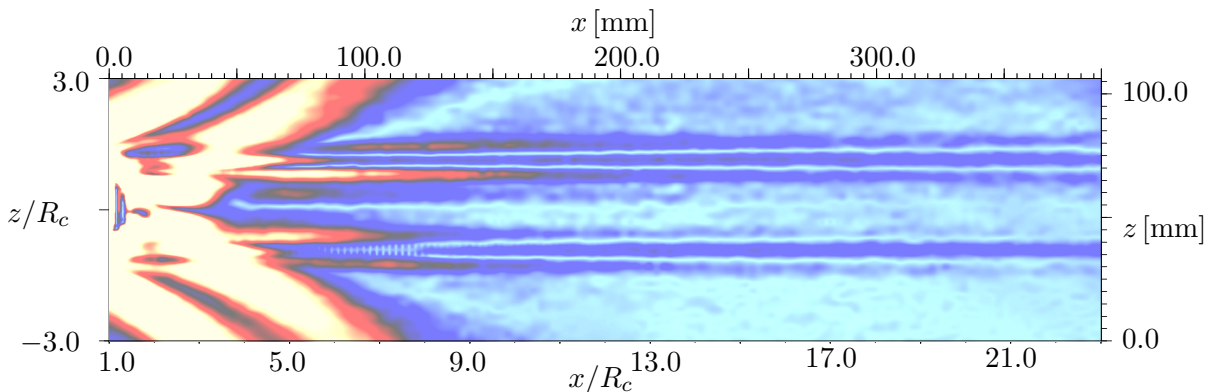


Figure 3.24: Zoom of section near cylinder in figure 3.23 (c). Scaling as in figure 3.23.

were performed with the cylinder oscillating continuously at a fixed frequency of $\sigma/N = 0.59$ for 120 minutes in order to assess the influence of this mixing on generated wavefields. Figure 3.23 shows RMS_T images of the cylinder (located in the top left-hand corners of the images) and one wave beam taken from three periods of oscillation beginning at times of (a) $\hat{t} + 0$, (b) $\hat{t} + 40$ and (c) $\hat{t} + 80$ minutes after the oscillation was initiated, where $\hat{t} = 4$ minutes. The wavefield remained qualitatively the same for each of these times except for the development of horizontal disturbances at the level of the source. The disturbances appeared to originate at the top and bottom of the cylinder and became more pronounced and increased in length as time progressed, extending beyond the field of view by $t = \hat{t} + 40$ minutes. The intrusions were caused by mixed fluid

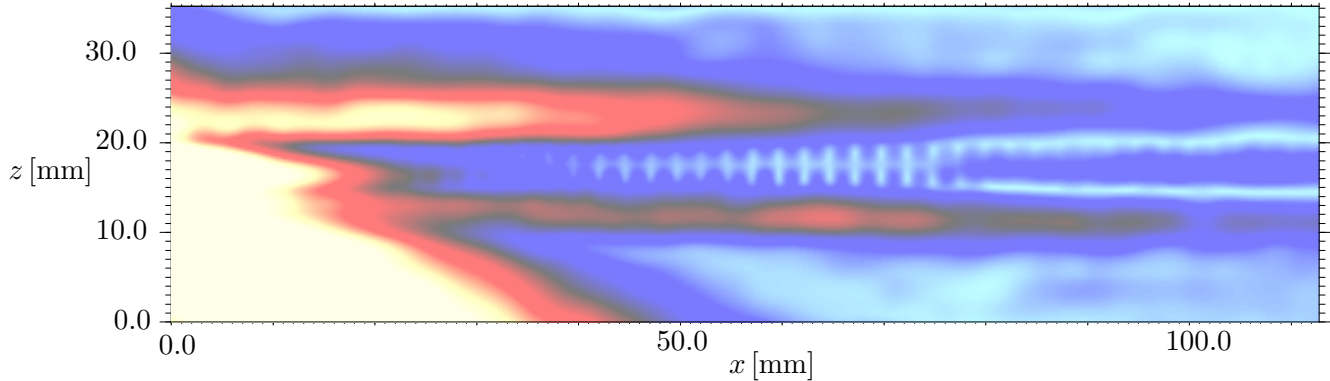


Figure 3.25: Zoom of section near cylinder in figure 3.24. Scaling as in figure 3.23.

generated in the region near the cylinder and expelled into the stratification at levels where the fluid was neutrally buoyant. The vertical density gradient decreased relative to the originally constant gradient within the layers and increased at the upper and lower vertical bounds of the layers. Figure 3.24 shows a larger version of the intrusions corresponding to figure 3.23 (c). Gradients in the perturbed buoyancy field were peaked in three horizontal bands originating at the base of the cylinder and three horizontal bands originating at the top of the cylinder. The outer two bands of each set exhibited sharp vertical gradients indicating the vertical bounds of the intruding fluid. The inner band of each set corresponds with the intruding fluid. Horizontal bands of mixed fluid generated near an oscillating cylinder were also commented on briefly in Mowbray & Rarity (1967) and Sutherland & Linden (2002). In the present study, oscillations were supported in the region adjacent to the cylinder and are most clearly visualised along the intrusion extending from the base of the cylinder in figure 3.24. Vertical bands can be seen at positions near $x/R_c \in [4, 9]$ and $z/R_c \sim 1$ (an enlargement of this region is shown in figure 3.25). These represent waves propagating in the horizontal direction with horizontal length scale 5.1 mm (measurements averaged over 18 peaks in the RMS_T field, corresponding to 9 wavelengths). The frequency of these oscillations was measured from time series images of a vertical section corresponding to the position $x/R_c = 7$ in figure 3.24 and averaged over 15 oscillations. The frequency was measured as 0.79 rad s^{-1} which was equal to the cylinder frequency σ . The presence of wave-like fluctuations about the horizontal level of the mean position of the source that oscillated at *twice* the forcing frequency with $2\sigma/N < 1$ were noted in experiments by Sutherland *et al.* (1999). However, $2\sigma/N = 1.18$ here and so an oscillation at 2σ corresponds to an evanescent mode. Propagating modes at this frequency are not expected to be generated unless they are supported by a local change in the stratification.

The influence of these features on the wavefields of interest in this study were negligible since they were confined to the vertical level of the source and only protruded significant horizontal distances into the stratification after sustained forcing and on time scales much larger than those for a series of experiments.

3.7.1 Removal of unwanted waves

The oscillating cylinder produced a characteristic ‘St Andrew’s Cross’ formation of four wave beams, where two of these were generally surplus to the requirements of experiments. Each of the four beams propagated away from the cylinder and reflected from the tank walls, bottom boundary and the free surface of the stratification. Viscosity acted to attenuate wave energy with distance from the generation site and had the fastest dissipative effect on the energy associated with the smaller across-beam scales, which had the greatest gradients in that direction. Structures of beam reflections returning to the region near the cylinder were therefore more dominantly characterised by larger scales and hence smaller wavenumbers. However their interaction with the oscillating cylinder or topography could regenerate larger wavenumbers. Wave energy contacting sloping boundaries (such as topography inserted into the tank) could be focused. This resulted in an increase in energy density and the associated energy redistributed to higher wavenumbers. It was therefore necessary to dampen the unwanted reflections at the tank boundaries and free surface as much as possible in order to remove their contaminating influence on the viewed wavefields.

Wave trap

In order to trap superfluous wave beams that had group velocities directed upwards away from the cylinder, a narrow sloping barrier was carefully inserted into the stratification at the free surface at least 2 hours before experiments were carried out. The angle made between the barrier and the vertical, α_w , was required to be greater than that made between the beam centreline and the vertical, θ . Since θ is conserved at first order during reflection, such an arrangement focused the beam into the wedge formed between the free surface and the barrier (see for example Hurley 1970) where the wave energy was dissipated by viscosity. Figure 3.26 shows a schematic of a wave beam interacting with the wave trap. Figure 3.27 shows a similar interaction occurring in experiments. To minimise mixing of the stratification caused by the inclusion of the wave trap, the trap was inclined at the chosen angle α_w prior to its insertion and the angle maintained whilst it was pushed smoothly into the tank. Wave energy incident on the submerged end of the wave trap was observed to generate up to four narrow beams that propagated away from the end of the wave trap in directions making an angle θ with the vertical, determined by the incident wave frequency (see figure 3.27). In general, the generation of these additional beams limited the configurations in which the trap could be usefully employed.

Wave damping by sponges

Three layers, S_1 , S_2 and S_3 , of coarse plastic sponge (reticulated foam) with a typical pore size of a few millimetres were combined to dampen wave beam reflections at the ends of the tank. At each tank end, sponges of thickness 0.5 mm, 15 mm, and 20 mm respectively, height ~ 600 mm and width 150 mm were layered in order of increasing thickness and sewn together at the sponge ends (see figure 3.28). Each sandwich of sponges was placed at a tank end prior to stratification, with the

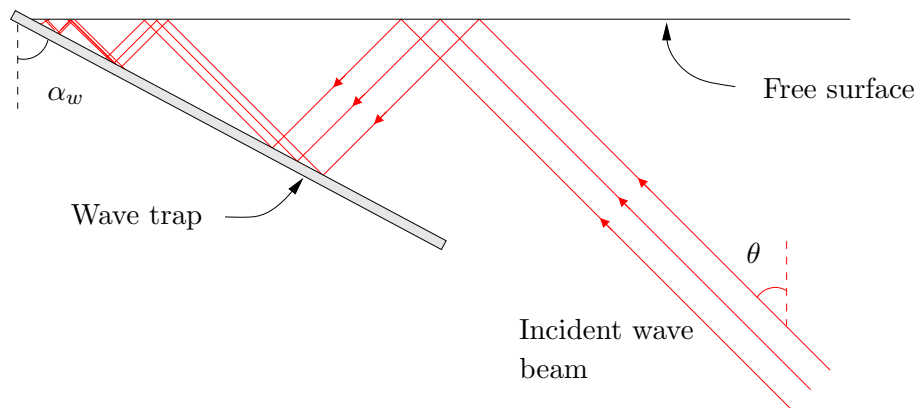


Figure 3.26: Wavetrapping schematic.

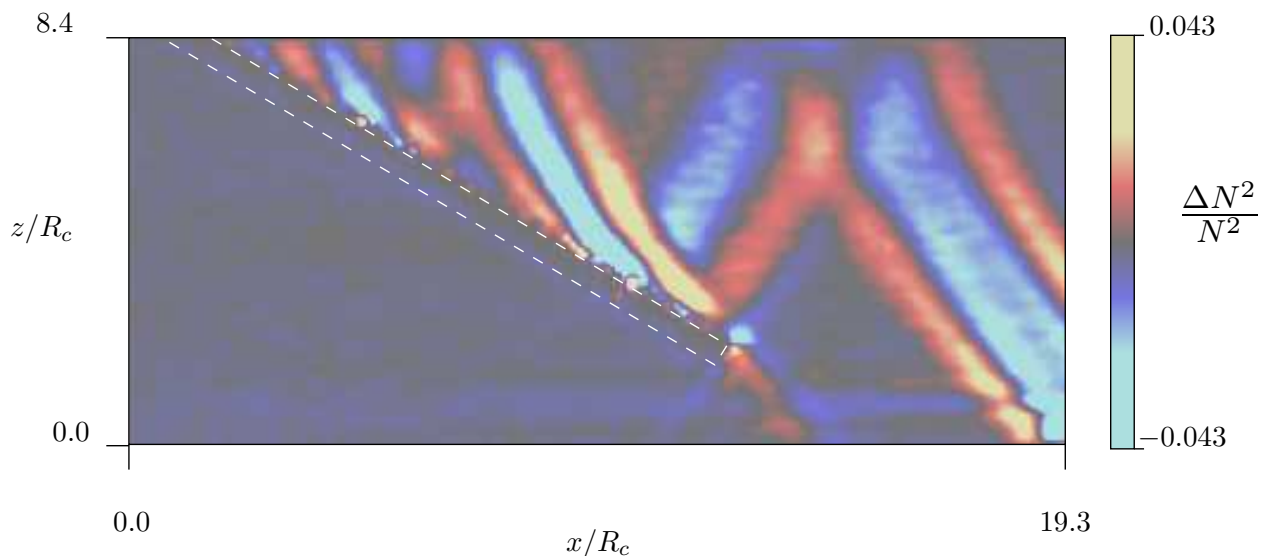


Figure 3.27: Experiment picture of focusing of wave beams wave trap. Wave trap is highlighted with dashed white line.

thickest sponge, S_3 , flat against the end wall. The thinner sponge layers, S_1 and S_2 , were allowed to bow out away from the end wall at about the mid-depth of the tank so that there were gaps between the layers. Propagation of wave energy through the layers of sponge was inhibited by the layer thickness, resulting in varying degrees of transmission through and reflection from each of the layers. Transmitted wave energy was subsequently reflected and diffracted by the plastic joins of the coarse internal structure of the sponge. These processes aided the conversion of incident energy to smaller spatial scales which was then dissipated more rapidly by viscosity as well as partitioning the incident energy density between different directions of subsequent propagation. Most wave beams contacted the sponges at mid-depths of the tank, where the sponge layers were

most spread out. This resulted in a large proportion of the incident wave energy being transmitted through the thinnest layer, S_1 , with small amounts of dissipation and reflection. Wave energy was transmitted through the next thickest layer, S_2 , to a lesser degree but with the transmitted flux subject to greater dissipation. Partial reflections from S_2 were further damped by their reverse transit through S_1 . Flux reaching the final and thickest layer, S_3 , was again partially transmitted and reflected. Reflected wave energy at S_3 was subject to further transmission or reflection at S_2 and S_3 so that wave energy propagating back into the main body of the stratification was significantly reduced.

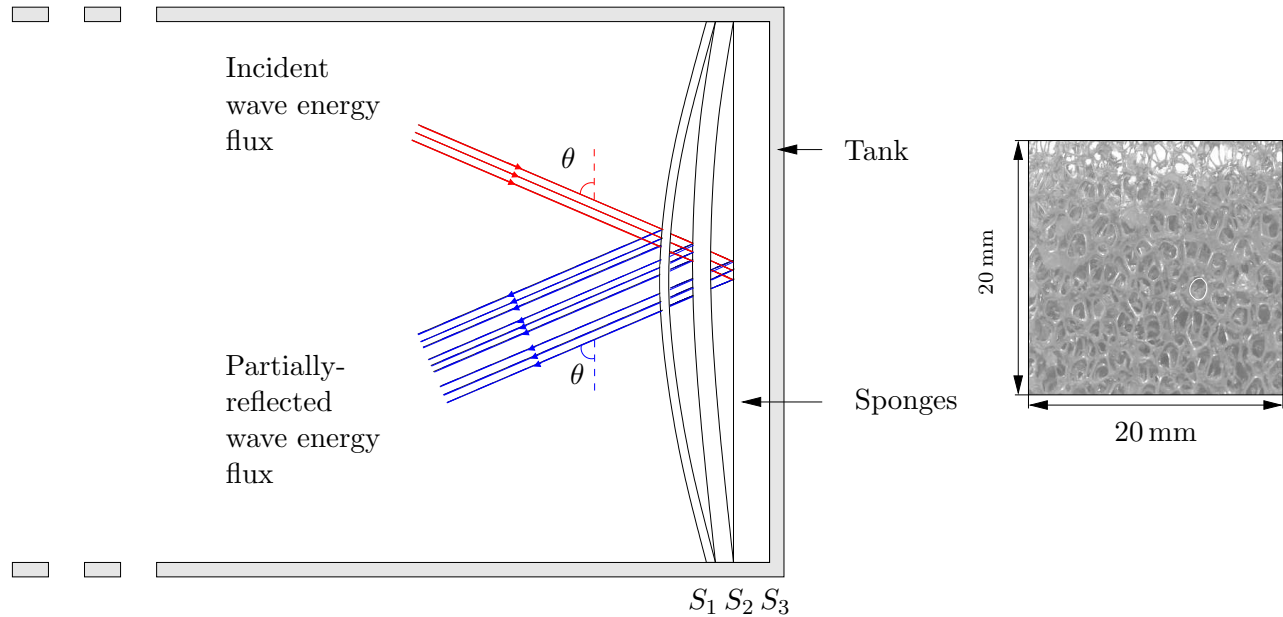


Figure 3.28: Schematic of wave beam reflection and transmission behaviour at layers of sponge. Red lines denote lines of constant phase associated with the incident wave beam. Blue dashed lines denote lines of constant phase associated with partial reflection at the sponge layers. Only primary reflections are shown for each of the layers. Arrows denote the direction of energy propagation. A 20 mm square section of the sponge material is also shown and a typical pore (~ 3 mm) is highlighted in white.

Alternative wave damping methods using netting and aluminium ‘honey comb’ to dissipate wave energy were used in experimental studies by Kwon *et al.* (2003) and Scase (2003) respectively. Several different materials and porosities of each were tested in this study and the sponge formation described above was the most successful.

Figure 3.29 shows the interaction of a wave beam propagating from the bottom left-hand corner of the picture with the sponge formation (highlighted in white at the top of the picture). A reflection with significantly reduced amplitudes can be seen propagating down from the sponge towards the right-hand side of the field of view. Figure 3.30 compares the superposition of across-beam amplitudes of cross-sections of wave beams over the course of one period of the motion. The cyan set of curves are those relating to cross-sections taken of a beam with centre point at a

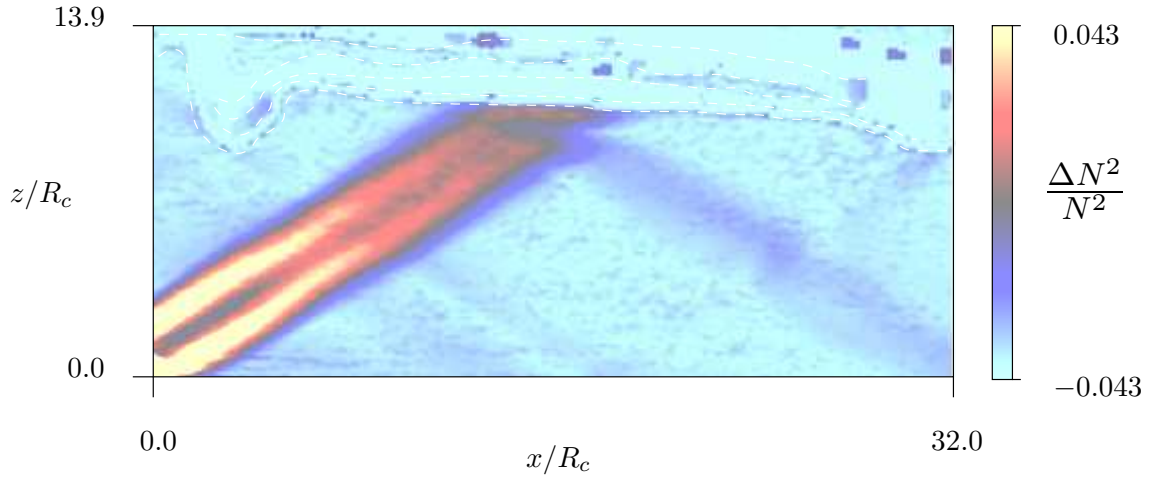


Figure 3.29: Wave damping by sponge layers (highlighted by white dashed lines).

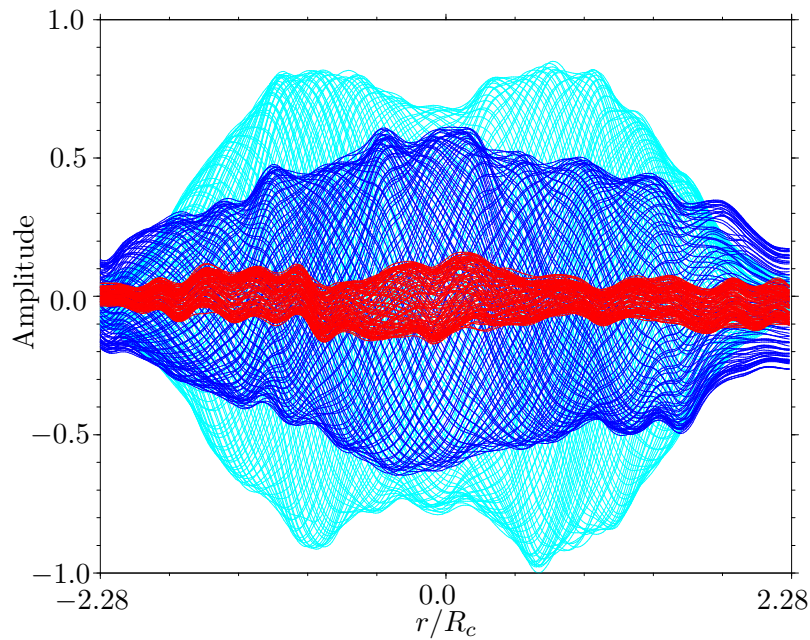


Figure 3.30: Amplitude reduction in wave beam reflections from sponges compared with those from a solid horizontal boundary. The curves are magnitudes of the perturbed buoyancy field throughout a period of the motion. Curves represent cross-sections taken from the incident beam (cyan); a beam after reflection from a solid horizontal boundary (dark blue) and a beam after interaction with the sponge formation (red). Amplitudes are normalised by the maximum amplitude of the incident beam.

horizontal distance of $\sim 10R_c$ from the centre of the cylinder prior (physically) to its interaction with the sponges. The dark blue set of curves are cross-sections of a beam with centre point at a horizontal distance $28R_c$ from the cylinder centre after reflection from a solid boundary. The red set of curves are cross-sections of a beam with centre point at a horizontal distance $28R_c$ from the

cylinder centre after reflection from the sponges. The reflections of the wave beams at the solid boundary and sponges occurred at similar distances from the centre of the cylinder.

A rest period of 50 minutes was allowed between experimental runs to ensure that all the wave energy, and in particular the enduring portion associated with smaller wavenumbers, was dissipated and the stratification had returned to its undisturbed state before subsequent runs.

3.8 Topography

Experiments were performed to investigate the interaction of wave beams with smooth horizontal and sloping boundaries, and with topographies which had sinusoidal, sawtooth, square-wave and approximately knife-edge profiles. Detailed descriptions of the specifications and positioning and insertion of the boundaries are given below together with a discussion of their influence on the density profile of the stratification over relevant time scales.

3.8.1 Smooth horizontal boundary

This study aims to determine the influence of rough boundaries on internal gravity wave propagation. It is therefore desirable to be able to compare the structure and evolution of a wave beam interacting with a boundary that has a specified profile with those of an unbounded wave beam. The finite extent and geometry of the tank used limited the distance over which a wave beam could be observed before it contacted and reflected from the tank base and sides or the free surface. The simplest reflective behaviour to study was that of a wave impinging on a smooth horizontal boundary. Comparisons were therefore made instead between the wavefields associated with scatter at rough topography and those associated with a wave beam reflecting at a smooth horizontal boundary. The mechanism used for the generation of internal wave beams (see section 3.6) aided this comparison since four beams of identical structure, allowing for phase shifts between upward and downward propagating beams and symmetry, are simultaneously produced by a cylinder oscillating in a linear, Boussinesq stratification. Provided that two of these beams were damped sufficiently that their influence on the observed wavefield was negligible (see section 3.7.1), the interaction of one of the two remaining beams with rough topography could be compared with the simultaneous reflection of the other beam at a smooth horizontal boundary.

An obvious choice for a solid reflecting boundary would be the base of the tank, however this was not ideal due to the form of the stratification there. Density profiles of stratifications used in experiments were discussed in section 3.2.2. A layer with a nonlinear density profile and a typical depth of ~ 30 mm inevitably formed at the base of the tank due to mixing during the filling process. As a result, the Brunt Väisälä frequency varied in this region and wave beams interacting with this layer and the base of the tank were observed to curve. Partial reflections could occur at any abrupt changes in N and some wave energy could even become trapped within the layer itself. In order to produce cleaner reflections, representative of those in a perfectly linear density profile,

the significance of the bottom boundary layer was reduced by the placement of a raised platform at the base of the tank prior to stratifying. The platform, or shelf, was made from a sheet of dark grey PVC (much denser than the saltwater) which measured 143 mm wide, 800 mm long and had a depth of 4 mm. The sheet was raised from the base of the tank by two strips made of the same material which ran along the underside of the shelf with a height of 45 mm. The total height of the shelf above the base of the tank was 49 mm which ensured that the shelf stood above the typical depth of the layer at the base of the tank. The dark colour of the PVC helped to reduce unwanted light reflections off the surface of the shelf which could have contaminated the synthetic schlieren processing. The PVC had negligible water absorption and so could be considered impermeable. Although a finite boundary layer of mixed fluid developed on the surface of the shelf due to its finite length, this was significantly shallower than the layer on the base of the tank. The finite length of the shelf also induced fluxes along its surface since horizontal density gradients in the fluid near the shelf ends generated baroclinic vorticity. These fluxes acted to reduce the depth of the boundary layer on the shelf as they provided a means of transporting and draining any mixed fluid forming along the boundary away into the stratification. The horizontal shelf was used in all experiments unless otherwise stated.

3.8.2 Smooth sloping boundaries

Experiments were performed to observe reflections of waves at smooth sloping boundaries that had surfaces making an angle α with the vertical. The data obtained is used to verify the behaviour predicted by linear inviscid theory (Phillips 1966) in chapter 4. (Data from these experiments also serve to validate the techniques used and described in this chapter.)

The sloping boundary was made from dark grey PVC of thickness 4 mm and was 148 mm wide and 800 mm long. A cushioning material was fixed with black tape along those edges of the slope which were in contact with the sides of the tank when it was in position within the stratification. The cushioned edges ensured that the slope spanned the entire width of the tank and completely sealed the part of the stratification on the front side of the slope from the part behind it.

The position at which the slope was inserted along the tank was selected based on the particular angle, α , of slope inclination, the position and frequency of the oscillating cylinder as well as consideration of the region of the stratification corresponding to the camera field of view. The geometries of wavefields were anticipated and the slope strategically placed to optimise the spatial extent of the reflected wavefields within the field of view and so that unwanted reflections and their interaction with the fields of interest were minimised.

The sloping boundary was inserted into the tank after stratification. A mount was constructed to support and maintain the inclination of the slope and so minimise mixing associated with its insertion into the tank. The mount consisted of a heavy steel base placed on top of the tank that had a flat upper section that could be inclined to a desired angle with an accuracy of $\pm 0.5^\circ$. Two rigid stainless steel runners of width 30 mm and length 550 mm were fixed onto the base of the mount a

distance 155 mm apart. The slope was placed onto the mount between the runners and these acted as a guide for the slope as it was slowly and smoothly pushed against the mount and into the tank. This was a difficult procedure to implement since the slope was necessarily only marginally narrower than the width of the tank to prevent seepage between the regions of the stratification separated by the slope. Several practise runs were performed in order to develop a suitable technique for pushing in the slope before this was actually done for experiments from which data was used in this study.

Insertion of a sloping boundary into the stratification did not significantly affect the linear stratification except for the diffusion driven flow in a boundary layer next to the slope (see section 3.7 and figure 3.22 (a)).

3.8.3 Rough topographic profiles

The main focus of the experimental study was to characterise the interactions of wave beams with rough topographies that had periodic sinusoidal, sawtooth, square-wave and approximately knife-edge profiles. Each topographic profile had a width of 143 mm and the profiles did not vary in the across-tank direction. Profiles were completely specified by their shape, a horizontal wavelength, $\hat{\lambda}_T$, a vertical length scale of variation, \hat{A}_T , and the total length of the topography L_T . An angle α is defined for each profile as

$$\alpha = \tan^{-1} \left(\frac{\hat{\lambda}_T}{4 \hat{A}_T} \right). \quad (3.23)$$

This angle corresponds to that made between the sloping sections of the sawtooth profiles and the vertical. In the case of other profile shapes, α indicates the relevant value of α for a sawtooth profile having the same values of $\hat{\lambda}_T$ and \hat{A}_T . Figure 3.31 shows the different profile shapes and defines the relevant length scales. Table 3.1 lists values of these length scales (to an accuracy of ± 0.05 mm) for the topographic profiles used and assigns a label to each different profile for ease of referencing. Topographic profiles *A* and *B* had sinusoidal shape; *C*, *D*, *E*, *F*, *G*, *H* and *I* had sawtooth shape; *J* and *K* had square-wave shape and *L* was a pseudo knife-edge profile with vertical approximate ‘knife-edges’ of finite width 2 mm.

Sinusoidal profiles *A* and *B* were made from sections of transparent PVC corrugated roofing material of thickness 1 mm and securely mounted with silicon based glue onto rigid dark grey PVC sheets of thickness 10 mm. The roofing material was sprayed matt black to reduce light reflections off its surface.

Sawtooth profiles *C* and *D* were made from sections of black plastic right-angled sections of thickness 2 mm that were cut into components measuring 143 mm and mounted adjacent to one another onto a base in the same way as profiles *A* and *B*. The radius of curvature at the corners of the angled-sections was therefore 2 mm.

The sawtooth profiles *E* - *I* and square-wave profiles *J* and *K* were cut in one complete piece directly from blocks of dark grey PVC using a milling machine. The milling machine cut lengths to an accuracy of ± 0.05 mm. Corners were sliced from the material so that their radius of curvature

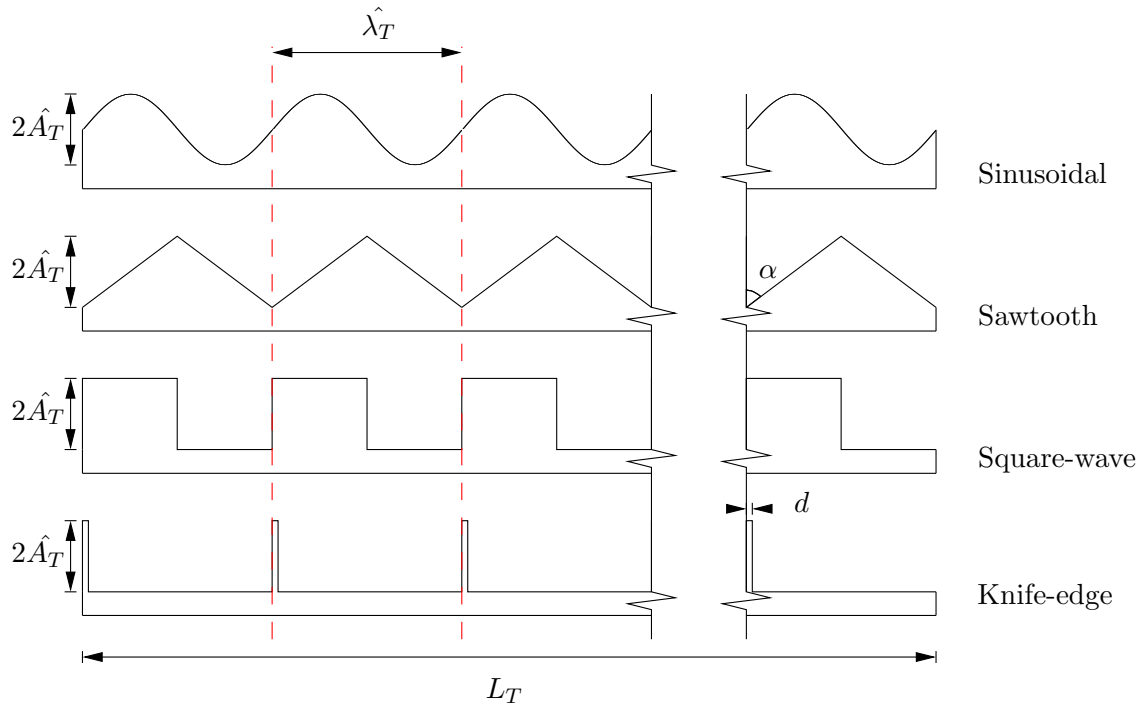


Figure 3.31: Topography side profiles and dimensions.

was minimal. A base of thickness 10 mm was also included into the form of the profile during the cutting process.

The ‘knife-edge’ profile L was made from a base of dark grey PVC of thickness 10 mm. The knife-edges were 2 mm wide prongs of acrylic. These were glued with silicon based glue into grooves of depth 2 mm cut across the width of the base at regular intervals. The transparent prongs were sprayed black to reduce light reflections. The radius of curvature of the knife-edges at the corners was ~ 2.5 mm.

Positioning and insertion of rough topography

To a good approximation, the stratifications could be considered Boussinesq (see section 3.2). As a result, the positioning of the topographic profiles at the top of the stratification or at the bottom could be arbitrarily chosen without influence on the behaviour of the wavefields. The rough topographies were positioned at the top of stratifications during synthetic schlieren experiments. This allowed the profiles to be lowered to a level where the stratification was linear as well as permitting the reuse of a stratification if possible for experiments with other profiles. The topographies were positioned at the base of the tank for the PIV experiments discussed in section 3.5.

The flat base of each rough topographic profile was drilled at mid-width in two positions approximately 50 mm from either end. Two rigid stainless steel threaded rods of diameter 6 mm and length 40 mm were screwed into the holes on the base of the profiles. The rods were threaded through and bolted to two stainless steel plates that were clamped firmly onto the top of the tank when

Profile Index T_i	Shape	α [degrees °]	$2\hat{A}_T$ [mm]	$\hat{\lambda}_T$ [mm]	$\hat{k}_T = 2\pi/\hat{\lambda}_T$ [mm ⁻¹]	$\hat{A}_T\hat{k}_T$	L_T [mm]
<i>A</i>	Sinusoidal	62.0	19.5	73.5	0.085	0.829	441.0
<i>B</i>	Sinusoidal	63.4	8.0	32.0	0.196	0.784	416.0
<i>C</i>	Sawtooth	40.0	19.0	31.9	0.197	1.872	416.0
<i>D</i>	Sawtooth	45.0	35.9	71.8	0.088	1.580	502.9
<i>E</i>	Sawtooth	45.0	18.0	35.9	0.175	1.575	431.1
<i>F</i>	Sawtooth	54.0	13.0	35.8	0.176	1.144	432.0
<i>G</i>	Sawtooth	63.5	18.0	72.2	0.087	0.783	432.0
<i>H</i>	Sawtooth	63.5	10.0	40.1	0.157	0.785	440.0
<i>I</i>	Sawtooth	69.5	10.0	53.5	0.117	0.585	432.0
<i>J</i>	Square-wave	45.0	20.0	36.0	0.175	1.750	414.0
<i>K</i>	Square-wave	61.0	18.0	72.0	0.087	0.783	432.0
<i>L</i>	Knife-edge	46.6	18.0	38.0	0.165	1.485	418.0

Table 3.1: Specifications of topographies used in experiments. Lengths are given to an accuracy of ± 0.05 mm.

the profile being studied was in position. The depth to which each profile was lowered within the stratification and also its horizontal levelling could therefore be controlled by adjusting the position of the bolts on the rods. Levelling was mainly assured before insertion into the tank by ensuring the bolts were the same distance along each of the rods. After insertion, the levelling was checked with a spirit level and any micro adjustments of the bolt positions could easily be done in a non-intrusive manner. The depth of each profile in the tank was chosen so that the vertical distance between the shelf and the topography was maximised for the density profile of the particular stratification. This required that stratifications were measured before topographies were inserted in order to determine the vertical level at which the stratification deviated from a linear density profile due to mixing and evaporation near the free surface. The profiles were then lowered so that the flat part of the base of the topography was just below this level (which made allowances for slight mixing induced whilst the profile was inserted into the tank). The profiles were slowly lowered into the stratification at the correct position along the tank to avoid unnecessary disturbance to the stratification from adjustments after insertion. As the profile was lowered through the free surface, care was taken to tilt the topography across the tank slightly so that the free surface contacted the underside of

the topography in a line which could be carefully moved across the topography as it was lowered further. This ensured that no pockets of air were trapped on the underside of the topography which both obscured the visualisation as well as making the fluid behave compressibly in that region.

Profiles were positioned centrally between the two side walls of the tank. Their location along the length of the tank required that they were as far away as possible from the end walls as well as being constrained by the relative position of the cylinder. Topographies needed to be far enough away from the cylinder that any component of the scattered wavefield with group velocity vector directed back towards the cylinder should be sufficiently damped by viscosity before reaching there and so have minimal second order influence on the wavefield propagating away from the cylinder.

Also, geometrical considerations due to the finite nature of each profile required that for a given frequency of cylinder oscillation, beams generated were incident on the topography at a position at least a beam width from its ends. Total lengths of the profiles were between 414.0 mm and 502.9 mm. Beam widths were approximately 35.6 mm near to the cylinder and widened slightly with distance as a result of viscosity (see chapter 2). For the range of beam angles, θ , viable in experiments, the largest horizontal component of beam widths occurred for large angles (corresponding to low frequency cylinder oscillation). For a maximum value of θ of about 75° , the horizontal component of the beam width was calculated as $\sim 35.6/(\cos(90 - 75)) \approx 38$ mm so that even the shortest topographic profile was ~ 10 times greater than the width of an impinging wave beam. The profiles were positioned within the tank such that incident wave beams did not contact the boundary close to its ends (at least a beam width away for quantitative results). In general the cylinder and topographic profiles were located fairly close to one another near the centre of the tank.

Once the relevant topography was in place, the phase-triggered LED attached to the cylinder oscillating mechanism was taped to the tank wall in front of a section of the topography in the field of view. Care was taken to keep the LED at least 10 mm from the edge of the topography so that light from the LED did not interfere with the synthetic schlieren visualisation. Figure 3.32 shows the relative positions of experiment equipment from the perspective of the camera.

Influence of topographic profiles on stratifications

The positioning of topographic profiles at the top of the tank minimised disturbances to density profiles of stratifications. Fluid displaced by the topography insertion was averaged over the length of the tank. The profiles intercepted isopycnals however and in a static stratification diffusion-driven mixing was induced at the sloping sides and sharp corners of topography as discussed in section 3.7.

Experiments were performed with the cylinder oscillating continuously at a fixed frequency of $\sigma/N = 0.59$ for 120 minutes in order to assess the influence of the presence of a topographic profile with a sustained wavefield on the density profile of the stratification. Figure 3.33 shows RMS_T images of a wave beam propagating from the bottom left-hand corner of the picture and interacting with topography, with a forward scattered wavefield evident propagating to the right-hand side of the field of view (a back-scattered wavefield is also evident). The RMS_T images were calculated

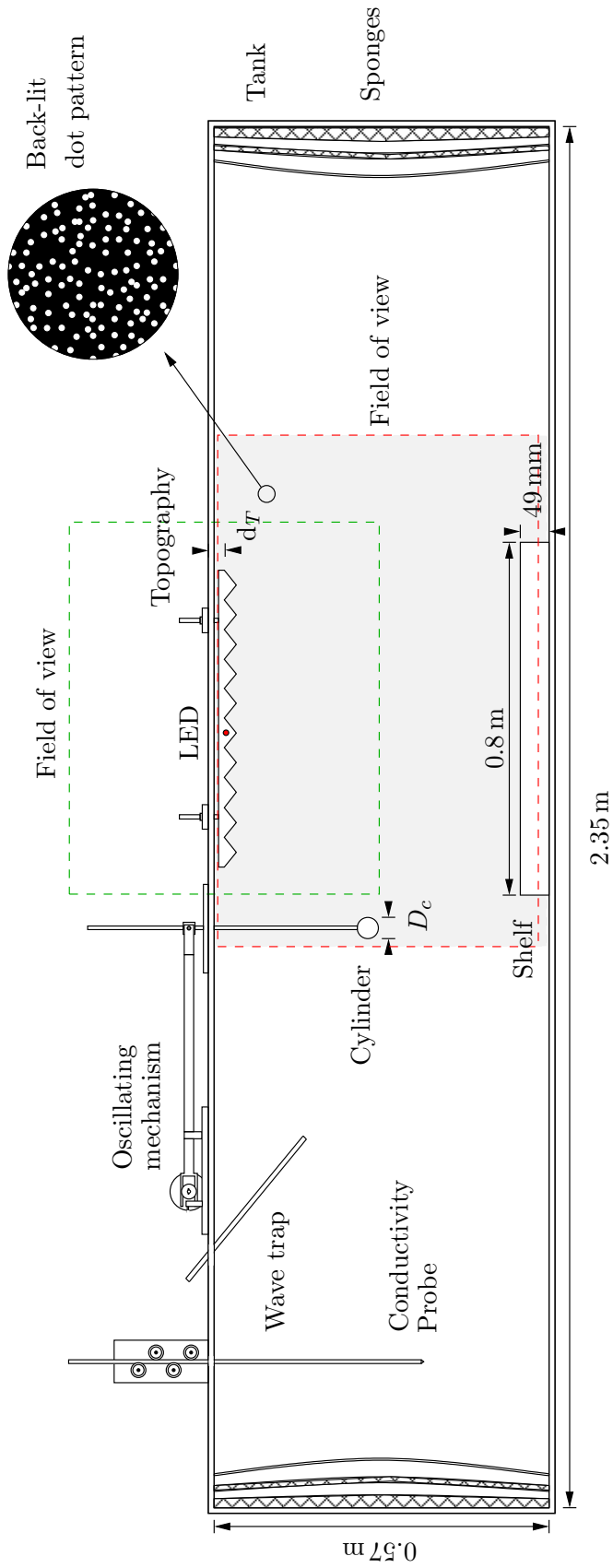


Figure 3.32: Camera view.

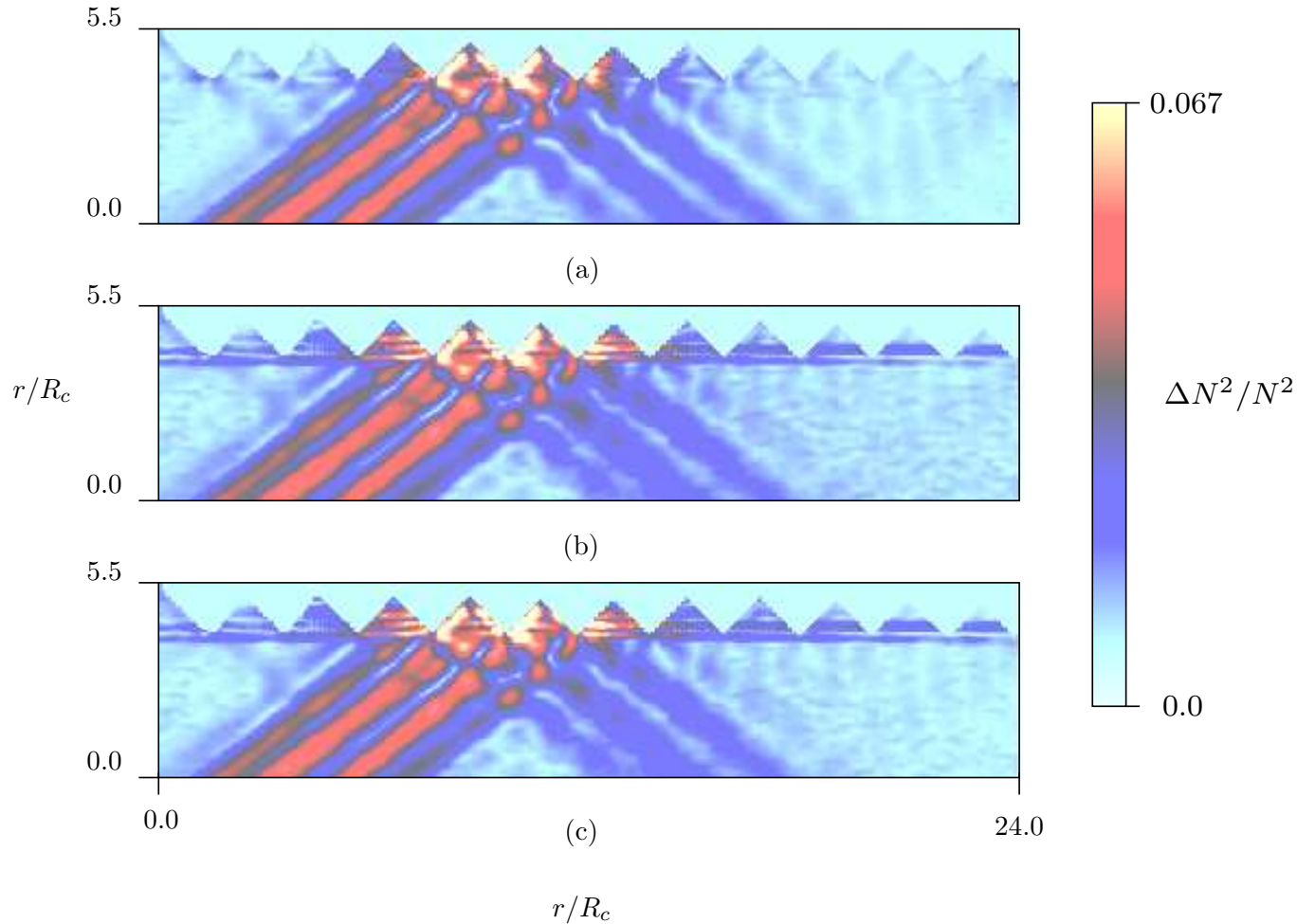


Figure 3.33: RMS_T images showing development of horizontal intrusions near sawtooth topography after cylinder oscillation at frequency $\sigma = 0.79$, *i.e.* $\sigma/N = 0.59$, for durations of (a) $\hat{t} + 0$, (b) $\hat{t} + 40$ and (c) $\hat{t} + 80$ minutes, where $\hat{t} = 4$ minutes.

from three periods of oscillation beginning at times of (a) $\hat{t} + 0$, (b) $\hat{t} + 40$ and (c) $\hat{t} + 80$ minutes, with $\hat{t} = 4$ minutes, after the oscillation was initiated. The wavefield remained qualitatively the same over the sequence of images except for the development of horizontal bands indicating mixed fluid. The bands were positioned about the vertical level of the topographic corners where the fluid mixed along the slopes and at the corner drained into the stratification and spread laterally. An oscillatory feature similar to that observed in figure 3.24 was also seen near the corners of the topography. These features are discussed further in chapters 5-8. A slight smoothing of the forward scattered wavefield structure was evident at the later times (figure 3.24 (b) and (c)) as presumably some of the incident wave energy reflected from the mixed layers as well as at the slopes of topography. However, the integrity of the stratification was maintained over the time scales of experiments. Stratifications were discarded whenever the vertical density gradient $\partial\rho_0/\partial z$ deviated significantly from a constant value or whenever the height of the section characterised by

the constant gradient became shorter than ~ 400 mm.

3.9 Summary

Methods used to collect data from experiments of internal gravity wave scatter at various topographic profiles have been outlined in this chapter. Some key features of the wavefield have been introduced and illustrated with experimental data. Results collected from the experimental study are analysed and discussed in chapters 4-8.

Chapter 4

Smooth topography

4.1 Overview

The previous chapters have established a context for the present research and have described experimental methods employed. This chapter presents results from this study that focus on reflections of wave beams from smooth boundaries that have continuous gradients. These include reflections at horizontal or sloping planar boundaries, at a smooth curved boundary and at sinusoidally varying topographic profiles. The wavefields are compared with linear theories based on geometrical ray tracing and methods of characteristics. Reflection behaviour is investigated in terms of parameters describing the relative slopes and length scales of the waves and topography. Results from this chapter are compared and contrasted with those relating to reflections at rough boundaries in chapters 6-8.

4.2 Reflection at a smooth horizontal boundary

Literature on internal gravity wave reflection at planar boundaries was discussed in sections 2.4.1-2.4.2. Experimental results for reflection at a horizontal boundary are presented here. Along-beam structures and amplitudes of incident and reflecting wave beams are compared with those of ‘freely’ propagating wave beams and reflecting wavefields as predicted by linear theory. The experimental setup employed in the present study (see chapter 3) allowed results to be collected of higher resolution and over a broader range of parameters than those described in previous studies. This permitted more detailed analyses (presented in this section) such as the generation of power spectra for the wavefields.

4.2.1 Qualitative results

Experiments were performed to view the reflected wavefields produced by wave beams reflecting at a horizontal boundary for incident wave frequencies in the range $\sigma/N \in [0.33, 0.71]$, corresponding to the range of propagation angles $\theta \in [44.5, 70.5]^\circ$. The synthetic schlieren processing used to

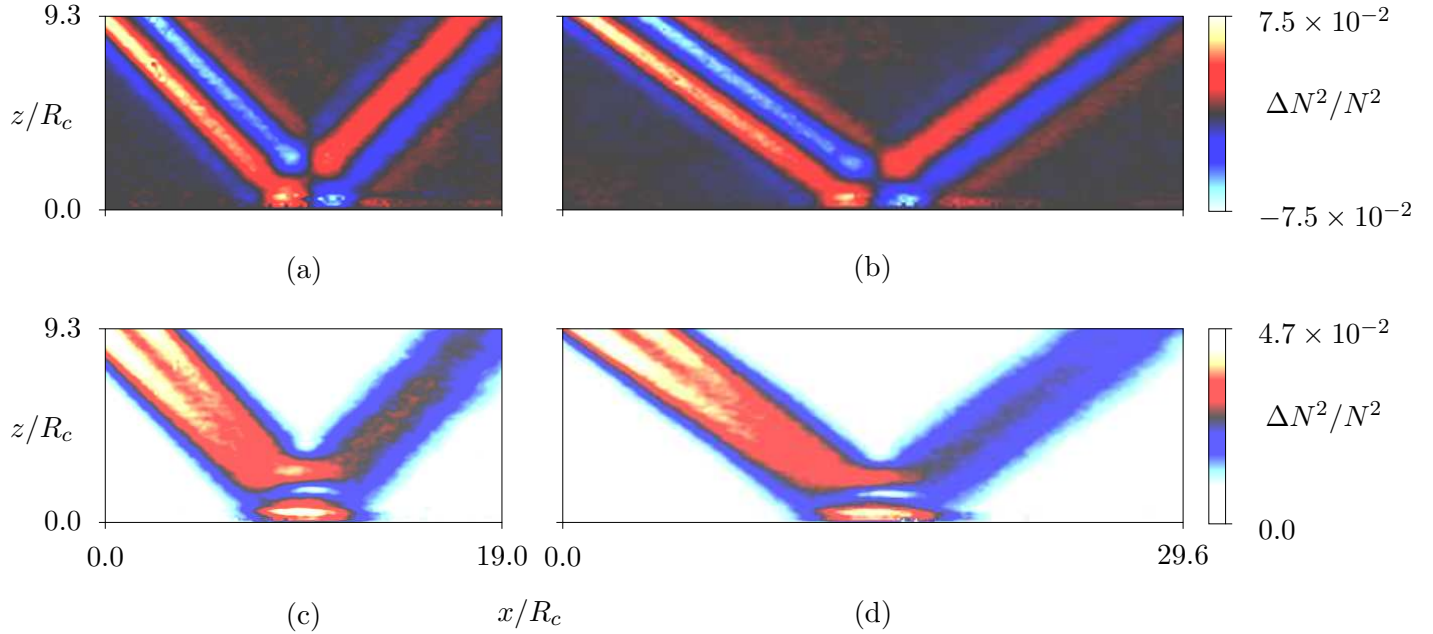


Figure 4.1: Images of the instantaneous perturbed buoyancy field for reflections at a smooth horizontal boundary with beams angles θ equal to (a) 44.8° and (b) 54.4° respectively, and corresponding RMS_T images shown in (c) and (d).

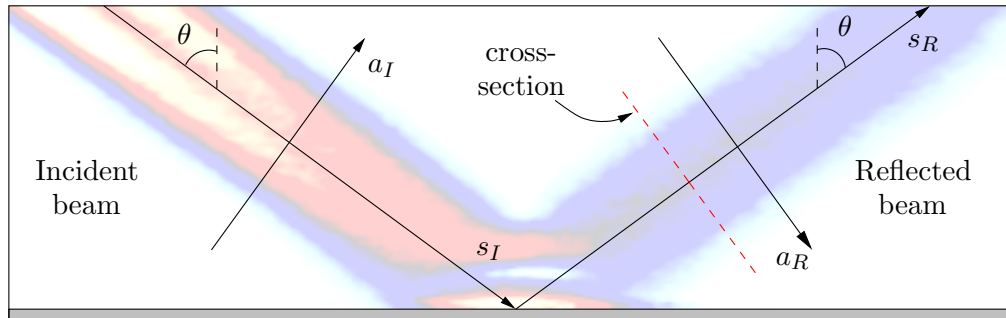


Figure 4.2: Coordinate systems used for incident and reflected wave beams.

visualise experiments readily yields the perturbed buoyancy field

$$\Delta N^2 = -\frac{\hat{g}}{\hat{\rho}} \frac{\partial \rho'}{\partial z}, \quad (4.1)$$

where ρ' indicates the perturbed density field. Root mean square averages of this field over several periods give a qualitative insight into the variation of the structure of wave beams (see chapter 3). Such an average is denoted here by RMS_T for convenience. Figure 4.1 shows both instantaneous (a and b) and RMS_T (c and d) $\Delta N^2/N^2$ images of wave beams reflecting at a horizontal boundary for values of θ (a, c) 44.8° and (b, d) 54.4° . Each figure shows an incident wave beam propagating from the top left-hand corner and reflecting at a horizontal boundary positioned at the bottom

of the image. Reflected wave beams subsequently propagate towards the top right-hand corners, making the same angles to the vertical as those made by the respective incident beams, indicating conservation of frequency at first order as predicted by linear theory (Lamb 1932, Phillips 1966).

Coordinate systems for the beams shown in figure 4.1 are defined in figure 4.2. Along-beam coordinates aligned with directions of energy propagation are denoted by s_I and s_R for the incident and forward reflected beams respectively. Across-beam coordinates are aligned with directions of phase propagation and are denoted a_I and a_R for the incident and forward reflected beams respectively. In the characteristic coordinate system of section 2.2.3, $a_I \equiv \xi$ and $a_R \equiv -\eta$. The origin of the coordinate system for the incident beam was taken as the center of the cylinder, given in cartesian coordinates by (x_c, z_c) . The origin of the coordinate system for the forwards reflecting wave beam was taken as the intersection of the centerline (i.e. specified by the centerpoint of the cylinder and the angle θ) of the incident beam with the vertical level of the boundary. In reality, from the perspective of the camera, the incident wave energy reflected from a vertical level slightly above the boundary due to minor parallax effects associated with the extremities of larger fields of view. An additional physical offset also occurred since wave energy also reflected from a narrow boundary layer that formed along the boundary (see section 3.8). However, these effects resulted in a negligible misalignment of the line $a_R = 0$ from the centerline of the reflected beam and so were ignored. The coordinates for the incident beam can therefore be written

$$a_I = x \cos \theta + z \sin \theta, \quad s_I = x \sin \theta - z \cos \theta \quad (4.2)$$

and those for the forward reflected beam

$$a_R = x \cos \theta - z \sin \theta, \quad s_R = x \sin \theta + z \cos \theta, \quad (4.3)$$

where the respective origins are those defined above. Note that the along and across-beam coordinates of the reflected beam have opposite vertical orientations to those of the incident beam.

At small distances along the incident beams shown in figure 4.1, maxima of the density perturbations lie along two tangents to the cylinder parallel to the beams. These maxima gradually converge with distance as viscosity acts to reduce gradients across each beam, acting preferentially on the higher wavenumber components. This is the well known bimodal to unimodal transition. The incident beams exhibit symmetry about their centerlines and their widths are approximately constant in the views shown.

The horizontal extent of the reflecting region, where the incident and reflected beams overlap and the wavefields superpose at the horizontal boundary, can be estimated from geometrical arguments using ray tracing to be

$$L_R = \frac{\hat{B}}{\cos \theta}, \quad (4.4)$$

where \hat{B} is the approximate incident beam width in the region near the boundary. As discussed in section 2.3.3, \hat{B} is dependent on the along-beam distance, s_I , and the viscous dissipation. The

height of the reflecting region above the horizontal boundary is similarly estimated to be

$$H_R = \frac{\hat{B}}{2 \sin \theta}. \quad (4.5)$$

Outside this region, the reflected beams shown have a unimodal structure, exhibiting maxima along their centerlines and have across-beam symmetry about the maxima. Values of the perturbed buoyancy field diminish and the beams gradually become narrower in width with along-beam distance s_R . The values associated with the reflected beams at small values of s_R , *i.e.* just outside the reflection region, are significantly smaller than those associated with large s_I , *i.e.* just prior (physically) to reflection. This perhaps indicates some enhanced dissipation in the reflection regions. Possible mechanisms for this enhancement could be interaction with the viscous boundary layer or nonlinear interactions where superposed amplitudes of the incident and reflected wavefields become large. Slight deviations of N in the region near the boundary from the constant interior stratification value (see section 3.8.1) could also contribute to this effect.

Time series images were formed from movies of the perturbed buoyancy fields along cross-sections of the beam of width $10R_c$. The cross-sections were taken at two along-beam positions for each beam and the time series produced typically represented 6 or more periods, T , of the first order wave motion. As an example, the cross-section indicated in figure 4.2 by the red dashed line is $6R_c$ wide and is located at a distance along the reflected beam of $s_R = 6R_c$. Figure 4.3 shows time series images taken from cross-sections positioned at (a) $s_I = 7R_c$, (b) $s_I = 12R_c$, (c) $s_R = 7R_c$ and (d) $s_R = 12R_c$ for $\sigma/N = 0.58$, corresponding to the RMS_T image shown in figure 4.1 (b). Frequency conservation is clearly evident in the time series of figure 4.3 as well as the shift from the distinct bimodal across-beam structure with amplitude peaks at $a_I/R_c = \pm 1$ in (a), and to a lesser extent in (b), to a unimodal structure with peak along the centerline $a_R/R_c = 0$ in (c) and (d).

4.2.2 Quantitative results: amplitudes

The amplitudes and structures of the incident and reflected beams corresponding to the experiment relating to figure 4.3 are compared here with the linear theory of Hurley & Keady (1997) for a freely propagating beam in a viscous fluid and with the linear inviscid theory of Phillips (1966) for reflection at a smooth boundary.

The theory of Hurley & Keady (1997) yields solutions for the stream functions for wave beams generated by a cylinder of radius R_c oscillating with vertical amplitude A_c such that $A_c/R_c \ll 1$ and at the temporal frequency σ in a viscous fluid. The stream function $\psi(x, z, t) = \hat{\psi}(x, z)e^{-i\sigma t}$ satisfies

$$\sigma^2 \nabla^2 \hat{\psi} - i\sigma\nu \nabla^4 \hat{\psi} - N^2 \frac{\partial^2 \hat{\psi}}{\partial x^2} = 0, \quad (4.6)$$

where ν is the kinematic viscosity. This is a form of (2.11) with the additional viscous contribution $-i\sigma\nu \nabla^4 \hat{\psi}$. Solutions for the stream function are found by rotating to the coordinate system

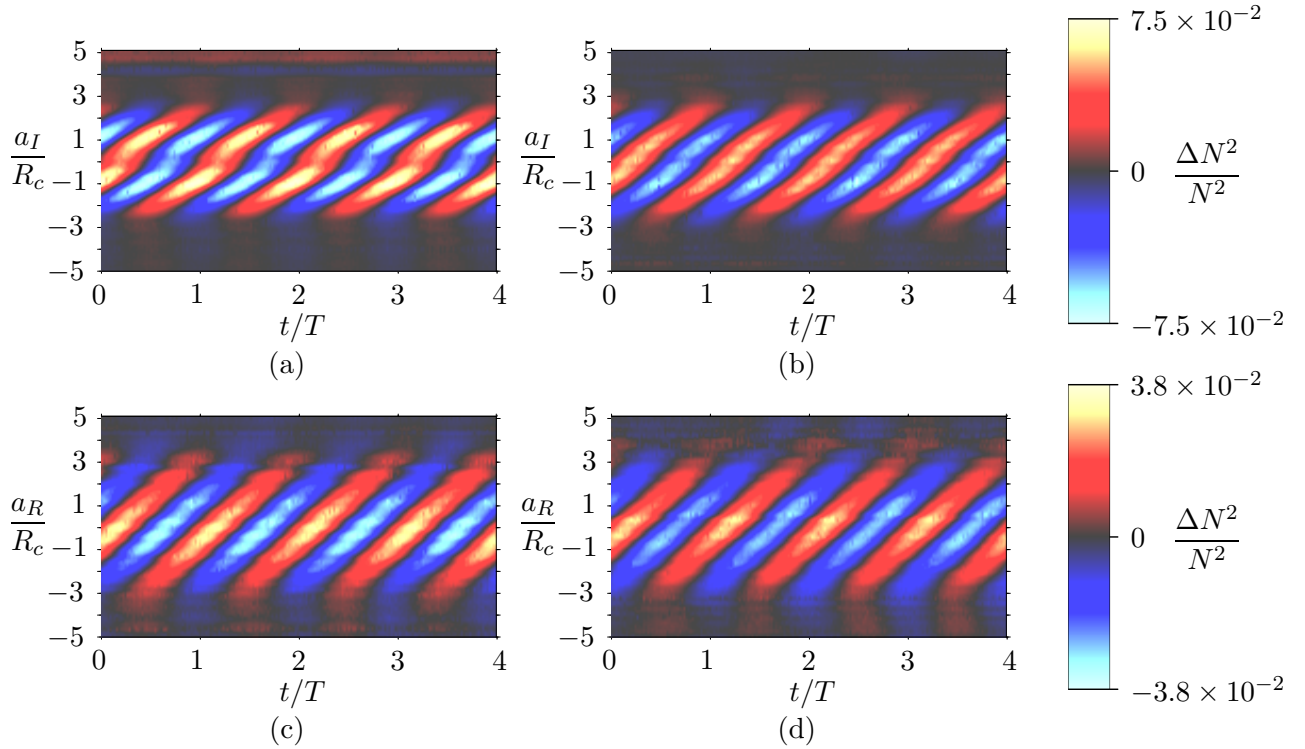


Figure 4.3: Time series images for cross-sections of established wave beams at positions (a) $s_I = 7$ and (b) $12R_c$ and (c) $s_R = 7$ and (d) $12R_c$ for $\sigma/N = 0.58$ and $T = 7.4$ s.

described above for the incident beam. The assumptions are made that

$$\frac{\partial \phi}{\partial s_I} \ll \frac{\partial \phi}{\partial a_I} \quad (4.7)$$

throughout the fluid, where ϕ represents a field variable, and that the depth of the boundary layer surrounding the cylinder is much smaller than R_c so that

$$\lambda = \frac{\nu}{2R_c^2 \sigma \tan \theta} \quad (4.8)$$

is a small quantity (Thomas & Stevenson 1972). The relevant linear viscous solution of the stream function for the incident wave beam is

$$\psi = \frac{iA_c \sigma R_c}{2} e^{i(\theta - \sigma t)} \int_0^\infty \frac{J_1(K)}{K} \exp\left(-K^3 \lambda \frac{s_I}{R_c} - iK \frac{a_I}{R_c}\right) dK, \quad s_I > 0 \quad (4.9)$$

where the function J_1 is the first order Bessel function of the first kind (Hurley & Keady 1997). The factor multiplying the integral in (4.9) encompasses the temporal variation of the wavefield and the form of generated wave groups as imposed by the shape and dimensions of the cylinder (*c.f.* chapter 5 where cylinders with elliptical cross-sections are also considered). The influence of viscosity is enforced by the first term of the exponent within the integral and indicates that as they

propagate away from the cylinder, wave components are attenuated at a rate $\sim k^3$, where k is the wavenumber, so that high wavenumber, *i.e.* small length scale, components are attenuated most rapidly. This solution can be used to derive a linear analytical approximation for the square of the perturbed buoyancy field ΔN^2 by solving

$$\Delta N^2 = - \left[\frac{iN^2}{\sigma} \frac{\partial^2 \hat{\psi}}{\partial x \partial z} \right] e^{-i\sigma t} \quad (4.10)$$

to give

$$\Delta N^2 = \frac{A_c R_c N^2}{2} e^{i(\theta - \sigma t)} \int_0^\infty \left(-\frac{1}{2} (\lambda^2 k^4 R_c^4 + 1) k^2 \sin 2\theta + i \lambda k^4 R_c^2 \cos 2\theta \right) \frac{J_1(R_c k)}{k} \exp(-R_c^2 k^3 \lambda s_I - i k a_I) dk, \quad (4.11)$$

where $k = K/R_c$ (Sutherland *et al.* 1999). Wave beams with group velocities directed with the same horizontal sense but opposite vertical sense exhibit a negative symmetry so that the solution for ΔN^2 for a beam oriented with the forward reflected beam is simply the negative of (4.11). Solutions of (4.11) were obtained in this study using numerical integration in Matlab.

Figure 4.4 shows instantaneous across-beam values of the perturbed buoyancy field at along-beam positions (a) $s_I = 7R_c$ and (b) $s_R = 12R_c$ for time series sections shown in figure 4.3 (a) and (d) respectively and at the four times $t/T = 0, 1/4, 1/2$ and $3/4$. The bold red line illustrates extrema for the time series. The distinct bimodal amplitude envelope of the cross-section of the incident beam is evident in figure 4.4 (a). The envelope is almost symmetric about $a_I/R_c = 0$, with peaks of ~ 0.079 at $a_I/R_c = \pm 1$ and tending to zero at $a_I/R_c \approx \pm 3$. In contrast, amplitudes along the cross-section of the reflected beam shown in figure 4.4 (b) follow a symmetric unimodal envelope structure, with a peak value of ~ 0.033 at $a_R/R_c = 0$.

Linear inviscid theory predicts that energy density is conserved on reflection at a horizontal boundary (Phillips 1966). At first order, it can therefore be expected that any decay in energy flux, and hence amplitude, in the along-beam direction is due to the diffusive action of viscosity alone. Figure 4.4 (c) and (d) compares across-beam amplitude predictions of the linear viscous theory of (4.11) with the corresponding amplitudes measured in the experiments shown in figure 4.4 (a) and (b) respectively. The along-beam distance, s , used in the calculation of (4.11) for the cross-section of the reflected beam (figure 4.3 (d)), is $s = \hat{s}_I + s_R$, where \hat{s}_I is the total distance along the centerline of the incident beam between the center of the cylinder and the intersection of the line with the horizontal boundary. The change in direction of propagation of the phase for the reflected beam was also accounted for in the calculation. The theoretical predictions compare closely with those measured along the cross-section of the incident beam corresponding to figure 4.4 (c). The linear theory also correctly models the unimodal across-beam structure of the cross-section of the reflected beam corresponding to figure 4.4 (d) but significantly overpredicts the magnitude

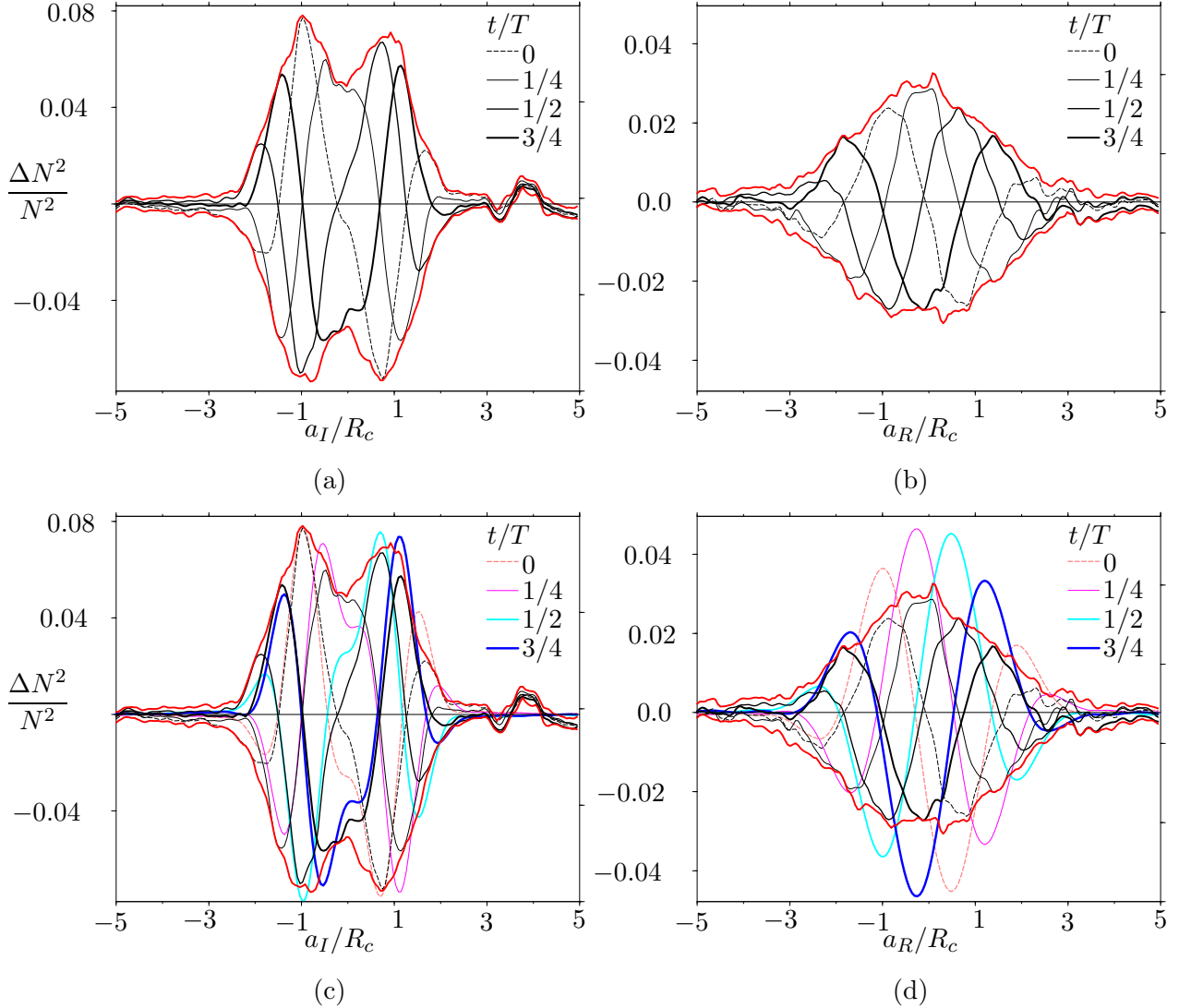


Figure 4.4: Instantaneous cross-beam values of the perturbed buoyancy field along cross-sections of (a) incident and (b) reflected beams associated with figure 4.1 (b) and comparisons of the measured cross-sections with linear theory in (c) and (d) respectively.

of the perturbed buoyancy field with peak values ~ 0.048 compared with measured peaks of ~ 0.033 . This discrepancy suggests that a proportion of the incident energy flux is lost from the reflected wavefield, either through enhanced viscous dissipation or nonlinear mechanisms where the incident and reflected wavebeams overlap near the boundary. The more complex structure of the overlap regions results in larger spatial gradients that promote viscous attenuation, whilst larger amplitudes caused by superposition of the incident and reflected wavefields in this region may enhance other nonlinear behaviour. However, since $\sigma/N = 0.58 > 1/2$, higher propagating harmonics of the primary wavefield cannot be generated. Instead energy can be dissipated in this regime by disturbances that decay exponentially in space away from their generation region.

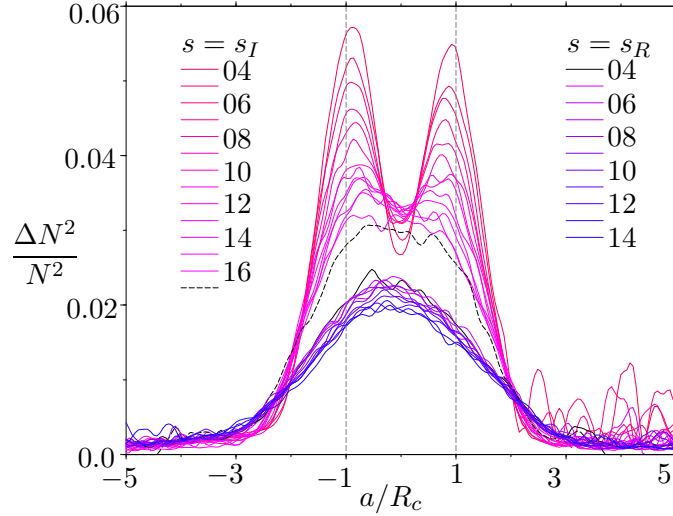


Figure 4.5: Across-beam RMS_T amplitudes at different values of s_I and s_R for $\sigma/N = 0.58$. Grey dashed lines indicate locations of tangents to cylinder in along-beam directions. The dashed black line indicates the cross-section measured closest to the horizontal boundary, positioned at $s_I/R_c = 17$.

Figure 4.5 shows RMS_T amplitudes of the perturbed buoyancy field taken along cross-sections of the incident and reflected beams of the experiment shown in figure 4.1. Note that due to the presence of the boundary, it was not possible to obtain measurements along cross-sections of the desired width on either beam for sections located within a distance of $s \sim 4R_c$ from the boundary. The figure clearly shows the erosion of the bimodal across-beam structure that is evident at small distances s_I from the cylinder, to a unimodal structure at large s_I . RMS_T amplitudes along the cross-sections of the reflected beam also have a unimodal structure that decreases in amplitude as s_R increases. The transition between a bimodal and unimodal form of the incident wave beam envelope is estimated to occur between $s_I = 15$ and $17R_c$. However, viscous theory (see section 2.3.2) calculates the transition distance, s_ν , to be $s_\nu \approx 462R_c$ (Makarov *et al.* 1990). Sutherland *et al.* (1999) found similar discrepancies with a predicted transition distance of $279R_c$ compared with an observed value of $\sim 8R_c$ and hence questioned the validity of (2.24). In particular, the viscous theory omits the inclusion of a viscous boundary layer on the surface of the oscillating cylinder.

Quantitative results: spectral techniques

In order to determine the partitioning of wave energy between different wavenumber components and its redistribution on reflection, various spectral methods were investigated for their suitability in the present study for analysis of time series of quantities along cross-sections of wave beams. A data set $f(a)$, where here a denotes a spatial quantity, can be represented in terms of the relative contributions from its constituent components that are associated with different wavenumbers. The most common representation of this is the power spectrum, $P(k)$, which can be found from

transforms using e.g. Fourier, maximum entropy or wavelet methods that use basis functions to map the spatial data into wavenumber space. The choice of analysis tool depends on the nature of the particular data set. Data sets used in the present study are discrete in their spatial sampling and finite in extent. Unless otherwise stated, cross-sections of wavefields measured $10R_c$ in length, corresponding to a resolution of $N_f \sim 200$ pixels in a field of view of dimensions $\sim 681 \text{ mm} \times 500 \text{ mm}$. As the present interest was in analysing the scattering behaviours of the wavefields at ‘rough’ boundaries, the spectral method employed was required to correctly capture rapidly varying in space and typically localised features of the data sets. A brief overview of the methods listed above is given here and the reader is directed to Press *et al.* (1992) for more detail on each method and associated power spectra calculation. Whilst other techniques for spectra calculation exist, such as the method of matching pursuits (e.g. Addison 2002), these are not discussed here further.

The Fourier transform, FT, or in the case of discretely sampled data, the discrete Fourier transform, DFT, is perhaps the most commonly used spectral technique. Fourier methods determine a unique and invertible representation of a data vector in wavenumber space using sine and cosine basis functions. The Fourier transform, $F(f)$, is given by

$$F(f) = \int_{-\infty}^{\infty} f(a)e^{ika} da \quad (4.12)$$

and its discrete analogy by

$$F(f_n) = \sum_{n=0}^{N_f-1} f_n(a)e^{ink_a}, \quad (4.13)$$

(e.g. Press *et al.* 1992; Sneddon 1995; Bracewell 2000). Efficiency of numerical computations of the DFT are often improved by employment of fast Fourier transforms, FFT, which significantly reduce the number of operations from $O(N_f^2)$ to $O(N_f \log_2 N_f)$ (Cooley & Tukey 1965). The sinusoidal basis functions of DFT have infinite spatial extent and hence allow the accurate representation of periodic data sets. The application of the DFT to a finite data set, however, effectively employs the assumption that the data is a truncated sample with length equal to one period of an infinite data set. This can therefore introduce false wavenumber components into the calculated spectra. In the same manner, the DFT is also unable to correctly resolve localised features in the data. An adaptation of the DFT that aims to resolve these features is the ‘windowed Fourier transform’ (Press *et al.* 1992). This splits the data into equal sections, or ‘windows’, and calculates the DFT for the data from a composite of DFT’s performed in each of these windows. Again, due to the periodicity of the basis functions, this method is highly sensitive to the choice of window size and positioning within the data.

In contrast, the maximum entropy method fits a chosen number of rational basis functions to the data set, assuming exponential decay of the data set outside the region of definition. The combination of these functions used to represent the data is selected using methods from Bayesian statistics. Effectively, for a particular selected level of detail or ‘trueness’ (specified by the number

of rational functions used in the calculation) to be maintained, the simplest representation of the data is chosen by maximising the ‘Shannon entropy’ (e.g. Cornwell & Evans 1985). This statistical measure is greatest for the most simplified version of the data. Hence the maximum entropy method involves some smoothing of the data, which may or may not be beneficial in the given application, and is therefore not exactly invertible. The use of rational functions, which support poles, allows the identification of both local physical and spectral features of the data provided that the number of rational functions is correctly specified for the particular data set.

Wavelet methods use basis functions known as ‘wavelets’ or ‘mother functions’ to perform rotations between physical and wavenumber space (e.g. Addison 2002). The wavelet transform, WT, or discrete wavelet transform, DWT, for a given data set uses a family of wavelets that are completely defined by scalings of the ‘mother function’ form chosen (e.g. Daubechies 1988). An infinite number of possibilities exist for the choice of the mother function and the most appropriate shape can be selected for the particular type of data being analysed. Unlike the Fourier basis functions, wavelets have finite spatial extent, *i.e.* ‘compact support’. These wavelets are translated along the data vector and scaled locally to fit the data structure there - hence allowing detailed representation of isolated features of the data. This localised analysis of the data also allows the locations within the data vector of its different spectral components to be identified, which is not possible with either Fourier or maximum entropy methods. Wavelet transforms are invertible and are most commonly used in data compression. Detailed reviews of wavelet methods and their applications can be found in Kaiser (1994), Kumar & Foufoula-Georgiou (1997), Mertins (1999), Walker (1999) and Mix & Olejniczak (2003).

Each of the spectral methods introduced above benefit from the selection of data that has magnitudes that tend to zero at its end points, hence reducing inaccuracies (‘spectral leakage’) introduced to the spectra caused by the assumption in the FFT of periodicity of the finite data set, etc. It is possible to multiply the data by a ‘window function’, which would enforce a tapering of the measured fluid motion towards the ends of cross-sections. However, this precaution is instead satisfied by the choice of broad cross-sections of length $10R_c$ (described above) that are carefully positioned within the field of view, since the across-beam structures of incident and reflected wave beams are generally of width $\sim 6R_c$, with negligible fluid motion outside this region. This condition is further enforced by the use of ‘zero padding’ at the ends of the data (e.g. Press *et al.* 1992; Mertins 1999; Addison 2002). Zero padding involves artificially widening the data vector with zero values. In the present study, data vectors were widened by a factor of 10 to a width of $100R_c$, where the original data was centered within the padded vector. Various degrees of zero padding were tested (in a similar manner as described below) and no significant improvement was observed for data extensions beyond the cross-section width of $\sim 100R_c$, though processing time was increased as data vectors were lengthened. In order to reduce the effects of transient noise in the data, which had high temporal frequency, spectra calculated from instantaneous measurements along a cross-section were also averaged over several complete periods of the first order wave motion.

Tests were made to assess the performance of the various spectral methods, with zero padding

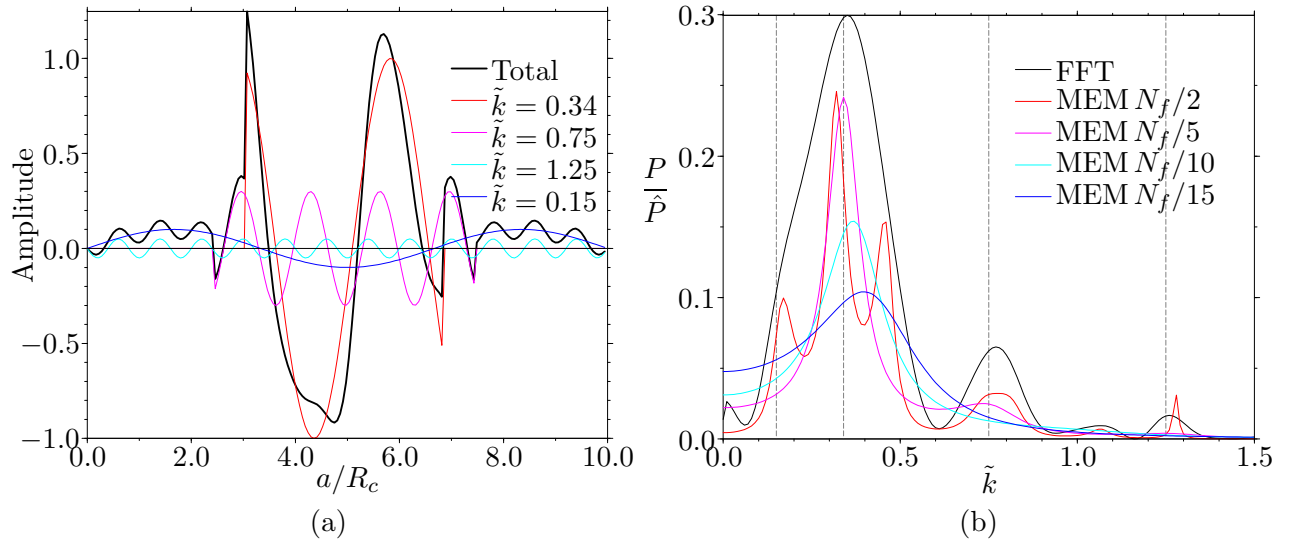


Figure 4.6: Tests of spectral methods for a specified data set. Here (a) plots a prescribed data set and its individual wavenumber components and (b) plots power spectra calculated with Fourier and maximum entropy methods. \tilde{k} is a nondimensional wavenumber representing the number of waves in an across-beam section of length R_c .

employed in all calculations in the manner described above. Figure 4.6 (a) shows an artificially prescribed data set (thick black line) together with its individual locally sinusoidal components, which have the wavenumbers indicated. The data was constructed with features typical of data collected in this study, with similar spatial resolution and an abruptly varying profile composed of several dominant components as well as a component representing relatively small amplitude, high frequency noise. Figure 4.6 (b) compares the various power spectra calculated from the artificial data using FFT and MEM (with different numbers of rational functions as indicated) techniques. The grey dashed lines indicate the actual positions of the known peak wavenumbers at $\tilde{k} = 0.15, 0.34, 0.75$ and 1.25 , where, unless otherwise stated, units of wavenumbers presented with the tilde, $\tilde{\cdot}$, notation are henceforth understood to correspond to the number of waves per cross-section of length R_c . The FFT method performs the best, correctly predicting peaks at, or closest to, the actual wavenumbers. The peak at $\tilde{k} = 0.2$ is amalgamated with that at $\tilde{k} = 0.34$, though its presence is evident in the asymmetry of the peak. There also appears to be a weak signal of a false wavenumber component predicted near $\tilde{k} = 1.1$. Of the various MEM spectra, the most accurate at locating positions of peaks appears to be the spectra calculated using $N_f/5$ rational functions. However, this fails to display a convincing signal at $\tilde{k} = 0.2$ or 1.25 , and consistently produces peaks that are less pronounced, and hence less distinct for analysis purposes, than those generated by the FFT method. The other MEM spectra exhibit peak splitting or wavenumber omissions - illustrating the sensitivity of this method to the choice of the number of rational functions used. Several tests with other data sets yielded similar behaviour to that shown in figure 4.6. A wavelet transform using the Daubechies-20 wavelet mother function (see Press *et al.* 1992; Addison 2002) was also compared to the FFT and MEM techniques, producing similar spectra to the FFT. The

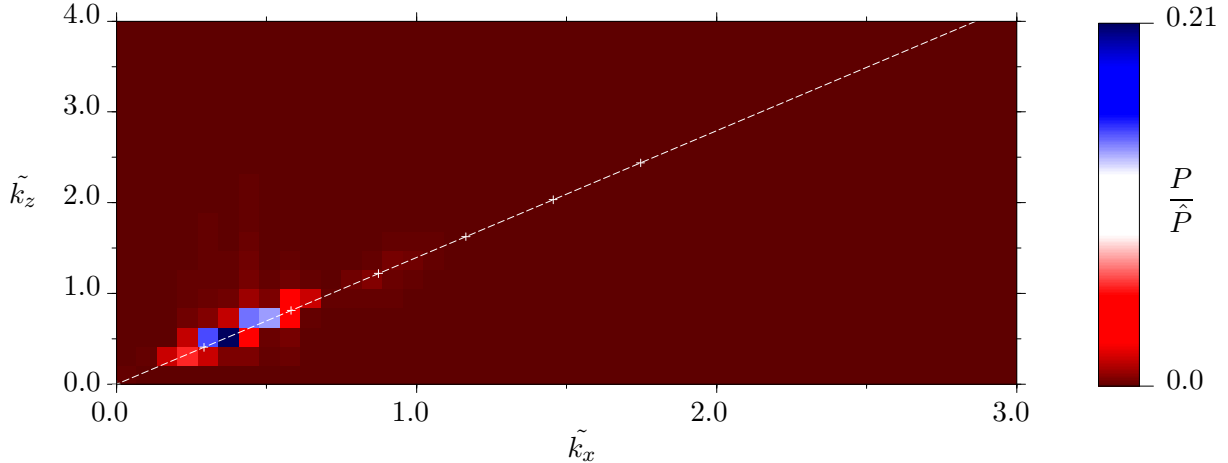


Figure 4.7: Two-dimensional power spectra for the sequence of images associated with the experiment of figure 4.1 (b) and (d). Power, P , is normalised by total power, \hat{P} . \tilde{k}_x and \tilde{k}_z denote nondimensional wavenumbers representing the number of waves in horizontal and vertical sections, respectively, of length R_c . The dashed white line indicates the orientation of the corresponding nondimensional across-beam wavenumber \tilde{k} , *i.e.* the wavenumber aligned with those directions making an angle $\theta = 54.4^\circ$ with the horizontal. Marks along the dashed line indicate magnitudes in the across-beam direction of $\tilde{k} \in [0, 3]$ incremented by 0.5.

wavelet transform also produced additional spatial information about the location of the different wavenumber components within the data. However, since FFT are more commonly used in internal gravity wave studies, and hence some validation of the wavelet transform is desirable before its use here, and as the processing time of the DWT was greater than that of the FFT, unless otherwise stated, the FFT was used for spectral analysis throughout this research. Study of the data using wavelet transforms will be the subject of future work.

Quantitative results: spectral analysis at a fixed frequency

Figure 4.7 shows the two-dimensional power spectra averaged over $2T$ of the motion for $\sigma/N = 0.58$. Wavenumbers represent the number of waves per unit distance equal to R_c . The dashed line, given by $\tilde{k}_z = \tan \theta \tilde{k}_x$, indicates the across-beam orientation of the wavenumber of the first order wave motion, \tilde{k} . The distribution of power along the dashed line indicates that the fluid motion is dominantly associated with across-beam phase propagation. Normalised power values are greatest for $\tilde{k} \in [0.50, 1.0]$, with the maximum value, $P/\hat{P} = 0.21$, located near $\tilde{k} \approx 0.60$. Interpretation of the two-dimensional power spectra such as that shown in figure 4.7 is restricted. In particular, the evolution of across-beam wavenumber spectra as waves propagate away from the source can not be deduced from the two-dimensional power spectra and so one-dimensional spectra taken along cross-sections of wave beams are used instead throughout this thesis.

Figure 4.8 (a) shows power spectra of time series taken at across-beam sections located at

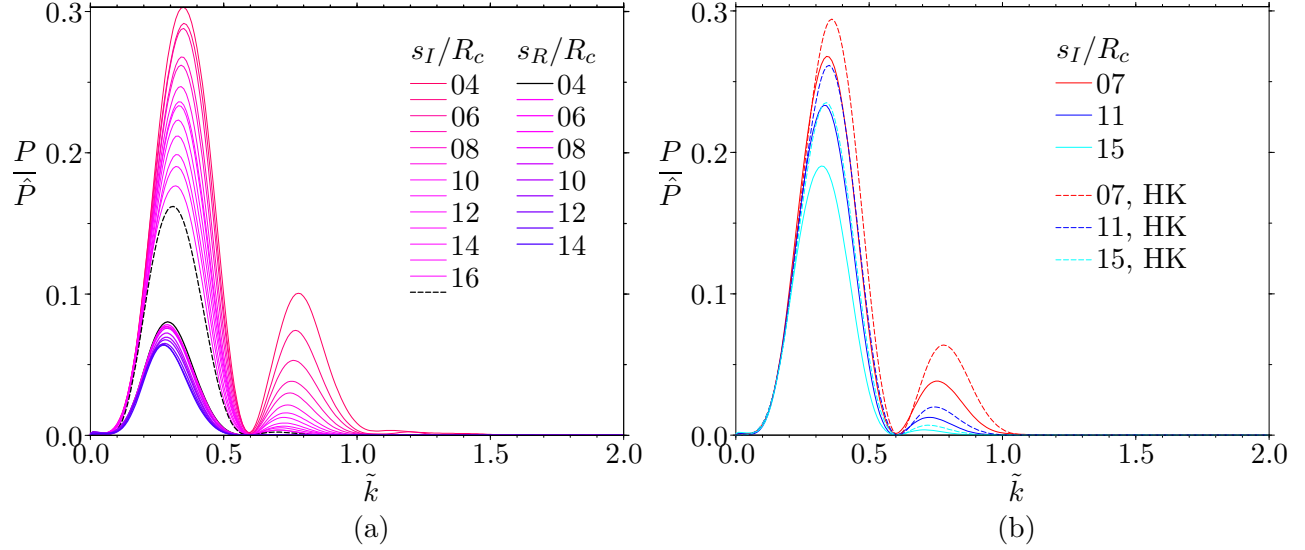


Figure 4.8: Power spectra of across-beam sections associated with figure 4.5. Power, P , is normalised by total power, \hat{P} , associated with the section at $s_I = 4R_c$. The dashed black line indicates the cross-section in (a) measured closest to the horizontal boundary, positioned at $s_I/R_c = 17$. Predictions of linear theory (dashed lines, HK = Hurley & Keady 1997) are compared in (b) with power spectra calculated from experiment cross-sections (solid lines) located at $s_I/R_c = 7, 11$ and 15 .

distances $s_I = 4 - 17 R_c$ along the incident beam associated with figure 4.5 and $s_R = 4 - 14 R_c$ along the beam reflecting from the horizontal boundary (corresponding to a total distance of $s = \hat{s}_I + s_R \approx 27 - 37 R_c$ from the cylinder centre). Since potential energy is proportional to the square of the displacement, the potential energy density is proportional to P^2 . Omitted power spectra at distances from the cylinder between 17 and $\sim 27 R_c$ are those for which complete cross-sections were not possible near the reflection region. Spectra for the incident cross-sections show two distinct peaks. The largest peaks are found for spectra corresponding to the cross-section positioned closest to the cylinder at $s_I = 4R_c$, with the largest of these located at a wavenumber of $\tilde{k} \approx 0.36$ and a second peak located at a wavenumber of $\tilde{k} \approx 0.78$. As the along-beam distance of the cross-sections is increased, the power associated with these peaks decreases and is accompanied by a slight skew of the peak to smaller wavenumbers. The general reduction in power with increasing distance from the cylinder is predominantly a result of viscous attenuation of the wave motion, whilst the skew to lower wavenumbers can be understood as the preferential action of viscosity on larger wavenumber components, which are associated with larger across-beam gradients and hence larger degrees of shear as discussed in section 2.3.2. Power associated with the higher wavenumber component is reduced to a negligible value prior to reflection. As a result, spectra associated with the reflected beam show peaks only near a wavenumber of $\tilde{k} = 0.31$. This peak is consistent with the lower wavenumber peak of the incident spectra and hence suggests that, in agreement with linear theory (Lamb 1932; Phillips 1966), wavenumbers associated with the incident wavefield are conserved on reflection at the horizontal boundary. The peak magnitude of the spectra for the cross-section at

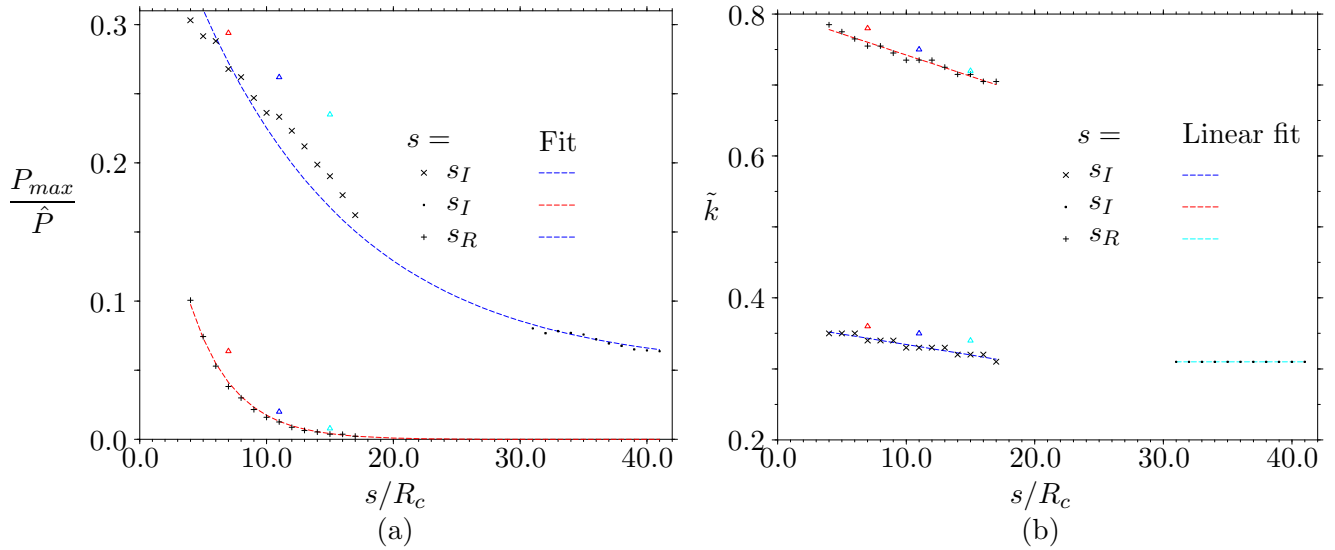


Figure 4.9: Wavenumber calculations from across-beam sections associated with figure 4.5. Here (a) shows variation of maximum normalised power, P_{max}/\hat{P} , of spectra with s and corresponding exponential fits and (b) shows variation of wavenumbers of spectra peaks with s and corresponding linear fits. Triangular symbols in both panels indicate predictions of linear theory, with colours corresponding to those of predicted spectra plotted in figure 4.8 (b).

$s_R = 4R_c$ along the reflected beam is approximately half that of the spectra for the cross-section at $s_I = 17R_c$ along the incident beam. This reduction occurs over a distance of $s \approx 10R_c$ and is likely to be caused by both viscous attenuation as well as some enhanced dissipation in the region near the boundary where incident and reflected wavefields overlap.

Figure 4.8 (b) plots spectra for cross-sections positioned at $s_I/R_c = 7, 11$ and 15 calculated from experimental data (solid lines), also shown in figure 4.8 (a), together with spectra calculated from viscous linear theory (Hurley & Keady 1997) at these positions (dashed lines). Magnitudes of spectra predicted by linear theory are consistently larger than those measured in experiments. This discrepancy increases with along-beam distance. A slight offset in the positions of the peak wavenumbers also occurs between the theory and experiments, with peak experimental wavenumbers slightly smaller than those predicted.

Figure 4.9 (a) compares power magnitudes of the experiment and theoretical spectral peaks shown in figures 4.8 (a) and (b) for increasing along-beam distances. Black ‘cross’ and ‘plus’ symbols represent magnitudes of the experimental peaks associated with the incident spectra near $\tilde{k} \approx 0.35$ and 0.78 respectively. Black ‘dot’ symbols represent those associated with the reflected spectra near $\tilde{k} \approx 0.35$. Coloured triangles indicate the corresponding positions of peaks for the incident spectra predicted by linear theory. The dashed blue line is a fit to the experiment data with form $P_{max}/\hat{P} \approx 0.05 + 0.39 \exp[-0.08s]$, indicating an exponential decay in the power associated with the peak near $\tilde{k} \approx 0.35$ with increasing s . The red dashed line is a fit to the experimental data

for the magnitude of the peak near $\tilde{k} \approx 0.78$ that has the form $P_{max}/\hat{P} \approx 0.12 \exp[-0.29(s + 0.9)]$, with the decay of this peak exhibiting a strong exponential tendency. Whilst the linear theory overpredicts the magnitude of the peaks, the predicted decay, $\sim \exp(-\nu k^3 s/R_c)$, follows a very similar trend to that of the experimental data for the high wavenumber peak, though it shows a weaker correlation with that for the lower wavenumber peak.

Figure 4.9 (b) plots the variation with along-beam distance, s , of wavenumbers at each of the peaks of the spectra associated with the incident and reflected beam. Plotted symbols correspond to those described for figure 4.9 (a). Whilst a linear representation is not suggested for the wavenumber decay, gradients of linear fits to these wavenumbers are used here (since resolution constraints restrict more detailed analyses) to indicate the rate of decrease of the peak wavenumbers with along-beam distance. As expected, the highest wavenumber component associated with the incident wave beam (red line) experiences a more rapid decrease, with a gradient of -5.98×10^{-3} , whilst the lower wavenumber peak for the incident wave beam (black line) has a gradient of -2.95×10^{-3} . At the spatial resolution used, no decrease was discernable in the peak wavenumber associated with the reflected beam (blue line). Whilst some inaccuracy of the calculated wavenumber positions of spectral peaks are possible through the use of FFT as discussed above, it is unlikely that the observed trends for a shift in wavenumber peak to lower values with along-beam distance are a consequence of the spectral method. The trend for the decrease in the low wavenumber peak of the incident beam, for example, can be observed over 14 sequential cross-sections separated by $s/R_c = 1$. As for the peak magnitudes, predictions of linear theory for wavenumber positions of peaks exceed those measured from experimental data but exhibit similar rates of reduction as the along-beam distance increases.

Power spectra variation with frequency

Time series along cross-sections of a beam incident on a horizontal boundary and those of its reflection were analysed in the preceding subsection for a single forcing frequency σ . In order to determine whether the behaviour reported is representative of other values of the parameter σ/N , a comparison was made of spectra calculated from cross-sections of incident beams for ten values of $\sigma/N \in [0.33, 0.71]$. Figure 4.10 shows power spectra calculated for each frequency from cross-sections positioned at distances s_I/R_c equal to (a) 7, (b) 11 and (c) 15 along the incident beam together with the corresponding RMS_T amplitudes along the given cross-sections in (d), (e) and (f) respectively. Peaks of the spectra associated with the cross-section closest to the cylinder, shown in figure 4.10 (a), are located for each frequency at wavenumbers of ~ 0.34 and ~ 0.77 , with the exception of $\sigma/N = 0.33$ and 0.37 , for which the spectra are skewed slightly as a result of significant overlaps (also evident in (d)) between the beams propagating upwards and downwards away from the cylinder. As the frequency increases from $\sigma/N = 0.33$ to 0.50 , the power associated with each peak also increases, with the frequencies $\sigma/N = 0.50$ and 0.54 having similar power magnitudes. Since the group velocity decreases with an increase in frequency according to (2.17), with $\theta =$

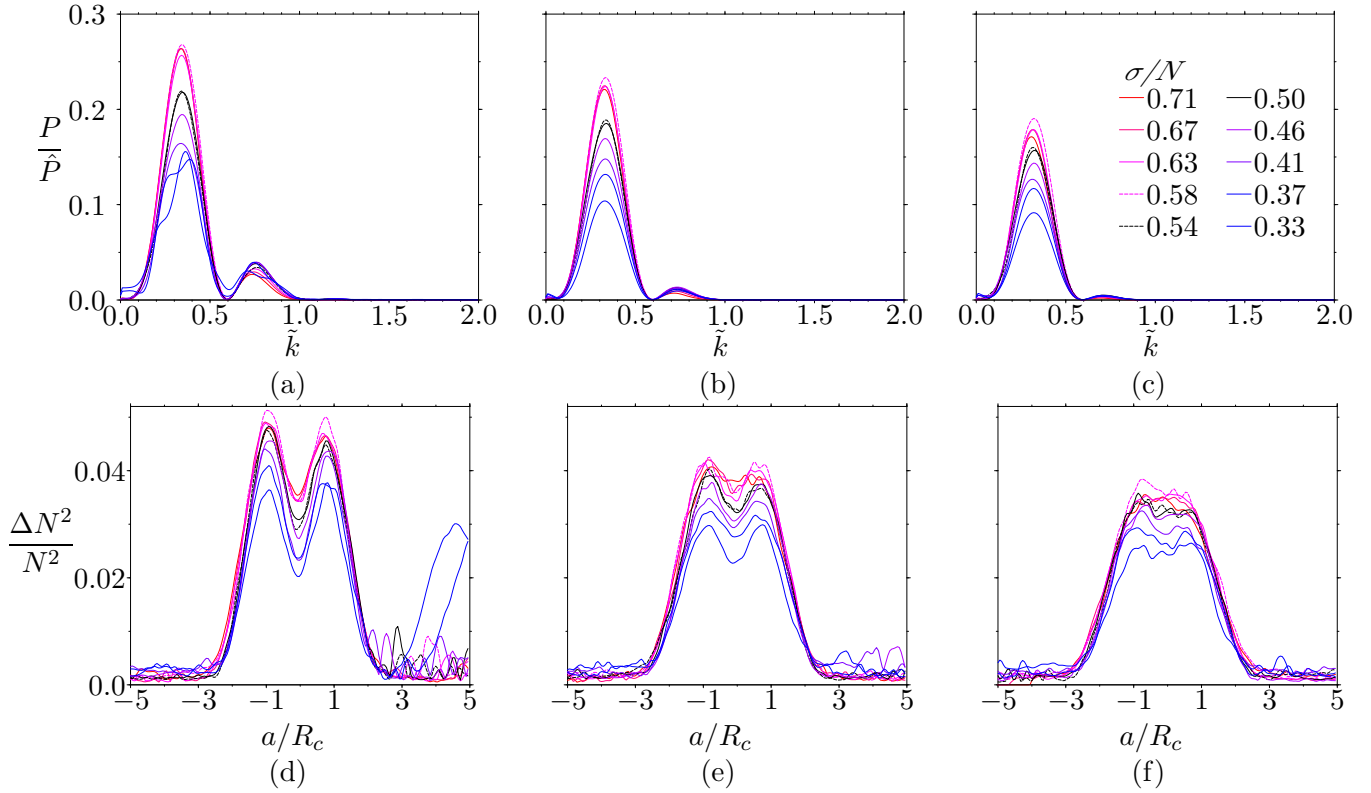


Figure 4.10: Power spectra variation with forcing frequency at along-beam distances s_I/R_c equal to (a) 7, (b) 11 and (c) 15. Corresponding RMS_T amplitudes along these sections are shown in (e), (f) and (g) respectively. Peaks of spectra for black dashed line are located at (a) $\tilde{k} = 0.34, 0.77$; (b) $\tilde{k} = 0.33, 0.74$; and (c) $\tilde{k} = 0.32, 0.72$. Power, P , is normalised by the total power, \hat{P} , in the spectra corresponding to $\sigma/N = 0.58$ at $s_I/R_c = 4$.

$\cos^{-1}(\sigma/N)$, energy densities and hence amplitudes therefore increase with σ/N . This trend can also be seen in figure 4.10 (d) for $\sigma/N \in [0.33, 0.54]$. Amplitude variation with frequency was also studied experimentally by Sutherland *et al.* (1999) for four frequency values in the narrower range $\sigma/N \in [0.26, 0.55]$. The study compared instantaneous across-beam amplitudes for these frequencies at just one along-beam distance $s_I/R_c = 9$ and, in agreement with the results of the present study for this frequency range, found a slight increase in amplitude with increases in frequency.

The largest power and amplitude maxima are those of frequencies $\sigma/N \in [0.58, 0.71]$. Whilst power peaks for these frequencies are similar in magnitude, surprisingly these show a slight *decrease* in magnitude between $\sigma/N = 0.58$ and 0.71 . RMS_T amplitude values are also largest for $\sigma/N = 0.58$. This behaviour is inconsistent with the argument used to explain the trend shown in the power magnitudes of the set $\sigma/N \in [0.33, 0.50]$ - especially since the group velocity varies more rapidly with increasing frequency. Note that the generation of secondary harmonic waves is only possible for $\sigma/N < 1/2$.

The trends in power spectra and RMS_T amplitudes described above for the cross-section closest to the source, are repeated in figure 4.10 (b)-(c) and (e)-(f) respectively, with magnitudes decreasing

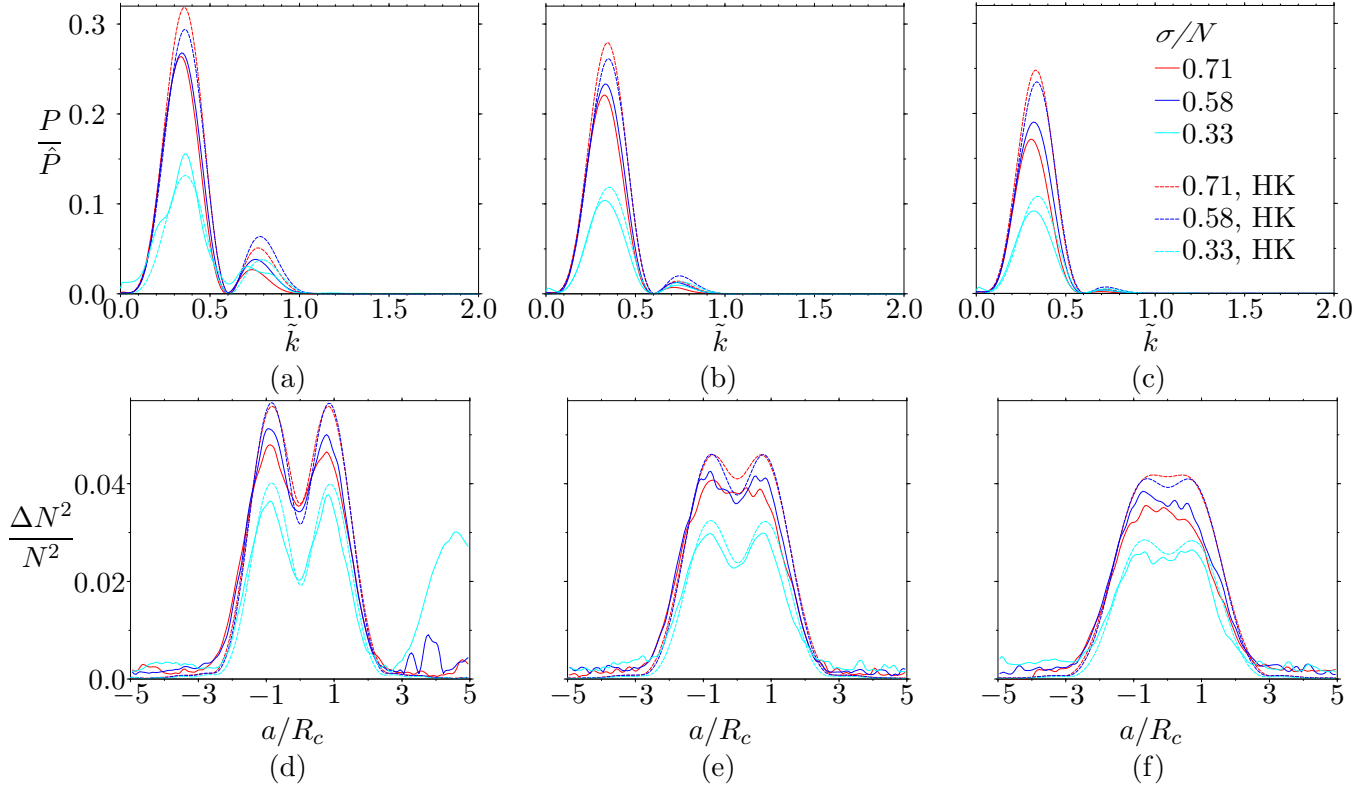


Figure 4.11: Power spectra variation with forcing frequency for three frequencies $\sigma/N = 0.71$, 0.58 and 0.33 at along-beam distances s_I/R_c equal to (a) 7 , (b) 11 and (c) 15 . Solid lines indicate spectra calculated from experiment data (*c.f.* figure 4.10) whilst dashed lines indicate predictions of linear theory (Hurley & Keady 1997). Corresponding RMS_T amplitudes for both experiment data and theoretical predictions along these sections are shown in (e), (f) and (g) respectively. Power, P , is normalised by the total power, \hat{P} , in the spectra calculated from experiment data corresponding to $\sigma/N = 0.58$ at $s_I/R_c = 4$.

with along-beam distance as expected due to viscous attenuation. Peaks for the spectra for $s_I/R_c = 11$ and 15 are found at wavenumbers of (b) $\tilde{k} = 0.33, 0.74$; and (c) $\tilde{k} = 0.32, 0.72$ respectively. This agrees with the behaviour shown in figure 4.9, where the wavenumber peak of spectra is skewed to lower values with greater distance from the cylinder as a result of preferential viscous attenuation of the higher wavenumber components.

Unfortunately, since the value $s_I = \hat{s}_I \approx z_c \cos(\sigma/N)$ at which each of the incident beams reflected at the boundary varied with frequency, it was not possible to make consistent comparisons between spectra calculated for the reflected beams. However, individual analysis of spectra for the incident and reflected beams for each frequency revealed power spectra consistent with those presented in figure 4.8 (a), subject to variation with frequency of the power magnitude associated with each peak in a similar manner to that observed for the incident spectra shown in figure 4.10 (a)-(c).

Figure 4.11 compares spectra and RMS_T amplitudes measured from experiment data (solid

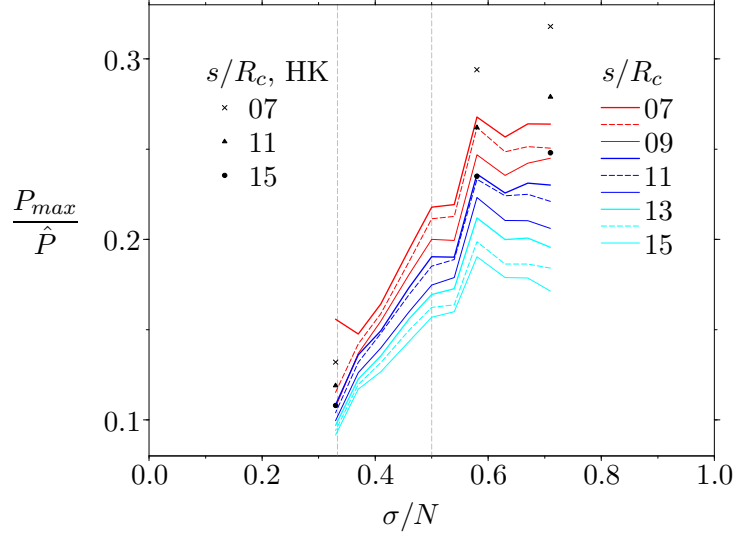


Figure 4.12: Variation of power spectra maxima, P_{max}/\hat{P} , with σ/N for different along-beam distances. Symbols indicate values of P_{max}/\hat{P} predicted by linear theory (Hurley & Keady 1997). Grey dashed vertical lines highlight the frequency values $\sigma/N = 1/2$ and $1/3$, below which the generation of second and third temporal harmonics, respectively, is possible.

lines) along cross-sections at $s_I/R_c = 7, 11$ and 15 for the three frequencies $\sigma/N = 0.71, 0.58$ and 0.33 (also shown in figure 4.10) with the predictions made by viscous linear theory (dashed lines) of Hurley & Keady (1997). Linear theory follows similar trends to those of the experimental data but consistently overestimates magnitudes of each of the spectra and plots of across-beam RMS_T amplitudes, with the discrepancy increasing with frequency.

Figure 4.12 compares the variation with σ/N of magnitudes of peaks of spectra calculated from experiment data at along-beam distances of $s_I/R_c = 7$ to 15 . Cross, triangle and dot symbols plot predictions of viscous linear theory (Hurley & Keady 1997) at along-beam distances $s_I/R_c = 7, 11$ and 15 , respectively, at the three frequencies $\sigma/N = 0.71, 0.58$ and 0.33 . A similar trend is seen at all along-beam distances, with the peak power increasing to a maximum at $\sigma/N = 0.58$, and then decreasing more gradually for further increases in the forcing frequency. The maximum power magnitudes predicted by theory again overestimate those measured by experiments but show a similar rate of increase for the lower frequencies. Theory predictions at $\sigma = 0.71$ do not however exhibit the slump evident in power values calculated from experiment data for the larger frequencies. The slump may be caused by enhanced attenuation near to the source where beams increasingly overlap at the higher frequencies.

4.2.3 Scatter to higher harmonics

Linear theory predicts the conservation of frequency during reflection of a wavefield at a horizontal boundary (Lamb 1932; Phillips 1966). Hence for an incident wavefield satisfying the amplitude constraint $A_c/D_c \ll 1$, all incident wave energy associated with a primary frequency σ is predicted

to reflect to a wavefield with the same frequency. Linear theory becomes less applicable in systems where the condition $A_c/D_c \ll 1$ is weaker, or in regions of the system for which the parameter is not representative of local amplitudes of the wavefield, such as in regions of superposition (where wavefields overlap in the reflection region adjacent to a boundary). In such cases, wave behaviour may deviate from the predictions of linear theory by the generation of higher harmonic components. As discussed in sections 2.3.2 and 3.7, the dispersion relation (2.16) permits the generation of harmonic wave components with frequency $\sigma_n = n\sigma$ provided that the primary frequency satisfies $0 \leq \sigma/N \leq 1/n$, for $n \in \mathbb{Z}_{\geq 0}$.

Figure 4.13 shows results from harmonic filtering of the $\Delta N^2/N^2$ field of an experiment of reflection at a horizontal boundary with forcing frequency $\sigma/N = 0.46 < N/2$ and $A_c/D_c = 0.066$. Each image shows incident wave energy propagating from the top left-hand corner towards the horizontal boundary at the bottom of the image. Figure 4.13 (a), (c) and (e) show the amplitude and phase fields as well as their products from filtering for the primary frequency. Figure 4.13 (a) is essentially the RMS_T image for the primary harmonic and can be interpreted in a similar manner to those shown in figure 4.1. The phase component shown in figure 4.13 (c) represents the structural form of the primary wavefield. In particular, the phase is constant in the along-beam direction and the beam is seen to widen with distance from the cylinder, corresponding to the transition between a bimodal and unimodal structure of the across-beam form. In addition to the primary wave beam and its reflection, the phase image reveals motion corresponding to reflected waves propagating within the tank of much lower amplitude than those associated with the main beam. However, the amplitudes associated with this motion are several orders of magnitude smaller than those associated with the primary wave beam and, as a result, these motions are not evident in the composite image shown in figure 4.13 (e).

Figure 4.13 (b), (d) and (f) show the amplitude and phase fields and their product from filtering for the secondary harmonic frequency $\sigma_2/N = 0.92$. Unfortunately, due to the finite temporal resolution of experimental movies, it was not possible to completely remove evidence of the primary harmonic during filtering for the secondary harmonic. The wave period was not an integer number of frames and only a relatively small number of wave periods were sampled. As a result, a slight amplitude peak can be seen along the location of the primary beam in figure 4.13, and similarly signatures of the primary harmonic can be seen in the corresponding regions of figures 4.13 (d) and (f). The generation of a secondary harmonic beam by the cylinder with amplitudes that are an order of magnitude less than that of the primary harmonic is clearly evident in figure 4.13 (b). This beam reflects at the bottom boundary and decays rapidly in amplitude as it propagates away from the boundary. Subsequent repeated reflections of this harmonic between the upper surface of the stratification and the bottom of the tank can be seen in the phase image shown in figure 4.13 (d). A second weaker beam also appears to be generated along the region of the boundary at which the primary harmonic reflects (figure 4.13). Inspection of figure 4.13 (d) and (f) indicates that the second beam is generated during the primary reflection, rather than being a reflection associated with the secondary harmonic generated by the cylinder. The generation of higher harmonics during

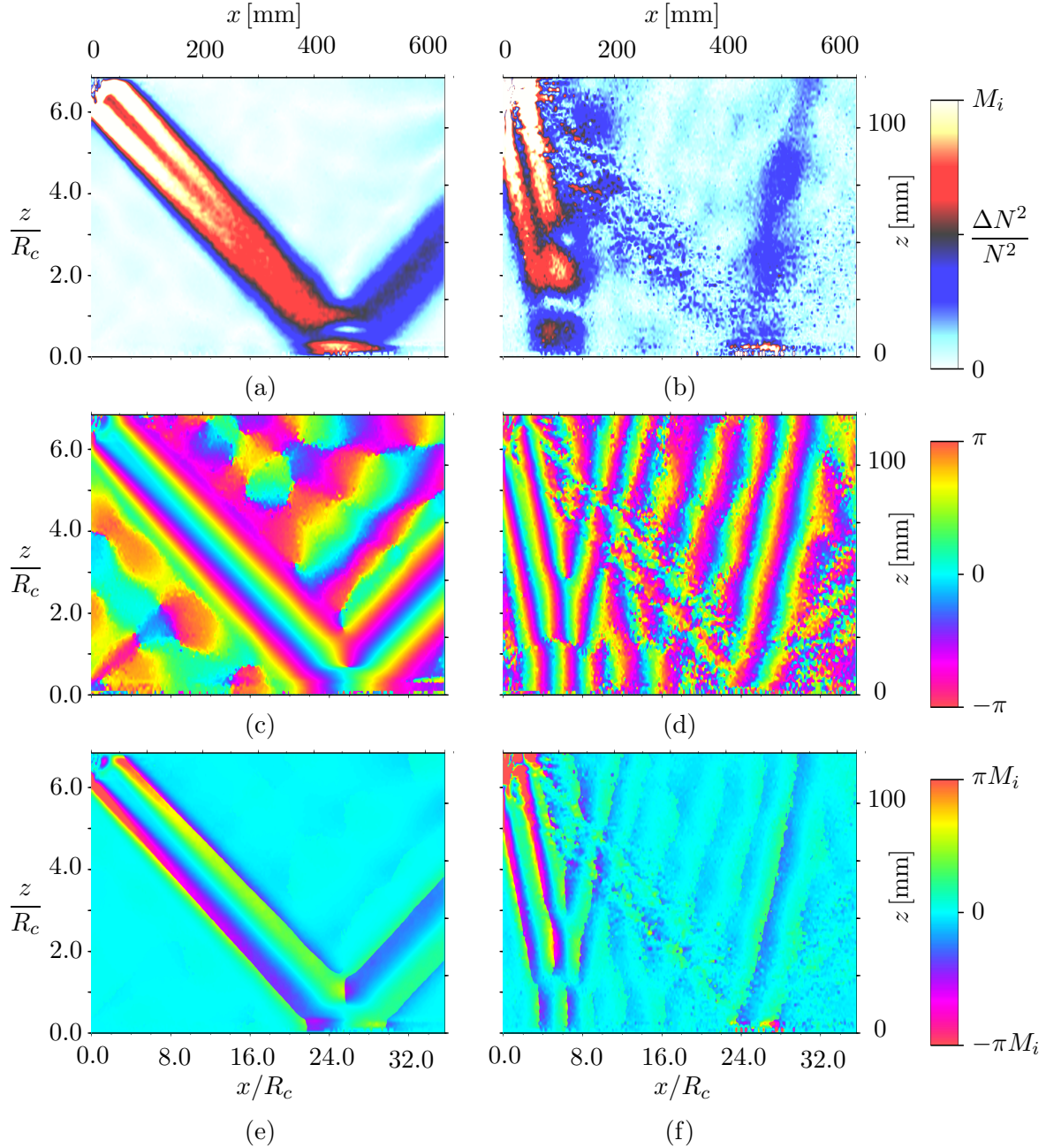


Figure 4.13: Temporal filtering for primary and secondary harmonics of reflection at a horizontal boundary with primary frequency $\sigma/N = 0.46$. Here (a) and (b) show amplitude components for the primary ($i = 1$) and secondary ($i = 2$) harmonics respectively with maxima $M_1 = 5.6 \times 10^{-2}$ and $M_2 = 3.8 \times 10^{-3}$; (c) and (d) show phase components corresponding to (a) and (b) respectively; (e) and (f) are products of the amplitude and phase components for (a) and (b) respectively.

the reflection process shows the weakening of linear theory even at the moderately small value of the parameter $A_c/D_c = 6.6 \times 10^{-2}$, presumably due to the local enhancement of wave amplitudes where the primary incident and reflected wavefields overlap in the reflection region.

This section has presented and discussed experimental results of wave reflection at a horizontal boundary. More detailed analyses have been presented than in other studies, such as for amplitude trends with variation of σ/N and s/R_c , as well as new data, including power spectra and harmonic filtering. Whilst the qualitative predictions of linear theory, such as the first order conservation of frequency and the incident wavenumber, have been supported by these results, a quantitative analysis has revealed that the incident energy undergoes enhanced dissipation during the reflection process and that for incident frequencies such that $\sigma < N/2$, forwards propagating secondary harmonic wavefields can also be generated. The following section considers reflection behaviour at sloping boundaries.

4.3 Reflection at a smooth sloping boundary

Consideration of wave interactions with boundaries that are inclined by an angle α relative to the vertical introduces the parameter θ/α , which compares the relative slopes of the wave energy vector and boundary. Reflection at a smooth sloping boundary inclined by the angle α is referred to here as subcritical, supercritical and near-critical for the ranges $\theta/\alpha < 1$, $\theta/\alpha > 1$ and $\theta/\alpha \approx 1$ respectively (see section 2.4.2). Experiments were performed with slope angles $\alpha = 32.4^\circ$, 37.0° , 37.3° and 50.1° . Values of θ/α for which the experiment setup could be manipulated so that just one wave beam, generated by the oscillating cylinder, was incident along the slope were restricted by the geometry of the tank (see chapter 3). Results for reflection at subcritical, supercritical and near-critical parameter values possible within these constraints are presented here.

4.3.1 Qualitative results: subcritical and supercritical

Instantaneous and RMS_T images of the perturbed buoyancy field are shown in figure 4.14 (a) and (c) for wave beams reflecting at a subcritical slope with $\sigma/N = 0.71$ and $\theta/\alpha = 0.89$, and in figure 4.14 (b) and (d) for wave beams reflecting at a supercritical slope with $\sigma/N = 0.34$ and $\theta/\alpha = 2.17$. In all images, incident beams propagate downwards from the top left-hand corner. In both subcritical and supercritical cases, the reflected beam propagates along a direction that makes the same angle with the vertical as the incident beam, hence demonstrating the conservation of frequency at first order (Phillips 1966). However, as predicted by ray tracing for this particular geometrical arrangement of the incident group velocity and boundary (see e.g. figures 2.4 (a) and 2.5 (a)), the reflected beams propagate in different vertical directions, with the subcritical reflection having an upwards oriented group velocity and that of the supercritical reflection directed downwards. The subcritical and supercritical reflected beams are narrower than the incident beams and are characterised by smaller across-beam length scales, which are most clearly seen in figure 4.14 (a) and (b). Geometric ray tracing predicts that widths of reflected beam vanish in the critical case as $|\theta/\alpha - 1| \rightarrow 0$. Since the supercritical value of $|\theta/\alpha - 1| = 1.17$ is greater than that for the subcritical case, for which $|\theta/\alpha - 1| = 0.11$, the width of the reflected beam is not constricted as

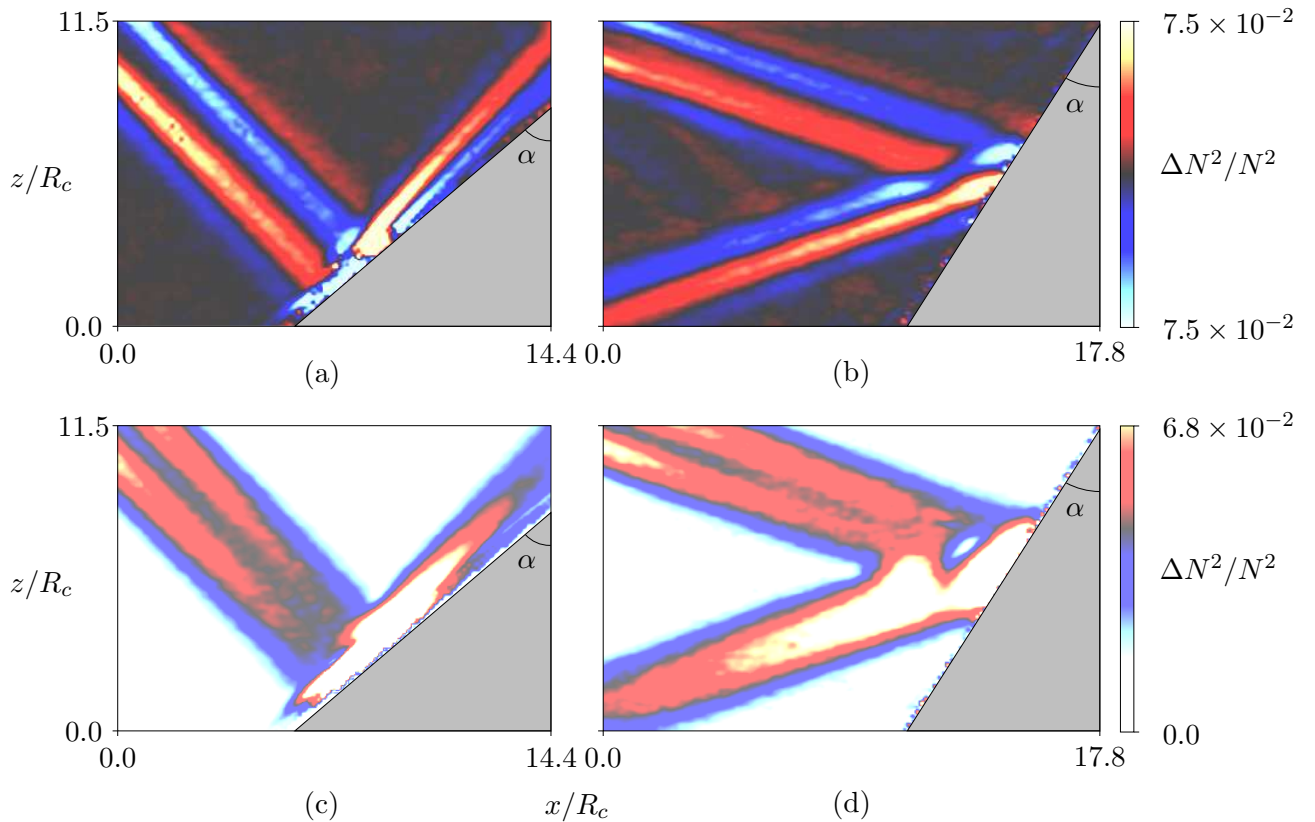


Figure 4.14: Images of the instantaneous perturbed buoyancy field for sub and supercritical reflections with slope ratios θ/α equal to (a) 0.89 and (b) 2.17 respectively, with corresponding RMS_T images shown in (c) and (d). Regions on right-hand side of slopes are shaded grey.

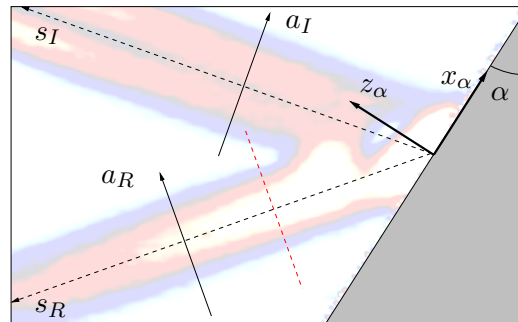


Figure 4.15: Coordinate systems used at boundaries inclined at an angle α to the vertical.

much in the supercritical reflection. Similarly, across-beam scales, evident in figure 4.14 (b), are reduced by a lesser degree in the supercritical case. Wave amplitudes are enhanced in each reflection as a result of the beam constriction and lower group velocities associated with the higher reflected wavenumbers. The across-beam structures of the reflected beams are evident in figure 4.14 (c) and (d), exhibiting maxima aligned with the centerlines of the beams. These observations agree with ray tracing predictions outlined in section 2.4.2. For both subcritical and supercritical reflections,

amplitudes of the fluid motion are particularly enhanced in the region where the incident and reflected beams overlap along the boundaries.

4.3.2 Quantitative results: supercritical

Quantitative measurements associated with only supercritical reflections are presented here. Unfortunately, experiments in the present study of subcritical reflections that had parameter values $\theta/\alpha < 0.7$ were contaminated by the presence of other reflecting wave beams, which could not be avoided with the experimental arrangement used. At larger values of θ/α , these overlapping wave beams could be avoided, but the quantitative analysis of the subcritical reflections was hindered by the close proximity of the reflected beam to the slope - preventing cross-sections of sufficient length to be made of the reflecting beams so as to allow accurate amplitude or spectral analysis (see e.g. figure 4.14 (c)). These subcritical results are therefore omitted here. The experimental arrangement did, however, permit reliable quantitative measurements of supercritical reflections for which $\theta/\alpha > 1.5$.

The coordinate system illustrated in figure 4.15 was employed for analysis of supercritically reflecting wave beams. Across-beam coordinates a_I and a_R for the incident and reflected beams are aligned with the direction of phase propagation. Note that, in contrast to the coordinate system described in figure 4.15 for reflections at a horizontal boundary, the along-beam coordinates s_I and s_R of the incident and reflected beams respectively are directed along beams and are *both* taken to originate at the point of interception of the incident beam with the boundary. Whilst this orientates s_I in the opposite direction to the incident group velocity, this coordinate system is adopted in order to allow more convenient comparisons with wave reflection behaviours described in later sections, for which this convention is more natural. Coordinates parallel, x_α , and perpendicular, z_α , to the boundary are also defined for convenience.

Figure 4.16 (a) shows amplitudes of the perturbed buoyancy field calculated from measurements made along cross-sections of the incident and reflected wave beam for a supercritical reflection with $\sigma/N = 0.64$ and $\theta/\alpha = 1.55$. Smaller values of s_I correspond to locations along the incident beam that are further from the oscillating cylinder and closer to boundary. Hence, measured RMS_T amplitudes of $\Delta N^2/N^2$ for the incident wavefield are greatest along the cross-section at $s_I/R_c = 11$ with a maximum value of 2.3×10^{-2} and smallest at $s_I/R_c = 4$ (dashed black line), just prior to reflection, having a maximum value of 1.9×10^{-2} , due to viscous attenuation. The incident beam amplitudes have a unimodal across-beam structure, symmetric about $a_I/R_c = 0$ and tending to zero at $a_I/R_c \approx \pm 3$. The reflected amplitudes are significantly larger than those of the incident beam with largest values closest to the boundary along the cross-section at $s_R/R_c = 6$ (bold black line), which has a maximum of 5.7×10^{-2} , and reducing to the maximum value of 3.0×10^{-2} along the cross-section at $s_R/R_c = 14$. The reflected wave beam has a narrower unimodal across-beam structure than that of the incident beam, with values tending to zero at $a_R/R_c \approx \pm 2$. Nonnegligible values occurring at the extremities of cross-sections are caused by some overlapping with adjacent

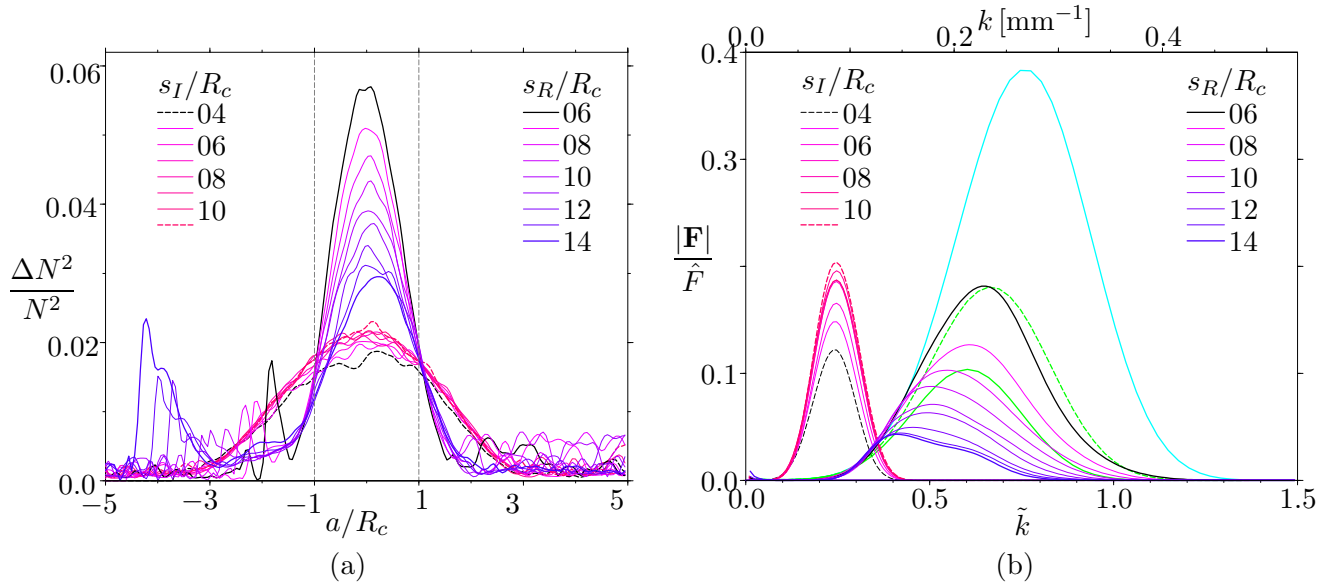


Figure 4.16: (a) Across-beam RMS_T amplitudes for cross-sections positioned at different s_I and s_R along incident and reflected beams in a supercritical configuration; and (b) corresponding energy flux, \mathbf{F} , spectra, normalised by total flux, \hat{F} , in cross-section $s_R/R_c = 6$. Grey dashed lines indicate locations of tangents to cylinder in along-beam directions. The dashed bold red line corresponds to measurements along the section located at $s_I/R_c = 11$. The cyan line in (b) represents predictions of inviscid linear theory for reflected spectra. Green solid and dashed lines indicate viscous adaptations of inviscid linear theory.

wave beams.

Figure 4.16 (b) shows energy flux spectra calculated from measurements made along the cross-sections displayed in figure 4.16 (a). The energy flux is related to the energy density, E , by

$$\mathbf{F} = E \mathbf{c}_g, \quad (4.14)$$

where $|\mathbf{c}_g| \sim 1/k$ by (2.20). Flux spectra are thereby deduced according to (4.14) from spectra for the energy density, E (representing twice the potential energy), which are calculated from the square of the FFT of cross-section data. Spectra for the incident beam exhibit peaks located at a wavenumber $\tilde{k}_I = 0.26$, with peak magnitudes at $s_I/R_c = 4$ (dashed black line) and 11 of 0.12 and 0.20 respectively. Peaks of spectra calculated from measurements of the reflected beam are broader and located at higher wavenumbers than those of the incident spectra, with the largest peak magnitude of 0.18 at $\tilde{k}_R = 0.67$ (solid black line) and smallest of magnitude 4.3×10^{-2} at $\tilde{k}_R = 0.43$. The apparent flattening and skew of the peaks corresponding to $s_R/R_c \approx 12 - 14$, relative to the reflected spectra at smaller s_R/R_c , is thought to be due to the overlapping of cross-sections identified in the amplitude profiles in figure 4.16 (a). As in power spectra values shown in figure 4.9 relating to reflections at a horizontal boundary, the reflected spectra in figure 4.16 also exhibit a general reduction in peak wavenumber with increasing s_R caused by the more rapid viscous decay of energy associated with higher wavenumber components.

The cyan line shows the predictions of inviscid linear theory (Phillips 1966) for the reflected energy flux spectra based on values of the spectra calculated for the incident beam cross-section located at $s_I/R_c = 4$ (dashed black line). The average energy flux per unit area of the reflected wavefield, \mathbf{F}_R , can be expressed as a ratio of the incident flux, \mathbf{F}_I , by

$$\left| \frac{\mathbf{F}_R}{\mathbf{F}_I} \right| = \left(\frac{\sin(\alpha + \theta)}{\sin(\alpha - \theta)} \right), \quad (4.15)$$

(Phillips 1966).

The predicted spectrum has a peak located at a wavenumber of $\tilde{k}_{thy} = 0.81$ with a peak magnitude of 0.38. Both the wavenumber and magnitude of this peak are significantly greater than those of the reflected spectra located closest to the boundary at $s_R/R_c = 6$. The ratio of the measured peak wavenumber to that predicted by theory can therefore be calculated as $\tilde{k}_R/\tilde{k}_{thy} \approx 0.83$, with the corresponding peak magnitude ratio of ~ 0.47 . In part, this discrepancy occurs due to the choice of incident spectra used in the calculation as well as the fact that the smallest distance s_R at which spectra can be compared with the theory is $6R_c$ from the boundary. Hence, a total along-beam distance discrepancy of $(s_I + s_R)/R_c = 10$ exists between the cross-sections of the incident and reflected wave beams used to compare with the theory, over the course of which wave energy is attenuated by viscosity. Some enhanced level of dissipation may also occur in the region next to the boundary through other nonlinear interactions caused by enhanced amplitudes due to property changes on reflection and also where the incident and reflected beams overlap and wave amplitudes superpose. Notably, whilst propagating higher harmonics cannot be generated at this value of $\sigma/N = 0.64$, the presence of exponentially decaying modes (in space) that can contribute locally to the dissipation is possible.

Linear viscous dissipation

The linear theory of Phillips (1966) described above is adapted here to include the effects of linear viscous dissipation on a packet of energy E_0 associated with a wavenumber k that propagates at the group velocity \mathbf{c}_g . The loss of energy from the packet with time t can be described by

$$\frac{dE}{dt} = -\nu k^2 E, \quad (4.16)$$

which yields the energy of the packet after a time t to be

$$E(k, t) = E_0(k) \exp[\nu k^2 t(k)], \quad (4.17)$$

where $t(k) = s/c_g$. Substituting the wavenumber dependence of the group velocity, \mathbf{c}_g (*c.f.* (2.17) and (2.20)), (4.17) can be rewritten as a function of the distance, s , travelled by the packet according to

$$E(k, s) = E_0(k) \exp\left[\frac{\nu k^3 s}{\sigma \tan \theta}\right]. \quad (4.18)$$

The associated flux can be calculated using (4.14). Adaptations of the inviscid linear theory (cyan line) by (4.18) are indicated by the green solid and dashed lines plotted in figure 4.16 (b). Wave groups experience viscous attenuation as they propagate an along-beam distance of $10R_c$ between the two experiment cross-sections located at $s_I = 11R_c$ and $s_R = 6R_c$. The green solid line plotted is the spectra calculated with linear dissipation applied firstly to the spectra associated with the cross-section positioned on the incident beam at $s_I/R_c = 11$ for a distance $s_I/R_c \approx 4$, in order to account for viscous dissipation of wave groups between the cross-section position and the boundary. Linear dissipation was subsequently applied to the inviscid linear theory prediction for the reflection of this attenuated spectra over the along-beam distance $s_R/R_c = 6$ as wave groups propagated away from the boundary. The predicted peak has a maximum magnitude of 0.10. Whilst some *enhancement* in dissipation might be expected in the region near the boundary where the incident and reflected wavefields overlap, the inclusion of linear dissipation predicts a maximum energy flux that is *lower* than that measured from the experimental data. Some small reduction in the total energy dissipated from both the incident and reflected wave beams during the reflection process may occur as a result of the incident wave beam effectively reflecting at locations slightly away from the boundary due to the presence of boundary layers there. This is unlikely to account for a large proportion of the discrepancy shown however. Rather than a smaller degree of viscous attenuation of the wave energy occurring, it is more likely that an inclusion of additional wave energy within the measured reflected spectra is experienced. As is shown in figure 4.13 (c) for example, an unavoidable background wavefield, ordinarily associated with very weak amplitudes relative to the primary wavefield, propagates throughout the entire tank. This energy becomes more significant near the sloping boundary where it is focused, so that it is able to form a nonnegligible contribution to the measured spectra.

The total along-beam distance required by the linear dissipation in order to match the peak energy fluxes of the inviscid linear theory to those calculated from the experiment cross-section at $s_R = 6R_c$ was estimated as a means of indicating the discrepancy between the attenuated linear predictions and the experimental data. The matched spectra (green dashed line) is plotted in figure 4.16 (b). The line was calculated by decreasing the along-beam distance s_R over which the dissipation was applied to the spectra represented by the solid green line, from $6R_c$ to $3R_c$. A slight shift in the wavenumber peak position to higher values also occurs between the spectra calculated from experimental data at $s_R/R_c = 6$ and the dashed green line. This is also consistent with the expectation, described above, that wave motion within nearby regions of the stratification contribute to the measured spectra. The background wave motions, having been present in the tank for a longer duration than the primary wavefield and therefore having experienced a greater degree of viscous attenuation, preferentially on higher wavenumbers, consist dominantly of lower wavenumber components.

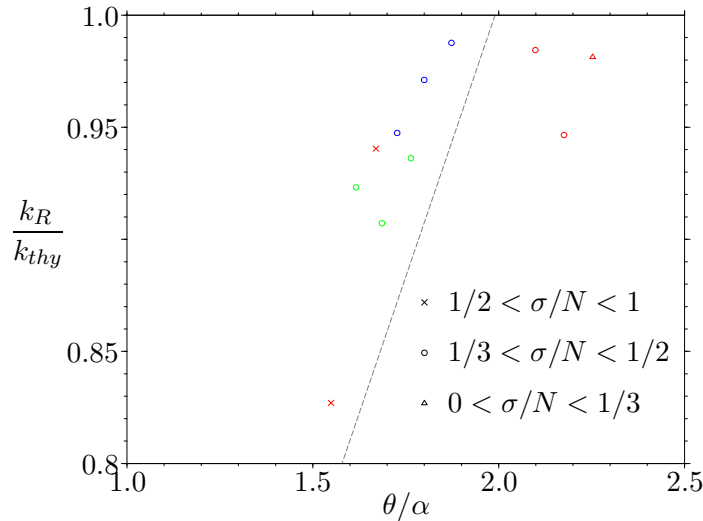


Figure 4.17: Comparison of measured peak wavenumbers with inviscid linear theory for supercritical slopes with $\alpha = 32.4^\circ$ (red symbols), 37.0° (blue symbols) and 37.3° (green symbols). Grey dashed line is a linear fit with gradient = 4.86×10^{-1} and y -intercept = 3.25×10^{-2} .

Variation of spectra with θ/α

Comparisons of peak wavenumbers of spectra calculated from experiment data and those predicted by inviscid linear theory (Phillips 1966) were also made for 11 supercritical reflections that had values of $\theta/\alpha \in [1.55, 2.25]$. Results are plotted in figure 4.17. At near-critical values of $\theta/\alpha \approx 1$, linear theory is expected to become less applicable since the widths of reflected wave beams are predicted to vanish in this limit, with wavenumbers and wave amplitudes becoming infinite as a result of the beam constriction. The smallest value of 0.827 for the ratio of measured to predicted peak wavenumbers, k_R/k_{thy} , occurs for $\theta/\alpha = 1.55$. With the exception of the experiment with $\theta/\alpha = 2.18$, there is indeed a general tendency for k_R/k_{thy} to increase, reaching values of greater than 0.98 for $\theta/\alpha \geq 1.87$. Whilst the convergence of reflection behaviour towards that predicted by linear theory is not expected to be linear, a linear fit to the data, with gradient = 4.86×10^{-1} and passing through the point $\theta/\alpha = 1.58$ at the peak ratio of $k_R/k_{thy} = 0.8$, is included in figure 4.17 for illustration. Many factors influence the measured behaviours. In each case, calculations were made using incident and reflected spectra located at the smallest possible along-beam distances s_I/R_c and s_R/R_c . This introduced some unavoidable discrepancy between the calculations of k_R/k_{thy} for each experiment due to the attenuating influence of viscosity with along-beam distance. Measured wavenumbers are also expected to be consistently lower than those predicted because of the preferential action of viscosity on higher wavenumber components, acting to skew the measured peak wavenumbers to lower values. In addition, as indicated in figure 4.17, the experiments measured ranged over several regimes of the parameter σ/N , with the generation of second and third temporal harmonics possible in a number of the experiments, which hence allowed scatter of the incident wave energy in different physical directions. Despite these factors, the strong trend towards increasingly linear

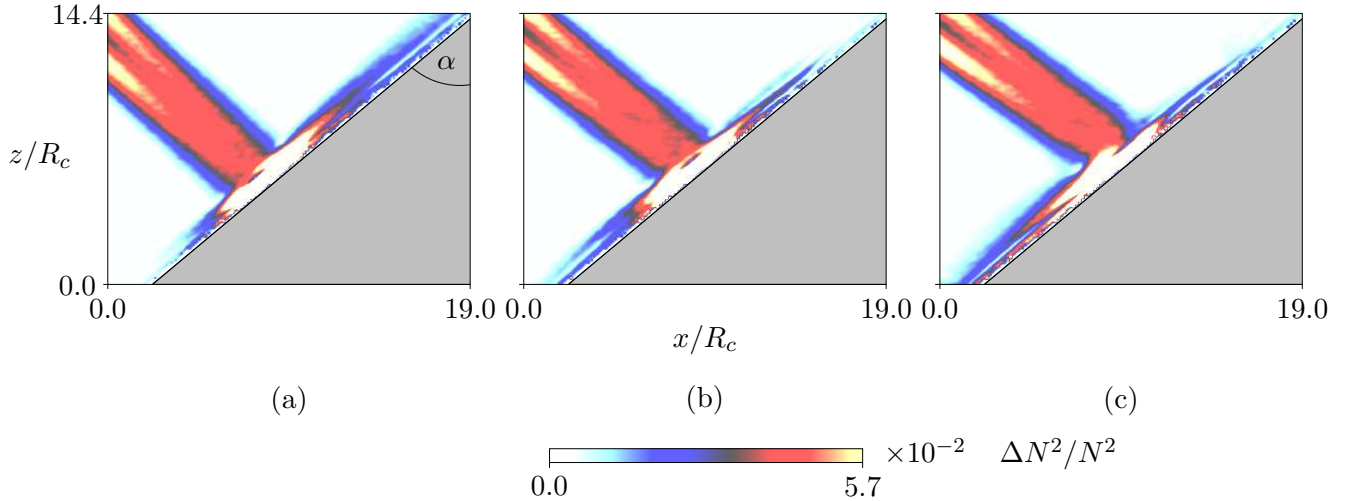


Figure 4.18: RMS_T image of perturbed buoyancy field for near critical reflections with slope ratios θ/α (a) 0.95, (b) 1.02 and (c) 1.08. Here $\alpha = 50.1^\circ$.

behaviour as the parameter θ/α is increased from the critical value of 1 is clearly evident in the plot shown. The results also suggest that the choice of delimiting values of θ/α for the ‘near-critical’ and ‘supercritical’ regimes is nontrivial.

4.3.3 Qualitative results: near-critical

Results from experiments of near-critical reflections are presented here. Figure 4.18 shows RMS_T images of wave beams undergoing near-critical reflection at values of $\theta/\alpha =$ (a) 0.95, (b) 1.02 and (c) 1.08, corresponding to values of $\sigma/N = 0.67, 0.62$ and 0.58 respectively. Figure 4.18 (a) shows a marginally subcritical reflection. Amplitudes of motion are greatly enhanced in the region where the incident wave contacts the boundary, and rapidly decrease in the direction along the boundary. A narrow upslope subcritical reflection propagating close to the boundary is clearly evident. Contrary to the predictions of inviscid linear theory however, significant perturbations of the buoyancy field are also present in the direction downslope from the reflection region. As discussed in section 2.4.2, inviscid linear theory predicts infinite reflected wavenumbers in the critical limit, and hence vanishing group velocities and locally infinite energy densities. Typical measured values of the perturbed buoyancy frequency near the boundary are $\Delta N^2/N^2 \sim 0.25$, an order of magnitude larger than typical peak values of $\Delta N^2/N^2$ of the incident wavefield near the boundary, so that the wave motion no longer represents a small perturbation to the background flow in this region and a nonlinear fluid response is expected. Significant perturbations to the perturbed buoyancy frequency field that decay rapidly in the direction along the slope also occur in the approximately critical and marginally supercritical reflections shown in figure 4.18 (b) and (c) respectively. As in the marginally subcritical reflection, reflected wave energy can be seen to propagate a short distance from the reflection region in upslope *and* downslope directions in both cases, with the downslope propagation most dominant in the marginally supercritical reflection of figure 4.18 (c).

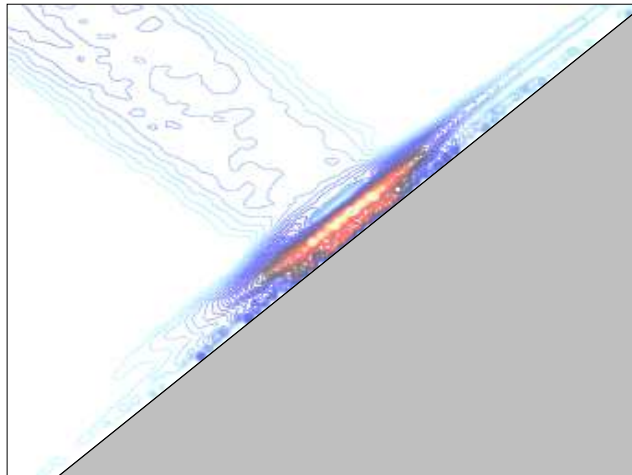


Figure 4.19: Contours of instantaneous perturbed buoyancy field for near-critical reflection with $\theta/\alpha = 1.02$. Colour scaled with magnitudes four times that of figure 4.18.

For the three values of θ/α discussed in this section, regular boundary motion is observed, with small regular vortical structures aligned in layers along the slope in the reflection region. Typical dimensions of individual vortices are several millimetres compared with a dominant incident wavelength, estimated from spectra, of $\lambda_I \sim 60$ mm. The viscous boundary layer thickness, for a homogeneous fluid, is calculated from (2.26) to be $\sim 1 - 2$ mm (Batchelor 1967). Due to the large amplitudes of the fluid motion in this region, the boundary structure was most clearly seen as it evolved during movies rather than in instantaneous images of the wavefield. However, some suggestion of the structure can be seen in the contour plot of the RMS_T field associated with $\theta/\alpha = 1.02$ shown in figure 4.19. These structures are reminiscent of those described in the experiments of Cacchione & Wunsch (1974), discussed in section 2.4.3. Ivey & Nokes (1989) later parameterised the reflection regimes in terms of the Reynolds number, defined in (2.42), and predicted a laminar to turbulent boundary layer transition for $Re \sim 15 - 20$. The experiments of Cacchione & Wunsch (1974) corresponded to $Re \sim 2$, whilst the present study had similar values of Re of 3.7, 3.5 and 3.2 for the experiments relating to figure 4.18 (a), (b) and (c) respectively. Such structures have not been reported in other studies, which were characterised by larger Reynolds numbers. Over the duration of experiments of $\sim 40T$ s, where T represents the period of the primary wave motion, horizontal intrusions of mixed fluid, such as those reported in Cacchine & Wunch (1974) associated with turbulent mixing along the boundary, were not observed to propagate away from the boundary. However, such observations are expected to require a longer duration of experiments than those performed in the present study.

4.4 Reflection at a smooth curved boundary

The previous sections described reflection at smooth flat or sloping boundaries characterised by the constant angle, α , made between the boundary surface and the vertical. This section briefly describes qualitative observations of scattering behaviours introduced when the boundary slope, and hence the angle α , is a smoothly varying function of position, $\alpha(x)$.

Experiments were performed of the scatter at an isolated cylindrical boundary, with axis of symmetry aligned perpendicular to the field of view and constant radius of curvature $R_T = 101.6$ mm, so that $R_T/D_c = 2.85$ (*c.f.* the numerical study by Legg & Adcroft 2003 and discussion in section 2.5.2). Figure 4.20 shows RMS_T images of the scatter on different regions of the boundary surface for incident beam angles θ equal to (a) 56.6° , (b) 62.7° and (c) 67.6° . It is believed that these are the first laboratory experiments examining scatter of a wavefield at a curved boundary feature presented in the literature. Wave beams are incident from the bottom left-hand corners of the field of view, with the bimodal structure of the wave beams clearly visible close to this region. The phase velocity of the incident beam propagates along the direction aligned with $-\eta$ (see also section 2.2.3). The incident wavefield shown in figure 4.20 (a) reflects dominantly along two directions, with corresponding phase velocities aligned with $\pm\xi$. This configuration is classified here as a ‘split-reflection’ configuration similar to that described in the inviscid theory of Baines (1971b) (see section 2.5.2). Baines predicts the split-reflection scenario for wave energy incident on a convex boundary feature that is symmetrical in form about a critical point such that the incident wave energy propagates perpendicular to the boundary tangent at that point. In the characteristic coordinate system associated with the present experiments, Baines (1971b) finds that reflected wave energy propagates in two directions along the tangent to the boundary at the critical point, *i.e.* corresponding to phase propagations along $\pm\xi$. Singular wave motion is expected in both directions of energy scatter. The enhancement of wave amplitudes associated with phase propagation along $\pm\xi$ can be seen clearly in figure 4.20 (a) as the incident wave energy becomes focused into two narrow beams. The incident flux is dominantly scattered in the downwards direction, whilst amplitudes of the upwards propagation decay rapidly away from the boundary. Movies of the experiment reveal a weak phase propagation along η superimposed on the incident phase propagation along $-\eta$. This coincides with a group velocity directed back along the incident beam - *i.e.* a back-scattered component. Though Baines (1971b) does not predict back-scatter for an idealised boundary feature that is symmetric about the critical point, back-scatter *is* predicted by Sandstrom (1972) for a more general convex boundary feature with a high radius of curvature. Sandstrom predicted a back-scattered component at critical reflection points, which became more prominent as the radius of curvature of the boundary decreased. Whilst the radius of curvature of the boundary studied in the present study is relatively large compared with those considered by Sandstrom (1972), the observed presence of a weak back-scattered component for $R_T/D_c = 2.85$ is consistent with the limiting behaviour of that predicted by Sandstrom.

Figure 4.20 (b) shows reflection configurations consistent with both the ‘split-reflection’ and

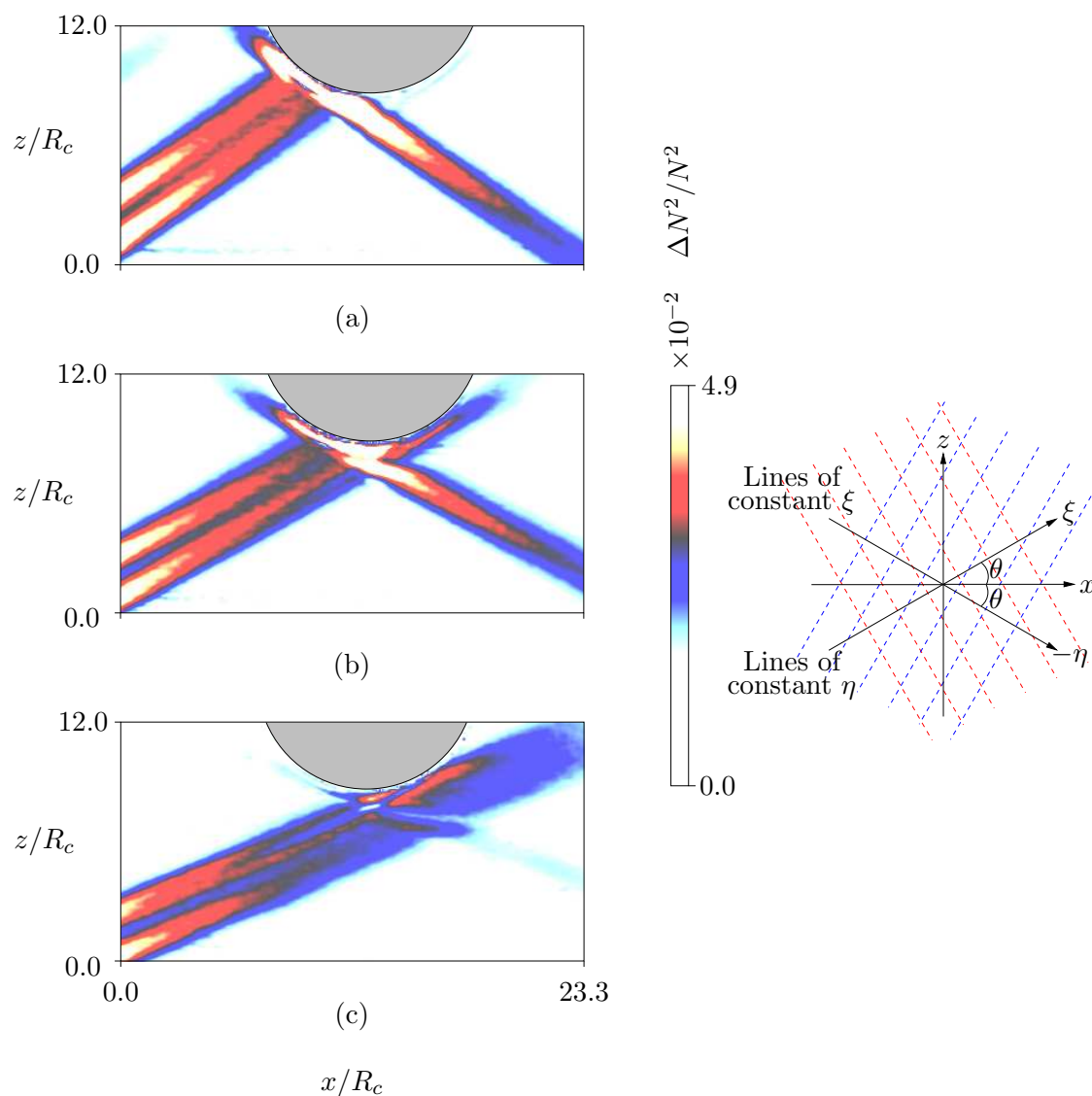


Figure 4.20: RMS_T images of perturbed buoyancy field for scatter at a curved boundary. The boundary and regions enclosed therein are shaded grey.

‘diffraction’ described in Baines (1971b) across the region of boundary directly exposed to the incident wave beam. Diffraction is defined by Baines (1971b) in a similar way to split-reflection, except that the incident wave energy propagates *parallel* to the tangent at a critical point along the boundary. In a diffraction configuration, Baines predicts singular behaviour along directions corresponding to phase propagation along $\pm\eta$, with the scattered energy in these directions decaying rapidly with distance from the boundary, and also a diffracted wave with phase propagating along ξ . As in figure 4.20 (a), the wave energy is seen to reflect dominantly in the direction corresponding to phase propagation along ξ . Other scattered beams are also present with phase directions along $\pm\xi$. Wave energy is focused in all directions of scatter but decays rapidly with distance from

the boundary for the latter two components. The phase propagating along $-\xi$ is thought to be that associated with split-reflection, whilst the phase propagating along ξ is that associated with diffraction. In addition to these components, and in accordance with the predictions of Baines for the diffraction configuration, a more significant back-scattered component is observed in movies of the experiment, compared with that present in the experiment associated with figure 4.20 (a). The back-scatter is visible in the change of RMS_T structure of the incident beam in figure 4.20 (b) in the region near to the curved boundary, particularly in the lower section of the incident beam. Over extended runs of the experiments at the frequency associated with figure 4.20 (b), mixed fluid generated in the reflection region was seen to protrude outwards as a thin horizontal layer into the surrounding stratification at the level of the bottom of the curved boundary (*c.f.* section 3.6.1).

The experiment shown in figure 4.20 (c) represents a dominantly diffraction configuration. The downwards scattered beam in this reflection regime is relatively weak in comparison to those seen in figure 4.20 (a) and (b). The diffracted wave, with phase propagating along $-\eta$, appears to be more significant than components scattered with phase propagations along $\pm\xi$. In part this is a result of the coincidence of the diffracted wave with the direction of propagation of incident wave energy that is unobstructed by the boundary. A significant feature of this scattering configuration is the dominant back-scattered component, which can be clearly seen in the RMS_T images to propagate along the direction of the incident beam a distance greater than $\sim 8R_c$ from the curved boundary.

4.5 Reflection at a smoothly varying rough topographic profile

The previous sections discussed detailed experimental results of reflection of wave energy incident at smooth horizontal or inclined slopes and scatter at an isolated boundary feature that had a constant radius of curvature. The present section discusses results from experiments performed of scatter at two sinusoidal boundary profiles, T_A and T_B , characterised by horizontal wavenumbers \hat{k}_T equal to 0.085 and 0.196 mm^{-1} respectively (see table 3.1). Experiments of internal wave scatter at sinusoidal topography are not previously reported in the literature. A parameter describing the aspect ratio of the topographic profile is defined as in section 2.5.1 as the product $\hat{A}_T \hat{k}_T$, where \hat{A}_T is the vertical amplitude of the sinusoid with respect to the mean level. This has values of $\hat{A}_T \hat{k}_T = 0.829$ and 0.784 for profiles T_A and T_B respectively. Another parameter comparing length scales associated with the incident wave relative to those of the topography is defined here as k_c/\hat{k}_T , where $k_c = 2\pi/R_c = 0.353 \text{ mm}^{-1}$. This parameter has values 4.15 and 1.80 for T_A and T_B respectively. The scatter is compared with ray tracing predictions (e.g. Longuet-Higgins 1969) and inviscid linear theory derived from characteristic methods (e.g. Baines 1971a) in sections 4.5.1 and 4.5.2 respectively. Further discussions of the scattered wavefields are given in chapters 6-8.

Figure 4.21 shows an RMS_T image of the perturbed buoyancy field associated with a typical experiment. The oscillating cylinder is located at the middle of the left-hand side of the field of view, with two of the generated wave beams emanating from this region. Wave energy propagating along the upwards directed wave beam is denoted B_I and interacts with sinusoid T_A at the top

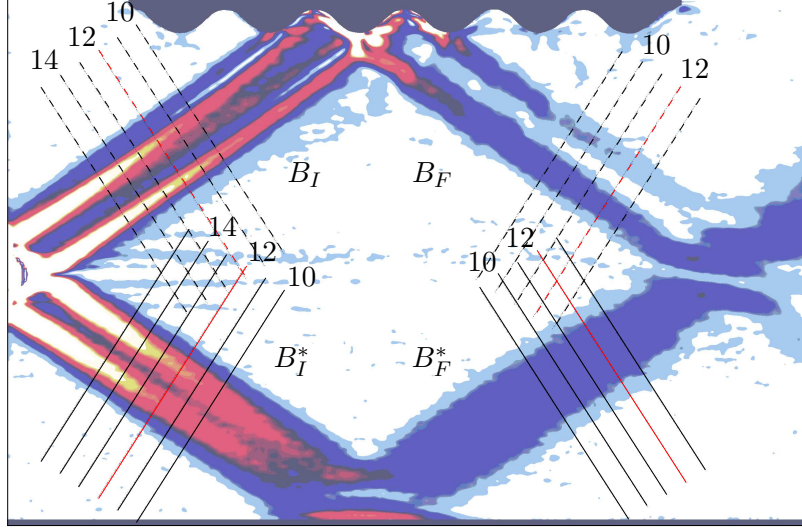


Figure 4.21: Example of positioning of cross-sections taken for incident (B_I , B_I^*) and reflected (B_F , B_F^*) beams at (top of picture) sinusoid, T_A , and (bottom of picture) horizontal boundary, respectively.

of the field of view, with the resulting forwards scattered wave beam denoted B_F . The beam directed downwards from the cylinder, denoted B_I^* , reflects at a horizontal boundary located at the bottom of the field of view. The reflection of this beam is denoted B_F^* . Coordinate systems are defined for beams B_I and B_F with across- and along-beam coordinates (a_I, s_I) and (a_R, s_R) . The origin of both of these beams is defined as the cartesian point $\mathbf{x}_{int} = (x_{int}, z_{int})$, where x_{int} is the x -coordinate of the intersection of the centerline of B_I with the mid height of the topographic profile z_{int} . Similarly, coordinate systems are defined for B_I^* and B_F^* as (a_I^*, s_I^*) and (a_R^*, s_R^*) . The origin for these beams is defined as the cartesian point $\mathbf{x}_{int}^* = (x_{int}^*, z_{int}^*)$, where $x_{int}^* = x_{int}$ and z_{int}^* is the corresponding z -coordinate for a point on the centerline of B_I^* so that values of s_R^* were taken as the length along the centerline of B_I^* from \mathbf{x}_{int}^* to the intersection with the horizontal boundary and from there along the centerline of B_F^* .

4.5.1 Ray tracing analysis

Ray tracing predicts purely subcritical boundary interactions, and hence no back-scatter, for values of θ such that the condition

$$\hat{A}_T \hat{k}_T < c, \quad (4.19)$$

where $c = \cot \theta$ (*c.f.* section 2.2.3), holds everywhere along the boundary. The maximum angle for which this is true is denoted $\theta = \alpha_s$ corresponding to a minimum forcing frequency denoted by σ_s/N , which has values of $\sigma_s/N = 0.64$ and 0.62 for T_A and T_B respectively. A subcritical ray tracing regime is therefore defined here for values of the parameter $\theta/\alpha_s < 1$. Subcritical, critical

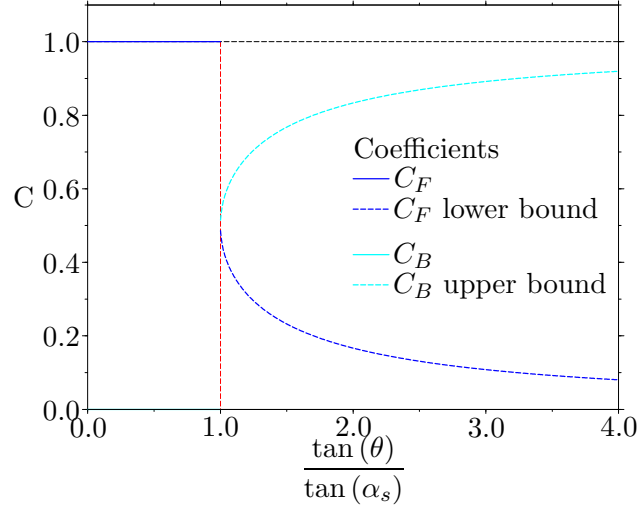


Figure 4.22: Geometrical ray tracing predictions for upper and lower bounds of reflection coefficients in forward and backward propagation directions (Longuet-Higgins 1969).

and supercritical interactions are possible in different regions along a boundary for values $\theta/\alpha_s \geq 1$. In such cases, ray tracing predicts downwards reflections of supercritical incident rays, resulting in multiple reflections before rays escape the topographic profile and propagate into the far-field in either the forwards or backwards directions. The total proportion of incident rays reflected in the forwards or backwards directions after interaction with a topographic profile can be described by the coefficients $0 \leq C_F \leq 1$ and $C_B = 1 - C_F$ respectively. As θ/α_s is increased, values of these coefficients calculated using a ray tracing analysis oscillate between the upper and lower bounds shown in figure 4.22 (Longuet-Higgins 1969). The oscillatory nature of the solution arises since the direction in which an incident wave ray is predicted to scatter is determined by whether the number of repeated reflections that an incident wave ray makes with the boundary is odd or even, with this property clearly oscillating as a function of the boundary angle, α_s . In particular, $C_F = 1$, *i.e.* $C_B = 0$, for the subcritical range $\theta/\alpha_s < 1$, with the red dashed line indicating the ‘critical’ value of $\theta/\alpha_s = 1$. In contradiction to these predictions, direct observations in the present study of movies of subcritical wave beams reflecting at sinusoidal topography reveal a back-scatter phase propagation in the opposite direction to that of the incident wave beam. Figure 4.23 (a) and (b) shows RMS_T images of the perturbed buoyancy field for (a) a section of a wave beam, with the wave beam denoted here by B_I^* , reflecting specularly at a smooth horizontal boundary positioned beyond the section shown at a distance $s/R_c \approx 16$ from the cylinder centre; and (b) the corresponding section of a wave beam, with the wave beam denoted here by B_I , that has subcritical interaction with sinusoid T_A at a distance of $s/R_c \approx 16$ along the beam. At small along-beam distances, maxima of the density perturbations associated with figure 4.23 (a) lie along two tangents to the cylinder parallel to the beam. These maxima gradually converge with distance as viscosity acts to reduce the gradients across the beam. This is the bimodal to unimodal transition discussed in more detail in section 4.2.1. The beam exhibits symmetry about its centerline and its width is approximately

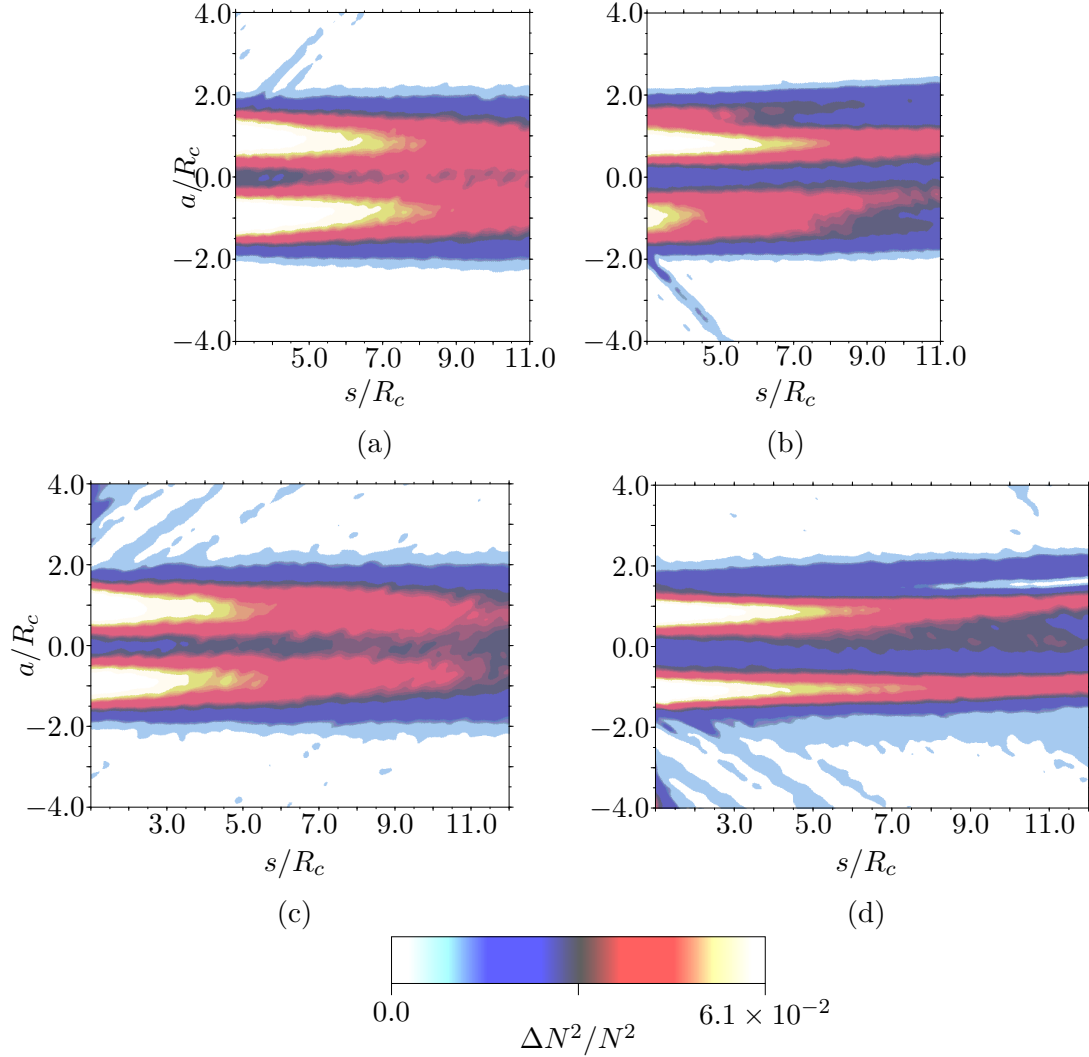


Figure 4.23: Comparison of RMS_T beam structures (a) B_I^* and (b) B_I , for topographic profile T_A and $\sigma/N = 0.67$, $\theta/\alpha_s = 0.95$. Similarly, (c) and (d) compare RMS_T beam structures B_I^* and B_I respectively, for parameter values $\sigma/N = 0.54$, $\theta/\alpha_s = 1.14$.

constant within the section shown. In contrast to the specular case, the beam RMS_T section shown in figure 4.23 (b) becomes asymmetric close to the topography and is characterised by smaller across-beam scales, indicating the imposition of higher wavenumber components on the wavefield by a back-scattered flux in this region. The structure becomes less distinctive and gradually adjusts to approximately bimodal nearer to the cylinder. As the backward flux propagates away from the topography it is attenuated by viscosity as well as encountering an incident flux with greater strength close to the cylinder. It is possible to filter the experiment data using Hilbert transforms in order to separate those fluid motions associated with wave groups propagating towards the boundary and those propagating in the opposite direction back towards the cylinder. This method and the filtered wavefields it produces are described in chapter 6.

Ray tracing comparisons with scatter observed at T_A

RMS $_T$ images of beam reflections for more general values of the parameter θ/α_s are shown for profiles T_A in figure 4.24 (a) and (c) together with the corresponding overlays of incident rays and their primary reflections as predicted by ray tracing in figure 4.24 (b) and (d). Ray tracing predictions, including primary *and* subsequent reflections of incident rays with the boundary, for the corresponding parameter values are shown in figure 4.25. In each case, wave energy is incident from the top left-hand corner and interacts with the topographic profiles positioned at the bottom of the field of view. Beams formed from the superposition of incident and back-scattered wavefields are denoted B_I and forwards scattered wave beams are denoted B_F . Colour schemes for the incident and reflected rays are described in the figure captions.

Figure 4.24 (a) shows the RMS $_T$ image of the perturbed buoyancy field for interaction of an incident beam at sinusoid T_A , with $\sigma/N = 0.58$ and $\theta/\alpha_s = 1.08$. Forwards scattered wave energy is focused into narrow beam-like structures, collectively referred to as B_F , that are characterised individually by smaller across-beam length scales than those associated with the incident wave beam, though the overall width of B_F is comparable to that of the incident beam B_I . Amplitudes of the forwards scattered wavefield decay rapidly with distance from the topography. The asymmetric structure of B_I , in comparison with the beam structure shown in figure 4.23 (a) for example, suggests the generation of a back-scattered flux. This is confirmed by observation of two directions of phase propagation across B_I in movies of the experiment. The experiment observations are compared here with ray tracing predictions. The locations of the peaks in B_F coincide with the focusing of rays predicted by ray tracing for the primary reflection shown in figure 4.24 (c) and for the complete wavefield shown in figure 4.25 (a). With regards to the back-reflected wavefield, a significant number of the incident rays are indeed predicted to back-reflect after multiple reflections with the topography, as shown in figure 4.25 (a). The back-reflected rays are focused into a periodic series of narrow ray tubes, with ray tracing estimating a value of $C_B \approx 0.49$ for $\theta/\alpha_s = 1.08$, suggesting nearly half of the incident wave energy will be back-reflected in the inviscid limit. Whilst ray tracing is able to suggest increases or decreases in wavenumbers and energy density through the focusing and defocusing of rays, it does not provide explicit information on amplitudes of the wave motion. Phase changes introduced through multiple reflections of rays are not clear from the analysis. In addition, as discussed in chapter 2, ray tracing does not resolve behaviour at critical points of the topography or the effects of viscosity.

Figure 4.24 (c) shows the RMS $_T$ image of the perturbed buoyancy field for interaction of an incident beam, B_I , at sinusoid T_A , with $\sigma/N = 0.33$ and $\theta/\alpha_s = 1.41$. The forwards scattered wavefield has a similar structure to that observed in figure 4.24 (a), though it exhibits smaller across-beam length scales and significantly weaker amplitudes. As in figure 4.24 (a), a back-scattered component of the incident flux is also evident from inspection of B_I . Ray tracing predicts that B_F is composed of rays reflecting directly in the forwards direction as well as rays reflecting there after multiple interactions with the topography (figures 4.24 (d) and 4.25 (b)). This allows an additional

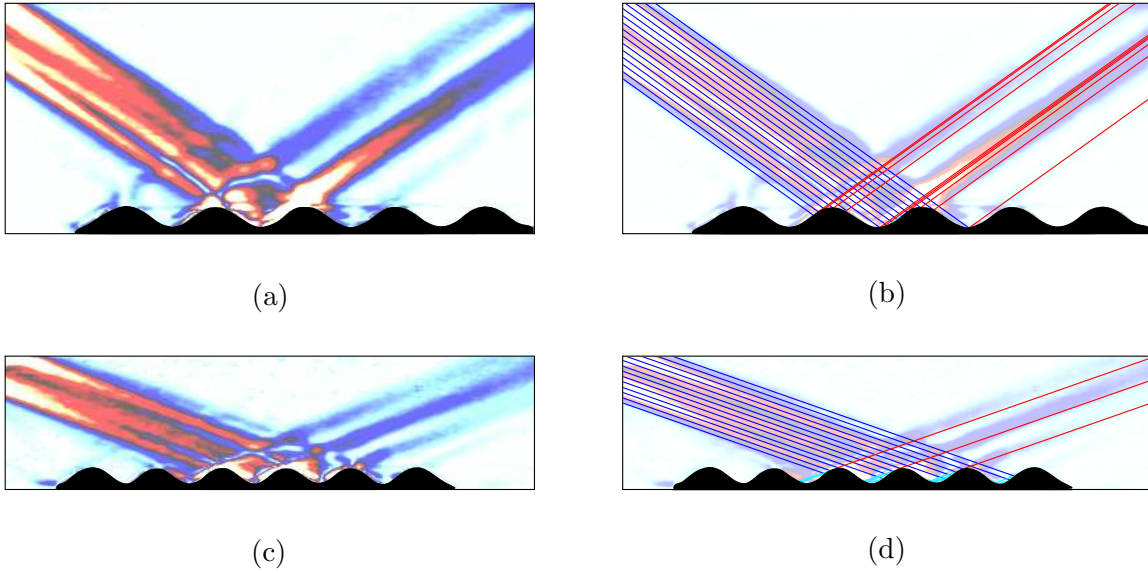


Figure 4.24: RMS_T images for topographic profile T_A with (a) $\sigma/N = 0.58$, $\theta/\alpha_s = 1.08$ and (c) $\sigma/N = 0.33$, $\theta/\alpha_s = 1.41$. These are compared with linear geometrical ray tracing predictions in (b) and (d) respectively. Blue lines denote wave rays within the incident ray tube; red lines denote forwards reflected rays; and cyan lines denote downwards reflected rays.

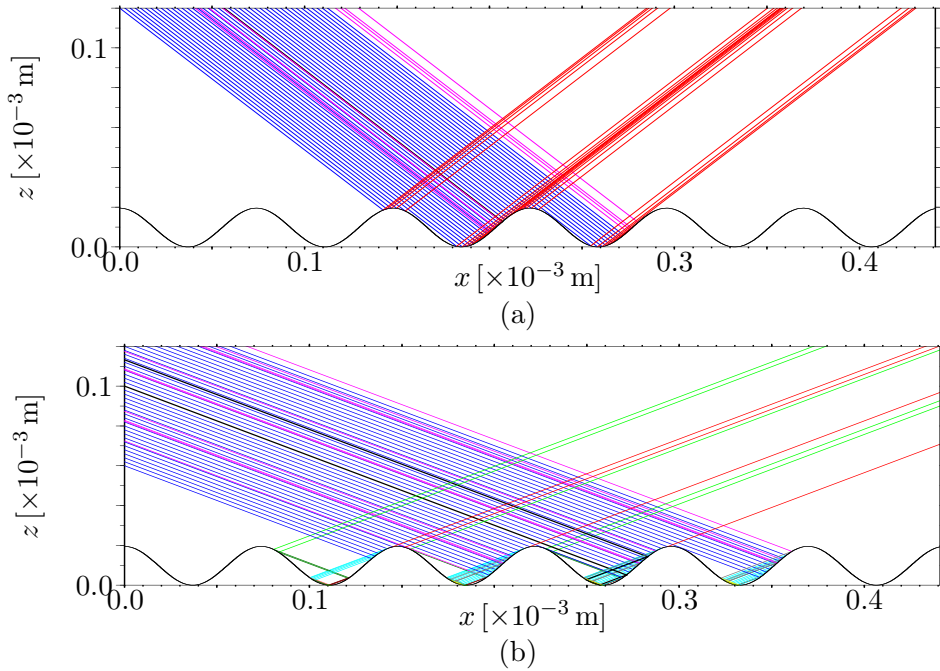


Figure 4.25: Ray tracing predictions for T_A . Here (a) $\sigma/N = 0.58$, $\theta/\alpha_s = 1.08$ and (b) $\sigma/N = 0.33$, $\theta/\alpha_s = 1.41$. Blue lines denote incident rays (constituents of B_I); red denote forwards reflected rays from primary reflection ($\in B_F$); green denote forwards reflected rays after multiple reflections ($\in B_F$); magenta denote back-reflected rays after multiple reflections ($\in B_I$). Cyan, dark green, dark red, grey and yellow denote topography-topography reflections.

mechanism for the introduction of phase shifts as well as other length scales into the wavefield. In the case of back-reflection, although more of the boundary is classified as supercritical than in the experiment associated with figure 4.24 (a), ray tracing values for C_F and C_B are oscillatory and so the proportion of back-reflected wave energy is not necessarily increased with increases in θ/α . In this case, however, ray tracing predicts a value of $C_B \approx 0.84$, again with back-reflected rays grouped into narrow ray tubes. The effect of the value of C_B is seen in the comparatively weak forwards scattered wavefield of the RMS_T image. The finer length scales introduced into B_F also enhance dissipation of the wave energy.

Ray tracing comparisons with scatter observed at T_B

Figure 4.26 (a) shows the RMS_T image of the perturbed buoyancy field for interaction of an incident beam, B_I , at sinusoid T_B , with $\sigma/N = 0.63$ and $\theta/\alpha_s = 0.98$. The forwards scattered wavefield is structured into narrow beams that have smaller across-beam scales than those observed for scatter at T_A due to the smaller wavenumber \hat{k}_T imposed by the topographic profile T_B . Forward scattered wave energy is hence not focused to the degree observed in figure 4.24 (a) for example, since it is partitioned between a greater number of beams. In addition, wave energy scattered from T_B might be anticipated to dissipate more rapidly due to the action of viscosity than in the case of T_A , since the smaller across-beam scales imposed by the topography introduce larger across-beam gradients. As the beams propagate away from the topography, the beams becomes less distinct from one another and converge into a larger beam structure, in a similar manner to the bimodal to unimodal structure transition seen for wave beams propagating away from an isolated source (see section 2.3). Under the predictions of ray tracing, this is a purely subcritical interaction and all incident rays are expected to be forward scattered (see figures 4.26 (c) and 4.27 (a)) so that $C_B = 0$. However, a back-scattered component is again observed in the present study (*c.f.* figure 4.23) in movies of the experiment and can be distinctly seen in figure 4.26 (a) to disturb the RMS_T structure of the incident wave beam, with the disturbance decaying with distance from the topography.

Figure 4.26 (c) shows the RMS_T image of the perturbed buoyancy field for interaction of an incident beam, B_I , at sinusoid T_B , with $\sigma/N = 0.41$ and $\theta/\alpha_s = 1.27$. The forwards scattered field is again similar in structure to that of figure 4.26 (a), though having smaller across-beam scales and amplitudes. A back-scattered wavefield can also be observed in figure 4.26 (c). Ray tracing predicts that only a small proportion of rays are directly reflected forwards and that a significant proportion of the forwards scatter is composed of rays that have undergone multiple reflections (figures 4.26 (d) and 4.27 (b)). In the back-reflected direction, ray tracing predicts a relatively small value of $C_B \approx 0.09$. It is difficult to estimate from these graphs the proportion of back-scattered and forwards scattered wave energy.

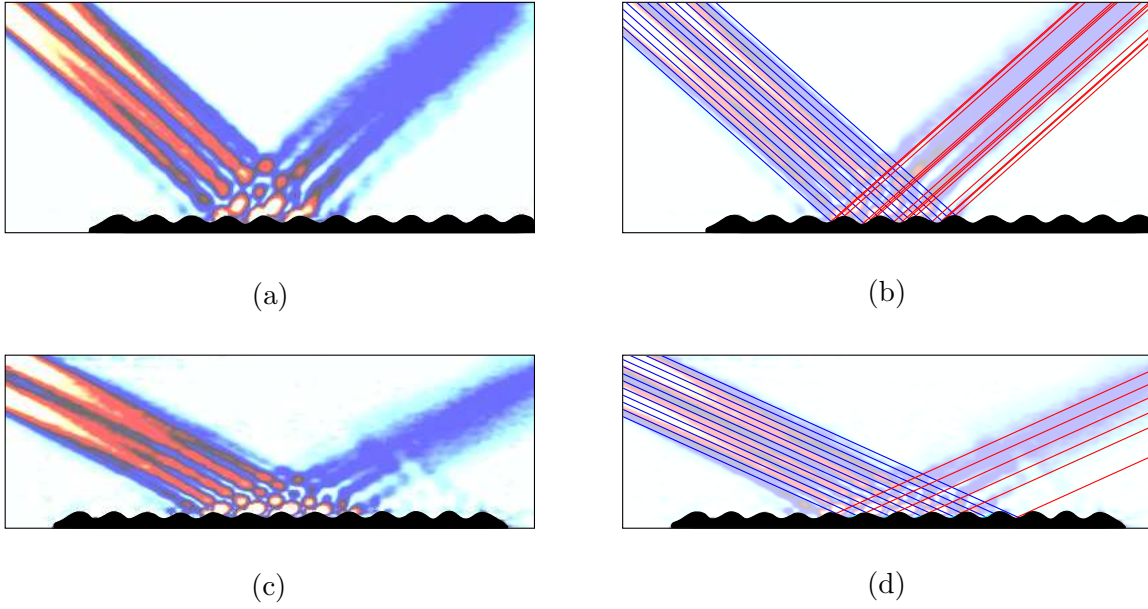


Figure 4.26: RMS_T images for topographic profile T_B with (a) $\sigma/N = 0.63$, $\theta/\alpha_s = 0.98$ and (c) $\sigma/N = 0.41$, $\theta/\alpha_s = 1.27$. These are compared with linear geometrical ray tracing predictions in (b) and (d) respectively. Line colouring as is figure 4.24.

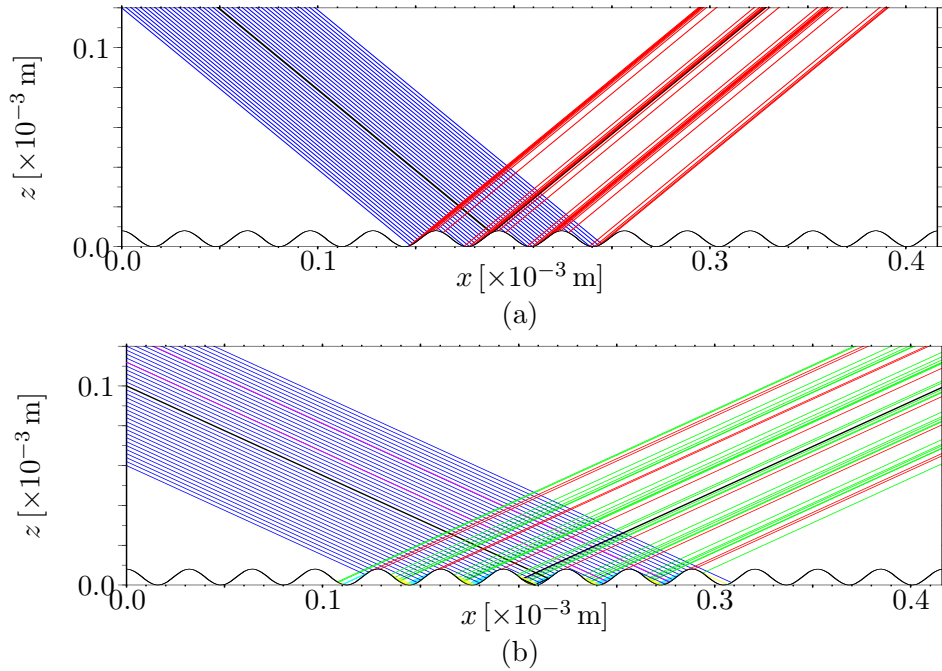


Figure 4.27: Ray tracing predictions for T_A . Here (a) $\sigma/N = 0.63$, $\theta/\alpha_s = 0.98$ and (b) $\sigma/N = 0.41$, $\theta/\alpha_s = 1.27$. Line colouring as in figure 4.25.

Applicability of ray tracing

Correct application of linear geometrical ray tracing is restricted to the propagation of rays within *slowly varying* media as discussed in section 2.5. The sinusoidal topographies discussed here, and

the other rough boundaries discussed later in this thesis, are *not* slowly varying on the scale of the incident waves, with parameters comparing length scales associated with the topography and those of the incident wavefield, k_c/k_T and $\hat{A}_T k_c$, having values $\sim 0(1)$. Despite its invalidity in this context, ray tracing provides a description of the wavefields generated if each incident ray were to reflect specularly at the boundary according to the local gradient at its point of incidence. Such predictions are used here to illustrate the degree to which reflection behaviours deviate from the specular description as wave groups encounter varying reflection conditions across their breadth. Similarly, applications of ray tracing in chapters 6-8 are intended as purely qualitative comparisons, used to suggest some of the underlying physics, and are not to be understood as mathematically legitimate.

In general, the ray tracing presented in the present section predicts some aspects of the qualitative behaviour of the scatter discussed but quantitative comparisons of the ray tracing are limited. A significant contradiction of the ray tracing analysis is obvious however, in the observation of a back-scattered flux in subcritical conditions, also observed in results presented in section 4.4. There are also other notable features of the scatter. In all RMS_T images shown, regions where the incident and forwards reflected beams overlap exhibit complicated structure, with both regions of large and vanishing RMS_T amplitudes caused by superposition. In particular, shadow zones, defined in section 2.5.2 as regions of the boundary not directly exposed to the rays, in the scattered wavefields predicted by ray tracing are not observed in experiments (e.g. compare the large RMS_T amplitudes present in the lee of crests in figure 4.25 (c) with figure 4.24 (b)). Thin horizontal intrusions of mixed fluid are also generated at crests of the topography (see e.g. figure 4.25 (a)). The near-field structures of wavefields are discussed in more detail in chapter 6.

4.5.2 Energy density spectra

The measurement of spectra of wavefields scattered at sinusoidal topography and their comparison with inviscid linear theory of Baines (1971a) is discussed here. In the example shown in figure 4.21, measurements of the wavefields were made at the cross-sections located along the lines superimposed on the image. Dashed lines indicate cross-sections of wave beams interacting with rough topography and solid lines indicate cross-sections of wave beams interacting with the horizontal boundary. The numbering shown represents the along-beam location of the centerpoint of the cross-section so that the dashed red line numbered ‘12’ on B_I , for example, represents a cross-section with centerpoint at $a_I = 0$ and $s_I = 12R_c$ relative to \mathbf{x}_{int} . The solid red line on B_I^* is the corresponding cross-section of the beam directed downwards from the cylinder.

Consider an experiment where the rough topographic profile is replaced with a *smooth* horizontal boundary. For each wave group generated by the cylinder with group velocity directed along B_I , a wave group with identical spectral form is simultaneously generated with group velocity directed along B_I^* . Any particular wavenumber component generated on B_I at a given time, $t = t_0$, propagates in the along-beam direction at the same speed as its counterpart on B_I^* , as specified by

the group velocity dependence on wavenumber (2.20), and hence the particular wavenumber components reach the locations of $s_I = 12R_c$ and $s_I^* = 12R_c$, respectively, at the same time, $t = t_1$, say. Wavenumber magnitude, and hence group velocity, is preserved on reflection at a smooth horizontal boundary (Lamb 1932, Phillips 1966) so that, subsequent to the given wavenumber components reflecting at their respective boundaries, they also both reach sections located at $s_R = 12R_c$ and $s_R^* = 12R_c$ at the same time $t = t_2$ (red sections on figure 4.21). It follows that, in this configuration, the form of wave groups on B_I and B_I^* should be the same at along-beam locations $s = s_I = s_I^*$, and similarly wave groups on B_F and B_F^* should have the same form at $s = s_R = s_R^*$. In the experiments performed in this study, measurements along cross-sections of B_I^* and B_F^* were therefore used as ‘control’ measurements, for comparison with measurements at the corresponding cross-sections of B_I and B_F .

Spectral analysis of scatter at T_A

Figure 4.28 (a), (c), (e) and (g) shows energy density spectra, $E(k)$, calculated for T_A along cross-sections at various distances along B_F and B_F^* with $\sigma/N = 0.71, 0.63, 0.54$, and 0.50 and $\theta/\alpha_s = 0.89, 1.01, 1.14$ and 1.19 respectively. Energy density values are normalised by the total energy, \hat{E} , associated with the closest cross-section to the cylinder measured on B_I^* for each frequency (specific locations for these can be deduced from figure 6.21). Spectra relating to B_F are coloured in blue shades, whilst the corresponding ‘control’ spectra measured from cross-sections of beams reflecting at the horizontal boundary are coloured in red shades.

Spectral differences, with $E_{\Delta F} = (E_F - E_F^*)$ are shown in (b), (d), (f) and (h), where E_F and E_F^* indicate spectra for B_F and B_F^* respectively. Regions of spectral difference graphs shaded light grey indicate estimated error margins for the experimental data. A measure of the error associated with noise and artefacts from data processing is calculated here by comparing energy density spectra obtained from measurements made along cross-sections of two separate wave beams simultaneously generated by an oscillating cylinder in the case where no rough topographic profile was put in the path of either beam. The two wave beams are represented here by the labels B_1 and B_2 , with corresponding along-beam distances (originating at the cylinder center) denoted s_1 and s_2 and energy densities E_1 and E_2 respectively. For a given along-beam distance $s = s_1 = s_2$, the discrepancy between the energy density spectra of B_1 and B_2 is calculated as $|E_{\Delta}| = |E_1 - E_2|$. Figure 4.29 shows values of $|E_{\Delta}|/\hat{E}$, where \hat{E} is the total energy associated with the closest cross-section to the cylinder measured on B_1 , located at $s_1 = 9R_c$, with $\sigma/N = 0.54$ and for a range of values of s typical of those used for back-scatter calculations presented in this research. The dominant discrepancy between the spectra of the two beams is localised in the region of peaks of the power spectra presented in figures 4.8 and 4.10 for individual wave beams, being the most significant for the cross-sections located closest to the cylinder, with spectral difference peak magnitudes of $\sim 5.8 \times 10^{-3}$ at $\tilde{k} \sim 0.3$. The magnitude of the error is therefore less than 1% of \hat{E} and decreases significantly for cross-sections associated with lower energy densities. The error margins shaded on

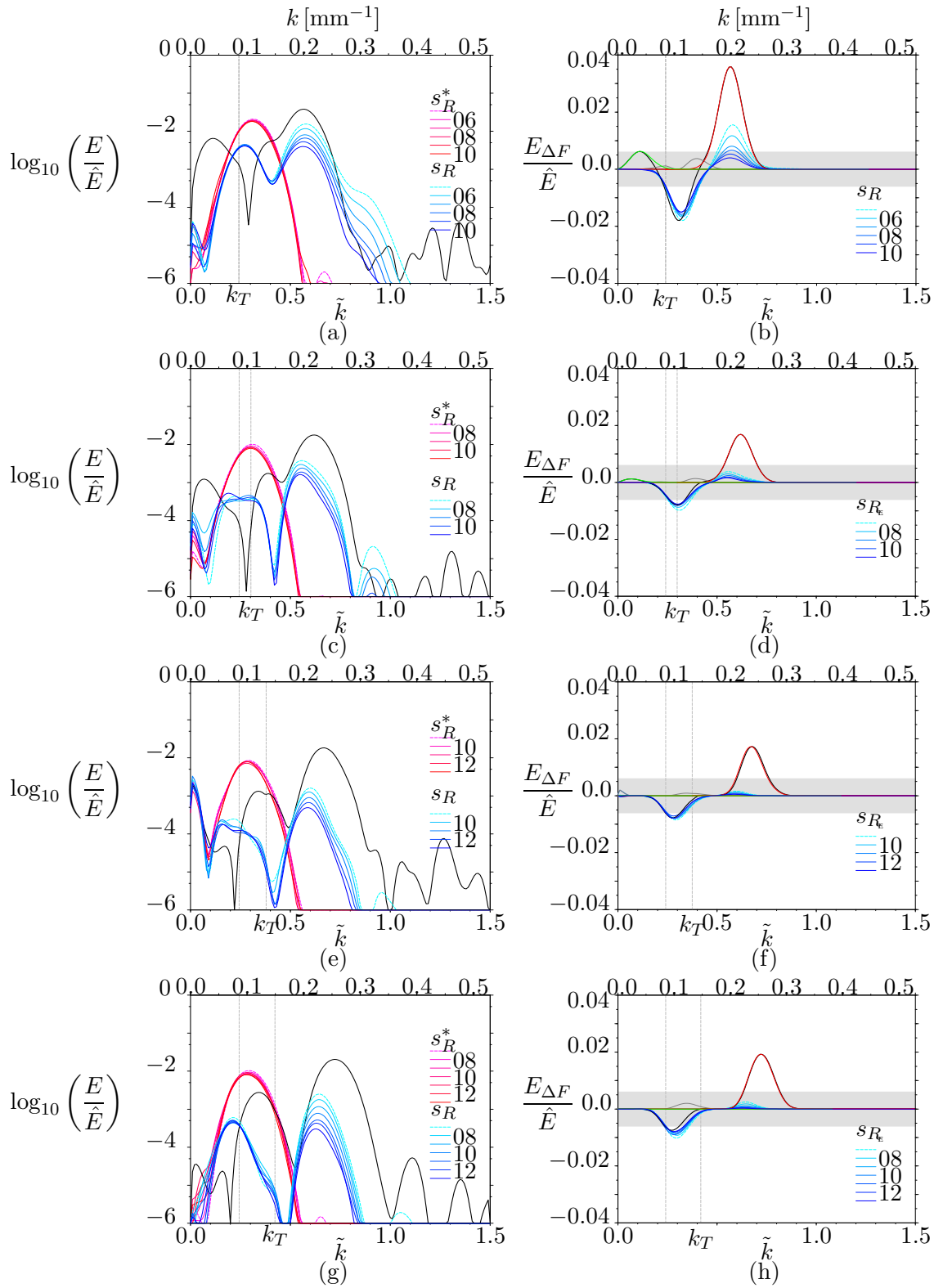


Figure 4.28: Forward-scattered energy density spectra for T_A are plotted in (a, c, e, g). Corresponding spectral differences are plotted in (b, d, f, h). Frequencies decrease down the page.

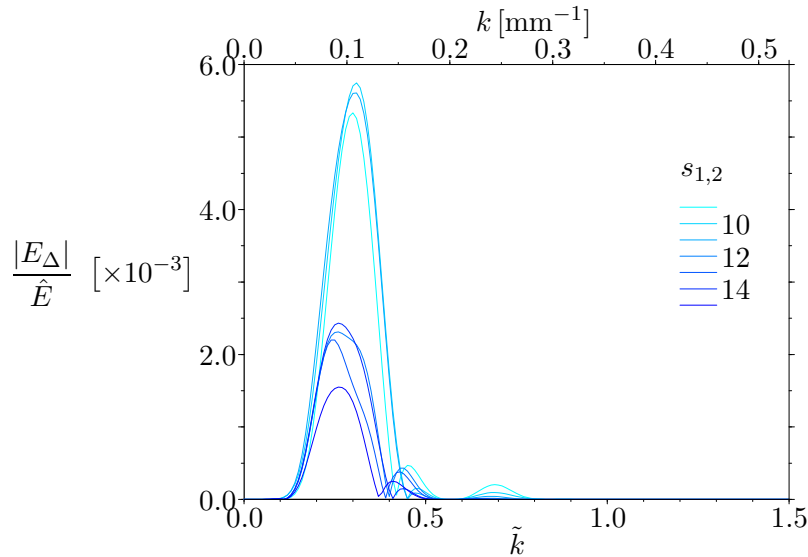


Figure 4.29: Error estimation for energy density spectra. Spectral differences, $|E_{\Delta}| = |E_1 - E_2|$, between energy density spectra calculated at different along-beam distances for two simultaneously generated wave beams, B_1 and B_2 respectively, at $\sigma/N = 0.54$, where $|E_{\Delta}|$ is normalised by the total energy, \hat{E} , associated with the closest cross-section to the cylinder.

spectral difference graphs are therefore very conservative estimates. In addition, the form of the actual error tends to be localised about spectral peaks of the data. Spectral difference graphs are presented in this research as a means of more clearly showing spectral locations of the individual *predicted* wavenumber components than is possible in full spectra, as well as those of measured components with spectral differences of magnitude $\sim O(10^{-2})$ and greater. Interpretations of spectral differences with magnitudes of $\sim O(10^{-3})$ are dependent on factors such as the associated energy densities of the relevant cross-sections. Spectral difference graphs are not intended as a rigorous method of analysis here but do provide some qualitative insights into the scatter that are less clear on graphs of full spectra.

Bold black lines superimposed on the spectra of figure 4.28 indicate the predictions of linear theory for the forwards scattered spectra (Baines 1971a), which assumes small topographic aspect ratios $\hat{A}_T \hat{k}_T \ll 1$ (see section 2.5.1). Dark grey, red and green lines (only plotted on graphs of spectral differences) indicate the individual contributions from forwards scattered ‘primary’, ‘sum’ and ‘difference’ wavenumber components respectively. Predictions for the forwards scatter are calculated from spectra associated with the cross-section located on B_F^* at the largest distance s_R^* measured for each particular frequency. For an incident plane wave associated with a streamfunction ψ_I and wavenumber k_I , Baines (1971a) calculates the relative amplitudes and wavenumbers associated with the streamfunctions for the primary, ψ_R , sum, ψ_+ , and difference, ψ_- , scattered wave components (see section 2.5.1). For a given wavenumber component k , with phase propagating

along ξ and amplitude ε , which can be expressed in terms of a streamfunction ψ with form

$$\psi = \varepsilon \exp [i(k\xi - \sigma t)], \quad (4.20)$$

Baines gives the magnitude of the associated average energy flux per unit area, \mathbf{F} , as

$$|\mathbf{F}| = \varepsilon^2 k \rho_0 [\sigma (N^2 - \sigma^2)]^{\frac{1}{2}}. \quad (4.21)$$

Energy density ratios of primary, sum and difference forwards scattered components relative to those of the incident wavefield are therefore calculated as

$$\frac{E_R}{E_I} = \begin{cases} (1 - k_I^2 \hat{A}_T^2)^2, & k_T < k_I, \\ (1 - k_I k_T \hat{A}_T^2)^2, & k_T > k_I, \end{cases} \quad (4.22)$$

$$\frac{E_+}{E_I} = (k_I + k_T) k_I \hat{A}_T^2, \quad (4.23)$$

and

$$\frac{E_-}{E_I} = \begin{cases} |k_I - k_T| k_I \hat{A}_T^2, & k_T < k_I, \\ 0, & k_T > k_I, \end{cases} \quad (4.24)$$

respectively.

Measured spectra associated with the incident wavefields at T_A plotted in figure 4.28 (a), exhibit dominant peaks at $\tilde{k}_I \approx 0.3$ with magnitudes of $E/\hat{E} \sim O(10^{-2})$. Forwards reflected spectra exhibit two dominant peaks, with maxima located at wavenumbers of $\tilde{k} \approx 0.6$ and at $\tilde{k} \approx 0.3$, both with magnitudes of $\sim O(10^{-2})$. The composite predicted spectra, indicated by the bold black line, exhibits three dominant peaks. The largest of these, dominantly representing ‘sum’ components of the scatter, approximately coincides with the largest peak of the measured spectra (blue lines), with slightly lower magnitudes in the measured spectra. This discrepancy is most likely dominantly caused by enhanced viscous attenuation during the scatter as a result of the greater proportion of energy associated with high wavenumber components. The second peak of the predicted spectra is associated with the ‘primary’ scattered component, with the third generated by a combination of ‘primary’ and ‘difference’ scattered components, located at $\tilde{k} \approx 0.4$ and $\tilde{k} \approx 0.1$ respectively, both with magnitudes of $\sim O(10^{-3})$. The second peak of the measured forward spectra has a similar magnitude to the two predicted components and is positioned midway between them. It is possible that the FFT used to calculate the spectra has merged two separate peaks.

Spectral *differences* for the forwards scatter (see figure 4.28 (b)) exhibit both positive (peaks) and negative (troughs) values. Generally, peaks of the spectral differences represent scatter of the incident wave energy to wavenumbers in this region. Troughs suggest that energy from that region of the spectrum has been redistributed during the scatter, either being transferred to other

wavenumber (or higher harmonic frequency) components, or being dissipated through viscous or other mechanisms. Measured spectral differences shown in figure 4.28 (b) have peak differences of magnitude $O(10^{-2})$ located at $\tilde{k} \approx 0.6$, coinciding with the high wavenumber peak of the predicted sum component. The measured spectral differences sharply decrease to negative values at $\tilde{k} \approx 0.45$, with spectral troughs of magnitude $O(10^{-2})$ located at $\tilde{k} \approx 0.3$. In part, the negative values may represent back-reflected wave energy. Additional losses near this region of the spectrum, relative to those predicted by the linearised boundary theory (bold black line), which is centered about the location of peaks of the incident spectra, also occur through enhanced dissipation of the incident beam during the reflection process. Larger spatial gradients in the overlap region of the incident and scattered beams near the topography combined with large amplitudes of the wave motion as the scattered energy is focused there enhances the action of viscosity. In addition, dissipation is promoted by the production of higher wavenumber components during the scatter, keeping the wave energy closer to the boundary for longer as group velocities therefore decrease. The spatial scatter of wave energy to propagating higher harmonics is not possible at $\sigma/N = 0.71 > 0.5$.

Variation in the scattering behaviour resulting from a decrease in the incident wave frequency, corresponding to an increase in k_T , is described here. As the frequency is decreased, locations of predicted sum components shift to higher wavenumbers, whilst peaks for the primary and difference components shift to lower wavenumbers. Measured peaks in the sum region of the spectrum are positioned within the predicted peaks of the sum components but decrease in magnitude from $O(10^{-2})$ to $O(10^{-3})$ over the frequencies shown in figure 4.28, with predicted magnitudes remaining at $O(10^{-2})$. For all frequencies the measured spectra have negligible magnitudes for wavenumbers greater than $\tilde{k} \sim 0.8$, well below the maximum wavenumber for synthetic schlieren measurements. This seems to suggest that discrepancies between predictions and experiments for the sum component are indeed caused primarily by enhanced viscous action or through instability mechanisms as greater proportions of the incident energy are scattered to higher wavenumbers, with a critical wavenumber existing beyond which wave energy in this region of the spectrum is rapidly dissipated. In dimensional terms, this wavenumber corresponds to $k \approx 0.28 \text{ mm}^{-1}$. A wavenumber corresponding to the viscous length scale, defined by (2.23), can be calculated as $k \approx 0.43 \text{ mm}^{-1}$. The second peak of the measured spectra in figure 4.28 (a), (c), (e) and (g), located at lower wavenumbers, similarly decreases in magnitude with decreasing frequency and the peak location shifts from $\tilde{k} \approx 0.3$ to $\tilde{k} \approx 0.2$. The form of spectral difference graphs is similar for all frequencies shown, with peak differences associated with sum components qualitatively following the trends described above, though magnitudes of spectral differences in this region are within the indicated error margin at lower frequencies. Magnitudes and locations of troughs of spectral differences remain approximately the same as the frequency decreases, though the discrepancy with *predicted* spectral differences increases possibly indicating enhanced dissipation. Multiple reflections of wave energy with the boundary are possible for $\theta/\alpha_s > 1$ (as in experiments relating to figure 4.28 (c), (e) and (g)), which increases the propagation distances of wave energy. The enhanced focusing and longer durations near the boundary results in increased dissipation.

In summary, spectra of forwards scattered wavefields at T_A show some tendency for scatter to the lower wavenumbers associated with predictions for primary and difference components. Spectra exhibit high wavenumber scatter corresponding to predicted sum components, though the measured scatter is limited at high wavenumbers by dissipation processes. In general, a larger total scatter to higher wavenumbers is observed for higher incident wave frequencies, *i.e.* at lower values of k_T . Losses from the measured spectra, relative to the specular control cases, occurring in the region of peaks of the incident spectra, suggest dissipative interactions between the scattered and incident wavefields.

Figure 4.30 (a), (c), (e) and (g) show spectra associated with superposition of the incident and back-scattered fields calculated for T_A along cross-sections at various along-beam distance of B_I and B_I^* for $\sigma/N = 0.71, 0.63, 0.54,$ and 0.50 respectively. Corresponding spectral differences, with $E_{\Delta I} = (E_I - E_I^*)$, are shown in (b), (d), (f) and (h), with theoretical predictions displayed as in figure 4.28. Predictions for the backward scatter are calculated using linearised boundary theory from spectra associated with the cross-section located on B_I^* at the largest distance s_I^* measured for each particular frequency (black lines in plots of full spectra, green lines in spectral difference plots). The spectra shown in figure 4.30 (a) for measured incident and scattered wavefields, as well as the predicted spectra are not easily distinguished from one another, showing little perceptible variation with decreasing frequency. All spectra exhibit two dominant peaks located at $\tilde{k} \approx 0.3$ and $\tilde{k} \approx 0.75$, with magnitudes of $O(10^{-1})$ and $O(10^{-2})$ respectively. Clearer distinctions between the spectra can be made from the corresponding spectral differences of figure 4.30 (b). For the relevant parameter value of $\theta/\alpha_s = 0.89$, the reflection is categorised as everywhere subcritical and ray tracing hence predicts that $C_B = 0$. In contrast, the linearised boundary theory of Baines (1971a) predicts a back-scattered flux at wavenumbers close to zero, with a peak magnitude of $O(10^{-4})$ (green line). The presence of this component in the experimental data can not be ascertained here however, due to its small magnitude. However, a peak representing high wavenumber scatter, *not predicted by either theoretical approach*, is present in the spectral differences, located at $\tilde{k} \approx 0.7$, with a magnitude of $O(10^{-3})$. Whilst the magnitude of this peak is within the error margin indicated, back-scatter characterised by small across-beam length scales can be clearly observed in movies and RMS_T images of the related experiments (*c.f.* figure 4.23 (b) and (d), for example). This high wavenumber scatter is not caused by scatter to higher harmonic components as $\sigma/N = 0.71 > 0.5$. The spectral differences also contain a distinct trough, again not anticipated by the inviscid linearised boundary theory, located at $\tilde{k} \approx 0.4$ with peak difference magnitude $O(10^{-2})$. In this case, ‘losses’ from the incident beam spectrum relative to the specular control case suggest that greater across-beam gradients introduced with the observed presence of back-scattered wave energy propagating along the incident beam direction cause enhanced viscous action. The trough of the back-scattered difference spectra lies at slightly higher wavenumbers than that seen in the forwards spectral differences since the incident beams are composed of a larger proportion of high wavenumber components and these are preferentially attenuated by viscosity.

As the frequency of the incident wavefields decrease, ray tracing predicts back-reflection coef-

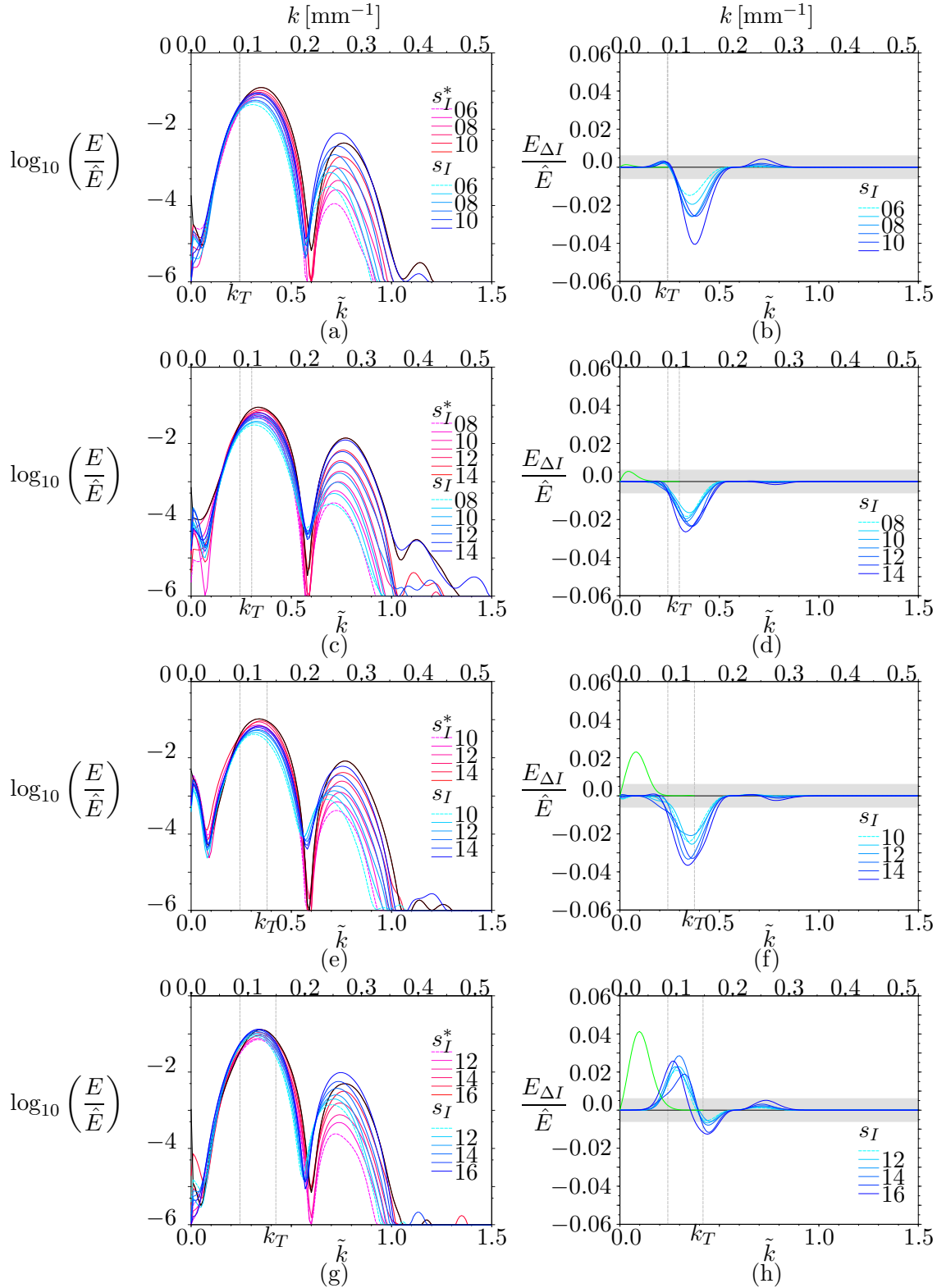


Figure 4.30: Back-scattered energy density spectra for T_A are plotted in (a, c, e, g). Corresponding spectral differences are plotted in (b, d, f, h). Frequencies decrease down the page.

ficients, dominantly associated with high wavenumber scatter, of $C_B = 0.11, 0.68$ and 0.50 corresponding to the spectra shown in figure 4.30 (d), (f) and (h) respectively. Baines (1971a) predicts an increasingly prominent back-scattered flux, with magnitudes increasing to $O(10^{-2})$ and peak located at $\tilde{k} \approx 0.1$ for the smallest frequency shown. Spectral difference graphs of the measured wavefields are not consistent in this region, in part due to artefacts of the FFT method used to create the spectra, though a well formed peak difference of magnitude $O(10^{-2})$ at $\tilde{k} \approx 0.4$ is present in the spectral differences of figure 4.30 (h). The weak signal of the second peak difference seen in figure 4.30 (b), located at higher wavenumbers, diminishes at lower frequencies. Whilst magnitudes of this peak are not reliable, the second peak difference may indicate the spectral location of high wavenumber back-reflection predicted by ray tracing, though notably, the peak is present even when $C_B = 0$. Similarly, the spectral difference trough at $\tilde{k} \approx 0.4$ is also present in lower frequency spectra.

In summary, low wavenumber back-scatter that may be associated with predicted difference components is observed at the lowest frequency. A region of weak high wavenumber scatter, noted in RMS_T images of the relevant experiments, may also be present in spectra, though magnitudes of these signals are not reliable. This high wavenumber scatter may be associated in part with back-reflected wave energy, which is not possible in the linearised boundary theory of Baines (1971a) though it is predicted by ray tracing for boundaries that are somewhere supercritical. However, the high wavenumber scatter also contradicts ray tracing predictions as it is also generated in those experiments with purely subcritical wave-boundary interactions. The high wavenumber back-scatter is therefore likely to arise from nonlinear mechanisms caused by high amplitude wave motion arising from energy focusing and superposition of the wavefields near the boundary.

Spectral analysis of scatter at T_B

Figure 4.31 (a), (c), (e) and (g) show spectra relating to forwards scattered wavefields for T_B , calculated along cross-sections positioned at various distances along B_F and B_F^* for $\sigma/N = 0.71, 0.63, 0.54$, and 0.50 and $\theta/\alpha_s = 0.86, 0.98, 1.10$ and 1.16 respectively. Corresponding spectral differences, with $E_{\Delta F} = (E_F - E_F^*)$, are shown in (b), (d), (f) and (h). Measured spectra for the incident and scattered wavefields shown in figure 4.31 (a) exhibit a single dominant peak located at $\tilde{k} \approx 0.3$ with magnitude $O(10^{-2})$. However, inviscid linearised boundary theory predicts *two* peaks located at $\tilde{k} \approx 0.3$ (the primary component) and $\tilde{k} \approx 0.8$ (dominantly the sum component) with magnitudes $O(10^{-2})$. The measured lower wavenumber peak has magnitudes slightly *larger* than those of the predicted spectra in this region. This may indicate the inclusion of background wave energy, ordinarily associated with much smaller wave amplitudes and larger length scales than the incident wave energy, in the measured spectra, which is focused at the topography and hence becomes more significant. As in previous discussion, some features of the predicted and measured spectra are more readily interpreted from the corresponding spectral differences in figure 4.31 (b). Theory for a linearised boundary predicts a single peak in the difference spectra of the scattered

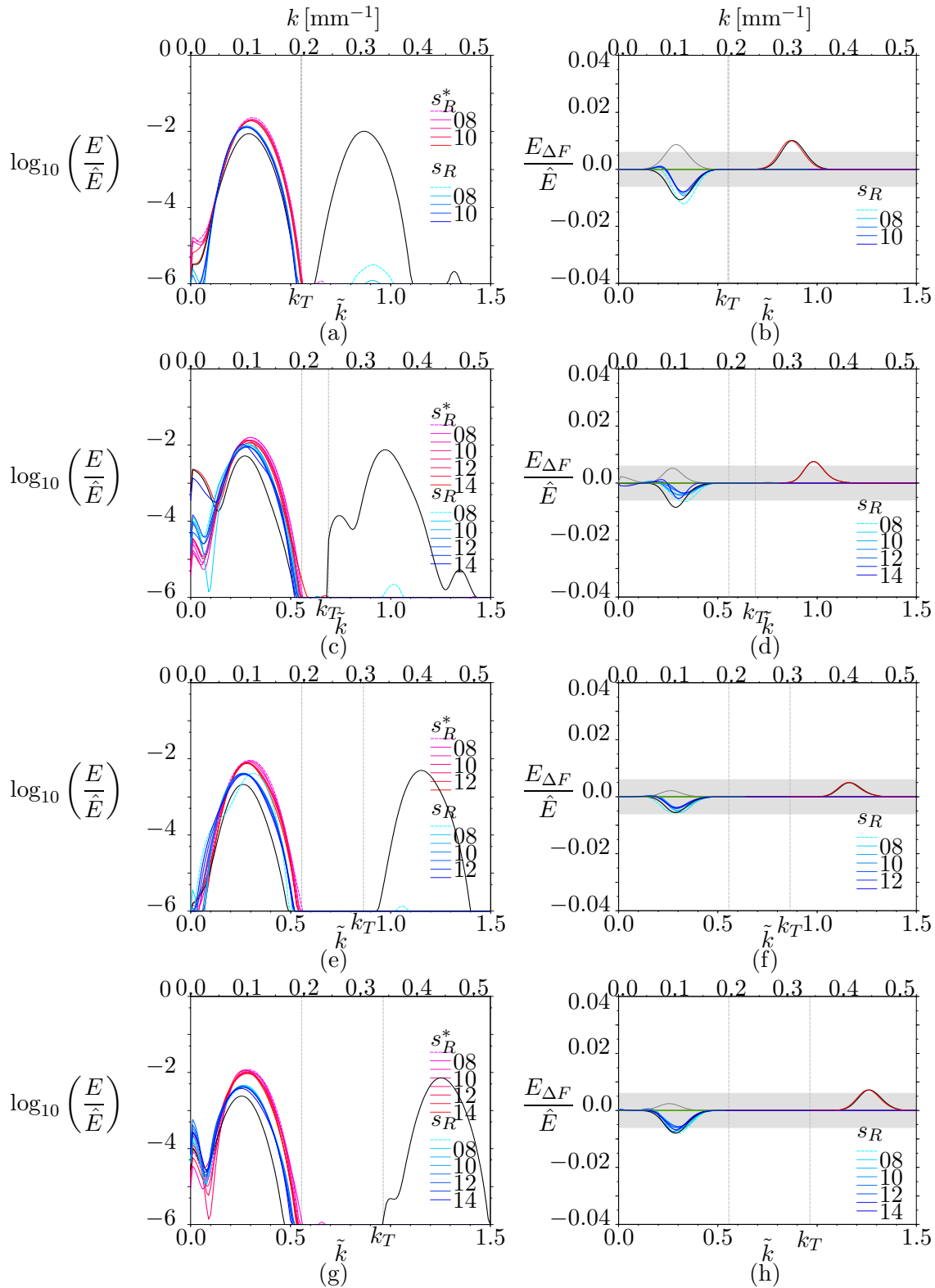


Figure 4.31: Forward-scattered energy density spectra for T_B are plotted in (a, c, e, g). Corresponding spectral differences are plotted in (b, d, f, h). Frequencies decrease down the page.

wavefield in the region of the sum component located at $\tilde{k} \approx 0.9$, with magnitude $O(10^{-2})$, together with a trough of similar magnitude located in the region of the peak in the incident spectra at $\tilde{k} \approx 0.3$. As frequency decreases, the contribution from the primary component shifts to lower wavenumbers and reduces in magnitude slightly, whilst the contribution from the sum component shifts to higher wavenumbers. Measured spectra in figure 4.31 (b) have a trough centered at $\tilde{k} \approx 0.3$ of magnitude $O(10^{-2})$. No significant low wavenumber scatter corresponding to the predicted primary component and, as identified in the full spectra, no high wavenumber scatter corresponding to the predicted sum component are observed however. Scattering behaviours at lower frequencies are similar and so, in contrast to the scattering behaviour reported at T_A , no high wavenumber forward scatter is observed in spectra relating to T_B . Notably, however, smaller length scales, introduced at the boundary and rapidly decaying away from there, are evident in movies and RMS_T images of scatter at T_B . It may be concluded therefore that their absence in spectra is dominantly a consequence of rapid viscous dissipation on the smaller length scales imposed on the wavefield by T_B .

Figure 4.32 (a), (c), (e) and (g) show spectra for the superposition of the incident and backwards scattered fields at T_B calculated along cross-sections at various along-beam distances of B_I and B_I^* for $\sigma/N = 0.71, 0.63, 0.54$, and 0.50 respectively. Corresponding spectral differences, with $E_{\Delta I} = (E_I - E_I^*)$, are shown in (b), (d), (f) and (h). As for figures 4.30 and 4.31, the distinction between spectra is best seen in the spectral *differences* of figure 4.32. At the highest two frequencies, ray tracing predicts a back-reflection coefficient of $C_B = 0$. Application of the theory of Baines (1971a) to these frequencies, however, predicts back-scattered components represented by peak differences of $O(10^{-2})$ centered at $\tilde{k} \approx 0.2$ and $\tilde{k} \approx 0.35$ respectively. Measured spectra are not consistent in the region of these peaks. However, a peak difference, unpredicted by either theoretical approach and suggesting high wavenumber scatter is measured at $\tilde{k} \approx 0.7$, most prominent for the experiment of figure 4.32 (d) with a peak difference magnitude in this case of $O(10^{-2})$. As in back-scatter spectra for T_A , the high wavenumber scatter is therefore thought to be generated by nonlinear mechanisms. A trough of magnitude $O(10^{-2})$ at $\tilde{k} \approx 0.35$ is also observed, caused by dissipation arising from interaction of back-scattered components with the incident wavefield.

As the frequency of the incident wavefield decreases, ray tracing predicts back-reflection coefficients of $C_B = 0.58$ and 0.71 corresponding to the spectra shown in figure 4.32 (f) and (h) respectively. The predicted back-scattered component of Baines (1971a) becomes more pronounced and shifts to higher wavenumbers with decreasing frequency and a second predicted peak difference of $O(10^{-3})$ emerges at low wavenumbers. The corresponding measured spectra are again not consistent at low wavenumbers. The trough observed at high frequencies persists at lower frequencies.

This section has examined spectra associated with forward and back-scatter at two sinusoidal topographic profiles. The spectra have been compared with ray tracing and theory for a linearised boundary (Baines 1971a). Whilst both theoretical approaches correctly predict some aspects of the spectra, the scatter at rough topography is clearly a more complex process and spectra dominantly exhibit the effects of viscous dissipation and other nonlinear mechanisms, especially for topography

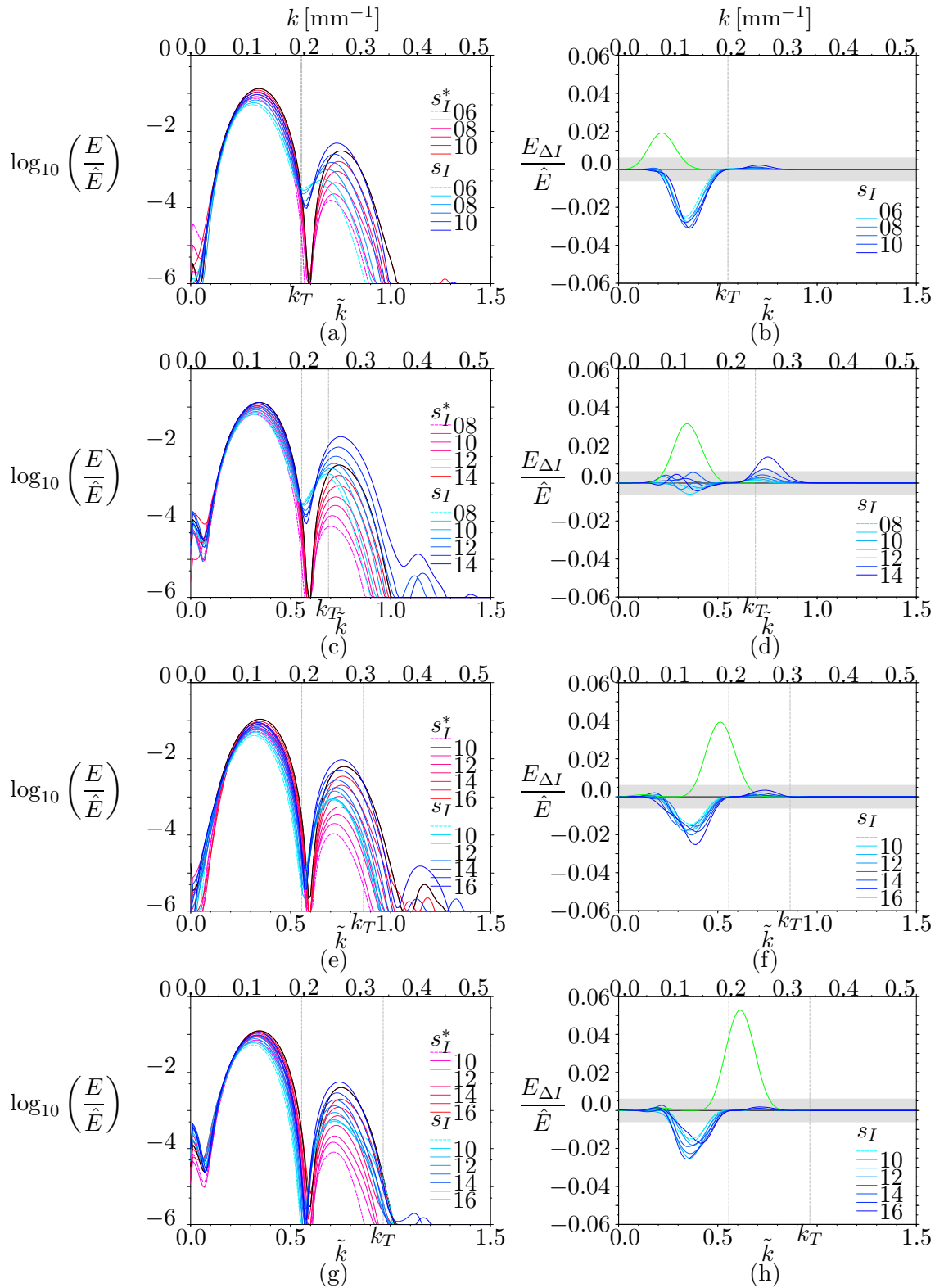


Figure 4.32: Back-scattered energy density spectra for T_B are plotted in (a, c, e, g). Corresponding spectral differences are plotted in (b, d, f, h). Frequencies decrease down the page.

with higher wavenumber variation. In particular, neither approach resolves behaviour in near-critical regions of the boundary. High wavenumber forwards scatter is observed at T_A and there is evidence for the presence of high wavenumber back-scatter at both T_A and T_B , though it is clear that high wavenumber components are rapidly dissipated as they propagate away from the topography.

4.6 Summary

This chapter has presented and discussed experimental results of reflection and scatter at flat sloping boundaries as well as topography with smoothly varying profiles. Where possible, the results have been compared with existing linear theory. In particular, ray tracing predictions capture most aspects of scattering behaviour at non-critical, slowly varying boundaries but fail to predict back-scatter or diffraction or split-reflection near critical regions. Quantitative applications of this first order approximation are also greatly restricted. However, other theoretical approaches based on linearised boundary theory, which are more quantitative and make predictions of back-scatter, are restricted to linearised and hence necessarily subcritical boundaries.

Viscous dissipation, both in the reflection region and as the scattered energy propagates into the far-field, has been shown to greatly influence the far-field wavefields. In particular, the preferential action of viscosity on wave motion characterised by small length scales cannot be ignored in studies aiming to quantify the proportion of wave energy scattered to higher wavenumber components.

A number of parameters, comparing relative length scales and slopes associated with the incident wavefield and topography, have been shown to influence scattering behaviours. The following chapter considers the effect of curvature and sharp corners by studying the generation of internal gravity waves from elliptical and square cylinders.

Chapter 5

Wave generation by different cylinder shapes

5.1 Overview

The reflection of wave beams at flat, sloping and smoothly varying rough topography was considered in chapter 4. Such topographic profiles are highly idealised and in particular do not contain features such as sharp corners, defined here as regions where the topographic slope becomes discontinuous. The influences of topographic curvature and the presence of sharp corners are investigated in the present chapter. Experimental results are presented of internal wave generation by elliptical and rectangular cylinders that have a range of aspect ratios. The generated beam structures are compared with the theory of Hurley & Keady (1997). Results from this chapter are used in order to understand the scattering behaviour at rough topographic profiles featuring sharp corners in chapters 6-8.

5.2 Wave generation by elliptical cylinders

Literature relating to the generation of internal gravity wavefields by the vertical oscillation of cylinders with circular and elliptical cross-sections was discussed in section 2.3. Preliminary experiments from the present study relating to wavefields generated by a circular cylinder were presented in sections 3.6 and 4.2. Many of these results have not been published in previous studies of this nature, or have been described over a much narrower range of parameters than is given here. This section compares experimental results of the established wavefields generated by circular and elliptical cylinders prior (physically) to the wavefields interacting with boundaries of the laboratory tank. Cylinders were oscillated at frequencies within the range $\sigma/N = [0.36, 0.77]$, corresponding to primary wavefield responses with energy propagating at angles $\theta \in [39.6, 68.9]^\circ$ to the vertical. Results relating to the wavefields generated by square and rectangular cylinders are discussed in section 5.3.

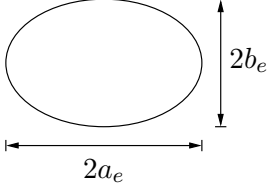
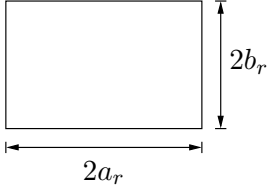
	Profile Index	$2a$	$2b$	Aspect Ratio
	C_i	[mm]	[mm]	a/b
	A	16.6	50.0	0.30
	B	21.5	43.0	0.50
	C	35.6	35.6	1.00
	D	43.0	21.5	2.00
	E	50.0	16.6	3.00
	F	38.5	59.0	0.65
	G	38.5	38.5	1.00
	H	59.0	38.5	1.53

Table 5.1: Specifications of cylinders used in experiments. Length scales a and b denote a_e or a_r and b_e or b_r for elliptical and rectangular cylinders respectively.

Lengths of the horizontal and vertical axes of elliptical cylinders are denoted $2a_e$ and $2b_e$ respectively, with cylinder aspect ratios defined by the ratio a_e/b_e . The top section of table 5.1 shows the dimensions of circular and elliptical cylinders used in experiments, which had aspect ratios of 0.3, 0.5, 1.0, 2.0 and 3.0. All cylinders were made of the same materials, and positioned and operated as described in section 3.6.1. An exception to this was that the vertical metal rods connected to the elliptical cylinders (see figure 3.12) measured 4 mm in diameter, *i.e.* 2 mm narrower than the rod connected to the circular cylinder. This reduced the effects on the wavefield due to the rod, which were anticipated to become more significant for ellipses with smaller aspect ratios. Note that the rigidity of the rod was not compromised by this reduction in diameter. A similarly narrow rod was not attached to the circular cylinder since its construction predated that of the elliptical cylinders and such a small rod diameter was not considered necessary for a cylinder with a diameter of 35.6 mm and unit aspect ratio.

Across-beam geometry

The perpendicular distance between two parallel tangents to an elliptical cylinder that make an angle $\theta = \cos^{-1}(\sigma/N)$ to the vertical is denoted here as $2c_e$, where

$$c_e^2 = a_e^2 \cos^2 \theta + b_e^2 \sin^2 \theta \quad (5.1)$$

(e.g. Sutherland & Linden 2002). These distances are indicated in figure 5.1 (a). Red and blue lines indicate tangents to the cylinder inclined at the angle θ . In particular, c_e varies with frequency as

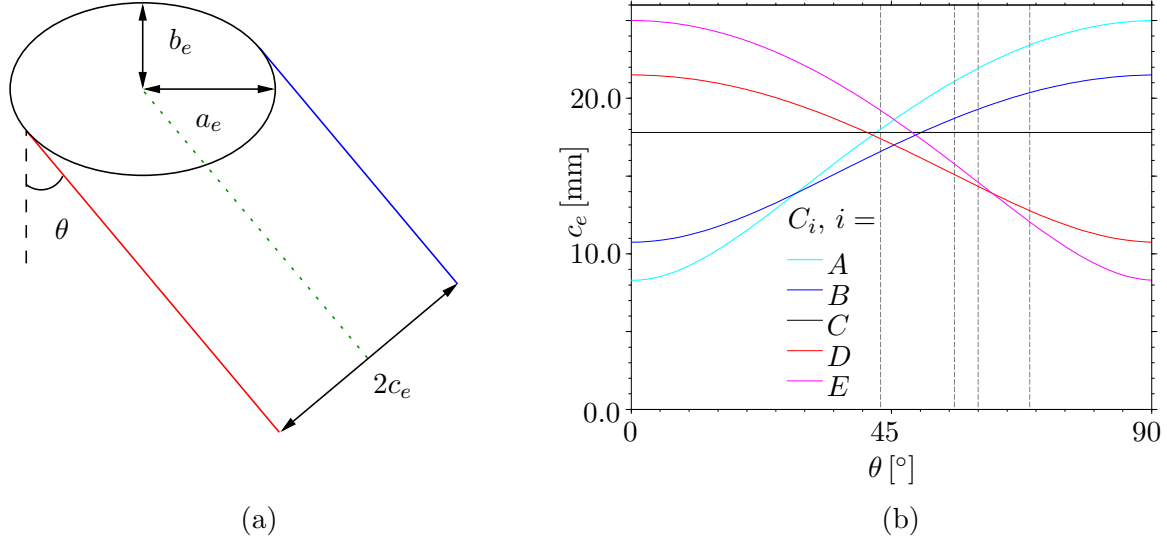


Figure 5.1: Geometrical schematic of an elliptical cylinder and definition of c_e are shown in (a). Variation of c_e with θ for elliptical cylinders, C_i , $i = A - E$, is plotted in (b).

plotted in figure 5.1 (b) for cylinders $C_A - C_E$. An analogous length scale, c_c , is also defined for a given ellipse that corresponds to the radius of the circle that has the same cross-sectional area, so that

$$c_c = (a_e b_e)^{\frac{1}{2}}, \quad (5.2)$$

where c_c has values of 14.2, 15.2, 17.8, 15.2 and 14.2 mm for cylinders C_A to C_E respectively. A coordinate system is defined for each cylinder with across-beam (*i.e.* aligned with the phase propagation) and along-beam (*i.e.* aligned with the energy propagation) coordinates denoted as in previous chapters by (a, s) respectively, which originate at cylinder centers.

The variation with aspect ratio of the amplitude and spectral structure of wave beams are considered in the following subsections, together with the generation of higher harmonic components and other features of the wavefields in regions near the cylinders. Specifically, results are discussed for wave beams with energy propagation from cylinders oriented downwards and to the right, with results for beams with other propagation directions inferred by symmetry.

5.2.1 Across-beam amplitudes

Across-beam structures of the wavefields generated by the different cylinders can be analysed in a similar manner to that described in section 4.2 for a circular cylinder. Figure 5.2 presents across-beam amplitudes of perturbed buoyancy fields (without filtering for temporal harmonics) for each cylinder along cross-sections of length $10c_e$ at different along-beam distances, s/c_e , and at the four forcing frequencies $\sigma/N = 0.36, 0.50, 0.59$ and 0.73 . Each individual panel represents results relating to one cylinder at a fixed forcing frequency σ/N . Frequencies increase across the page, from left to right, whilst aspect ratios of cylinders increase down the page, from top to bottom. Since the

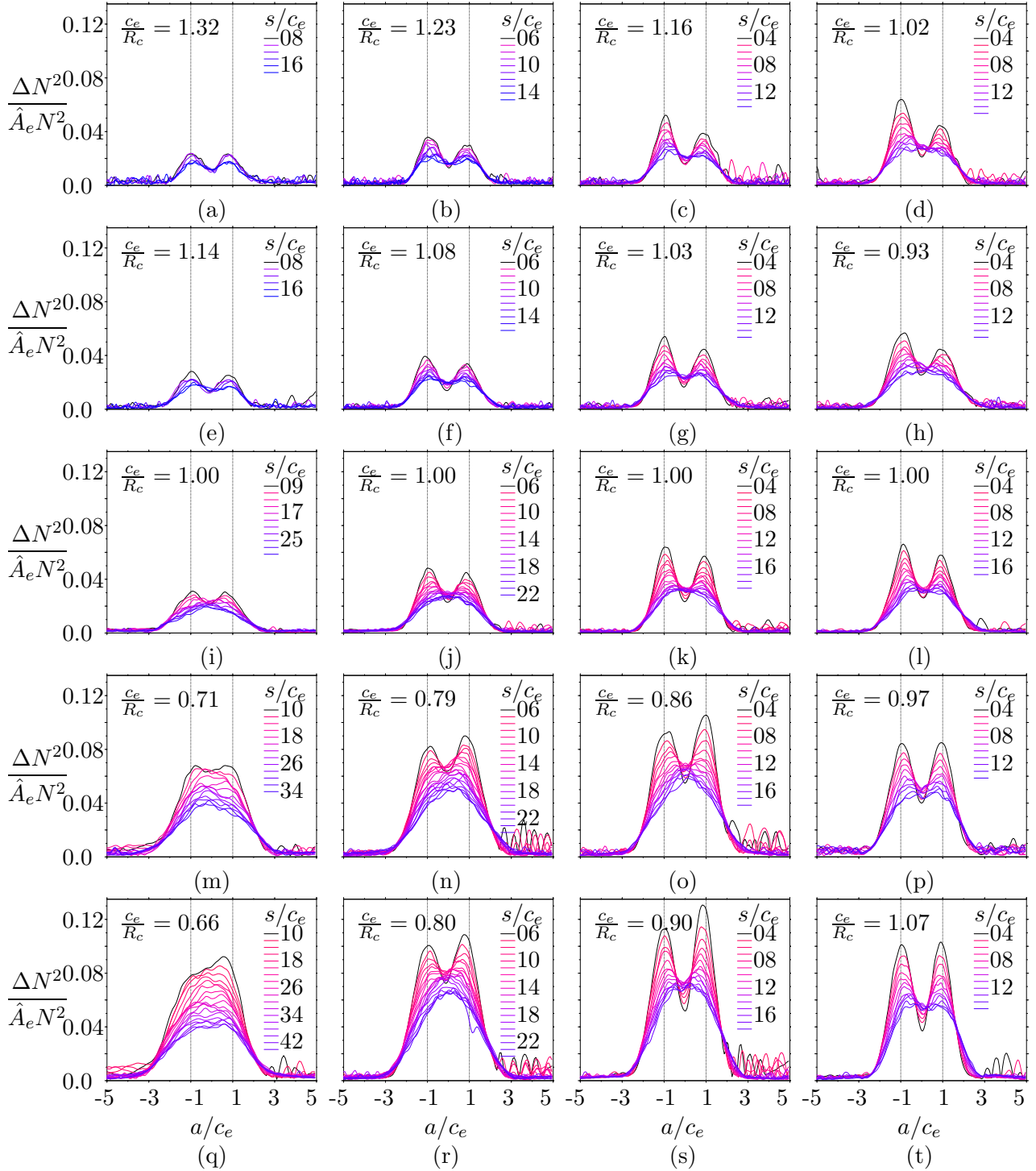


Figure 5.2: Across-beam RMS_T amplitudes at different values of s for $\sigma/N = 0.36, 0.50, 0.59$ and 0.73 (corresponding to columns from left to right) are plotted for ellipse aspect ratios $0.3, 0.5, 1.0, 2.0$ and 3.0 (corresponding to rows from top to bottom). Perturbed buoyancy values are multiplied by the factor $1/\hat{A}_e = (R_c/c_e)^2$.

cross-sectional areas of the cylinders of different aspect ratios vary (though those of C_A and C_E are equal, as are those of C_B and C_D), the amplitudes are normalised by the ratio $(R_c/c_c)^2$. This represents the ratio of the cross-sectional area of the circular cylinder, C_C , relative to that of each elliptical cylinder. Dashed vertical grey lines indicate the positions of tangents to the cylinders in each case.

The across-beam amplitudes of a circular cylinder and their variation with frequency and along-beam distance were described and analysed in detail in section 4.2. A brief summary of these results is given here as a comparison with those for elliptical cylinders. At small along-beam distances, s , envelopes of across-beam amplitudes measured from wavefields generated by a circular cylinder have a bimodal structure, with two maxima located along the tangents to the cylinder that are aligned parallel to the direction of energy propagation. As s increases, viscosity preferentially erodes wave energy associated with smaller length scales of the motion, corresponding to larger across-beam gradients. As a result, the across-beam structure of the wave beam gradually develops a unimodal structure at larger s , characterised by a single maximum positioned at the center of the wave beam. The bimodal to unimodal transition distance was estimated in section 4.2 to be $s \approx 15 - 17R_c$. Amplitudes of the fluid motion increase as the frequency of the cylinder oscillation increases, peaking, for the frequencies measured in the present study, at $\sigma/N = 0.58$, and subsequently decreasing with further increases in frequency. These trends are again evident in figure 5.2 (i)-(l).

Envelopes of across-beam amplitudes along cross-sections for the elliptical cylinders also exhibit bimodal structures at small values of s/c_e , with peaks located near the cylinder tangents at $a = \pm c_e$ in each case. Bimodal structures gradually transition to unimodal at similar values of s/c_e to those observed for the circular cylinder. It was noted in section 4.2 that a slight asymmetry exists between the magnitudes of the two peaks of the bimodal structure in the circular case, with the higher value of the two peaks lying on the lower side of the wave beam. This is attributed to enhanced viscous attenuation of the upper side of the wave beam where the beam overlaps with the wave beam propagating in the upwards direction from the cylinder. Asymmetries in the bimodal envelopes associated with the elliptical cylinders are also evident. At aspect ratios $a_e/b_e \leq 1$, the larger of the peaks lie on the lower sides of the measured beams, whilst the opposite is true at larger aspect ratios. This is consistent with the explanation given above for the circular cylinder case based on enhanced attenuation of wave energy where beams overlap. In general, at lower aspect ratios, greater overlaps are experienced between the measured beam and the beam propagating upwards and to the right away from the cylinder. In addition, wave amplitudes measured along the tangent at $a = +c_e$ are smaller than those measured at a given along-beam distance s on the tangent $a = -c_e$ since wave energy propagating along the former travels, and hence is subject to viscous attenuation over, a greater distance from the cylinder edge than the latter. At larger aspect ratios however, the measured beam overlaps more significantly with the beam propagating downwards and to the left of the cylinder, so that the *lower* portion of the measured beam experiences the greater attenuation. In these cases, along-beam distances measured from the edge of cylinder to a given s are greater

along $a = -c_e$ than $a = +c_e$.

Non negligible amplitudes, typically an order of magnitude smaller than the maximum amplitude shown for a particular frequency and aspect ratio, can be seen at small s/c_e and for positive values of $a/c_e \in [\sim 2, 5]$. This region lies on the upper section of the wave beam in each case and hence the non negligible amplitudes are unlikely to relate to higher propagating harmonics of the wavefield, which would correspond to smaller angles θ and hence the signatures of which would be expected to lie in the region of negative a/c_e . Instead, these amplitudes are related to horizontally propagating features that are discussed in more detail in section 5.2.4.

Variation with aspect ratio and frequency

Variation of across-beam amplitudes with aspect ratio and frequency is discussed here. The trend observed for the circular cylinder of increasing amplitudes with increasing frequency is also seen for the elliptical cylinders, with maxima for aspect ratios less than one occurring at the highest frequency shown, $\sigma/N = 0.73$, whilst the higher aspect ratios have maxima at $\sigma/N = 0.59$. At the lowest frequency $\sigma/N = 0.36$ (*i.e.* figure 5.2 (a, e, i, m, q)), an increase in amplitude of the envelopes occurs with increasing aspect ratio. At this frequency, the increase in aspect ratio corresponds to a narrowing of the across-beam structure from $c_e/R_c = 1.32$ to $c_e/R_c = 0.66$. Dashed grey vertical lines on figure 5.1 (b) indicate the values of c_e and θ for experiments presented in figure 5.2. Hence at lower aspect ratios, the wave energy is spread over a broader beam so that the energy density and therefore amplitudes of the wave motion are reduced, whilst at larger aspect ratios, wave energy is squeezed into a narrower beam resulting in larger amplitudes. The bimodal structure of the wave beam is less obvious in *e.g.* figure 5.2 (q), where the two peaks are close enough and have high enough amplitudes to merge. As for the circular cylinder, the trend of increasing amplitudes with aspect ratio is observed at higher frequencies.

Comparison with linear theory

The linear viscous solution for the stream function of a beam propagating away from an elliptical cylinder with group velocity directed downwards and to the right is

$$\psi = \frac{iA_c\sigma c_e}{2} \left(\frac{a_e^2}{c_e^2} \left[\frac{b_e}{a_e} \sin \theta - i \cos \theta \right] \right) e^{-i\sigma t} \int_0^\infty \frac{J_1(K)}{K} \exp \left(-K^3 \lambda \frac{sI}{c_e} - iK \frac{aI}{c_e} \right) dK, \quad sI > 0 \quad (5.3)$$

(Hurley & Keady 1997; Sutherland & Linden 2002), where the function J_1 is the first order Bessel function of the first kind and

$$\lambda = \frac{\nu}{2c_e^2\sigma \tan \theta} \quad (5.4)$$

is a small quantity. Solutions for (5.3) are found in the present study in a similar manner to those for (4.9) and (4.10) (Sutherland *et al.* 1999; Sutherland & Linden 2002).

Figure 5.3 compares across-beam RMS_T amplitudes measured from the experiments (solid lines,

also displayed in figure 5.2) with the corresponding predictions (dashed lines) calculated using (5.3). Results are displayed for the three forcing frequencies $\sigma/N = 0.36, 0.59$ and 0.73 (increasing across the page) and for the five cylinder aspect ratios (increasing down the page). Results at three along-beam distances $s/c_e = 7$ (red lines), 11 (blue lines) and 15 (cyan lines) are plotted in each case. The viscous linear theory (Hurley & Keady 1997, denoted ‘HK’) best compares to the experiment measurements at $a_e/b_e = 1$, *i.e.* for the circular cylinder, with tendencies to slightly underpredict amplitudes at smaller cylinder aspect ratios. The theory tends to overpredict amplitudes at $a_e/b_e > 1$, with the largest discrepancies observed at the largest measured aspect ratio of $a_e/b_e = 3.0$. Notably, the asymmetry in a/c_e associated with the peaks predicted by the theory has opposite sign to that measured in experiments (particularly evident in figure 5.3 (m)-(o)). The maxima for experimental measurements lies at positive a/c_e . The discrepancy with theory either suggests enhanced dissipation for negative a/c_e , *i.e.* lower side of wave beams, relative to that for positive a/c_e , and/ or that amplitudes are enhanced in regions of the wavefield with positive a/c_e . In support of the latter explanation, additional features of the wavefield that propagate horizontally away from the cylinder (discussed in section 5.2.4) may contribute to the measurements of amplitudes for positive a/c_e . Power spectra corresponding to the results shown in figures 5.2 and 5.3 are discussed below.

5.2.2 Across-beam spectra

Figure 5.4 plots power spectra, normalised by the total power, \hat{P} , associated with the cross-section for C_C at $s/c_e = 4$ and $\sigma/N = 0.59$, corresponding to amplitude plots in figure 5.2. In each case the nondimensional wavenumber \tilde{k} represents the number of waves in an across-beam section of length c_e . For each cylinder and forcing frequency, the maximum power is located at wavenumbers close to $\tilde{k} = 0.36$ and a second peak with maximum value located at $\tilde{k} = 0.78$, which are the locations of the maximum power of the two main spectral peaks measured for the circular cylinder (see section 4.2, in particular figure 4.8). In dimensional terms, these peaks correspond to the highest wavenumbers for the largest aspect ratio, *i.e.* C_E , and smallest frequency, *i.e.* spectra plotted in figure 5.4 (q). In this case, the ratio $c_e/R_c = 0.66$ and so the wavenumber of the dominant peak is $k \approx 0.19 \text{ mm}^{-1}$, compared with $k \approx 0.13 \text{ mm}^{-1}$ for the circular cylinder, C_C . In general, the largest power coupled with the largest (dimensional) wavenumbers are therefore generated by the cylinder with the highest aspect ratio. The smallest dimensional peak wavenumber, $k \approx 0.096 \text{ mm}^{-1}$, occurs for the cylinder with the smallest aspect ratio, C_A , and at the smallest frequency. Maximum power values associated with cylinder C_E , having aspect ratio $a_e/b_e = 3.0$, are an order of magnitude greater than those associated with C_A , with aspect ratio $a_e/b_e = 0.3$.

Figure 5.5 (a) plots the variation with the logarithm base two of cylinder aspect ratio of the maximum power value for power spectra of cross-sections at $s/c_e = 7$ for seven forcing frequencies $\sigma/N \in [0.36, 0.73]$. At all frequencies, the maximum power value increases with aspect ratio. Figure 5.5 (b) plots variation with frequency of the maximum power for each cylinder aspect ratio.

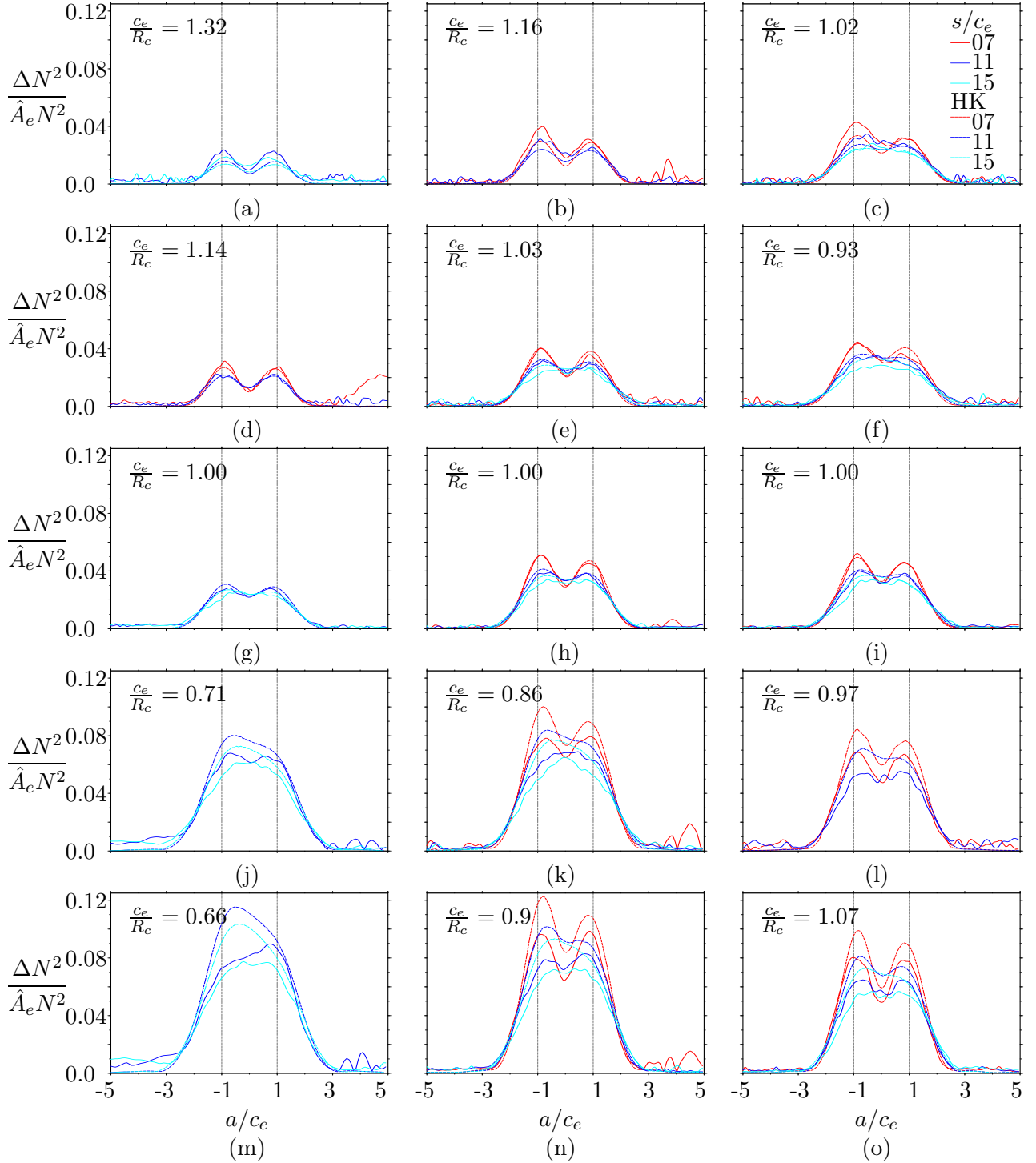


Figure 5.3: Across-beam RMS_T amplitudes at different values of s for $\sigma/N = 0.36, 0.59$ and 0.73 (corresponding to columns from left to right) are plotted for ellipse aspect ratios 0.3, 0.5, 1.0, 2.0 and 3.0 (corresponding to rows from top to bottom). Perturbed buoyancy values are multiplied by the factor $1/\hat{A}_e = (R_c/c_e)^2$.

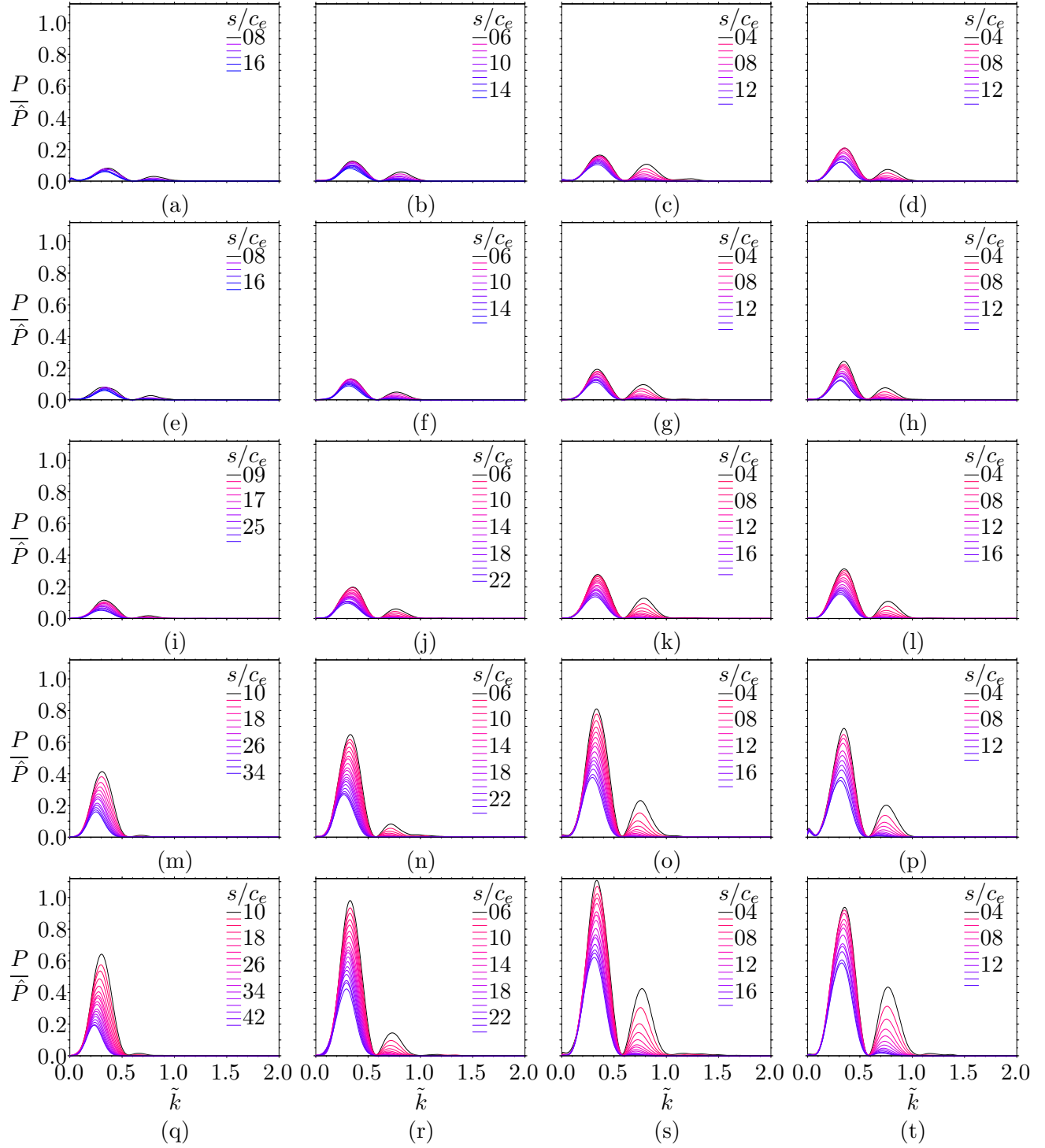


Figure 5.4: Across-beam power spectra corresponding to figure 5.2. Perturbed buoyancy values are multiplied by the factor $1/\hat{A}_e = (R_c/c_e)^2$. Power is normalised by the total power, \hat{P} , associated with the cross-section for C_C at $s/c_e = 4$ and $\sigma/N = 0.59$. Wavenumbers \tilde{k} represent the number of waves per across-beam section of length c_e .

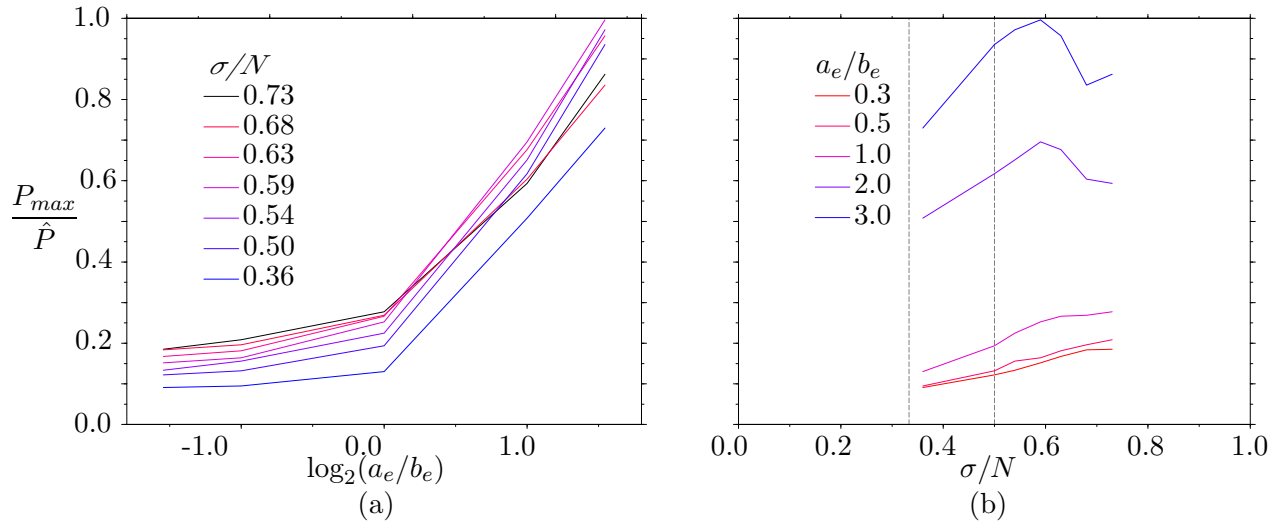


Figure 5.5: Variation of maximum power, P_{max} , with (a) aspect ratios a_e/b_e of the elliptical cylinders at seven forcing frequencies, σ/N , for cross-sections at along-beam distance $s = 7c_e$ and (b) forcing frequency for each cylinder aspect ratio for $s = 7c_e$.

Dashed grey lines indicate the values $\sigma/N = 1/3$ and $1/2$, below which the generation of propagating higher harmonics is possible. At aspect ratios less than one, the maximum power increases approximately linearly with frequency. At larger cylinder aspect ratios the maximum power increases with frequency up to a maximum at $\sigma/N \approx 0.59$, then decreasing at larger forcing frequencies. This slump in maximum power value at high forcing frequencies, noted for the circular cylinder in section 4.2, becomes more pronounced at higher cylinder aspect ratios.

Figure 5.6 compares predictions of viscous linear theory (Hurley & Keady 1997, dashed lines) with experiment measurements (solid lines) of power spectra corresponding to the amplitude plots shown in figure 5.3. Power spectra are displayed on logarithmic scales, rather than linear, to aid visual comparison of the experimental measurements and theoretical predictions. An estimation of the background noise in these experiments is therefore given in figure 5.7, which shows an example of typical spectra calculated from two images of the undisturbed stratification in the circular cylinder case, C_C . The spectra is indicative of the level and composition of the background noise, with peaks over a wide spectral range of maximum magnitudes $\sim O(10^{-4})$. Similar power magnitudes are shown in the spectra of figure 5.4 and 5.6 for wavenumbers larger than $\tilde{k} \approx 1.0$. In general, locations of the dominant power peaks shown in figure 5.6 for the wavefield predictions of linear theory correspond well with those calculated from experiment measurements, though, as in section 4.2, the theory tends to predict peak locations to lie at slightly higher wavenumbers than measured. The underprediction and overprediction of power values at low and high aspect ratios respectively, corresponding to the overprediction and underprediction of maximum RMS_T amplitudes of the perturbed buoyancy field described above for figure 5.3, are also evident in the spectra. Whilst the theory of Hurley & Keady (1997) includes the effects of viscous attenuation along the direction of energy propagation, the influence of viscous boundary layers that form around the cylinders are

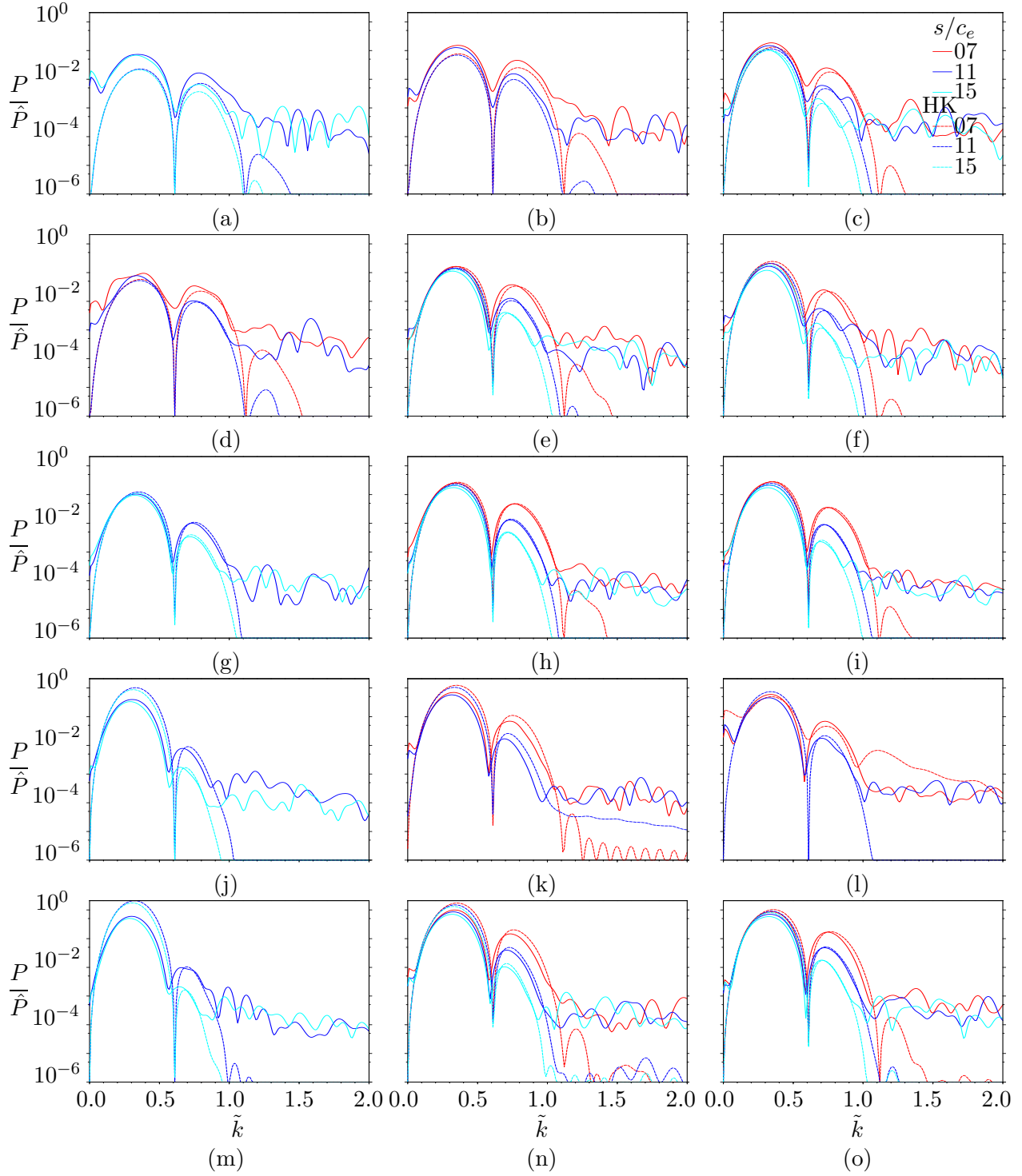


Figure 5.6: Comparisons of power spectra from experiments and predictions of viscous linear theory corresponding to the amplitude plots of figure 5.3 for the three forcing frequencies (increasing across page) $\sigma/N = 0.36$, 0.59 and 0.73 and five elliptical cylinders $C_A - C_E$ (aspect ratios increase down page). \hat{P} is the total power associated with the cross-section at $s/c_e = 4$ and $\sigma/N = 0.59$ for C_C .

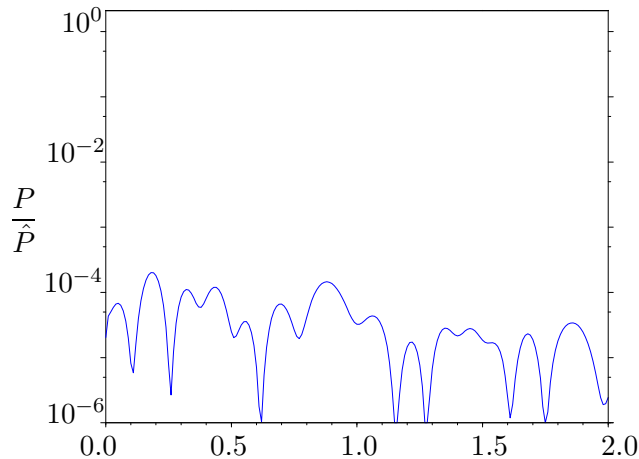


Figure 5.7: Spectra calculated from measurements of undisturbed stratification in circular cylinder case, C_C , relating to figures 5.4 and 5.6.

not accounted for. Such layers tend to simulate conditions such that the cylinder appears slightly wider, hence imposing larger length scales, corresponding to smaller wavenumbers, on the generated wavefields. This may account for the slight shifts observed between the predicted and measured spectra. In a stratified fluid, the discrepancy in effective source dimensions resulting from the formation of boundary layers around the source is expected to be at least the depth predicted for the boundary layer in a homogeneous fluid $\sim (\nu/\sigma)^{1/2}$ (Batchelor 1967).

5.2.3 Higher harmonics

The partitioning of wave energy between primary, secondary and tertiary harmonic components for different cylinder aspect ratios is discussed here. Figure 5.8 shows results from harmonic filtering of the $\Delta N^2/N^2$ field for experiments with cylinders C_B and C_D and forcing frequency $\sigma/N = 0.32 < N/3$. The cross-sectional areas of C_B and C_D , which have aspect ratios $a_e/b_e = 0.5$ and 2.0 respectively, are equal. Each image shows incident wave energy propagating away from cylinders located in the top left-hand corner towards the horizontal boundary at the base of the wave tank, *i.e.* along the bottom of the image. Figure 5.8 (a)-(c) show amplitudes and (d)-(f) show phase fields after filtering for the primary, secondary and tertiary harmonics respectively for cylinder C_B . Figure 5.8 (g)-(i) show amplitudes and (j)-(l) show phase fields after filtering for the primary, secondary and tertiary harmonics respectively for C_D . Black lines, overlaid on phase images, are inclined at the angles $\theta_1 = 71.6^\circ$, $\theta_2 = 50.9^\circ$ and $\theta_3 = 18.7^\circ$ to the vertical corresponding to angles of energy propagation predicted by the dispersion relation for the primary, secondary and tertiary harmonics at frequencies $\sigma_1/N = 0.32$, $\sigma_2/N = 0.64$ and $\sigma_3/N = 0.96$ respectively. Note that maximum amplitude magnitudes of the filtered primary harmonics are one and two orders of magnitude greater than that for the secondary and tertiary harmonics respectively. Amplitude and phase images from harmonic filtering of the wavefield generated by the circular cylinder C_C were also analysed in section 4.2.

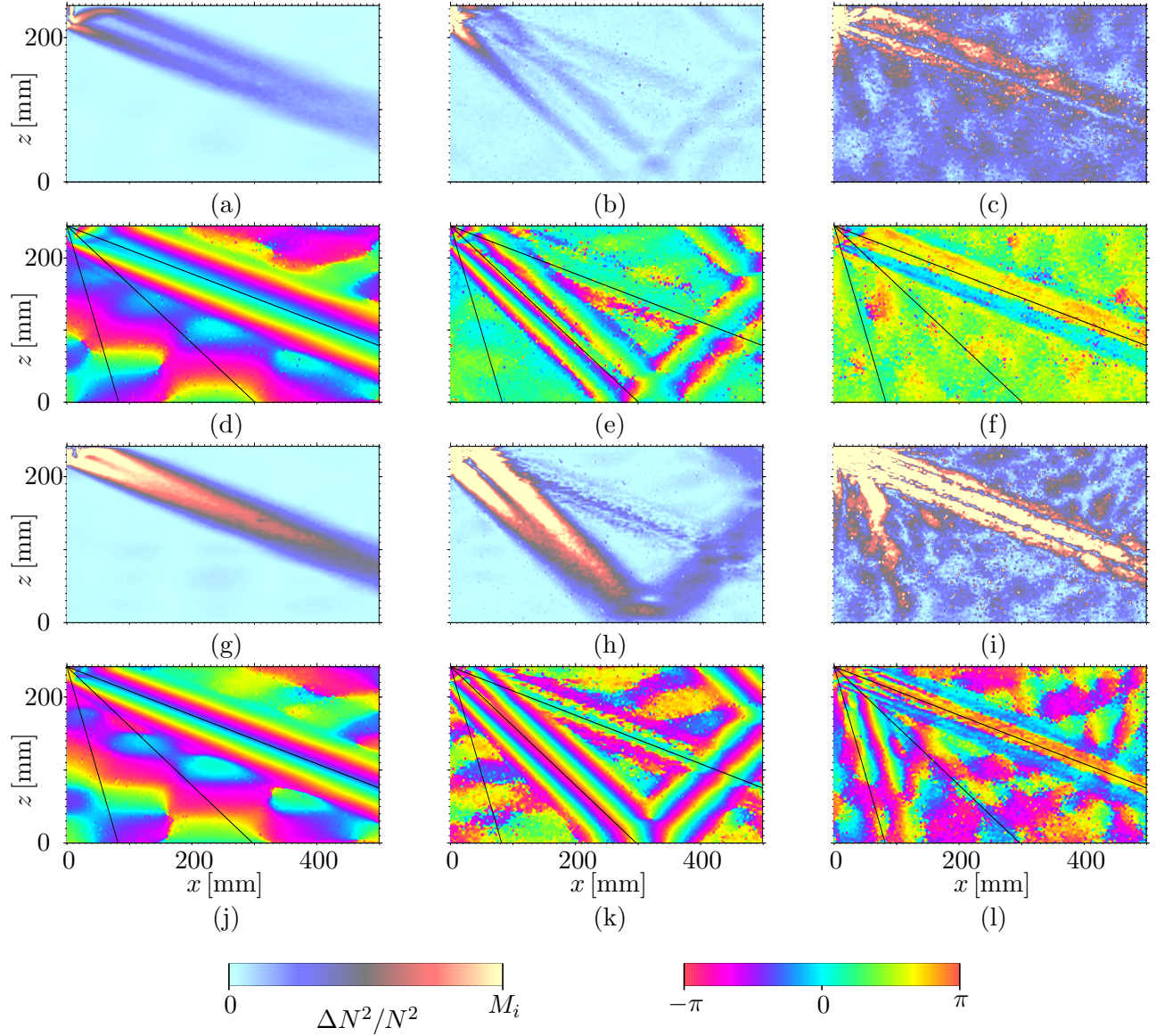


Figure 5.8: Amplitude and phase images of temporal harmonics generated by elliptical cylinders at forcing frequency $\sigma/N = 0.32$. RMS $_T$ images of primary, secondary and tertiary harmonics are shown in (a-c) and (g-i) for C_B and C_D respectively. Corresponding phase images are shown in (d-f) and (j-l). Dashed lines are shown at angles 71.6° , 50.9° and 18.7° to the vertical, corresponding to predicted values of θ_i for primary ($i = 1$), secondary ($i = 2$) and tertiary ($i = 3$) harmonics respectively. Amplitude maxima M_i have values 7.8×10^{-2} , 7.8×10^{-3} and 7.8×10^{-4} for $i = 1, 2$ and 3.

Figure 5.8 (a) shows amplitudes associated with the primary harmonic for C_B . Close to the cylinder, a distinct bimodal across-beam structure is visible that gradually converges with along-beam distance and diminishes in amplitude as the wave energy is attenuated by viscous action. The bimodal structure is very clear in the corresponding phase image (figure 5.8 (d)). Amplitudes associated with the secondary harmonic, shown in figure 5.8 (b), are an order of magnitude smaller

than those for the primary harmonic. A bimodal across-beam structure of the secondary harmonic can also be seen in both the amplitude and phase images. As discussed in section 4.2, the finite time step necessary in the collection of experimental data caused slight signatures of other harmonic components to remain in images even after the wavefield was filtered for a specific harmonic component. As a result, evidence of the primary component can be seen in the amplitude and phase images for the secondary and tertiary filtered images for both C_B and C_D . The filtered images for the tertiary components also exhibit signatures for the secondary components. A very weak suggestion of the tertiary harmonic component is evident in figures 5.8 (c) and (f), being of comparable amplitude to the weak background wavefield within the tank. For each harmonic, amplitudes associated with C_D , figures 5.8 (g)-(i), are significantly larger than those for C_B , which has a smaller aspect ratio. The primary beam associated with C_D is slightly narrower than that for C_B (see figure 5.1 comparing values of c_e for the different cylinders at each angle of energy propagation). Bimodal across-beam structures and their transition to a unimodal form are clearly visible for cylinder C_D at the primary and secondary levels, whilst the structure of the tertiary harmonic is less clear due to the small amplitudes associated with this component. For all phase images displayed in figure 5.8, angles of propagation for each harmonic component are consistent with the angles predicted by the dispersion relation, as indicated by the black lines.

For completeness, the wavefield for C_C at forcing frequency $\sigma/N = 0.32$ was also filtered for the subharmonic frequencies $\sigma/2N$ and $3\sigma/2N$. However, no perceptible signal was observed for these frequencies of wave motion.

5.2.4 Influence on background stratification

The structure of wavefields and their influence on the background stratification in the immediate vicinity of a circular cylinder was discussed in section 3.6.1 for a forcing frequency of $\sigma/N = 0.59$ at times after cylinder motion was initiated \hat{t} equal to 4, 40 and 120 minutes. The evolution of horizontally propagating disturbances extending from the vertical level of the top and bottom of the cylinder, *i.e.* at $z = \pm R_c$ mm, were described. The disturbances developed as mixed fluid generated near the cylinder spread horizontally into the adjacent stratification, characterised in RMS_T images of the perturbed buoyancy field as regions bounded above and below by enhanced vertical density gradients. Oscillations at the cylinder frequency, σ , of these thin layers were also described.

Figure 5.9 (a)-(e) shows RMS_T images of the perturbed buoyancy field of regions adjacent to elliptical cylinders $C_A - C_E$, respectively, taken from three periods of oscillation at cylinder frequency $\sigma/N = 0.59$ beginning at time $\hat{t} = 4$ minutes. RMS_T amplitudes are scaled by the factor $\hat{A}_e = (R_c/c_c)^2$. Cylinder centres are positioned at the middle left-hand side of images, so that sections of upward and downward propagating beams are visible in the images. In each case, intrusions, similar to those described in section 3.6.1, were observed at the vertical levels of the top and bottom of the cylinders, *i.e.* $z = \pm b_e$ mm, though these protruded a shorter distance

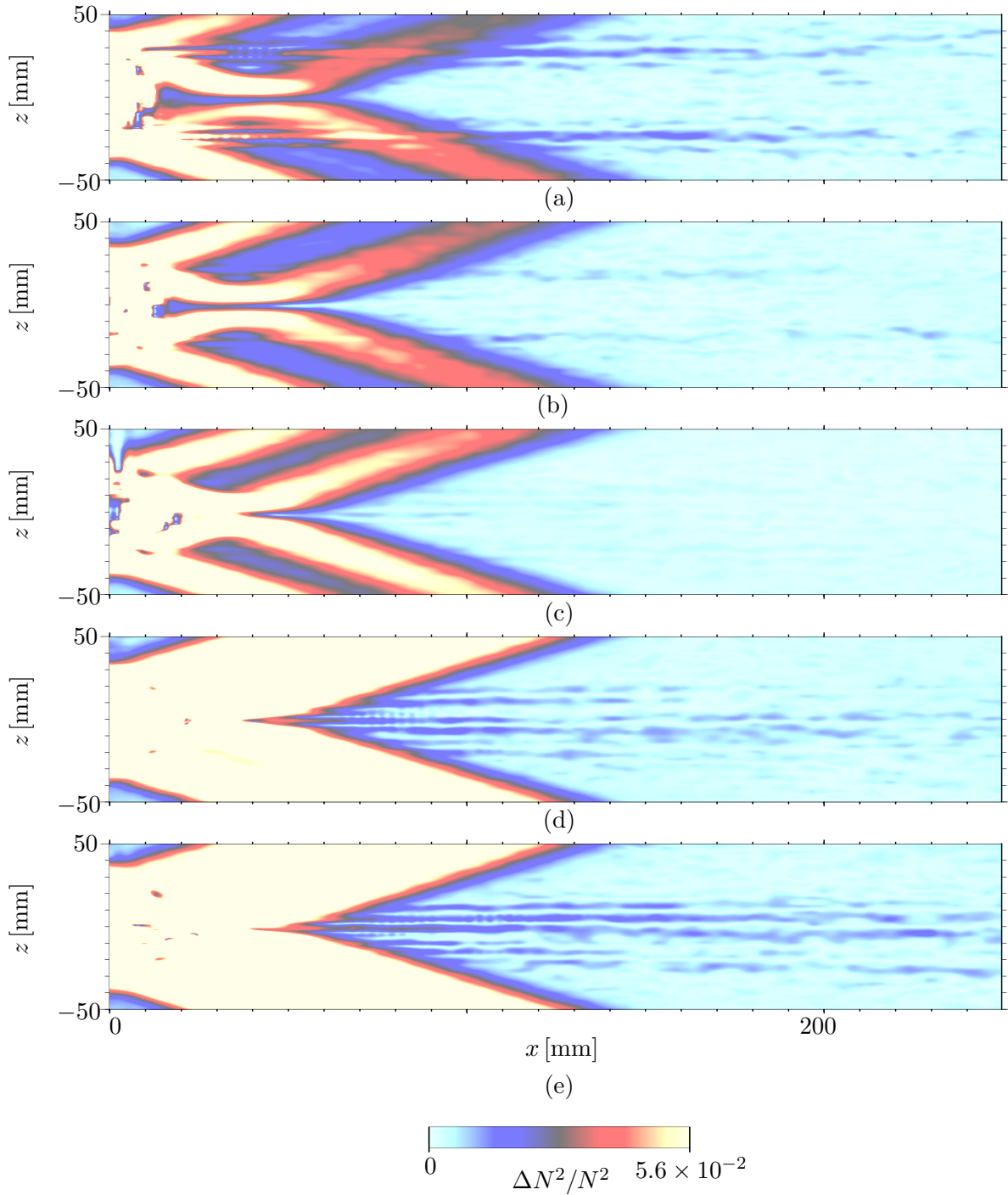


Figure 5.9: RMS_T images of $\Delta N^2/N^2$ fields in regions adjacent to cylinders $C_A - C_E$ (centre-left of field of view) are shown in (a)-(e) respectively. Amplitudes are multiplied by the factor $\hat{A}_e = (R_c/c_c)^2$.

into the stratification than those shown in figures 3.24 and 3.25, for example, due to the shorter experimental run times employed for the elliptical cylinders. The disturbances were the least distinct in experiments (see figure 5.9 (c)) relating to the circular cylinder, C_C , and appeared to become

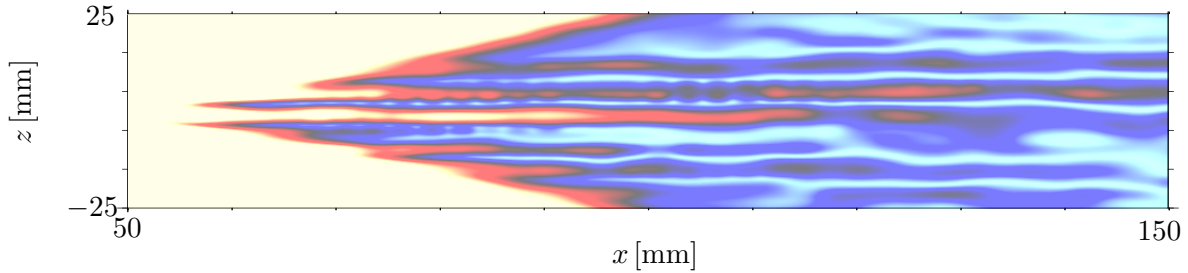


Figure 5.10: Zoom of section near cylinder in figure 5.9 (e). Scaling as in figure 5.9.

more pronounced with either decreasing or increasing aspect ratios. In particular, amplitudes of disturbances shown in figure 5.9 (e) for the cylinder C_E , with aspect ratio $a_e/b_e = 3.0$, are the most significant. Mixing of the stratified fluid is enhanced in regions of the cylinder surfaces that have high curvature. For cylinders C_A and C_B these regions coincide with the vertical extremities of the cylinders, $z = \pm b_e$ mm, whereas the regions of high curvature are positioned at the level of the cylinder centres for C_D and C_E . Indeed, additional intrusions are visible in figure 5.9 (d) and (e) at $z = 0$ mm.

As for the experiments with the circular cylinders that had longer run times (see section 3.6.1), evidence of oscillatory motion along mixed fluid layers can also be seen in varying degrees in movies of the experiments corresponding to figure 5.9. The clearest of these is for C_E in the region defined by $x \in [50, 150]$ mm and $z \in [-25, 25]$ mm. A zoom of this section is shown in the RMS_T image of figure 5.10. A periodic horizontal pattern can be seen at $x \in [80, 110]$ mm and $z \approx 5$ mm. This is a less developed version of that shown in figure 3.25 for the longer run time of $\hat{t} = 120$ minutes. The mixed fluid did not intrude sufficiently far into stratifications over the much shorter duration of the experiments for the elliptical cylinders to allow more detailed analysis of the intrusions and the oscillations they support.

5.3 Wave generation by rectangular cylinders

With the exception of a study by Dalziel (2000), which exemplified the use of synthetic schlieren for studying the wavefield generated by a square cylinder, there are no experimental, numerical or theoretical results presented in the literature of internal wave generation by either square or rectangular cylinders. This section describes experimental results from the present study of wavefields generated by square and rectangular cylinders and compares them with those for elliptical cylinders and the predictions of viscous linear theory (Hurley & Keady 1997). In particular, square and rectangular cylinders have sharp corners and the effect of these on the wavefield is investigated here.

The width and height of a rectangular cylinder are denoted $2a_r$ and $2b_r$ respectively, with cylinder aspect ratios defined by the ratio a_r/b_r . The bottom section of table 5.1 shows the dimensions of square and rectangular cylinders used in experiments, $C_F - C_H$, which had aspect ratios of 0.65,

1.0, and 1.53. Square and rectangular cylinders were constructed and operated as described in section 3.6.1.

Across-beam geometry

The perpendicular distance between two parallel lines that make an angle $\theta = \cos^{-1}(\sigma/N)$ to the vertical and that pass through opposite corners of a rectangular cylinder of width $2a_r$ and height $2b_r$ is denoted here as $2c_r$ where

$$c_r = \frac{1}{2} (a_r \cos \theta + b_r \sin \theta). \quad (5.5)$$

As for the elliptical cylinders, an analogous length scale, c_c , is also defined for a given rectangle that corresponds to the radius of the circle that has the same cross-sectional area, so that

$$c_c = 2 \left(\frac{a_r b_r}{\pi} \right)^{\frac{1}{2}}, \quad (5.6)$$

where c_c has values of 26.9, 21.7 and 26.9 mm for cylinders $C_F - C_H$ respectively. The coordinate system employed in section 5.2 is applied here also.

A second across-beam distance, \tilde{c}_e , is also defined here as the analogy with c_e for the elliptical cylinder, with horizontal and vertical axes lengths \tilde{a}_e and \tilde{b}_e , that has the same aspect ratio and cross-sectional area as the rectangular cylinder. The horizontal and vertical axes half-lengths of the ellipse can be calculated to be

$$\tilde{a}_e = \frac{2a_r}{\sqrt{\pi}} \quad \text{and} \quad \tilde{b}_e = \frac{2b_r}{\sqrt{\pi}} \quad (5.7)$$

and the across-beam half-length as

$$\tilde{c}_e^2 = \tilde{a}_e^2 \cos^2 \theta + \tilde{b}_e^2 \sin^2 \theta. \quad (5.8)$$

These distances are indicated on figure 5.11.

As in section 5.2, this section considers the variation with aspect ratio of the amplitude and spectral structure of wave beams as well as the generation of higher harmonic components and other features of the wavefields in regions near the cylinders.

5.3.1 Across-beam amplitudes

Figure 5.12 shows across-beam amplitudes of $\Delta N^2/N^2$ for each rectangular cylinder along cross-sections of length $10\tilde{c}_e$ at different along-beam distances, s/\tilde{c}_e , and at the four forcing frequencies $\sigma/N = 0.36, 0.50, 0.59$ and 0.73 . Each panel presents results relating to one cylinder at a fixed forcing frequency, with frequencies associated with each panel increasing across the page. Panels (a)-(d) show envelopes for the circular cylinder C_C . Envelopes for the rectangular cylinders C_F , C_G and C_H , which have aspect ratios 0.65, 1.0 and 1.53 respectively, are shown in panels (e)-(h), (i)-(l)

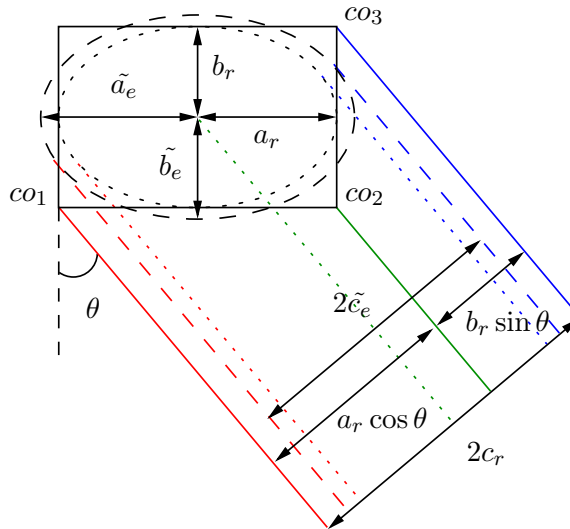


Figure 5.11: Ray geometry for rectangular cylinders.

and (m)-(p). Amplitudes are normalised by the ratio $(R_c/c_c)^2$. Dashed vertical lines indicate the positions of lines inclined at angles θ to the vertical, *i.e.* parallel to the group velocity vector of the primary wave component, that pass through the cylinder corners. For convenience, these lines are referred to here as ‘corner asymptotes’ (indicated by solid red, green and blue lines originating at corners co_1 , co_2 and co_3 denoted in figure 5.11).

In contrast to the bimodal and unimodal across-beam amplitude structures described in sections 3.6.1 and 5.2 and shown in figure 5.12 (a)-(d) for circular and elliptical cylinders, envelopes of across-beam amplitudes for rectangular cylinders exhibit peaks having locations coincident with the across-beam positions of the cylinder corners. At small s/\tilde{c}_e , the across-beam structures are therefore characterised by a generally asymmetric form that has three peaks. At larger s/\tilde{c}_e , distinct peaks positioned along adjacent corner asymptotes are observed to gradually merge with increasing values of s into single peaks positioned between the two corner asymptotes. This transition occurs more rapidly with increasing s for corners in closer proximity (e.g. see figure 5.12 (1)). The transition occurs through the same mechanism as described for the bimodal-unimodal transition associated with the circular cylinder. Viscosity preferentially acts to reduce wavefield motions associated with rapid variations, *i.e.* high wavenumbers, in the across-beam direction. The across-beam structure therefore gradually becomes dominantly characterised by larger across-beam length scales as s increases.

The symmetries of circular and elliptical cylinders and the location of peaks of amplitude envelopes along tangents to the cylinders results in an equal partitioning of wave energy near $s = 0$ between the two peaks. Length scales imposed on the wave motion are therefore dominantly controlled by c_e . However, in the case of rectangular cylinders, the across-beam positions of the corner asymptotes are in general *asymmetric* about $a = 0$, varying with both cylinder aspect ratio and the frequency of the wave motion. Additional length scales may therefore be imposed on the wave

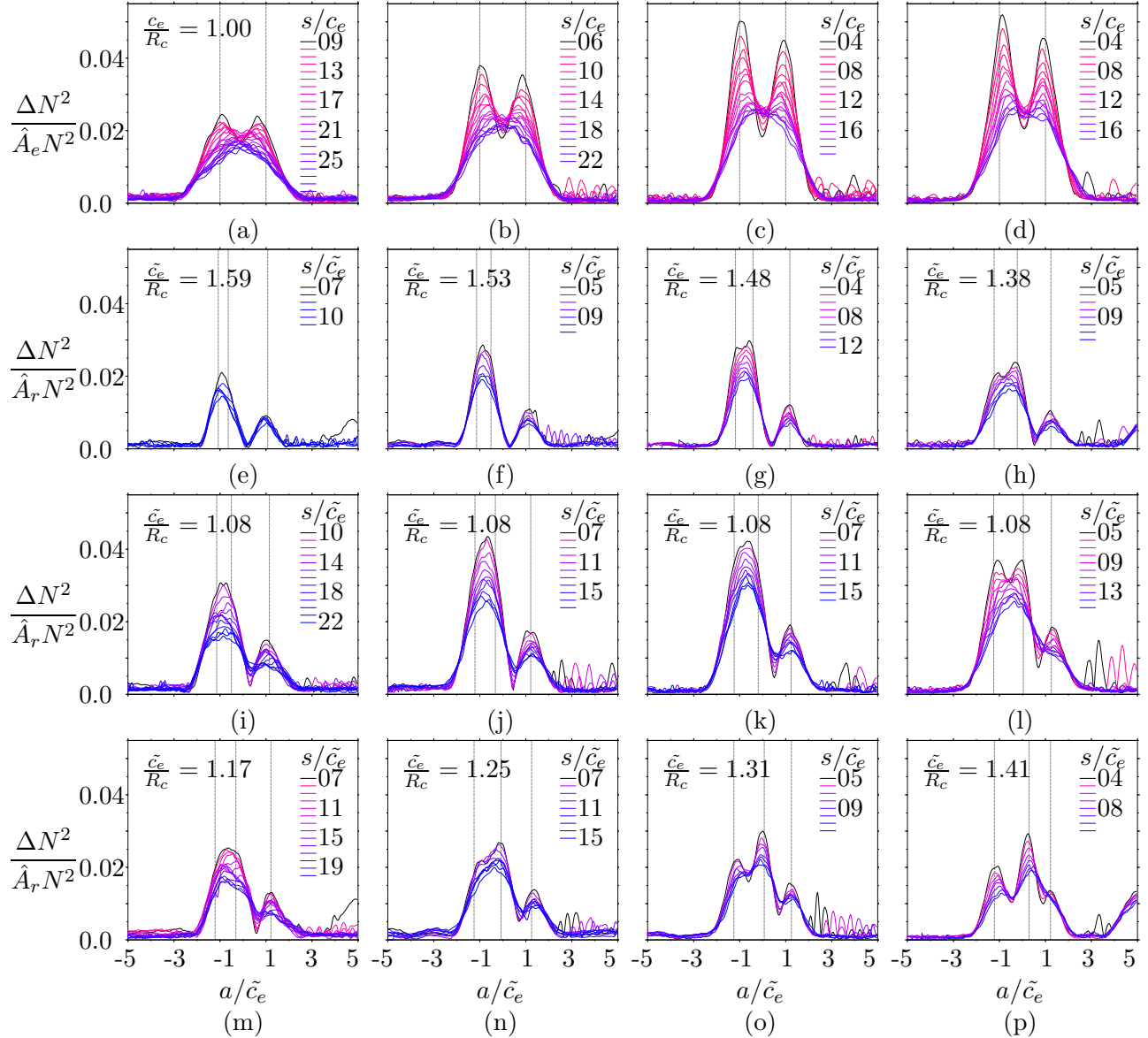


Figure 5.12: Across-beam RMS_T amplitudes at different values of s for $\sigma/N = 0.36, 0.50, 0.59$ and 0.73 (corresponding to columns from left to right) are plotted for a circular cylinder (top row) and rectangle aspect ratios $0.65, 1.0$ and 1.53 (corresponding to rows from second from top to bottom). Perturbed buoyancy values are multiplied by the factor $1/\hat{A}_r = (R_c/c_c)^2$. Dashed lines indicate across-beam positions of corners of rectangular cylinders.

motion, including c_r , $a_r \cos \theta$ and $b_r \sin \theta$.

Figure 5.13 compares RMS_T across-beam amplitudes of $\Delta N^2/N^2$ from experimental measurements for the rectangular cylinders with those predicted by linear viscous theory for elliptical cylinders (Hurley & Keady 1997, referred to as ‘HK’) that have the same cross-sectional areas and aspect-ratios as the rectangular cylinders. Each panel plots results for one cylinder at a fixed frequency, σ/N , and at three along-beam distances, $s/\tilde{c}_e = 7$ (red lines), 11 (blue lines) and 15 (green

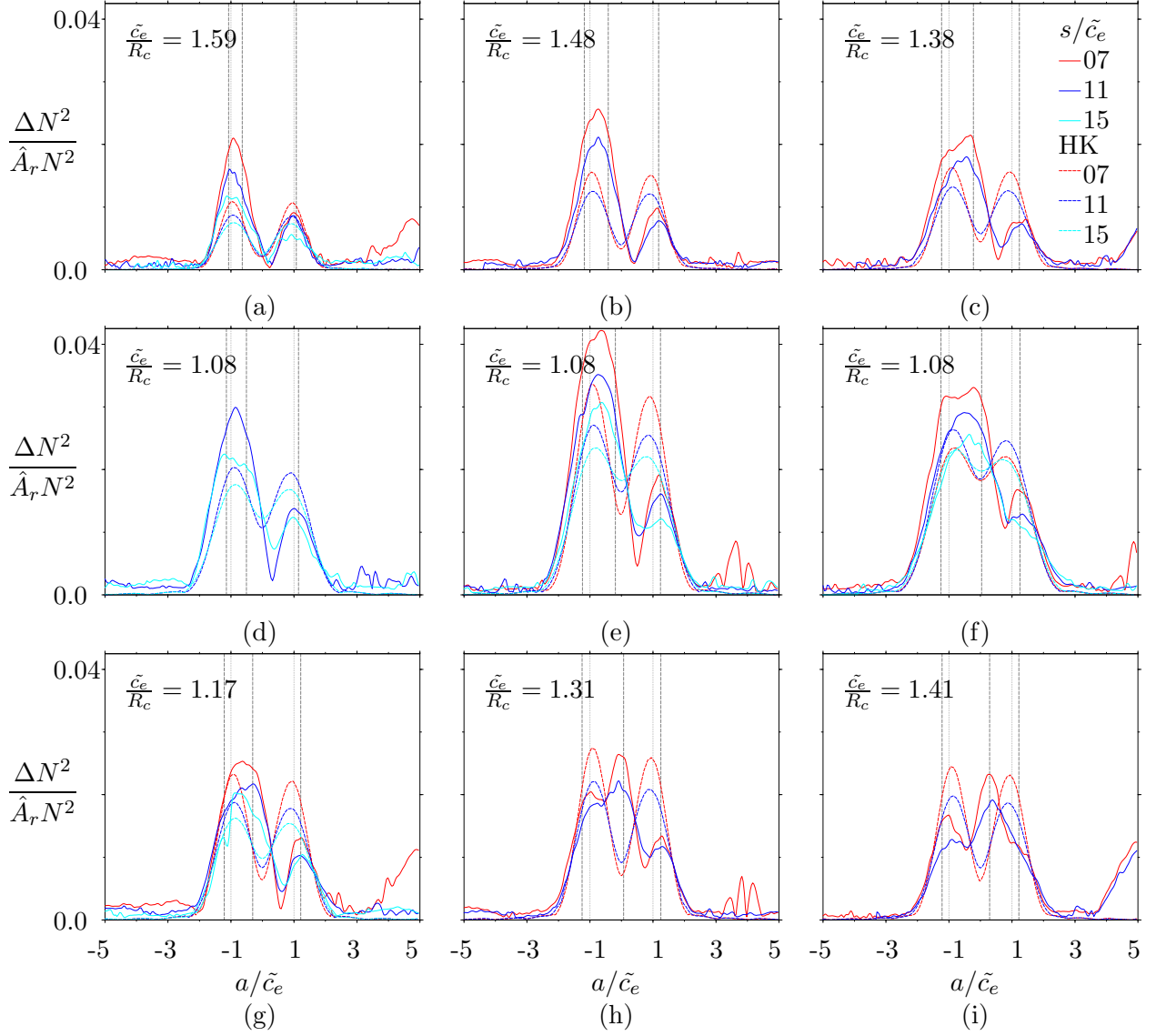


Figure 5.13: Across-beam RMS_T amplitudes at different values of s for $\sigma/N = 0.36$, 0.59 and 0.73 (corresponding to columns from left to right) are plotted for a circular cylinder (top row) and rectangle aspect ratios 0.65 , 1.0 and 1.53 (corresponding to rows from second from top to bottom). Perturbed buoyancy values are multiplied by the factor $1/\hat{A}_r = (R_c/c_c)^2$. Dashed grey vertical lines indicate across-beam positions of corners of rectangular cylinders.

lines). Results are shown for cylinders $C_F - C_H$, with aspect ratios increasing down the page, and the three forcing frequencies $\sigma/N = 0.36$, 0.59 and 0.73 , increasing across the page. Solid coloured lines indicate measurements from experiments and dashed coloured lines indicate predictions of viscous linear theory for the elliptical cylinder analogy. In each case the across-beam form of the amplitude envelopes generated by the rectangular cylinders differs from that for the corresponding elliptical cylinder analogy, with peaks positioned approximately along the corner asymptotes at small s/\tilde{c}_e rather than at $a/\tilde{c}_e \approx \pm 1$ as predicted for the ellipses. The asymmetric distribution of

wave energy between the peaks associated with the envelopes of the rectangular cylinders results in larger maximum amplitudes when compared with those predicted for the elliptical cylinder. This implies greater shearing motion in the along-beam direction and hence suggests enhanced viscous attenuation in such regions for the rectangular cases.

The discontinuities introduced at the corners of a rectangular cylinder make linear analytical approaches of the kind used in the analysis of elliptical cylinders (Hurley & Keady 1997) unfeasible. A first order analytical model of the wavefield generated by a rectangular cylinder is perhaps suggested by the results of the present study. This would include the modelling of the cylinder as an array of four sources of vanishingly small dimensions located at the corner positions of the rectangle. The linear theory for wave generation by a cylinder requires that the dimensions of the source are much larger than the amplitude of oscillation however, which is violated in such an analysis. The effects of diffusion are also expected to become non negligible in the region of sharp corners of the source.

5.3.2 Across-beam spectra

Power spectra corresponding to RMS_T perturbed buoyancy field measurements presented in figure 5.12 are shown in figure 5.14. Spectra for C_C at frequencies $\sigma/N = 0.36, 0.50, 0.59$ and 0.73 are shown in figure 5.14 (a)-(d) respectively. Spectra for cylinders $C_F - C_H$ are plotted in (e)-(h), (i)-(l) and (m)-(p). Note that values on vertical scales of plots for C_C are almost twice those shown for the rectangular cylinders. In particular, spectra of the square cylinder, which has the same aspect ratio as C_C , display the largest maxima of the rectangular cylinders and the peaks are only around half as large in magnitude as those for the circular cylinder. The contrast of these values with the maxima for the circular cylinder indicates significantly enhanced levels of dissipation of wave energy in the rectangular cylinder cases. This could occur through the generation of high wavenumber components at the cylinder corners that are dissipated rapidly by viscosity near the cylinder. As noted above, viscous attenuation is also promoted as length scales related to the across-beam distances between the cylinder corners, which are smaller than those imposed by the circular cylinder and so generate higher wavenumbers, are also introduced to the wavefield. In addition, the proximity of adjacent corners determines the *energy density* of, and hence the shear related to, the wavefield propagating from that region. The spectra for C_C exhibit peaks located at wavenumbers near $\tilde{k} \approx 0.3$ and 0.7 with the partitioning of wave energy between these peaks varying with frequency. The largest magnitude for the high wavenumber peak occurs at $\sigma/N = 0.50$, whilst that for the lower wavenumber peak occurs at $\sigma/N = 0.73$. Qualitatively, this variation correlates well with the change in the across-beam distances between cylinder corners, and hence the wavenumbers and energy densities imposed on the wavefield, with frequency.

Spectra for cylinders C_F and C_H exhibit smaller maxima than those for the square cylinder. The peak locations and magnitudes are again a complicated function of frequency as the length scales imposed by the cylinders vary with the angle of the group velocity vector, θ .

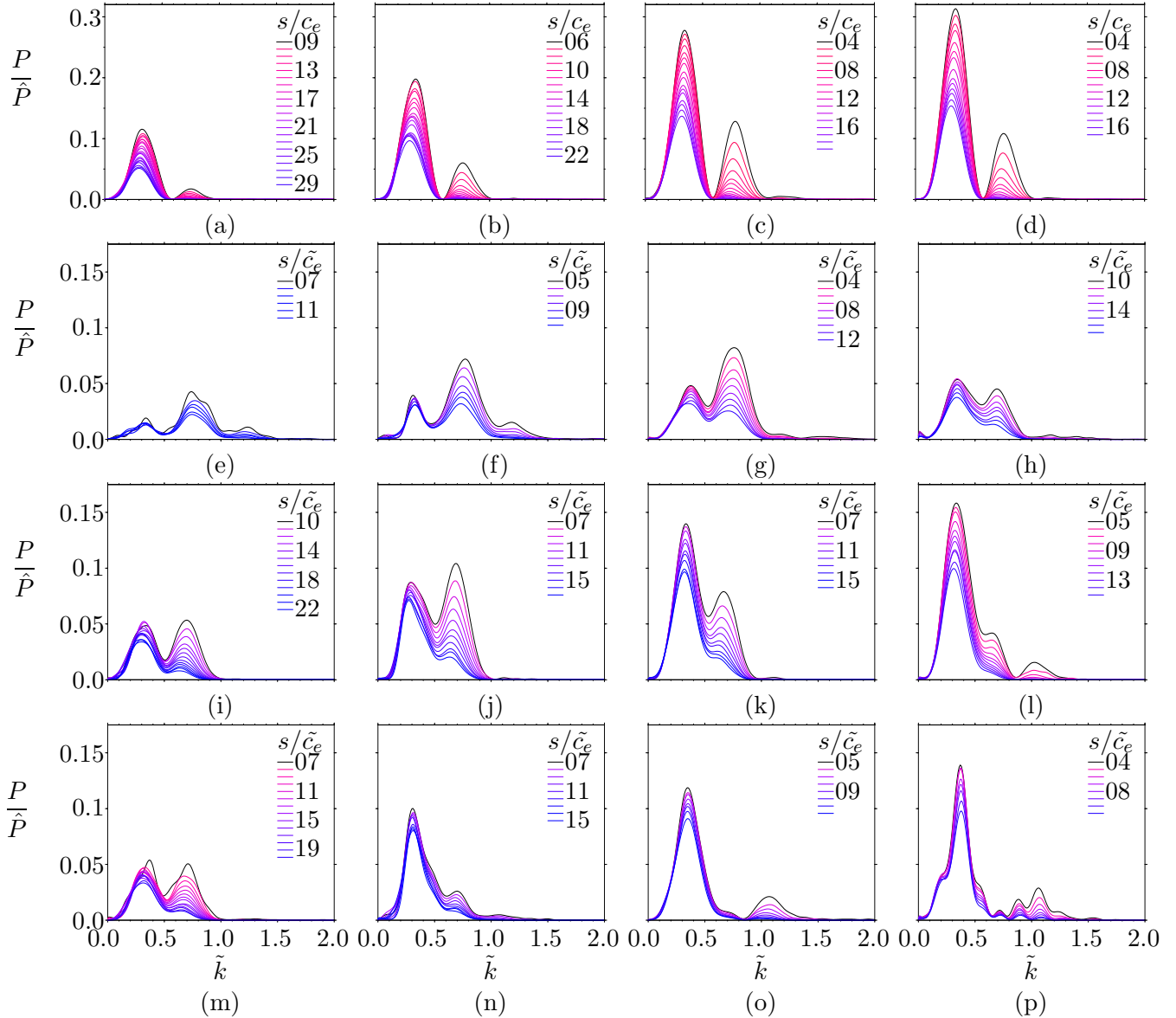


Figure 5.14: Across-beam power spectra corresponding to figure 5.12. Perturbed buoyancy values are multiplied by the factor $1/\hat{A}_r = (R_c/c_c)^2$. Power is normalised by the total power, \tilde{P} , associated with the cross-section for C_C at $s/c_e = 4$ and $\sigma/N = 0.59$. Wavenumbers \tilde{k} represent the number of waves per across-beam section of length c_e and \tilde{c}_e for the circular and rectangular cylinders respectively.

Figure 5.15 compares spectra calculated from experiments with $C_F - C_H$ (solid coloured lines, aspect ratios increasing down page) with those predicted by viscous linear theory (Hurley & Keady 1997) for elliptical cylinder analogies (dashed coloured lines) at three forcing frequencies (increasing across the page) and three along-beam distances, corresponding to the amplitude plots presented in figure 5.13. Peaks of spectra located near $\tilde{k} \approx 0.3$, calculated from the experimental data correspond well to locations of peaks predicted for the analogous elliptical cylinders, with magnitudes of the

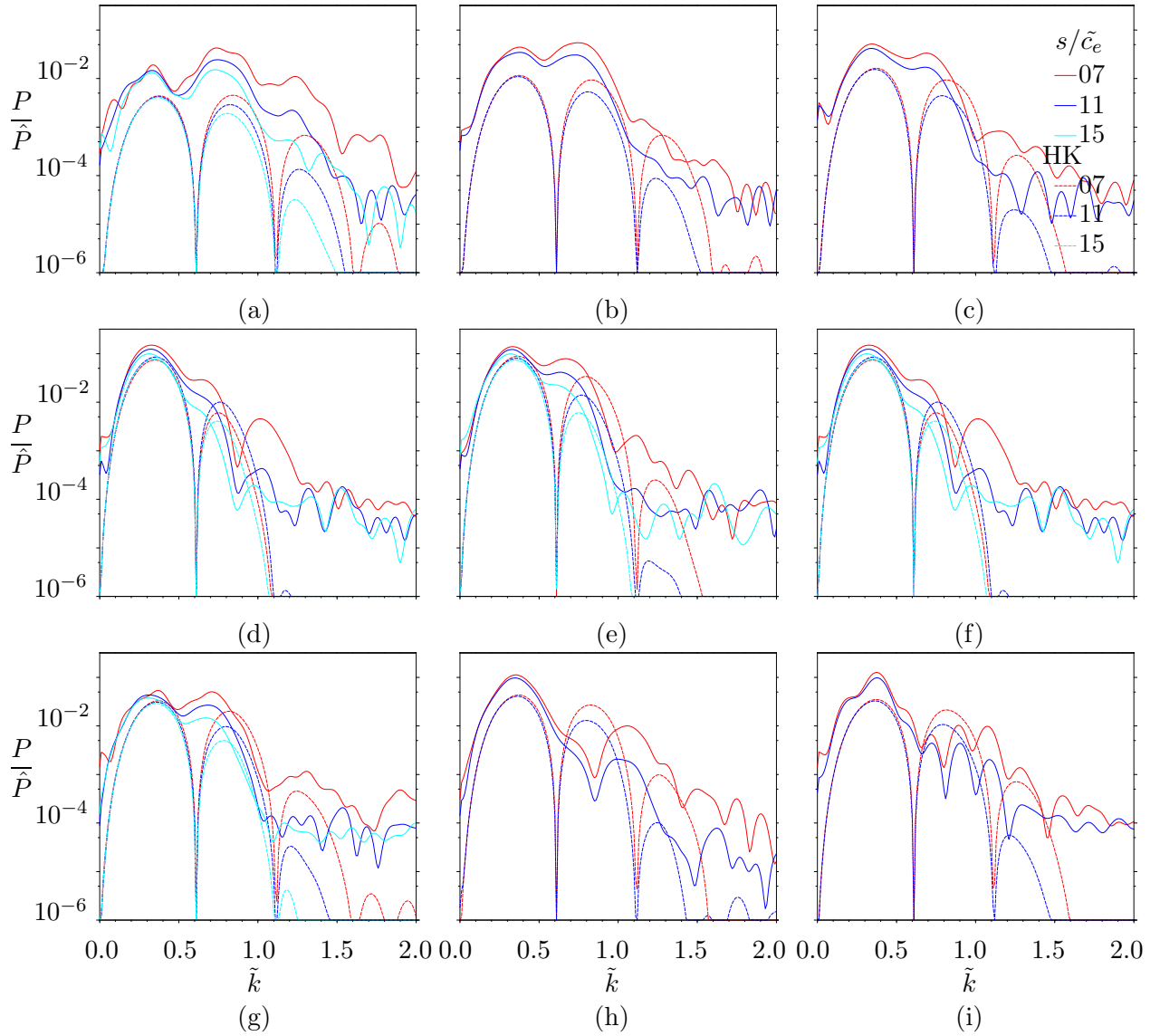


Figure 5.15: Comparisons of power spectra from experiments with rectangular cylinders $C_F - C_H$ (aspect ratios increase down the page) and predictions of viscous linear theory (Hurley & Keady 1997) for analogous elliptical cylinders corresponding to the amplitude plots of figure 5.13. Forcing frequencies $\sigma/N = 0.36, 0.59$ and 0.73 increase across the page. \hat{P} is the total power associated with the cross-section at $s/c_e = 4$ and $\sigma/N = 0.59$ for C_C .

peaks for both the experiments and predictions closest for C_G . The spectra illustrate the complex dependence of the wavenumber composition of the generated wavefields on frequency, aspect ratio and cylinder shape.

5.3.3 Higher harmonics

The partitioning of wave energy between first, second and third temporal harmonic components is compared here for circular, C_C , and square, C_G , cylinders at forcing frequency $\sigma/N = 0.32 < N/3$.

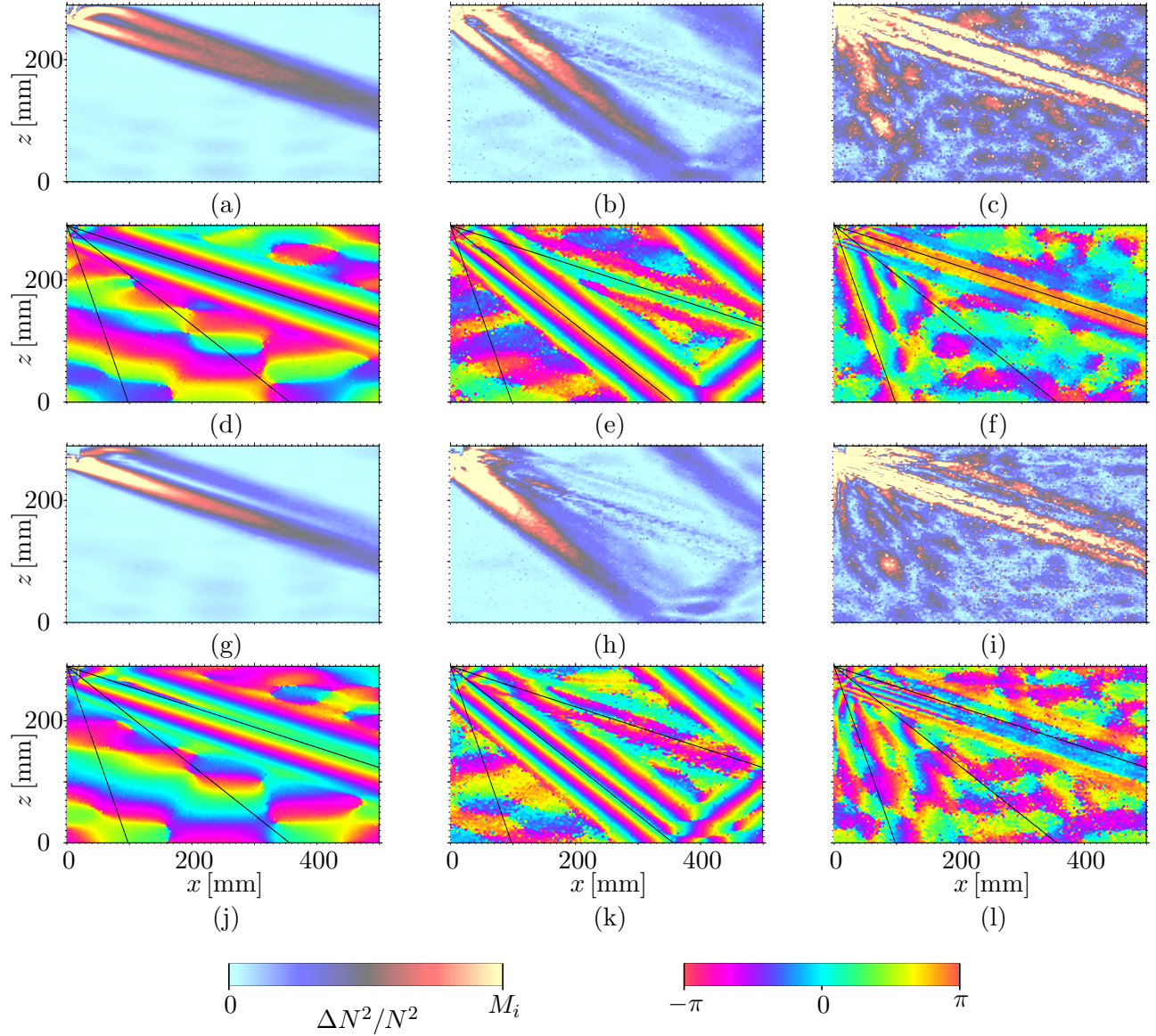


Figure 5.16: Amplitude and phase images of temporal harmonics generated by circular and square cylinders. RMS_T images of primary, secondary and tertiary harmonics are shown in (a-c) and (g-i) for C_C and C_G respectively. Corresponding phase images are shown in (d-f) and (j-l). Dashed lines are shown at angles 71.6° , 50.9° and 18.7° to the vertical, corresponding to predicted values of θ_i for primary ($i = 1$), secondary ($i = 2$) and tertiary ($i = 3$) harmonics respectively. Amplitudes relating to square cylinder are scaled by the factor $1/\hat{A}_r = (R_c/c_c)^2$. Amplitude maxima M_i have values 5.6×10^{-2} , 5.6×10^{-3} and 5.6×10^{-4} for $i = 1, 2$ and 3 .

In a similar manner to figure 5.8, figure 5.16 shows amplitude images (a-c), (g-i) and phase images (d-f), (j-l) after harmonic filtering of $(R_c/c_c)^2 \Delta N^2/N^2$ for cylinders C_C and C_G respectively. The first, second and third columns of images in figure 5.16 correspond to filtering for primary, secondary and tertiary harmonics respectively. Black dashed lines superimposed on phase images are inclined at angles $\theta_1 = 71.6^\circ$, $\theta_2 = 50.9^\circ$ and $\theta_3 = 18.7^\circ$ relative to the vertical, which are the angles predicted

by the dispersion relation for the orientation of the group velocity vector for wave motions with temporal frequencies $\sigma_1/N = 0.32$, $\sigma_2/N = 0.64$ and $\sigma_3/N = 0.96$.

Primary (figure 5.16 (a), (d)), secondary (figure 5.16 (b), (e)) and weak tertiary harmonics (figure 5.16 (c), (f)) were observed for the circular cylinder, with wave beams inclined at the predicted value of θ_i , $i = 1, 2, 3$, in each case. The bimodal to unimodal transition of the across-beam RMS_T amplitude structure for the circular cylinder can be seen for the primary harmonic in figure 5.16 (a). The distinct bimodal structure of the second harmonic is evident in figure 5.16 (b), though some asymmetry occurs as a result of the smaller amplitudes of the wave motion associated with this harmonic (an order of magnitude less than those of the primary component), hence making interactions with other components of the wavefield more distinct in images. Except in regions close to the cylinders, amplitudes associated with the tertiary harmonic, shown in figure 5.16 (c), are comparable with those of the background wavefield and hence the structural form of this component is best seen in the corresponding phase image.

Evidence of each harmonic was also observed for the square cylinder. The across-beam structure of the primary harmonic, figure 5.16 (g), exhibits two distinct peaks. The most prominent of these lies on the lower side of the wave beam and occurs as wave motion generated at the two adjacent corners of the cylinder there, in the notation of figure 5.11: co_1 and co_2 , merges near the cylinder. A comparably weaker peak is also generated at co_3 . Amplitudes along the dominant peak are greater than those observed for the circular cylinder at small along-beam distances, s , but decay more rapidly with increasing s due to the higher wavenumbers and larger shearing motions associated with the square cylinder at this forcing frequency and hence enhanced viscous attenuation. Similar behaviour is observed for the second and third harmonics.

Figure 5.17 compares amplitude and phase images from harmonic filtering for primary, secondary and tertiary harmonics at $\sigma/N = 0.32$ for rectangular cylinders C_F and C_H , which have aspect ratios $a_r/b_r = 0.65$ and 1.53 respectively but equal cross-sectional areas. The ordering (*i.e.* across and down the page) of images in figure 5.17 is the same as those in figures 5.8 and 5.16. As in the elliptical cylinder case at this frequency, the amplitudes of each of the harmonics is more significant for the cylinders with highest aspect ratio, with the greatest contrast occurring between the secondary harmonics. The tertiary harmonics for both cylinders are very weak, being most prominent at small s . Their presence is more distinct in the phase images however.

5.3.4 Influence on background stratification

Intrusions of mixed fluid extending horizontally from the vertical extremities, $z = \pm b_e$ mm, and regions of high curvature of oscillating elliptical cylinders were described in section 5.2.4. Similar features were also observed in regions near square and rectangular cylinders. Figure 5.18 shows RMS_T images of the perturbed buoyancy fields for (a) C_C , (b) C_F , (c) C_G and (d) C_H at forcing frequency $\sigma/N = 0.54$, where the RMS_T values are calculated from averages over one period of the wave motion commencing at time $\hat{t} = 4$ minutes after the cylinder oscillation was initiated.

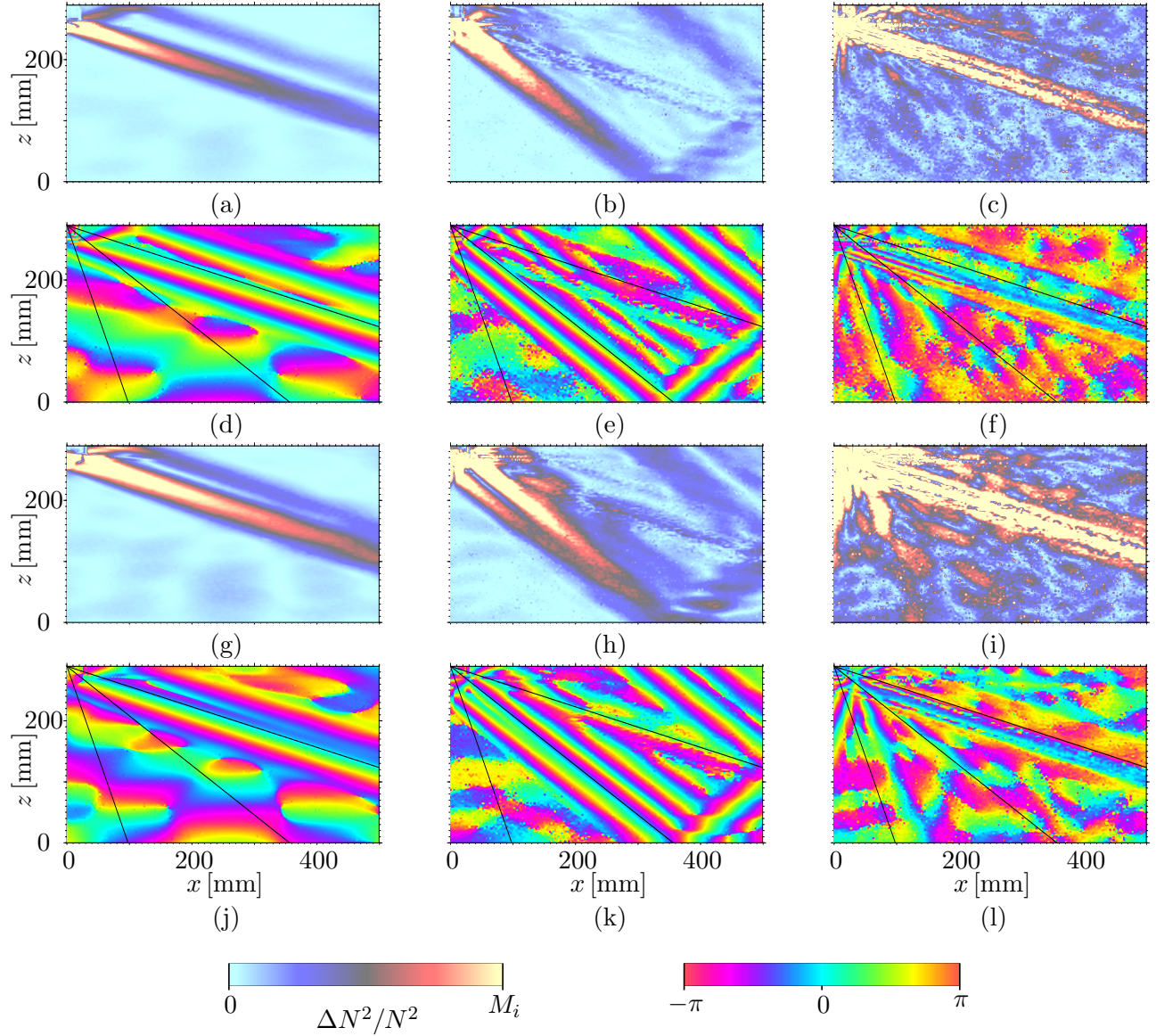


Figure 5.17: Amplitude and phase images of temporal harmonics generated by rectangular cylinders. RMS_T images of primary, secondary and tertiary harmonics are shown in (a-c) and (g-i) for C_F and C_H respectively. Corresponding phase images are shown in (d-f) and (j-l). Dashed lines are shown at angles 71.6° , 50.9° and 18.7° to the vertical, corresponding to predicted values of θ_i for primary ($i = 1$), secondary ($i = 2$) and tertiary ($i = 3$) harmonics respectively. Amplitude maxima M_i have values 9.5×10^{-2} , 9.5×10^{-3} and 9.5×10^{-4} for $i = 1, 2$ and 3 .

Amplitudes of $\Delta N^2/N^2$ fields are multiplied by the factor $\hat{A}_r = (R_c/c_c)^2$. Intrusions generated by each of the rectangular cylinders, $C_F - C_H$, are more distinct than that generated by the circular cylinder, C_C . In each case, the disturbances extend from the vertical levels of the top and bottom of the cylinders, *i.e.* $z = \pm b_r$ mm, which coincides with the vertical positions of the cylinder corners. The intrusions appear to become more prominent with increasing aspect ratio and, as in the elliptical cases, oscillatory motions are again observed in movies of the experiments to propagate along the

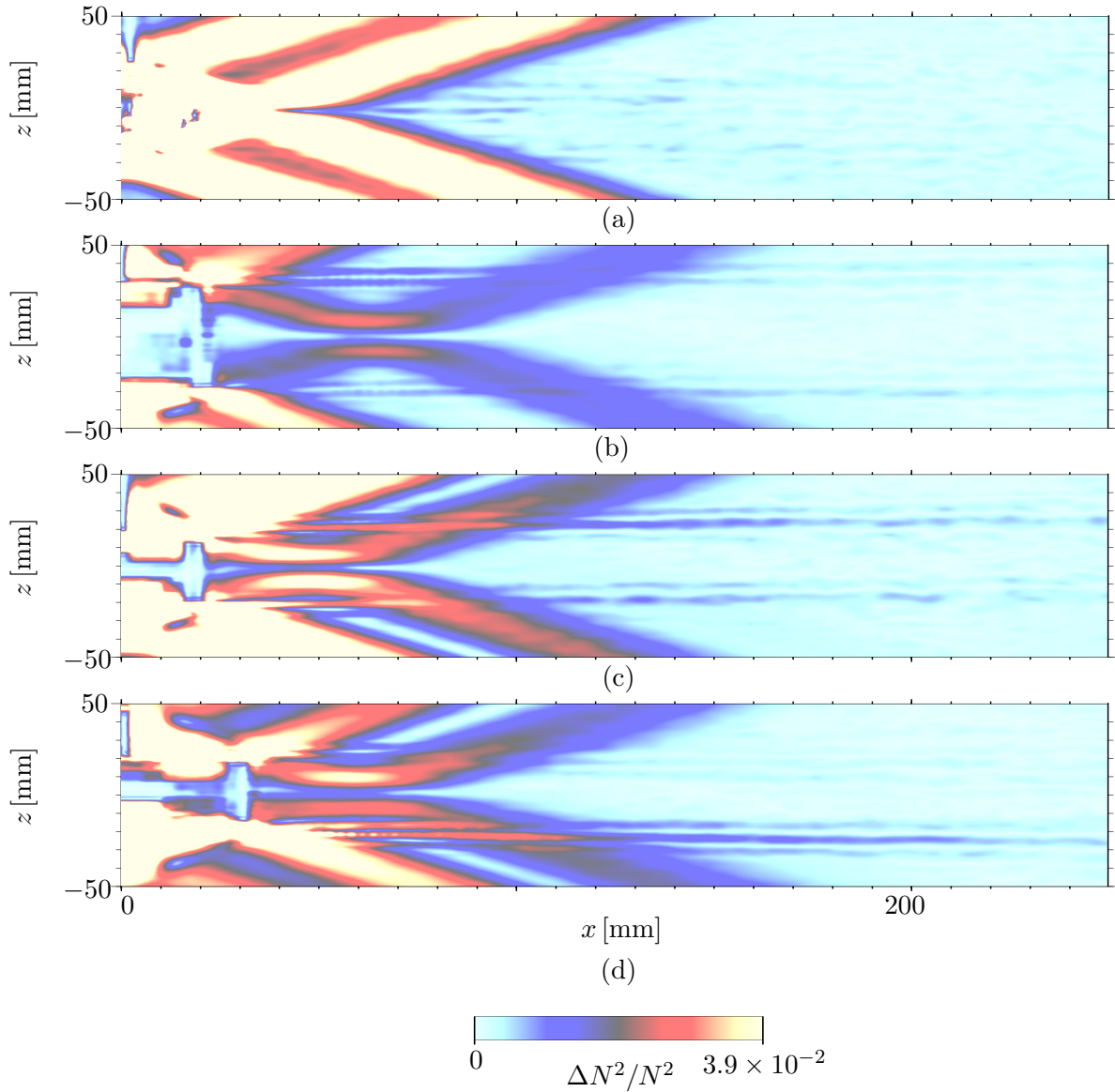


Figure 5.18: RMS_T images of regions adjacent to cylinders (centre-left of field of view) (a) C_C and (b) to (d) C_F to C_H respectively. Amplitudes are multiplied by the factor $\hat{A}_r = (R_c/c_c)^2$.

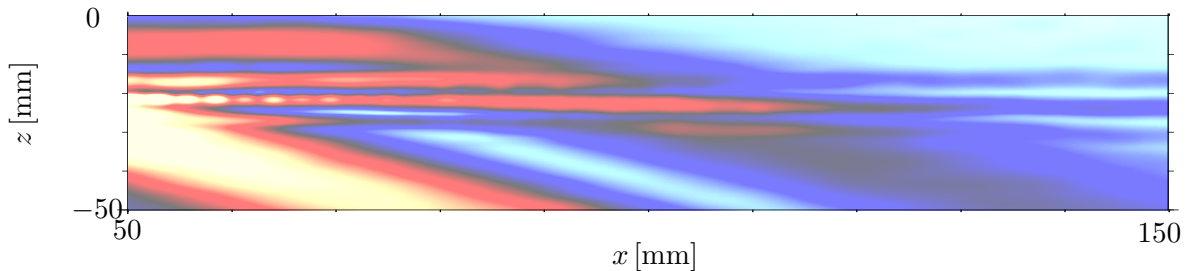


Figure 5.19: Zoom of section near cylinder in figure 5.18 (e). Scaling as in figure 5.18.

thin layers of mixed fluid. Figure 5.19 shows a zoomed section of figure 5.18 (d) for the cylinder

C_H of the region $x \in [50, 150]$ mm and $z \in [-50, 0]$ mm. Evidence of the horizontal oscillation is perhaps best seen by the periodic undulation of the horizontal band at $x \in [55, 70]$ mm and $z \approx -22$ mm. As in experiments with the elliptical cylinders, experiment run times were not long enough to generate sufficiently developed intrusions and hence to allow more detailed analyses of these features here.

5.4 Summary

A study was made of the established wavefields generated by a vertically oscillating circular cylinder prior (physically) to their interaction with boundaries. These were compared with those produced by vertically oscillating elliptical and square cylinders with a view to determining the influence of aspect ratio and sharp corners of the cylinders on the spatial structure of the generated wave beams.

The RMS_T across-beam structure of wave beams generated by elliptical cylinders is characterised at small along-beam distances, s , by two peaks positioned along tangents to the cylinder. Both aspect ratio and frequency control the separation of these peaks and hence the length scales imposed on the wavefield and the associated energy densities. The aspect ratio is defined here as the ratio of horizontal to vertical length scales of the oscillating cylinders. In particular, the maximum power at a given frequency increases with aspect ratio, with primary, secondary and tertiary harmonics of the wavefield more prominent for high aspect ratios. As in the circular cylinder case, viscosity acts to modify the form of the across-beam envelope as wave energy propagates along the beam. High wavenumber components generated at regions of high surface curvature of the elliptical cylinders result in enhanced viscous dissipation of the wave energy as compared with the circular case. Energy is also dissipated near the vertical extremities of the cylinders as well as regions of high surface curvature by the generation of mixed fluid that is expelled into the stratification, forming thin horizontally propagating intrusions along which oscillations can be supported.

In contrast to the elliptical case, across-beam envelopes associated with rectangular cylinders, which feature sharp corners, are generally characterised at small s by three peaks, which originate at the corners of the cylinder. The positions of these peaks vary with frequency and aspect ratio, and the envelopes are generally highly asymmetric as a result, with regions of high energy density where corner asymptotes lie close together. Smaller length scales, which are related to the across-beam displacement of the cylinder corners, are imposed on the wavefields than those in circular or elliptical analogies, as well as a significant proportion of energy focused, generating high wavenumber components, at the sharp corners themselves. The energy associated with these high wavenumber components is rapidly attenuated by viscosity and consequently across-beam amplitudes associated with the rectangular cylinders are significantly lower than those for a circular cylinder. As for the elliptical cylinders, harmonics of the wavefield are more prominent at higher aspect ratios and mixed fluid intrusions are also observed, originating at the top and bottom of the cylinders.

In summary, the wavefields generated by oscillating sources are controlled by a number of length scales. The circular radius analogy, c_c , for a particular cylinder is indicative of the area and hence the

total energy introduced to the system for a given forcing frequency and amplitude. The projected beam width, denoted in this chapter by c_e and \tilde{c}_e , for a wavefield dictates the energy density associated with a generated wave beam. This also therefore influences the shear and rate of viscous dissipation of the wave energy propagating along the beam. Horizontal and vertical length scales of the cylinders determine the spectral partitioning of the wave energy.

The interaction of wave energy with regions of high topographic curvature and with sharp corners in the near-field of topographies, and the influence of these regions on the far-field structure of scattered wavefields is investigated in chapters 6-8.

Chapter 6

Subcritical rough topography

6.1 Overview

Scatter at boundaries for which the angle α made between the boundary surface and the vertical is constant or varies smoothly in space was described in chapter 4. In particular, the imposition of a wavenumber on a wavefield was investigated using laboratory experiments of scatter at sinusoidally varying topographic profiles. Scattering behaviours at ‘rough’ periodic topographic profiles are considered again in the present chapter. Specifically, scattering behaviour is investigated at piece-wise linear topographic profiles such as the sawtooth, square-wave and, as a limiting case of the square-wave, the pseudo knife-edge. These all exhibit discontinuities in slope, and hence α , at sharp corners. The simplest piece-wise linear topographic profile that contains the smallest number of sharp corners per topographic wavelength is the sawtooth profile (see section 3.8). Such profiles are characterised here by a horizontal wavenumber $\hat{k}_T \neq 0$ and vertical amplitude from the mean level $\hat{A}_T \neq 0$. A unique angle, α , of inclination to the vertical of the sloping surfaces of a given sawtooth is therefore defined as

$$\alpha = \tan^{-1} \left(\frac{\pi}{2\hat{A}_T\hat{k}_T} \right). \quad (6.1)$$

As discussed in chapter 4, regimes of scatter can be defined as subcritical, $\theta/\alpha < 1$, near-critical, $\theta/\alpha \approx 1$, or supercritical, $\theta/\alpha > 1$. Linear geometrical ray tracing treatments predict specular behaviour of incident rays based on local values of θ/α . With the exception of topographic corners, for which the slope of the topography is not defined, and the critical case, *i.e.* $\theta = \alpha$, inviscid linear geometric ray tracing predicts either purely subcritical or purely supercritical scattering regimes at the sawtooth (Longuet-Higgins 1969). This contrasts with ray tracing predictions for the sinusoid (section 4.5.2), that define scatter to be either purely subcritical in cases where $\theta < \alpha$ everywhere, or to be a mixed regime for which the topography simultaneously contains subcritical, critical and supercritical regions somewhere along the boundary.

In the present study, experiments were performed to investigate scatter at seven sawtooth profiles $T_C - T_I$ (see table 3.1) with $\alpha \in [40.0, 69.5]^\circ$ corresponding to aspect ratios $\hat{A}_T\hat{k}_T \in [0.585, 1.872]$.

The range of values of the angle parameter θ/α that could be investigated for a particular topographic profile were inevitably limited by the geometrical constraints of the experimental setup. Consequently, results are presented from subsets of the sawtooth profiles for subcritical values in the present chapter and for supercritical and near-critical values in chapters 7 and 8 respectively. Each chapter describes the far-field structure of scattered wavefields, which vary slowly in the direction of energy propagation, as well as near-field wave behaviour, *i.e.* in the immediate vicinity of the boundary. Results are reported for laboratory experiments and compared with predictions made by linear geometrical ray tracing and a linearised boundary model based on the method of characteristics (Baines 1971a). In particular, the effect of variation of θ/α , α , k_T and topographic shape on spectral scatter of incident wave energy in the forwards and backwards directions is studied, as well as the transfer of energy to higher temporal harmonics and in the mixing of stratified fluid near the topography. With the exception of the inviscid linear geometric ray tracing study of Longuet-Higgins (1969), which calculated general formulae for reflection coefficients at sawtooth and square-wave topographies, no other theoretical, numerical or experimental studies of internal gravity wave scatter at discontinuous periodic profiles are known to the present author so that all results presented here are new.

6.2 Sawtooth topography

This section discusses results relating to subcritical scatter at sawtooth topographies T_G , T_H and T_I . Comparisons with wavefield behaviour near sinusoid T_A and square-wave T_K are made in section 6.3.

6.2.1 Subcritical ray tracing

With the exception of the ray tracing approach applied by Longuet-Higgins (1969), scatter at periodic piece-wise linear topographic profiles has not been modelled theoretically. In the case of subcritical scatter at a sawtooth, with $\theta/\alpha < 1$, ray tracing predicts an entirely forwards scattered wavefield so that the forward and backward scattering coefficients are $C_F = 1$ and $C_B = 0$, respectively. Rays incident on sections of the boundary that are inclined in the same direction relative to the vertical as that of the incident wave energy vector are defocused on reflection, whilst those contacting slopes with the opposite sign of inclination are focused. In particular, ray tracing does not predict a back-scattered wavefield for the subcritical regime.

Another possibility for modelling subcritical scatter is the Fourier superposition of Baines' (1971a) linearised boundary solution for a sinusoidal boundary, summarised in sections 2.5.1 and 4.5.2. The Fourier series representing the height, $A_T(x)$, of a boundary that has a sawtooth profile specified by an amplitude, \hat{A}_T , and horizontal wavenumber, \hat{k}_T , as defined above, can be calculated to be

$$A_T(x) = \hat{A}_T - \frac{8\hat{A}_T}{\pi^2} \sum_{m=1}^{\infty} \frac{1}{(2m-1)^2} \cos\left(\frac{(2m-1)\hat{k}_T x}{2\pi}\right). \quad (6.2)$$

Baines' solution requires that the aspect ratio, *i.e.* the product of the amplitude and horizontal wavenumber, of *each component* be much less than unity. This translates here to the condition

$$\frac{4\hat{A}_T\hat{k}_T}{\pi^3(2m-1)} \ll 1, \quad (6.3)$$

which can be simplified to a condition for $m \in \mathbb{Z}_{\geq 1}$ as

$$m \gg \left(\frac{1}{2} + \frac{2}{\pi^2} \hat{A}_T \hat{k}_T \right). \quad (6.4)$$

Even for $\hat{A}_T\hat{k}_T \ll 1$, this condition is violated by the larger amplitude components, *i.e.* those corresponding to values of $m \sim O(1)$, of the Fourier series. Hence this approach is not used here. Subcritical experiment results of the present study are instead compared with ray tracing predictions and Baines' (1971a) linearised boundary solution for a *sinusoidal* topographic profile. Results from experiments of scatter at sawtooth topographies are presented here.

6.2.2 Basic sawtooth (T_G)

Sawtooth profile T_G is characterised by the horizontal topographic wavenumber $\hat{k}_T = 0.087 \text{ mm}^{-1}$ and an aspect ratio of $\hat{A}_T\hat{k}_T = 0.783$. Length scales of the incident wavefield are compared with those of T_G with the parameters $k_c/\hat{k}_T = 4.06$ and $\hat{A}_Tk_c = 3.18$, where k_c is defined as in section 4.5.

Qualitative description of scatter

As in earlier chapters, RMS_T images are presented here to illustrate the spatial structure and amplitudes of scattering wavefields. In addition, Hilbert transforms are used to isolate internal wave components according to their direction of phase propagation as described in a recent paper by Mercier *et al.* (2008). The method successively applies Fourier transforms in time and space to time evolving two-dimensional experimental data, ultimately allowing individual wave components to be identified in complex space by the direction associated with their wavenumber vector. An outline of the Hilbert transform method and its implementation in this study is given here.

Isolating wave components using Hilbert transforms

The Fourier decomposition in time of a real-valued data set, $\phi(x, z, t)$, contains both negative and positive frequency components, with the frequency distribution symmetric about zero frequency due to Hermitian symmetry. As a consequence of this symmetry, the data can be trivially reformulated as the complex-valued field $\tilde{\phi}(x, z, t)$, consisting of only the positive frequency components, where

$$\Re[\tilde{\phi}(x, z, t)] = \phi(x, z, t), \quad (6.5)$$

provided that suitable magnitude adjustments are made to compensate for the halving of the total energy incurred through filtering out the negative frequency components. By representing the wavefield in this manner, interpretation of the phase of the fluid motion is simplified. The two-dimensional spatial Fourier transform of the complex field, $\tilde{\phi}$, yields a wavenumber domain for which each quadrant representing a particular orientation of the wavenumber vector, with horizontal and vertical components k_x and k_z respectively, also represents that orientation of *phase* propagation.

A similar method to that of Mercier *et al.* (2008), following the principles outlined above, is applied in the context of the present study using data processing package Digiflow (Dalziel 2007) to filter scattering wavefields for wave components with phase velocities oriented with those defined in section 2.3 by c_{p++} , c_{p+-} , c_{p-+} or c_{p--} . For convenience, these phase directions will be referred to in terms of the corresponding directions of energy propagation c_{g+-} , c_{g++} , c_{g--} , and c_{g-+} respectively. Incident and forward scattered wave components therefore have group velocity vectors directed as c_{g+-} and c_{g++} , respectively, and hence may be isolated individually using the transforms described.

The two main stages of application of the Hilbert transform method, *i.e.* (i) the Hilbert transform, crucially generating a complex-valued formulation, $\tilde{\phi}$, of the wavefield ϕ , and (ii) filtering $\tilde{\phi}$ in the two-dimensional wavenumber domain for wave components with specific phase orientation, are demonstrated here for scatter at sawtooth T_G , $\theta/\alpha = 0.88$. The associated wavefield, ϕ , (e.g. the perturbed buoyancy field) is firstly subject to temporal filtering for the primary harmonic wavefield, with the filtering transform being applied in this study over three periods of the primary wave motion. The harmonic analysis is completed by an inverse transform, reconstructing the filtered wavefield as the complex field $\tilde{\phi}$ in the physical domain. Figure 6.1 shows the RMS_T image of the perturbed buoyancy field for subcritical scatter at T_G with $\theta/\alpha = 0.88$ after filtering for the primary harmonic wavefield.

The second stage of the Hilbert transform method involves application of a two-dimensional fast Fourier transform (FFT) to the frequency filtered data $\tilde{\phi}$. Figure 6.2 (a) shows a schematic of the corresponding two-dimensional wavenumber domain and the group velocity directions associated with each quadrant. The fourth quadrant, for example, represents wave motion with positive horizontal, k_x , and negative vertical, k_z , wavenumbers, *i.e.* those with phase velocity denoted as c_{p+-} and hence with group velocity c_{g++} , which is oriented with the forward scattered wavefield. Similar deductions can be made for the other quadrants. Filtering the data for forwards scattered wave components, for example, is therefore reduced in the wavenumber domain to a simple multiplication by a binary mask that filters the wave motion associated with the first, second and third quadrants, whilst preserving that of the fourth. Figure 6.2 (b) and (c) show the magnitude M/\hat{M} of the two-dimensional FFT of the frequency-filtered data relating to figure 6.1 before and after filtering for the forward scattered wave motion, where \hat{M} is the maximum value of M over the domain. The wavenumber filtered physical data is then reconstructed by an inverse two-dimensional FFT. Figure 6.3 shows the RMS_T image of the perturbed buoyancy field after both stages of the Hilbert transform method are performed, *i.e.* harmonic analysis for the primary wave motion and filtering for the forwards scattered wavefield in the two-dimensional wavenumber domain. The image there-

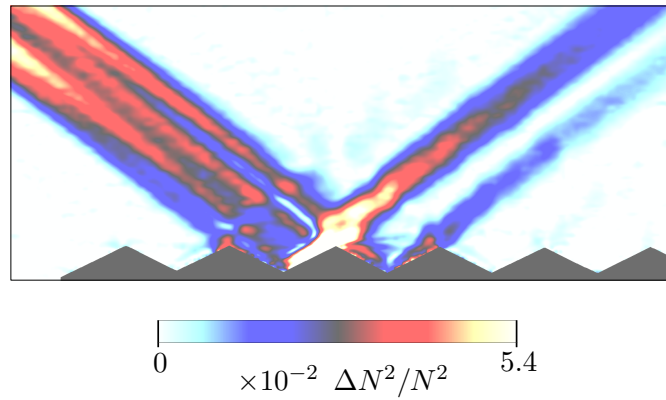


Figure 6.1: RMS_T image of perturbed buoyancy field for subcritical scatter at sawtooth T_G and $\theta/\alpha = 0.88$ after filtering at the primary frequency, σ .

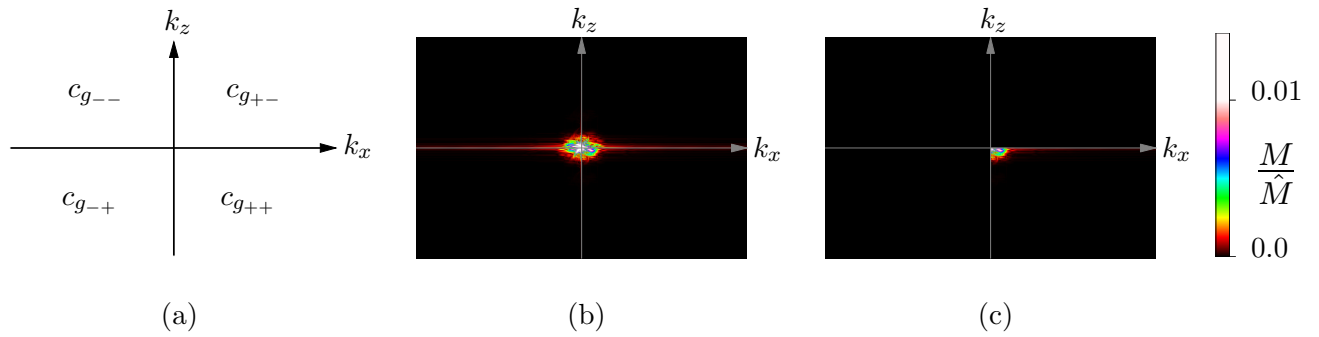


Figure 6.2: Two-dimensional wavenumber domain represented as (a) a schematic indicating the orientation of group velocity vectors for fluid motion associated with each quadrant (nomenclature as defined in figure 2.2); magnitudes, M/\hat{M} , of the two-dimensional FFT of data relating to figure 6.1 (b) before and (c) after filtering for wavenumber components associated with $c_{g_{++}}$ (*i.e.* forwards scatter), where \hat{M} denotes the maximum value of the transform in (b).

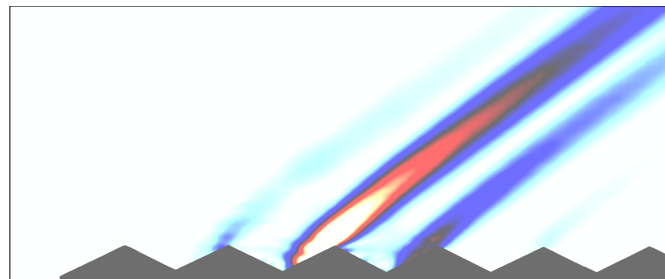


Figure 6.3: RMS_T image of perturbed buoyancy field for subcritical scatter at sawtooth T_G and $\theta/\alpha = 0.88$ after filtering at the primary frequency, σ , and for wavenumbers associated with forwards scatter. Scale for $\Delta N^2/N^2$ as in figure 6.1.

fore displays only the forwards scattered wavefield of the primary wave motion.

Figure 6.4 (a-c) shows RMS_T images of subcritical scatter at profile T_G . In each image, an incident wave beam can be seen to propagate from the top left-hand corner towards the sawtooth topography positioned at the bottom of the field of view. Composite beams formed by the superposition of incident and back-scattered wavefields are denoted B_I and forwards scattered wave beams are denoted B_F . As described in section 4.2.3, in an unbounded stratification, the incident beam has a bimodal structure close to the wave source that gradually erodes by viscous action to a unimodal structure as wave energy propagates away. At a horizontal boundary (see e.g. figure 4.1 (c-d)), the reflected wavefield propagates in the forwards direction away from the boundary, *i.e.* towards the right, with little change to its unimodal beam structure except for a reduction in amplitude, dominantly caused by viscous attenuation of the wave energy.

Figure 6.4 (a-c) shows scatter of an incident wave beam at T_G for subcritical values of θ/α equal to (a) 0.77, (b) 0.88 and (c) 0.97, corresponding to incident wave frequencies such that $\sigma/N = 0.66, 0.56$ and 0.48 respectively. Whilst results are presented for only three frequencies, experiments at intermediate values were also performed and analysed in a similar manner to that presented here. Unless otherwise stated, trends described in this chapter for the wavefields hold for the experiments presented as well as for those experiments performed at intermediate frequencies. In each RMS_T image of figure 6.4, forwards scattered wave energy is focused into narrow beam-like structures emanating from topographic slopes with positive gradient, collectively referred to as B_F , that are characterised individually by smaller across-beam length scales than those associated with the incident wave beam, and is defocused in the regions seen as gaps between the focused beams. The forwards scattered beams are narrower and closer together for larger values of θ/α , in accordance with the predictions of ray tracing in which ray tubes become more constricted as $\theta/\alpha \rightarrow 1$. Amplitudes of the forwards scattered wavefields are largest in the near-field, at the sloping sections of the topography, with maximum values there increasing with θ/α as the wavefield becomes more focused. Amplitudes decay, however, with increasing distance from the topography as viscosity attenuates the wave energy. Viscous action on the wave energy is enhanced in conditions of increased shear and acts most rapidly on the smaller length scales of the motion. The greater focusing of the wavefield as θ/α approaches critical results in wave energy becoming associated with smaller length scales, *i.e.* higher wavenumbers, and larger shearing motions. Consequently, decay of amplitudes can be seen in figure 6.4 to occur more rapidly with distance from the topography as θ/α increases, so that the forward scattered wavefield associated with the *smallest* value of θ/α (shown in figure 6.4 (a)) is the most prominent in the far-field. Some weakening of the amplitudes of the wavefields can be attributed to the lower frequencies (and hence larger group velocities) corresponding to the larger values of θ/α . Also note that secondary harmonic generation is possible (which requires $\sigma/N < 1/2$) for the experiment corresponding to figure 6.4 (c). The generation of higher harmonic wave components is discussed further in section 6.4.

Forward scatter at profile T_G can be viewed more directly in figure 6.4 (d-f), where the wavefields, with incident wave frequencies corresponding to those in figure 6.4 (a-c), have been filtered using Hilbert transforms as described above. The frequency and wavenumber filtered images of figure 6.4 (d-f), where the images are snapshots of the wavefields based on the harmonically analysed data with the phase chosen in each case to be such that the oscillating cylinder is located at the midpoint of its oscillation, confirm the trends discussed above for the forward scatter at T_G . An additional feature visible in the filtered images is the slight reduction of θ in the immediate vicinity of the topography, perhaps suggesting weakening of the buoyancy frequency, N , in this region.

Ray tracing predicts complete forwards scatter, *i.e.* $C_F = 1$ and $C_B = 0$, for wave energy interacting subcritically with sawtooth topography. However, the asymmetric structure of B_I in each of the RMS_T images of figure 6.4, as compared with the beam structure shown in figure 4.23 (a) of the incident beam for a reflection at a horizontal boundary for example, suggests the generation of a *back-scattered* flux (*i.e.* with group velocity directed as $c_{g_{-+}}$) in each case. This is confirmed by the observation of two directions of phase propagation across B_I in movies of the experiments. As in figure 6.4 (d-f), for the forward scattered wavefields, Hilbert transforms are used in figure 6.4 (g-i) to filter for the corresponding back-scattered wave energy. The general spatial form of the back-scattered wavefields is similar to that for the forwards scatter but with the group velocity directed away from the topography and to the left. However, in contrast to the forwards scatter, amplitudes associated with back-scattered wave energy are typically an order of magnitude weaker than those of the forwards scatter and *increase* as the value of θ/α approaches critical. Maximum amplitudes of back-scattered fields are near the corners of the topography and the wavefields attenuate as they propagate away. The action of viscosity on components of B_I is likely to be enhanced by the presence of the incident wavefield propagating along $c_{g_{+-}}$, which increases gradients in the across-beam direction and shear. Incident beams interacting with rough topography viewed in images filtered using Hilbert transforms for $c_{g_{+-}}$ are essentially identical to those in experiments of reflection at a *flat* bottom, indicating that there is no significant influence of back-scatter on wave generation at the oscillating cylinder.

Variation with θ/α

The variation of subcritical scattering behaviour for increasing values of θ/α is discussed here. Linear geometrical ray tracing predicts complete forward scatter at the sloping sections of subcritical sawtooth topography (*i.e.* $C_F = 1$, $C_B = 0$) but does not resolve behaviour at the topographic corners. Figure 6.5 shows a schematic of subcritical ray geometry at sawtooth topography. Wave rays are incident from the top left-hand side of the diagram and make an angle θ with the vertical. Rays incident on the sections of topography with negative gradient (*i.e.* lying between the red and green lines denoted) are defocused as they reflect in the forwards direction, whilst those incident between the green and blue lines are focused. Simple geometrical calculations can be made to determine the proportions of focused and defocused wave energy, denoted here by C_f and C_{df} ,

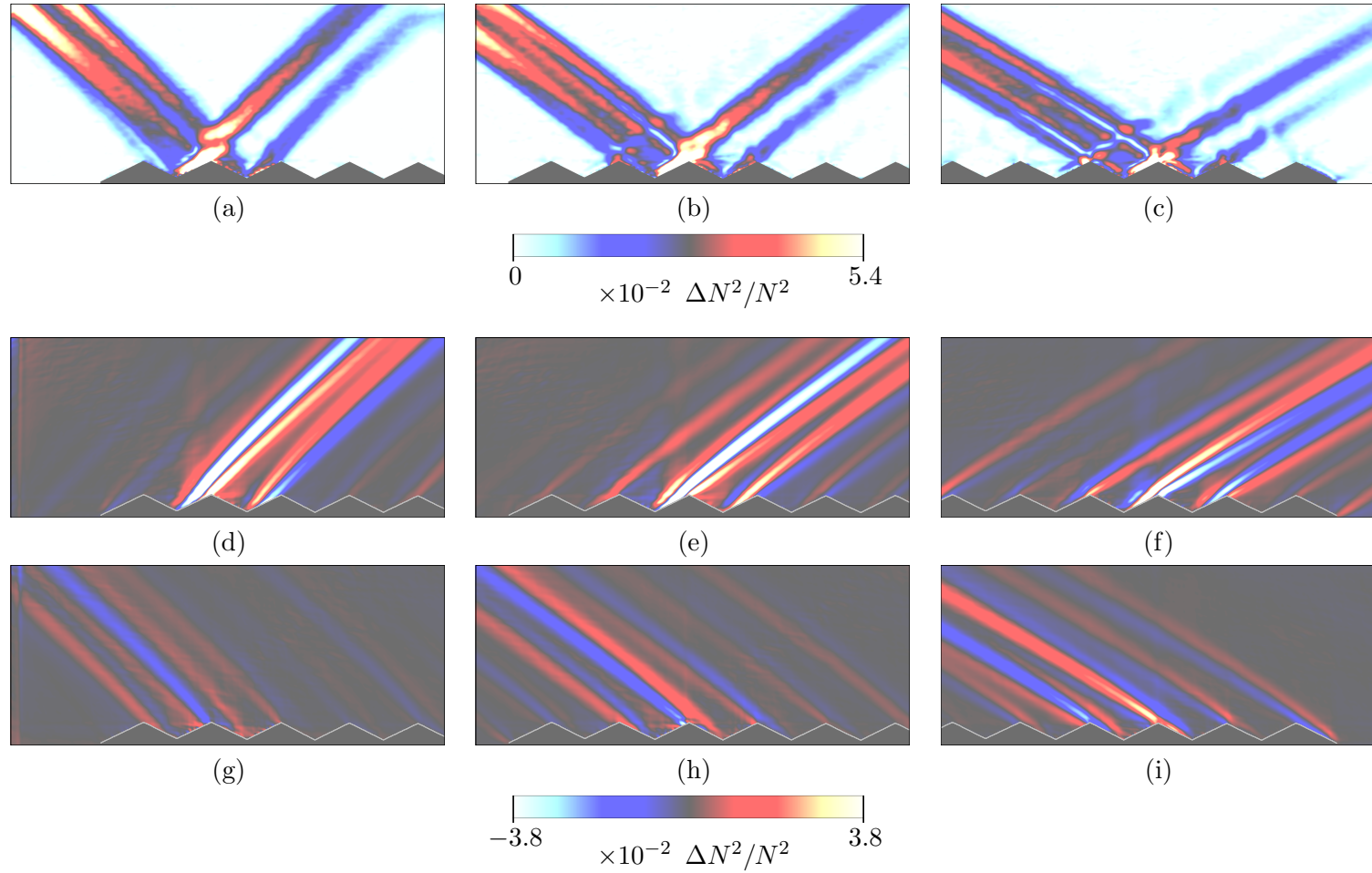


Figure 6.4: RMS_T images of perturbed buoyancy fields for subcritical scatter at sawtooth T_G , with $\alpha = 63.5^\circ$, at forcing frequencies such that θ/α is equal to (a) 0.77, (b) 0.88 and (c) 0.97. Images of corresponding forward and back-scattered wavefields after filtering using the Hilbert transform are shown in (d)-(f) and (g)-(i) respectively, with upper edge of topography highlighted in grey. Fields of view measure 449×186 mm.

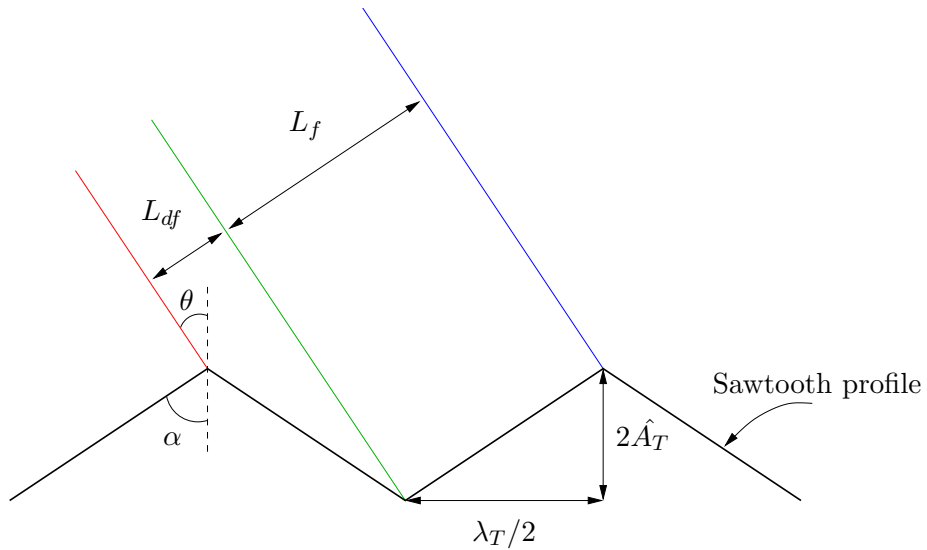
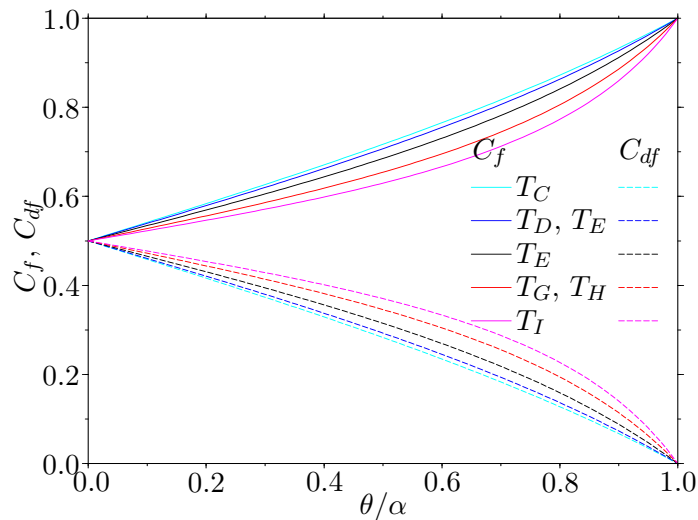


Figure 6.5: Ray geometry for subcritical sawtooth.

Figure 6.6: Variation with θ/α of coefficients for focusing, C_f , and defocusing, C_{df} , of wave energy incident at sawtooth topographies.

respectively. The total across-beam distance per topographic wavelength over which wave energy is focused, using specular theory, is denoted L_f , whilst the corresponding distance over which wave energy is defocused is denoted L_{df} . These lengths are indicated in figure 6.5. The coefficients for the focused and defocused wave energy can therefore be calculated from geometrical arguments, assuming specular reflection of incident rays at the slopes of the boundary, to be

$$C_f = \frac{1}{2} \left(1 + \frac{\tan \theta}{\tan \alpha} \right) \quad \text{and} \quad C_{df} = \frac{1}{2} \left(1 - \frac{\tan \theta}{\tan \alpha} \right). \quad (6.6)$$

Figure 6.6 plots the variation of these coefficients with θ/α for sawtooth topographies $T_C - T_I$. The proportion of energy predicted by ray tracing arguments to be focused (defocused) after subcritical interaction with a sawtooth profile increases (decreases) with θ/α , with a greater degree of focusing occurring for a given value of θ/α at those profiles defined by smaller α , *i.e.* steeper slopes.

Spectral analysis of scatter at T_G

Energy spectra are calculated for the wavefields scattered at T_G in the same manner and using the same terminology as in section 4.5.2, where spectra were calculated for scatter at sinusoids T_A and T_B . Figure 6.7 (a), (b) and (c) shows energy density spectra, $E(k)$, calculated for T_G along cross-sections at various distances along B_F (lines coloured in blue scales) and B_F^* (lines coloured in red scales) for experiments corresponding to those shown in figure 6.4 (a)-(c) respectively. Corresponding spectral differences, with $E_{\Delta F} = (E_F - E_F^*)$, are shown in (d)-(f). As for the spectra shown in section 4.5.2, bold black lines superimposed on the spectra indicate the predictions of inviscid linearised boundary theory for the forwards scattered spectra at the analogous *sinusoid* to T_G (Baines 1971a), which assumes $\hat{A}_T \hat{k}_T \ll 1$ and that $\hat{A}_T k_c \ll 1$. Dark grey, red and green lines (only plotted on graphs of spectral differences) indicate the individual contributions from forwards scattered ‘primary’, ‘sum’ and ‘difference’ wavenumber components respectively (calculated as in section 4.5.2), which are characterised by the wavenumbers k_I , $k_I + k_T$ and $|k_I - k_T|$, with $k_T = \hat{k}_T / \cot \theta$. Dashed vertical lines indicate locations of \hat{k}_T and k_T (with one labelled on each graph). Regions shaded grey indicate error estimates calculated as in section 4.5.2. Note that the actual form of the error tends to be localised to spectral peaks and the actual magnitude of the error tends to reduce significantly as energy densities associated with measured cross-sections decrease. It is expected that maximum magnitudes of the error associated with energy density values typical in regions of forwards scatter measurements are an order of magnitude smaller than that indicated by the shaded regions, *i.e.* $\sim O(10^{-4})$. Measured spectra associated with the incident wavefields at T_G (coloured in red shades) plotted in figure 6.7 (a), exhibit dominant peaks at $\tilde{k}_I \approx 0.3$ with magnitudes of $E/\hat{E} \sim O(10^{-2})$. Measured forwards scattered spectra exhibit two dominant peaks, with maxima located at $\tilde{k} \approx 0.25$ and at $\tilde{k} \approx 0.6$, both with magnitudes $\sim O(10^{-3})$. The lower wavenumber peak is located in the region of the predicted primary component, whilst the higher wavenumber scatter seems to be associated with the sum component. As noted in section 4.5.2, some features of the scattered spectra can be more readily interpreted from the corresponding spectral differences, shown in figure 6.7 (b). Peaks of the spectral difference graphs generally represent scatter of incident wave energy to wavenumbers in the peak region. Troughs are located in regions of the spectra where energy has been redistributed to other wavenumber or frequency components, or dissipated by viscous action or mixing. The linearised boundary theory for a sinusoidal boundary with the same specifications as T_G predicts two peaks in the difference spectra for the scattered wavefield that correspond to difference and sum components and are located at $\tilde{k} \approx 0.1$ and $\tilde{k} \approx 0.6$ respectively, with magnitudes of $O(10^{-3})$ and $O(10^{-2})$, and a trough at

$\tilde{k} \approx 0.3$ of magnitude $O(10^{-2})$. As θ/α increases towards critical value, the peak difference of the predicted sum component shifts to higher wavenumbers, with little change in magnitude, and the predicted difference component shifts to even lower wavenumbers and reduces in magnitude by several orders. Measured spectra in figure 6.7 (b) exhibit peak differences centered at $\tilde{k} \approx 0.6$ with largest magnitude $\sim O(10^{-3})$, coinciding with the peak predicted for the sum component, and troughs located in the same region and with approximately the same magnitude as the trough of the predicted spectra. The measured peak lies well within the indicated error region. However, as noted above, it is anticipated that the actual error associated with energy density magnitudes typical of those in regions of forwards scatter is an order of magnitude smaller than that indicated. Measured spectra magnitudes are not significant in the very low wavenumber region of the predicted difference component. Similar scattering behaviour is observed in the measured spectra as θ/α increases. However, magnitudes of the measured energy density in the region of the predicted sum component decrease with increasing θ/α as viscous attenuation acts more rapidly on the higher wavenumbers generated as the scatter becomes near-critical (see also behaviour noted for figure 6.4 (d)-(f)). As noted in section 4.5.2, at all values of θ/α , magnitudes of the measured spectra tend to zero at a wavenumber of $\tilde{k} \sim 0.8$, indicating that energy scattered to wavenumbers greater than this is rapidly dissipated in the near-field of the topography by viscous action or instability mechanisms. Note that the spatial scatter of wave energy to propagating higher harmonics is only possible for the experiment corresponding to figure 6.7 (c).

Figure 6.8 (a), (b) and (c) shows spectra associated with back-scattered fields calculated for T_G along cross-sections at various along-beam distance of B_I (*i.e.* beam composed of incident and back-scattered fields at rough topography) and B_I^* (analogous incident beam at flat boundary) for experiments corresponding to those shown in figure 6.4 (a)-(c) respectively. Corresponding spectral differences, with $E_{\Delta I} = (E_I - E_I^*)$, are shown in (b), (d), (f), with theoretical predictions for the analogous sinusoid as in figure 6.7. The spectra show in figure 6.8 (a) for the measured incident and scattered wavefields are not easily distinguished from one another but clearer distinctions, such as the locations of predicted components, can be made in the corresponding spectral differences in figure 6.8 (b). Note that, as in difference spectra for the forward scatter, areas shaded grey indicate the estimated maximum magnitude of the error, with the *form* of the actual error tending to be localised about peaks in the measured spectra. The inviscid linearised boundary theory of Baines (1971a) predicts a back-scattered flux at wavenumbers close to zero, with peak magnitude $\sim O(10^{-2})$ (green line). A signature of this component is not observed in the measured spectra. A suggestion of a second possible peak, which is *not predicted* by the linearised boundary theory, can be seen in the spectral difference graphs at $\tilde{k} \approx 0.65$, with a maximum magnitude of $O(10^{-3})$, *i.e.* within the error estimate. However, note that smaller across-beam length scales are observed in RMS_T images of figure 6.4 for B_I , indicating that high wavenumber back-scatter is indeed present. The spectral differences for the back-scatter also contain two distinct troughs centered at $\tilde{k} \approx 0.35$ and $\tilde{k} \approx 0.8$, coinciding with the spectral regions of the two peaks of the incident spectra, with magnitudes $O(10^{-2})$ and $O(10^{-3})$ respectively. As discussed in section 4.5.2 for the sinusoid, these ‘losses’ from

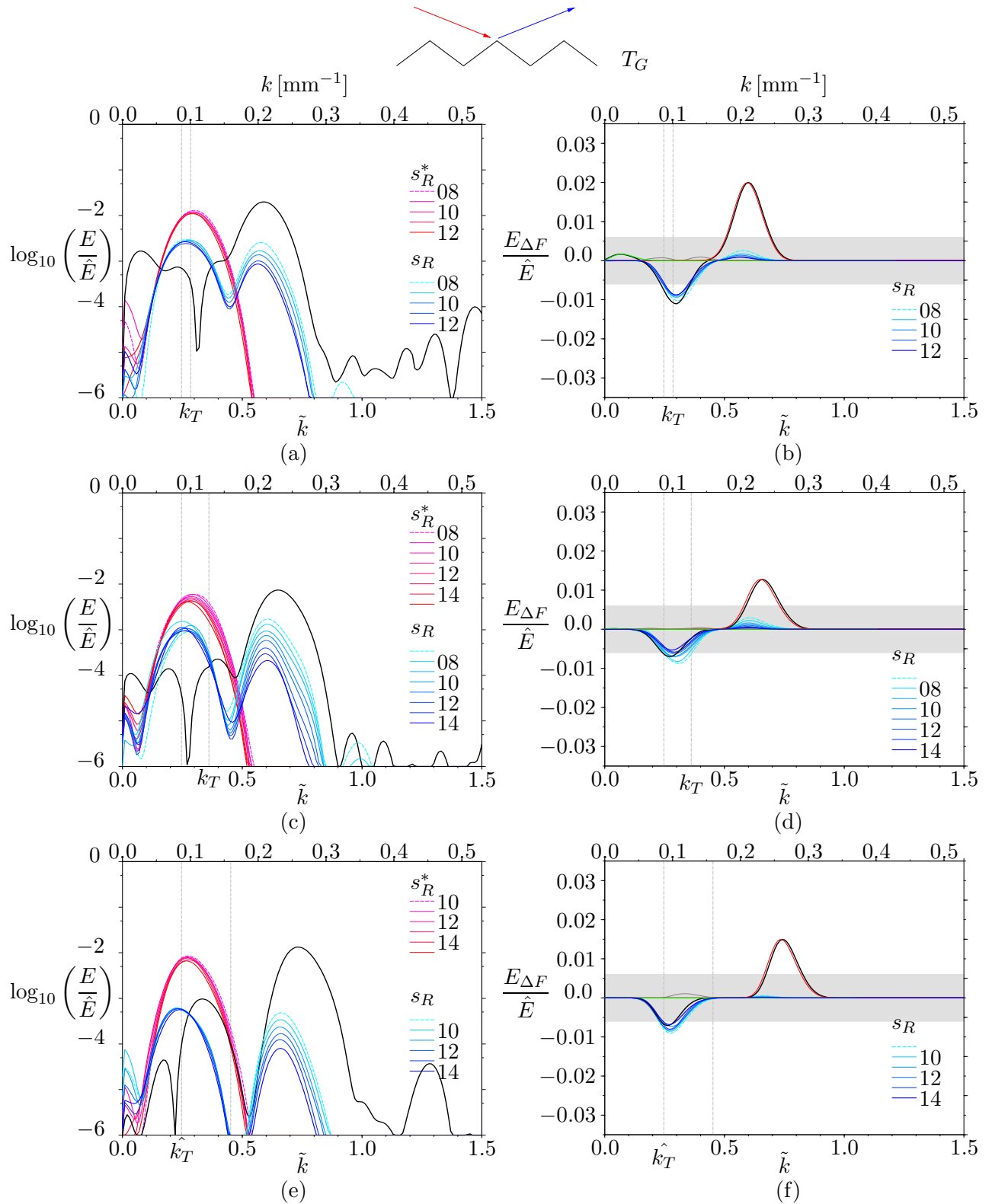


Figure 6.7: Forward-scattered energy density spectra for sawtooth T_G are plotted in (a, c, e). Corresponding spectral differences are plotted in (b, d, f). Frequencies decrease down the page with θ/α equal to (a,b) 0.77, (c,d) 0.88 and (e,f) 0.97.

the incident beam spectrum relative to the specular control case indicate enhanced viscous action caused by an increase in across-beam gradients in the presence of a back-scattered flux. As the value of θ/α is increased for the experiments shown in figure 6.8 (c,d) and (e,f), Baines (1971a) predicts a more pronounced back-scattered flux, with a shift to slightly higher wavenumbers. There is no significant evidence of this component in the measured difference spectra at the larger values of θ/α . The second, though equivocal, higher wavenumber peak difference seen in figure 6.8 (b), is also present at larger θ/α , as are the two troughs.

In general, the subcritical forwards scattering behaviour at sawtooth T_G is modelled well by the inviscid linearised boundary theory of Baines (1971a) for a sinusoidal boundary, despite the relatively large values of the parameters $\hat{A}_T \hat{k}_T$ and $\hat{A}_T k_c$. The forwards scattered spectra exhibit evidence of high wavenumber scatter that seems to be associated with predicted sum components. However, viscosity reduces amplitudes of the measured spectra for all wavenumbers and the more acute action of dissipation processes on higher wavenumber components truncates the scatter to the far-field at a finite wavenumber. As a result, whilst inviscid theory predicts the generation of the highest wavenumber components during scatter at near-critical values of θ/α , in reality wave energy of these components does not propagate into the far-field. In addition to the preferential action of viscosity on the higher wavenumbers, the associated energy is kept near the boundary for longer due to the smaller group velocities, hence enhancing the dissipation. Consequently, the largest proportion of high wavenumber scatter propagating away from the near-field of the topography is measured for the smallest value of θ/α . No significant low wavenumber scatter was measured for any value of θ/α . The *back-scattered* spectra for T_G also show little evidence of low wavenumber back-scatter propagating away from the near-field but possibly indicate a region of *high* wavenumber scatter that is not predicted by either geometrical ray tracing, for which $C_B = 0$, or the linearised boundary theory. If indeed genuine, such scatter is therefore likely to be generated by nonlinear mechanisms, which are promoted by focusing of the wave energy, particularly at the corners of the topography, and superposition of the wavefields in the near-field. Some features of the near-field behaviour are described in the following section.

Influence on background stratification

The influence of topographic corners on the background stratification was discussed briefly in section 3.8. Fluid mixed near the slopes and corners of a sawtooth profile appeared to drain into the stratification at the vertical level of the topographic corners and spread out horizontally into the surrounding fluid (see figure 3.33). These horizontal layers are identified in RMS_T images of the wavefield as regions bounded vertically by horizontal bands of enhanced perturbations to the background stratification. Observation of time evolving movies of the perturbed buoyancy fields reveals oscillations along the thin layers of mixed fluid. Similar features were also described near elliptical and rectangular cylinders in sections 5.2.4 and 5.3.4. In particular, mixed fluid is generated in these cases near the vertical extremities of the elliptical cylinders and the corners of the square

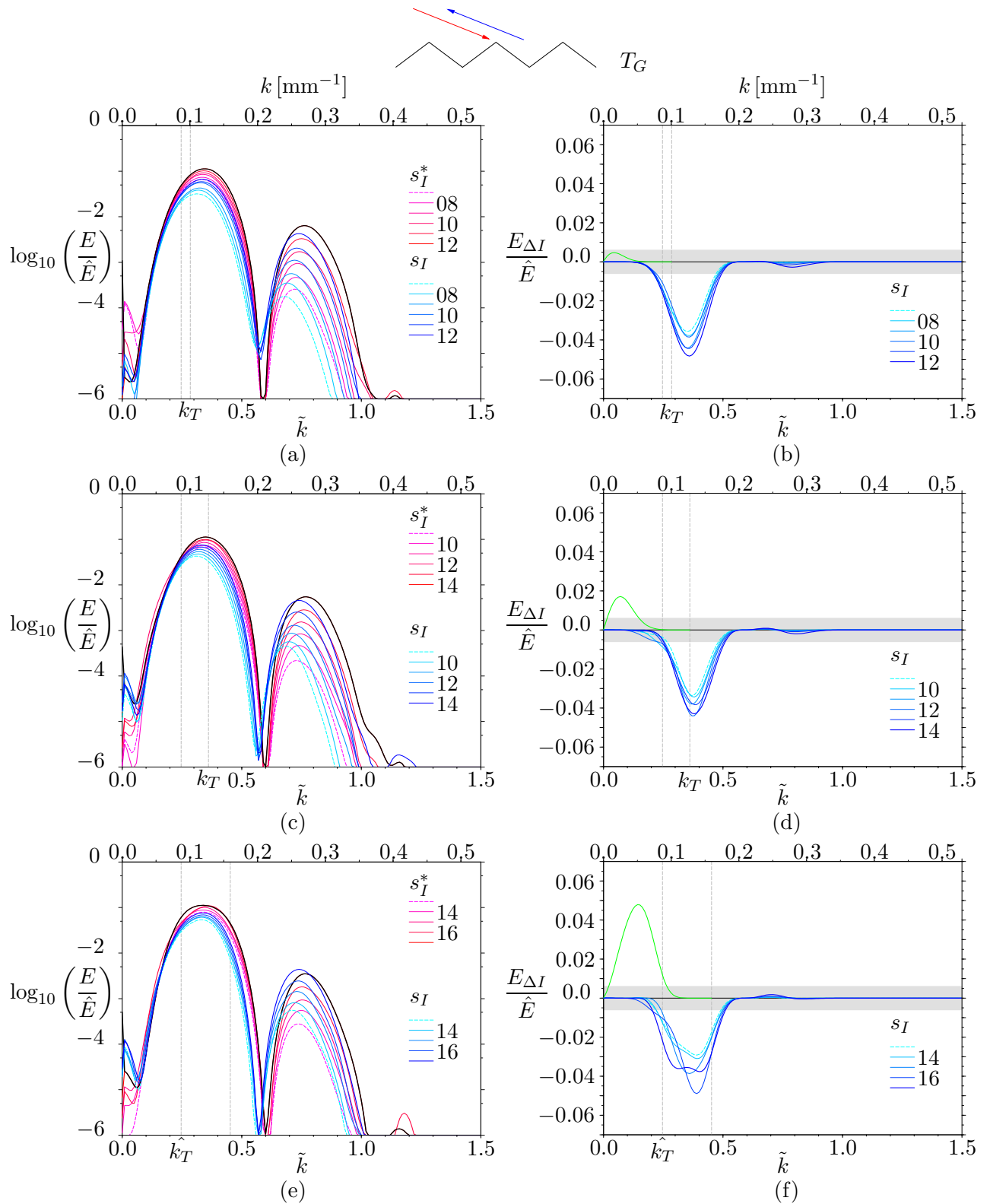


Figure 6.8: Back-scattered energy density spectra for sawtooth T_G are plotted in (a, c, e). Corresponding spectral differences are plotted in (b, d, f). Frequencies decrease down the page with θ/α equal to (a,b) 0.77, (c,d) 0.88 and (e,f) 0.97.

and rectangular cylinders. The production of mixed fluid was found to be more pronounced for cylinders that had larger aspect ratios.

Figure 6.9 (a-c) shows RMS_T images of near-field scatter at sawtooth T_G for subcritical values of θ/α equal to (a) 0.76, (b) 0.86 and (c) 0.96 with σ/N equal to 0.67, 0.58 and 0.49 respectively. As in figure 3.33, horizontal bands are again visible in each case, occurring most significantly at the corner positioned at the centre of the views, where amplitudes of the incident and scattering wavefields are greatest. The mixed fluid behaviour near the corner becomes more pronounced for values of θ/α closer to critical, when the scattered wave energy is the most focused. Figure 6.10 shows a close-up RMS_T image of the wavefield corresponding to that shown in figure 6.9 (c) for the near-critical value $\theta/\alpha = 0.96$. As reported in section 3.8, disturbances that propagate away from the topographic corners along the mixed fluid layers are visible in movies of the perturbed buoyancy fields. In addition to the horizontal intrusions extending outwards from the corners of the topography, periodic arrays of vortex-like structures are seen along the sloping sections of the sawtooth. These features are several millimeters in diameter and are similar to those described for near-critical reflection at a smooth sloping boundary in section 4.3.3. The structures were compared in section 4.3.3 with vortices, which mixed boundary layer fluid, that were observed in near-critical reflection at smooth slopes in experiments by Cacchione & Wunsch (1974) (see also section 2.4.2). The lack of reports of such structures in other studies was attributed by Ivey & Nokes (1989) to the relatively small Reynolds number value, $Re \sim 2$, of the experiments of Cacchione & Wunsch (1974). Ivey & Nokes (1989) suggested that at Reynolds numbers of this magnitude the boundary layer exhibited regular structures but transitioned to the turbulent boundary layer behaviour more often observed in other studies at $Re \sim 15 - 20$. Experiments of the present study had Reynolds numbers comparable with those of the experiments of Cacchione & Wunsch (1974), with typical values of $Re \sim 3 - 4$. In the experiments of Cacchione & Wunsch (1974), the vortices observed along the boundary were most significant for near-critical values of θ/α , but were also prominent in supercritical conditions. The vortices were not consistently observed for subcritical cases in their smooth slope experiments however, though the boundary structures seen in the present study at sawtooth topography are visible in all images of figure 6.9. For completeness, RMS_T images from the present study of marginally *supercritical* scatter at T_G are included here in figure 6.9 with θ/α equal to (d) 1.05, (e) 1.09 and (f) 1.13 and σ/N equal to 0.40, 0.35 and 0.31 respectively. Note also that secondary harmonic generation is possible for each of the experiments shown in figures 6.9 (c-f), and tertiary harmonics for that shown in figure 6.9 (f). The development of the features discussed here are looked at further in chapter 8 for near-critical scatter at sinusoidal, sawtooth, square-wave and knife-edge topographies.

6.2.3 High wavenumber sawtooth (T_H)

This section discusses the effect on scattered wavefields of variation of the horizontal topographic wavenumber, \hat{k}_T , for a fixed aspect ratio, $\hat{A}_T \hat{k}_T$, and hence topographic slope angle, α . Sawtooth

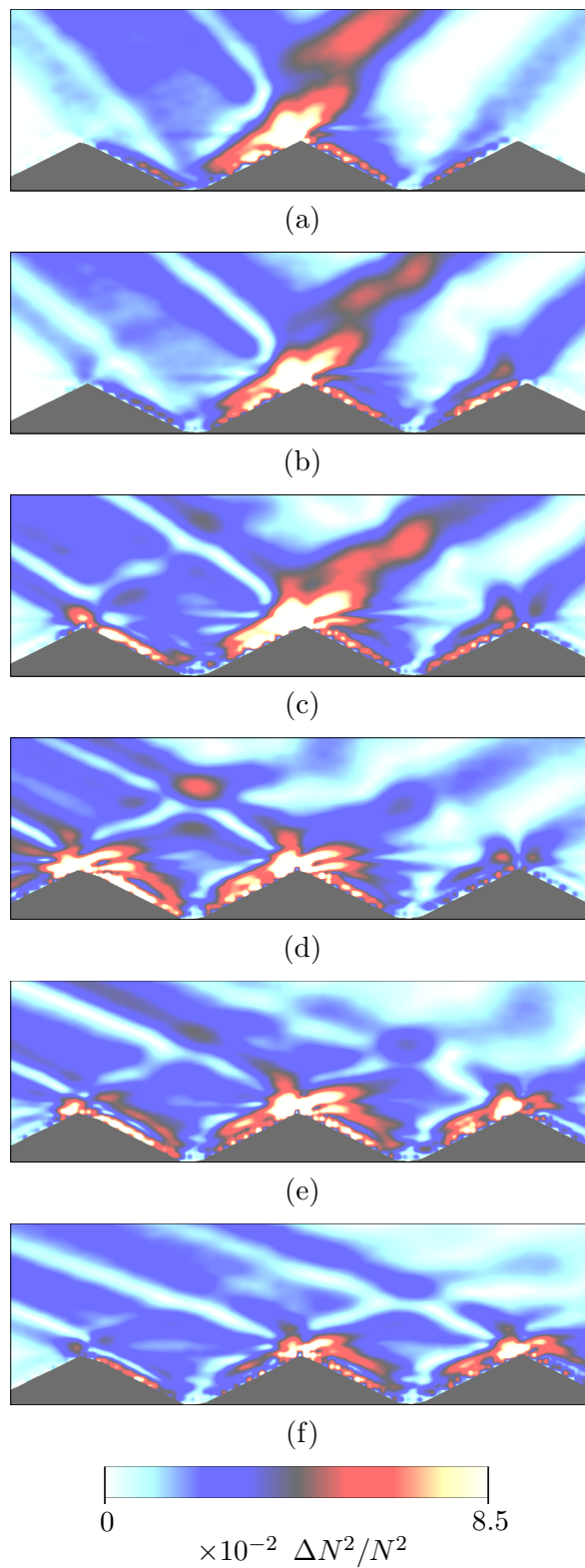


Figure 6.9: Close-up RMS_T images of perturbed buoyancy field near corners of topography for profile T_G with subcritical θ/α equal to (a) 0.76, (b) 0.86 and (c) 0.96, and supercritical θ/α equal to (d) 1.05, (e) 1.09 and (f) 1.13. Fields of view measure 188×59 mm.

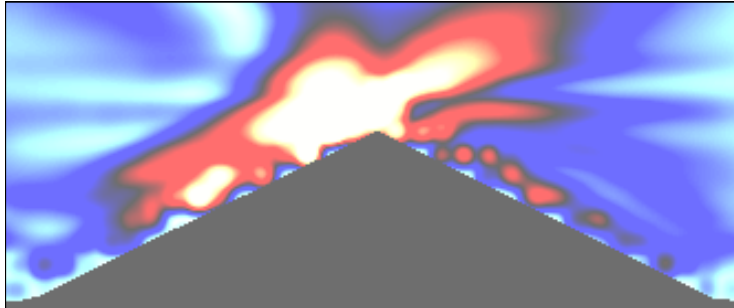


Figure 6.10: Close-up of figure 6.9 (c) for profile T_G and $\theta/\alpha = 0.96$. Colour scale as in figure 6.9 except with maximum value 0.12. Field of view measures 68×29 mm.

topography T_H is defined by the horizontal wavenumber $\hat{k}_T = 0.157 \text{ mm}^{-1}$, almost double that of sawtooth T_G discussed above, and an aspect ratio $\hat{A}_T \hat{k}_T = 0.785$, approximately equal to that of T_G . The length scale ratios for T_H have values $k_c/\hat{k}_T = 2.25$ and $\hat{A}_T k_c = 1.77$.

Qualitative description of scatter

Figure 6.11 (a-c) shows RMS_T images for wavefields with θ/α equal to (a) 0.77, (b) 0.88 and (c) 0.97 and σ/N equal to 0.66, 0.56 and 0.48 respectively, as well as corresponding forward, (d-f), and backward, (g-i), scattered wavefields after filtering using Hilbert transforms. The same conventions used in figure 6.4 are applied here. In general, the nature of the wavefields shown in the RMS_T images of figure 6.11 (a-c) are qualitatively the same as the corresponding ones for the scatter at T_G except that the forward scattered wavefields of T_H , which has the larger topographic wavenumber \hat{k}_T , are characterised by smaller across-beam length scales. Consequently, the partitioning of wave energy between a greater number of beam-like structures and the enhancement of viscous action on the smaller length scales results in a general reduction of the energy density of the forward scattered wavefields at T_H relative to those at T_G . The Hilbert transform filtered forwards and back-scattered wavefields of figure 6.11 (d-f) and (g-i) also show the same trends as discussed for T_G . A more quantitative comparison of the scattering behaviours at the two sawtooth profiles can be made by inspection of the energy density spectra.

Spectral analysis of scatter at T_H

Figure 6.12 (a), (c) and (e) show spectra relating to forwards scattered wavefields for T_H , calculated along cross-sections positioned at various distances along B_F and B_F^* for values of θ/α and σ/N corresponding to those of figure 6.11 (a)-(c), respectively. The corresponding spectral differences are shown in figure 6.12 (b), (d) and (f). Measured spectra for the incident and scattered wavefields shown in figure 6.12 (a) show a dominant peak located at $\tilde{k} \approx 0.3$ with magnitude $\sim O(10^{-2})$. The peak locations in the scattered spectra coincide with those of the spectra predicted by linearised boundary theory for the primary components. However, magnitudes of the measured primary low-

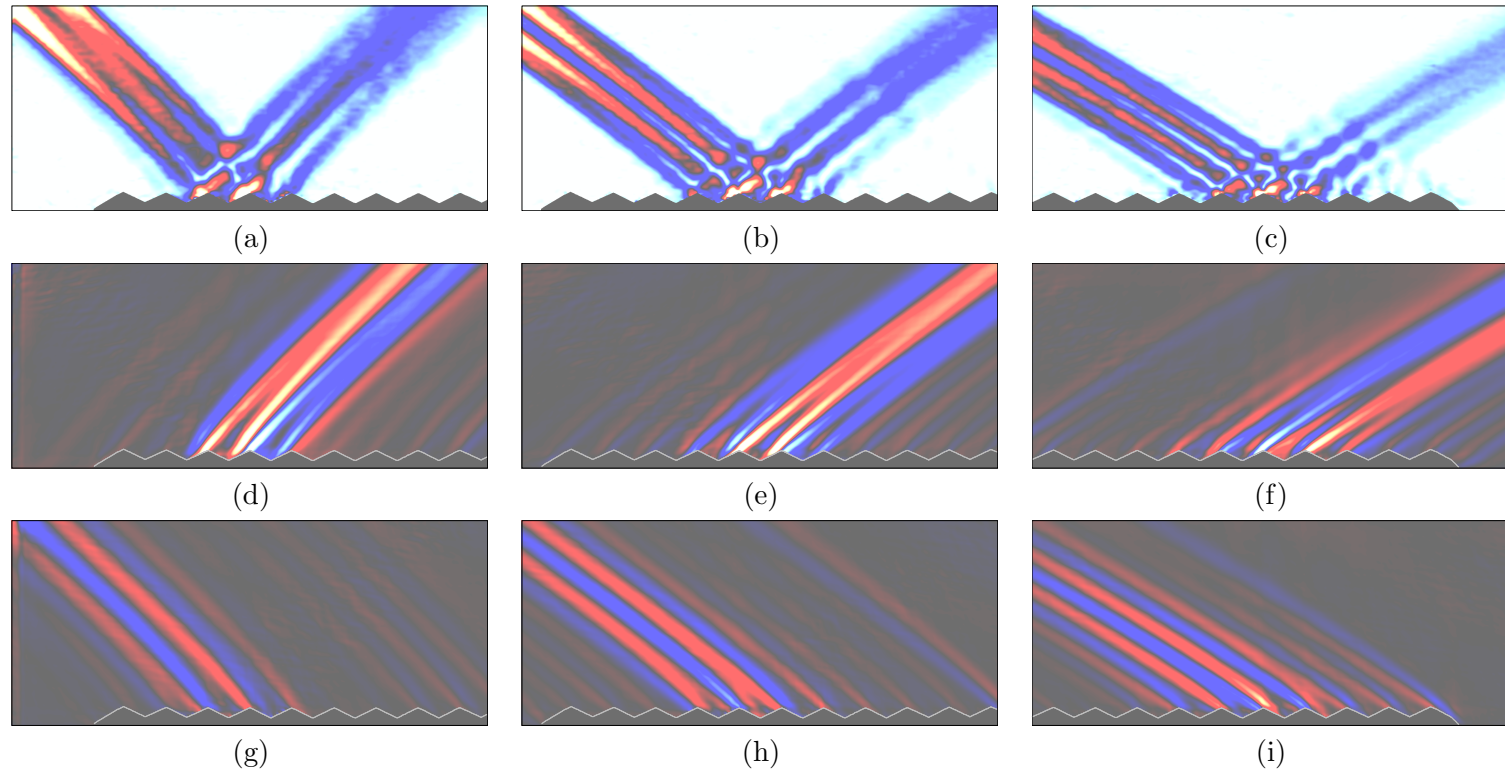


Figure 6.11: RMS_T images of perturbed buoyancy fields for subcritical scatter at sawtooth T_H , with $\alpha = 63.5^\circ$, at forcing frequencies such that θ/α is equal to (a) 0.77, (b) 0.88 and (c) 0.97. Images of corresponding forward and back-scattered wavefields after filtering using the Hilbert transform are shown in (d)-(f) and (g)-(i) respectively, with upper edge of topography highlighted in grey. Fields of view measure 449×193 mm. Colour scale as in figure 6.4.

wavenumber spectral peak are *greater* than those predicted by the theory. This underprediction may in part be because the theory is calculated for scatter at a sinusoidal boundary rather than a sawtooth. In addition, background wave energy, composed of superfluous waves that reflect around the tank and are normally associated with larger length scales and weaker wave amplitudes relative to those of the incident wavefield, may also be included in the measured spectra. The background wavefield is focused by the slopes of the sawtooth and hence becomes more significant in the measured spectra. In contrast, no significant signal is seen in the measured spectra in the region of the predicted *sum* component. However, the presence of small across-beam length scales is clear in the forwards scattered wavefields in RMS_T images of figure 6.11. This discrepancy is most likely caused by the rapid viscous attenuation of the wave energy associated with the higher wavenumber components there. The net scattering behaviour and the spectral locations of predicted components is more clearly interpreted in the corresponding spectral differences of figure 6.12 (b). Linearised boundary theory predicts a peak in the difference spectra in the region of the sum component at $\tilde{k} \approx 0.85$, of magnitude $O(10^{-2})$, and a trough centered at $\tilde{k} \approx 0.3$, *i.e.* in the region of the peak in the measured incident spectra, of magnitude $O(10^{-2})$. As θ/α increases, the contribution of the predicted primary component of the spectra shifts to lower wavenumbers and reduces slightly in magnitude, whilst the contribution from the predicted sum component shifts to higher wavenumbers. Measured spectra show no significant have peak differences located in the high wavenumber sum component region of the spectrum but do exhibit troughs of maximum magnitudes $O(10^{-2})$. Similar behaviour is seen as θ/α increases.

Figure 6.13 (a), (c) and (e) show spectra for the superposition of the incident and backwards scattered wavefields at T_H calculated along cross-sections at various along-beam distances of B_I and B_I^* for values of θ/α and σ/N corresponding to those in the spectra of figure 6.12 (a), (c) and (e) respectively. Corresponding spectral differences are shown in (b), (d) and (f). Features of the spectra, such as spectral locations of predicted components, are best seen in the spectral *differences* of figure 6.13. The measured back-scattered difference spectra of T_H have similar form to those of T_G . Whilst linearised boundary theory predicts a more prominent and relatively higher wavenumber back-scattered difference component for T_H as compared with that for T_G , no significant evidence of this is observed in the spectra.

Sawtooth topographies T_G and T_H have approximately equal aspect ratios of $\hat{A}_T \hat{k}_T = 0.783$ and 0.785, respectively, but the horizontal wavelength and amplitude of T_H are almost half that of T_G . For both profiles, the measured forward scatter qualitatively follow the predictions of inviscid linearised boundary theory for a *sinusoidal* boundary (Baines 1971a), despite not satisfying the linearity condition of the theory that $\hat{A}_T \hat{k}_T \ll 1$. Most notably, there is evidence in the measured spectra of high wavenumber scatter to the predicted sum components, which are characterised by wavenumbers $k_I + k_T$, where $k_T = \hat{k}_T / \cot \theta$. However, the influence of viscosity, and in particular its tendency to attenuate higher wavenumber components most rapidly, significantly modifies the spectra. Wave energy that is forward scattered to the high wavenumbers associated with the sum component predicted for T_H is dissipated in the near-field so that little is measured in the far-

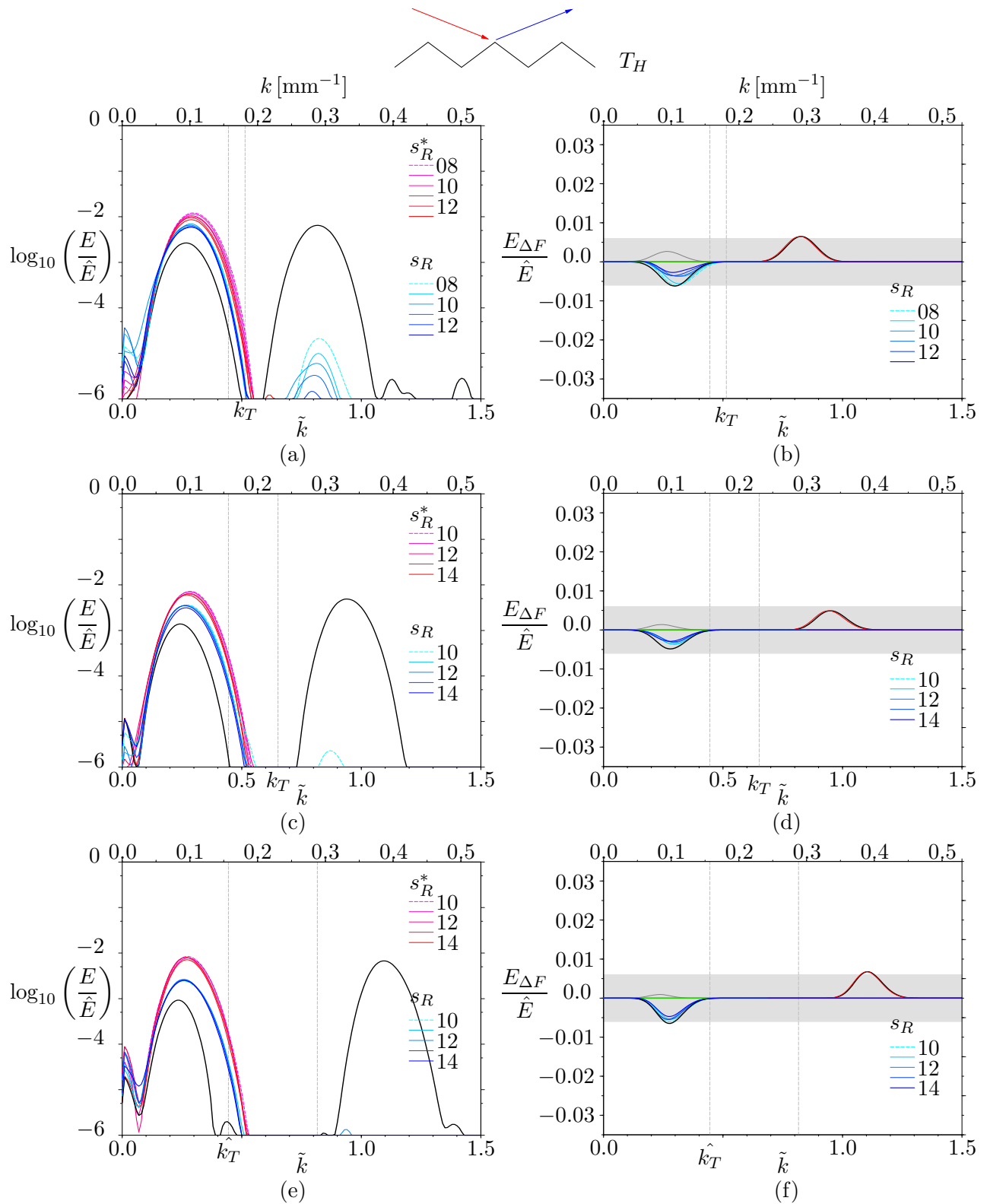


Figure 6.12: Forward-scattered energy density spectra for sawtooth T_H are plotted in (a, c, e). Corresponding spectral differences are plotted in (b, d, f). Frequencies decrease down the page with θ/α equal to (a,b) 0.77, (c,d) 0.88 and (e,f) 0.97.

field. However, the corresponding forward scatter at T_G to slightly lower wavenumbers than those predicted for the scatter at T_H is not attenuated as rapidly and hence energy associated with the high wavenumber scatter of the sum component in this case propagates further away from the near-field. In effect, despite the larger length scales associated with T_G as compared with those of T_H , and its larger value of k_c/\hat{k}_T (*i.e.* length scales associated with T_H , rather than those of T_G , are more comparable with those of the incident wavefield), scatter at this profile produces the *greatest* proportion of high wavenumber scatter into the far-field. There is no significant distinction between the measured back-scatter behaviour at T_G and T_H , with both showing evidence of high wavenumber back-scatter that is not predicted by either ray tracing or the linearised boundary theory, suggesting a nonlinear generation mechanism. For both profiles, far-field amplitudes of the forward scattered wavefields decrease as θ/α increases, whilst those of the back-scattered wavefields appear to increase. Near-field amplitudes become more focused in each case, particularly at topographic corners, as θ/α increases.

6.2.4 Varying the slope (T_I)

This section discusses the effect on scattered wavefields of variation in the topographic wavenumber, \hat{k}_T , and hence topographic aspect ratio, $\hat{A}_T\hat{k}_T$, and slope angle, α , for a fixed topographic amplitude, \hat{A}_T .

Qualitative description of scatter

Sawtooth topography T_I is defined by the horizontal wavenumber $\hat{k}_T = 0.117 \text{ mm}^{-1}$ and an aspect ratio of $\hat{A}_T\hat{k}_T = 0.585$, so that the slopes of T_I are less steep than those of T_H . Length scale ratios for T_I have values $k_c/\hat{k}_T = 3.02$ and $\hat{A}_Tk_c = 1.77$, the latter equal to that of sawtooth T_H . Figure 6.14 (a-c) shows RMS_T images for wavefields with θ/α equal to (a) 0.80, (b) 0.87 and (c) 0.95, and with σ/N equal to 0.56, 0.49 and 0.41 respectively, as well as corresponding forward, (d-f), and backward, (g-i), scattered wavefields after filtering using Hilbert transforms. The same conventions used in figures 6.4 and 6.11 are applied here. The structure of the wavefields shown in RMS_T and forward and back-scatter filtered images of figure 6.14 (a-c), (d-f) and (g-i), respectively, is generally qualitatively the same as corresponding images for scatter at T_H . Sawtooth T_I is characterised by a smaller topographic wavenumber than T_H and hence larger across-beam length scales are visible in the scattered wavefields for T_I than T_H . As a consequence of these larger length scales, viscous attenuation of wave energy scattering from T_I is less rapid, as is observed in the larger RMS_T amplitudes of the forward scattered wavefield as compared with those at T_H .

Spectral analysis of scatter at T_I

Figure 6.15 (a), (c) and (e) show spectra relating to forwards scattered wavefields for T_I , calculated along cross-sections positioned at various distances along B_F and B_F^* for values of θ/α and σ/N corresponding to those of figure 6.14 (a)-(c) respectively. The corresponding spectral differences

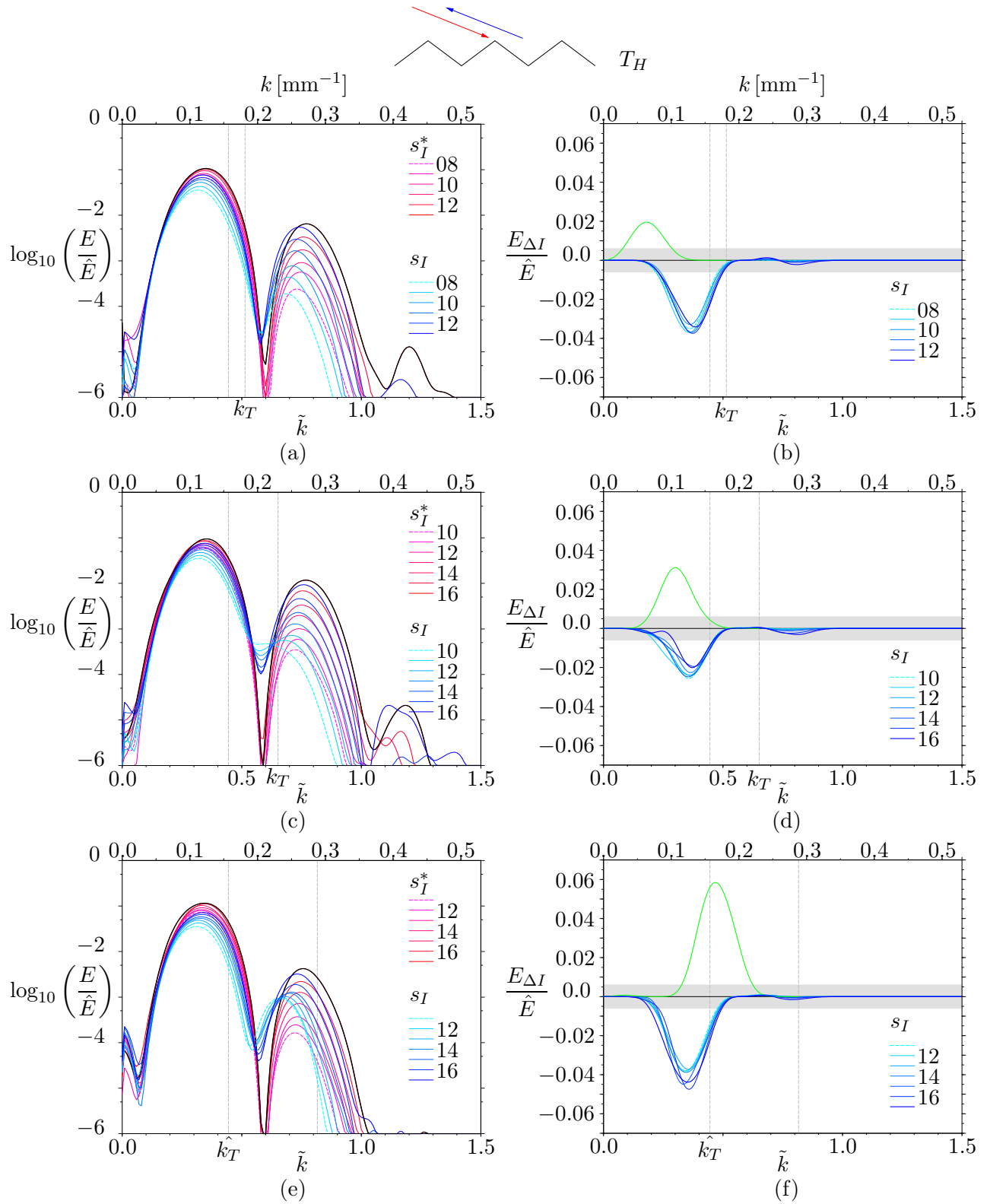


Figure 6.13: Back-scattered energy density spectra for sawtooth T_H are plotted in (a, c, e). Corresponding spectral differences are plotted in (b, d, f). Frequencies decrease down the page with θ/α equal to (a,b) 0.77, (c,d) 0.88 and (e,f) 0.97.

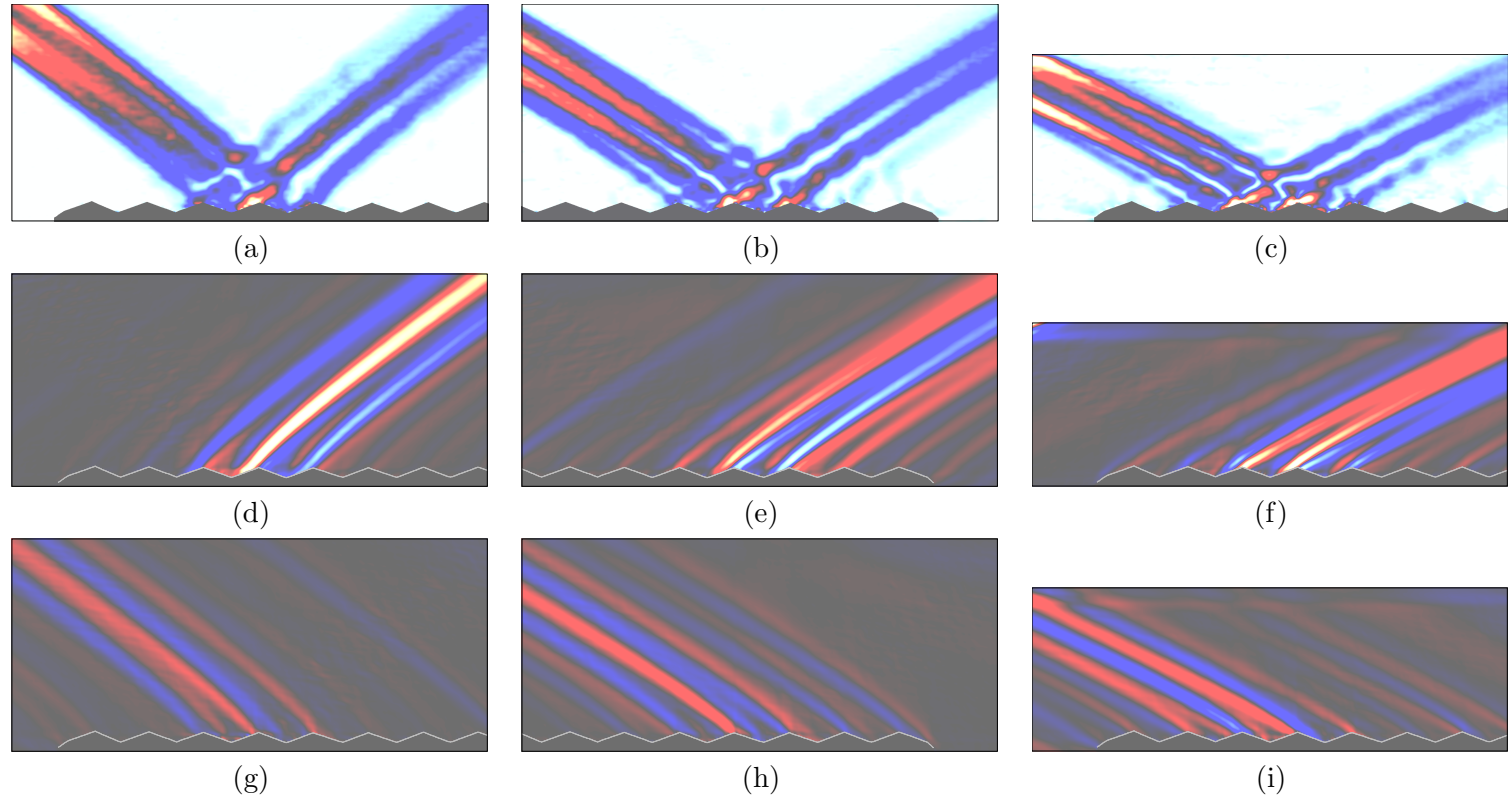
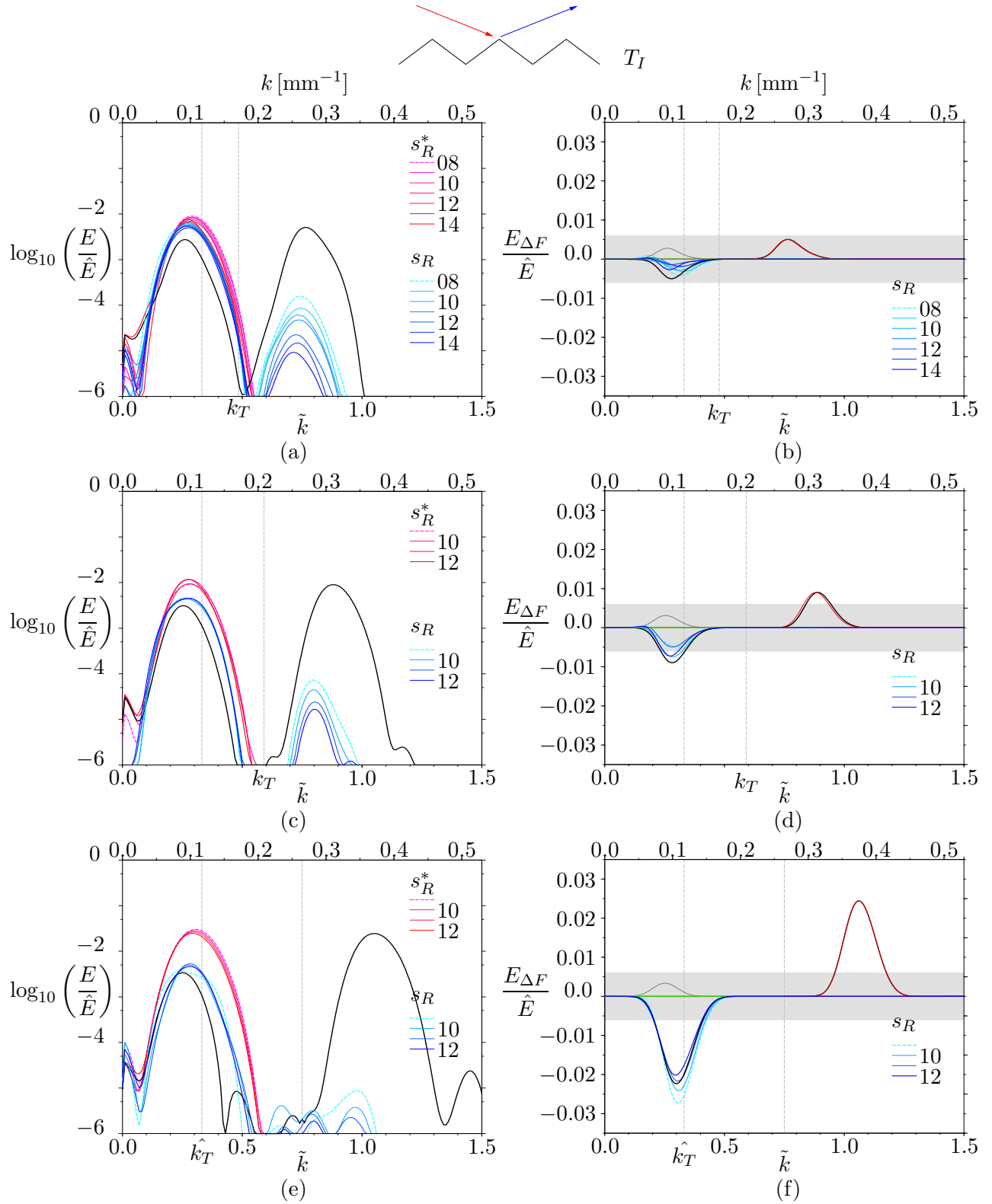


Figure 6.14: RMS_T images of $\Delta N^2/N^2$ fields for subcritical scatter at sawtooth T_I , with $\alpha = 69.5^\circ$, at forcing frequencies such that θ/α is equal to (a) 0.80, (b) 0.87 and (c) 0.95. Images of corresponding forward and back-scattered wavefields after filtering using the Hilbert transform are shown in (d)-(f) and (g)-(i) respectively, with upper edge of topography highlighted in grey. Fields of view measure 449×193 mm and 449×148 mm. Colour scale as in figure 6.4.



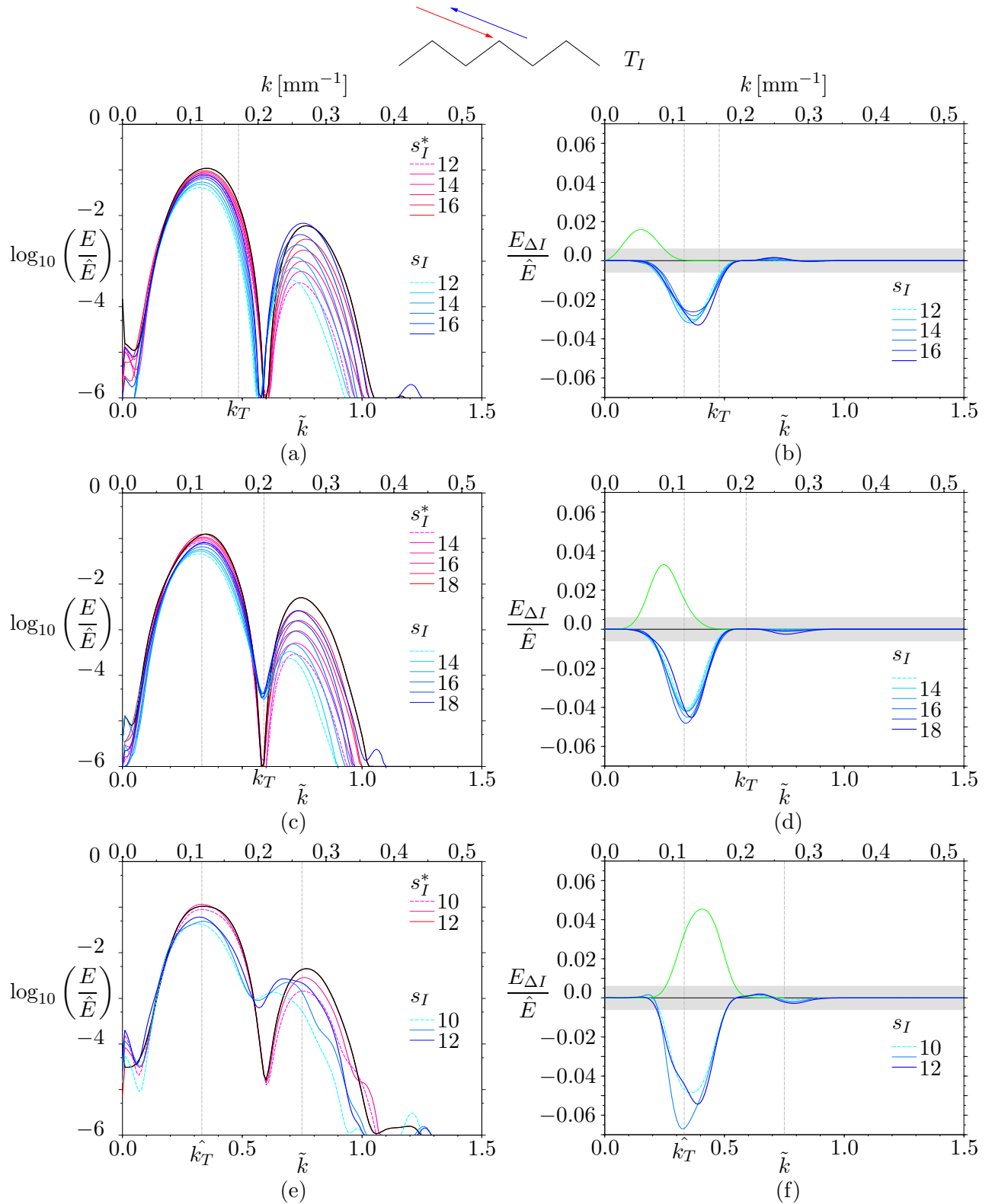


Figure 6.16: Back-scattered energy density spectra for sawtooth T_I are plotted in (a, c, e). Corresponding spectral differences are plotted in (b, d, f). Frequencies decrease down the page with θ/α equal to (a,b) 0.80, (c,d) 0.87 and (e,f) 0.95.

are shown in figure 6.15 (b), (d) and (f). Predicted (Baines 1971a) and measured spectra for the forwards scatter at T_I are qualitatively very similar to those for the corresponding scatter at T_H . The predicted behaviour is most closely followed by scattered wavefields associated with T_I . In part this may be due to the smaller value of $\hat{A}_T \hat{k}_T$, which is closer to satisfying the linearity condition of the theory and hence may suggest a reduction in nonlinear behaviour as compared with that for scatter at T_H . In addition, ray theory predictions suggest incident wave energy is focused less at the shallower slopes of T_I , which is also characterised by a smaller topographic wavenumber. Hence wavenumbers, energy densities and shear in the scattered wavefields of T_I are smaller in the near-field than for those of T_H , so that near-field viscous dissipation on the wave energy propagating away from T_I is also smaller. Scatter at T_I therefore produces a *greater* amount of high wavenumber scatter in the far-field than T_H , which has the larger aspect ratio and topographic wavenumber.

Figure 6.16 (a), (c) and (e) show spectra for the superposition of the incident and backwards scattered wavefields at T_I calculated along cross-sections at various along-beam distances of B_I and B_I^* for values of θ/α and σ/N corresponding to those in the spectra of figure 6.15 (a), (c) and (e) respectively. Corresponding spectral differences are shown in (b), (d) and (f). There are no significant distinctions between measured back-scatter spectra of T_I and the corresponding spectra of T_H .

6.3 Topographic shape

This section discusses the effect on scattered wavefields of variation of the topographic shape. Forward and back-scattered wavefields at sawtooth profile T_G are compared with those at sinusoid T_A , for which $\hat{k}_T = 0.085 \text{ mm}^{-1}$, $\hat{A}_T \hat{k}_T = 0.829$, $k_c/k_T = 4.15$ and $\hat{A}_T k_c = 3.44$, and square-wave T_K , for which $\hat{k}_T = 0.087 \text{ mm}^{-1}$, $\hat{A}_T \hat{k}_T = 0.783$, $k_c/\hat{k}_T = 4.06$ and $\hat{A}_T k_c = 3.18$, as well as the associated scatter to higher temporal harmonics.

6.3.1 Scatter from a sinusoid (T_A)

Scatter at sinusoidal profiles was discussed in sections 2.5 and 4.5 in the context of smoothly varying topographies. The discussion of scatter at the sinusoid given in the present chapter is included as a comparison to scatter at rough topography. In contrast to sawtooth profiles, which are piece-wise linear, the sinusoid is a smoothly varying profile that does not exhibit sharp corners. An angle α can be defined for a given sinusoid as in (6.1) (see also section 2.5), *i.e.* that of the analogous sawtooth, which has the same values of \hat{k}_T and \hat{A}_T . The angle made between the tangent to a sinusoid and the vertical varies continuously along its surface and purely subcritical behaviour, as defined by geometrical ray tracing, is only achieved for values of θ such that $\cot \theta > \hat{A}_T \hat{k}_T$. Consequently, whilst scatter of a given wavefield at a sawtooth can be defined as purely subcritical away from corners for $\theta/\alpha < 1$, a mixed scattering regime is typical for the corresponding sinusoidal profile, with regions of sub, super and near-critical scatter simultaneously predicted along its surface. A

maximum value of α below which values of θ are everywhere subcritical along the boundary is therefore defined for a given sinusoid as $\alpha_s = \cot^{-1}(\hat{A}_T \hat{k}_T)$ (see also section 4.5.1). Geometrical ray tracing predicts complete forward scatter of incident wave energy at a sinusoid for purely subcritical regimes (e.g. Longuet-Higgins 1969), *i.e.* $\theta/\alpha_s < 1$, whilst linearised boundary theory (Baines 1971a), which assumes a small boundary aspect ratio such that $\hat{A}_T \hat{k}_T \ll 1$, predicts an additional back-scattered component at second order provided that the incident wavenumber, k_I , satisfies $k_I < \hat{k}_T / \cot \theta$.

At sinusoidal boundaries that are not purely subcritical, linear geometrical ray tracing predicts both forwards and back-reflected wave energy through direct and multiple specular interactions of rays with the boundary. Ray tracing does not resolve behaviour at critical points along the boundary. Forwards and back-reflected coefficients (Longuet-Higgins 1969), oscillate in magnitude for increasing θ/α , in contrast to scatter at sawtooth topographies for which $C_F = 1$ and $C_B = 0$ in subcritical interactions and $C_F = 0$ and $C_B = 0$ in supercritical interactions. Shadow zones are also predicted for the sinusoid.

Qualitative description of scatter

Sinusoid T_A is closely analogous to sawtooth profile T_G . Figure 6.17 (a-c) shows RMS_T images for wavefields scattering at sinusoid T_A with θ/α equal to (a) 0.78, (b) 0.88 and (c) 0.97 for σ/N equal to 0.66, 0.58 and 0.50 respectively, as well as corresponding forward, (d-f), and backward, (g-i), scattered wavefields after filtering using Hilbert transforms. The same conventions used in figure 6.4 are applied here. The structure of wavefields shown in RMS_T and forward and back-scattered filtered images of figure 6.17 (a-c), (d-f) and (g-i), respectively, is generally qualitatively the same as in corresponding images for scatter at T_G . Forward scattered wavefields in RMS_T images of T_A appear to be associated with slightly larger amplitudes than those for T_G . According to ray tracing predictions for the sinusoid, incident wave energy can be both focused and defocused (to varying degrees) at different points along the boundary, whilst wave energy incident at the sawtooth is *focused everywhere* along sections of the boundary that have positive slope (see focusing coefficients in figure 6.6). It might therefore be expected that energy densities of forwards scattered fields associated with T_G would be greater than those for T_A , particularly for θ/α near-critical. However, viscous attenuation of the more focused scattered wave energy at T_G , which is characterised by higher wavenumber components and larger shear, is greater than the attenuation of that of T_A , so that the scattered wavefields observed at T_G are weaker in the far-field. A localised source of high wavenumber scatter is also introduced by the sharp corner of sawtooth T_G . The forwards and back-scattered wavefields at T_A follow the same trends with increases in θ/α as are observed for sawtooth T_G . The near-field structures of T_A also exhibit mixing features similar, though less pronounced, to those discussed for T_G in section 6.2.2. This could be compared to the behaviour seen for elliptical and rectangular cylinders in sections 5.2.4 and 5.3.4, for which the mixing feature was seen to be most pronounced for the rectangular cylinders, which had sharp corners.

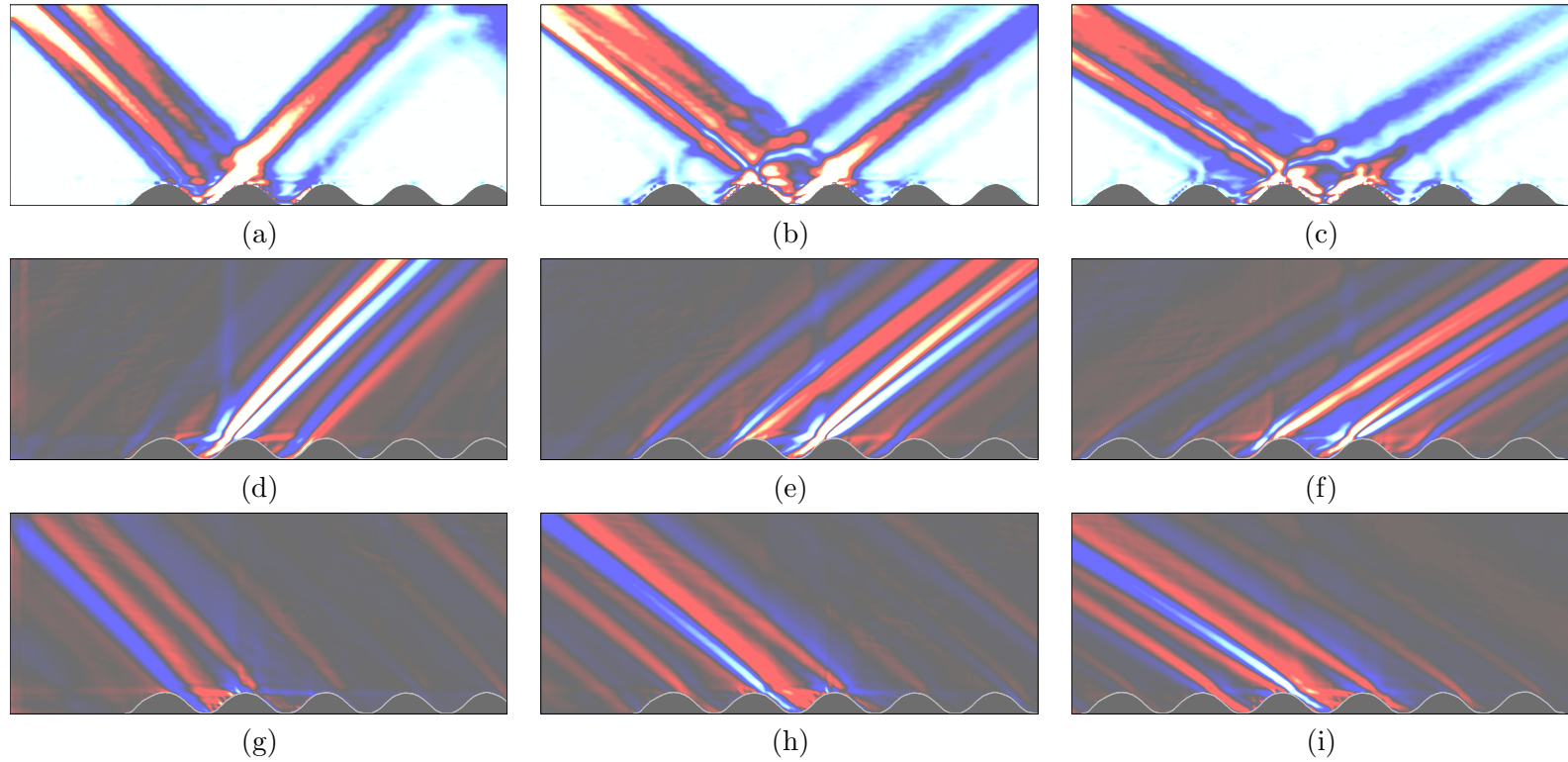


Figure 6.17: RMS_T images of perturbed buoyancy fields for subcritical scatter at sinusoid T_A , with $\alpha = 62.0^\circ$, at forcing frequencies such that θ/α is equal to (a) 0.78, (b) 0.88 and (c) 0.97. Images of corresponding forward and back-scattered wavefields after filtering using the Hilbert transform are shown in (d)-(f) and (g)-(i) respectively, with upper edge of topography highlighted in grey. Fields of view measure 449×182 mm. Colour scale as in figure 6.4.

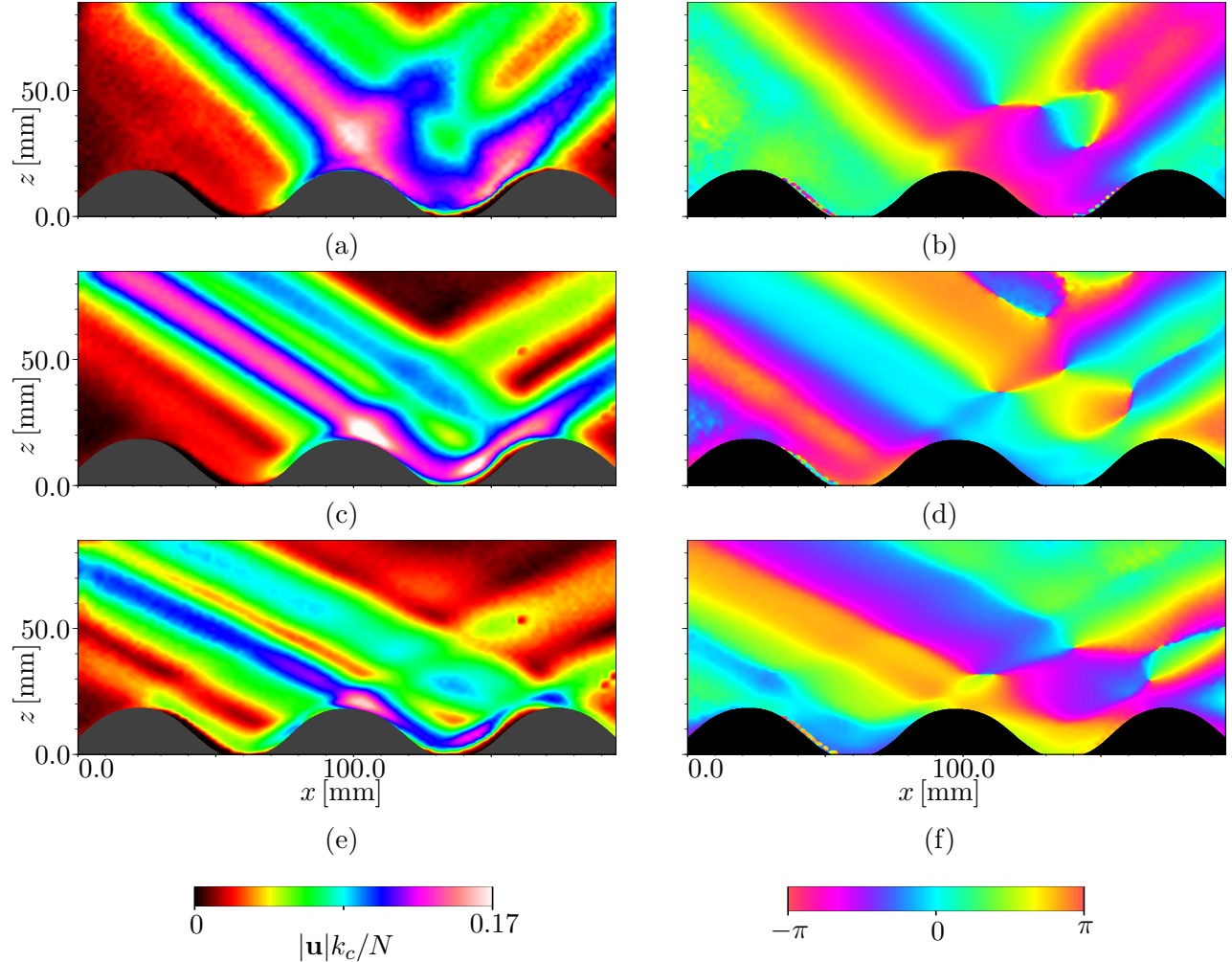


Figure 6.18: RMS_T velocity images of primary harmonics generated by subcritical scatter at sinusoid T_A with θ/α equal to (a) 0.68, (c) 0.87 and (e) 0.98 with σ/N equal to 0.74, 0.59 and 0.49 respectively (topography shaded in grey). Corresponding phase images are shown in (b), (d) and (f) (topography shaded in black).

Figure 6.18 presents results from PIV experiments in the near-field of the sinusoid profile T_A . Figure 6.18 (a), (c) and (e) show RMS_T velocity, denoted $|\mathbf{u}|$, values after filtering for the primary harmonic at θ/α equal to 0.68, 0.87 and 0.98 respectively. Velocities are normalised by the quantity N/k_c . Corresponding phase images are shown in figure 6.18 (b), (d) and (f). In general, fluid speeds decrease as θ/α increases to near-critical. The speeds appear to be most pronounced in the region of critical points along the boundary and along characteristics emanating from these points. An increase in θ/α coincides with a decrease in the forcing frequency, σ/N . Note that whilst this implies an increase in the *group* velocities of the wavefield (*i.e.* the rate of energy propagation), a reduction is seen in the associated fluid speeds at the larger values of θ/α . Typical particle displacements can be calculated as ~ 1 mm, with maxima of ~ 2 mm.

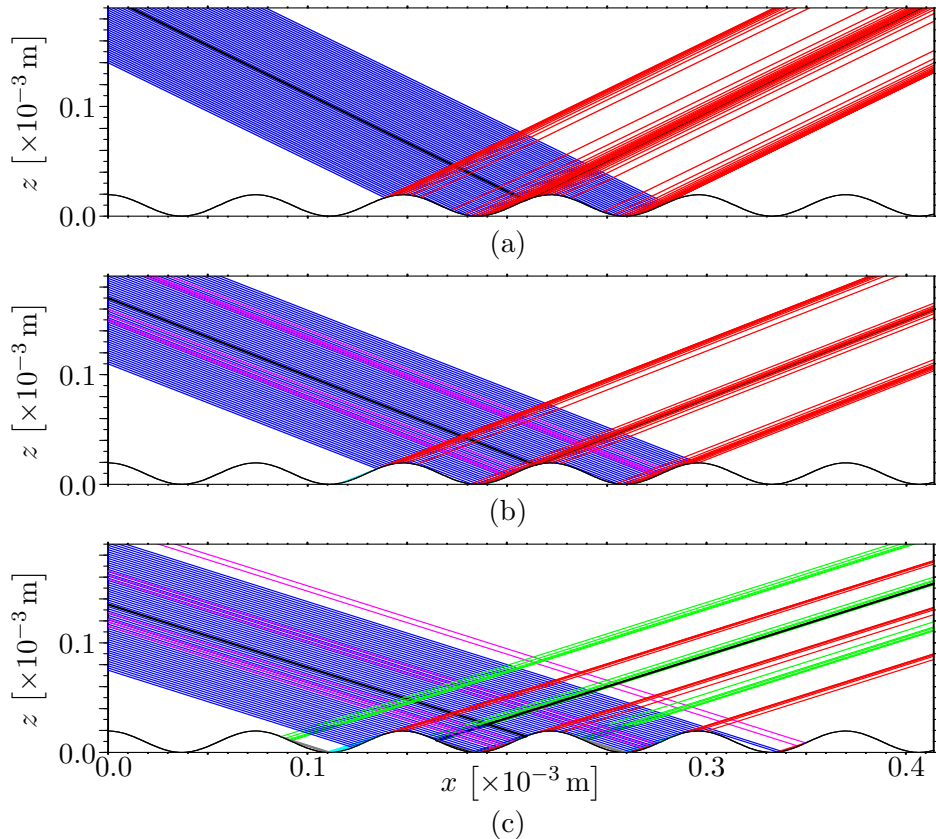


Figure 6.19: Ray tracing predictions for T_A . Here (a) $\sigma/N = 0.66$, $\theta/\alpha = 0.78$, (b) $\sigma/N = 0.58$, $\theta/\alpha = 0.88$ and (c) $\sigma/N = 0.50$, $\theta/\alpha = 0.97$. Blue lines denote incident rays (constituents of B_I); red denote forwards reflected rays from primary reflection ($\in B_F$); green denote forwards reflected rays after multiple reflections ($\in B_F$); magenta denote back-reflected rays after multiple reflections ($\in B_I$). Cyan, dark green, dark red, grey and yellow denote topography-topography reflections.

Ray tracing analysis of scatter at T_A

Ray tracing predictions, including primary and subsequent reflections of rays (blue) incident at sinusoid T_A , for parameter values corresponding to those in figure 6.17 (a)-(c) are shown in figure 6.19 (a)-(c) respectively. In each case, wave energy is incident from the top left-hand corner and interacts with the topography positioned at the bottom of the fields of view. Colour schemes for the incident and reflected rays are described in the figure captions. Similar figures were also presented in section 4.5.1 for sinusoids T_A and T_B . The forwards scattered wavefield predictions shown in the ray tracing diagrams of figure 6.19 compare *qualitatively* well with the corresponding RMS_T images of figure 6.17. The scatter is defined as purely subcritical for the parameter values of figure 6.19 (a) and ray tracing therefore predicts complete forward scatter for this configuration, *i.e.* $C_B = 0$. However, the corresponding filtered image for the back-scatter shown in figure 6.17 (g) contradicts this. Note that a back-scattered component *is* predicted at second order by the linearised boundary theory of Baines (1971a). The ray tracing back-reflection coefficients corresponding to figure 6.19 (b)

and (c) are calculated as $C_B = 0.36$ and 0.32 respectively, *i.e.* a larger degree of back-reflection is predicted for the *smaller* value of θ/α for these two experiments. Back-reflection coefficients, C_B , are calculated using a macro written to trace paths of 1000 rays incident over a region of the boundary measuring $\sim 5\lambda_T$. Coefficients calculated using the macro were invariant with further increases in incident ray densities. Back-reflection is shown by the magenta lines on ray tracing diagrams. By comparison, ray tracing predicts $C_B = 0$ at sawtooth T_G for *all* experiments at the parameter values associated with figure 6.17. As discussed in section 4.5.1, the applicability of ray tracing beyond qualitative structural predictions and estimates of proportions of back-reflection is limited and, as shown for the experiment corresponding to figure 6.19 (a), incorrect. Ray tracing is unaware of time and hence whether a wave is propagating in the correct direction. In particular, for subcritical scatter as defined for T_G , points of critical scatter at the sinusoid and scatter at corners of the sawtooth are not modelled by the ray tracing theory. Moreover, the effects of viscosity are not accounted for. More quantitative comparisons between scatter at T_A and T_G are made here.

Spectral analysis of scatter at T_A

Figure 6.20 (a), (c) and (e) show spectra relating to forwards scattered wavefields for sinusoid T_A , calculated along cross-sections positioned at various distances along B_F and B_F^* for values of θ/α and σ/N corresponding to those of figure 6.17 (a)-(c) respectively. The corresponding spectral differences are shown in figure 6.20 (b), (d) and (f). Spectra of T_A were presented and discussed in detail in section 4.5.2. Spectra included here are for experiments with similar parameter values to those for sawtooth T_G . The trends observed in the spectra for sinusoid T_A compare well with those shown for T_G in figure 6.7. The spectra for T_A follow the predictions of linearised boundary theory (Baines 1971a) more closely than those of the sawtooth, which is to be expected as the theory is calculated for a sinusoidal boundary. Chapter 5 compared wavefields *generated* by smooth elliptical cylinders and by rectangular cylinders, which featured corners. Figure 5.14 showed spectra associated with these wavefields and, in particular, compared those generated by circular and square cylinders. The influence of corners on the wavefields is apparent in these cases, with spectra of the two cylinders differing in form. Peaks of spectra for the square cylinder are around half the magnitude of those for the circular cylinder. This behaviour is attributed to significant generation of high wavenumber components, which are acted on rapidly by viscosity, at the corners of the square cylinder. In addition, the small group velocities of these components causes the associated wave energy to accumulate near the corners, promoting dissipation through nonlinear mechanisms. Spectra from wavefields scattered at the sawtooth exhibit discrepancies in magnitude with those at the sinusoid that are comparable with the discrepancies noted between spectra for square and circular cylinders in the generation case. It is therefore noteworthy that the spectra for *scatter* at the sinusoid and analogous sawtooth are so *similar* in form, whilst those for wavefields generated at the square and circular cylinders were more distinct.

Figure 6.21 (a), (c) and (e) show spectra for the superposition of the incident and backwards

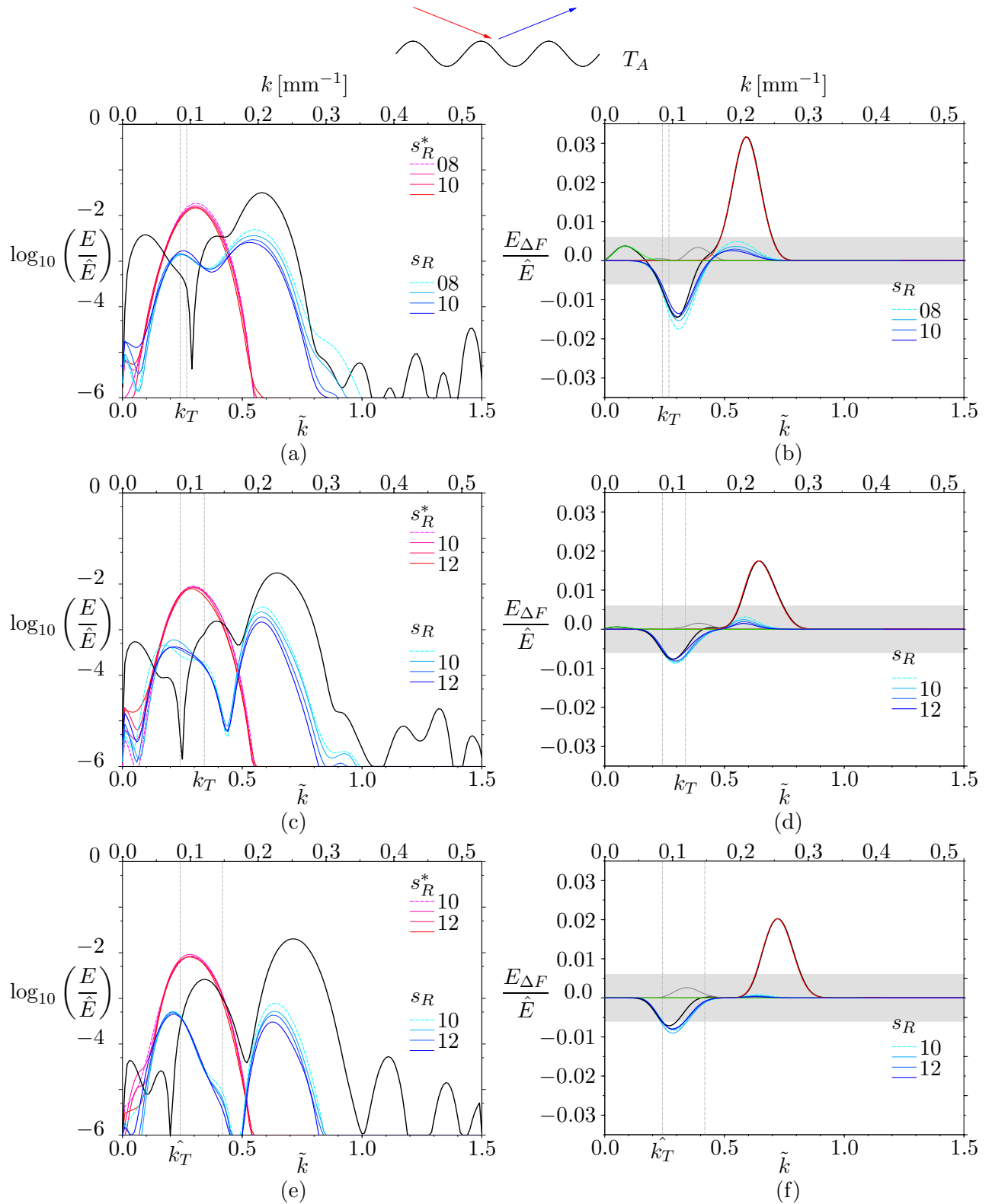


Figure 6.20: Forward-scattered energy density spectra for sinusoid T_A are plotted in (a, c, e). Corresponding spectral differences are plotted in (b, d, f). Frequencies decrease down the page with θ/α equal to (a,b) 0.78, (c,d) 0.88 and (e,f) 0.97.

scattered wavefields at T_A calculated along cross-sections at various along-beam distances of B_I and B_I^* for values of θ/α and σ/N corresponding to those in the spectra of figure 6.20 (a), (c) and (e) respectively. Corresponding spectral differences are shown in (b), (d) and (f). There is significantly stronger evidence in the difference spectra of figure 6.21 (d) and (f) than in those of sawtooth T_G for back-scatter to the predicted low wavenumber difference component. Measured difference spectra for the back-scatter at T_A exhibit a peak difference in the region of the predicted back-scattered component that increases in magnitude and breadth with θ/α to a maximum value for the experiments shown of $O(10^{-2})$. This difference peak is not seen in corresponding spectra for T_G . Back-scattered difference spectra for T_A also feature the equivocal region of high wavenumber scatter, as noted for spectra of T_G , which is not predicted by the linearised boundary theory. The predicted back-reflection coefficient has value $C_B = 0$ for the experiment corresponding to figure 6.21 (a,b), so that high wavenumber scatter contradicts ray theory in this case. However, at the other values of θ/α for which $C_B \neq 0$, high wavenumber scatter may in part represent the back-reflection predicted by ray theory.

Forward scatter at sinusoid T_A compares qualitatively well with that at sawtooth T_G . Both are generally consistent in form with the predictions of inviscid linearised boundary theory (Baines 1971a), with some suggestion of the generation of high wavenumber components in the spectral region of the predicted sum component. Dissipation of wave energy is enhanced in the case of the sawtooth, however, as the corners and linear slopes promote high wavenumber scatter and large energy densities. Near-field features such as mixing near the boundary are therefore most pronounced at the sawtooth, whilst high wavenumber scatter propagating away from this region is greatest for the sinusoid. Back-scattered wavefields for both topographies exhibit high wavenumber scatter, again largest in the far-field for the sinusoid, which is not predicted by the linearised boundary theory. The predicted low wavenumber difference component is only generated for the sinusoid however.

6.3.2 Scatter from a square-wave (T_K)

A square-wave topographic profile comprises of horizontal and vertical sections joined by 90° corners. Subcritical and supercritical regimes cannot be defined directly for the square-wave. Instead, a pseudo slope angle α is defined here for square-wave profiles as in (6.1) (see also section 3.8) and analogous periodic profiles that are not square-wave in shape are taken to be those sharing the same values of \hat{A}_T and \hat{k}_T . In the context of square-wave profiles, sub, super and near-critical regimes therefore refer here to those of the analogous sawtooth profile. The square-wave profile has four corners per topographic wavelength, twice the number of the sawtooth. Linear geometrical ray tracing predicts specular reflection behaviour of rays incident at the horizontal and vertical sections of the square-wave but does not resolve behaviour at the corners (e.g. Longuet-Higgins 1969). Specular reflection at infinite horizontal and vertical boundaries was discussed in detail in sections 2.4.1 and 4.2. The magnitude of the incident wavenumber is preserved at these boundaries,

with complete forward scatter, *i.e.* $C_F = 1$ and $C_B = 0$. The square-wave does not contain sloping surfaces like those of the sawtooth at which incident wave energy can be focused or defocused. However, the wavenumber spectra of a wavefield incident at a square-wave profile does not remain unchanged since topographic variation across the breadth of an incident wave group causes changes in phase between component rays of the group. Rays may reflect directly forwards or undergo multiple interactions with the topography before either reflecting away from the boundary in the forwards or backwards directions. As for ray tracing predictions for the sinusoid, coefficients for the forward and back-reflection are calculated to oscillate in magnitude for varying θ/α (Longuet-Higgins 1969). Ray tracing also predicts shadow zones, defined in section 2.5, for square-wave profiles.

Qualitative description of scatter

Square-wave T_K is closely analogous to sawtooth profile T_G and sinusoid T_A . Figure 6.22 (a-c) shows RMS_T images for wavefields scattering at square-wave T_K with values of θ/α equal to (a) 0.79, (b) 0.89 and (c) 0.99 for σ/N equal to 0.67, 0.58 and 0.49 respectively, as well as corresponding forward, (d-f), and backward, (g-i), scattered wavefields after filtering using Hilbert transforms. The same conventions used in figure 6.4 are applied here. The structure of forwards scattered wavefields shown in RMS_T and forward scatter filtered images of figure 6.22 (a-c) and (d-f), respectively, differs from those of the corresponding wavefields for sawtooth T_G in a number of ways. Forward scattered beam structures are broader and associated with lower energy densities than for those seen at T_G . In part, this is a consequence of the large proportion of horizontal surfaces comprising T_K , which do not focus wave energy directly as is the case at the slopes of T_G . The trend observed for sawtooth T_G of decreasing far-field wave amplitudes with increasing θ/α is also seen for T_K however, suggesting near-field dissipation is *increased* in this limit. The back-scattered fields shown in figure 6.22 (g-i) are more pronounced in all cases for the square-wave than those for sawtooth T_G . The variation of the back-scattered wavefield with increasing θ/α is not clear from these images though, in contrast to the behaviour at T_G and T_A , the weakest back-scattered field appears to be generated at the *largest* value of θ/α .

Figure 6.23 presents results from PIV experiments in the near-field of the square-wave profile T_K . Figure 6.23 (a), (c), (e) and (g) show normalised RMS_T velocity values after filtering for the primary harmonic at θ/α equal to 0.63, 0.70, 0.89 and 1.00 respectively. Corresponding phase images are shown in figure 6.23 (b), (d), (f) and (h). As in the experiments for sinusoid T_A , the fluid speeds tend to decrease as θ/α increases towards critical value. The speeds are the most pronounced in the region of corners of the topography and along characteristics emanating from these points. In critical conditions, the largest fluid speeds are confined to regions at the vertical level of the crests of the topography. As θ/α increases, spatial gradients in the wavefields can be seen to reduce significantly in phase images.

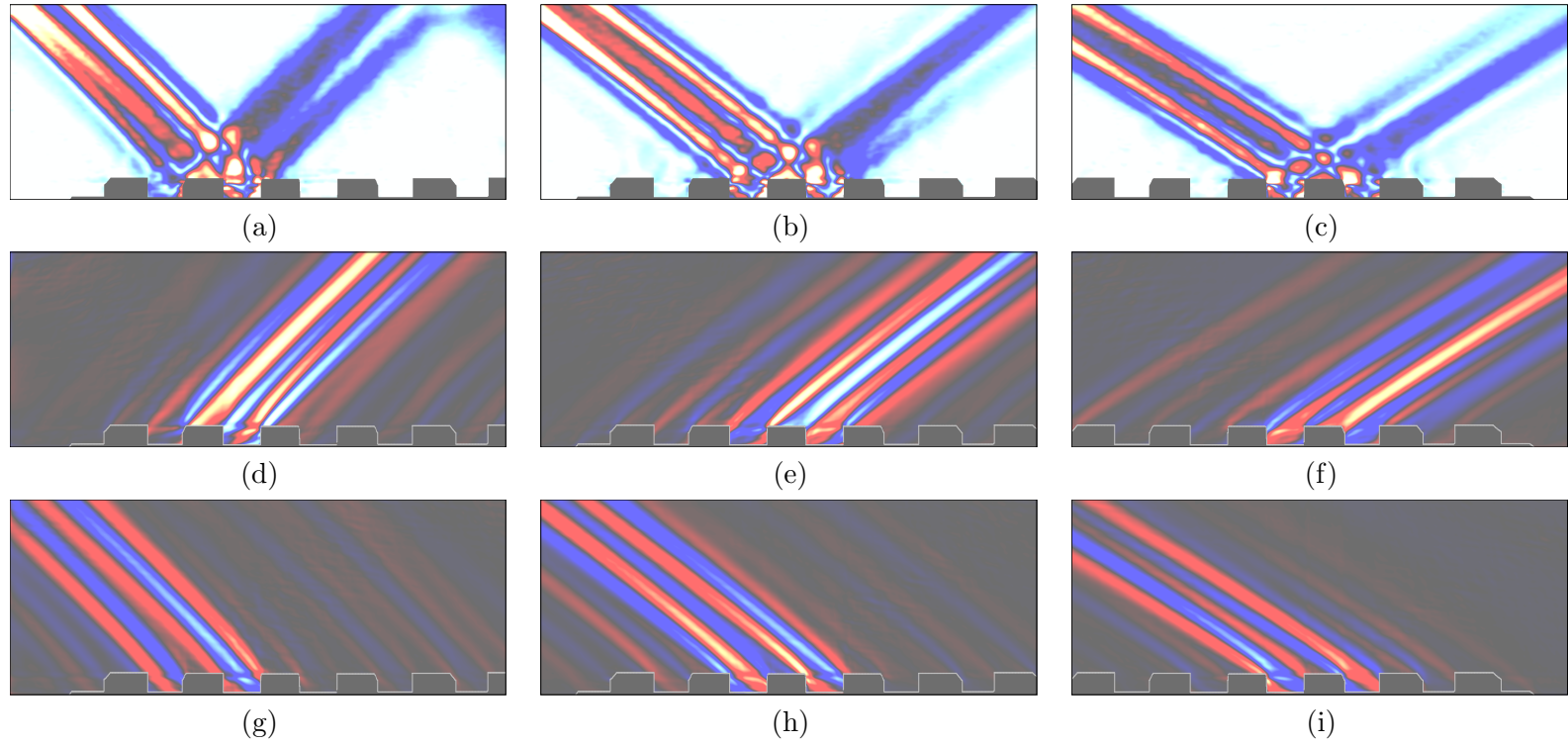


Figure 6.22: RMS_T images of perturbed buoyancy fields for subcritical scatter at square-wave T_K , with $\alpha = 61.0^\circ$, at forcing frequencies such that θ/α is equal to (a) 0.79, (b) 0.89 and (c) 0.99. Images of corresponding forward and back-scattered wavefields after filtering using the Hilbert transform are shown in (d)-(f) and (g)-(i) respectively, with upper edge of topography highlighted in grey. Fields of view measure 449×177 mm. Colour scale as in figure 6.4.

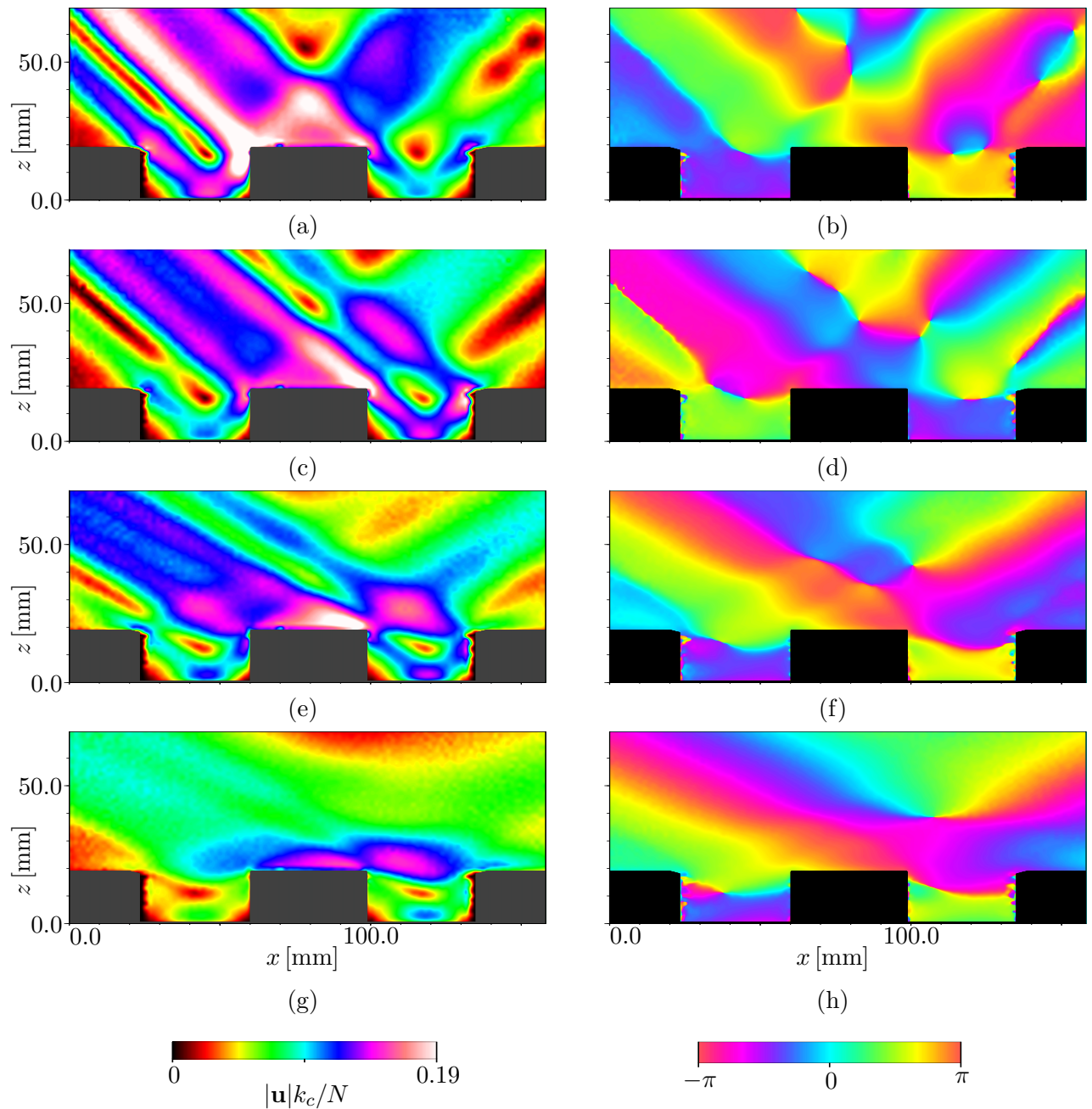


Figure 6.23: RMS_T velocity images of primary harmonics generated by subcritical scatter at square-wave T_K with θ/α equal to (a) 0.63, (c) 0.70, (e) 0.89 and (g) 1.00 with σ/N equal to 0.79, 0.74, 0.59 and 0.49 respectively (topography shaded in grey). Corresponding phase images are shown in (b), (d), (f) and (h) (topography shaded in black).

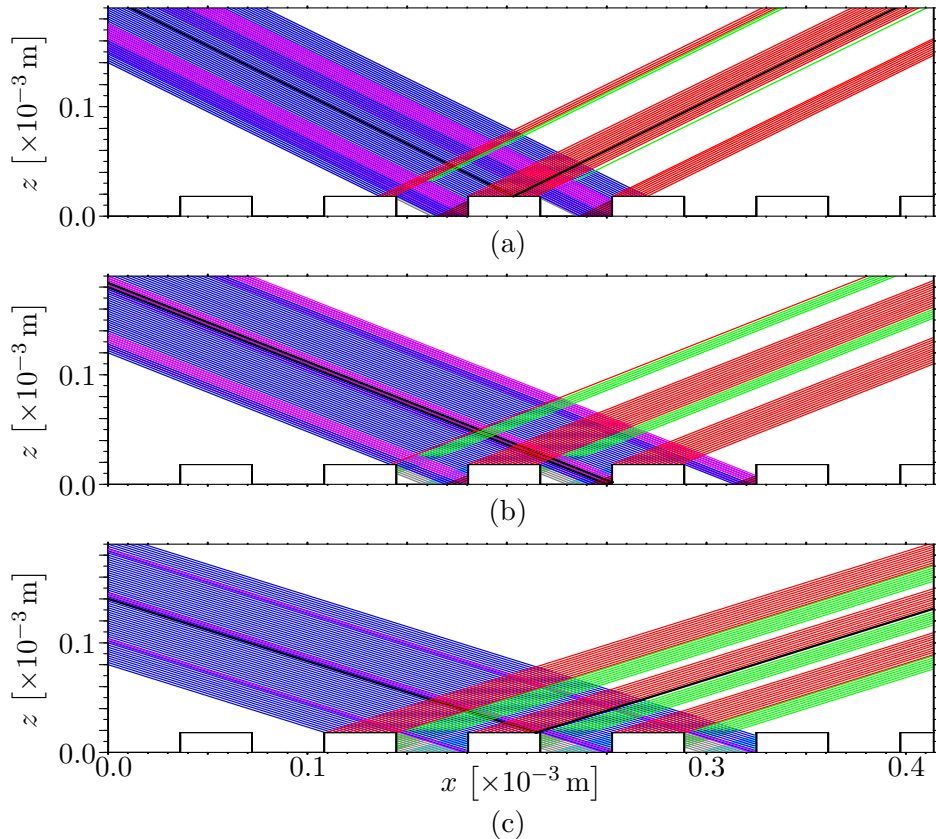


Figure 6.24: Ray tracing predictions for T_K . Here (a) $\sigma/N = 0.67$, $\theta/\alpha = 0.79$, (b) $\sigma/N = 0.58$, $\theta/\alpha = 0.89$ and (c) $\sigma/N = 0.49$, $\theta/\alpha = 0.99$. Line colouring as in figure 6.19.

Ray tracing analysis of scatter at T_K

Figure 6.24 (a)-(c) shows ray tracing predictions, including primary and subsequent reflections of rays (blue) incident at square-wave T_K , for parameter values corresponding to those in figure 6.22 (a)-(c), respectively. Conventions of the ray tracing diagrams are the same as those used in figure 6.19. Structures of the forwards scattered wavefield predictions shown in the ray tracing diagrams of figure 6.24 compare *qualitatively* well with the corresponding RMS_T images of figure 6.22. However, ray tracing predictions for the proportions of forwards scatter corresponding to figure 6.24 (a)-(c) are $C_F = 0.56$, 0.69 , and 0.88 respectively.

Figure 6.25 plots the variation with θ/α of C_F at T_K (cyan line), together with those for square-wave T_J (red line), knife-edge T_L (discussed in section 3.8, blue line) and the lower bound for sinusoid T_A (dashed green line). The coefficients are calculated using the method described by Longuet-Higgins (1969). In contrast to the behaviour seen in figure 6.22, ray tracing therefore predicts the greatest forward scatter at the largest value of θ/α . However, the experiment observations *are* consistent with the trends seen for the forwards scatter at sawtooth T_G and sinusoid T_A . As discussed for these cases, the spatial focusing of wave energy and redistribution to higher wavenumbers as

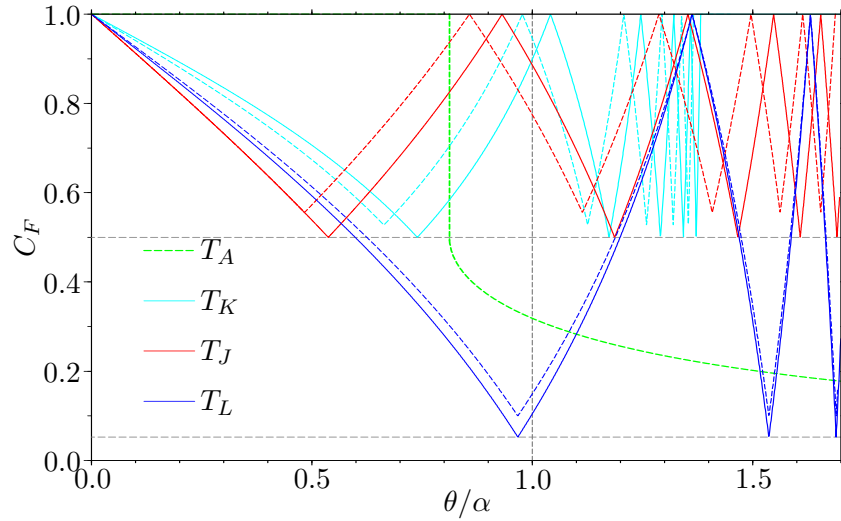


Figure 6.25: Ray tracing predictions for forward scatter coefficients at square-wave profiles T_J and T_K and pseudo knife-edge T_L , derived from method of Longuet-Higgins (1969). Dashed green line indicates the predicted lower bound for C_F at sinusoid T_A and horizontal dashed grey lines indicate lower bounds for C_F at T_J , T_K and T_L . Vertical dashed grey line indicates critical value for θ/α . Curve for T_J is truncated for clarity. Dashed cyan, red and blue lines are explained in chapter 7.

θ/α approaches critical promotes viscous and nonlinear behaviour so that near-field dissipation is enhanced and hence less wave energy propagates into the far-field. In addition, the length of near-field ray paths for the sinusoid and square-wave can be increased, relative to those reflecting at the sawtooth, by multiple interactions with the topography. In configurations for which this occurs, wave energy is retained in the near-field region, which is characterised by large gradients and high amplitudes, for a longer duration, *i.e.* conditions promoting nonlinear interactions, as well as being subject to an increased *period* of viscous attenuation before it propagates to the far-field.

Back-scatter coefficients calculated by ray tracing for figure 6.24 (a)-(c) are $C_B = 0.44$, 0.31 and 0.12 , respectively, with the weakest predicted for the near-critical value of θ/α . This is qualitatively consistent with the images of figure 6.22 (g)-(i). Note that the corresponding ray tracing predictions for the sawtooth of $C_B = 0.0$ in all cases, and for the sinusoid of $C_B = 0.0$, 0.36 and 0.32 , differ significantly from those for the square-wave. Observed back-scatter for both the sawtooth and sinusoid is most pronounced in the near-critical case, whereas back-scatter for the square-wave is *weakest* for this value of θ/α . Whilst it has been shown for the square-wave and sinusoid (sections 6.3.2 and 6.3.1) that *back-reflection* (*i.e.* through multiple specular reflections of wave rays with the topography) is not the only mechanism for back-scattered wave energy, it seems that there is at least consistency between maxima/ minima predicted by the ray tracing coefficients for the back-scatter and those of the observations. As for the sawtooth, the ray tracing fails to resolve scatter at corners of the topography.

Spectral analysis of scatter at T_K

Figure 6.26 (a), (c) and (e) show spectra relating to forwards scattered wavefields for square-wave T_K , calculated along cross-sections positioned at various distances along B_F and B_F^* for values of θ/α and σ/N corresponding to those of figure 6.22 (a)-(c) respectively. The corresponding spectral differences are shown in figure 6.26 (b), (d) and (f). The trends observed in the spectra for square-wave T_K compare well with those for sawtooth T_G and sinusoid T_A in figures 6.7 and 6.20. In particular, the spectra for T_K follow the predictions of inviscid linearised boundary theory (Baines 1971a) as convincingly as in the case of the sinusoid, *i.e.* more so than for the sawtooth. This suggests that dissipation of wave energy promoted by focusing along the linear slopes of the sawtooth, affecting most of the incident wave energy, is more significant than the enhancement in dissipation caused by focusing at the localised topographic corners, affecting only a small fraction of the incident wave energy, since the square-wave has twice as many corners per topographic wavelength than the sawtooth yet seems to exhibit less attenuation in spectra relative to the theoretical predictions for a sinusoidal boundary.

Figure 6.27 (a), (c) and (e) show spectra for the superposition of the incident and backwards scattered wavefields at T_K calculated along cross-sections at various along-beam distances of B_I and B_I^* for values of θ/α and σ/N corresponding to those in the spectra of figure 6.26 (a), (c) and (e) respectively. Corresponding spectral differences are shown in (b), (d) and (f). The difference spectra for the square-wave do not exhibit significant difference peaks in the spectral region of the difference component predicted by linearised boundary theory. Some evidence of higher wavenumber back-scatter is also observed in difference spectra for the square-wave.

6.3.3 Corners, slopes and curves

In summary, forward scatter at square-wave T_K compares qualitatively well with that at sawtooth T_G and sinusoid T_A . Scatter at each topography is generally consistent in form with the predictions of linearised boundary theory and high wavenumber scatter that appears to be in the spectral region of the predicted sum component is observed in each case. Forward scatter at T_A and T_K show less discrepancy with the theoretical predictions than that of sawtooth T_G , so that high wavenumber scatter measured in the far-field is most prominent for the sinusoid and square-wave profiles. For T_A , T_K and T_G , back-scattered wavefields exhibit high wavenumber scatter, which is again most significant for the sinusoid and square-wave. In the case of the sawtooth experiments and for one value of θ/α for the sinusoid, the back-scatter was *not* predicted by linear ray tracing. Additional low wavenumber scatter, predicted by linearised boundary theory, is measured for the sinusoid. Near-field mixing features are the most prominent for the sawtooth profile.

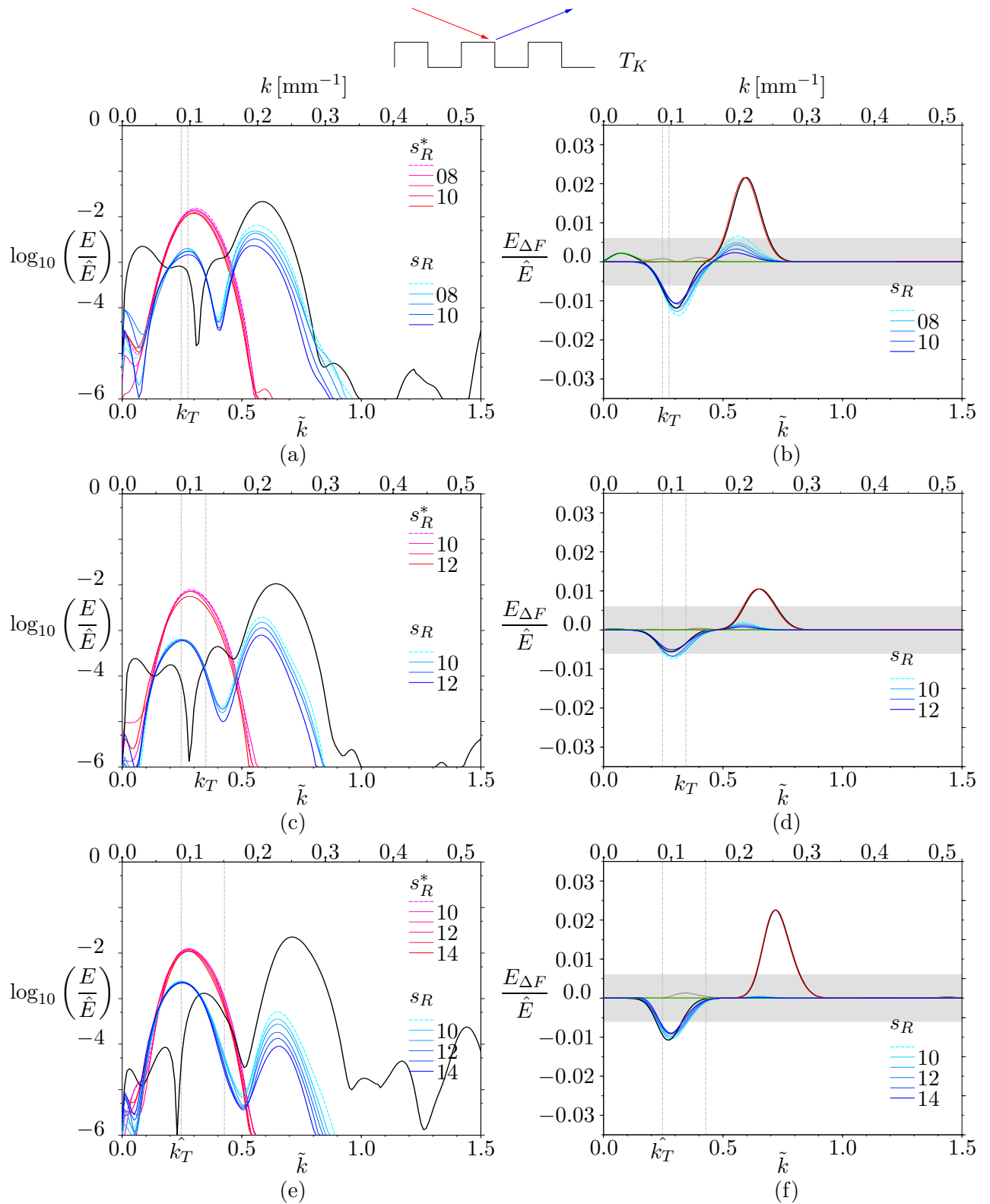


Figure 6.26: Forward-scattered energy density spectra for square-wave T_K are plotted in (a, c, e). Corresponding spectral differences are plotted in (b, d, f). Frequencies decrease down the page with θ/α equal to (a,b) 0.79, (c,d) 0.89 and (e,f) 0.99.

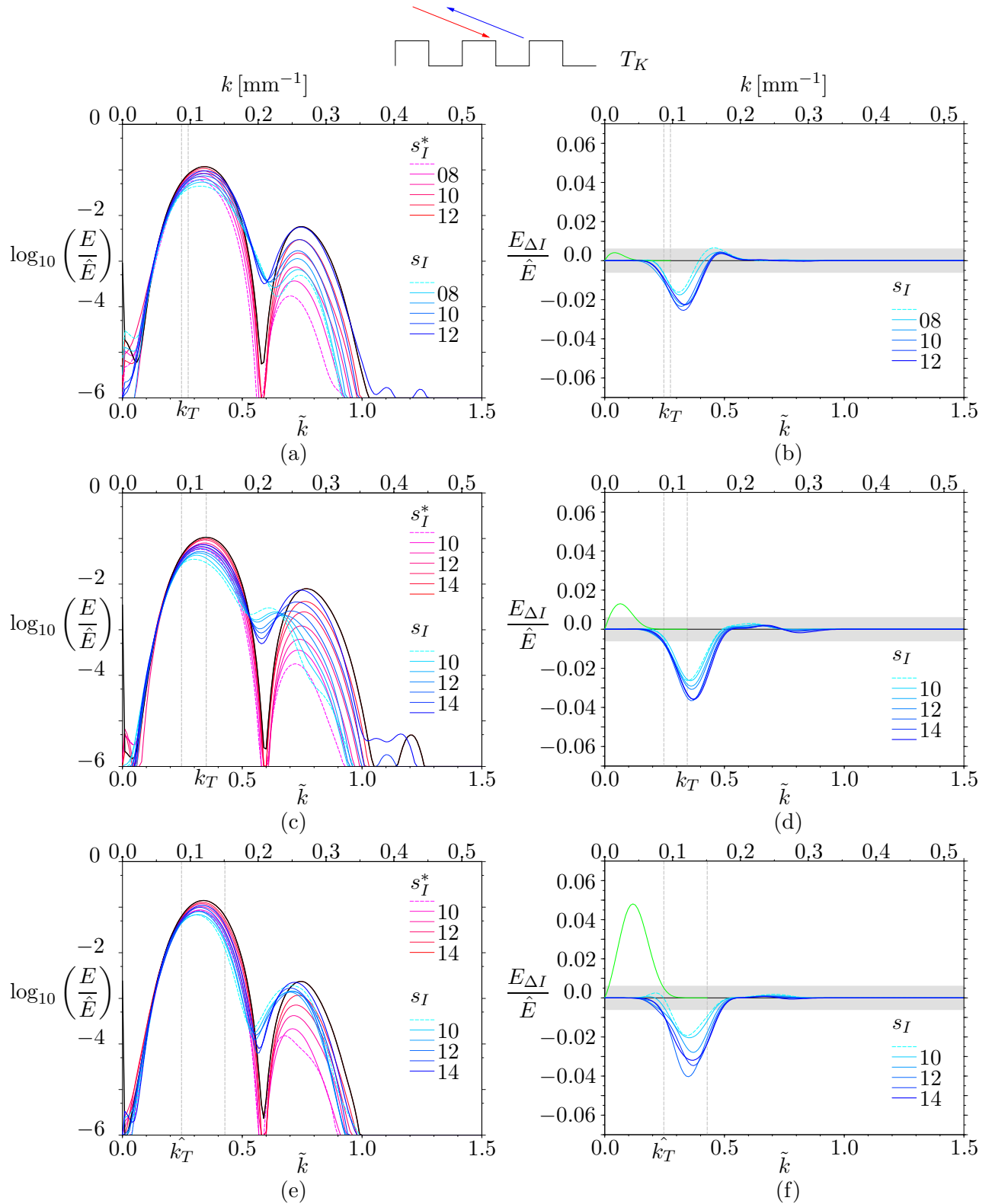


Figure 6.27: Back-scattered energy density spectra for square-wave T_K are plotted in (a, c, e). Corresponding spectral differences are plotted in (b, d, f). Frequencies decrease down the page with θ/α equal to (a,b) 0.79, (c,d) 0.89 and (e,f) 0.99.

6.4 Scatter to higher harmonics

Linear theory requires that the frequency of an internal gravity wavefield incident at a boundary is conserved on reflection (Lamb 1932; Phillips 1966). However, linear theory is less applicable in systems where amplitudes of the wavefield become comparable with characteristic length scales of the wavefield and in these cases higher temporal harmonics may be generated. The dispersion relation permits the generation of higher harmonic components that have frequencies $\sigma_n = n\sigma$ provided that the primary frequency satisfies $0 \leq \sigma/N \leq 1/n$ for $n \in \mathbb{Z}_{\geq 0}$. Scatter to secondary and tertiary harmonics of twice and three times that of the incident wave frequency, σ/N , respectively, were discussed in section 2.4.3 and described for experiment results of scatter at a flat boundary in section 4.2.3. Higher harmonic generation by cylinders of different shapes and dimensions was also presented in sections 3.7, 5.2.3 and 5.3.3. Secondary harmonic generation is described here for subcritical scatter at sinusoidal profile T_A , sawtooth T_G and square-wave T_K .

Figure 6.28 shows results from harmonic filtering of $\Delta N^2/N^2$ fields from experiments of marginally subcritical scatter at (a-d) sinusoid T_A , (e-h) sawtooth T_G and (i-l) square-wave T_K for θ/α equal to 0.97, 0.97 and 0.99 and incident frequencies, σ/N , equal to 0.50, 0.48 and 0.50 respectively, *i.e.* $1/3 < \sigma/N \leq 1/2$ in each case. Each image shows the incident wave energy propagating from the top left-hand corner towards the topographic profile positioned at the bottom of the image. Figure 6.28 (a), (e) and (i) show the amplitude fields (essentially the RMS_T field) from filtering for the primary frequency and figure 6.28 (c), (g) and (k) are the corresponding phase fields. The forwards and back-scattered wavefield structures shown in figures 6.17, 6.4 and 6.22 for the primary harmonic are clearly evident in the amplitude and phase images of the primary harmonic filtering shown in figure 6.28 (a,c), (e,g) and (i,k), respectively.

Figure 6.28 (b), (f) and (j) show the amplitude fields from filtering for the secondary harmonic frequency, $2\sigma/N$, and figure 6.28 (d), (h) and (l) are the corresponding phase fields. As described in section 4.2.3, a weak signature of the wavefield associated with the primary frequency remains in the images produced after filtering the wavefields for the secondary harmonic. This is an unavoidable consequence of the finite temporal resolution and lack of phase locking of the experimental movies. Since the primary harmonics are, albeit marginally, subcritical in each case, so are the secondary harmonics with values of θ_2/α for T_A , T_G and T_K equal to 0.13, 0.26 and 0.13 respectively, where θ_2 are the angles made between the group velocity vectors of the secondary harmonics and the vertical. Secondary harmonic generation is evident in the region where incident wave energy interacts with each of the topographic profile shapes, with maximum amplitudes approximately second order in the incident wave amplitude. Only secondary harmonic wave motion in the forwards direction is visible in phase images. These harmonics decay rapidly with distance away from the topography. The frequencies of each of the secondary harmonic components shown in figure 6.28 are close to N , resulting in small group velocities of these components and hence the confinement of the associated wave energy near to the boundary since the waves cannot propagate far before they have decayed. Also, the small values of θ_2/α , most clearly visible in the phase images, suggest

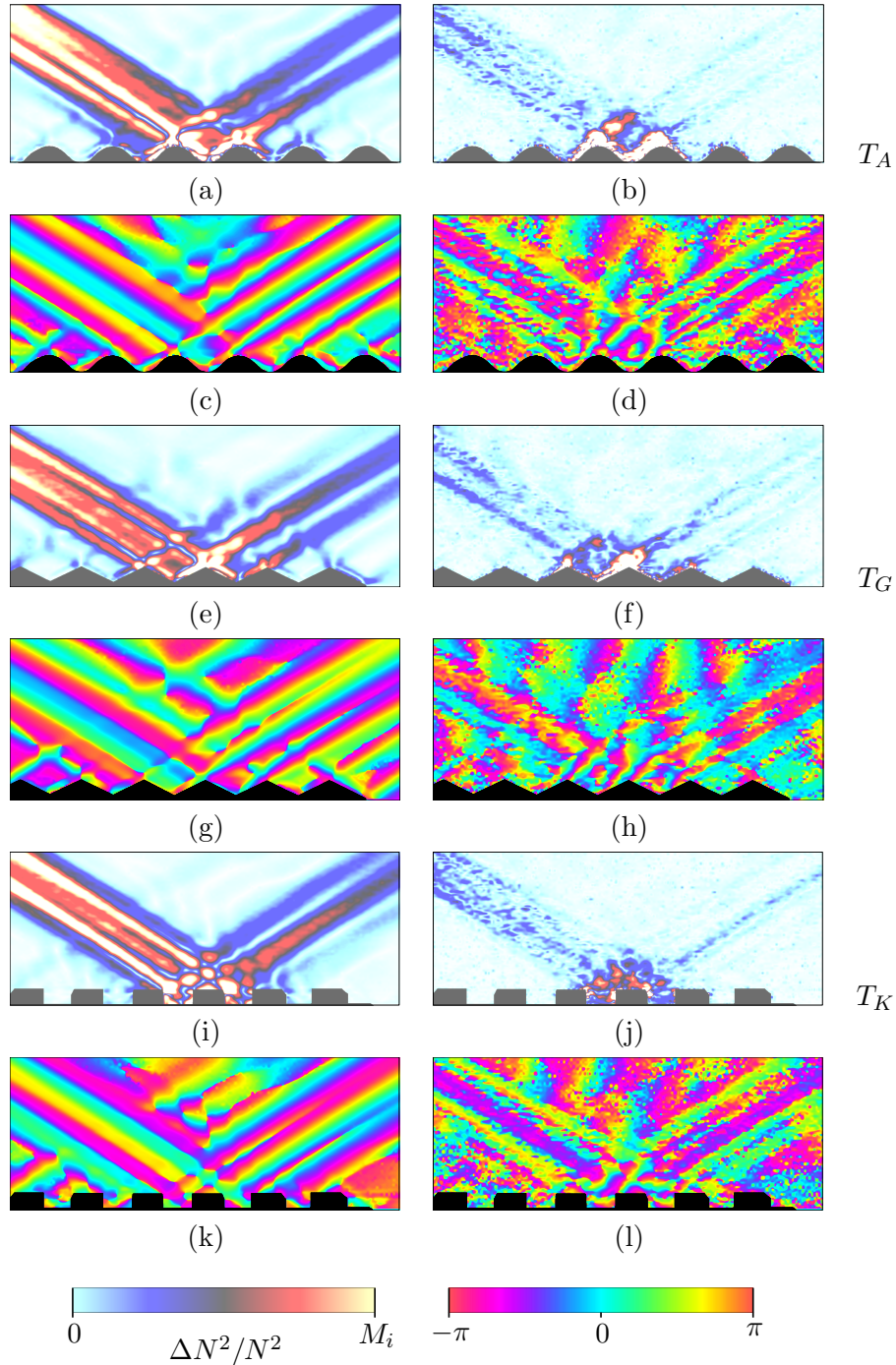


Figure 6.28: Amplitude and phase images of temporal harmonics generated by marginal subcritical scatter at sinusoidal, sawtooth and square-wave profiles T_A , T_G and T_K with $\sigma/N = 0.50$, 0.48 and 0.50 , $\theta/\alpha = 0.97$, 0.97 and 0.99 . RMS_T images of primary and secondary harmonics are shown in (a-b), (e-f) and (i-j) respectively. Corresponding phase images are shown in (c-d), (g-h) and (k-l). Amplitude maxima M_i have values of 5.4×10^{-2} , 5.4×10^{-3} and 5.4×10^{-4} for $i = 1, 2$ and 3 .

relatively small degrees of focusing of the secondary harmonic wave energy at the sloping regions of the boundaries, yielding weak amplitudes of the secondary harmonic wavefields there. The most pronounced secondary harmonic wavefield appears to be generated at the sinusoid, T_A , see figure 6.28 (b) and (d), with the wavefield generated across the entire region ‘lit’ by the incident wave beam. Secondary harmonics generated by scatter at the sawtooth, T_G , and square-wave, T_K , profiles are most prominent near the corners of these topographies, with the weakest wavefield generated at the square-wave. Wavefield amplitudes in the near-field of sawtooth T_G are expected to be greater (hence enhancing nonlinear behaviour) than those at the square-wave since wave energy is focused at the sloping sections of the sawtooth.

The generation of higher harmonics by elliptical and rectangular cylinders was analysed in, e.g. , section 5.3.3. There it was shown that amplitudes of the secondary harmonic wave motion generated were most pronounced near corners of the cylinders, but that the focusing of wave energy and high wavenumber skew of the spectra at the corners resulted in enhanced viscous attenuation of the wave energy as it propagated away from the source. This behaviour seems similar to that observed in the scattering experiments, with secondary harmonic wave energy most focused near topographic corners and rapidly decaying away from these regions.

Since the forcing frequencies, σ/N , in each of the experiments relating to figure 6.28 had values such that $\sigma/N > 1/3$, propagating tertiary harmonics of the wavefields were not predicted and no signatures were visible in images produced from filtering experiment data at this frequency. However, exponentially decaying (in space) disturbances could still be generated at third order.

6.5 Summary

This chapter has discussed subcritical scatter at various sawtooth topographies and compared this behaviour with scatter at analogous sinusoidal and square-wave profiles. The inviscid theoretical approaches of linear geometrical ray tracing (e.g. Longuet-Higgins 1969) and linearised boundary theory (Baines 1971a) have also been evaluated. In general, forwards and back-reflection coefficients calculated by ray tracing compare well qualitatively with behaviour observed in experiments. However, ray tracing fails to model scatter at corners or the critical value $\theta/\alpha = 1$ and does not yield quantitative predictions for the spectral scatter. In addition, some experimental results directly contradict the predictions of ray tracing with e.g. the presence of back-scatter at sawtooth profiles and purely subcritical scatter at a sinusoid. The linearised boundary theory of Baines (1971a) for a sinusoidal boundary, however, corresponds well with scatter at the sinusoid *and* sawtooth and square-wave profiles discussed, despite the violation of the conditions $\hat{A}_T \hat{k}_T \ll 1$ and $\hat{A}_T k_c \ll 1$. Wavenumber spectra exhibit regions of high wavenumber scatter associated with the predicted sum component characterised by the wavenumber $k_I + k_T$. High wavenumber scatter *not* predicted by the theory is also seen in the back-scattered spectra. The influence of viscosity significantly modifies scattered spectra, in particular reducing energy associated with high wavenumber scatter propagating into the far-field. Consequently, the least amount of high wavenumber scatter is mea-

sured in the far-field of the sawtooth, compared with those of the sinusoid and square-wave, since efficient focusing of wave energy along the linear slopes of the sawtooth and the introduction of high wavenumber components at the sharp corners enhances viscous attenuation of the scattered wave energy. Near-field features of the scatter, such as the generation of mixed fluid at topographic corners, are therefore more pronounced at the sawtooth, with high energy densities there promoting nonlinear behaviour. Experimental results of supercritical scatter at various rough topographic profiles are described in the following chapter.

Chapter 7

Supercritical rough topography

7.1 Overview

The previous chapter discussed subcritical scatter at rough sawtooth topographies and compared the observed behaviour with that at a sinusoid and a square-wave. The present chapter considers supercritical scatter, *i.e.* $\theta/\alpha > 1$, at sawtooth as well as square-wave and knife-edge topographic profiles.

Inviscid linear geometrical ray tracing predicts that wave energy incident at the sloping sections of supercritical sawtooth topography is repeatedly focused into the topographic troughs so that the predicted forward, C_F , and back-scatter, C_B , are both zero. Ray tracing does not, however, resolve behaviour at topographic corners and does not satisfy the radiation condition at rough boundaries. As in chapter 6, far-field and near-field scattering behaviour is discussed for variations in θ/α , \hat{k}_T (section 7.2) and topographic shape (section 7.3) as well as scatter to higher harmonics (section 7.4). Experimental results of this chapter are compared solely with the predictions of ray tracing, since the supercritical configuration has not been modelled by any other theoretical means. In addition, no other experimental or numerical studies of supercritical scatter at periodic rough topography are known to the present author.

7.2 Sawtooth topography

This section presents results relating to supercritical scatter at sawtooth topographies T_D and T_E . Comparisons are made in section 7.4 with wavefield behaviour near square-wave T_J and pseudo knife-edge T_L .

7.2.1 Basic sawtooth (T_D)

Supercritical scatter in experiments with sawtooth T_D and its variation with θ/α is discussed here. Sawtooth profile T_D is characterised by the horizontal topographic wavenumber $\hat{k}_T = 0.088 \text{ mm}^{-1}$

and an aspect ratio of $\hat{A}_T \hat{k}_T = 1.58$. Length scales of the incident wavefield are compared with those of T_D with the parameters $k_c/\hat{k}_T = 4.01$ and $\hat{A}_T k_c = 6.34$.

Qualitative description of scatter

Figure 7.1 (a-c) shows RMS_T images for wavefields with θ/α equal to (a) 1.23, (b) 1.36 and (c) 1.55 and σ/N equal to 0.57, 0.48 and 0.35 respectively, as well as corresponding forward, (d-f), and backward, (g-i), scattered wavefields after filtering using Hilbert transforms. The same conventions used in figure 6.4 are applied here. Contrary to ray tracing predictions of $C_F = 0$, the presence of a forward scattered wavefield is clearly visible in RMS_T and filtered images for the forward scatter. The forward scattered fields have a similar structural form to those observed for subcritical interactions, with scattered wave energy focused into narrow beam-like structures, which propagate away from the corners of the topography. In the fields of view shown, amplitudes associated with the forward scattered wavefields are typically two orders of magnitude smaller than those associated with the incident wavefield and are largest for values of θ/α nearest critical in both the near-field and far-field. Amplitudes of the forwards scatter are generally an order of magnitude smaller than those typical of the subcritical case for topography T_G , which has a topographic wavenumber approximately equal to that of T_D . Primary *downward* scatter is also visible within the troughs of topography T_D (see figure 7.3). Notably, non zero amplitudes are present in the lee of the each crest, contradicting the prediction of ‘shadow zones’ by ray tracing (illustrated in figure 7.2). The mixing feature described in section 6.2.1 near the corners of sawtooth T_G is present in supercritical conditions with T_D and is most prominent near-critical (e.g. see figure 7.1 (a)). In addition to the supercritical forward scatter, *back-scattered* wavefields, similar to those observed for subcritical scatter at T_G in figure 6.4 (g)-(i), are also evident in the RMS_T and filtered images for the back-scatter, despite ray tracing predictions of $C_B = 0$. The back-scatter appears to emanate from the corners of the sawtooth. Amplitudes of the back-scattered wavefields are of similar magnitudes to those for the forwards scatter and, as for the forward scatter and in the subcritical case, these amplitudes are most significant for values of θ/α closer to critical. It is anticipated that there is some relationship between the back-scatter of the subcritical case and the scatter, in both directions, of the supercritical case. The decrease in amplitudes of the forwards and back-scattered wavefields at larger θ/α may in part be due to the reduction in σ/N of the wavefields in these cases, which causes an increase in the group velocities and hence a decrease in energy densities. Figure 7.4 presents results from PIV experiments in the near-field of the sawtooth profile T_D . Figure 7.4 (a), (c) and (e) show normalised RMS_T velocity values after filtering for the primary harmonic at θ/α equal to 1.01, 1.08 and 1.49 respectively. Corresponding phase images are shown in figure 7.4 (b), (d) and (f). In general, fluid speeds tend to decrease as θ/α increases away from the critical value. As in the subcritical experiments at square-wave T_K , the speeds are the most pronounced in the region of corners of the topography and along characteristics emanating from these points. Maximum particle displacements of almost 4 mm occur for the near-critical value of θ/α in the region of the

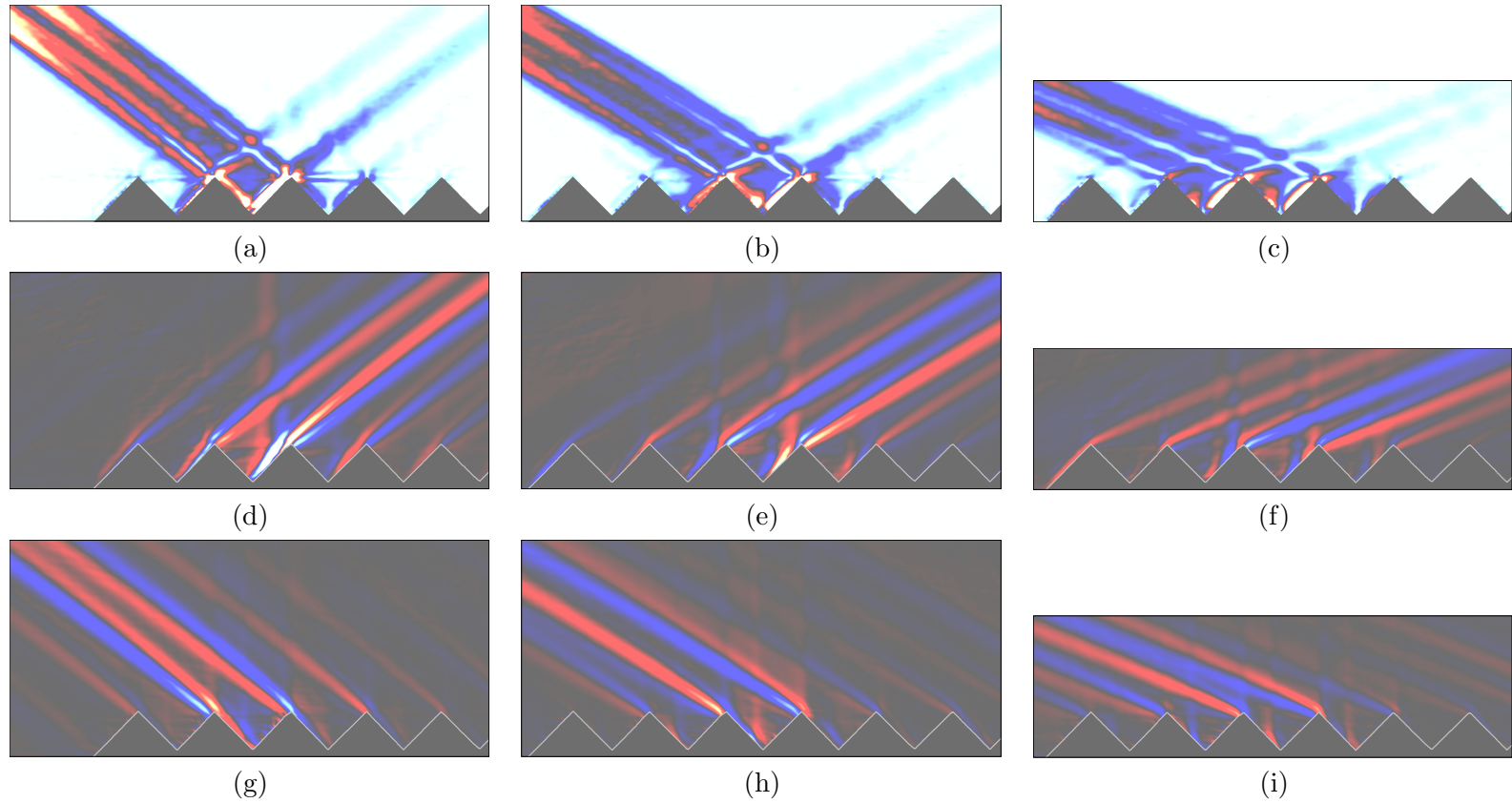


Figure 7.1: RMS_T images of perturbed buoyancy fields for supercritical scatter at sawtooth T_D , with $\alpha = 45.0^\circ$, at forcing frequencies such that θ/α is equal to (a) 1.23, (b) 1.36 and (c) 1.55. Images of corresponding forward and back-scattered wavefields after filtering using the Hilbert transform are shown in (d)-(f) and (g)-(i) respectively, with upper edge of topography highlighted in grey. Fields of view measure 449×203 mm and 449×133 mm, with unit aspect ratio. Colour scale as in figure 6.4.

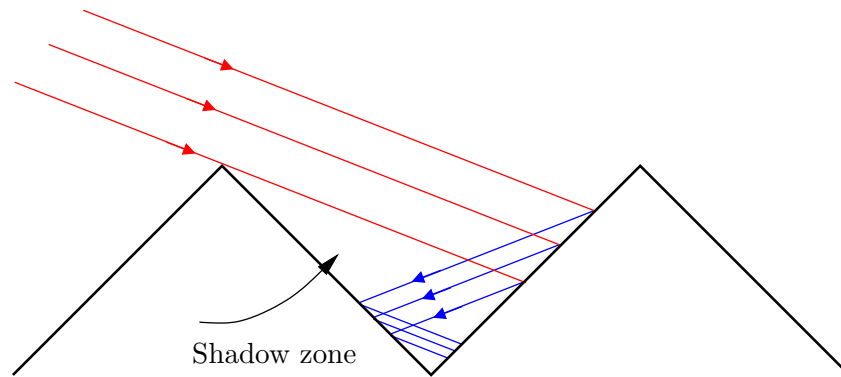


Figure 7.2: Ray schematic of shadow zone for supercritical scatter at sawtooth T_D .

topographic corner at the centre of the field of view.

Spectral analysis of scatter at T_D

Figure 7.5 (a), (c) and (e) show spectra relating to forwards scattered wavefields for T_D , calculated along cross-sections along B_F and B_F^* for values of θ/α and σ/N corresponding to those of figure 7.1 (a)-(c) respectively. The corresponding spectral differences are shown in figure 7.1 (b), (d) and (f). As in chapters 4 and 6, grey shaded regions of spectral difference graphs in this chapter indicate experiment and data processing error estimates based on figure 4.29. Whilst these regions indicate the estimated maximum magnitude of the error, the actual spectral *form* of the error is expected to be localised around peaks of the measured spectra. Magnitudes of the error calculated in figure 4.29 also decrease as energy density measurements associated with beam cross-sections decrease at along-beam locations further from the cylinder. It is therefore estimated that actual error values corresponding to cross-sections of B_F and B_F^* , *i.e.* forwards scatter, may in practice be an order of magnitude smaller than that indicated. In contrast to the subcritical configurations discussed in section 6.2.1, there is an absence of theoretical models for supercritical scatter except for those of ray tracing, which predicts that there is no forward or back-scatter to the far-field. Hence, spectra in the present section only display results from experiments. Measured spectra associated with the incident wavefields at T_D plotted (red shades) in figure 7.5 (a), exhibit dominant peaks at $\tilde{k} \approx 0.3$ with magnitudes of $\sim O(10^{-2})$. Measured forwards spectra (coloured in blue shades) exhibit two dominant peaks of magnitudes $\sim O(10^{-4})$, with maxima located at $\tilde{k} \approx 0.2$, possibly suggesting a ‘primary’ forwards scattered component, and at $\tilde{k} \approx 0.55$. Whilst forwards scatter *is* observed in RMS_T images of figure 7.1, these peak magnitudes lie within the estimated error value and therefore cannot be interpreted as an accurate quantitative measurement. However, the spectra may still have some *qualitative* value in indicating approximate spectra locations of scattered components. If true, the peak of the forward scattered spectra located at higher wavenumbers is positioned near $\tilde{k} \approx 0.3 + k_T$, which could indicate the presence of a ‘sum’ component. Corresponding difference spectra of figure 7.5 (b) exhibit a trough with magnitude $\sim O(10^{-2})$ in the region

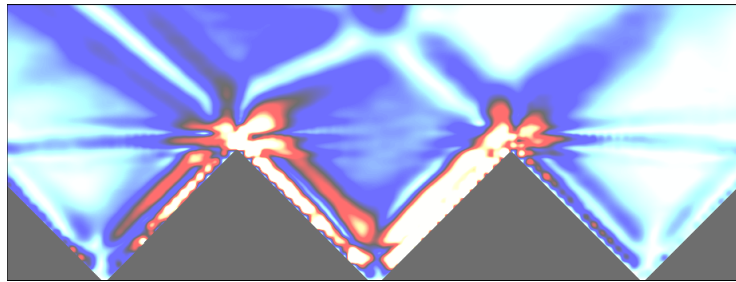


Figure 7.3: Close-up of scatter at profile T_D for $\theta/\alpha = 1.23$. Colour scale as in figure 6.9 except with maximum value 11.72×10^{-2} . Field of view measures 68×29 mm.

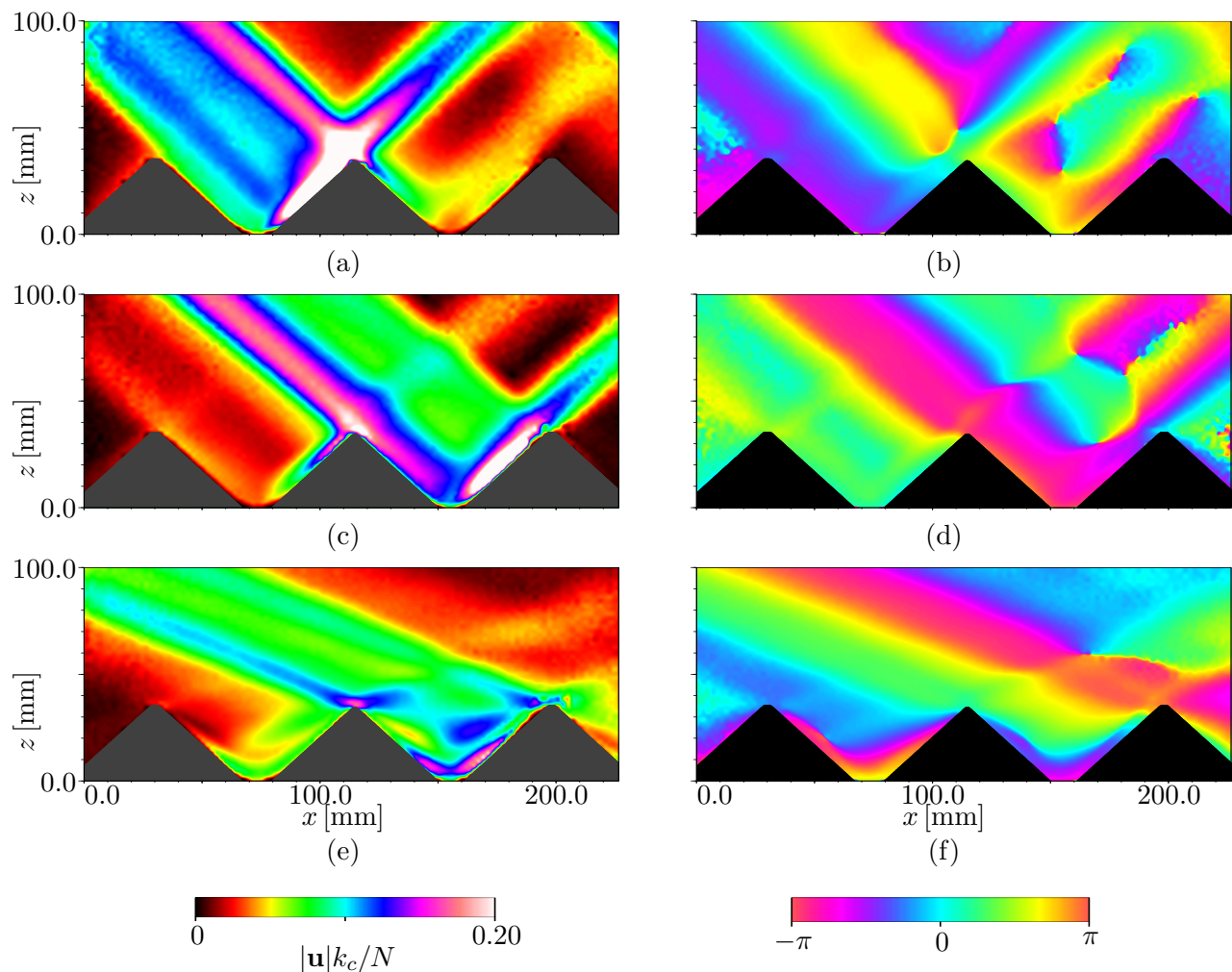


Figure 7.4: RMS_T velocity images of primary harmonics generated by supercritical scatter at sawtooth T_D with θ/α equal to (a) 1.01, (c) 1.08 and (e) 1.49 with σ/N equal to 0.70, 0.66 and 0.39 respectively (topography shaded in grey). Corresponding phase images are shown in (b), (d) and (f) (topography shaded in black).

of the spectral peak of the incident wavefield. There does not appear to be a significant scatter to lower wavenumbers in this supercritical configuration.

Figure 7.6 (a), (c) and (e) show spectra for the superposition of the incident and backwards scattered fields at T_D calculated along cross-sections of B_I and B_I^* for values of θ/α and σ/N corresponding to those in the spectra of figure 7.5 (a), (c) and (e) respectively. Corresponding spectral differences are shown in (b), (d) and (f), with regions shaded grey indicating error estimates based on figure 4.29. Distinctions between spectra are most easily seen in the spectral differences of figure 7.6. A high wavenumber difference peak is present in the spectral difference graph of figure 7.6 (b) at $\tilde{k} \approx 0.7$ with a peak difference magnitude comparable with that of the estimated error. No significant evidence of this peak difference is seen as θ/α increases. As for the forward scatter, back-scatter is *not predicted* by ray tracing. However, back-scatter associated with small across-beam length scales *is* observed in RMS_T images of figure 7.1 for each value of θ/α and the presence of peaks at high wavenumbers are therefore anticipated in the corresponding spectra. No significant back-scatter to *lower* wavenumbers is observed for this supercritical configuration. As in the subcritical spectra, the spectral differences also exhibit troughs located in the regions of the spectral peaks of the incident wavefield. These suggest that the spatial coincidence of the back-scattered and incident wavefields, which increases across-beam gradients, particularly since the phase velocities are opposing, results in enhanced viscous attenuation of the wave energy in the incident beam.

In contrast to ray tracing predictions, forwards and backwards supercritical scatter *is* observed at sawtooth T_D , with evidence of high wavenumber scatter in both directions. Energy densities associated with the scattered components appear to decrease as values of θ/α increase from critical.

7.2.2 High wavenumber sawtooth (T_E)

This section discusses the effect on scattered wavefields of variation of the topographic wavenumber, \hat{k}_T , for a fixed aspect ratio, $\hat{A}_T \hat{k}_T$, and hence topographic slope angle, α . Scattering behaviour at sawtooth T_E is compared here with that at T_D . Sawtooth profile T_E is characterised by the horizontal topographic wavenumber $\hat{k}_T = 0.175 \text{ mm}^{-1}$, almost twice that for T_D , and an aspect ratio of $\hat{A}_T \hat{k}_T = 1.58$, approximately equal to that for T_D . Length scale ratios of T_E have values $k_c/\hat{k}_T = 2.02$ and $\hat{A}_T k_c = 3.18$.

Qualitative description of scatter

Figure 7.7 (a-c) shows RMS_T images for wavefields with θ/α equal to (a) 1.20, (b) 1.38 and (c) 1.56 and σ/N equal to 0.59, 0.47 and 0.34 respectively, as well as corresponding forward, (d-f), and backward, (g-i), scattered wavefields after filtering using Hilbert transforms. The same conventions used in figure 6.4 are applied here. The nature of the wavefields shown in the RMS_T images of figure 7.7 (a-c) are generally qualitatively the same as the corresponding ones for the scatter at T_D except that the forward scattered wavefields of T_E , which has the larger topographic wavenumber,

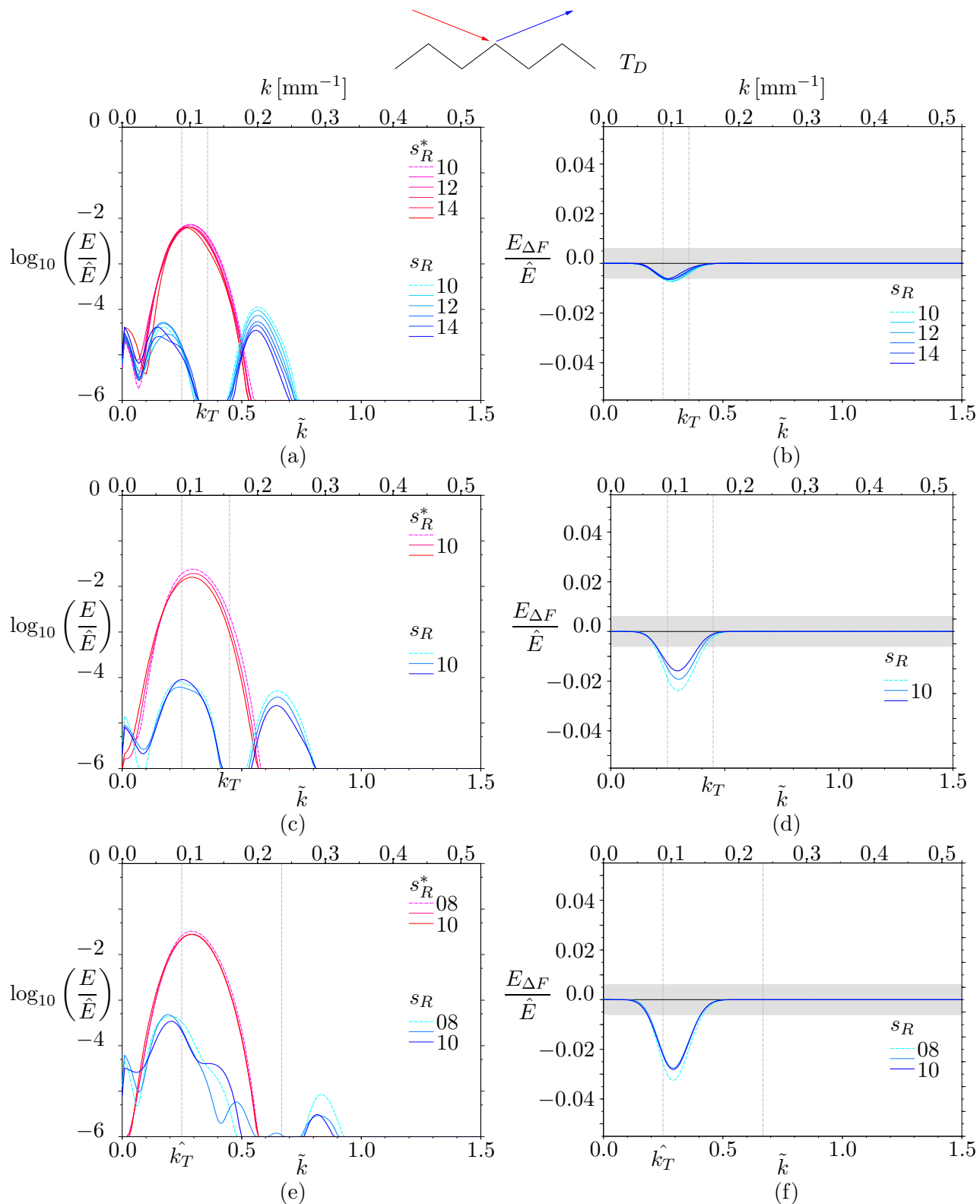


Figure 7.5: Forward-scattered energy density spectra for sawtooth T_D are plotted in (a, c, e). Corresponding spectral differences are plotted in (b, d, f). Frequencies decrease down the page with θ/α equal to (a,b) 1.23, (c,d) 1.36 and (e,f) 1.55.

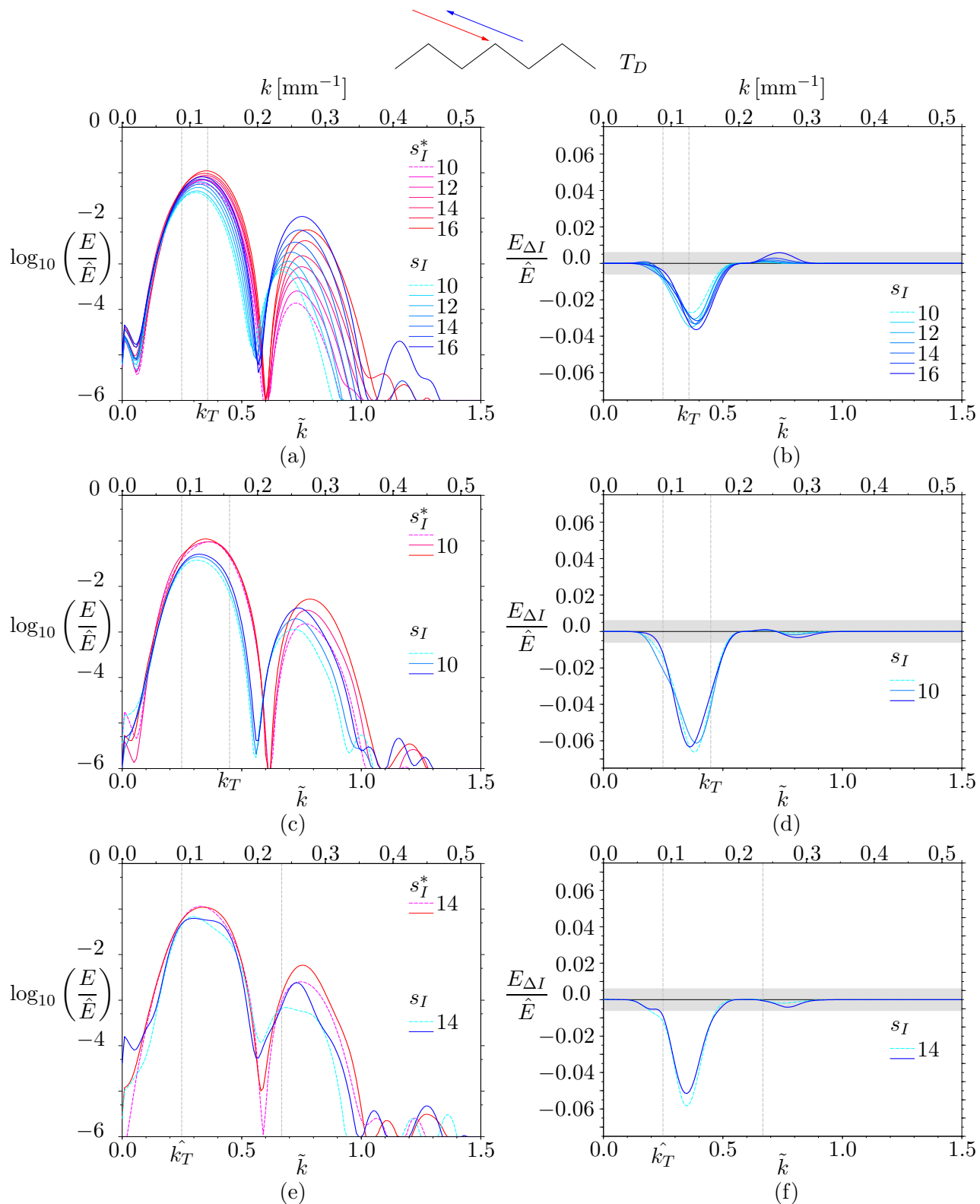


Figure 7.6: Back-scattered energy density spectra for sawtooth T_D are plotted in (a, c, e). Corresponding spectral differences are plotted in (b, d, f). Frequencies decrease down the page with θ/α equal to (a,b) 1.23, (c,d) 1.36 and (e,f) 1.55.

\hat{k}_T , are characterised by smaller across-beam length scales and also slightly larger amplitudes. Similar observations were made for the comparison of subcritical scatter at sawtooths T_G and T_H , which had aspect ratios of $\hat{A}_T \hat{k}_T = 0.783$ and 0.785 respectively. Quantitative comparisons of the scattering behaviours at T_D and T_E can be made by inspection of the energy density spectra.

Spectral analysis of scatter at T_E

Figure 7.8 (a), (c) and (e) show spectra relating to forwards scattered wavefields for T_E , calculated along cross-sections of B_F and B_F^* for values of θ/α and σ/N corresponding to those of figure 7.7 (a)-(c) respectively. The corresponding spectral differences are shown in figure 7.7 (b), (d) and (f). Measured spectra for the incident and scattered wavefields shown in figure 7.8 (a) show a dominant peak in the scattered spectra in the region of $\tilde{k} \approx 0.3$ (incident) and $\tilde{k} \approx 0.25$ (scattered), with peak magnitudes $\sim O(10^{-2})$ and $\sim O(10^{-3})$, respectively. The magnitude of the peak for the primary scattered component at T_E is an order of magnitude greater than that observed for scatter at T_D . This contrast in primary scatter is consistent with the behaviour shown in section 6.2.1 for subcritical interactions with sawtooths T_H and T_G , which were also related by length scale doubling with preserved aspect ratio. Some of the contrast in scatter between the large and small scale topographies might be caused by the relatively greater significance of any imperfections in the stratification within troughs of the topography, though inspection of RMS_T and Hilbert transform filtered images of the scatter suggests this influence remains small in both cases over the time scales of experiments used in this study. Whilst no significant high wavenumber forwards scatter is observed in the measured spectra for T_E , its presence is clear in the corresponding RMS_T images. The lack of signal is accounted for with the preferential action of viscosity at the higher wavenumbers.

Figure 7.9 (a), (c) and (e) show spectra for the superposition of the incident and backwards scattered fields at T_E calculated along cross-sections of B_I and B_I^* for values of θ/α and σ/N corresponding to those in the spectra of figure 7.8 (a), (c) and (e) respectively. Corresponding spectral differences are shown in (b), (d) and (f). Distinctions between spectra are most easily seen in the spectral differences of figure 7.9. The measured back-scattered difference spectra of T_E have similar form to those of T_D , with the high wavenumber signal expected from observation of small across-beam length scales in RMS_T images again too small to have prominence in the measured spectra.

In summary, comparisons have been made between supercritical scatter at sawtooths T_D and T_E . The profiles have approximately equal aspect ratios of $\hat{A}_T \hat{k}_T = 1.58$ but the horizontal wavelength and amplitude of T_E are almost half that of T_D . Contrary to ray tracing predictions, forward and back-scattered wavefields are observed at both profiles and in both cases the scatter is most prominent at values of θ/α nearer critical. The presence of primary (*i.e.* located at wavenumbers in the region of the peak of the incident spectra at $\tilde{k} \approx 0.3$) and sum (*i.e.* high wavenumber scatter located near $\tilde{k} \approx 0.3 + k_T$) components, similar to those observed in subcritical scatter are suggested in the forward scattered spectra. High wavenumber scatter is expected to be located at higher

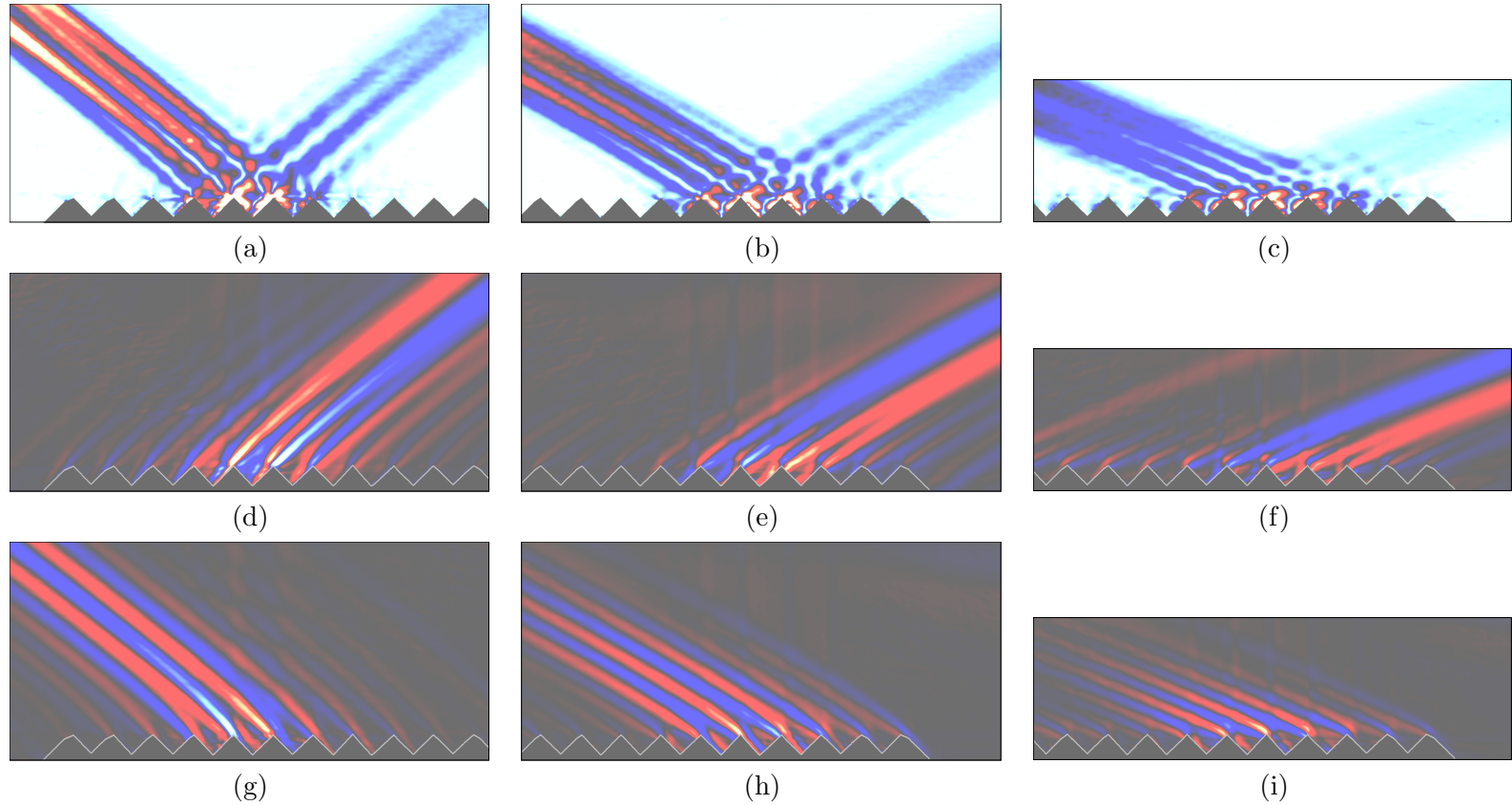


Figure 7.7: RMS_T images of perturbed buoyancy fields for supercritical scatter at sawtooth T_E , with $\alpha = 45.0^\circ$, at forcing frequencies such that θ/α is equal to (a) 1.20, (b) 1.38 and (c) 1.56. Images of corresponding forward and back-scattered wavefields after filtering using the Hilbert transform are shown in (d)-(f) and (g)-(i) respectively, with upper edge of topography highlighted in grey. Fields of view measure 449×205 mm and 449×134 mm, with unit aspect ratio. Colour scale as in figure 6.4.

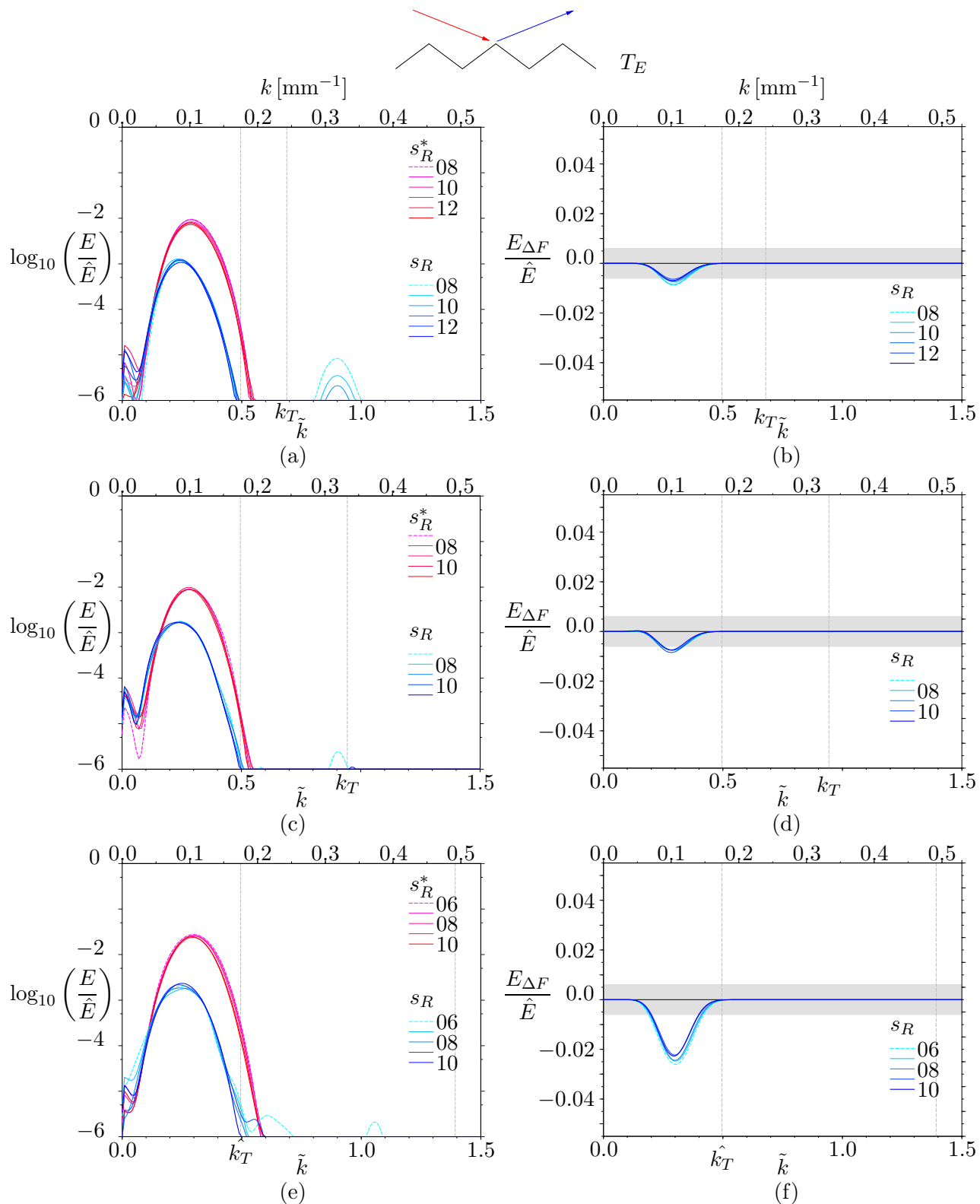


Figure 7.8: Forward-scattered energy density spectra for sawtooth T_E are plotted in (a, c, e). Corresponding spectral differences are plotted in (b, d, f). Frequencies decrease down the page with θ/α equal to (a,b) 1.20, (c,d) 1.38 and (e,f) 1.56.

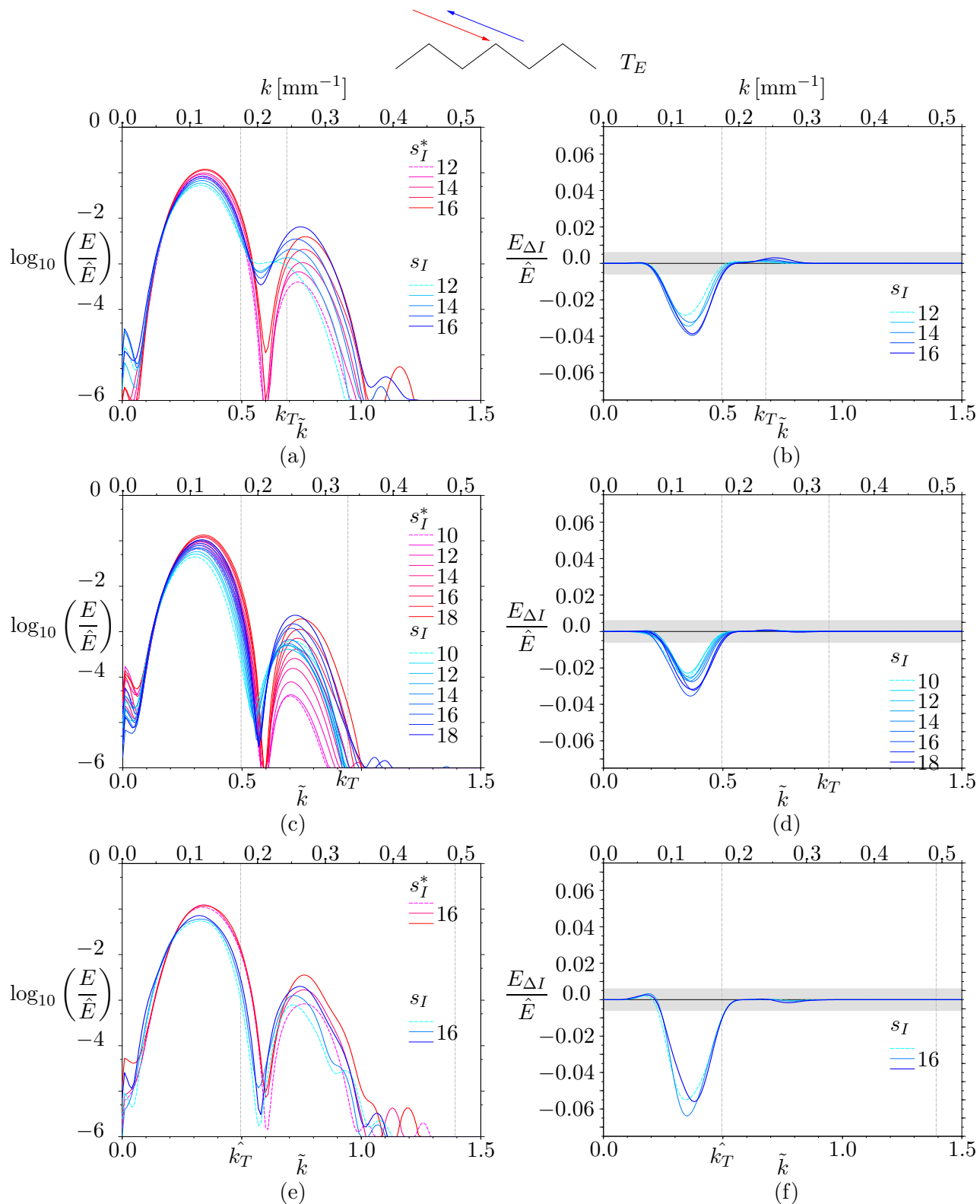


Figure 7.9: Back-scattered energy density spectra for sawtooth T_E are plotted in (a, c, e). Corresponding spectral differences are plotted in (b, d, f). Frequencies decrease down the page with θ/α equal to (a,b) 1.20, (c,d) 1.38 and (e,f) 1.56.

wavenumbers for T_E , which has the greater topographic wavenumber, but since the smaller length scales promote viscous attenuation, the observed high wavenumber scatter is most prominent for T_D . This result is similar to that found for comparisons of subcritical scatter at T_H and T_G . Properties of the high wavenumber back-scatter observed at T_E compare well with that at T_D . Energy densities observed for the back-scatter appear to be comparable in magnitude in supercritical and subcritical configurations, both being most significant near-critical. Sawtooths T_G and T_D are characterised by approximately the same topographic wavenumbers, $\hat{k}_T = 0.087$ and 0.088 , respectively, but have different aspect ratios of $\hat{A}_T \hat{k}_T = 0.783$ and 1.58 , *i.e.* the aspect ratio of T_D is approximately twice that of T_G . Near-field RMS_T images for supercritical scatter at each of the topographies can be seen in figures 6.9 and 7.3, with values of $\theta/\alpha = 1.13$ and 1.23 respectively. As might be anticipated, the near-field features are most prominent at T_D , which has the greatest aspect ratio and hence steepest slopes.

7.3 Topographic shape

This section discusses the effect on scattered wavefields of variation of the topographic shape. Forward and back-scattered wavefields at sawtooth profile T_E are compared with those at square-wave T_J , for which $\hat{k}_T = 0.175 \text{ mm}^{-1}$, $\hat{A}_T \hat{k}_T = 1.75$, $k_c/\hat{k}_T = 2.02$ and $\hat{A}_T k_c = 3.53$, and pseudo knife-edge T_L , for which $\hat{k}_T = 0.165 \text{ mm}^{-1}$, $\hat{A}_T \hat{k}_T = 1.49$, $k_c/\hat{k}_T = 2.14$ and $\hat{A}_T k_c = 3.18$ as well as the associated scatter to higher temporal harmonics. Geometrical constraints of the experimental set up prevented comparison of the supercritical results with scatter at either sinusoid. Higher harmonic generation for supercritical scatter is also considered for T_A , T_G and T_K .

7.3.1 Scatter from a square-wave (T_J)

Qualitative description of scatter

Square-wave T_J is closely analogous to sawtooth profile T_E . An angle α is defined for T_J to be the angle made between the slopes and vertical of a sawtooth characterised by the same values of \hat{A}_T and \hat{k}_T . Whilst regimes are defined here for scatter at the square-wave in terms of values of θ/α , the component vertical faces of the square-wave are always supercritical and the horizontal faces are always subcritical. Figure 7.10 (a-c) shows RMS_T images for wavefields with θ/α equal to (a) 1.20, (b) 1.38 and (c) 1.56 and σ/N equal to 0.59, 0.47 and 0.34 respectively, as well as corresponding forward, (d-f), and backward, (g-i), scattered wavefields after filtering using Hilbert transforms. The same conventions used in figure 6.4 are applied here. The structure of forwards scattered wavefields at T_J shown in RMS_T and forwards scatter filtered images of figure 7.10 (a-c) and (d-f), respectively, differs from those for scatter at sawtooth T_E in a number of ways. The amplitudes of forwards scattered wavefields are larger at the square-wave topography and scattered beam-like structures are broader. The behaviour of wavefields during specular reflection at sloping boundaries suggest that, in the supercritical case, the slopes of the sawtooth focus the energy into troughs of the

topography. Whilst the presence of scattered wavefields indicates that other scattering mechanisms are also occurring, such as scatter at the topographic corners and nonlinear processes, the downward focusing of wave energy at the sawtooth certainly appears to reduce the fluxes of wave energy to the far-field as compared with behaviour at the square-wave. As in the case of sawtooth T_E , energy densities of the forward scatter at square-wave T_J are greatest for values of θ/α nearest critical. The back-scattered wavefields shown in figure 7.10 (g-i) are associated with lower amplitudes than those for T_E and, in contrast to the trend shown by the sawtooth, are most pronounced for the intermediate value of θ/α . Near-field features such as those shown in figure 6.9 can also be seen in movies of supercritical scatter at T_J , though are less visible in figure 7.10.

Ray tracing analysis of scatter at T_J

Ray tracing predictions, including primary and subsequent reflections of rays (blue) incident at square-wave T_J , for parameter values corresponding to those in figure 7.10 (a)-(c) are shown in figure 7.11 (a)-(c) respectively. Conventions of the ray tracing diagrams are the same as those used in figure 6.19. Ray tracing predictions for the forwards scatter corresponding to figure 7.11 (a)-(c) are $C_F = 0.53, 0.90$ and 0.91 respectively (as derived using the method described by Longuet-Higgins (1969) - see figure 6.25). In contrast to the behaviour seen in figure 7.10, ray tracing therefore predicts the greatest proportion of forward scatter at the largest value of θ/α . However, the observed trend *is* consistent with that seen for the forwards scatter at sawtooth T_E , which was most prominent near the critical value of θ/α .

Back-scatter coefficients calculated by ray tracing for figure 7.11 (a)-(c) are $C_B = 0.47, 0.10$ and 0.09 , respectively, with the weakest predicted for the largest value of θ/α . This is not consistent with the images of figure 7.10, with the back-scattered wavefield at the smallest value of θ/α being weaker than that for the intermediate value of θ/α . Note that propagating secondary temporal harmonics are possible in the latter two experiments. Amplitudes of the back-scattered wavefields at T_J are typically an order of magnitude less than those for T_E .

Spectral analysis of scatter at T_J

Figure 7.12 (a), (c) and (e) show spectra relating to forwards scattered wavefields for T_J , calculated along cross-sections along B_F and B_F^* for values of θ/α and σ/N corresponding to those of figure 7.10 (a)-(c) respectively. The corresponding spectral differences are shown in figure 7.10 (b), (d) and (f). The scatter shown in figure 7.12 (a), for the smallest value of θ/α , is mainly to the primary component, with no measured high wavenumber scatter. Troughs in the difference spectra for the square-wave are less pronounced than those for the sawtooth and are in fact virtually absent in figure 7.12 (b) and (d). This is a consequence of the weaker back-scatter observed for T_J , which does not enhance viscous attenuation of the incident wave beam to the same degree as is seen for the sawtooth. As was discussed earlier, viscous action is promoted in the incident beam as the spatially coincident back-scattered field introduces greater across-beam gradients and shear. As

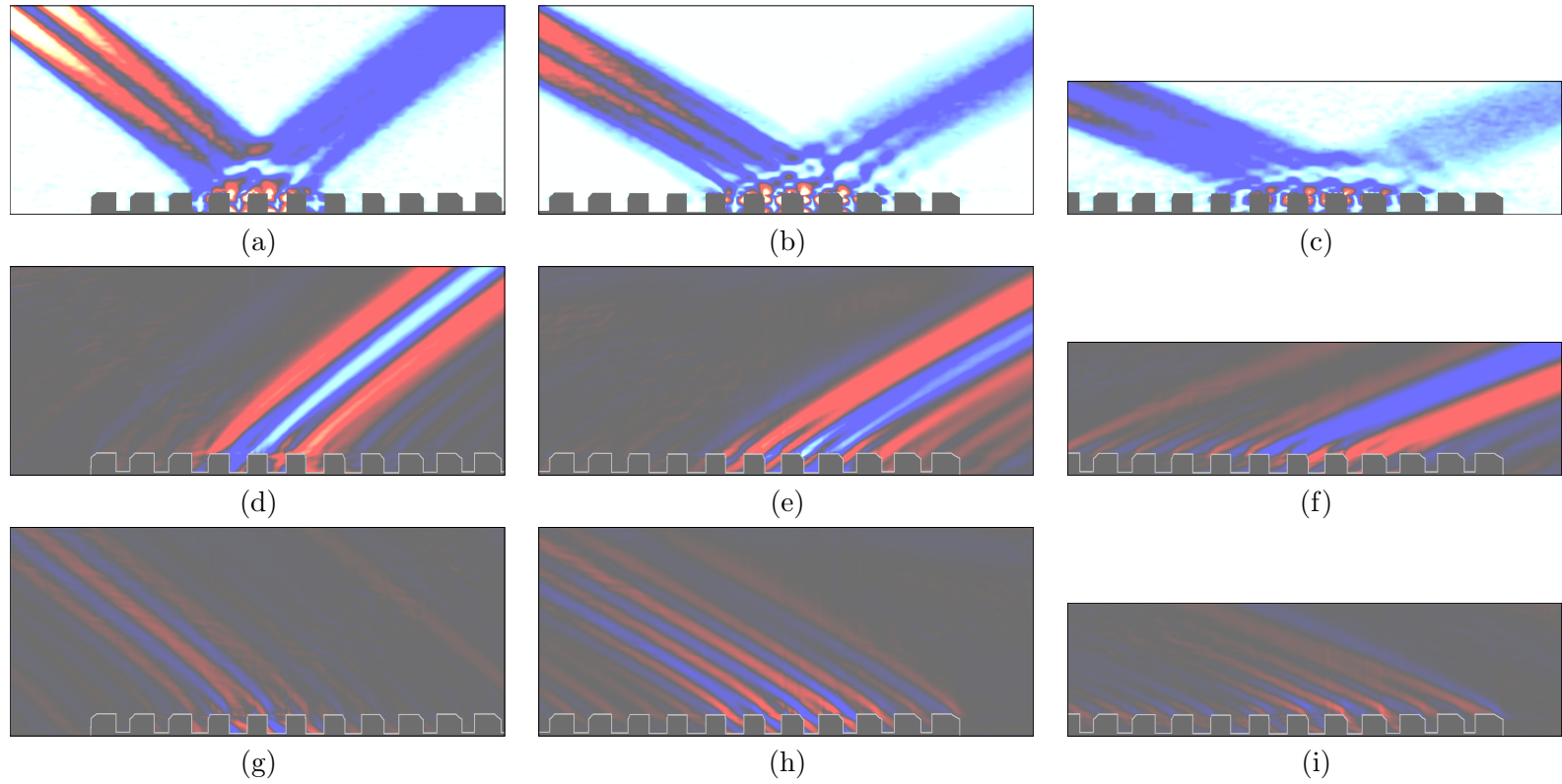


Figure 7.10: RMS_T images of perturbed buoyancy fields for supercritical scatter at square-wave T_J , with $\alpha = 45.0^\circ$, at forcing frequencies such that θ/α is equal to (a) 1.20, (b) 1.38 and (c) 1.56. Images of corresponding forward and back-scattered wavefields after filtering using the Hilbert transform are shown in (d)-(f) and (g)-(i) respectively, with upper edge of topography highlighted in grey. Fields of view measure 449×190 mm and 449×121 mm, with unit aspect ratio. Colour scale as in figure 6.4.

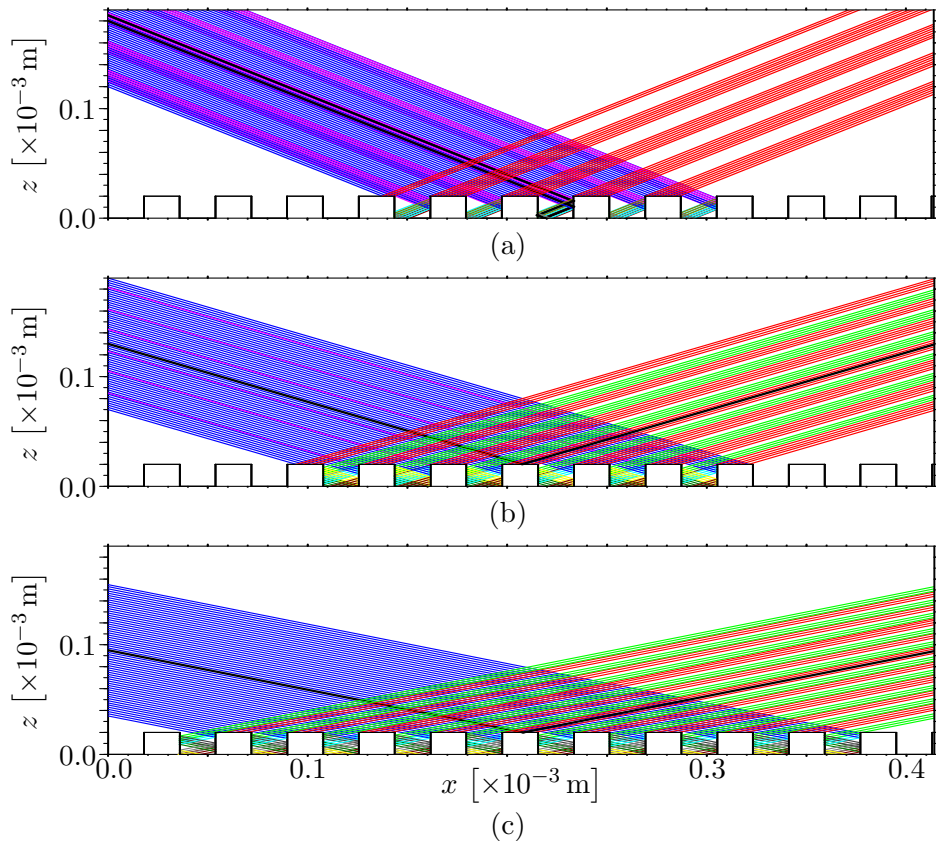


Figure 7.11: Ray tracing predictions for T_J . Here (a) $\sigma/N = 0.59$, $\theta/\alpha = 1.20$, (b) $\sigma/N = 0.47$, $\theta/\alpha = 1.38$ and (c) $\sigma/N = 0.34$, $\theta/\alpha = 1.56$. Line colouring as in figure 6.19.

θ/α increases, the primary scatter is seen to decrease in the forwards spectra for T_J .

Figure 7.13 (a), (c) and (e) show spectra for the superposition of the incident and backwards scattered fields at T_J calculated along cross-sections of B_I and B_I^* for values of θ/α and σ/N corresponding to those in the spectra of figure 7.12 (a), (c) and (e) respectively. Corresponding spectral differences are shown in (b), (d) and (f). Distinctions between spectra are most easily seen in the spectral differences of figure 7.13. The measured back-scatter at T_J shows little variance with θ/α . As for scatter at sawtooth T_E , despite observations in corresponding RMS_T images of small across-beam lengths scales indicating high wavenumber back-scatter, energy densities associated with these components are too small to feature significantly in the measured spectra.

In general, energy densities associated with forward scattered wavefields generated at square-wave T_J are greater than those at sawtooth T_E . The variation of the scattered wavefields with θ/α does not correlate with ray tracing predictions of coefficients for the square-wave forward scatter. Instead, the wavefields follow the observed trend for forward scatter at the sawtooth, with energy densities appearing to increase towards critical values of θ/α . Spectra suggest that scatter at both the square-wave and sawtooth topographies generates a primary component. In addition, high wavenumber forward scatter is also observed in RMS_T images of the forward scatter. In contrast to

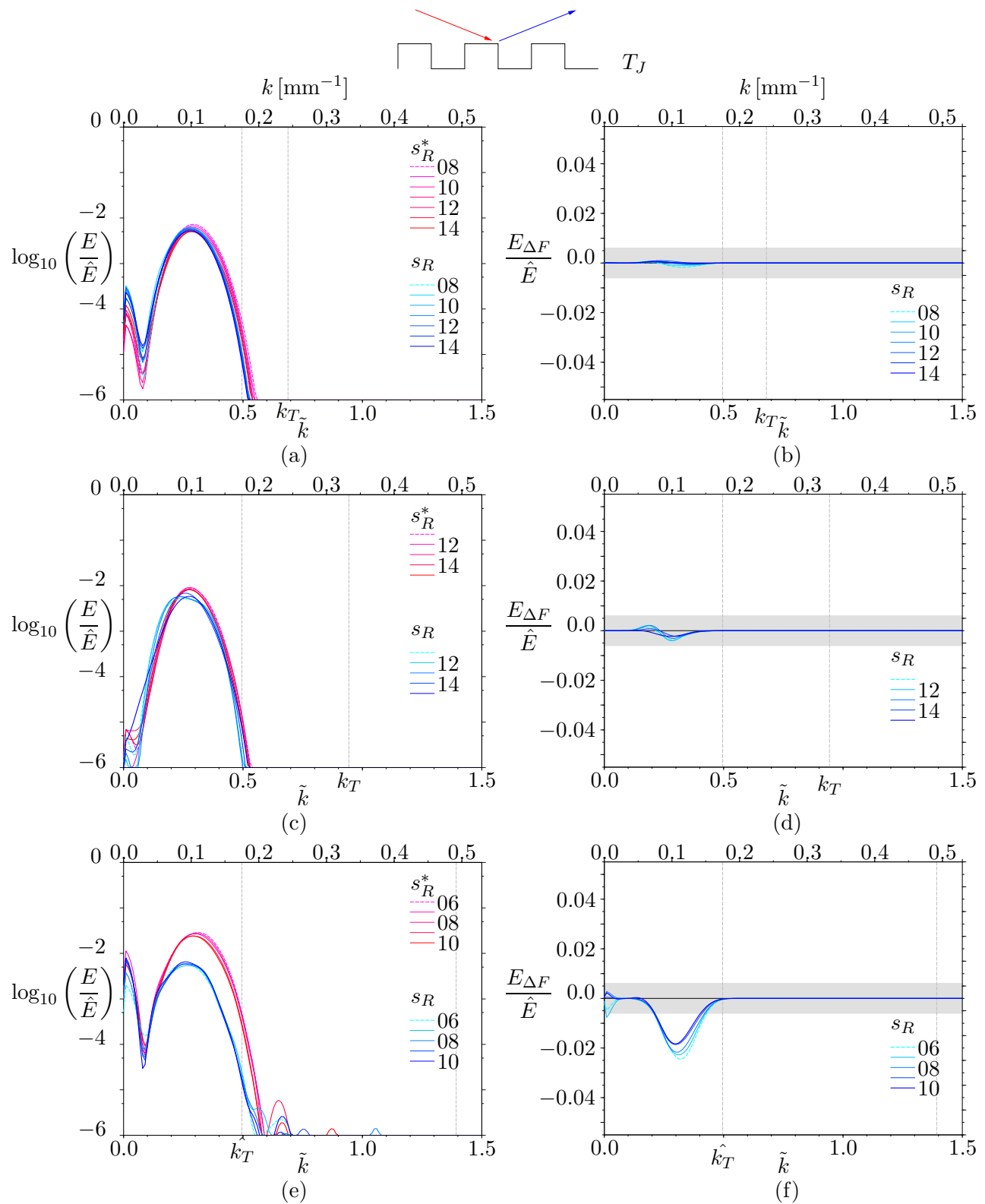


Figure 7.12: Forward-scattered energy density spectra for square-wave T_J are plotted in (a, c, e). Corresponding spectral differences are plotted in (b, d, f). Frequencies decrease down the page with θ/α equal to (a,b) 1.20, (c,d) 1.38 and (e,f) 1.56.

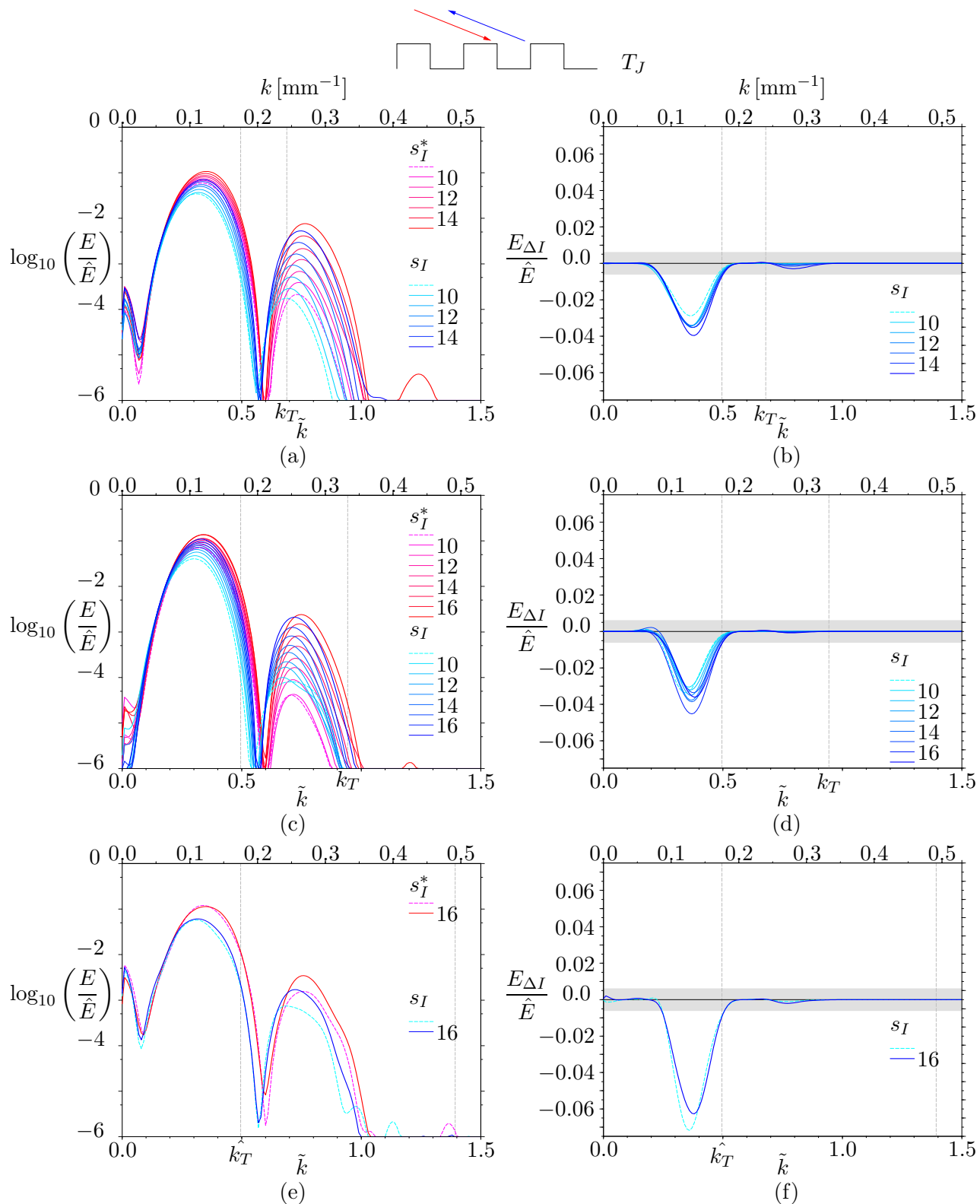


Figure 7.13: Back-scattered energy density spectra for square-wave T_J are plotted in (a, c, e). Corresponding spectral differences are plotted in (b, d, f). Frequencies decrease down the page with θ/α equal to (a,b) 1.20, (c,d) 1.38 and (e,f) 1.56.

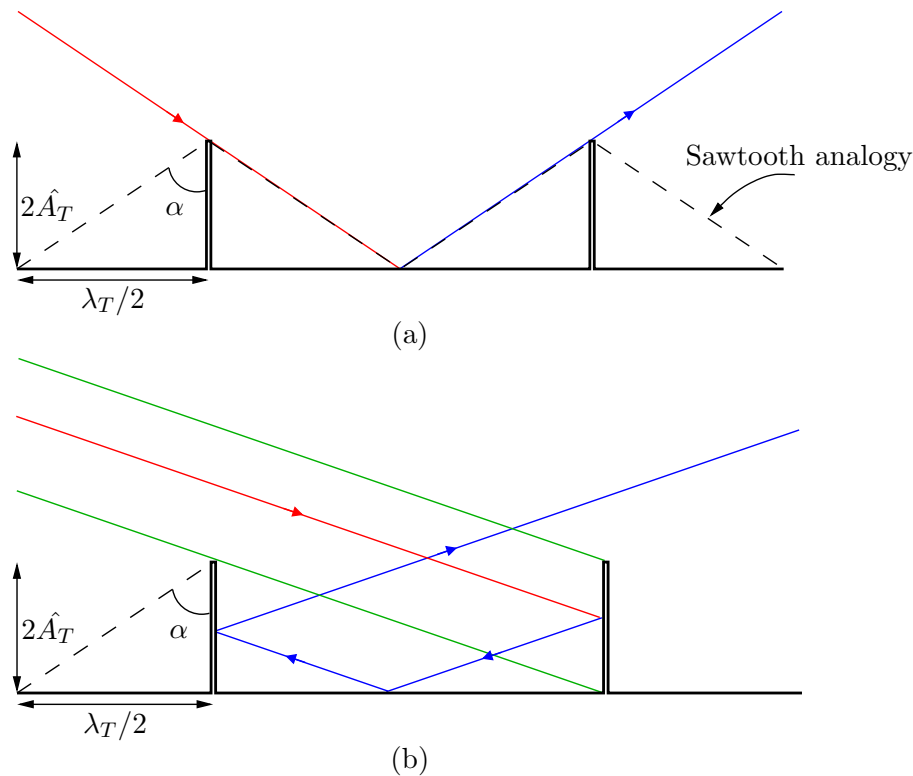


Figure 7.14: Ray geometries for critical configurations at knife-edge with critical configurations (a) as defined for analogous sawtooth and (b) where reflection of incident rays is purely supercritical (green lines in the latter indicate region where incident ray reflection is possible).

the behaviour for the forward scatter, energy densities associated with back-scatter at the square-wave are weaker than those for the sawtooth and do not follow ray tracing predictions or the trend seen for the sawtooth of decreasing magnitudes at larger values of θ/α . Near-field amplitudes and mixing features are more pronounced at the sawtooth.

7.3.2 Scatter at a knife-edge (T_L)

The geometry of knife-edge profiles is described in section 3.8. As for the sinusoid and square-wave, an angle α is defined for the knife-edge that describes the slopes of the sawtooth characterised by the same values of \hat{A}_T and \hat{k}_T . As for the sawtooth, a critical value of the slope parameter is therefore defined as $\theta/\alpha = 1$. However, a second critical angle, for which geometrical ray tracing predicts $C_F = 1$, can also be defined for the knife-edge. This occurs when $\theta = \tan^{-1}(\pi/\hat{A}_T\hat{k}_T)$, *i.e.* the configuration where all incident rays reflect initially at *vertical* sections of the knife-edge (*i.e.* supercritical reflection), subsequently reflecting specularly three times before scattering forwards. These two critical configurations are illustrated in figure 7.14 (a) and (b) respectively.

Qualitative description of scatter

Knife-edge T_L is closely analogous to sawtooth profile T_E and square-wave T_J . Figure 7.15 (a-c) shows RMS_T images for wavefields with θ/α equal to (a) 1.22, (b) 1.40 and (c) 1.56 and σ/N equal to 0.55, 0.42 and 0.30 respectively, as well as corresponding forward, (d-f), and backward, (g-i), scattered wavefields after filtering using Hilbert transforms. The same conventions used in figure 6.4 are applied here. The forwards scattering behaviour seen in RMS_T and filtered images for knife-edge T_L shown in figure 7.15 (a-c) and (d-f), respectively, have strong similarities with those for sawtooth T_E , with the largest amplitude forward scatter at the value of θ/α nearest critical. The tips of the knife-edge appear to transfer energy associated with the background wavefield to high wavenumbers more efficiently than the corners of the sawtooth however, so that more prominent scatter is observed to propagate from the knife-edges adjacent to the main region of the topography lit by the incident wave beam than from the sawtooth crests in corresponding positions. The influence of this adjacent scatter can be seen in RMS_T images such as figure 7.15 (a), where it interferes constructively and destructively with the forwards scatter to produce a visually ‘crisscross’ wavefield. The effect is most visually dramatic at this value of θ/α , as compared with figures 7.15 (b) and (c), due to the weaker far-field forwards scatter in this case. The more pronounced gradients introduced into the near-field of the knife-edge in this way are anticipated to enhance viscous attenuation of wave energy there. Back-scattered wavefields at the knife-edge are also similar to those at the sawtooth, with the near-critical scatter again most pronounced. In the knife-edge case however, the near-critical back-scatter (see figure 7.15 (a) and (g)) is far more significant than that at the sawtooth or square-wave and indeed that of the corresponding *forward* scatter at the knife-edge. As for the sawtooth, near-field mixing features are observed near the tips of the knife-edge.

Figure 7.16 presents results from PIV experiments in the near-field of the knife-edge profile T_L . Figure 7.16 (a), (c), (e) and (g) show normalised RMS_T velocity values after filtering for the primary harmonic at θ/α equal to 1.01, 1.22, 1.36 and 1.54 respectively. Corresponding phase images are shown in figure 7.16 (b), (d), (f) and (h). As for the experiments at sawtooth profile T_D , fluid speeds tend to decrease as θ/α increases away from critical and the speeds are most pronounced in the region of corners (*i.e.* the tips of the pseudo knife-edges) of the topography and along the characteristics emanating from these points. It appears that fluid speeds are largest along the direction of characteristics directed in the back-scatter direction. At the largest value of θ/α , there is very little discernable forwards scatter in the RMS_T velocity or phase images.

Ray tracing analysis of scatter at T_L

Ray tracing predictions, including primary and subsequent reflections of rays (blue) incident at pseudo knife-edge T_L , for parameter values corresponding to those in figure 7.15 (a)-(c) are shown in figure 7.17 (a)-(c) respectively. Conventions of the ray tracing diagrams are the same as those used in figure 6.19. Ray tracing predictions for the forwards scatter corresponding to figure 7.17 (a)-(c) are $C_F = 0.55, 0.85$ and 0.25 respectively (see figure 6.25). These predictions are not validated

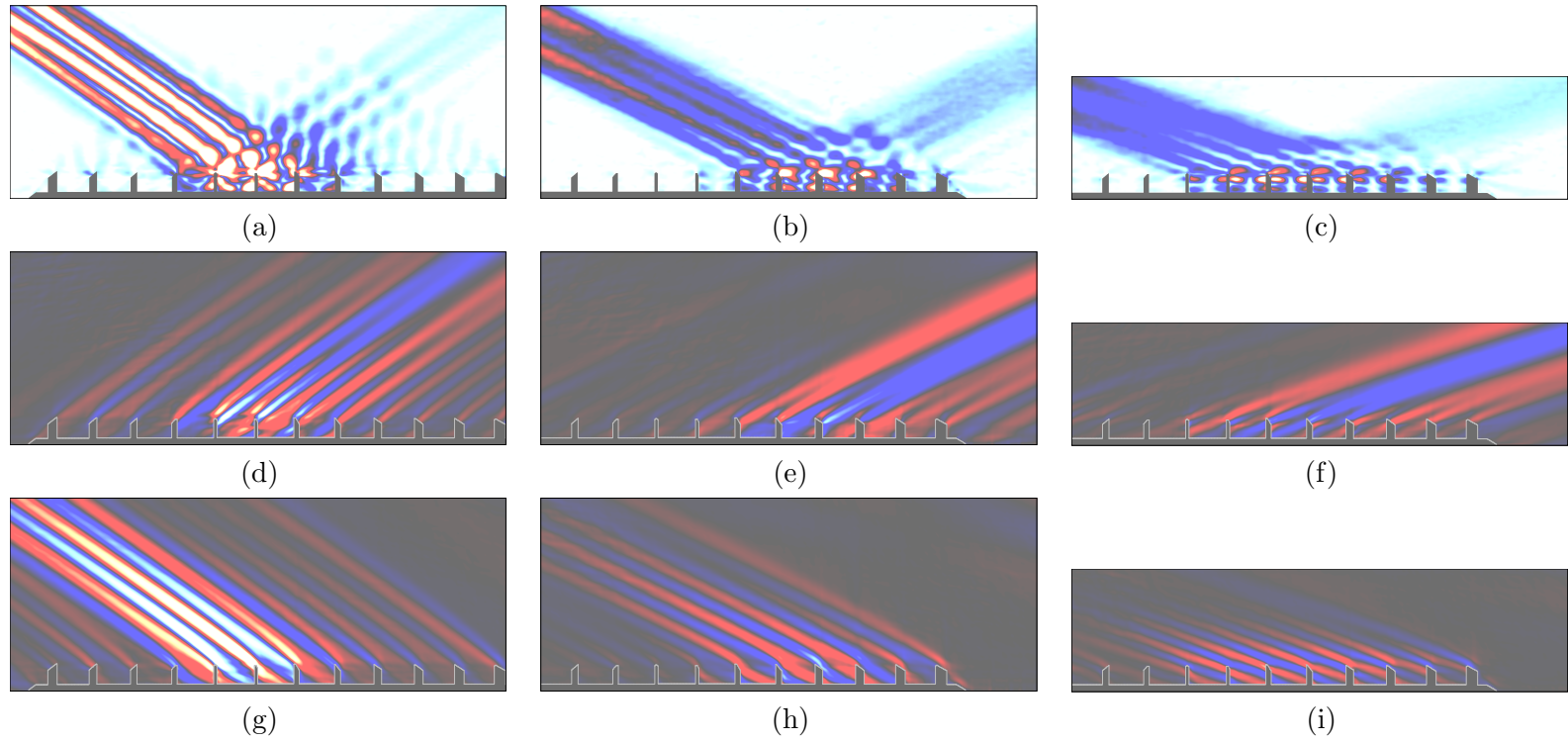


Figure 7.15: RMS_T images of perturbed buoyancy fields for supercritical scatter at knife-edge T_L , with $\alpha = 46.6^\circ$, at forcing frequencies such that θ/α is equal to (a) 1.22, (b) 1.40 and (c) 1.56. Images of corresponding forward and back-scattered wavefields after filtering using the Hilbert transform are shown in (d)-(f) and (g)-(i) respectively, with upper edge of topography highlighted in grey. Fields of view measure 449×175 mm and 449×112 mm, with unit aspect ratio. Colour scale as in figure 6.4.

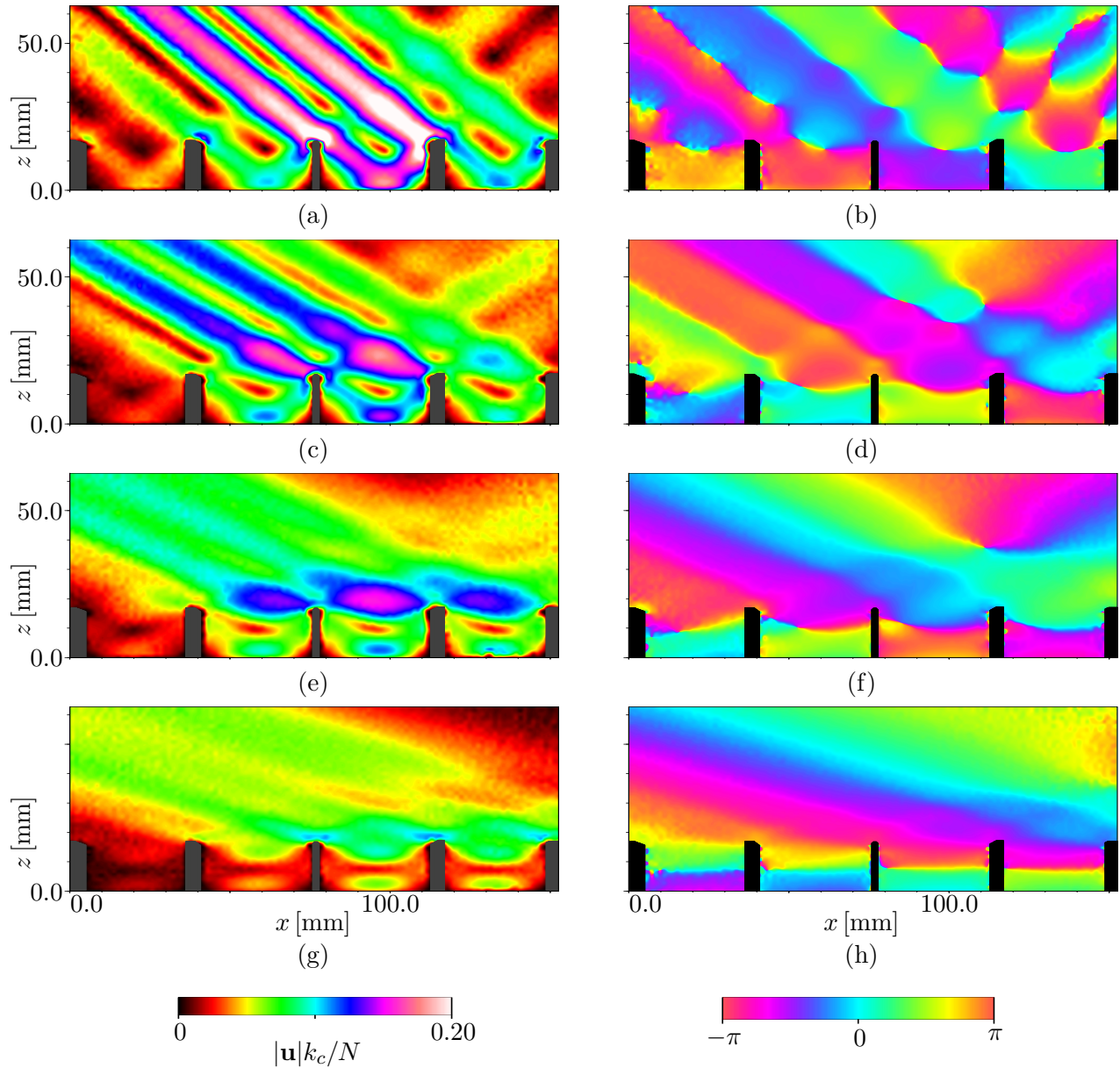


Figure 7.16: RMS_T velocity images of primary harmonics generated by supercritical scatter at knife-edge T_L with θ/α equal to (a) 1.01, (c) 1.22, (e) 1.36 and (g) 1.54 with σ/N equal to 0.68, 0.54, 0.45 and 0.32 respectively (topography shaded in grey). Corresponding phase images are shown in (b), (d), (f) and (h) (topography shaded in black).

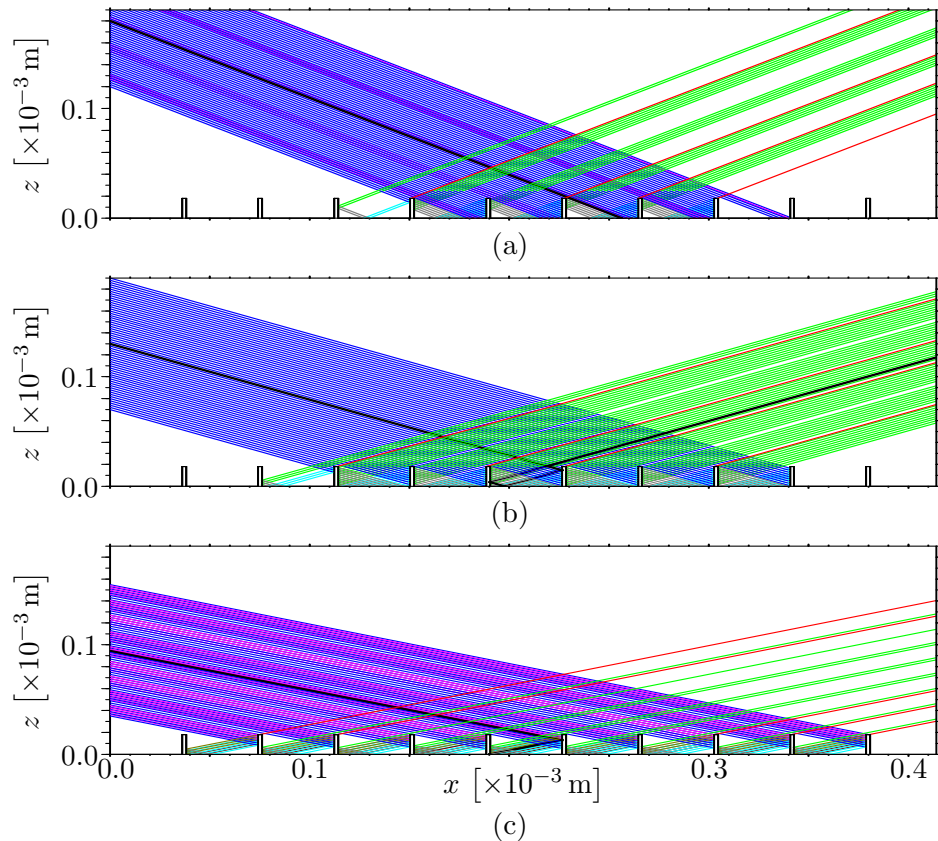


Figure 7.17: Ray tracing predictions for T_J . Here (a) $\sigma/N = 0.58$, $\theta/\alpha = 1.22$, (b) $\sigma/N = 0.45$, $\theta/\alpha = 1.45$ and (c) $\sigma/N = 0.34$, $\theta/\alpha = 1.56$. Line colouring as in figure 6.19.

by RMS_T images of figure 7.15, with forward scatter, at least in the near-field, at the smallest value of θ/α more pronounced than at the intermediate value. In addition, the ray tracing predictions differ from those at corresponding parameter values for the sawtooth, for which $C_F = 0$, and the square-wave, for which $C_F = 0.53, 0.90$ and 0.91 .

Back-scatter coefficients calculated by ray tracing for figure 7.17 (a)-(c) are $C_B = 0.45, 0.15$ and 0.75 , respectively. As for the forward scatter, the experiment results contradict these predictions. Note that generation of propagating secondary harmonic wavefields is possible at the parameter values of the latter two experiments.

Spectral analysis of scatter at T_L

Figure 7.18 (a), (c) and (e) show spectra relating to forwards scattered wavefields for T_L , calculated along cross-sections along B_F and B_F^* for values of θ/α and σ/N corresponding to those of figure 7.15 (a)-(c) respectively. The corresponding spectral differences are shown in figure 7.15 (b), (d) and (f). Spectra for the forwards scatter at T_L compares well with that at sawtooth T_E . However, energy densities of scatter at the knife-edge to the primary component for the near-critical value of θ/α are an order of magnitude smaller than those for the sawtooth.

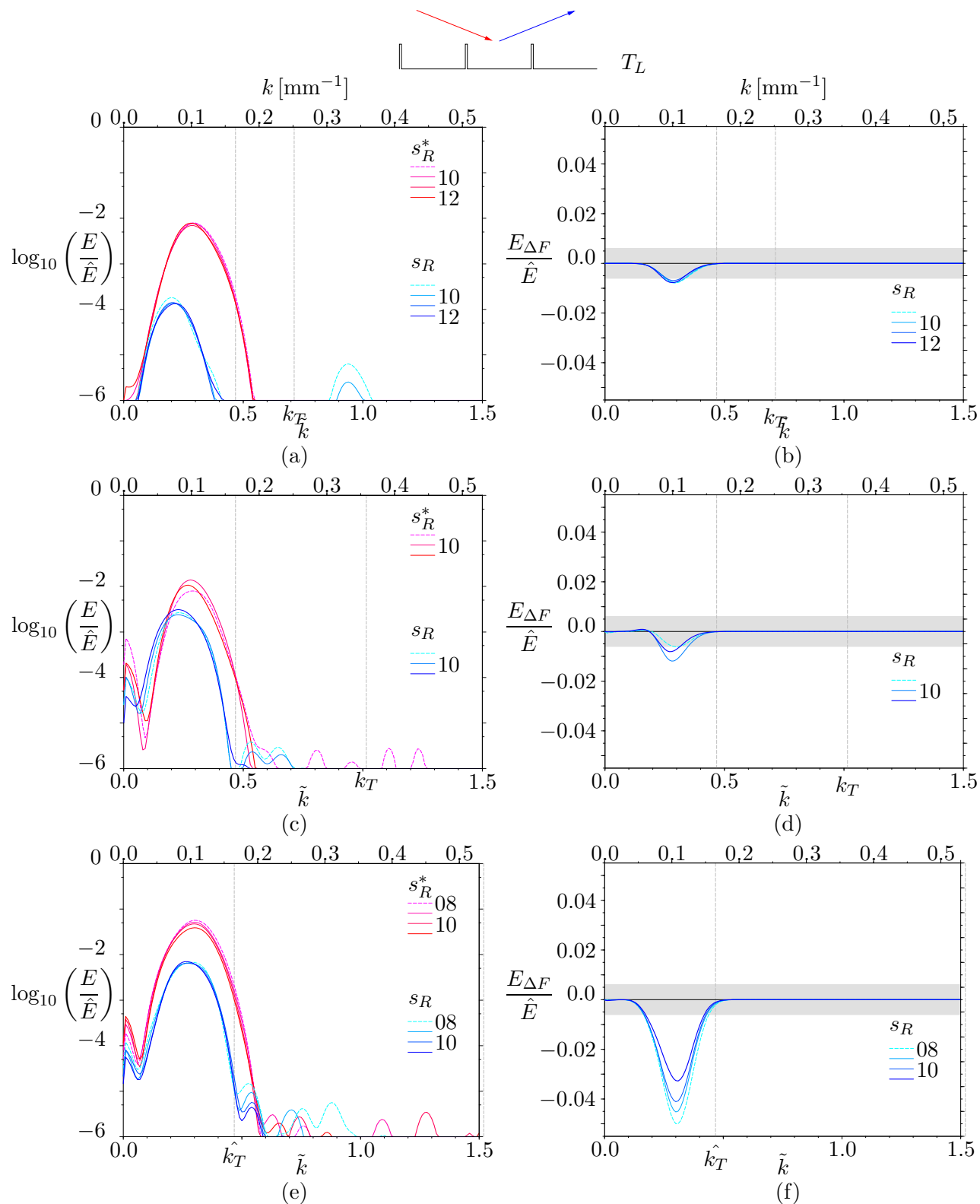


Figure 7.18: Forward-scattered energy density spectra for pseudo knife-edge T_L are plotted in (a, c, e). Corresponding spectral differences are plotted in (b, d, f). Frequencies decrease down the page with θ/α equal to (a,b) 1.22, (c,d) 1.40 and (e,f) 1.56.

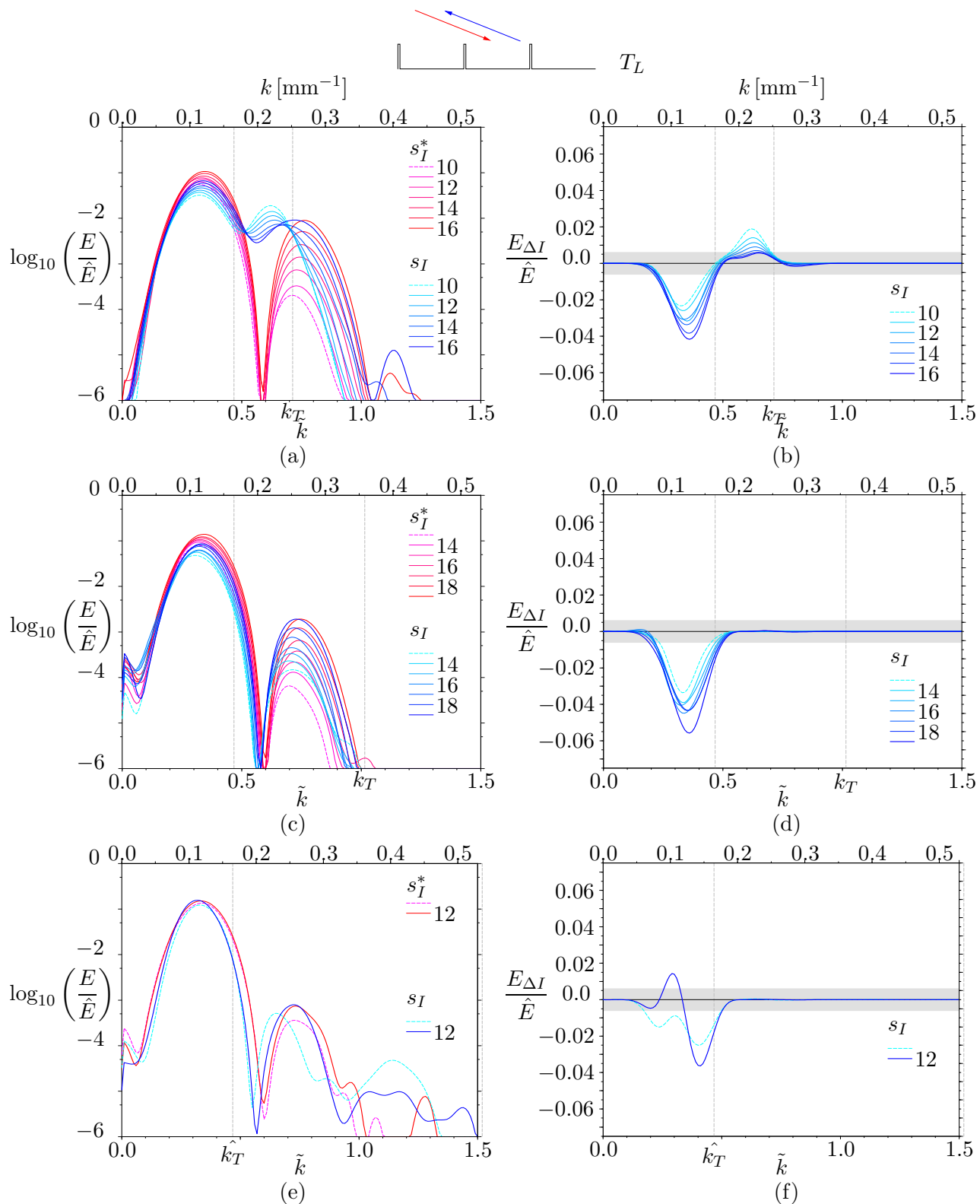


Figure 7.19: Back-scattered energy density spectra for pseudo knife-edge T_L are plotted in (a, c, e). Corresponding spectral differences are plotted in (b, d, f). Frequencies decrease down the page with θ/α equal to (a,b) 1.22, (c,d) 1.40 and (e,f) 1.56.

Figure 7.19 (a), (c) and (e) show spectra for the superposition of the incident and backwards scattered fields at T_L calculated along cross-sections of B_I and B_I^* for values of θ/α and σ/N corresponding to those in the spectra of figure 7.18 (a), (c) and (e) respectively. Corresponding spectral differences are shown in (b), (d) and (f). Distinctions between spectra are most easily seen in the spectral differences of figure 7.19. The spectra measured at T_L compare well with those for sawtooth T_E , except at the value of θ/α closest to critical, where the back-scattered spectra for the pseudo knife-edge T_L exhibits a prominent region of high wavenumber scatter at $\tilde{k} \approx 0.65$ with maximum peak magnitude $\sim O(10^{-2})$.

7.3.3 Corners, slopes and edges

In general, forward scattered wavefields generated at pseudo knife-edge T_L compare well with those at sawtooth T_E . As for the square-wave T_J , the variation of the scattered wavefields with θ/α does not correlate with ray tracing predictions of coefficients for the knife-edge forward scatter. Instead, the wavefields follow the observed trends for forward scatter at the sawtooth and square-wave, with energy densities increasing towards critical values of θ/α . Energy densities of the primary component generated at the knife-edge are an order of magnitude smaller than those at the sawtooth. In addition, high wavenumber forward scatter, like that generated at the sawtooth, was also observed at T_L . Back-scatter at the knife-edge increases towards critical θ/α and does not follow ray tracing predictions. In particular, back-scatter at the knife-edge is dramatically enhanced for near-critical θ/α . Near-field amplitudes and mixing features are more pronounced at the knife-edge than the sawtooth or square-wave.

7.4 Scatter to higher harmonics

Scatter to higher harmonics at subcritical sinusoidal, sawtooth and square-wave topographies was discussed in section 6.3. Higher harmonic generation during *supercritical* scatter is described here for sawtooth profiles T_E and T_G , square-wave T_J and T_K and pseudo knife-edge profile T_L .

Figure 7.20 shows results from harmonic filtering of $\Delta N^2/N^2$ fields from experiments of supercritical scatter at (a-d) sawtooth T_E , (e-h) square-wave T_J and (i-l) knife-edge T_L for θ/α equal to 1.51, 1.51 and 1.46, respectively, and at the incident frequency $\sigma/N = 0.38$, *i.e.* $1/3 \leq \sigma/N \leq 1/2$, in each case. As in figure 6.28, each image shows the incident wave energy propagating from the top left-hand corner towards the topographic profile positioned at the bottom of the image. Figure 7.20 (a), (e) and (i) show the amplitude fields from filtering for the primary frequency and figure 7.20 (c), (g) and (k) are the corresponding phase fields. The forwards and back-scattered wavefield structures discussed above for figures 7.7, 7.10 and 7.15, which dominantly show the primary harmonic, are evident in the amplitude and phase images of the primary harmonic filtering shown in figure 7.20 (a,c), (e,g) and (i,k), respectively.

Figure 7.20 (b), (f) and (j) show the amplitude fields from filtering for the secondary harmonic

frequency, $2\sigma/N$, and figure 7.20 (d), (h) and (l) are the corresponding phase fields. As noted in section 6.3, due to experimental constraints, a weak signature of the wavefield associated with the primary frequency is present in the images produced after filtering the wavefields for the secondary harmonic. A secondary harmonic beam generated at the source, together with its reflection at the topography, is also evident in each image. However, this additional ‘incident’ beam reflects sufficiently far to the left of the images to avoid ambiguity as to the source of the generation of the secondary harmonic wavefields, which are visible at the topographic profiles in the region lit by the primary incident beam in each case. Maximum amplitudes of the components generated by scattering of the primary incident beam are approximately second order in the incident wave amplitude. Whilst the primary harmonics are supercritical, the secondary harmonics are subcritical with values of θ_2/α equal to 0.90, 0.90 and 0.87 for T_E , T_J and T_L respectively. These harmonics decay rapidly with distance away from the topography, though less so than for the secondary harmonics shown in figure 6.28. This is in part due to the greater group velocity of the secondary components shown in figure 7.20, which permits the transport of wave energy more rapidly away from the topography. The larger value of θ_2/α for the secondary harmonic components shown in figure 7.20 (b) and (d), compared with those in figure 6.28, suggests a greater degree of focusing of the wave energy at the sloping sections of T_E and hence more pronounced wave amplitudes as a result. As for the subcritical cases of figure 6.28, the secondary harmonic components of figure 7.20 appear to be most pronounced in the vicinities of the corners of the sawtooth, square-wave and knife-edge topographies, with the sawtooth exhibiting the strongest wavefield here. Whilst the scatter at this order is dominantly in the forwards direction for each topography, inspection of the phase images in figure 7.20 (d), (h) and (l) suggest back-scattered secondary harmonic wave energy is also generated. Since the forcing frequency satisfies $\sigma/N > 1/3$, no tertiary harmonic components are predicted and their generation was not observed here.

Figure 7.21 shows results from harmonic filtering of $\Delta N^2/N^2$ fields from experiments of supercritical scatter at (a-d) sinusoid T_A , (e-h) sawtooth T_G and (i-l) square-wave T_K for θ/α equal to 1.14, 1.10 and 1.16 and incident frequencies σ/N equal to 0.33, 0.35 and 0.33, respectively, *i.e.* $\sigma/N \leq 1/2$, in each case. As in figure 6.28, each image shows the incident wave energy propagating from the top left-hand corner towards the topographic profile positioned at the bottom of the image. Figure 7.21 (a), (e) and (i) show the amplitude fields from filtering for the primary frequency and figure 7.21 (c), (g) and (k) are the corresponding phase fields. Similar forwards and back-scattered wavefield structures to those discussed for sinusoid T_A in section 4.5.1 and above for sawtooth and square-wave topographies are evident in the amplitude and phase images of the primary harmonic filtering shown in figure 7.21 (a,c), (e,g) and (i,k).

Figure 7.21 (b), (f) and (j) show the amplitude fields from filtering for the secondary harmonic frequency, $2\sigma/N$, and figure 7.21 (d), (h) and (l) are the corresponding phase fields. Again, as noted above, a weak signature of the wavefield associated with the primary frequency is present in the images produced after filtering the wavefields for the secondary harmonic as well as a secondary harmonic beam generated at the source, together with its reflection at the topography.

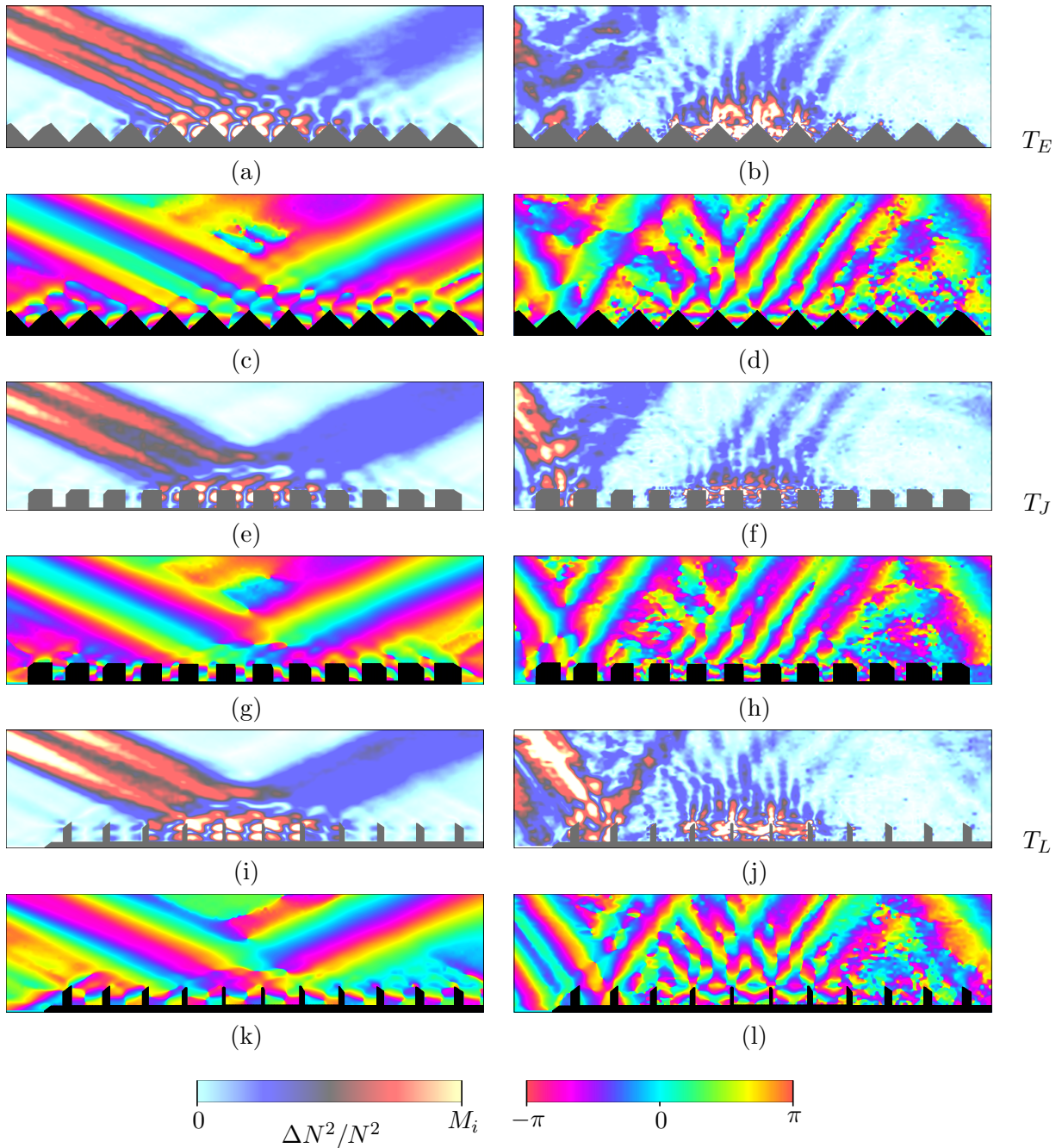


Figure 7.20: Amplitude and phase images of temporal harmonics generated by supercritical scatter at sawtooth, square-wave and knife-edge profiles T_E , T_J and T_L with $\sigma/N = 0.38$ and $\theta/\alpha = 1.51$, 1.51 and 1.46 . RMS_T images of primary and secondary harmonics are shown in (a-b), (e-f) and (i-j) respectively. Corresponding phase images are shown in (c-d), (g-h) and (k-l). Amplitude maxima M_i have values of 5.4×10^{-2} , 5.4×10^{-3} and 5.4×10^{-4} for $i = 1, 2$ and 3 .

Maximum amplitudes of the components generated by scattering of the primary incident beam are approximately second order in magnitude, with the largest amplitudes generated at the sawtooth profile (*c.f.* figure 6.28, where the most prominent secondary harmonic wavefield was generated at

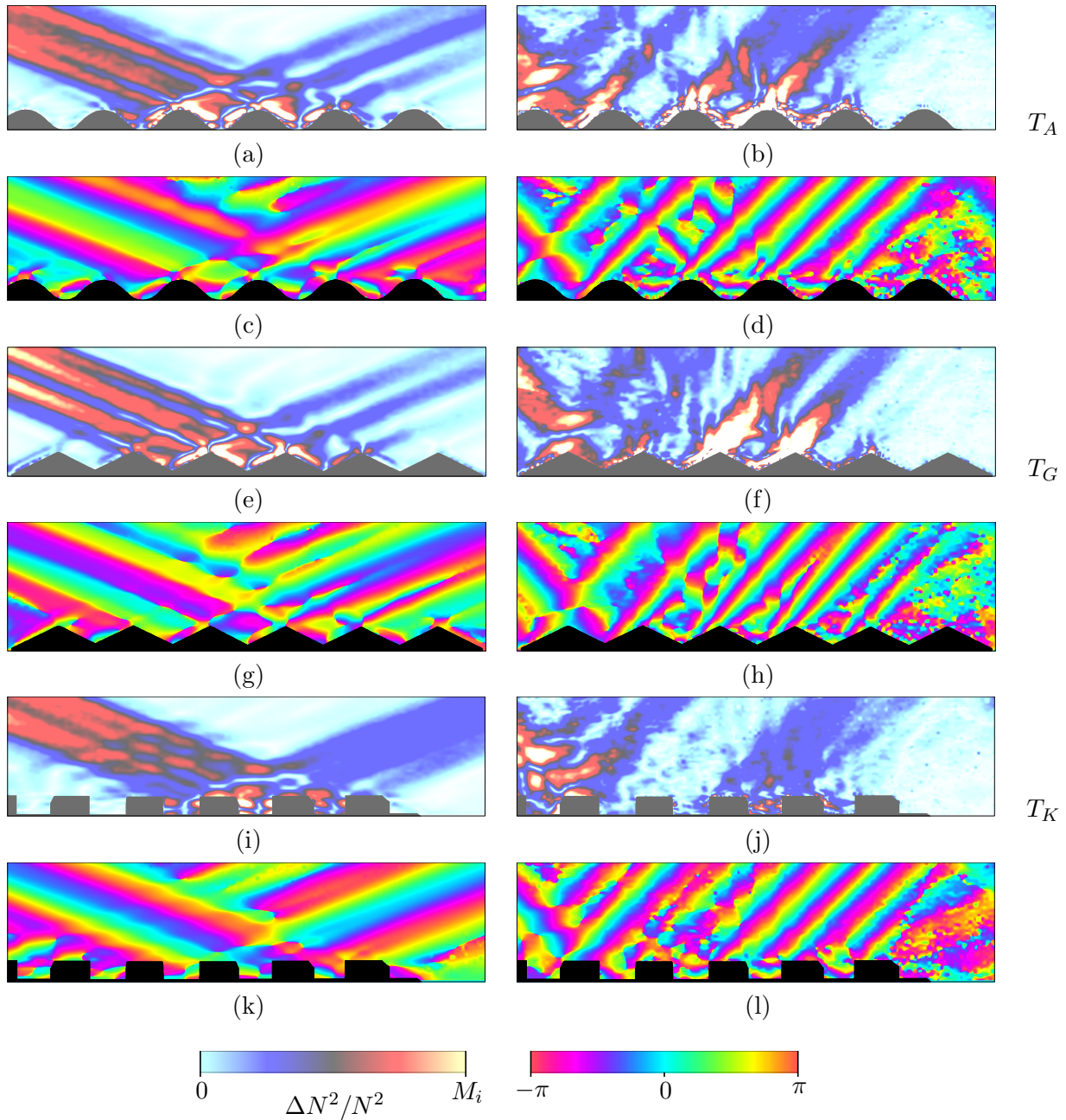


Figure 7.21: Amplitude and phase images of temporal harmonics generated by supercritical scatter at sinusoidal, sawtooth and square-wave profiles T_A , T_G and T_K with $\sigma/N = 0.33$, 0.35 and 0.33 , $\theta/\alpha = 1.14$, 1.10 and 1.16 . RMS_T images of primary and secondary harmonics are shown in (a-b), (e-f) and (i-j) respectively. Corresponding phase images are shown in (c-d), (g-h) and (k-l). Amplitude maxima M_i have values of 5.4×10^{-2} , 5.4×10^{-3} and 5.4×10^{-4} for $i = 1, 2$ and 3 .

the sinusoid T_A). As for the experiments relating to figure 7.20, the secondary harmonics for the experiments shown in figure 7.21 are *subcritical* with values of θ_2/α equal to 0.79, 0.72 and 0.80 for T_A , T_G and T_K respectively. These harmonics decay less rapidly as the wave energy propagates away from the topography than those for the secondary harmonics shown in figures 6.28 and 7.20. Wave frequencies associated with figure 6.28 were close to N and hence, in these experiments, the resulting small group velocities confined secondary harmonic wave energy near the boundary. In contrast, the smaller frequencies and hence larger group velocities of the secondary harmonics in figure 7.21 allowed the wave energy to ‘escape’ from the region near the topography and so a further reaching secondary harmonic wavefield is therefore seen in this case. Also, secondary harmonic wave energy with values of θ_2/α as in experiments shown in figure 7.21 is less focused than the wave energy associated with the scatter in figure 7.20 (b) and (d), for example, for which values of θ_2/α are closer to critical. Hence viscous attenuation of the wave energy is less pronounced at the smaller values of θ_2/α . In addition, the secondary harmonics shown for the scatter in figure 7.21 experience a weaker interaction with the corresponding forwards scattered primary component, due to the supercritical nature of the scatter at first order, relative to that encountered by the secondary harmonics generated during the subcritical scatter shown in figure 6.28, for which the forwards scattered wavefield at first order is more pronounced. As for the subcritical cases of figure 6.28 and supercritical cases of figure 7.20, magnitudes of secondary harmonic wavefield perturbations are greatest near corners of the sawtooth and square-wave topographies shown in figure 7.21, with the sawtooth exhibiting the strongest wavefield. Again, scatter at this order is dominantly in the forwards direction for each topography but inspection of the phase images of figure 7.21 (d), (h) and (l) also indicates the presence of *back-scattered* secondary harmonic wave energy. The scatter in this direction is also weakly visible in the corresponding amplitude images in figure 7.21 (b), (f) and (j).

Tertiary harmonic component generation is also possible for the experiments shown with profiles T_A and T_K in figure 7.21. However, as a consequence of the weak third order magnitude of the perturbations associated with the tertiary harmonic wavefields, which rapidly became comparable with levels of experiment background noise as this wave energy propagated away from the topography, images produced after filtering at the frequency $3\sigma/N$ did not yield any clear signature for the tertiary harmonics. This was also due in part to the limitations imposed by the finite temporal resolution of the experimental movies that caused signals from the primary and secondary harmonics to leak into the filtered tertiary data.

7.5 Summary

This chapter has presented results from supercritical scatter at various sawtooth topographies and compared these with scattering behaviour at analogous square-wave and pseudo knife-edge profiles. Only theoretical predictions of inviscid linear geometrical ray tracing have been available for comparison to the experimental results, which predicted no forwards or back-scatter at the saw-

tooth topographies. Contrary to these ray tracing predictions, both forward and back-scattered supercritical wavefields were observed at the sawtooths, including scatter to higher wavenumbers. Forward and back-scattered wavefields were most prominent as θ/α became closer to critical value. In general, scatter at the knife-edge profile compared well with that of the sawtooth, whilst scatter at the square-wave was more pronounced and followed different trends with increasing θ/α . The similarities between behaviour at the sawtooth and knife-edge might be expected. Since the fluid is not inviscid, the tips of the knife-edges of T_L may effectively influence the wave motion as *one* topographic discontinuity, rather than as the *two* corners featured on the crests of the square-wave. In this sense the knife-edge therefore behaves like the sawtooth, which also has one corner on each crest. However, unlike the knife-edge, the slopes of the sawtooth focus wave energy down into the troughs of the topography and hence weaken the scattered wavefields. Near-field features of the scatter, such as the generation of mixed fluid at topographic corners, were most prominent for the sawtooth and knife-edge. In particular, the intense high wavenumber scatter and enhanced energy densities at the tips of the knife-edge, as compared with behaviour near the corners of the sawtooth, and therefore promoted viscous attenuation of the wave energy as it propagated away. Hence, despite the reductions in scattered wave energy propagating away from the topography caused by down focusing into troughs of the sawtooth, far-field energy densities of the sawtooth and knife-edge are comparable as a result of the enhanced viscous action in the region of the knife-edge. Observed scatter at the square-wave and knife-edge also exhibit discrepancies with ray tracing predictions. To some degree, the failure of the inviscid ray tracing to correctly model the scatter may be attributed to the presence of thin boundary layers along the surface of the topography, which would act to effectively change the dimensions of the profiles. As an illustration of how the coefficients might be effected by this, figure 6.25 compares ray tracing predictions for square-wave profiles T_K and T_J and pseudo knife-edge T_L with predictions for these profiles with an additional 1 mm along each of their surfaces (dashed cyan, red and blue lines respectively). In addition, the ignorance of time of the ray tracing method results in violations of the radiation condition. Experimental results of near-critical scatter at various rough topographic profiles are described in the following chapter.

Chapter 8

Near-critical rough topography

8.1 Overview

Chapters 6 and 7 discussed subcritical ($\theta/\alpha < 1$) and supercritical ($\theta/\alpha > 1$) scatter at sinusoidal, sawtooth, square-wave and knife-edge topographies. Effects on forwards and back-scattered wavefields from varying θ/α and the topographic wavenumber, amplitude and aspect ratio of sawtooth topographies were described, as well as the influence of topographic shape.

As the angle of incident wave energy propagation becomes closer to the angle of inclination of topographic slopes, *i.e.* θ/α approaches the critical value of unity, inviscid linear ray tracing predicts an increasing degree of focusing (see figure 6.6) of the wave energy that is incident on the slopes of the sawtooth that are oriented with positive gradient (*i.e.* for wave energy incident between the green and blue lines depicted on figure 6.5). Also, a smaller fraction is incident on the defocusing slopes. The constriction of wave energy in this manner causes reductions in the associated length scales of the wave motion in the direction perpendicular to that of the energy propagation and hence results in scatter to increasingly higher wavenumbers as $\theta/\alpha \rightarrow 1$. However, geometrical ray tracing breaks down in this limit and there is an absence of theoretical predictions for the critical case. As for the subcritical and supercritical cases presented in chapters 6 and 7, experimental and numerical results of near-critical scatter at rough topographic profiles are also unprecedented. This chapter discusses experiment results of scatter in near-critical, *i.e.* as $\theta/\alpha \rightarrow 1$, configurations.

8.2 Sawtooth topography

Results of near-critical scatter at sawtooth topographies are presented here.

8.2.1 Varying the wavenumber

This section discusses the effect on scattered wavefields of variation of the horizontal topographic wavenumber, \hat{k}_T , for a fixed aspect ratio, $\hat{A}_T \hat{k}_T$, and hence topographic slope angle α .

Comparison of near-critical scatter at sawtooths T_D and T_E

Sawtooth profiles T_D and T_E have approximately equal aspect ratios with values $\hat{A}_T \hat{k}_T = 1.580$ and 1.575 , respectively, but are characterised by different horizontal topographic wavenumbers of $\hat{k}_T = 0.088 \text{ mm}^{-1}$ and 0.175 mm^{-1} . Length scales of the incident wavefield are compared with those of T_D and T_E with the parameters $k_c/\hat{k}_T = 4.01$ and 2.02 , and $\hat{A}_T k_c = 6.34$ and 3.18 . Hence length scales associated with T_D are approximately twice those of T_E . Chapter 7 compared supercritical scatter at T_D and T_E . In contrast to inviscid ray tracing predictions, high wavenumber scatter was measured in the supercritical conditions at each topography in both the forward and back-scatter directions. The scatter is most prominent for the experiments with values of θ/α closest to critical. Despite the higher topographic wavenumber associated with T_E , the greatest proportion of high wavenumber scatter was measured in the far-field of T_D . This behaviour is attributed here to the more rapid attenuation of scattered wave energy in the near-field of T_E , which imposes smaller length scales on the scattered wavefield than T_D . Figure 8.1 shows far-field RMS_T images of scatter at sawtooth profiles (a) T_D and (c) T_E for near-critical (marginally supercritical) values of θ/α equal to 1.08 and 1.05 respectively. Corresponding zooms of the wavefields are shown in figure 8.1 (b) and (d). Forwards and back-scattered wavefields are also evident at both topographies in these near-critical configurations. Figure 8.1 (a) and (c) can be compared with those at larger values of θ/α shown in figures 7.1 and 7.7. The near-critical scatter is similar in character to that observed at larger θ/α but is associated with larger amplitudes in the far-field. As in the specular case, this can be understood by geometrical ray tracing arguments for which reflecting rays are constricted more, and hence wave energy focused more, as the inclination of group velocity vectors approach that of the topographic slopes. Near-field energy densities are also more pronounced for the near-critical cases (figure 8.1 (b) and (d)), with the largest amplitudes occurring near the sawtooth corners and most dominantly for T_D since more incident wave energy can be focused into each scattered ‘beam’ along the slopes of T_D , which have greater surface areas than those of T_E . Speeds associated with the near-critical fluid motion for experiments at sawtooth T_D are shown in figure 7.4 (a) and (c). These are greatest at the smallest value of θ/α near the sawtooth corners and along the slopes and characteristics emanating from the corners. As a consequence of the greater energy densities and fluid speeds, the mixing feature described in earlier sections (e.g. figure 7.3) is promoted in the near-critical configuration, and is particularly significant near the corners of T_D (see figure 8.1 (b)).

Comparison of near-critical scatter at sawtooths T_G and T_H

Sawtooth profiles T_G and T_H have approximately equal aspect ratios with values $\hat{A}_T \hat{k}_T = 0.783$ and 0.785 , respectively, but are characterised by different horizontal topographic wavenumbers of $\hat{k}_T = 0.087 \text{ mm}^{-1}$ and 0.157 mm^{-1} . Length scales of the incident wavefield are compared with those of T_G and T_H with the parameters $k_c/\hat{k}_T = 4.06$ and 2.25 , and $\hat{A}_T k_c = 3.18$ and 1.77 . Hence length scales associated with T_G are approximately twice those of T_H . Slopes of these sawtooth profiles are shallower than those of sawtooths T_D and T_E , discussed above. Section 6.2.1 compared

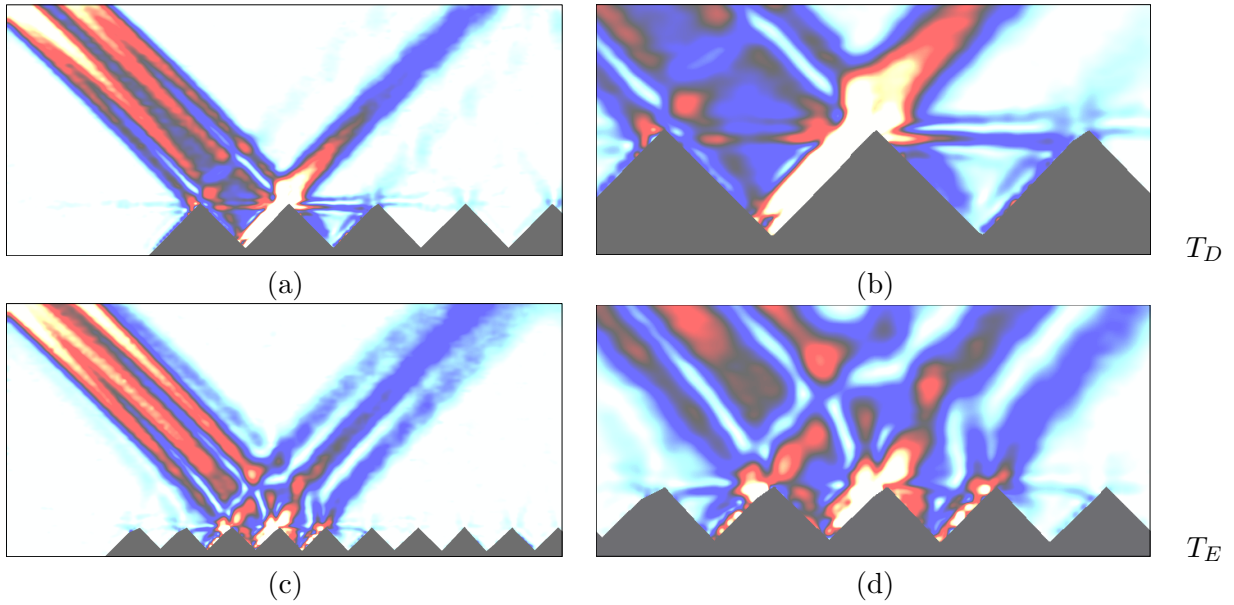


Figure 8.1: RMS_T images of $\Delta N^2/N^2$ fields for near-critical scatter at sawtooth profiles T_D and T_E with θ/α equal to (a-b) 1.08 and (c-d) 1.05 respectively. Fields of view shown in (a) and (c) measure 449 mm across and have unit aspect ratio. Colours are scaled as in figure 6.4. Corresponding zooms by factor 24/7 and colours scaled with maxima 10% greater than the larger fields of view are shown in (b) and (d).

subcritical scatter at T_G and T_H . In accordance with theoretical predictions based on inviscid linearised boundary theory, high wavenumber scatter was measured in subcritical conditions at each topography in both the forward and back-scatter directions. Far-field forward scatter is most prominent for experiments with the smallest values of θ/α , *i.e.* furthest from the critical value, whilst far-field back-scatter is most prominent for experiments with θ/α closest to critical. As noted for scatter at sawtooths T_D and T_E , the greatest proportion of high wavenumber scatter is measured in the far-field of the sawtooth characterised by the larger length scales, in this case T_G . Figure 8.2 shows far-field RMS_T images of scatter at sawtooth profiles (a) T_G and (c) T_H for the near-critical (marginally supercritical) value of $\theta/\alpha = 1.02$. Corresponding zooms of the wavefields are shown in figure 8.2 (b) and (d). Forwards and back-scattered wavefields are also evident for near-critical conditions at both T_G and T_H . Figure 8.2 (a) and (c) compares qualitatively well with scatter at smaller values of θ/α shown in figures 6.4 and 6.11. Amplitudes of forward scattered wavefields are weakest in the near-critical case for both topographies, whilst those of back-scattered wavefields are enhanced near-critical. As for sawtooths T_D and T_E , near-field energy densities are most pronounced for near-critical configurations (figure 8.2 (b) and (d) and figure 6.9), at sawtooth corners and for the sawtooth with the largest length scales, in this case T_G .

In summary, both forward and back-scattered wavefields are generated in near-critical scattering conditions at the sawtooth profiles considered. Far-field amplitudes of the forward scatter decrease as θ/α increases from subcritical values towards critical, and decrease further as θ/α increases into

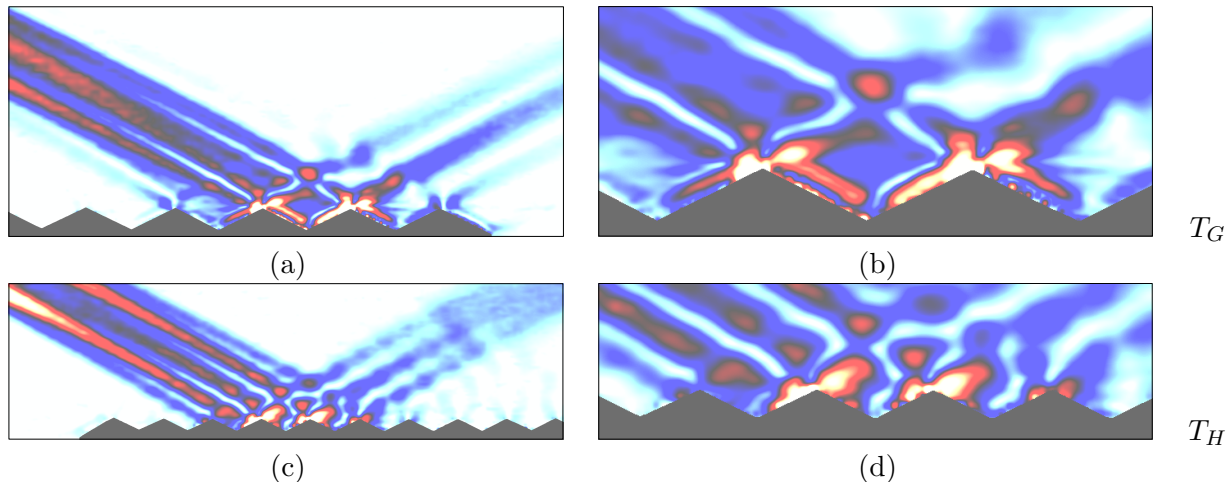


Figure 8.2: RMS_T images of $\Delta N^2/N^2$ fields for near-critical scatter at sawtooth profiles T_G and T_H with θ/α equal to 1.02 in each case. Fields of view shown in (a) and (c) measure 449 mm across and have unit aspect ratio. Colours are scaled as in figure 6.4. Corresponding zooms by factor 24/7 and colours scaled with maxima 10% greater than the larger fields of view are shown in (b) and (d).

supercritical values. By contrast, the far-field structure of back-scattered wave energy and near-field amplitudes become more prominent as $\theta/\alpha \rightarrow 1$ from either sub or supercritical values. Comparisons between pairs of topographies that have the same aspect ratios but different wavenumbers suggest that near-critical far-field behaviour and high wavenumber scatter as well as near-field nonlinear features are most pronounced for those topographies of the present study characterised by *larger* length scales, *i.e.* T_D and T_G .

8.2.2 Varying the slope

This section discusses the effect on scattered wavefields of variation in the topographic wavenumber, \hat{k}_T , and hence the topography aspect ratio, $\hat{A}_T \hat{k}_T$, and slope angle, α , for a fixed topographic amplitude, \hat{A}_T .

Comparison of near-critical scatter at sawtooths T_C , T_E and T_G

Sawtooth profiles T_C , T_E and T_G have approximately equal amplitudes with values $\hat{A}_T = 9.5$, 9.0 and 9.0 mm, respectively, but are characterised by different horizontal topographic wavenumbers of $\hat{k}_T = 0.197$, 0.175 and 0.087 mm^{-1} and hence aspect ratios $\hat{A}_T \hat{k}_T = 1.872$, 1.575 and 0.783. Length scales of the incident wavefield are compared with those of T_C , T_E and T_G with the parameters $k_c/\hat{k}_T = 1.79$, 2.02 and 4.06, and $\hat{A}_T k_c = 3.35$, 3.18 and 3.18 respectively. As was observed in the results presented above, inspection of sequences of experiments for scatter with subcritical and supercritical values of θ/α at profiles T_C , T_E and T_G indicates that far-field energy densities associated with the forward scattered wave energy decrease with increasing θ/α , whilst those associated with the *back-scatter* become less prominent as θ/α is decreased or increased from the critical value.

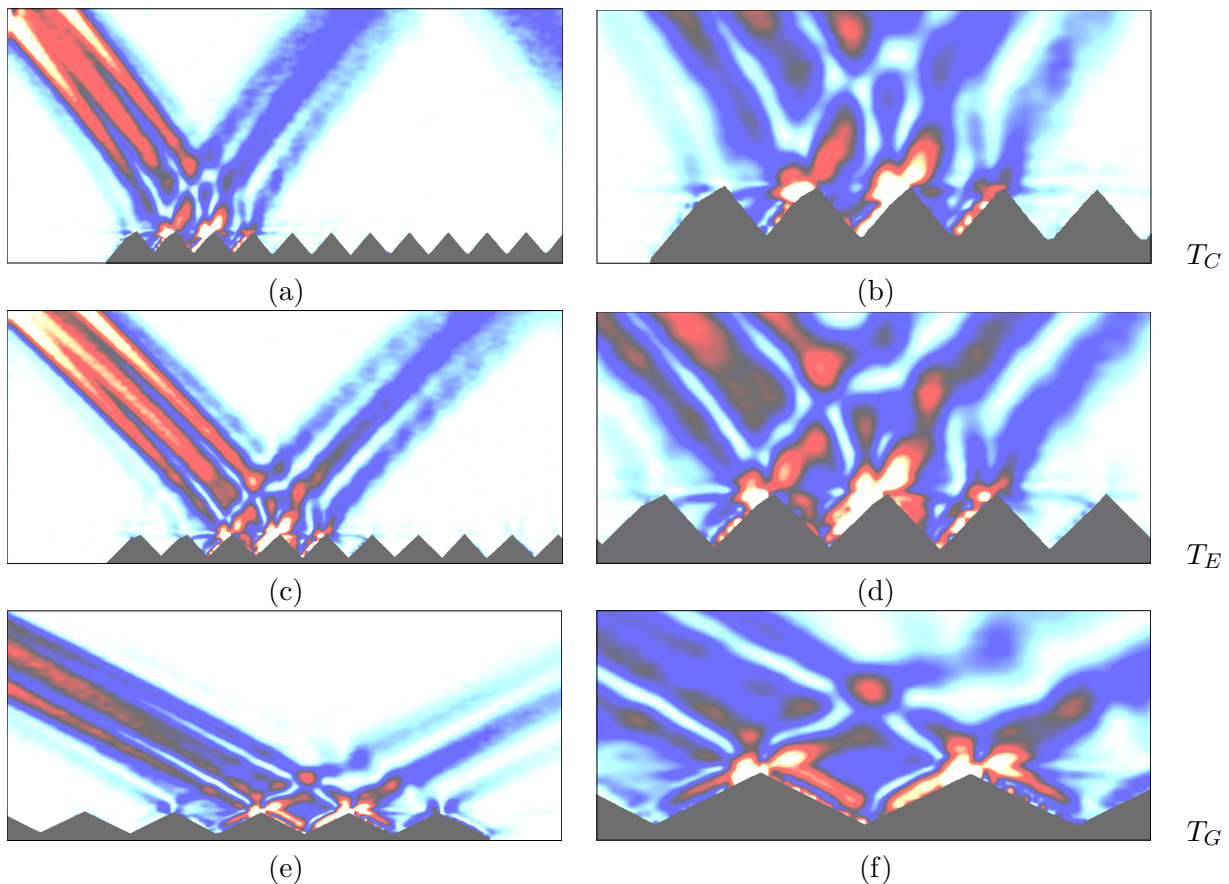


Figure 8.3: RMS_T images of $\Delta N^2/N^2$ fields for near-critical scatter at sawtooth profiles T_C , T_E and T_G with θ/α equal to (a-b) 1.06, (c-d) 1.05 and (e-f) 1.02 respectively. Fields of view shown in (a), (c) and (e) measure 449 mm across and have unit aspect ratio. Colours are scaled as in figure 6.4. Corresponding zooms by factor 24/7 and colours scaled with maxima 10% greater than the larger fields of view are shown in (b), (d) and (f).

Figure 8.3 shows RMS_T images of scatter at sawtooth profiles (a) T_C , (c) T_E and (e) T_G for near-critical (marginally supercritical) values of θ/α equal to 1.06, 1.05 and 1.02 respectively. Corresponding zooms of the wavefields are shown in figure 8.3 (b), (d) and (f). There is little distinction between back-scattered wavefields, and amplitudes of the near-field wave motion are also similar for all profiles. Most notably for these profiles, far-field forward scattered energy densities are greatest for T_C , *i.e.* the profile with the largest horizontal wavenumber. In part, this may be a result of the greater value of σ/N used for this experiment, which implies lower group velocities and hence higher energy densities. It is also possible that since the corners of T_C are so close together, with this profile having the largest horizontal wavenumber and hence the largest number of topographic corners per incident wave group, the influence of the mixed fluid expelled into the stratification at the corners is more significant. It could be expected that a proportion of incident wave energy reflects from the discontinuity introduced into the otherwise continuous background stratification by the mixed fluid intruding from the corners (see also section 3.8.3) and hence promotes scatter

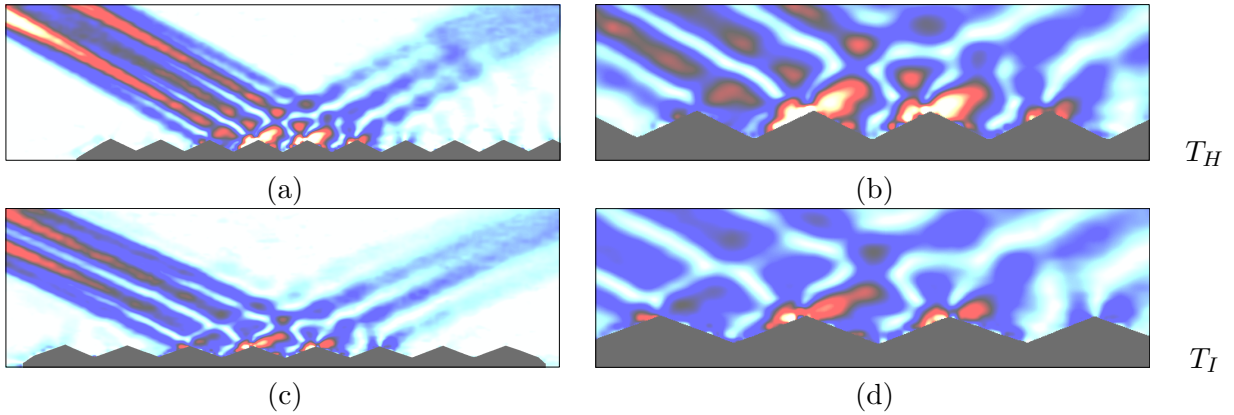


Figure 8.4: RMS_T images of $\Delta N^2/N^2$ fields for near-critical scatter at sawtooth profiles T_H and T_I with θ/α equal to (a-b) 1.02 and (c-d) 0.99 respectively. Fields of view shown in (a) and (c) measure 449 mm across and have unit aspect ratio. Colours are scaled as in figure 6.4. Corresponding zooms by factor 24/7 and colours scaled with maxima 10% greater than the larger fields of view are shown in (b) and (d).

to the primary component rather than higher wavenumbers, which would be expected to attenuate more rapidly by viscous action than corresponding scatter at T_E and T_G . In general, however, the mixed fluid generated during experiments of the duration used in this study did not have a significant influence on scattered wavefields (see figure 3.33).

Comparison of near-critical scatter at sawtooths T_H and T_I

Sawtooth profiles T_H and T_I have equal amplitudes of value $\hat{A}_T = 10.0$ mm but are characterised by different horizontal topographic wavenumbers of $\hat{k}_T = 0.157$ and 0.117 mm^{-1} and hence aspect ratios $\hat{A}_T \hat{k}_T = 0.785$ and 0.585 . Length scales of the incident wavefield are compared with those of T_H and T_I with the parameters $k_c/\hat{k}_T = 2.25$ and 3.02 , and $\hat{A}_T k_c = 1.77$ respectively. Figure 8.4 shows RMS_T images of scatter at sawtooth profiles (a) T_H and (c) T_I for near-critical values of θ/α equal to 1.02 (*i.e.* marginally supercritical) and 0.99 (*i.e.* marginally subcritical) respectively. Corresponding zooms of the wavefields are shown in figure 8.4 (b) and (d). Section 6.2.1 compares subcritical scatter at T_H and T_I . The trends described there include the near-critical case so that the proportion of high wavenumber scatter propagating to the far-field is greatest for T_I , despite this profile having the smaller horizontal wavenumber, since viscosity preferentially attenuates small length scales of the fluid motion. As for scatter at T_C , T_E and T_G described above, little distinction can be made between the near-critical back-scattered wavefields at T_H and T_I .

This section has discussed effects of variation in the topographic wavenumber, \hat{k}_T , for a fixed topographic amplitude, \hat{A}_T . As values of k_c/\hat{k}_T approach unity and below, wavefield behaviour, such as those causing fluid mixing, occurring near topographic corners becomes more significant. Local ‘steps’ introduced into the background stratification in the region of corners, which decrease in strength with distance from corners, can reflect incident wave energy (as shown for a marginally

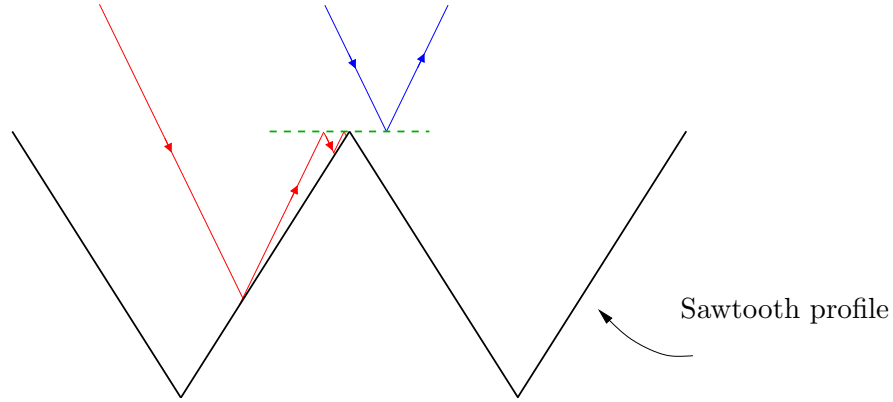


Figure 8.5: Schematic of rays (red and blue lines - incident from top left) reflecting specularly at a discontinuity in the background stratification (green dashed line) near a corner of a sawtooth topographic profile.

subcritical ray (blue) assumed to reflect specularly in the schematic of figure 8.5) and possibly trap, and thereby focus, wave energy reflecting away from the topographic slopes near the corner (red ray). As the number of corners per incident wave group increases with topographic wavenumber, a greater proportion of incident wave energy reflects at the changes in background stratification in the manner described rather than at the slopes of the topography. In addition, the high wavenumber scatter that *is* generated at profiles characterised by the larger horizontal wavenumbers is acted on more rapidly by viscosity than corresponding scatter at profiles with smaller wavenumbers. Hence, for fixed topographic amplitudes, high wavenumber scatter measured in the far-field is greatest for the profiles used in this study that are characterised by the largest horizontal length scales.

8.2.3 Varying the aspect ratio

This section discusses the effect on scattered wavefields of variation of topography aspect ratio, $\hat{A}_T \hat{k}_T$, and hence slope angle α , for a fixed horizontal topographic wavenumber, \hat{k}_T .

Comparison of near-critical scatter at sawtooths T_D and T_G

Sawtooth profiles T_D and T_G have approximately equal topographic wavenumbers of values \hat{A}_T equal to 0.088 and 0.087 mm^{-1} but are characterised by different aspect ratios of values $\hat{A}_T \hat{k}_T = 1.580$ and 0.783 and hence slope angles $\alpha = 45.0^\circ$ and 63.5° . Length scales of the incident wavefield are compared with those of T_D and T_G with the parameters $k_c/\hat{k}_T = 4.01$ and 4.06, and $\hat{A}_T k_c = 6.34$ and 3.18 respectively. Figure 8.6 shows RMS_T images of scatter at sawtooth profiles (a) T_D and (c) T_G for near-critical (marginally supercritical) values of θ/α equal to 1.08 and 1.02 respectively. Corresponding zooms of the wavefields are shown in figure 8.6 (b) and (d). The near-critical wave energy forward scattered at T_D , *i.e.* the profile with the greater amplitude, is dominantly focused into one beam like structure, whereas the forward scatter at T_G is partitioned between a greater

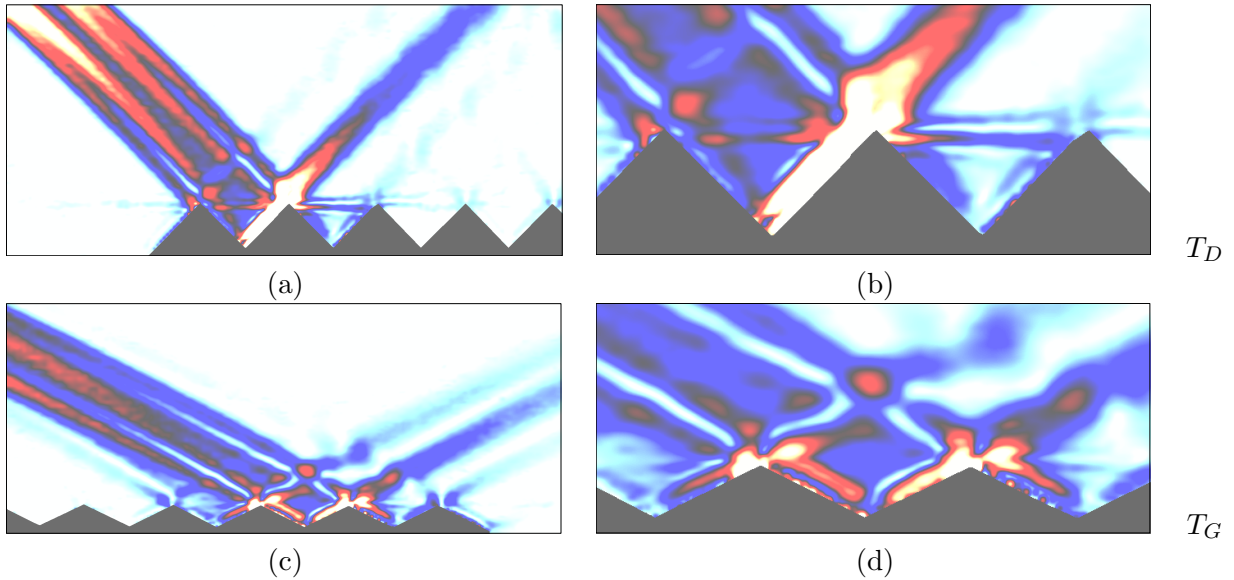


Figure 8.6: RMS_T images of $\Delta N^2/N^2$ fields for near-critical scatter at sawtooth profiles T_D and T_G with θ/α equal to (a-b) 1.08 and (c-d) 1.02 respectively. Fields of view shown in (a) and (c) measure 449 mm across and have unit aspect ratio. Colours are scaled as in figure 6.4. Corresponding zooms by factor 24/7 and colours scaled with maxima 10% greater than the larger fields of view are shown in (b) and (d).

number of such beams. The greater degree of focusing at the larger value of $\hat{A}_T \hat{k}_T$ results in greater near-field amplitudes, particularly near the topographic corners of T_D . Consequently, the mixing feature described in earlier sections is more prominent than for T_G . There is little distinction between back-scattered wavefields generated at the two profiles.

Comparison of near-critical scatter at sawtooths T_E and T_F

Sawtooth profiles T_E and T_F have approximately equal topographic wavenumbers of values \hat{k}_T equal to 0.175 and 0.176 mm^{-1} , respectively, but are characterised by different aspect ratios of values $\hat{A}_T \hat{k}_T = 1.575$ and 1.144 and hence slope angles $\alpha = 45.0^\circ$ and 54.0° . Length scales of the incident wavefield are compared with those of T_E and T_F with the parameters $k_c/\hat{k}_T = 2.02$ and 2.01, and $\hat{A}_T k_c = 3.18$ and 2.29, respectively. Figure 8.7 shows RMS_T images of scatter at sawtooth profiles (a) T_E and (c) T_F for near-critical (marginally supercritical) values of θ/α equal to 1.05 and 1.02 respectively. Corresponding zooms of the wavefields are shown in figure 8.7 (b) and (d). The smaller value of k_c/\hat{k}_T associated with T_E and T_F , as compared with that for T_D and T_G , implies that a wave group scattering at T_E or T_F encounters a greater number of topographic corners. As discussed above, this might imply a greater proportion of scatter to the primary component in these cases, instead of to higher wavenumbers, as wave energy reflects at mixed fluid patches generated near the corners. As for comparisons of profiles T_D and T_G , greater focusing of the forwards scattered wave energy is observed for the topographic profile with the largest amplitude and hence aspect

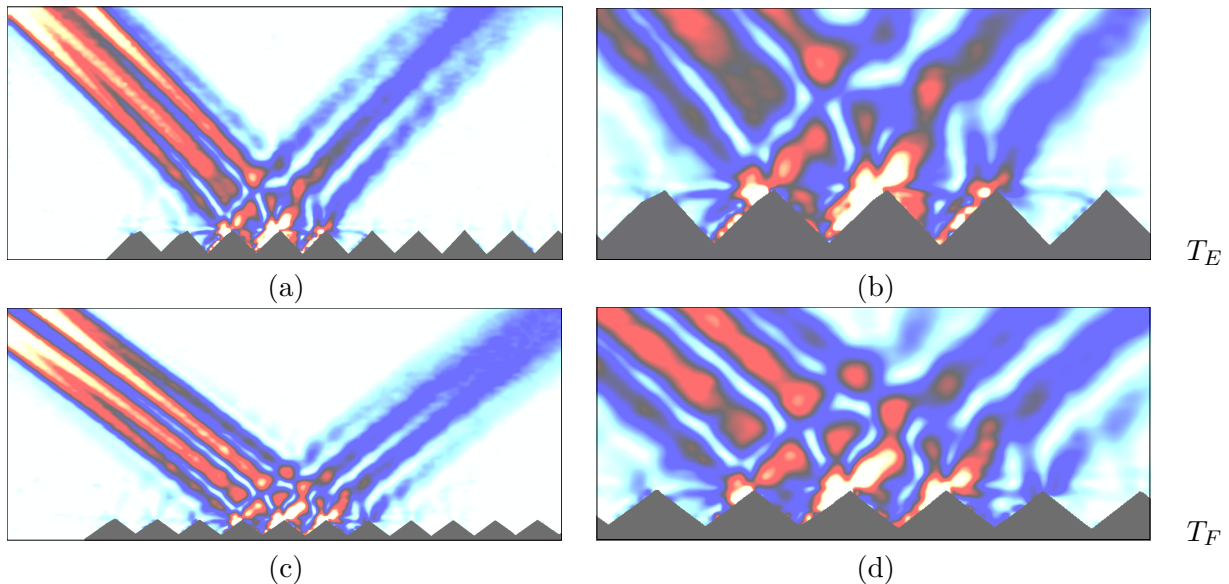


Figure 8.7: RMS_T images of $\Delta N^2/N^2$ fields for near-critical scatter at sawtooth profiles T_E and T_F with θ/α equal to (a-b) 1.05 and (c-d) 1.02 respectively. Fields of view shown in (a) and (c) measure 449 mm across and have unit aspect ratio. Colours are scaled as in figure 6.4. Corresponding zooms by factor 24/7 and colours scaled with maxima 10% greater than the larger fields of view are shown in (b) and (d).

ratio, *i.e.* T_E rather than T_F . However, there is little distinction between near-field features and back-scatter at these profiles.

The variation of amplitude, and hence aspect ratio, of topographies for a fixed topographic wavenumber essentially controls the distribution of the scattered wave energy in physical space. Larger topographic amplitudes result in wave energy being focused into a smaller region (*i.e.* narrower B_F). This increases near-field amplitudes and hence promotes nonlinear behaviour and instability near the topographic corners. The larger shear associated with larger wave amplitudes implies that viscous attenuation is enhanced and so high wavenumber scatter measured in the far-field is reduced.

8.3 Topographic shape

This section discusses the effect on scattered wavefields in the limit $\theta/\alpha \rightarrow 1$ of variation of the topographic shape.

8.3.1 Curves versus corners

Sinusoid T_A and square-wave T_K are approximately analogous to sawtooth profile T_G . In depth descriptions of scatter at these profiles for marginally subcritical values of θ/α were given in section 6.3. It was deduced that, contrary to inviscid linear geometrical ray tracing predictions, trends

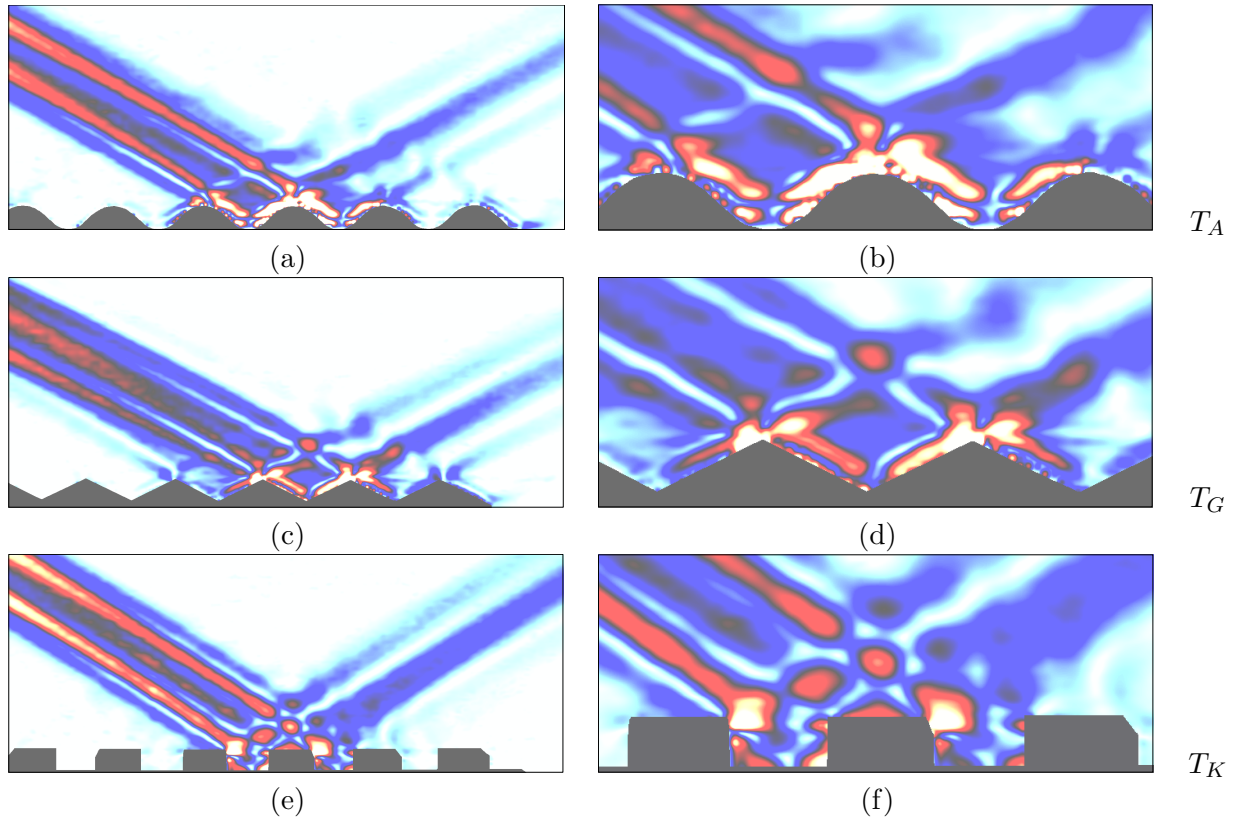


Figure 8.8: RMS_T images of $\Delta N^2/N^2$ fields for near-critical scatter at sinusoid T_A , sawtooth T_G and square-wave T_K with θ/α equal to (a-b) 1.01, (c-d) 1.02 and (e-f) 0.99 respectively. Fields of view shown in (a), (c), (e) and (g) measure 449 mm across and have unit aspect ratio. Colours are scaled as in figure 6.4. Corresponding zooms by factor 24/7 and colours scaled with maxima 10% greater than the larger fields of view are shown in (b), (d) and (f).

for scatter at the sinusoid and square-wave are strongly analogous to those for the sawtooth and scatter at each profile correlates well with predictions made by inviscid linearised boundary theory for the sinusoid. However, the influence of viscosity, which varies according to the profile shape, modifies energy density spectra for the scattered wavefields, causing the greatest discrepancies with theory as θ/α approaches critical. As a consequence of the large degree of focusing at the sawtooth slopes and corners, viscous action is most pronounced on wave motion associated with T_G so that far-field measurements of proportions of high wavenumber scatter are the least significant for this profile whereas near-field features, such as the generation of mixed fluid, are the most prominent.

Figure 8.8 shows RMS_T images of scatter at (a) sinusoid T_A , (c) sawtooth T_G and (e) square-wave T_K for near-critical values of θ/α equal to 1.01 (*i.e.* marginally supercritical), 1.02 (*i.e.* marginally supercritical) and 0.99 (*i.e.* marginally subcritical) respectively. Corresponding zooms of the wavefields are shown in figure 8.8 (b), (d) and (f). Wavefield behaviour for the near-critical experiments shown here is consistent with the trends reported for subcritical θ/α in section 6.3. For each topographic shape, proportions of high wavenumber forwards scatter measured in the far-field are

comparable with those of the back-scatter in near-critical conditions. The most pronounced wavefield in the far-field is measured for the square-wave since the focusing of wave energy along the slopes (absent for T_K) of the sinusoid and sawtooth enhances viscous attenuation of the scattered wavefields generated at these profiles. Near-field behaviour for T_G , most significant in near-critical conditions, was presented in section 6.3. The mixing feature is most pronounced for the sawtooth, near topographic corners, and is least evident in the square-wave case. Scatter to higher temporal harmonics at T_A , T_G and T_K for marginally subcritical values of θ/α was discussed in section 6.3.

8.3.2 Corners versus knife-edges

Square-wave T_J and knife-edge T_L are approximately analogous to sawtooth profile T_E . In depth descriptions of scatter at these profiles for supercritical values of θ/α were given in section 7.3. Measured scatter does not correlate well with ray tracing predictions for any of the profiles in supercritical conditions. In particular, forwards and back-scattered wavefields are observed at the sawtooth. Scatter at the knife-edge compares qualitatively well with that at the sawtooth, with forwards and back-scatter most significant near-critical. Forward scatter at the square-wave follows a similar trend to that of the sawtooth and knife-edge, but there is some contrast between the back-scattered fields. In addition, back-scatter at the knife-edge becomes greatly enhanced near-critical values of θ/α . Near-field mixing features are also enhanced in this limit, being the most prominent near knife-edges and sawtooth corners.

Figure 8.9 shows RMS_T images of scatter at (a) sawtooth T_E , (c) square-wave T_J and (e) pseudo knife-edge T_L for near-critical (marginally supercritical) values of θ/α equal to 1.05, 1.05 and 1.02 respectively. Corresponding zooms of the wavefields are shown in figure 8.9 (b), (d) and (f). Wavefield behaviour for the near-critical experiments is consistent with the trends reported in section 7.3 for supercritical θ/α . The most dramatic features to note are that of the strong back-scatter and also the near-field mixing near the knife-edge (figure 8.9 (e) and (f)), which are not observed to this degree at the other profiles. Another point to note is the close proximity of adjacent corners of the square-wave profile as compared with the spacings of corners on the other profiles. Any mixing occurring at the square-wave corners, though observed to be less than at the other profiles, may therefore have a more significant influence on the far-field scatter. In a similar manner to that illustrated by the schematic of figure 8.5, wave energy can reflect directly at any steps in the background stratification introduced at the topographic corners. Hence this might cause enhanced proportions of scatter to the primary wavenumber component at the square-wave topography and, correspondingly, reductions in high wavenumber scatter there.

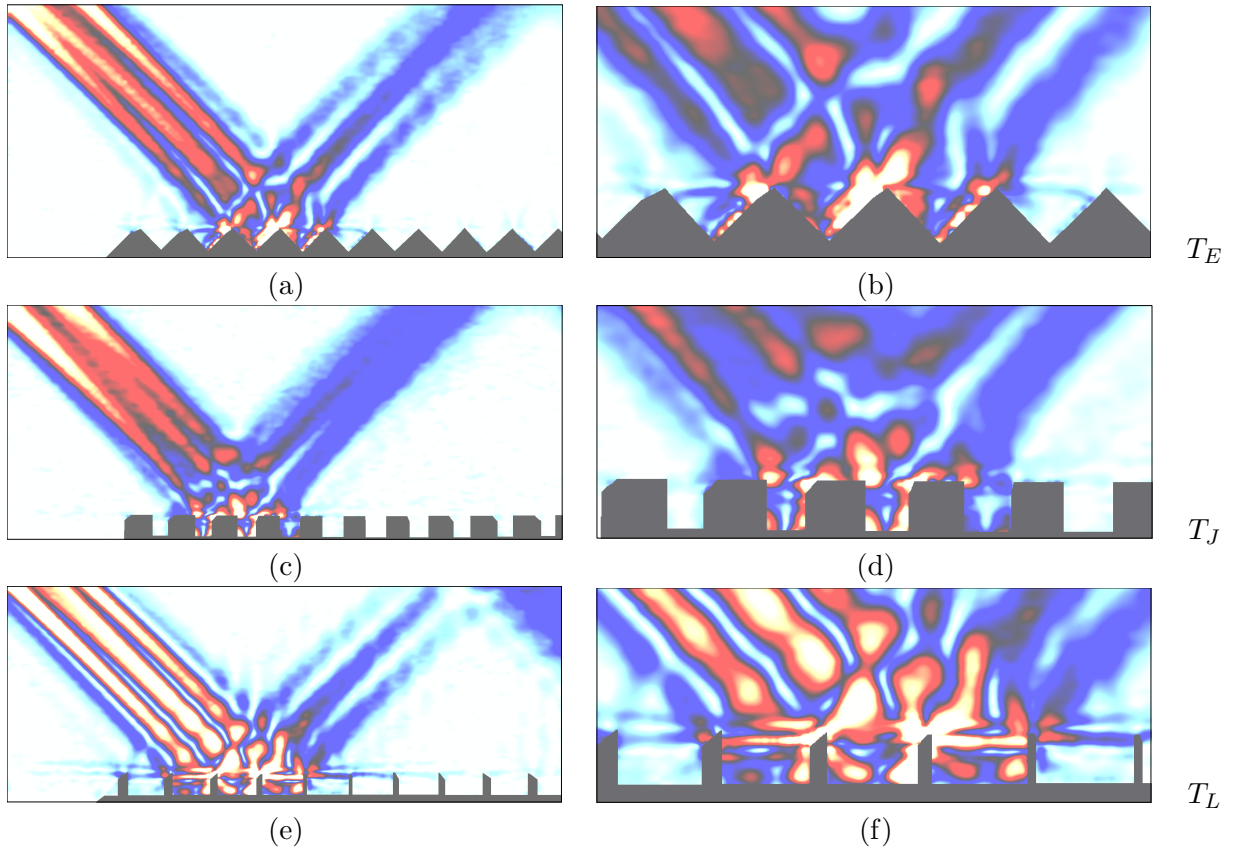


Figure 8.9: RMS_T images of $\Delta N^2/N^2$ fields for near-critical scatter at sawtooth T_E , square-wave T_J and knife-edge T_L with θ/α equal to (a-b) 1.05, (c-d) 1.05 and (e-f) 1.02 respectively. Fields of view shown in (a), (c), (e) and (g) measure 449 mm across and have unit aspect ratio. Colours are scaled as in figure 6.4. Corresponding zooms by factor 24/7 and colours scaled with maxima 10% greater than the larger fields of view are shown in (b), (d) and (f).

8.4 Summary

This chapter has presented unprecedented experimental results of scatter at rough periodic topographic profiles in near-critical configurations. These results represent the limiting case, *i.e.* $\theta/\alpha \rightarrow 1$, of the subcritical, $\theta/\alpha < 1$, and supercritical, $\theta/\alpha > 1$, behaviour described in chapters 6 and 7. The most significant observation as θ/α approaches critical is the enhancement in near-field dissipation and back-scatter, particularly at the knife-edge profile. This behaviour corresponds to a decrease in far-field scatter. As in the subcritical and supercritical configurations, the significant influence of viscosity on the evolution of the scattered wavefields has been highlighted. In particular, the form of scattered wavefields in the near and far-fields is subtly controlled by the combination of parameters comparing length scales of the topography and incident wavefield together with the relative degrees of viscous attenuation these parameters induce. In addition, the complexity of the scatter is increased by the presence of topographic corners and mixing in the near-field, as well as scatter to higher temporal harmonic components.

Chapter 9

Conclusions

This thesis has studied scattering behaviours of internal gravity waves using experimental approaches. Where possible, comparisons have been made between results from this study and the predictions of existing linear theory.

The experimental component of this research employed synthetic schlieren and PIV techniques. In order to accurately capture the phenomena being investigated, the visualisation methods were required to provide data with high spatial resolutions. To this end, careful customisations and optimisations of the techniques were made. In particular, these included damping of superfluous wavefields at the tank boundaries, precise alignment and rigorous tests to ensure an optimal camera setup and the minimisation of sources of light, heat and vibration in the surrounding environment. The use of artificial pearlescence in PIV experiments was tested with the aim of improving the spatial resolutions achievable for velocity measurements in this study and also as a technique for obtaining high resolution data with PIV in more general stratified contexts. Experiments were performed to observe two-dimensional wavefields generated by oscillating cylinders of various elliptical and rectangular cross-sections as well as reflection of internal wave beams at horizontal and sloping boundaries, a slowly varying curved boundary and a total of twelve sinusoidal, sawtooth, square-wave and pseudo knife-edge periodic rough topographic profiles. Very few of the phenomena reported here have been investigated in previous experimental studies and hence most of the results of the present research are the first of their kind.

9.1 Summary of results

9.1.1 Wave generation by oscillating cylinders

Results of wave generation by elliptical (including circular) and rectangular (including square) cylinders were presented in chapters 3 and 5. The form of wavefields generated in this manner are controlled by the parameters σ/N and A_c/D_c as well as the shape and aspect ratio of the cylinders. The frequency ratio σ/N controls the slope and magnitude of group velocity vectors and defines regimes for which propagating higher temporal harmonics may be generated. The amplitude

parameter A_c/D_c determines amplitudes, and hence stability, of the generated wave motion and the proportion of wave energy scattered to higher harmonics. Incident wavefields of this study are very small amplitude and are essentially linear, but still show some evidence of nonlinear effects. Previous studies have described wavefield generation by circular and square cylinders but the results presented here are of higher resolution than these studies and have been presented for a wider range of parameter values. Generation by elliptical and rectangular cylinders has not been documented in previous experimental studies. Results have been compared here with the linear theory of Hurley & Keady (1997).

Energy densities associated with the generated primary, secondary and tertiary harmonic wavefields increase with aspect ratios of the cylinders and, specifically, are focused along characteristics passing through corners or that are tangent to regions of high curvature along the surface of the cylinders. Length scales imposed on the wavefields are therefore determined by the across-beam locations of these characteristics, which, for a given cylinder, varies with σ/N . The regions of focused wave energy correspond with the generation of high wavenumber components, particularly at the corners of square and rectangular cylinders. The synthetic schlieren technique used in the experiments yields measurements of perturbations to *gradients* of the density field and so the method is sensitive to high wavenumber components. The preferential action of viscosity on high wavenumber components of the wave motion significantly modifies the wavefields as energy propagates to the far-field. Consequently, maxima of measured far-field energy density spectra are greatest in wavefields associated with *elliptical* cylinders. Conversely, near-field features such as mixed fluid generation observed near corners, regions of high curvature and vertical extremities of the cylinders are most prominent for the rectangular cylinders.

9.1.2 Reflection at horizontal and sloping boundaries

Results of reflection of internal gravity wave beams at horizontal boundaries and those inclined with an angle α relative to the vertical were described in chapter 4. Such configurations have been reported previously. However, as for the experiments of wavefield generation by cylinders, the present study provided results of higher resolution and over a wider range of parameter values. The results have also been analysed here in a more rigorous quantitative manner, including comparisons made with linear theory of Phillips (1966) together with simple adaptations to approximate the effects of viscous attenuation.

The slope parameter θ/α introduces sub-, near- and supercritical regimes defined for values $\theta/\alpha < 1$, $\theta/\alpha \approx 1$ and $\theta/\alpha > 1$ respectively. In general, sub- and supercritical experiments agree qualitatively with inviscid geometrical ray tracing predictions, though discrepancies owing to viscous attenuation of the wavefields are observed. As $\theta/\alpha \rightarrow 1$, ray tracing predicts greater focusing of incident wave energy and scatter to higher wavenumbers but the technique breaks down in the critical limit. This is illustrated by the observation of disturbances in near-critical experiments that propagate in both upslope *and* downslope directions. In addition, boundary layer structures, which

may mix fluid locally in more sustained wavefields, are seen to develop in near-critical configurations. The latter observations are consistent with those for experiments of Cacchione & Wunsch (1974) at similar values of Re .

9.1.3 Scatter at slowly varying topography

Chapter 4 also described original experiments of scatter at a section of cylindrical boundary, which was characterised by a constant radius of curvature, R_T , such that $R_T/D_c = 2.85$. In contrast to ray tracing predictions, the experiments illustrated configurations with split-reflection and diffraction, which *are* predicted at critical points of the boundary by Baines (1971b), and back-scatter, predicted by Sandstrom (1972). Generation of mixed fluid was also observed in the near-field over longer experimental runs.

9.1.4 Scatter at rough topographic profiles

Scatter at rough periodic topographic profiles was described in chapters 6-8. Behaviour at sinusoidal, sawtooth, square-wave and pseudo knife-edge profiles has been discussed and compared with inviscid linear predictions of geometrical ray tracing and an inviscid linearised boundary theory of Baines (1971a), requiring $\hat{A}_T \hat{k}_T \ll 1$, for a sinusoidal boundary.

Contrary to ray tracing predictions but consistent with the work of Baines, both forward *and* back-scattered wave energy is observed in purely subcritical scatter at sinusoidal boundaries with $\hat{A}_T \hat{k}_T \sim 1$. Energy density spectra suggest scatter to primary, *i.e.* characterised by the incident wavenumber k_I , sum, *i.e.* $(k_I + k_T)$, and difference, *i.e.* $|k_I - k_T|$, components as predicted by Baines (1971a). Unpredicted higher wavenumber scatter is also seen in the *back-scattered* spectra. Viscous attenuation, particularly of higher wavenumber scatter, causes additional discrepancies between measured and predicted far-field energy density magnitudes. As a consequence of the more rapid diffusion of smaller length scales of the wave motion, despite the prediction of scatter to higher wavenumbers at the sinusoid characterised by smaller length scales, a larger proportion of high wavenumber scatter is observed in the far-field of the *larger* scaled sinusoidal profile.

The spectral behaviour observed for experiments with the sinusoid is very similar to that measured in subcritical scatter at an analogous sawtooth profile. As in experiments investigating wave generation by rectangular cylinders, a significant proportion of incident wave energy is scattered to high wavenumber components at sawtooth corners, which propagate away from the boundary along all characteristics passing through the corner (see Baines 1971b and Sandstrom 1972 predictions for split-reflection, diffraction and back-scatter at isolated boundary features). The relatively small group velocities associated with these components allows energy to accumulate near the corners of the topography and nonlinear scatter to higher harmonics as well as the generation of mixed fluid are seen in these regions as a result. In addition to this enhanced dissipation in the near-field, the high wavenumber components are attenuated rapidly (with wave energy dissipating as $\sim \nu k^3 N$ per unit length) as they propagate away from the boundary, so that subcritical far-field energy densities

associated with the sawtooth are significantly less than those measured for the sinusoid.

Despite ray tracing calculations of forward and back-scatter coefficients for sawtooth profiles predicting wave trapping with $C_F = C_B = 0$ in supercritical conditions, scatter in both of these directions is observed in experiments. Forwards spectra indicate the presence of primary wavenumber components. The presence of high wavenumber components, which introduce small across-beam length scales into the forwards and back-scattered wavefields, are also observed in RMS_T images of the experiments. However, energy densities associated with high wavenumber scatter are often too small to produce significant signatures in spectra for the forwards and back-scatter, in part as a consequence of the rapid viscous attenuation of these components. Contrary to ray tracing predictions, magnitudes of forwards scatter to high wavenumbers observed in the far-field decrease as θ/α increases, whereas those for the back-scatter increase as θ/α approaches critical from either sub or supercritical values. Correspondingly, near-field mixing features are also enhanced as $\theta/\alpha \rightarrow 1$. Ray tracing fails to predict the observed behaviour because of its localised treatment, in both space and time, of individual rays. Ray tracing assumes that each ray contacting a boundary responds independently of adjacent rays, reflecting specularly according to the local slope of the boundary. This independence discards the phase information between rays and, critically, the time information, rendering the approach blind to causality, *i.e.* rays reflecting at rough boundaries can violate the radiation condition. In reality, adjacent rays within a wave group are coupled by factors such as finite Reynolds numbers, nonlinear wave interaction and, by the inclusion of time, causality. One influence of these factors is the introduction of back-scattered components.

In general, though there are exceptions, scatter at square-wave and pseudo knife-edge profiles also compare well with that for the sinusoid and sawtooth but do not agree with ray tracing predictions. Focusing of wave energy at the tips of the knife-edge is more intense than that observed at the sawtooth, yielding larger near-field energy densities and dissipation. Another interesting distinction for the behaviour of scatter at the knife-edge is the pronounced back-scattered wavefield generated as $\theta/\alpha \rightarrow 1$, which is significantly more prominent than that for the analogous sawtooth or square-wave profile. The knife-edge profile can be viewed in a number of different ways. One of these is as a square-wave profile in the limit where the width of the crests of the square-wave tend to zero, hence bringing the two corners close together. In this limit, the high wavenumber scatter introduced by the knife-edge can be understood to be the equivalent of the high wavenumber scatter contributions from *two* corners. Consequently, a greater proportion of wave energy accumulates in the region of the knife-edge than at each corner of a square-wave, leading to enhanced nonlinear and dissipative behaviour there. Alternatively, the knife-edge can be viewed as a limiting case of a periodic profile with trapezoidal shaped troughs. In this scenario, the knife-edge represents the limiting case of a *single* corner atop two sloping boundaries as the slopes tend to vertical. The sawtooth is another limiting case of this profile. The former description seems the most consistent with the behaviour observed.

Scatter at the sawtooth profiles has been investigated for the variation of several parameters. These include the topography aspect ratio $\hat{A}_T \hat{k}_T$ as well as ratios of length scales characterising

the incident wavefield and the topography: $\hat{A}_T k_c$ and k_c/\hat{k}_T . For a fixed aspect ratio, but variation of topographic length scales, it was found that observed high wavenumber scatter in the far-field was greatest for the profile characterised by the larger length scales. This is a result of enhanced viscous attenuation of wave energy scattered to smaller scales at the smaller scale profile. An increase in aspect ratio for a fixed topographic wavenumber yielded more focused wavefields in the near-field. This enhanced both near-field dissipation and mixing at the topographic corners, as well as viscous attenuation of wave energy as it propagated to the far-field due to greater shear associated with larger wave amplitudes. Hence observed high wavenumber forward scatter was the least in the far-field of profiles characterised by larger amplitudes. An increase in aspect ratio for a fixed topographic amplitude resulted in different behaviour depending on the value of \hat{k}_T . For large \hat{k}_T (*i.e.* small $k_c/\hat{k}_T \sim 1$), corners of the topography were close enough for a significant proportion of the incident wave energy to reflect at the local step in the background stratification introduced by the mixed fluid generated at the corners. Consequently, far-field forward scatter for such profiles exhibited a greater proportion of the primary component and hence a smaller degree of high wavenumber scatter. For larger topographic wavenumbers, enhanced viscous dissipation of wave energy scattered from the profiles imposing larger wavenumbers on the wavefield reduced the proportion of high wavenumber scatter measured in the far-field relative to that for a profile characterised by a smaller wavenumber. However, with each parameter variation, little change was observed between *back-scattered* wavefields.

In summary, linear geometrical ray tracing predictions have not provided reliable descriptions of the wavefields studied here at any value of θ/α . However, the inviscid linearised boundary theory of Baines (1971a) for a sinusoidal boundary compares qualitatively well with subcritical wavefields generated at sinusoid, sawtooth, square-wave and knife-edge profiles, despite the relaxation of the conditions $\hat{A}_T \hat{k}_T \ll 1$ and $\hat{A}_T k_c \ll 1$. The presence of topographic corners have been shown to have a significant effect on the form of scattered wavefields. Wave energy scattered at a corner is focused along characteristics passing through the corner. The associated high wavenumber scatter is subject to rapid viscous attenuation and hence fluxes to the far-field are reduced. Accumulation of energy near topographic corners due to the small group velocities of scattered high wavenumber components results in large energy densities that promote nonlinear behaviour and mixing there. These effects appear to be enhanced at ‘sharper’ corners, with near-field dissipation consistently observed to be greater for the knife-edge profile than for the sawtooths. As the separation between topographic corners is reduced (*i.e.* $k_c/\hat{k}_T \rightarrow 0$), the near-field mixing features cause a significant proportion of incident wave energy to reflect directly at local changes induced in the stratification at the vertical level of the corners, hence modifying far-field scatter.

9.2 Future work

The work presented in this thesis has highlighted the complex nature of scatter at both smooth and rough topographies. Consequently, there is great scope for development of this research, as

discussed here.

9.2.1 Extensions of experimental work

Investigations of wave phenomena always benefit from improvements in both spatial and temporal resolutions of the data collected in experiments. In particular, in the present context, enhanced spatial data could be used to better resolve scattering behaviour and mixing at topographic corners and of fluid motion in boundary layers along topography, whilst more temporal information would allow a more detailed study of scatter to higher temporal harmonics as well as permit filtering of the primary harmonic wavefield to remove high frequency background noise. Greater spatial resolution could be achieved if a dot mask with smaller dots was generated and additional measures taken to control the environment surrounding experiments in order to accommodate the resulting increase in sensitivity of the synthetic schlieren technique. The PIV method described could also be refined and optimised further. Temporal resolutions are easily improved by image capture at larger frame rates. The frame rate used in this study was restricted by capacities available to store and analyse the amount of data generated. Phase locking the camera with the oscillating cylinder would also produce cleaner harmonic analyses of the wavefields.

The experiments possible in the present study were also constrained by the geometry of the tank. A wider range of parameter values could be investigated with the use of a taller and longer tank. In addition, an alternative method of wave generation for the purposes of analysing wave reflection and scatter might be the use of a camshaft mechanism such as that described by Gostiaux *et al.* (2007), which generates plane waves that have more distinct spectra than those of wave *beams* generated by oscillating cylinders (see discussion in section 3.6). However, wave beams are prevalent in the environment and hence their use was preferred here. The experiments themselves could be extended to determine scattering behaviours at other topographic profiles, having different shapes and dimensions to those used in the present study. In particular, the influence of corners could be studied in more detail by the use of topographic profiles consisting of isolated, rather than periodic, smooth bumps, sawtooths, square-waves and knife-edges of various dimensions. Other possibilities include scatter at rough profiles inclined with a net slope or scatter with a non-Boussinesq or nonlinear background stratification or with a mean flow. Viscosity has been shown here to be a dominant mechanism of wave dissipation and hence investigation of larger Reynolds numbers could be conducted. Experiments could also be made of scatter of large amplitude wavefields in order to study nonlinear wavefields, wave breaking and the generation and long term evolution of mixed fluid. Specifically, it would be interesting to establish how fast a topographic trough must drain of mixed fluid generated there before it were to effectively become isolated from the surrounding stratification. In addition, even if the stratification within a trough were modified so that $\sigma/N > 1$ there, then how would the interaction of exponentially decaying modes with topography affect the scatter if $\hat{A}_T k_c < O(1)$ (*i.e.* evanescent wave energy interacting with relatively shallow topography)?

In reality, benthic topography is three-dimensional, and ideally, all the concepts described above

would be extended to three-dimensions. Experimentally, this would require significant development of visualisation techniques. Initially, a good starting point for such a study would be to consider scatter at an isolated axisymmetric hill. Studies could also look at scatter at isolated hills of various shapes, such as cubes, pyramids and irregular hills, or scatter at arrays of hills.

Analysis of the data collected in the present study could be extended to include evaluations of mixing in the near-field of topographies by calculations of diffusivities. Energy flux calculations could also be made in order to quantify scatter of wave energy to the far-field in each of the various directions. A greater use could be made of Hilbert transforms, and similar techniques, to decouple wave modes propagating in different directions.

9.2.2 Extensions of theoretical work

Existing theories describing scatter of internal gravity waves primarily include inviscid linear geometrical ray tracing and the inviscid linearised boundary theory of Baines (1971a). Limitations in the applicability of each these have been discussed in earlier chapters. In particular, the significance of viscosity in modifying wavefields has been emphasised and so viscous adaptations of the theory are desirable. Other important advances would include the extension of Baines' work to parameter values of $\hat{A}_T \hat{k}_T \sim O(1)$ and $k_c / \hat{k}_T \sim O(1)$ and also a theoretical model for scatter at a periodic profile featuring sharp corners, such as a sawtooth. Preliminary work (not presented in this thesis), which adds causality to geometrical ray tracing arguments, suggests that if ray tracing predicts a discontinuity in wavenumber and/or amplitude in the reflection of a monochromatic incident wave then scattered components propagating in non specular directions are generated in order to avoid a violation of the radiation condition.

9.2.3 Numerical work

A complementary numerical study was also conducted alongside the present research. Whilst the numerical simulations are not discussed in detail in this thesis, they are the subject of ongoing work and a brief overview of this aspect of the research and example results are given here.

The numerical component of the study involved the development of a code that used a stream function-vorticity formulation of the two-dimensional nonlinear Boussinesq equations of motion within a finite volume scheme. Internal waves were forced through the introduction of a patch of vorticity within the domain. Scattering behaviours of the waves have been observed at step and sawtooth topographies and artificial seeding of vorticity near topographic corners (to remove the velocity singularity and satisfy the Kutta condition) has been applied in order to evaluate the influence of flow separation on scattered wavefields. A significant challenge in the development of the numerical method was in the choice of boundary conditions that allowed wave energy to propagate 'transparently' through the regions of the domain boundary that were not specified as topography and the suppression of aliasing problems near topographic corners. This has been done successfully with the use of a combination of damping profiles for both the vorticity and perturbed

density fields across the numerical domain, effectively creating a numerical ‘sponge’ to dissipate the wave energy without significant reflections. Examples of some of the simulations possible with this numerical model are given here.

Transient ‘start-up’ motion

Figure 9.1 shows perturbed buoyancy frequencies for transient ‘start-up’ wavefields generated by the numerical internal gravity wave source located at the centre of the field of view and oscillating with frequency $\sigma/N = 0.54$ for times $t = 1T, \dots, 9T$ after the oscillation was initiated. The wavefields compare well with those generated in experiments by an oscillating circular cylinder (see figure 3.14), except that the structure of the numerical wave beams are unimodal everywhere, rather than bimodal as observed near oscillating cylinders in experiments. This is due to the continuous form of the numerical vorticity source profile, which does not introduce discontinuities into the wavefield at its edges.

Scatter at step topography

Figure 9.2 (a) shows an RMS_T image of the perturbed buoyancy field from numerical simulation of the scatter of an established wave beam of frequency $\sigma/N = 0.54$, generated near the centre of the left-hand side of the domain, incident at a single step topographic profile, located in the bottom right-hand corner of the domain. The Kutta condition is not applied at the corners in this example. A second wave beam is generated at the wave source that propagates upwards and to the right. The successful removal of this superfluous beam as well as others generated at the source by the diffusive boundary conditions can be observed near the top and left boundaries. A large proportion of the wave energy incident at the topography reflects specularly at the vertical section of the step. Wave energy reflected downwards is rapidly dissipated by the ‘sponge’ boundary conditions imposed at the lower boundary of the domain (thus avoiding any upward reflection from this boundary). High wavenumber scatter is observed in the region of the step corner, resulting in lowered group velocities and the associated accumulation of energy there. As observed in experiments at piecewise linear rough topographic profiles, scattered wave energy propagates away from the corner along characteristics in three directions, with wave amplitudes rapidly attenuated in these directions by diffusive terms imposed across the domain.

Figure 9.2 (b) shows an RMS_T image of the perturbed buoyancy field for the scatter of a similar wavefield at a four step ‘staircase’ topographic profile, again located in the bottom right-hand corner of the domain. Incident wave energy in this case becomes back-reflected through multiple reflections with the horizontal and vertical sections of the steps, as well as being back-scattered at the topographic corners in the manner observed at the isolated step in figure 9.2 (a). Consequently, a strong back-scattered wavefield is seen for the staircase profile, superposed with the incident wavefield. The largest energy densities are again observed at the corners of the steps.

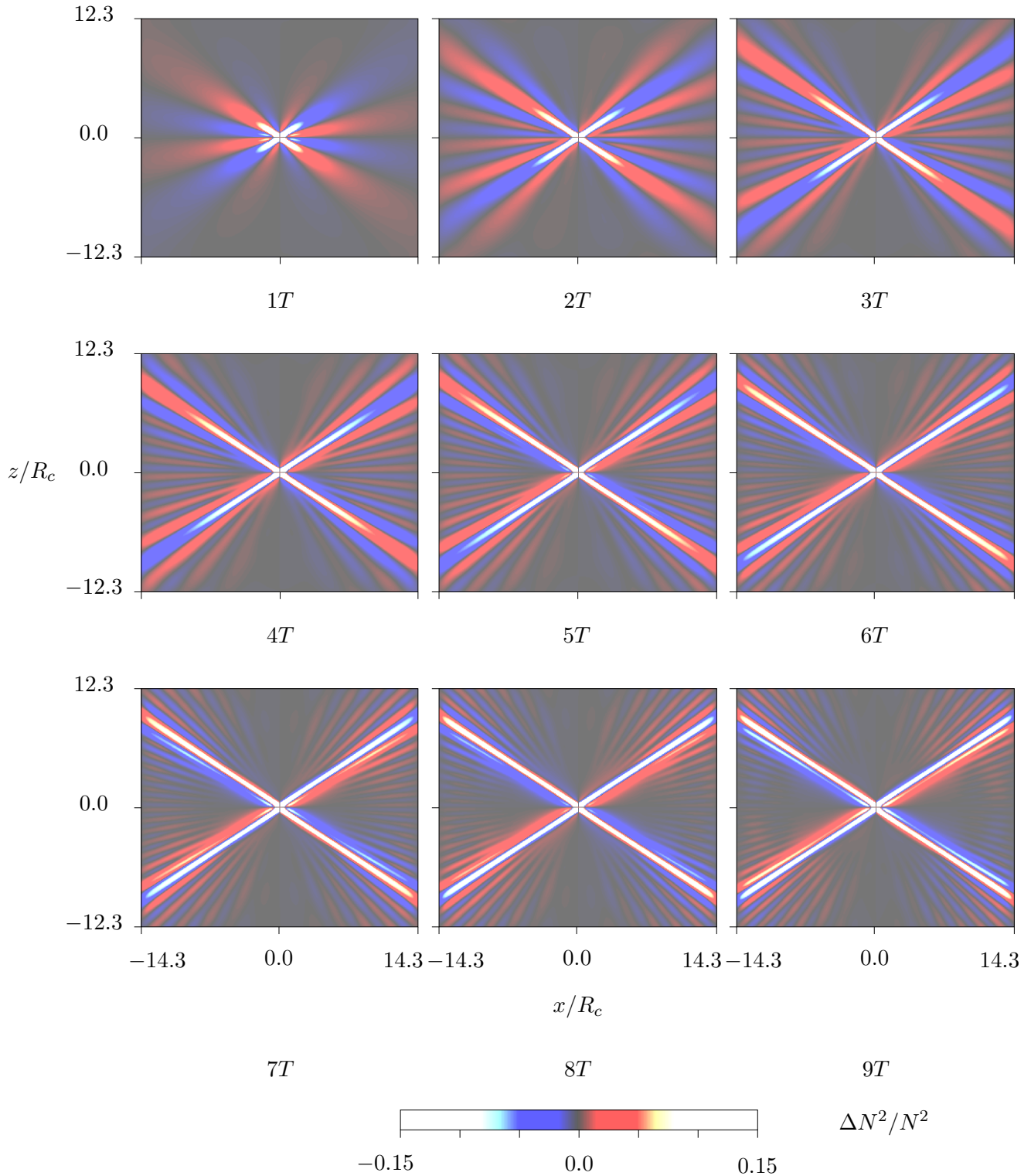


Figure 9.1: Sequence of transient start-up wavefield at times $t = 1T, 2T, \dots, 9T$ s. The cylinder oscillation was initiated at $t = 0T$ s with $T = 11.64$ s and $\sigma/N = 0.54$. Simulations run at domain resolution of 1024×1024 . Smaller regions with resolutions 915×787 are shown for direct comparison with figure 3.14.

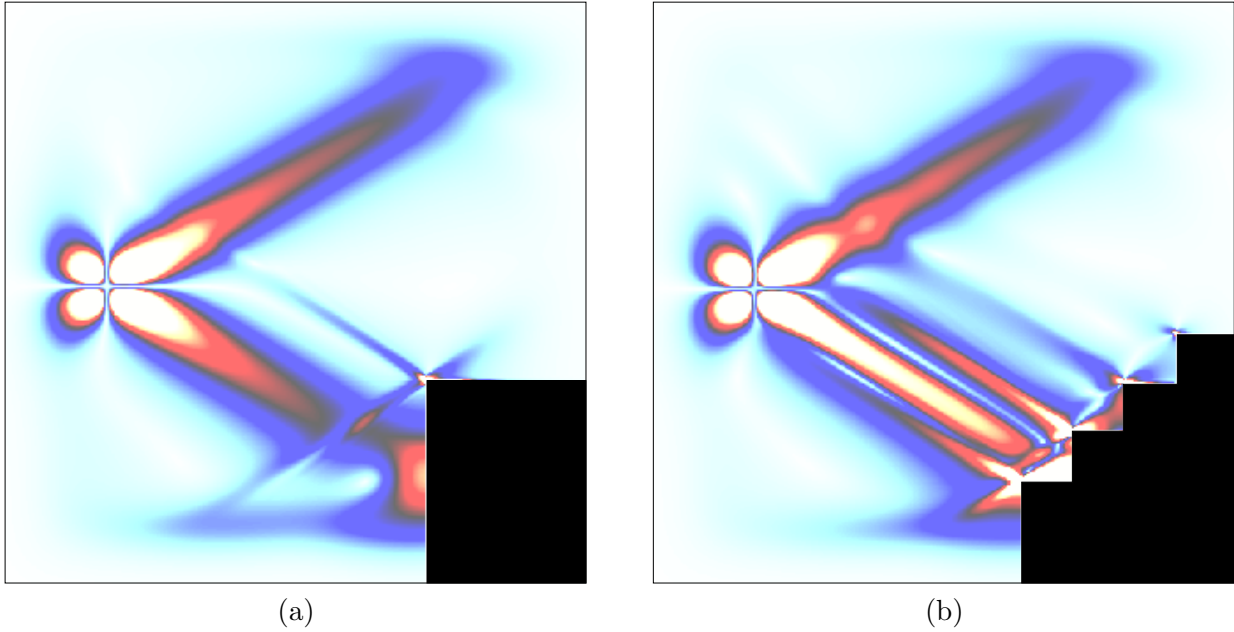


Figure 9.2: RMS_T images of $\Delta N^2/N^2$ from numerical simulations of scatter with $\sigma/N = 0.54$ at (a) an isolated step and (b) a four step staircase topographic profile. Colour scale as in figure 6.4, with amplitude maxima 2×10^{-2} and topography shaded in black. Simulations run at resolutions of 512×512 , with whole domain shown.

Extensions of numerical work

A continuing problem in numerical investigations of stratified fluids is in the determination of satisfactory open boundary conditions. These are particularly important in studies of scattering behaviours of internal gravity waves. Whilst a specific combination of diffusive profiles has been used in the simulations shown above, a more general boundary condition is desirable. The boundary conditions used here also had a significant impact on the available resolution since the ‘sponge’ was necessarily multiple times the wavelength in thickness. Numerical models could also be developed to accommodate other topographic shapes. The numerical model described here has been adapted for scatter at square-wave topographic profiles and also, after rotating the domain through an angle of 45° , sawtooth profiles.

9.3 Geophysical and environmental implications

Application of results discussed in this thesis to environmental contexts, such as in quantifying ocean mixing resulting from internal gravity wave scatter at benthic topography (see section 1.3), requires a detailed knowledge of the topography in question. Ocean bathymetry is typically composed of a broad range of scales and slopes with features such as sharp corners. In practice, a detailed description of the bathymetry is generally not available, and neither feasible to collect nor employ in numerical simulations. Ideally, both due to the resolution limitations of bathymetry maps and

for efficiency in calculations, bathymetry would be divided into larger regions that are defined by particular characterising properties, such as large abyssal plains with gentle undulations, deep canyons, large scale ridges, continental shelves, jagged topography, etc. Statistical methods could then be used to approximate the associated mixing in each of these regions based on knowledge of scattering properties of internal gravity waves at the typical profiles. The level of detail required remains an open question. When does a staircase look like a smooth slope? A rough bottom like a smooth one, etc. It is pertinent to ask, therefore, what generalisations can be made about scattering behaviours and the associated dissipation of wave energy for the topographies discussed in the present study? This is addressed here.

Results presented in this thesis have highlighted the complex nature of scatter at rough topographic profiles. Wave energy can be scattered spatially in forwards and backwards directions, as well as to higher temporal harmonic components. Wave energy can be dissipated in the near-field, generating mixed fluid there; through viscous attenuation of the wavefields as they propagate away from the boundary; or by instability and breaking (see section 1.2.3) of the scattered wavefields remote from the boundary, *i.e.* in the far-field. The evolution of mixed fluid generated either in the near-field or the far-field, by wave breaking, was discussed in section 1.2.3. How and where the energy is dissipated is subtly controlled by the shape and length scales of the topographic profile. Some generalisations are possible however.

Scatter at topographic profiles characterised by small horizontal length scales, *i.e.* $k_c/\hat{k}_T < O(1)$, is largely similar to specular reflection observed at a horizontal boundary. In such cases, crests of the topography are sufficiently close to one another for almost all, if not all, incident wave energy to reflect directly off local steps in the background stratification caused by mixed fluid generated in the crest region, isolating the detailed topographic features. Consequently, scatter at profiles of this type is dominantly conservative of wavenumbers associated with the incident wavefield. Apart from a small proportion of dissipation associated with near-field mixing, the incident wave energy, subject to viscous attenuation, is scattered to the far-field and is unlikely to develop instabilities and break unless it is destabilised by e.g. focusing at a local change in the buoyancy frequency, N , there. A mean slope of the topography can change this picture however. In the limit of a rough vertical wall, there would be no filling of the topography, but there would still be mixed layers propagating away, decaying as they do so. The layers themselves could produce scattering as discussed in section 1.2.3.

The present study concentrates on profiles characterised by $k_c/\hat{k}_T \sim O(1)$. Near-field dissipation of wave energy and generation of mixed fluid there are the most pronounced for near-critical values of θ/α , at knife-edge and sawtooth profiles, and for larger values of $\hat{A}_T\hat{k}_T$ and \hat{A}_Tk_c . As in the case of profiles characterised by small horizontal length scales, the generation and accumulation of mixed fluid in the near-field of the topography modifies the scatter by, to some extent, isolating topographic features from the incident wavefield. In this case, however, the effects of changes in the local stratification are likely to be more variable in time, with the behaviour dependent on the relative rates of generation of mixed fluid near the topography and its spreading, or ‘draining’, laterally into the surrounding stratification (see section 1.2.3). Scattering behaviour may assume

cycles where mixed fluid is generated at the topography and gradually accumulates, with the step in stratification isolating a large portion of the boundary from the incident wavefield. Hence near-field mixing generated during wave scatter decreases whilst the accumulated fluid drains. This coincides with a greater proportion of scattered energy being reflected, almost specularly, to the far-field, so that wave energy dissipation at this stage predominantly occurs remotely from the boundary. At some point, the local form of the stratification is restored sufficiently by fluid draining for the net rate of near-field mixed fluid generation to increase once more and the accumulation period of the cycle is resumed. Such temporal variations clearly add greater complexity to the scattering problem as a whole.

Measurements of forward scattered wave energy and high wavenumber scatter in the far-field are largest for smaller values of θ/α (*i.e.* subcritical regime) as well as for larger values of $\hat{A}_T \hat{k}_T$ and $\hat{A}_T k_c$, with little distinction between scatter at different topographic shapes. It might therefore be expected that scatter in these configurations would be associated with the greatest amount of far-field mixing. Viscous attenuation of the wave energy has been shown to have some stabilising influence on the scattered wavefield evolution by its preferential erosion of high wavenumber components. Figure 9.3 plots the variation in total enstrophy measured in forward scattered beam cross-sections with increasing distance from sawtooth, sinusoid and square-wave profiles. Measurements are given for two subcritical configurations, with $\theta/\alpha \approx 0.78$ and 0.88 , and one marginally subcritical configuration with $\theta/\alpha \approx 0.98$. Note that total enstrophies are normalised by the total in the cross-section measured closest to the topography in each case. Hence the plot is illustrative of the relative rates of attenuation of the forward scattered field at each topography rather than comparisons of actual values. Whilst some variation between plots for the different profiles is evident at the smallest two values of θ/α (dotted and dashed lines), enstrophy totals exhibit similar rates of dissipation, assumed to be primarily through viscous diffusion of wave energy, with s_R/R_c for each of the topographic profiles. Totals approximately halve over along-beam distances of $s_R \sim 4R_c$. Evolutions of wavefields scattered at each profile are more distinct from one another at the near-critical value of θ/α . At the along-beam distances measured, the most rapid decay occurs for the forward scatter at the sinusoid, whilst the slowest is of that for the square-wave, indicating the greater proportion of wave energy associated with high wavenumbers, and hence the enhancement of viscous dissipation, in the sinusoid case. An accurate description of topographic shape in the prediction of wave scatter and associated fluid mixing therefore becomes more important as $\theta/\alpha \rightarrow 1$.

Back-scattered wave energy is enhanced in near-critical conditions and, in particular, at the knife-edge profile studied. An increase in back-scatter generally coincides with a reduction in forwards scatter. As a consequence of this partitioning of the wave energy, forwards scattered wavefields become associated with smaller amplitudes and lower shear, which is likely to increase the stability of these components and allow wave energy to propagate further from the boundary in this direction. The back-scattered wavefields typically exhibit high wavenumber scatter, implying lower wave stability. However, the direction of propagation of back-scattered wave energy, aligned opposite to

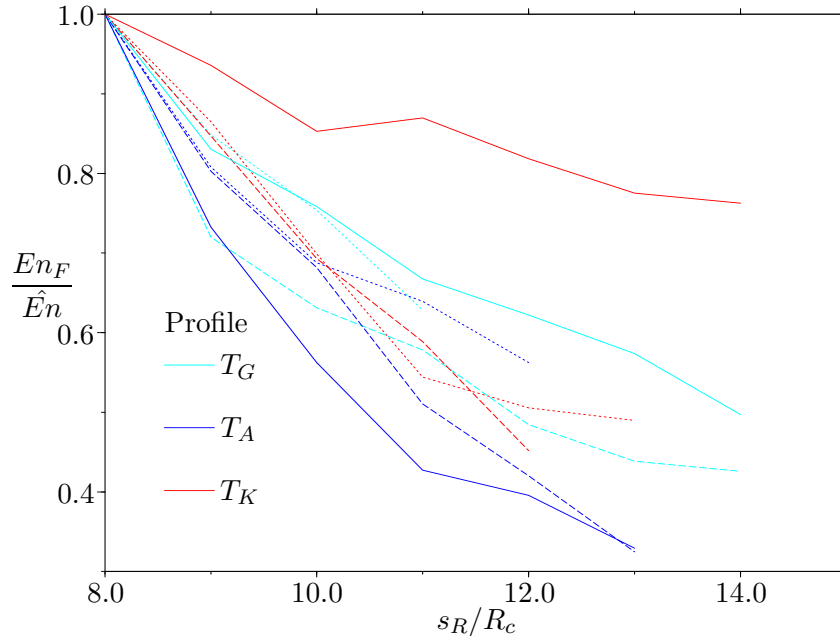


Figure 9.3: Variation with distance from topography of total wave enstrophy, En_F , measured along cross-sections of subcritical forwards scattered wavefields at sawtooth (T_G), sinusoid (T_A) and square-wave (T_K) profiles. Enstrophy is normalised by the total, $\hat{E}n$, in the cross-section measured closest to the topography in each case. Values of θ/α for configurations with T_G , T_A and T_K are 0.77, 0.78 and 0.79 (dotted lines); 0.88, 0.88 and 0.89 (dashed lines) and 0.97, 0.97 and 0.99 (solid lines) respectively.

that of the incident wavefield, induces greater viscous attenuation of the back-scatter due to the greater across-beam gradients and shear introduced by the superposing phases.

Scatter to higher temporal harmonics represents a further partitioning of the incident wave energy in space and hence causes a reduction in scatter to the, usually most dominant, primary harmonic forward scattered component. In the region of their generation, amplitudes associated with propagating secondary harmonics, *i.e.* $\sigma/N < 1/2$, are typically second order in the incident wave amplitude and hence, due to viscous attenuation, are only significant in the near-field. In general, energy associated with higher harmonics is therefore dissipated locally.

9.4 Final remarks

Accounting for and quantifying factors that contribute to oceanic mixing remains one of the most important issues in climate modelling and prediction. In particular, the ubiquity of internal gravity waves in the ocean and the strong coupling between mixing and regions of high wavenumber scatter, such as near rough benthic topography, highlights their significance to large scale numerical models, which currently do not account adequately for these effects. Ideally, parameterisations of near-field and far-field mixing caused by the interaction of wavefields with different types of topography

would be included in these models. Results presented in this thesis have highlighted the complex dependence of the scatter and diffusion of wave energy on the shape and dimensions of topography. Parameters shown to be of importance in conditioning scattered wavefields include characterisation of the incident wavefield: A_c/D_c and σ/N ; comparisons of the slope and length scales of the incident wavefield with those of the topography: θ/α , $\hat{A}_T k_c$ and k_c/\hat{k}_T , and characterisation of the topographic profile using $\hat{A}_T \hat{k}_T$ as well as the general shape of the profile and, in particular, the number and nature of corners. Further detailed analysis of internal gravity wave scatter is required before the physical mechanisms controlling the scatter are understood and quantifications of the associated mixing can be made and used to improve current predictive ocean models.

Bibliography

- ADDISON, P. 2002 *The illustrated wavelet transform handbook*. IOP.
- AGUILAR, D. & SUTHERLAND, B. 2006 Internal wave generation from rough topography. *Phys. Fluids* **18** (066603).
- AGUILAR, D., SUTHERLAND, B. & MURAKI, D. 2006 Laboratory generation of internal waves from sinusoidal topography. *Deep-Sea Res. II* **53**, 96–115.
- ANDREWS, D., HOLTON, J. & LEOVY, C. 1987 *Middle atmosphere dynamics*. Academic Press.
- ARMI, L. 1978 Mixing in deep ocean - importance of boundaries. *Oceanus* **21**, 14–19.
- BAINES, P. 1971*a* The reflexion of internal/ inertial waves from bumpy surfaces. *J. Fluid Mech.* **46**, 273–291.
- BAINES, P. 1971*b* The reflexion of internal/ inertial waves from bumpy surfaces. Part 2. Split reflexion and diffraction. *J. Fluid Mech.* **49**, 113–131.
- BAINES, P. 1974 The generation of internal tides over steep continental slopes. *Phil. Trans. Roy. Soc.* **277**, 27–58.
- BAINES, P. 1978 A note on momentum flux and orographic scattering of internal gravity waves. *J. Atmos. Science.* **35**, 922–925.
- BAINES, P. & HOINKA, K. 1985 Stratified flow over two-dimensional topography in fluid of infinite depth: a laboratory simulation. *J. Atmos. Sci.* **42**, 1614–1630.
- BAINES, W. & TURNER, J. 1969 Turbulent buoyant convection from a source in a confined region. *J. Fluid Mech.* **37**, 51–80.
- BALMFORTH, N., IERLEY, G. & YOUNG, W. 2002 Tidal conversion by subcritical topography. *J. Phys. Oceanogr.* **32**, 2900–2914.
- BARENBLATT, G. 1996 *Scaling, self-similarity and intermediate asymptotics*. Cambridge University Press.

- BATCHELOR, G. 1967 *An introduction to fluid dynamics*. Cambridge University Press.
- BAYDULOV, V. & CHASHECHKIN, Y. 1996 A boundary current induced by diffusion near a motionless horizontal cylinder in a continuously stratified fluid. *Izv., Acad. Sci., USSR, Atmos. Oceanic Phys.* **32**, 751.
- BENIELLI, D. & SOMMERIA, J. 1996 Excitation of internal wave and stratified turbulence by parametric instability. *Dyn. Atmos. Oceans* **23**, 335–343.
- BENIELLI, D. & SOMMERIA, J. 1998 Excitation and breaking of internal gravity waves by parametric instability. *J. Fluid Mech.* **374**, 117–144.
- BONNETON, P., CHOMAZ, J.-M. & HOPFINGER, E. 1993 Internal waves produced by the turbulent wake of a sphere moving horizontally in a stratified fluid. *J. Fluid Mech.* **254**, 23–40.
- BRACEWELL, R. 2000 *The Fourier transform and its applications*. Boston: McGraw-Hill.
- BROWAND, F. & WANG, Y. 1972 An experiment on the growth of small disturbances at the interface between two streams of different densities and velocities. In *Proc. Int. Symp. on Stratified Flows*. Novosibirsk, Soviet Union.
- CACCHIONE, D. & WUNSCH, C. 1974 Experimental study of internal waves over a slope. *J. Fluid Mech.* **66**, 223–239.
- CHANDRASEKHAR, S. 1961 *Hydrodynamic and hydromagnetic stability*. Oxford: Clarendon Press.
- COOLEY, J. & TUKEY, J. 1965 An algorithm for the machine calculation of complex Fourier series. *Math. Comput.* **19**, 297–301.
- CORNWELL, T. & EVANS, K. 1985 A simple maximum entropy deconvolution algorithm. *Astron. Astrophys.* **143**, 77–83.
- COX, C. & SANDSTROM, H. 1962 Coupling of internal and surface waves in water of variable depth. *J. Oceanogr. Soc. Japan* **20th Ann. Vol.**, 499–513.
- DALZIEL, S. 2000 Synthetic schlieren measurements of internal waves generated by oscillating a square cylinder. In *Proc. Int. Symp. on Stratified Flows*, pp. 743–748. Vancouver, Canada.
- DALZIEL, S. 2007 <http://www.damtp.cam.ac.uk/lab/digiflow/>.
- DALZIEL, S., CARR, M., SVEEN, K. & DAVIES, P. 2007 Simultaneous Synthetic Schlieren and PIV measurements for internal solitary waves. *Meas. Sci. Tech.* **18**, 533–547.
- DALZIEL, S., HUGHES, G. & SUTHERLAND, B. 1998 Synthetic schlieren. In *Proc. 8th Int. Symp. on Flow Visualisation*, pp. 743–748. Vancouver, Canada.

- DALZIEL, S., HUGHES, G. & SUTHERLAND, B. 2000 Whole-field density measurements by ‘synthetic schlieren’. *Exp. Fluids* **28**, 322–335.
- DAUBECHIES, I. 1988 Orthonormal bases of compactly supported wavelets. *Comm. Pure Appl. Math.* **41**, 909–996.
- DAUXOIS, T., DIDIER, A. & FALCON, E. 2004 Observation of near-critical reflection of internal waves in a stably stratified fluid. *Phys. Fluids* **16**, 1936–1941.
- DAUXOIS, T. & YOUNG, W. 1999 Near critical reflection of internal waves. *J. Fluid Mech.* **390**, 271–295.
- DAVIDSON, P., STAPLEHURST, P. & DALZIEL, S. 2006 On the evolution of eddies in a rapidly rotating system. *J. Fluid Mech.* **557**, 135–144.
- DE SILVA, I., IMBERGER, J. & IVEY, G. 1997 Localized mixing due to a breaking internal wave ray at a sloping bed. *J. Fluid Mech.* **350**, 1–27.
- DRAZIN, P. & REID, W. 2004 *Hydrodynamic stability*. Cambridge University Press.
- DUPONT, P., KADRI, Y. & CHOMAZ, J.-M. 2003 Internal waves generated by the wake of a gaussian hills. *Phys. Fluids* **13**, 3223–3233.
- DUPONT, P. & VOISIN, B. 1996 Internal waves generated by a translating and oscillating sphere. *Dyn. Atmos. Oceans* **23**, 289–298.
- DVORÁK, V. 1880 Über eine neue einfache Art der Schlieren - beobachtung. *Ann. Phys. Chem.* **9**, 502–512.
- EGBERT, G. & RAY, R. 2000 Significant dissipation of tidal energy in the deep ocean inferred from satellite altimeter data. *Nature* **405**, 775–778.
- ERIKSEN, C. 1982 Observations of internal wave reflection of sloping bottoms. *J. Geophys. Res.* **87**, 525–538.
- ERIKSEN, C. 1985 Implications of ocean bottom reflection for internal wave spectra and mixing. *J. Phys. Oceanogr.* **15**, 1145–1156.
- FELS, S. 1977 Momentum and energy exchanges due to orographically scattered gravity waves. *J. Atmos. Science.* **34**, 499–514.
- FELS, S. 1978 Notes and Correspondence: Reply. *J. Atmos. Science.* **35**, 925–927.
- FLYNN, M., ONU, K. & SUTHERLAND, B. 2003 Internal wave excitation by a vertically oscillating sphere. *J. Fluid Mech.* **494**, 65–93.

- FORTUIN, J. 1960 Theory and application of two supplementary methods of constructing density gradient columns. *J. Polym. Sci.* **44**, 505–515.
- FOUCAULT, L. 1859 Mémoire sur la construction des télescopes en verre argenté. *Ann. Obs. Imp. Paris* **5**, 197–203.
- FRITTS, D. & ALEXANDER, M. 2003 Gravity wave dynamics and effects in the middle atmosphere. *Rev. Geophys.* **41**, 1–64.
- GARRETT, C. & GILBERT, D. 1988 Estimates of vertical mixing by internal waves reflected off sloping topography. In *Small-scale turbulence and mixing in the ocean* (ed. J. Nihoul & B. Janard), pp. 405–423. Elsevier Scientific, New York.
- GARRETT, C. & MUNK, W. 1975 Space-time scales of internal waves: A progress report. *J. Geophys. Res.* **80**, 291–297.
- GAVRILOV, N. & ERMANYUK, E. 1997 Internal gravity wave generated by circular translational motion of a cylinder in a linearly stratified fluid. *J. Appl. Mech. Tech. Phys.* **38**, 224–227.
- GILBERT, D. & GARRETT, C. 1989 Implications for ocean mixing of internal wave scattering off irregular topography. *J. Phys. Oceanogr.* **19**, 1716–1729.
- GILL, A. 1982 *Atmosphere-ocean dynamics*. New York: Academic Press.
- GÖRTLER, H. 1943 Über eine schwingungserscheinung in flüssigkeiten mit stabiler dichteschichtung. *Z. Angew. Math. Mech.* **23**, 65–71.
- GOSTIAUX, L. & DAUXOIS, T. 2007 Laboratory experiments on the generation of internal tidal beams over steep slopes. *Phys. Fluids* **19** (028102).
- GOSTIAUX, L., DAUXOIS, T., DIDELLE, H., SOMMERIA, J. & VIBOUD, S. 2006 Quantitative laboratory observations of internal wave reflection on ascending slopes. *Phys. Fluids* **18** (056602).
- GOSTIAUX, L., DIDELLE, H., MERCIER, S. & DAUXOIS, T. 2007 A novel internal waves generator. *Exp. Fluids* **42**, 123–130.
- GYÜRE, B. & JÁNOSI, I. 2003 Stratified flow over asymmetric and double bell-shaped obstacles. *Dyn. Atmos. Oceans* **37**, 155–170.
- HAZEWINKEL, J., VAN BREEVOORT, P., DALZIEL, S. & MAAS, L. 2008 Observations on the wavenumber spectrum and evolution of an internal wave attractor. *J. Fluid Mech.* **598**, 373–382.
- VON HELMHOLTZ, H. 1868 Über discontinuierliche Flüssigkeits-Bewegungen. *Monatsbericht Akad. Wiss. Berlin* **23**, 215–228.

- HILL, D. 2002 General density gradients in general domains: The ‘two-tank’ method revisited. *Exp. Fluids* **32**, 434–440.
- HOLMBOE, J. 1962 On the behaviour of symmetric waves in stratified shear flows. *Geophys. Publ.* **24**, 67–113.
- HOLTON, J. 1979 *An introduction to dynamic meteorology*. Academic Press.
- HOOKE, R. 1665 Of a new property in the air. In *Micrographia*, Observation LVIII, pp. 217–219. London.
- HOWARD, L. 1961 Note on a paper of John W. Miles. *J. Fluid Mech.* **10**, 509–512.
- HURLEY, D. 1970 Internal waves in a wedge shaped region. *J. Fluid Mech.* **43**, 97–120.
- HURLEY, D. 1972 A general method for solving steady-state internal gravity wave problems. *J. Fluid Mech.* **56**, 721–740.
- HURLEY, D. 1997 The generation of internal waves by vibrating elliptic cylinders. Part 1. Inviscid solution. *J. Fluid Mech.* **351**, 105–118.
- HURLEY, D. & HOOD, M. 2001 The generation of internal waves by vibrating elliptic cylinders. Part 3. Angular oscillations and comparison of theory with recent experimental observations. *J. Fluid Mech.* **433**, 61–75.
- HURLEY, D. & KEADY, G. 1997 The generation of internal waves by vibrating elliptic cylinders. Part 2. Approximate viscous solution. *J. Fluid Mech.* **351**, 119–138.
- IVEY, G. & NOKES, R. 1989 Vertical mixing due to the breaking of critical internal waves on sloping boundaries. *J. Fluid Mech.* **204**, 479–500.
- IVEY, G., WINTERS, K. & DE SILVA, I. 2000 Turbulent mixing in a sloping benthic boundary layer energized by internal waves. *J. Fluid Mech.* **418**, 59–76.
- KAISER, G. 1994 *A friendly guide to wavelets*. Birkhäuser.
- KELLER, J. & MOW, V. 1969 Internal wave propagation in an inhomogeneous fluid of non-uniform depth. *J. Fluid Mech.* **38** (II), 365–374.
- KELVIN, L. W. 1871 Hydrokinetic solutions and observations. *Phil. Mag.* **42**, 362–377.
- KISTOVICH, Y. & CHASHECHKIN, Y. 1993 The reflection of packets of internal waves from a plane rigid boundary. *Izv. Ross. Akad. Nauk. Fiz. Atmos. Akeana* **29**, 831–836.
- KISTOVICH, Y. & CHASHECHKIN, Y. 1995a The reflection of beams of internal gravity waves at a flat rigid surface. *J. Appl. Math. Mech.* **59**, 579–585.

- KISTOVICH, Y. & CHASHECHKIN, Y. 1995*b* Reflection of packets of internal waves from a rigid plane in a viscous fluid. *Atmos. Ocean. Phys.* **30**, 718–724.
- KUMAR, P. & FOUFOULA-GEORGIU, E. 1997 Wavelet analysis. *Rev. Geophys.* **35**, 385–412.
- KUNZE, E. & TOOLE, J. 1997 Tidally driven vorticity, diurnal shear, and turbulence atop Fieberling Seamount. *J. Phys. Oceanogr.* **27**, 2663–2693.
- KWON, S., MOON, W. & LEE, H. 2003 Experimental and numerical studies on the development of a new wave absorber. *Ocean. Eng.* **30**, 185–203.
- LAM, F.-P. & MAAS, L. 2008 Internal wave focussing revisited: a reanalysis and theoretical links. *Fluid Dyn. Res.* **40**, 95–122.
- LAMB, H. 1932 *Hydrodynamics*. Cambridge University Press.
- LARSEN, L. 1969 Internal waves incident upon a knife edge barrier. *Deep-Sea Res.* **16**, 411–419.
- LAWS, P., PEAT, K. & STEVENSON, T. 1982 An interferometer to study density stratified flows. *J. Phys. E: Sci. Instrum.* **15**, 1327–1331.
- LEDWELL, J., MONTGOMERY, E., POLZIN, K., ST LAURENT, L., SCHMITT, R. & TOOLE, J. 2000 Evidence for enhanced mixing over rough topography in the abyssal ocean. *Nature* **403**, 179–182.
- LEDWELL, J., WATSON, A. & LAW, C. 1998 Mixing of a tracer in the pycnocline. *J. Geophys. Res.* **103**, 21499–21530.
- LEGG, S. 2003 Internal tides generated on a corrugated continental slope. Part I: Cross-slope barotropic forcing. *J. Phys. Oceanogr.* **34**, 156–173.
- LEGG, S. & ADCROFT, A. 2003 Internal wave breaking at concave and convex continental slopes. *J. Phys. Oceanogr.* **33**, 2224–2246.
- LEPPINEN, D. 1997 Aspects of convection. PhD thesis, University of Cambridge.
- LIGHTHILL, M. 1978 *Waves in fluids*. Cambridge University Press.
- LIU, X. 1998 Scattering of internal waves at finite topography. PhD thesis, University of Hawaii.
- LONGUET-HIGGINS, M. 1969 On the reflexion of wave characteristics from rough surfaces. *J. Fluid Mech.* **37**, 231–250.
- LUECK, R. & MUDGE, T. 1997 Topographically induced mixing around a shallow seamount. *Science* **276**, 1831–1833.
- MAAS, L. 2005 Wave attractors: linear yet nonlinear. *Int. J. Bifur. Chaos* **15**, 2757–2782.

- MAAS, L., BENIELLI, D., SOMMERIA, J. & LAM, F.-P. 1997 Observation of an internal wave attractor in a confined stably stratified fluid. *Nature* **388**, 557–561.
- MAAS, L. & LAM, F.-P. 1995 Geometric focusing of internal gravity waves. *J. Fluid Mech.* **300**, 1–41.
- MACH, E. & VON WELTRUBSKY, J. 1878 Über die Formen der Funkenwellen. *Sitzungsber. Kaiserl. Akad. Wiss Wien, Math.-Naturwiss. Kl. Abt.* **78**, 551–560.
- MARAKOV, S., NEKYLYUDOV, V. & CHASHECHKIN, Y. 1990 Spatial structure of two-dimensional and monochromatic internal-wave beams in an exponentially stratified liquid. *Inz. Atmos. Oceanic. Phys.* **26**, 548–554.
- MCEWAN, A. 1973 Interactions between internal gravity waves and their traumatic effects on a continuous stratification. *Boundary-Layer Met.* **5**, 159–175.
- MCPHEE-SHAW, E. & KUNZE, E. 2002 Boundary layer intrusions from a sloping bottom: a mechanism for generating intermediate nepheloid layers. *J. Geophys. Res.* **107**, C6, 3050.
- MERCIER, M., GARNIER, N. & DAUXOIS, T. 2008 Reflection and diffraction of internal waves analysed with the hilbert transform. *Phys. Fluids* **20** (086601).
- MERTINS, A. 1999 *Signal analysis. Wavelets, filter banks, time-frequency transforms and applications*. John Wiley & Sons.
- MERZKIRCH, W. 1974 *Flow visualisation*. New York: Academic.
- MERZKIRCH, W. & PETERS, F. 1992 Optical visualisation of internal gravity waves in stratified fluid. *Optics and lasers in engineering* **16**, 411–425.
- MIED, R. & DUGAN, J. 1976 Internal wave reflexion from a sinusoidally corrugated surface. *J. Fluid Mech.* **76**, 259–272.
- MILES, J. 1961 On the stability of heterogeneous shear flows. *J. Fluid Mech.* **10**, 496–508.
- MIROPOL'SKY, Y. 2001 *Dynamics of internal gravity waves in the ocean*. Kluwer Academic Publishers.
- MIX, D. & OLEJNICZAK, K. 2003 *Elements of wavelets for engineers and scientists*. Wiley.
- MOWBRAY, D. & RARITY, S. 1967 A theoretical and experimental investigation of the phase configuration of internal waves of small amplitude in a density stratified liquid. *J. Fluid Mech.* **28**, 1–16.
- MUNK, W. 1966 Abyssal recipes. *Deep-Sea Res.* **13**, 707–730.

- MUNK, W. & WUNSCH, C. 1998 Abyssal recipes II: energetics of tidal and wind mixing. *Deep-Sea Res. I* **45**, 1977–2010.
- NASH, J., ALFORD, M. H., KUNZE, E., MARTINI, K. & KELLY, S. 2007 Hotspots of deep ocean mixing on the Oregon continental slope. *Geophys. Res. Lett.* **34** (L01605).
- NASH, J., KUNZE, E., POLZIN, K., TOOLE, J. & SCHMITT, R. 2004 Internal tide reflection and turbulent mixing on the continental slope. *J. Phys. Oceanogr.* **34**, 1117–1134.
- ONU, K., FLYNN, M. & SUTHERLAND, B. 2003 Schlieren measurement of axisymmetric internal wave amplitudes. *Exp. Fluids* **35**, 24–31.
- OSTER, G. 1965 Density gradients. *Sci. Am.* **213**, 70–76.
- PATORSKI, K. 1993 *Handbook of the Moirè Fringe technique*. Amsterdam: Elsevier.
- PEACOCK, T., ECHEVERRI, P. & BALMFORTH, N. 2008 An experimental investigation of internal tide generation by two-dimensional topography. *J. Phys. Ocean* **38**, 235–242.
- PEACOCK, T., STOCKER, R. & ARISTOFF, J. 2004 An experimental investigation of the angular dependence of diffusion-driven flow. *Phys. Fluids* **16**, 3503–3505.
- PEACOCK, T. & TABAEI, A. 2005 Visualization of nonlinear effects in reflecting internal wave beams. *Phys. Fluids* **17** (061702).
- PEDLOSKY, J. 2003 *Waves in the ocean and atmosphere*. Springer.
- PETERS, F. 1985 Schlieren interferometry applied to a gravity wave in a density-stratified fluid. *Exp. Fluids* **3**, 261–269.
- PHILLIPS, O. 1966 *The dynamics of the upper ocean*. Cambridge University Press.
- PHILLIPS, O. 1970 On flows induced by diffusion in a stably stratified fluid. *Deep-Sea Res.* **17**, 435–443.
- POLZIN, K., TOOLE, J., LEDWELL, J. & SCHMITT, R. 1997 Spatial variability of turbulent mixing in the abyssal ocean. *Science* **276**, 93–96.
- PRESS, W., TEUKOLSKY, S., VETTERLING, W. & FLANNERY, B. 1992 *Numerical recipes in fortran, second edition*. Cambridge University Press.
- RAFFEL, M., WILLERT, C. & KOMPENHANS, J. 1998 *Particle image velocimetry, a practical guide*. Berlin: Springer.
- RAYLEIGH, L. 1883 Investigation of the character of the equilibrium of an incompressible heavy fluid of variable density. *Proc. R. Soc. Lond.* **XIV**, 170–177.

- RIENITZ, J. 1975 Schlieren experiments 300 years ago. *Nature* **254**, 293–295.
- RIENITZ, J. 1997 Optical inhomogeneities: schlieren and shadowgraph methods in the seventeenth and eighteenth centuries. *Endeavour* **21**, 77–81.
- RILEY, N. 2001 Steady streaming. *Annu. Rev. Fluid Mech.* **33**, 43–65.
- ROBERTS, J. 1975 *Internal gravity waves in the ocean*. Marcel Dekker.
- ROBINSON, R. 1969 The effects of a vertical barrier on internal waves. *Deep-Sea Res.* **16**, 421–429.
- ROBINSON, R. 1970 The effects of a corner on a propagating internal gravity wave. *J. Fluid Mech.* **42**, 257–267.
- RUBENSTEIN, D. 1988 Scattering of inertial waves by rough bathymetry. *J. Phys. Oceanogr.* **18**, 5–18.
- RUDNICK, D., BOYD, T., BRAINARD, R., CARTER, G., EGBERT, G., GREGG, M., HOLLOWAY, P., KLYMAK, J., KUNZE, E., LEE, C., LEVINE, M., LUTHER, D., MARTIN, J., MERRIFIELD, M., MOUM, J., NASH, J., PINKEL, R., RAINVILLE, L. & SANFORD, T. 2003 From tides to mixing along the Hawaiian Ridge. *Science* **301**, 355–357.
- SAKAI, S. 1990 Visualisation of internal gravity waves by Moiré method. *Kashika-Joho* **10**, 65–68.
- SANDSTROM, H. 1966 The importance of topography in generation and propagation of internal waves. PhD thesis, University of California.
- SANDSTROM, H. 1969 Effect of topography on propagation of waves in stratified fluids. *Deep-Sea Res.* **16**, 405–410.
- SANDSTROM, H. 1972 The effect of curvature on the reflection of internal waves. In *Proc. 4th Liège Colloq. on Ocean Hydrodynamics* (ed. J. Nihoul), pp. 183–190.
- SANDSTRÖM, J. 1908 Dynamische versuche mit meerwasser. *Ann. Hydrogr. Martimen Meteorol.* **36**, 6–23.
- SAVAŞ, O. 1985 On flow visualisation using reflective flakes. *J. Fluid Mech.* **152**, 235–248.
- SCASE, M. 2003 Vortex rings in a stratified fluid. PhD thesis, University of Cambridge.
- SCASE, M. & DALZIEL, S. 2006 Internal wave fields generated by a translating body in a stratified fluid: an experimental comparison. *J. Fluid Mech.* **564**, 305–331.
- SETTLES, G. 2001 *Schlieren and shadowgraph techniques*. Berlin: Springer-Verlag.
- SLINN, D. & RILEY, J. 1998 Turbulent dynamics of a critically reflecting internal gravity wave. *Theor. Comput. Fluid Dyn.* **11**, 281–303.

- SNEDDON, I. 1995 *Fourier transforms*. Dover.
- SOMMERFELD, A. 1949 *Partial Differential Equations in Physics*. New York: Academic Press.
- SRDIĆ-MITROVIĆ, A., MOHAMED, N. & FERNANDO, J. 1999 Gravitational settling of particles through density interfaces. *J. Fluid Mech.* **381**, 175–198.
- ST. LAURENT, L. & GARRETT, C. 2002 The role of internal tides in mixing the deep ocean. *J. Phys. Oceanogr.* **32**, 2882–2899.
- ST. LAURENT, L., STRINGER, S., GARRETT, C. & PERRAULT-JONCAS, D. 2003 The generation of internal tides at abrupt topography. *Deep-Sea Res. I* **50**, 987–1003.
- STAPLEHURST, P., DAVIDSON, P. & DALZIEL, S. 2008 Structure formation in homogeneous freely-decaying, rotating turbulence. *J. Fluid Mech.* **598**, 81–105.
- STAQUET, C. & SOMMERIA, J. 2002 Internal gravity waves: From instabilities to turbulence. *Ann. Rev. Fluid Mech.* **34**, 559–593.
- STEVENSON, T. 1969 Axisymmetric internal waves generated by a travelling oscillating body. *J. Fluid Mech.* **35**, 219–224.
- SUTHERLAND, B. 2002 Large-amplitude internal wave generation in lee of step-shaped topography. *Geophys. Res. Lett.* **29** (1769), 1–4.
- SUTHERLAND, B. & AGUILAR, D. 2006 Stratified flow over topography: Wave generation and boundary layer separation. *Advances in Fluid Mechanics VI, WIT press* pp. 317–326.
- SUTHERLAND, B., DALZIEL, S., HUGHES, G. & LINDEN, P. 1998 Laboratory observations of internal waves. In *Proc. 13th Aust. Fluid Mech. Conf.*, pp. 855–858. Melbourne.
- SUTHERLAND, B., DALZIEL, S., HUGHES, G. & LINDEN, P. 1999 Visualization and measurement of internal waves by ‘synthetic schlieren’. Part 1: Vertically oscillating cylinder. *J. Fluid Mech.* **390**, 93–126.
- SUTHERLAND, B., HUGHES, G., DALZIEL, S. & LINDEN, P. 2000 Internal waves revisited. *Dyn. Atmos. Oceans* **31**, 209–232.
- SUTHERLAND, B. & LINDEN, P. 1998 Internal wave excitation from stratified flow over a thin barrier. *J. Fluid Mech.* **377**, 223–252.
- SUTHERLAND, B. & LINDEN, P. 2002 Internal wave excitation by a vertically oscillating elliptical cylinder. *Phys. Fluids* **14**, 721–731.
- SVEEN, J. & DALZIEL, S. 2005 A dynamic masking technique for combined measurements of PIV and synthetic schlieren applied to internal gravity waves. *Meas. Sci. Technol.* **16**, 1954–1960.

- TABAEI, A. & AKYLAS, T. 2003 Nonlinear internal gravity wave beams. *J. Fluid Mech.* **482**, 141–161.
- TABAEI, A., AKYLAS, T. & LAMB, K. 2005 Nonlinear effects in reflecting and colliding internal wave beams. *J. Fluid Mech.* **526**, 217–243.
- TANNER, L. 1956 The optics of the Mach-Zehnder interferometer. In *Aero. Res. Council. R & M 3069*. London.
- TANNER, L. 1957 The design and use of interferometers in aerodynamics. In *Aero. Res. Council. R & M 3131*. London.
- TEOH, S., IVEY, G. & IMBERGER, J. 1997 Laboratory study of the interaction between two internal wave rays. *J. Fluid Mech.* **336**, 91–122.
- THOMAS, N. & STEVENSON, T. 1972 A similarity solution for viscous internal waves. *J. Fluid Mech.* **54**, 495–506.
- THORPE, S. 1987 On the reflection of a train of finite-amplitude internal waves from a uniform slope. *J. Fluid Mech.* **178**, 279–302.
- THORPE, S. 1992 Thermal fronts caused by internal gravity waves reflecting from a slope. *J. Phys. Oceanogr.* **22** (105108).
- THORPE, S. 1994 Statically unstable layers produced by overturning internal gravity waves. *J. Fluid Mech.* **260**, 333–350.
- THORPE, S. 1999 $75+25=99+1$, or some of what we still don't know: wave groups and boundary processes. In *Proc. Hawaiian Winter Workshop*, pp. 129–135.
- THORPE, S. 2001 Internal wave reflection and scatter from sloping rough topography. *J. Phys. Oceanogr.* **31**, 537–553.
- THORPE, S. & HAINES, P. 1987 On the reflection of a train of finite amplitude internal waves from a uniform slope. *J. Fluid Mech.* **178**, 279–302.
- TOEPLER, A. 1864 *Beobachtungen nach einer neuen optischen Methode*. Max Cohen u. Sohn, Bonn.
- TOOLE, J., SCHMITT, R., POLZIN, K. & KUNZE, E. 1997 Near-boundary mixing above the flanks of a midlatitude seamount. *J. Geophys. Res.* **102**, 947–959.
- TURNER, J. 1979 *Buoyancy effects in fluids*. Cambridge University Press.
- VENAYAGAMOORTHY, S. & FRINGER, O. 2005 Nonhydrostatic and nonlinear contributions to the energy flux budget in nonlinear internal waves. *Geophys. Res. Lett.* **32** (L15603).

- VENAYAGAMOORTHY, S. & FRINGER, O. 2006 Numerical simulations of the interaction of internal waves with a shelf break. *Phys. Fluids* **18** (076603).
- VENAYAGAMOORTHY, S. & FRINGER, O. 2007 On the formation and propagation of nonlinear internal boluses across a shelf break. *J. Fluid Mech.* **577**, 137–159.
- VOISIN, B. 1991 Internal wave generation in uniformly stratified fluids. Part 1. Green’s function and point sources. *J. Fluid Mech.* **231**, 439–480.
- WALKER, J. 1999 *A primer on wavelets and their scientific application*. Chapman & Hall/ CRC.
- WEAST, R. 1981 *Handbook of chemistry and physics*. C.R.C. Press.
- WELLER, R. & SHEPARD, B. 1948 Displacement measurement by mechanical interferometry. *Proc. Soc. Exp. Stress Anal.* **6**, 35–38.
- WEYL, F. 1954 Analysis of optical methods. In *Physical measurements in gas dynamics and combustion* (ed. R. Ladenburg), pp. 3–25. Princeton University Press.
- WHITHAM, G. 1974 *Linear and nonlinear waves*. Wiley-Interscience.
- WUNSCH, C. 1969 Progressive internal waves on slopes. *J. Fluid Mech.* **35**, 131–144.
- WUNSCH, C. 1970 On oceanic boundary mixing. *Deep-Sea Res.* **17**, 293–301.
- WUNSCH, C. 1975 Internal tides in the ocean. *Rev. Geophys.* **13**, 167–182.
- WUNSCH, C. 1985 Can a tracer field be inverted for velocity? *J. Phys. Oceanogr.* **15**, 1521–1531.
- WUNSCH, C. & FERRARI, R. 2004 Vertical mixing, energy, and the general circulation of the oceans. *Ann. Rev. Fluid Mech.* **36**, 281–314.
- YICK, K.-Y., STOCKER, R. & PEACOCK, T. 2007 Microscale synthetic schlieren. *Exp. Fluids* **42**, 41–48.
- ZHANG, H., KING, B. & SWINNEY, H. 2007 Experimental study of internal gravity waves generated by supercritical topography. *Phys. Fluids* **19** (096602).
- ZIENKIEWICZ, H. 1959 Wave theory of the Mach-Zehnder interferometer. In *Aero. Res. Council. R & M 3173*. London.